ATOMIC AND PLASMA–MATERIAL INTERACTION DATA FOR FUSION

VOLUME 5

The following States are Members of the International Atomic Energy Agency:

AFGHANISTAN	ICELAND	PERU
ALBANIA	INDIA	PHILIPPINES
ALGERIA	INDONESIA	POLAND
ARGENTINA	IRAN, ISLAMIC REPUBLIC OF	PORTUGAL
ARMENIA	IRAQ	QATAR
AUSTRALIA	IRELAND	ROMANIA
AUSTRIA	ISRAEL	RUSSIAN FEDERATION
BANGLADESH	ITALY	SAUDI ARABIA
BELARUS	JAMAICA	SENEGAL
BELGIUM	JAPAN	SIERRA LEONE
BOLIVIA	JORDAN	SINGAPORE
BRAZIL	KAZAKHSTAN	SLOVAKIA
BULGARIA	KENYA	SLOVENIA
CAMBODIA	KOREA, REPUBLIC OF	SOUTH AFRICA
CAMEROON	KUWAIT	SPAIN
CANADA	LEBANON	SRI LANKA
CHILE	LIBERIA	SUDAN
CHINA	LIBYAN ARAB JAMAHIRIYA	SWEDEN
COLOMBIA	LIECHTENSTEIN	SWITZERLAND
COSTA RICA	LITHUANIA	SYRIAN ARAB REPUBLIC
COTE D'IVOIRE	LUXEMBOURG	THAILAND
CROATIA	MADAGASCAR	THE FORMER YUGOSLAV
CUBA	MALAYSIA	REPUBLIC OF MACEDONIA
CYPRUS	MALI	TUNISIA
CZECH REPUBLIC	MARSHALL ISLANDS	TURKEY
DENMARK	MAURITIUS	UGANDA
DOMINICAN REPUBLIC	MEXICO	UKRAINE
ECUADOR	MONACO	UNITED ARAB EMIRATES
EGYPT	MONGOLIA	UNITED KINGDOM OF GREAT
EL SALVADOR	MOROCCO	BRITAIN AND NORTHERN
ESTONIA	MYANMAR	IRELAND
ETHIOPIA	NAMIBIA	UNITED REPUBLIC OF TANZANIA
FINLAND	NETHERLANDS	UNITED STATES OF AMERICA
FRANCE	NEW ZEALAND	URUGUAY
GABON	NICARAGUA	UZBEKISTAN
GERMANY	NIGER	VENEZUELA
GHANA	NIGERIA	VIET NAM
GREECE	NORWAY	YEMEN
GUATEMALA	PAKISTAN	YUGOSLAVIA
HAITI	PANAMA	ZAIRE
HOLY SEE	PARAGUAY	ZAMBIA
HUNGARY		ZIMBABWE

The Agency's Statute was approved on 23 October 1956 by the Conference on the Statute of the IAEA
held at United Nations Headquarters, New York;
it entered into force on 29 July 1957. The Headquarters of the Agency are situated in Vienna. Its principal objective is
"to accelerate and enlarge the contribution of atomic energy to peace, health and prosperity throughout the world".

ATOMIC AND PLASMA–MATERIAL INTERACTION DATA FOR FUSION

(Supplement to the journal Nuclear Fusion)

VOLUME 5

The volumes of ATOMIC AND PLASMA–MATERIAL INTERACTION DATA FOR FUSION are published by the International Atomic Energy Agency as supplements of the journal NUCLEAR FUSION.

For these supplements, papers, letters and reviews are accepted which deal with the following topics:

— Elementary collision processes in fusion plasmas involving photons, electrons, ions, atoms and molecules;
— Collision processes of plasma particles with surfaces of fusion relevant materials;
— Plasma–material interaction phenomena, including the thermophysical response of materials.

Each submitted contribution should contain fusion relevant data and information in either of the above areas. Original contributions should provide new data, using well established methods. Review articles should give a critical analysis or evaluation of a wider range of data. They are normally prepared on the invitation of the Scientific Editor or on prior mutual consent. Each submitted contribution is assessed by two independent referees.

Every manuscript submitted must be accompanied by a *disclaimer* stating that the paper has not been published and is not being considered for publication elsewhere. If no copyright is claimed by the authors, the IAEA automatically owns the copyright of the paper.

Guidelines for the preparation of manuscripts are given on the inside back cover. Manuscripts and correspondence should be addressed to: The Editor, NUCLEAR FUSION, International Atomic Energy Agency, Wagramerstrasse 5, P.O. Box 100, A-1400 Vienna, Austria.

EDITORIAL NOTE

The present volume of Atomic and Plasma–Material Interaction Data for Fusion is devoted to a critical review of the physical and thermo-mechanical properties of presently considered candidate plasma-facing and structural materials for next-generation thermonuclear fusion reactors. The material issue in the engineering design of fusion reactors is currently seen as one of the most complex ones, having a strong impact on the basic operational and engineering reactor parameters. The preparation of this volume was guided by the idea of providing the fusion reactor designers with a source of critically assessed material properties data, including information on the material response to high heat and particle fluxes and on the thermo-hydrodynamic coupling with coolants. Emphasis was given not on comprehensiveness, but rather on presentation of the most recent results for the materials considered as prime option for plasma-facing reactor materials.

The IAEA is indebted to the contributors to this volume for their dedicated effort and co-operativeness, and to Drs. W.B. Gauster and V.R. Barabash for their advice in formulating the scope of the compendium.

Vienna, December 1994

CONTENTS

REQUIREMENTS AND SELECTION CRITERIA FOR PLASMA-FACING MATERIALS AND COMPONENTS IN THE ITER EDA DESIGN

W. B. GAUSTER, W. R. SPEARS AND THE ITER JOINT CENTRAL TEAM
ITER Garching Joint Work Site
Max-Planck-Institut für Plasmaphysik
Boltzmannstraße 2
D-85748 Garching bei München, Germany

ABSTRACT. The goal of the International Thermonuclear Experimental Reactor (ITER) is to demonstrate the scientific and technological feasibility of fusion energy for peaceful purposes. The Engineering Design Activities (EDA) are developing the design of this next step experiment in controlled fusion energy research. Severe demands are placed on performance of materials, especially of those in contact with the plasma. The present status of the design is summarised, with emphasis on the vacuum vessel and the in-vessel components. The requirements to be met by plasma-facing materials and components are highlighted, and the research and development needs are described.

1. INTRODUCTION

The design of the International Thermonuclear Experimental Reactor (ITER) places unprecedented demands on materials performance in several areas if the projected performance goals are to be met [1]. Important topics include structural and electrical properties of superconducting magnet windings and the mechanical support elements of the magnet systems, structural and electrical properties of the vacuum vessel and blanket assemblies, and a wide range of requirements for the materials which come in contact with the plasma. The latter category is particularly extensive: it includes properties which influence plasma behaviour as well as those which relate to the functionality and lifetime of the material and the associated components.

In all cases, availability of the materials, their fabricability, the construction, maintenance, and replacement processes, as well as costs, also play important roles. In addition, ITER is the first fusion machine in which the degradation of properties due to neutron damage is a prime concern.

The first two years of the project's Engineering Design Activities (EDA) have resulted in an outline design [2,3,4]. Two operating phases for the machine are being considered. In the first, a Basic Performance Phase (BPP), breeding would not be needed. The function of the blanket is then to extract the fusion power that is produced and, together with the vacuum vessel, to shield the superconducting magnets. However, elementary breeding blanket modules would be tested functionally during this phase, in which the experience of a few thousand hours of plasma operation would be gained. In an Extended Performance Phase (EPP), tritium would be bred throughout the blanket. To be better able to test blankets for future devices in this later phase, attainment of an average first wall neutron fluence of up to 3 MWa/m^2 should not be precluded by the performance of any permanent machine component.

In this overview, the present design of the ITER machine is summarised, with emphasis on the vacuum vessel and the in-vessel components [4,5]. Materials needs are listed, especially for the elements facing the plasma. Finally, an outline is given of the associated research and development priorities.

2. SUMMARY OF THE DESIGN

The design of ITER is intended to be conservative in the sense that a high likelihood exists of achieving the intended operating parameters on the basis of extrapolations from results obtained on existing tokamaks. A modest margin is incorporated to sustain ignition while allowing for uncertainties in physics and operation. To achieve safety and economic objectives, emphasis is on minimising complexity in design and maintenance, on achieving a low tritium inventory where feasible, and on optimising performance for a given cost.

The design concept presently has the following characteristics:

- 24 toroidal and 7 poloidal (including the central solenoid) field coils of Nb_3Sn superconductor, using "cable in conduit" technology;
- toroidal field (TF) coils covered by outer structural bands and linked to a central bucking cylinder inside the central solenoid (CS), with the TF coils bucked against the CS; overturning moments on the TF coils are resisted by shear keys and outer mechanical supports, linking the separate TF coils into a complete toroidal structure; the TF coils generate a magnetic field of 5.7 T at the plasma major radius of 8.10 m, corresponding to 13 T at the Nb_3Sn conductor.
- a plasma configuration characterised by a moderately elongated cross-section and a single-null poloidal divertor: stability of the plasma is provided by the relatively low total resistance (5-$10\mu\Omega$) of the vacuum vessel and blanket structure, and by feedback control of the six outer poloidal field coils;
- inductive drive, with provision for moderate heating and (as a by-product) the capability for current drive by ion cyclotron, electron cyclotron, and/or neutral beam injection: the design foresees 50 MW of auxiliary heating, upgradable to 100 MW (by adding external equipment only).
- a divertor design based on physics concepts which allow thermal energy to be distributed over a relatively large area of the divertor channel's walls;
- for the BPP, a water-cooled shield: the first wall is integrated with the shield structure, although the two have separate cooling loops;
- a double-walled, fully welded vacuum vessel which acts as the first confinement barrier for purposes of safety; the vessel must be able to withstand the electrodynamic loads caused by disruptions, which cause transfer of forces both directly to the vessel and via the internal shield or blanket structures;
- a performance objective of about 1 MW/m² of neutron wall loading met at a nominal fusion power of 1.5 GW: due to the margin available to permit ignition in most cases, the possibility of temporary over- (or under-) power of 20% has also to be designed for.

The main design parameters are shown in Table 1. A cross-section of the device is shown in Figure 1.

| Table 1:	ITER EDA Machine Parameters		
Plasma density (averaged)	10^{20}	m^{-3}	
Ion temperature (averaged)	13	keV	
Fusion power (nominal)	1.5 ± 0.3		GW
Burn time	1000	s	
Major radius	8.1	m	
Minor radius	3.0	m	
Elongation	1.6		
Toroidal magnetic field at 8.1 m	5.7	Tesla	
Plasma current	24	MA	
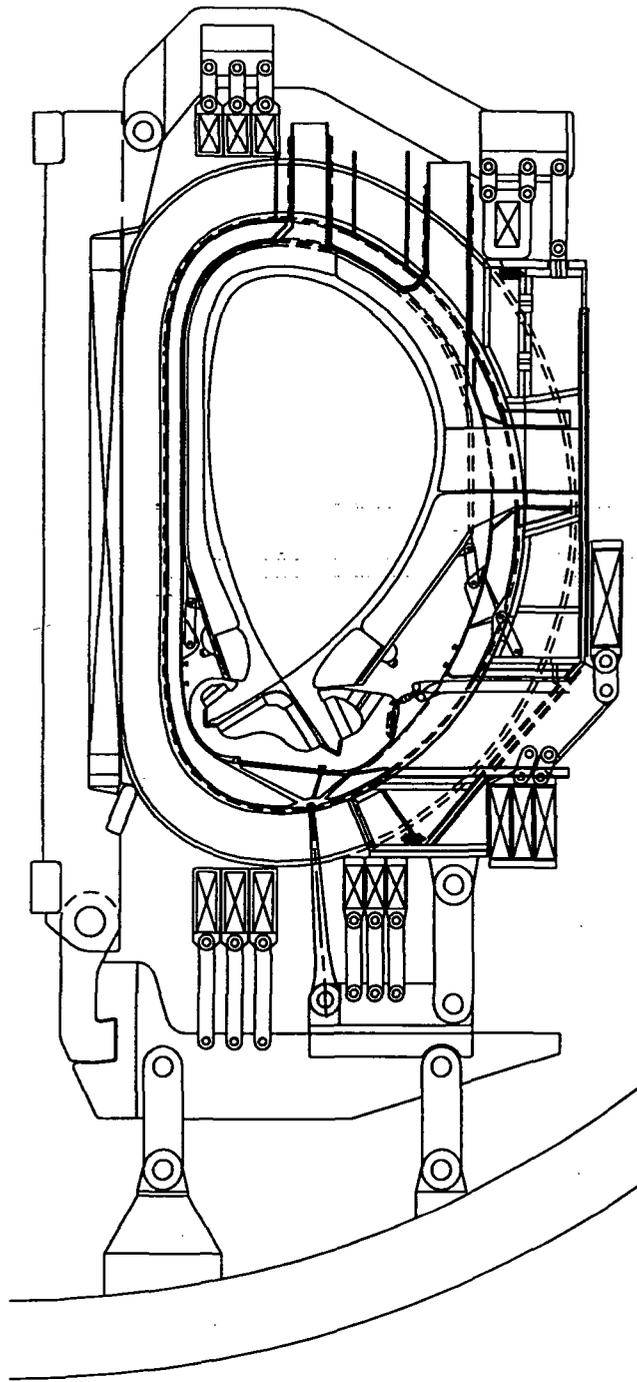
Figure 1.   Cross section of the ITER machine.

3. VACUUM VESSEL

3.1. Vessel Specifications

The vacuum vessel provides a high vacuum environment for the plasma. At the same time, it is a safety barrier, and needs to assure adequate confinement for plausible accidents. It is designed to support the electromagnetic loads which result from disruptions, vertical displacement events (VDE), and halo currents. These loads can act directly on the vessel and also indirectly by transfer of forces from the first wall and blanket structure.

Together with the blanket and shield, the vessel provides for shielding of neutrons, so that acceptable values of fluences to the insulators in the magnet system and of power dissipated in the conducting materials of the magnets are obtained. The electrical resistance of the vessel must be high enough to limit current flow in the vessel and low enough to aid vertical stability control. The maximum outlet temperature of the coolant is limited to 200°C, but higher temperatures are required for bakeout or during loss-of-coolant events. Detailed specifications are found in references [6] and [7].

3.2. Vacuum Vessel Design

The vessel is a double-walled structure, with shells that are made of welded plates, 30-40 mm thick, and joined by poloidal stiffening ribs [Figure 2] to provide the required strength. The total thickness of the vessel varies poloidally from 0.4 to 0.7 m, with an overall height of the toroidal shells of about 15 m. Coolant water flows between the shells at temperatures below 200°C at a maximum pressure of 2 MPa. The vessel can be baked at 300°C using gas or steam.

To provide neutron shielding, the space between the shells, i.e. the region of coolant water flow, is filled with electrically insulated steel balls. This approach was selected for its apparent simplicity and low cost relative to the alternative of a structure of steel plate inserts.

The vessel structure consists of 24 sectors, which are joined toroidally by field welding. The sector field joints need to accommodate the mismatch between adjacent vessel sectors. Research and development is needed on methods for field welding and non-destructive inspection, using remote handling techniques.

Ports are provided on top of the vessel, at the mid plane, and at the bottom. The upper ports provide blanket access and cooling. The mid-plane ports are used to access blanket test modules and blanket/shield modules that are integrated with ion (ICRF) and/or electron (ECRF) cyclotron heating and or diagnostic systems, and for the insertion of remote handling equipment. The lower horizontal ports are for replacement of divertor cassettes and for vacuum pumping.

3.3. Development Needs and Materials Choices

The vessel for ITER is considerably larger than vacuum vessels of similar design fabricated up to now. For that reason, methods of fabrication need to be established, and non-destructive, thermomechanical and dynamic testing need to be carried out on the basis of models and mock-ups. A critical development item is the region of the upper ports, which are used as feedthroughs for blanket coolant lines and as openings for the installation and replacement of blanket segments. A key issue is the feasibility of cutting and welding the port structure during maintenance of blanket or the vessel, using remote handling techniques, while maintaining the low tolerances and distortions required. Bellows are used around the blanket coolant feedthroughs to compensate for differences in thermal expansion between the blanket and the vacuum vessel, and to provide stress relief during off-normal events. For the insulated steel balls, coating methods and their QA, as well as the handling techniques for filling, also need to be investigated thoroughly.
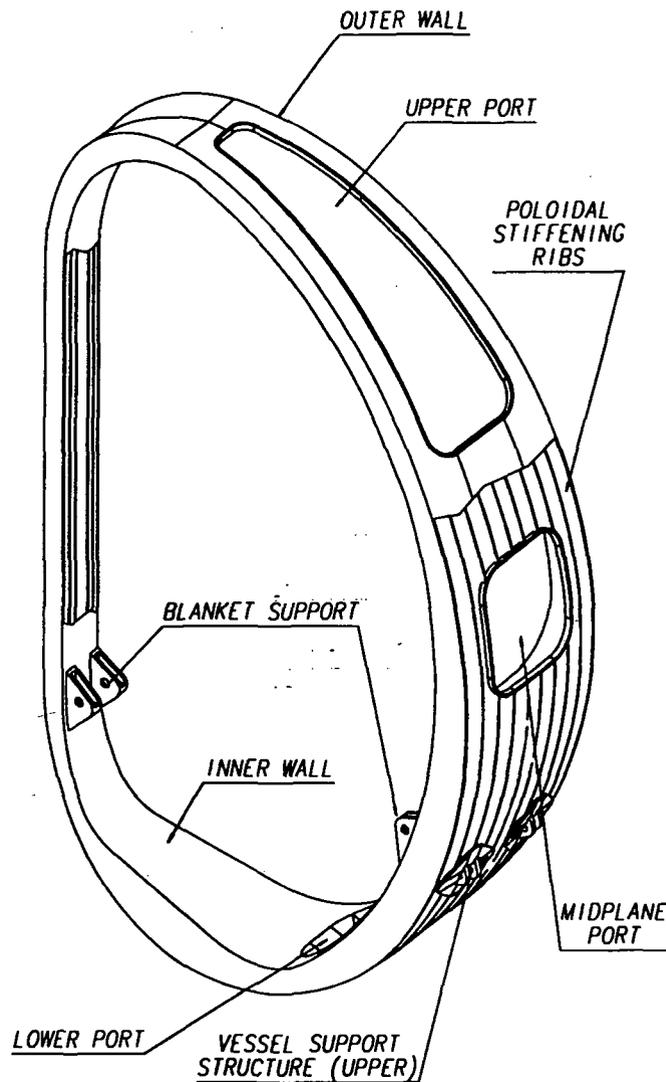
Figure 2. Vacuum vessel section view.

The selection of materials for the vacuum vessel is based on structural and electrical properties both before and after irradiation; fabricability and cost are of course also important factors. The prime candidate material for the vacuum vessel is at present Inconel 625, because of its high electrical resistivity and high yield strength even at elevated temperatures. However, under the expected radiation levels, the rate of production of helium is about twice that for stainless steel. Since reweldability is strongly affected by helium production, testing of reweldability after irradiation is needed. In addition, the induced activity with long decay times is higher for Inconel after irradiation, due to the significant concentrations of niobium and tantalum. To reduce this effect, the tantalum could be eliminated while still maintaining the required standard composition of, for example, Inconel 625. Due to these concerns, type 316 stainless steel is also under consideration. The most important advantages of steel are the larger database on its properties and its simpler fabrication technology. Cost is also expected to favour steel.

4. FIRST WALL, BLANKET, AND SHIELD

4.1. Design Requirements

The first wall and shielding blanket structure together has several functions. During the BPP, the first is to remove the surface heat flux impinging on the wall and the nuclear heating within its own structure while maintaining allowable temperatures and stresses. Next, it must reduce the nuclear responses in the vacuum vessel to levels such that rewelding during maintenance and repair is still possible. Practically, this means that helium production must be less than 1 appm and the atomic displacements less than 1 dpa until the end of the EPP. Third, together with the vacuum vessel, it protects the toroidal field coils from excessive nuclear heating and radiation damage. In the EPP, the additional function of tritium breeding is required. Options for tritium breeding have been summarised recently [8]; they are not discussed further here.

For 1.5±0.3 GW of fusion power in the ITER machine, the first wall encounters an average surface heat flux of 0.2 MW/m². For design specifications, a peak value of 0.5 MW/m² is assumed. The main design parameters for the first wall and shielding blanket are listed in Table 2. These design specifications also apply to plasma facing elements of the heating systems, which therefore have to be

Table 2:   Main Design Parameters of First Wall and Blanket/Shield

Nominal fusion Power	1500 MW
Average first wall neutron fluence	
- Basic performance phase	~0.3 MWa/m²
- Extended performance phase	≤3.0 MWa/m²
Peak first wall neutron wall loading	1.2 MW/m²
Average first wall heat load	0.2 MW/m²
Peak first wall heat load	0.5 MW/m²
First wall surface structure temperature	
- Baking	350°C
- Between Pulses	200°C
Total number of cycles	10^5
Pulse length	1000 s
Water coolant conditions (FW)	
- Inlet temperature	100°C
- Outlet temperature	150°C
- Inlet pressure	2 MPa
Structural material	316 SS
Heat sink material	copper alloy
First wall protection material	Be (≤ 10 mm)
	C (≤ 30 mm)
	W (≤ 3 mm)
First wall pressure load from disruption event	
- Inboard	1.5 MPa
- Outboard	1.0 MPa
First wall design approaches	
- Separately cooled first wall	
- Structurally integrated with blanket and shield	
Breeding Capability	Not required in BPP. Convertible or replaceable for EPP.

designed so as to be indistinguishable from the first wall. Limiters, integrated with the blanket, are also required. These will have performance requirements closer to those of the divertor baffle (described in the next section).

4.2. Modular Shielding Blanket

Recently a modular blanket design with a separately cooled first wall has been developed which serves as the basis for design analyses and for the development of maintenance and replacement scenarios [4,5]. Each toroidal blanket sector consists of a number of poloidal modules having on the order of 1 to 2 m² plasma-facing area. The modules are supported from the back plate. The sectors can in principle be connected electrically in the toroidal direction to minimise the electromagnetic loads during plasma disruptions, and several such schemes are under investigation. The individual modules and their attachments to the back plate, however, are intended to withstand the electromagnetic shear loads even without electrical connections at the first wall. The installation and replacement of the blanket sectors (through the upper port) or modules (through the mid-plane port) does not require cutting and rewelding the back plate. The mid-plane cross-section of an inboard shielding blanket module is shown in Figure 3. Also shown is the back plate, which is installed in the vacuum vessel before the blanket sectors are attached to it by welding.


3 mm Be Coating   Support Rib

FW-Coolant
Inlet Manifold

FW-Coolant
Outlet Manifold

Shielding Coolant
Inlet Manifold

Shielding Coolant
Outlet Manifold
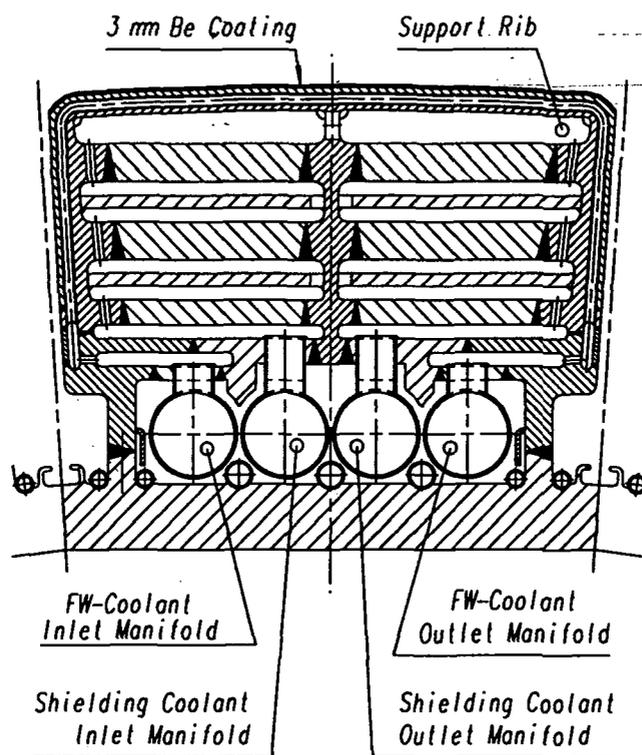
Figure 3.   Modular blanket design.

4.3. Fabrication, Development Needs and Material Choices

To fabricate the laminar structure of the first wall, hot isostatic pressing (HIP), diffusion bonding, explosive bonding, or a combination of the first two methods are being assessed. Attachment of the first wall to the blanket modules is by welding. As an alternative approach, tests are planned on HIP of powder to produce the blanket module and first wall in one step. This would eliminate welds from

the high radiation zone of the first wall and would simplify the process in terms of the numbers of parts and of processing steps.

To provide improved thermal response, a laminate of copper alloy and austenitic steel constitutes the first wall, with a layer of beryllium faces the plasma. The first wall is seen in the Figure to be structurally integrated with the blanket modules, but it is separately cooled. Under consideration are square or circular steel coolant channels with single or multiple coolant paths. While both designs provide adequate cooling, higher primary stresses and stress concentrations are found for the square channels. The square channels, however, can be joined directly to the steel blanket box. This leads to a more reliable joint than for circular tubes that are joined along only a portion of their perimeter. The final choice will be based on fabrication test results and on performance of the copper alloy.

For the main components of the blanket and the first wall structure, type 316LN stainless steel is currently proposed. The principal considerations for the choice are the extensive data base on unirradiated and irradiated material, good fabricability and experience in the material's use for non-nuclear and fission reactor applications, an acceptable temperature range from 20 to 450°C (and up to 600°C without irradiation), and good compatibility with coolant water in the range 20 - 150°C. As a second option type 316L is considered. For these materials the impact of low-temperature embrittlement, swelling, radiation-enhanced stress corrosion cracking, and weld characteristics, are being assessed.

R&D also includes the verification of neutronics code predictions by means of shielding experiments both on bulk materials and on penetrations.

5. DIVERTOR

The design of the divertor for ITER is based on the formation of a cold, dense plasma in the divertor chamber, and the consequent radiation of power over a large area [9,10]. This concept provides a plausible solution, evidence of which has been seen in operating tokamaks, to an extremely challenging problem. For a fusion power of 1.5 GW in ITER, 300 MW are carried by alpha-particles. Due to uncertainties in the distribution of power, the design calls for both the divertor and the first wall to be able to handle 80 % of the power. For a conventional target in the divertor, power loading peaks of 140 MW/m^2 would be expected, which could be reduced to 35 MW/m^2 by tilting the plates. In addition to the steady-state power, there are transient power excursions, edge localized modes, and disruptions. The concept proposed for ITER [11] reduces the nominal power value to sustainable peak-design levels of the order of 5 MW/m^2 as well as moderating particle fluxes in order to lower erosion rates.

5.1. Divertor Concept

In the "dynamic gas target" divertor, radiation from hydrogen and from impurities results in a transfer of energy from the plasma in the divertor to the walls of the chamber. Charge exchange collisions with neutrals that recycle in the divertor channel reduce ion momentum. This causes a reduction of the pressure in front of the target plates and a lowering of the ion flux to the plates; temperatures of about 5 eV and ion and neutral densities of 3×10^{19} to 10^{20} m^{-3} are predicted. The resulting power load is 2.5 MW/m^2 on the targets. The radiation to the side walls of the divertor channel gives an average load of 0.6 MW/m^2 over a 400 m^2 area.

5.2. Divertor Design

The concept is implemented in a divertor consisting of three main regions, all designed for heat loads up to 5 MW/m^2 to take account of uneven power distribution. These are the divertor targets, the power exhaust and recycling area in the divertor channels (the side walls), and a baffle area in the

lower first wall and divertor entrance region that reduces the flow of neutral particles into the main chamber. The prime candidate plasma-facing material is beryllium, but carbon fibre composites and tungsten are also being considered, and may be used instead of Be, or just in certain areas. A schematic view of the divertor assembly is shown in Figure 4 [10,11]. The side walls of the channels are "transparent", consisting of plates or vanes inclined toward the field lines and supported at the bottom by the cassette structure. This is the power exhaust region. The divertor targets, or energy dump targets, are at the bottom of the divertor throat. The central dome and toroidal limiters form the baffle area.


ITER DIVERTOR ASSEMBLY
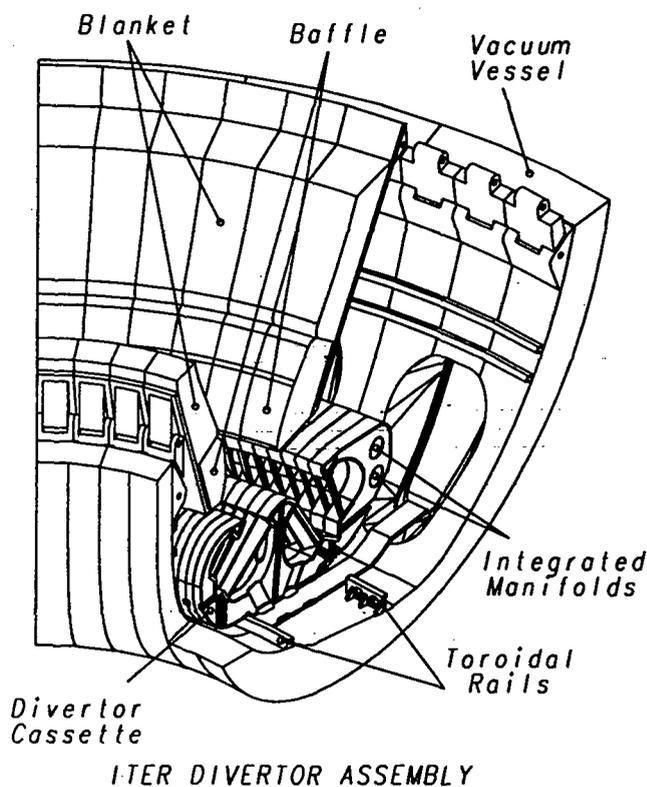
Figure 4.   Schematic view of divertor assembly.

Each of the 24-toroidal sectors contains 4 cassettes, for a total of 96 in the machine. Details of the present design are given in reference [12]. The divertor cassettes are stainless steel structures. Plasma-facing areas are covered by copper alloy panels with beryllium coatings. The cassettes are designed to resist impulsive loads due to eddy currents and halo currents during disruptions. In addition, they provide neutron shielding in the lower regions where there are no blanket modules. For this reason, 60% of the body is steel; the remainder is water at 2 MPa which cools the cassette structure itself and provides coolant for the high-heat-flux regions of the dump targets, dome, wings and the inboard divertor baffle.

The dome and the baffles shield the components in the power exhaust and momentum loss regions of the divertor. Leading edges of the latter would otherwise be exposed to the scrape-off layer plasma, which has a parallel power flux of >100 MWm^{-2}. The protection is also important during transient events such as plasma start-up and during disruptions. Thus these elements (along with any first wall/blanket limiters) are considered as the key high-heat-flux components.

15

The power exhaust and momentum loss region is essentially a large gas box, designed to optimise the recirculation of neutrals along the whole divertor channel. This may require a "transparent wall", which provides for thermalization of hot neutrals by collision with the structure, but also allows neutrals to pass through and participate in the recirculation. The wing-like structures, which are tilted at 45 degrees toroidally toward the magnetic field lines, must be designed to accept most of the ~ 200 MW power radiated in the divertor region as well as the momentum flux.

The energy dump targets receive the remainder of the power conducted into the divertor channels, that is not transferred to the side walls. This is estimated to be 10% of the total in steady state, resulting in a peak heat flux of 2.5 MW/m²; the design value is taken to be 5 MW/m². There is concern about disruptions or edge localized modes resulting in power excursions to the targets by burning through the gas target.

The divertor baffle is attached and may eventually be an integral part of the blanket segments. By restricting the flow of neutrals it reduces the leakage of high-density gas from the divertor chamber to the main plasma region. It is a steel structure of 2 m height, and also includes a copper alloy heat sink with a plasma-facing coating of beryllium.

5.3. Fabrication, Development Needs and Materials Choices

For all divertor components the structural and neutron-shielding material is presently considered to be stainless steel (type 316L or equivalent). The coolant, which is also part of the shielding, is water at a pressure of about 2 MPa and a maximum temperature of 200°C. The heat sink is copper alloy. The plasma-facing material will be chosen from beryllium, carbon fibre composite, and high-Z materials . The modular structure of the cassettes allows design modifications, including changes in plasma-facing materials, without re-designing the cassettes.

Several manufacturing technologies are under consideration. These include diffusion bonding and HIP between copper alloys and beryllium, with brazing as an alternate. For coating of surfaces and repair of damaged surfaces, plasma spraying of beryllium is being evaluated. Diffusion bonding, HIP, and explosive welding are being considered for the joining of stainless steel and copper alloy, with brazing as a back-up.

For non-neutron-irradiated materials, the manufacturing techniques are well established. Under neutron irradiation, creep, swelling, embrittlement, etc. will occur. The quantification of these phenomena for the ITER conditions, and the qualification of materials and processes are important items for research and development. The R&D will include also the improvement of existing materials. Particular emphasis is placed on lifetime limitations due to thermal fatigue because of ITER's pulsed operation. High-heat-flux tests with cyclic loading on non-irradiated and irradiated component mock-ups need to be done. Work is also planned to verify the maintenance of this component, which is likely to need rapid and frequent replacement during the early stages of operation.

Physical and chemical sputtering are major factors limiting the lifetime of the targets and the channel walls in the ITER divertor. Preliminary assessments indicate that a beryllium cladding of 1cm thickness and a 3 cm thick carbon fibre composite covering will behave in a similar way, having predicted target lifetimes on the order of a few 1000 full power, full length discharges. The greater thickness of the carbon material is possible because of its higher thermal conductivity. Chemical erosion of carbon fibre composite appears to be worse at low energies; data below 10-20 eV and flux scaling are uncertain. For a 1cm tungsten target, however, the lifetime is as great as 10^6 discharges, for neutral energies below 30 eV and plasma temperatures below 20 eV. Although tungsten and other high-Z metals have longer lifetimes against erosion by sputtering, the permitted impurity influx into the plasma is smaller because of radiation from the ionised impurities in the plasma core.

Another limitation to the lifetime of divertor components is the damage occurring during disruptions. The expected energy density during a disruption is of the order of 10 MJ/m²; for edge localized modes (ELMs) it can reach 100 MJ/m². Estimations of the allowable number of disruptions on a target need to account for vapour shielding effects and, for metals, the stability of melt layers. These are key research and development topics.

An important aspect of the choice of plasma-facing materials is the uptake and retention of tritium. Processes that are known to influence the resulting tritium inventories include the co-deposition of tritium with carbon that is redeposited after erosion, the role of impurities in beryllium as trapping sites, trapping at neutron damage sites, and tritium retention and release in dust and debris generated during disruptions.

ACKNOWLEDGEMENT

REFERENCES

[1]   ITER Joint Central Team, presented by W.B. Gauster, Proceedings of the 6th International Conference on Fusion Materials Research, Stresa, 1993; Rickerby, D.G., Stamm, H., Ehrlich, K., Victoria, M., eds., Elsevier Science B. V., Amsterdam, 1994.

[2]   P-H. Rebut et al., Proceedings of the 18th Symposium on Fusion Technology, Karlsruhe, 1994; Herschbach, K., Maurer, W., and Vetter, J., eds., Elsevier Science B. V., Amsterdam (to be published).

[3]   P-H. Rebut et al., IAEA-CN-60/E-1-I-1, Proceedings of the 15th International Conference on Plasma Physics and Controlled Nuclear Fusion Research, Seville, 1994, International Atomic Energy Agency, Vienna (to be published).

[4]   R.R. Parker, W.B. Gauster et al., Proceedings of the 18th Symposium on Fusion Technology, Karlsruhe, 1994; Herschbach, K., Maurer, W., and Vetter, J., eds., Elsevier Science B. V., Amsterdam (to be published).

[5]   R.R. Parker et al., IAEA-CN-60/E-1-I-6, Proceedings of the 15th International Conference on Plasma Physics and Controlled Nuclear Fusion Research, Seville, 1994, International Atomic Energy Agency, Vienna (to be published).

[6]   K. Ioki, G. Johnson, K. Shimizu and D. Williamson, Proceedings of the 3rd International Symposium on Fusion Nuclear Technology, Los Angeles, 1994 (to be published).

[7]   K. Ioki et al., Proceedings of the 18th Symposium on Fusion Technology, Karlsruhe, 1994, Herschbach, K., Maurer, W., and Vetter, J., eds., Elsevier Science B. V., Amsterdam (to be published).

[8]   Y. Gohar et al., ibid.

[9]   M. L. Watkins and P.-H. Rebut, Proc. 19th Europ. Conf. Contr. Fus. Plasma Phys., 16 C Part II (1992) 731.

[10] G. Janeschitz et al., Proceedings of the 11th International Conference on Plasma Surface Interactions in Controlled Fusion Devices, Mito, 1994 (to be published).

[11] J. Dietz, IAEA-CN-60/E-1-I-4, Proceedings of the 15th International Conference on Plasma Physics and Controlled Nuclear Fusion Research, Seville, 1994, International Atomic Energy Agency, Vienna (to be published).

[12] R. Tivey et al., Proceedings of the 18th Symposium on Fusion Technology, Karlsruhe, 1994, Herschbach, K., Maurer, W., and Vetter, J., eds., Elsevier Science B. V., Amsterdam (to be published).

18

THERMOMECHANICAL PROPERTIES OF BERYLLIUM

D.E. Dombrowski, E.B. Deksnis* and M.A. Pick*

Brush Wellman Inc., Cleveland, Ohio, USA
*JET Joint Undertaking, Abingdon, Oxon, OX14 3EA, UK

ABSTRACT

Beryllium is foreseen to be used as a cladding for plasma facing components and as a neutron multiplier in the tritium breeding blanket of a fusion reactor. Thermomechanical properties are presented for powder metallurgic and ingot sheet grades of beryllium that are commercially available. Additional characterisation under normal conditions is required for most grades of material particularly as regards Poissons ratio and fracture toughness at elevated temperatures. No radiation damage data has been found for a well characterised irradiation at any neutron fluence on a modern form of beryllium. Given the difficulties of obtaining fusion-relevant neutron spectra, it is suggested that even the effect of thermal neutrons on well-characterised beryllium samples, i.e. defined manufacturing method and impurity content would give valuable data on the behaviour of beryllium subject to neutron damage.

Most forms of beryllium presently considered for breeder blanket applications are porous forms and as such are not yet in a form that is commercially available.

1. INTRODUCTION

This review will summarise the properties of beryllium at temperatures of interest to application as a plasma-facing component (PFC) and in the breeder blanket. The principal advantages which Be has in PFC applications is its ability to getter oxygen and its low atomic number. These properties have been shown by experiment to eliminate density limit disruptions and to increase the time scale for magnetohydrodynamic instabilities [1]. It is now very likely that any future large tokamak fusion experiment will rely upon beryllium for PFC applications [2].

Like most metals, beryllium can be fabricated into a variety of forms such as block, sheet, rod, tube and wire. Historically, block has been of the most commercial interest and has been the most characterised form, however grades of beryllium developed

recently have significantly improved properties. Beryllium ingot sheet will be another focus for this review as there has been recent assessment of a commercial product, and because its lower beryllium oxide content has provoked interest in the fusion community.

The primary use of beryllium in tokamak experiments [3, 4] has been for PFC which absorb heat without active cooling. In future experiments actively cooled beryllium clad heat sinks [5] or perhaps even directly cooled beryllium components [6] will be required to operate under steady-state conditions. Thus the experience gained so far with beryllium PFC is only a guideline for the design of actively cooled components. The requirements for a beryllium PFC for ITER are principally that the cladding remains intact and does not crack when subjected to 10^3 cycles of long pulse (10^3s) steady state operation. This requirement is for the physics phase of ITER. The requirements for a later, engineering phase would require sustaining the same integrity for neutron irradiation of up to 2 dpa before replacement is required.

The cladding of beryllium to a copper heat sink, the latter being favoured for thermal reasons, intrinsically presents a problem in view of the formation of copper-beryllium eutectic at elevated temperatures and by the formation of brittle intermetallic compounds at lower temperatures [7]. Whereas there is some experience relating to the bonding of beryllium to heat-sinks, i.e. [8, 9], little published data has been found on the effect of fast neutrons on joints. One successful method of fastening, brazing, uses materials that are readily activated and which may be transmuted under neutron bombardment. The lifetime of PFC components may thus be limited by various considerations other than strength of the joint. Furthermore limitations arising from the joining technology may be more severe than the intrinsic limits of beryllium. Very considerable experimental work remains to be done in this field.

Beryllium is the material of choice as the neutron multiplier through (n, 2n) reactions in a solid breeder blanket design. Design optimisation studies [8] have shown that such a blanket, although based on lithium ceramics, would require up to 70% beryllium in order to maximise tritium production. The solubility and retention of hydrogen isotopes in beryllium both for PFC and for blanket applications under unirradiated and irradiated conditions is not fully understood. Widely scattered data have been presented for beryllium grades that are now obsolete. Furthermore new grades are at present being developed [11] which examine low density forms of beryllium that appear to have improved rates of desorption of tritium for use in breeder blankets.

Discharges in tokamaks using beryllium as wall and/or limiter material have produced encouraging physics results. Three different experiments, i.e. UNITOR, ISX-B and JET have relied upon beryllium material in the form of thick blocks. In many discharges however, plasma behaviour has been limited by a runaway accumulation of impurities due to loss of material from the PFC. In addition to the requirements for mechanical integrity, minimal deformation and resistance to large body forces during disruptions, the level of impurities within beryllium for fusion PFCs must be very low. In particular the presence of impurities with high atomic number must be minimised. JET has used material with very small amounts of impurities with high atomic number, i.e. <100 ppm total for elements above Fe in the atomic table [12].

2. SCOPE

Good summaries of beryllium data for grades that are no longer being produced may be found in the Reactor Handbook [13] and in an excellent review by Pinto [14] of the properties measured prior to 1979.

This review will focus on measurements taken after 1979 with an emphasis on commercially available grades of beryllium block and ingot sheet. Block has been the form most widely used and is the best characterised form. However, the low BeO content and high ductilities of ingot sheet has provoked interest in these materials for fusion applications. It is intended in this review to highlight those properties which require substantial additional characterisation, in particular for irradiated material. It is noted that the ITER programme foresees a need to develop even more robust forms of beryllium.

3. BACKGROUND

Beryllium is an element with atomic number 4 and atomic weight of 9.012. It is a metal with a hexagonal close packed structure. Beryllium in structural applications is notable for a combination of stiffness and low density. Due to its low atomic number, beryllium transmits x-rays seventeen times better than an equivalent thickness of aluminium. Excellent reflectivity for infrared radiation is observed; commercial grades are up to 98.5% effective in the 8-12 micron range. Beryllium is used for neutron reflectors and as a neutron multiplier due to its high neutron scattering cross-section, low thermal neutron capture cross-section and high (n, 2n) neutron

multiplication cross-section. It has a strong chemical affinity for oxygen. Like aluminium, beryllium has a protective oxide layer.

In aerospace and other applications beryllium has been used due to its low specific modulus, which means that distortion of components made out of beryllium is minimised with respect to applied stress. The combination of high specific heat, high thermal conductivity, low coefficient of thermal expansion with the structural properties given above makes beryllium components dimensionally stable under transient thermal loads [22].

Beryllium grades are brittle at room temperature and become ductile at elevated temperatures with maximum ductility reached typically at 400°C. The PFC beryllium component comprises cladding on an actively-cooled substrate. One important criterion for the choice of grades to be considered is the ductility at coolant temperatures, i.e. ~ 100°C. The fatigue lifetime of the cladding has to be maximised with respect to regular thermal cycling at strain rates of the order of 10^{-4}/sec.

Table 1: Thermophysical properties of beryllium at 300K (unless noted).

Property	Value	
Melting Temperature	1289°C	(7)
Boiling point at 1 atm	2470°C	(7)
Heat of Fusion	1132 KJ/Kg	(7)
Heat of Vaporisation	24770 KJ/Kg	(15)
Density	1848 Kg/m^3	(14)
Electrical resistivity	$\sim 4 \times 10^{-8}$ Ω – m	(16)
Thermal conductivity	204 W/m/K	(17, 18)
Coefficient of thermal expansion	11.5×10^{-6}/K	(19)
Specific heat	1.85 KW-sec/Kg/K	(7)
Viscosity at 1556K	$\sim 10^{-3}$ poises	(20)
Youngs modulus	~ 311 GPa	(21)
0.2% Yield Strength	~ 270 MPa	(21)

Beryllium, like many industrial materials, poses a health risk if mishandled. In its usual solid form, as well as for finished parts, and in most manufacturing operations, it is completely safe. However, breathing very fine particles may cause a serious lung

condition in a small percentage of individuals. Risk can be minimised with simple, proven, and readily available engineering controls such as ventilation of operations producing fine dust. JET has operated safely with beryllium in large quantities and under conditions producing fine particles. Details of the JET safety experience are given in Appendix A.

4.   TYPES OF BERYLLIUM MATERIAL

The mechanical properties of beryllium vary significantly from grade to grade and also are strongly dependent upon specific fabrication technology. This review considers those grades available in ingot or block form. One manufacturer offers structural, instrument and optical grades of material [23]. Cast and rolled material called ingot sheet offers low BeO content and greater ductility than powder sheet above 200°C [24].

In the course of writing this paper the authors became aware of recent publications concerning the thermomechanical properties of beryllium produced by countries of the former Soviet Union [25]. In this latter report a wide range of materials are described to be forged, cold worked, hot pressed and/or rolled. In view of the multi-lateral agreement on the design of the ITER project it is expected that more information on the commercial availability of beryllium grades from this source will be forthcoming. However, as there is no data at present on the reproducibility of these properties for quantities of at least several hundred kilograms no further reference will be made to this source of material without prejudice to the quality of beryllium manufactured there.

Further ongoing development is to be noted of the methods whereby beryllium powder is produced. In particular the availability of spherical beryllium powder with very low BeO concentration, circa 0.5wt%, may produce grades of interest to the design of fusion PFC. Spherical beryllium powder has been made by inert gas atomisation [26, 27] and centrifugal atomisation [28]. Both processes involve the break up and rapid cooling of a molten metal stream to form powder. This type of powder has only been made in limited quantities.

A glossary of terms now follows relevant to the manufacture of beryllium through powder metallurgical (PM) methods or through ingot-metallurgy (IM).

4a   Powder Metallurgy of Beryllium

4a.1   *Milling*

Production of most forms of beryllium begins with chipping of a vacuum cast beryllium ingot. Chips are then ground using one of three methods.

<u>Attrition Grinding (AG)</u>   Chips are ground into powder between two grooved beryllium plates, one fixed and one rotating. Plate-shaped particles are produced which tend to align preferentially during powder consolidation steps, resulting in anisotropic mechanical properties. This technique is becoming obsolete.

<u>Impact Grinding (IG)</u>   Beryllium chips are suspended in a stream of high velocity gas and then directed at a solid beryllium target. The blocky particles produced this way result in a less textured microstructure and more uniform properties in all directions than attrition milling. The largest volume of beryllium is made using impact ground powder.

<u>Ball Mill Grinding (BG)</u>   Ball mill grinding is an expensive and time consuming process which produces extremely fine particles and a higher BeO concentration. This results in an extremely fine grained microstructure in the final product. This microstructure confers enhanced resistance to thermo-mechanical distortion. Typically beryllium grades produced this way are used for precision guidance components.

4a.2   Atomisation

Inert gas atomisation produces spherical beryllium powder particles in contrast to the angular or blocky particles produced by grinding. Atomised spherical powder (ASP) generally has half as much as BeO or less as the other beryllium powders. This technology has only recently been successfully applied to beryllium.

4a.3   Powder Consolidation

<u>Cold Pressing (CP)</u>   Powder is fed into a steel die and then uniaxially pressed from the top and bottom. The cold pressed or green powder billet then goes to one of the hot consolidation processes, usually sintering. Cold pressing tends to yield anisotropic mechanical properties.

<u>Cold Isostatic Pressing (CIP)</u> Powder is fed into flexible rubber bags which are sealed and lowered into a water filled pressure vessel. Pressure is applied simultaneously from all directions (isostatically). The CIP billet then passes through one of the hot consolidation processes. Products made with a CIP step tend to have more isotropic mechanical properties than products produced with a CP step.

<u>Vacuum Hot Pressing (VHP)</u> Powder is poured into a vertical cylindrical die. Pressure is then applied from rams at the top and bottom of the die under temperature and vacuum. Mechanical properties are anisotropic; mechanical properties measured parallel to the pressing direction (longitudinal) are generally lower than properties measured perpendicular to the pressing direction (transverse).

<u>Hot Isostatic Pressing (HIP)</u> Loose powder or a CIP powder billet is placed in a steel can which is welded shut after degassing at elevated temperature. The sealed can is then placed into a pressure vessel where it is heated and then pressed from all directions simultaneously (isostatically) by argon gas. Simple shapes made by HIP have minimal anisotropy in mechanical properties. Complex near net shapes can be made by this technique.

<u>Sintering (S)</u> A CP or cold CIP billet is placed in a furnace and heated under vacuum. Diffusion of beryllium atoms produces bonding. Sintered products have a coarser grain structure than HIP products and show anisotropy in mechanical properties.

<u>Extrusion</u> Billets made by CP or CIP are generally used as input stock, although extrusion of loose powder has been done. The feedstock is put in a cylindrical steel can, and degassed at elevated temperatures. The can is then welded shut and heated in a furnace. The hot can is then extruded through a die by a ram. Extruded products have anisotropic properties; the properties in the ram direction (longitudinal) differ from those in material perpendicular to the ram direction (transverse).

4b   Ingot Metallurgy

4b.1   Cast   This covers any process where molten beryllium is poured into a mould and solidified. Cast beryllium generally has very coarse grain size and a different distribution of BeO compared to powder metallurgy beryllium. The strength and ductility of cast beryllium is much lower than powder metallurgy beryllium but can be improved by cold working and hot working to a fine grain size. Rolling is at present the only practical method to produce a fine grain size in cast beryllium. The most pure forms of beryllium are prepared by casting and zone refining techniques.

4b.2   Ingot Sheet   This is beryllium sheet produced from cast beryllium by rolling. It is notable for low BeO content and more ductility in the in-plane direction above 200°C than powder metallurgy sheet. The properties of these grades are anisotropic. It has been suggested that the out of plane ductility of these grades may be higher than powder metallurgy sheet which has an out of plane ductility of < 1%.

4c   Refining Processes

Beryllium can be refined using the same techniques as other metals, but zone refining and vacuum distillation are currently used the most.

4c.1   Zone Refining   A bar of beryllium is placed in such a way that a furnace moves axially along it. A very small molten zone is formed at one end of the furnace and impurities are driven into the liquid by thermodynamic forces. Very high purity beryllium with very large grain size is produced. There are no commercial scale facilities for beryllium zone refining.

4c.2   Vacuum Distillation   Beryllium is vaporised and separated from impurities by fractional condensation. A high purity, coarse grained product is produced.

4d   Summary of Commercial Grades

Although beryllium is used in relatively small quantities compared to steel or aluminium, specific grades have been tailored for the major aerospace applications: structural, guidance instruments and optics. Grain size, impurity content, anisotropy and BeO content are the principal differences between these grades. A brief summary now follows of commercial grades.

26

Table 2: Commercially available structural grades of beryllium

Material	S-65B/C	S-200-E[1]	S-200-F	S-200-FH	S-200-FC	MSC-100	SR-200
Powder	IG	AG	IG	IG	IG	ingot	AG
Compaction	VHP	VHP	VHP	HIP	CP&S	sheet	VHP Sheet
Composition							
Be, min %	99.0	98.0	98.5	98.5	98.5	99.5	98.0
BeO, max %	1.0	2.0	1.5	1.5	1.5	<100 ppm	2.0
Al, max ppm	600	1600	1000	1000	1000	1000	1600
C, max ppm	1000	1500	1500	1500	1500	1000	1500
Fe, max ppm	800	1800	1300	1300	1300	1500	1800
Mg, max ppm	600	800	800	800	800	NS	800
Si, max ppm	600	800	600	600	600	1000	800
Other, max ppm	400	400	400	400	400	100	400
UTS-min MPa	290	276	324	414	262	276	483
typ-L	372		372	441	317		
typ-T	397		393	414	262		345
YS-min MPa	207	207	241	297	172	138	
typ-L	251		255	345	207		
typ-T	251		241	345	172		
% elongation - min	3.0	1.0	2.0	3.0	2.0	3.0	10.0
typ-L	3.8		4.0	4.9	4.1	<1	<1
typ-T	6.0		6.0	4.9		<1	<1

(1) no longer commercially available
NS - not specified

Table 3: Commercially available Instrument and Optical Grades of Beryllium

Material	I-70	I-70-H	I-220-H	I-250	I-400	0-50
Powder	IG	IG	IG	IG	BG	IG
Compaction	VHP	HIP	HIP	HIP	VHP	HIP
Composition						
Be, min %	99.0	99.0	98.0	97.0	94.0	99.0
BeO, max%	0.7	0.7	2.2	2.5	4.25 min.	0.5
Al, max ppm	700	700	1000	1000	1600	700
C, max ppm	700	700	1500	1500	2500	700
Fe, max ppm	1000	1000	1500	1500	2500	1000
Mg, max ppm	700	700	800	600	800	700
Si, max ppm	700	700	800	600	800	700
Other, max ppm	400	400	400	400	100	400
UTS - min MPa	241	345	448	517	345	241
typ - L	N/A	503	634	606	N/A	N/A
typ - T	N/A	490	634	606	N/A	N/A
YS - min MPa	172	207	345	448	N/A	172
typ - L	N/A	338	542	524		N/A
typ - T	N/A	338	542	524	N/A	N/A
% elong - min	2.0	2.0	2.0	1.5		2
typ - L	N/A	5.1	3.7	3.0		N/A
typ - T	N/A	5.1	3.7	3.0		N/A
Microyield (MPa)[1]	12	21	41	69	62	NS

(1) Stress required to produce 2.5×10^{-2} mm permanent strain.
NS - not specified

<u>Structural Grades</u> (S-65, S-200-F, S-200-E, MSC-100, SR-200) are processed to provide the highest strength. They are the most versatile grades and are the most well characterised. Nominal properties of selected grades are shown in Table 2.

<u>Instrument Grades</u> (I-220-H, I-400, I-70) are designed to provide the least distortion in aerospace guidance instruments. They are optimised to provide the best micro yield strength which is the maximum stress which can be applied before one microinch of plastic strain is made. Nominal properties are shown in Table 3.

<u>Optical Grades</u> (0-50, I-70, I-220-H) are optimised for reflectivity and polishing characteristics. The principal application is for satellite mirrors, although there are some terrestrial mirror applications where weight and infrared reflectivity are important. Nominal properties are shown in Table 3.

The S-65 grade was originally chosen by JET for First Wall and Divertor applications because it combined low impurity level (for low plasma contamination) with low BeO content and superior ductility at elevated temperatures. However, in other applications where strength is the overriding factor, instrument grades are more appropriate. It should be noted that instrument grades have the highest BeO contents of the commercial beryllium grades, and often have higher impurity levels and lower ductility than the structural grades.
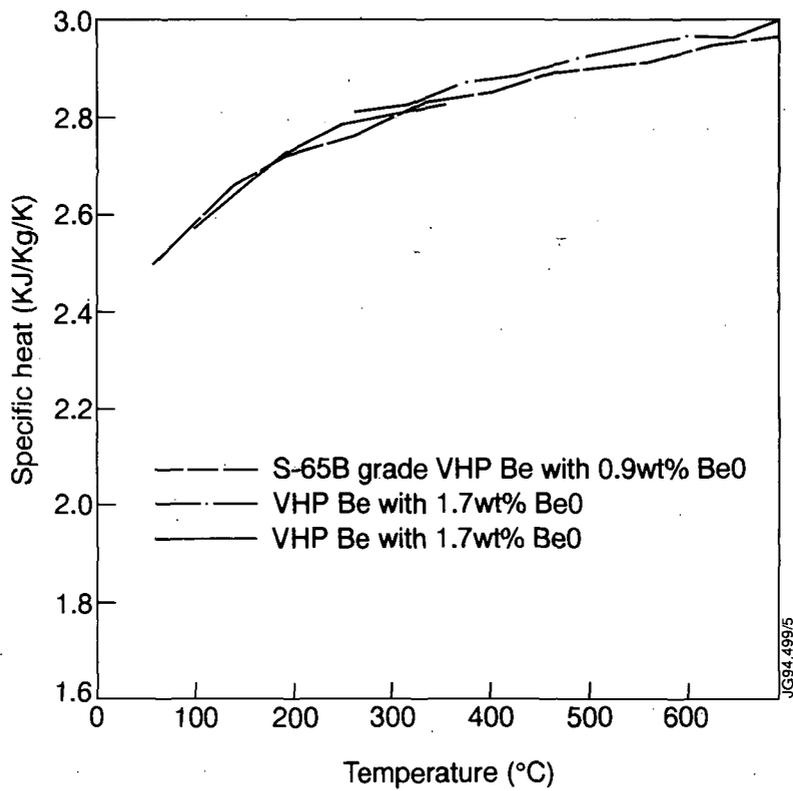
Fig. 1   Specific heat of VHP Be [16]. Specific heat of S-65B grade VHP Be [21].

IM sheet, BeO circa 100ppm
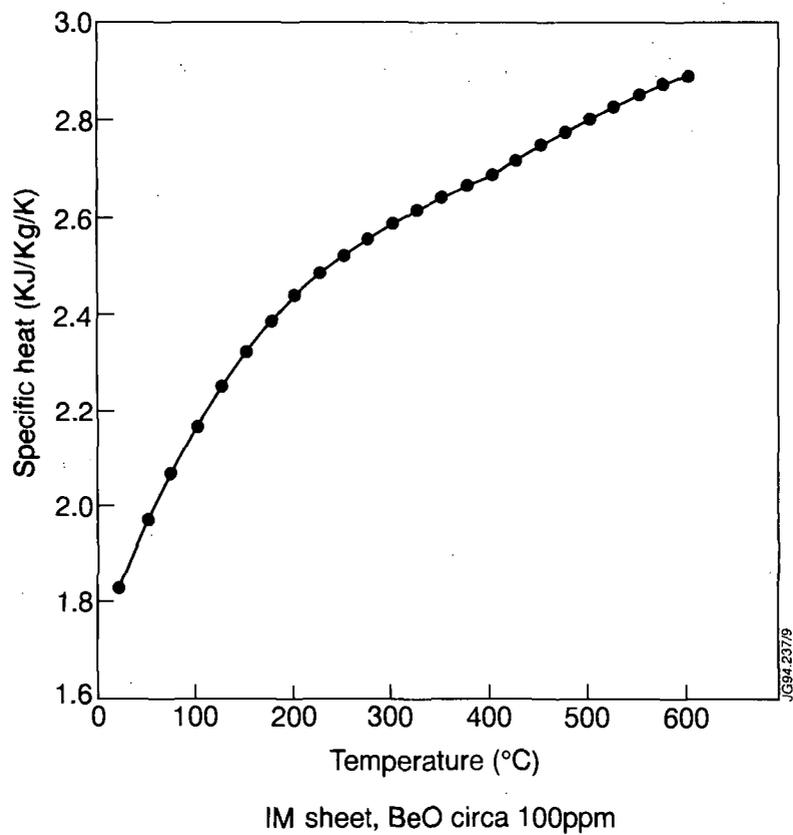
Fig. 2   Specific heat for IM Be [29] sheet with unknown BeO content [29].

5. BASELINE PROPERTIES

Many of the thermophysical properties of beryllium vary not only from grade to grade but also change substantially due to neutron irradiation. For example, yield strength, ultimate tensile strength and ductility are expected to be influenced substantially by radiation damage. These properties are discussed in detail in subsequent sections. This section presents data for those properties which are not expected to be influenced by neutron damage.

5a   Specific Heat

Recently measurements of specific heat have been made of commercially available grades for which the fabrication process and the impurity levels have been given. In Figure 1 specific heat is plotted for (a) VHP beryllium with 1.70% BeO by weight [16] using adiabatic calorimetry, (b) VHP beryllium with 1.70% BeO by weight [16] using the slope of an enthalpy curve, (c) VHP beryllium grade S-65B with 0.8% BeO by weight [21]. Figure 2 shows data for IM beryllium sheet [29] for which the BeO content is likely to have been less than 100 ppm.

The specific heat of S-65 material as tabulated in Table 4 below is seen to vary between 17.2J/mole/K at 51°C to 29.0J/mole/K at 996°C. For ingot sheet specific heat range is 16.5J/mole/K at 23°C and 26.0J/mole/K at 602°C.

The specific heat of liquid beryllium is relevant in the assessment of material loss from PFC due to disruptive events that produce surface melting. Values of 3.27 KJ/Kg/K at melting temperature rising linearly to 3.45 KJ/Kg/K at boiling point have been reported [14]. It is not clear that this result would vary greatly from grade to grade unless the percentage of BeO varies greatly from the values of up to 2% typical of modern forms of beryllium.

5b   Density

The density of any material varies with temperature as a consequence of thermal expansion. Variation of density with temperature is listed in Table 4 for commercially available VHP grade, S-65B beryllium with 0.9% by weight of BeO.
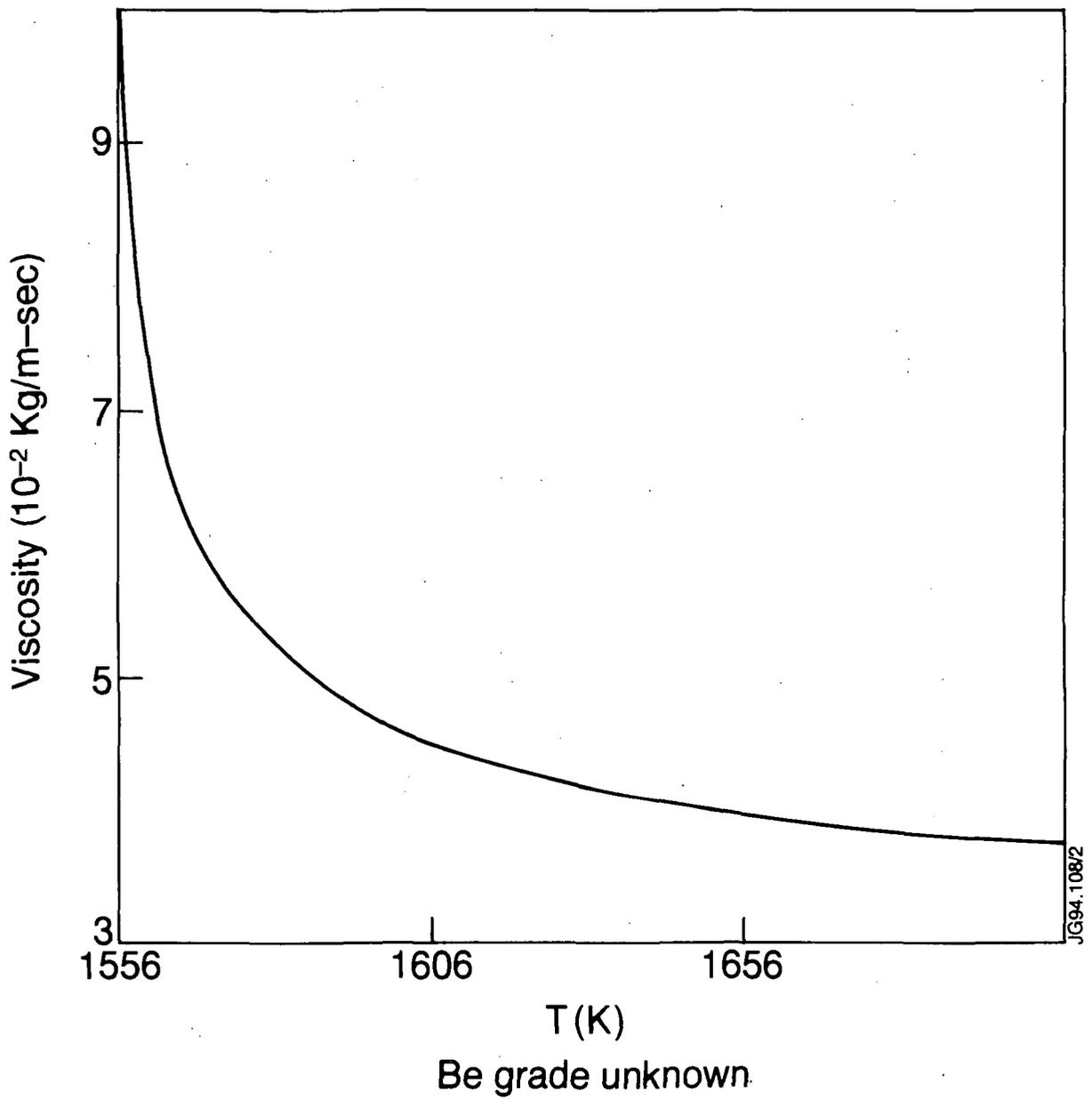
Fig. 3   Viscosity of molten beryllium [20]. The beryllium stock was 99.85 to 99.9%
pure and had an unknown amount of BeO.

Table 4: Reference thermal properties S-65b [21]

Temperature °C	Conductivity W/m/k	Specific heat KJ/Kg/K	Density Kg/m³
51.0	187.3	1.905	1820
139.0	152.3	2.240	1814
183.0	143.8	2.344	1806
242.0	133.8	2.441	1806
291.0	128.8	2.529	1801
336.0	125.2	2.613	1797
400.0	116.6	2.667	1791
464.0	110.4	2.734	1785
543.0	101.8	2.780	1777
619.0	96.1	2.860	1769
700.0	88.4	2.939	1760
854.0	75.8	3.086	1742
996.0	63.8	3.220	1725

5c   Viscosity

The development of Rayleigh-Taylor instabilities on the surface of liquid metal due to the interaction of electric currents induced in the liquid layer with magnetic fields at the edge of a plasma has been observed at JET in disruption damage of inconel heat shields [30]. The viscosity of beryllium has been measured to be 10^{-3} poise at melting temperature and decreases with temperature as shown in Figure 4. The material grade is not known [20].

5d   Vapour Pressure

In a PFC application the amount of wall material released into the plasma is crucial to the purity of the edge plasma and ultimately to the performance of the core plasma. In addition to the physical process of evaporation, sputtering by hydrogenic species, by other impurities and by beryllium particles already released contribute towards the net wall influx of beryllium atoms into the plasma.

The vapour pressure of beryllium in solid form is given by [15]

$$\log p \text{ (Torr)} = 11.279 - 0.56 \log T - 17.058 \, T^{-1} \quad 298 < T < 1560 \text{ K}$$

and for the liquid form by [15]

$$\log p \text{ (Torr)} = 12.483 - 1.04 \log T - 16.518 \, T^{-1} \quad 1560 < T < 2745 \text{ K}.$$
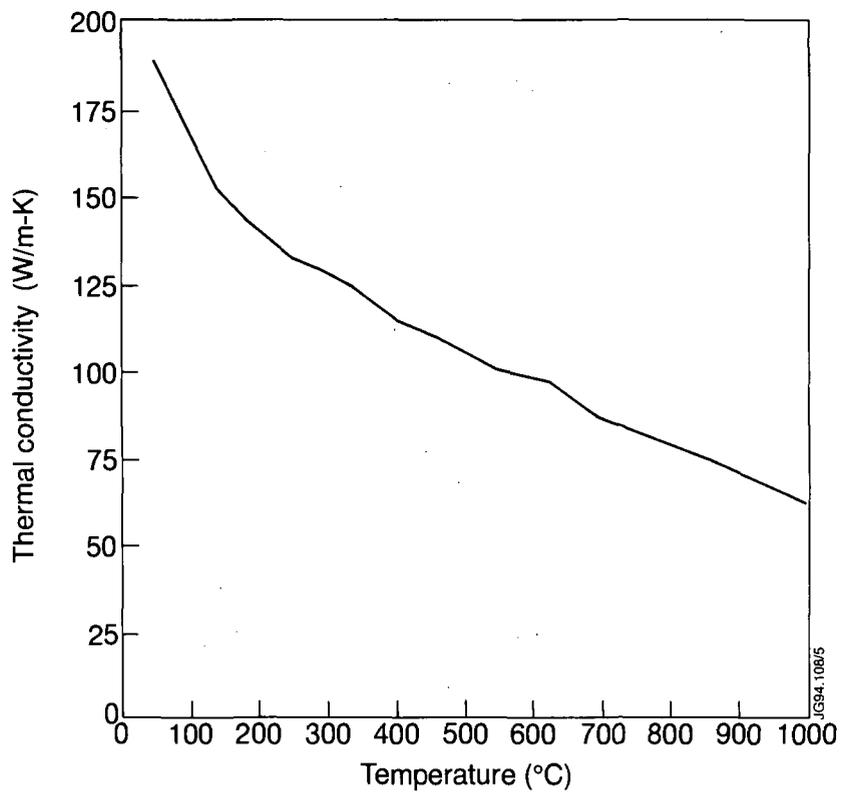
S65B VHP Beryllium

Fig. 4   Thermal conductivity of S-65B grade VHP Be [21].
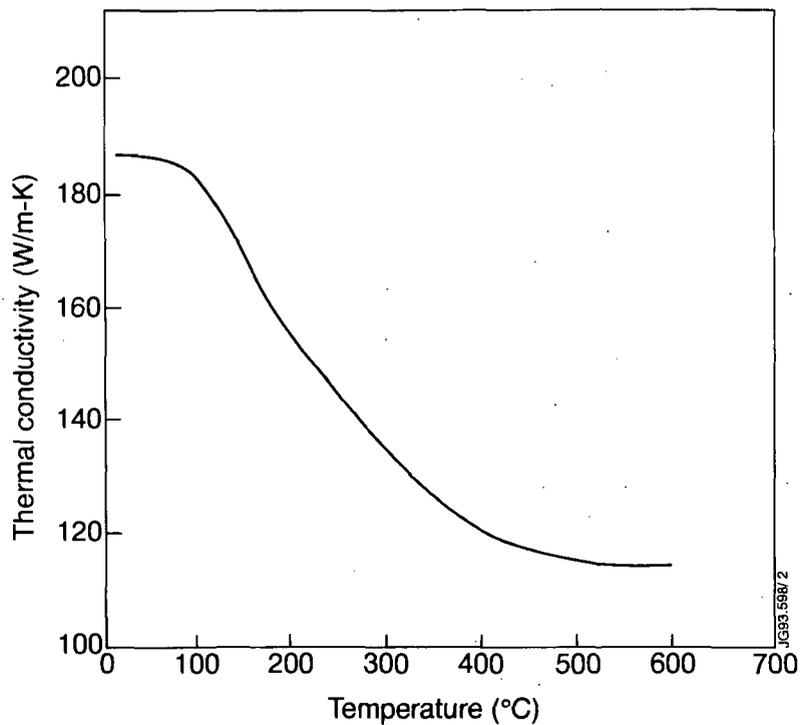
IM sheet with BeO circa 100ppm

Fig. 5   Thermal conductivity for IM sheet [29].

34

For commercially available beryllium material, experience at JET suggests that the method of fabrication i.e. casting versus powder metallurgical methods, does play a role in determining the total evaporation rate of beryllium from a surface. As BeO melts at substantially higher temperatures than Be, the preferential release of Be from a surface will tend to enrich the concentration of BeO and thus reduce the net total evaporation rate. Clearly the ionic and energetic bombardment of beryllium PFC in a tokamak will alter the geometric morphology of the surface. No systematic measurements of beryllium evaporation rates from samples modified this way have been reported.

6.   UNIRRADIATED PROPERTIES

In this section the behaviour of thermomechanical properties versus temperature will be reviewed with emphasis on measurements made according to published standards. For example ASTM volume 3.01 [31] lists accepted procedures for metals testing. VHP beryllium block has been the form for which the most extensive investigation of properties has been made since the review by Pinto [14]. New HIP grades have been shown to exhibit nearly isotropic properties. Thermomechanical data for these grades have yet to be fully measured at elevated temperatures.

6a   Thermal Conductivity

The majority of thermal conductivity data for beryllium was generated during the years 1940-1955. Although most of this data was obtained from tests conducted on single crystals at cryogenic temperatures, or on material in a strong magnetic field, there is some data which may pertain to the properties of beryllium made by the current PM process. The most complete review of the older data is to be found in Thermophysical Properties of Matter Vol. 1 [32]. Room temperature values quoted therein of thermal conductivity for material which has characteristics of commercial beryllium range from 135 to 200 W/m-K, with a recommended value of 180 W/m-K.

As shown in Table 5, beryllium of modern purity has a room temperature thermal conductivity in the range 204-219 W/m-K [17]. This is 15-20% higher than the widely accepted values for beryllium [32]. Note that the method of measurement for the longitudinal bars [17] follows ASTM standard C-1045-80. Since the most widely used commercial grade in the table is S-200F, the value 204 W/m-K is recommended as the thermal conductivity at room temperature.
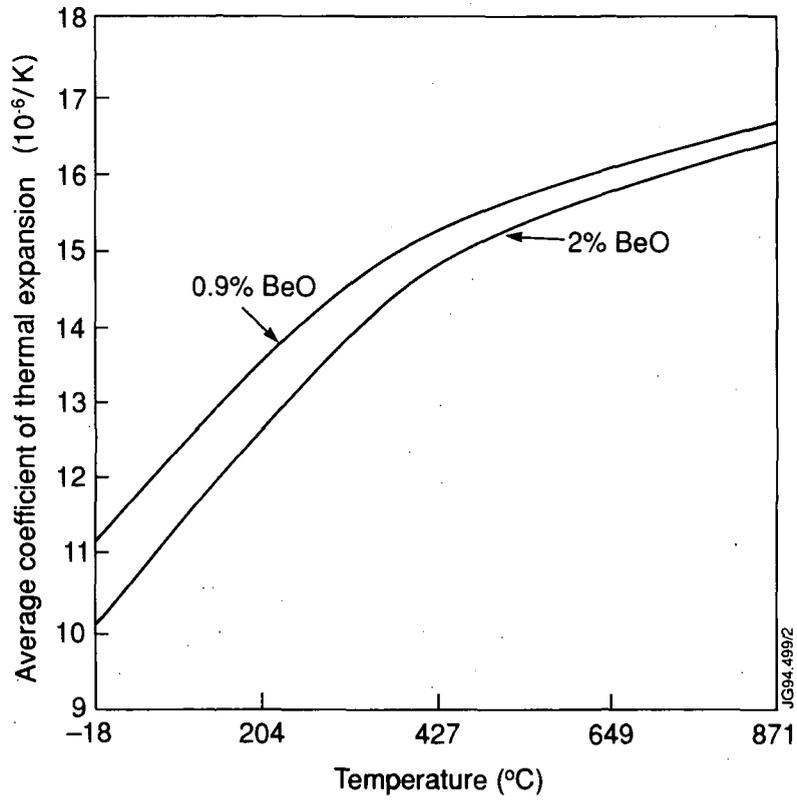
Fig. 6   Coefficients of thermal expansion [36].

S-200F VHP Be grade
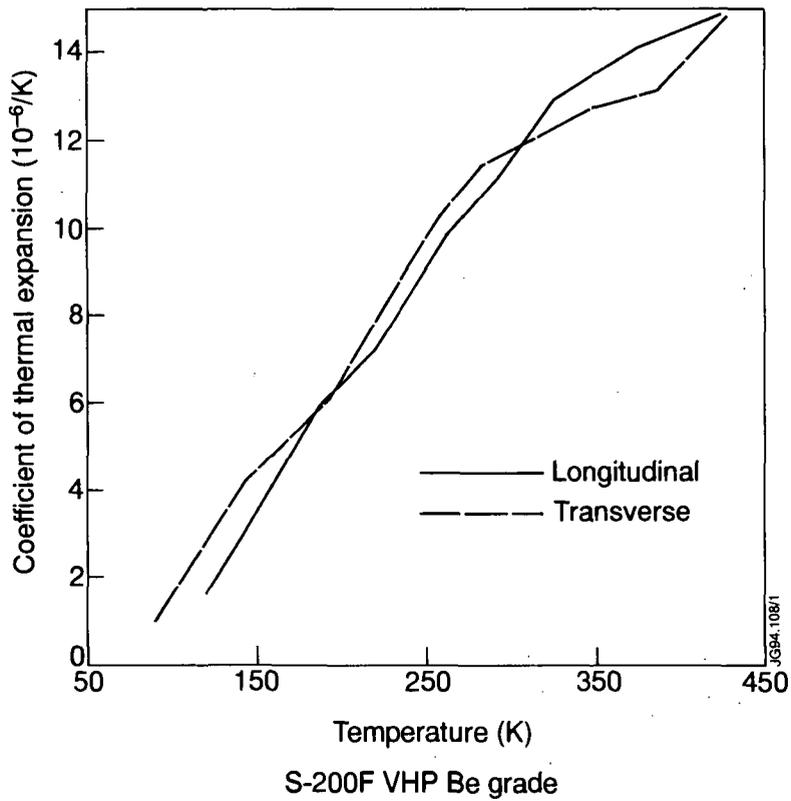
Fig. 7   Coefficient of thermal expansion [34].

Table 5 Thermal Conductivity of Be at 25°C

Grade	wt% BeO	Form	Process	Measurement Method	k (W/m-K)
Spherical Powder	~0.5	Block	HIP	Longitudinal Bar	204
Spherical Powder	~0.5	Block	VHP	Longitudinal Bar	216
BG-170	~2	Block	CIP/Sinter/ Coin	Longitudinal Bar	215
S-200F	< 1.50	Block	VHP	Longitudinal Bar	204
SR-200	< 2.0	Block	VHP/Roll	Laser Flash	219

Figures 4 and 5 show measured values of thermal conductivity as a function of temperature. Thermal conductivity of VHP grade S-65B with 0.9wt% of BeO is shown as a function of temperature in Figure 5 and also in Table 4 above. Figure 5 shows data for IM beryllium sheet for which the samples are likely to contain less than 100 ppm of BeO [29]. The measured value of 187 W/m/K at 20°C for ingot sheet is lower than the reference value of Table 1.

6b Coefficient of Thermal Expansion

For evaluation of older CTE data, the anisotropy of various Be products must be taken into account, as well as the %BeO content. The introduction of HIP Be products has provided grades that exhibit a more isotropic CTE response. However, these HIP products have not been characterised over the full temperature range of interest for fusion.

Figure 6 shows average values of CTE versus temperature for two different BeO contents: 0.9 wt% BeO and 2.0 wt% BeO [14]. As seen in Figure 6 CTE for the higher content to vary between 10×10^{-6}/K and 16.4×10^{-6}/K for a temperature span of -18 to 871°C. The CTE of beryllium with 0.9% BeO is seen to vary between 11×10^{-6}/K and 16.7×10^{-6}/K for the same temperature range. This indicates that higher BeO content decreases CTE. This trend is confirmed by comparing the CTE values for several high
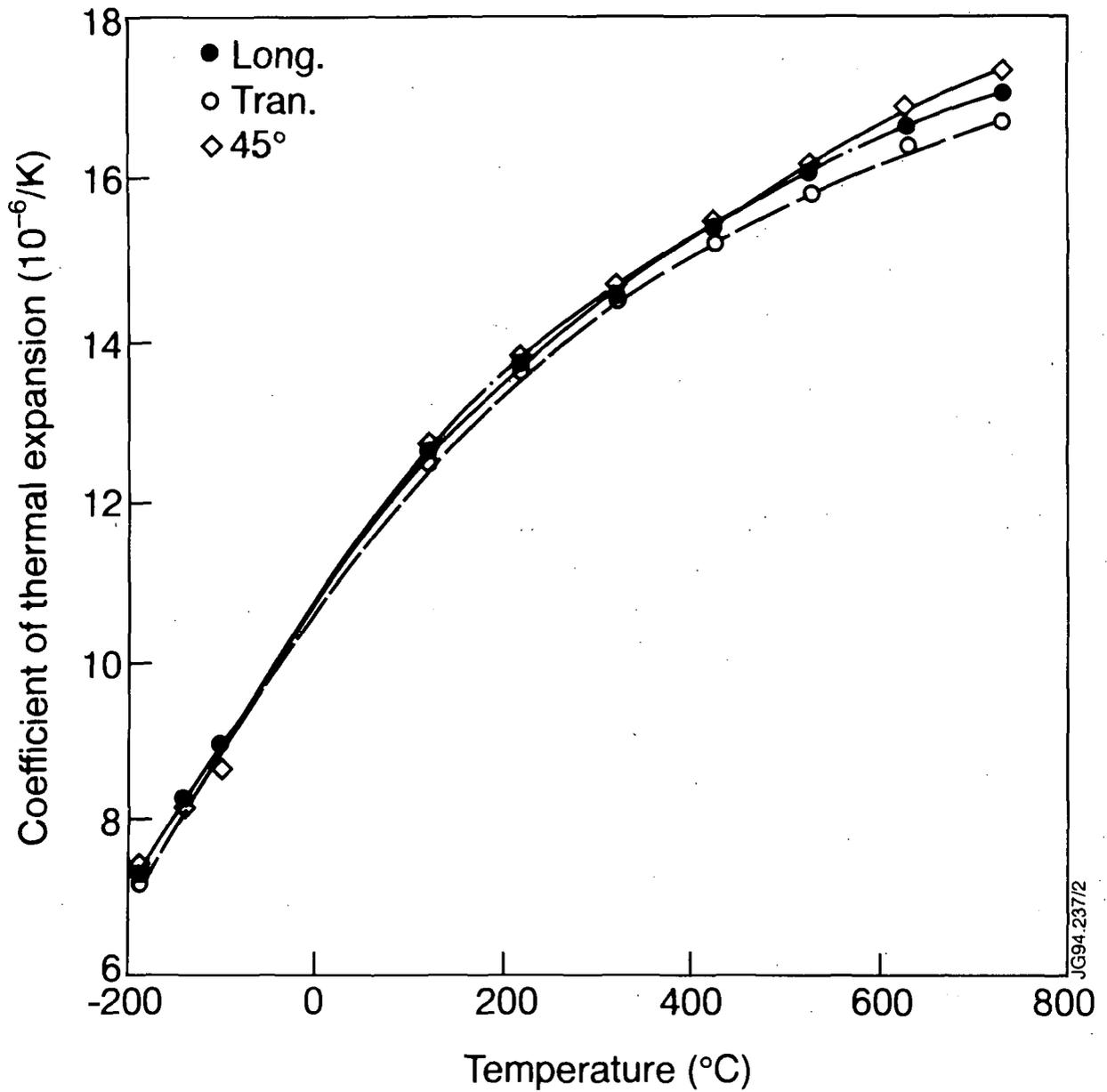
Fig. 8   Coefficient of thermal expansion [29].

BeO content, and Be/BeO composite materials. As the volume % BeO is increased from 20 to 60, the CTE for the 0 to 25°C temperature range drops by about 33% [33].

Figure 7 shows CTE values for VHP grade S-200F (1.06 wt%BeO) from 89 to 430 K [34]. In the longitudinal direction, CTE varies between 1.6×10^{-6} /K and 14.7×10^{-6}/K as the temperature ranges between 120 and 425 K. In the transverse direction, CTE varies between 0.9×10^{-6}/K and 14.7×10^{-6}/K as the temperature ranges between 89 and 430 K. Note that the difference in CTE between the two orientations decreases with temperature, and is negligible at 430 K.

CTE values over the temperature span 6 to 64°C for the S-65B grade of VHP beryllium are reported to be 11.66×10^{-6}/K in the transverse direction and 11.54×10^{-6}/K in the longitudinal direction [35]. This grade of VHP beryllium typically contains 0.9 wt% BeO, and has a lower CTE than the S-200F grade, as expected.

Figure 8 shows average CTE values for beryllium sheet made using IM [29]. There is little effect of orientation within the plane of the sheet. Although the BeO content was not reported, it was expected to be less than 100 ppm. Values for CTE range from 7.2×10^{-6}/K at -188°C to 17.2×10^{-6}/K at 707°C; CTE at 20°C is 11.3×10^{-6}/K.

6c   Electrical Resistivity

Resistivity is strongly affected by contaminant concentration and by heat treatments which determine whether the contaminants are in solution or are precipitates. Resistivity is lower when impurities have been precipitated out of solid solution for both PM and IM beryllium. High purity is always associated with lower electrical resistivity.

Figure 9 shows a plot of electrical resistivity as a function of temperature for VHP Be with 1.7 wt% BeO [16]. Values range from 4.47×10^{-8} Ohm-m at 23°C to 45.65×10^{-8} Ohm-m at 1000°C. There is little difference (2%) in electrical resistivity at 21°C between the longitudinal and transverse orientations in the VHP billet.

The electrical resistivity of beryllium ingot sheet is shown in Figure 10 for temperatures between 20°C to 527°C [29].

6d   Youngs Modulus

The most extensively documented and detailed measurements of Youngs modulus have been presented by Haws for a VHP billet of S-200F material [19]. For a sample
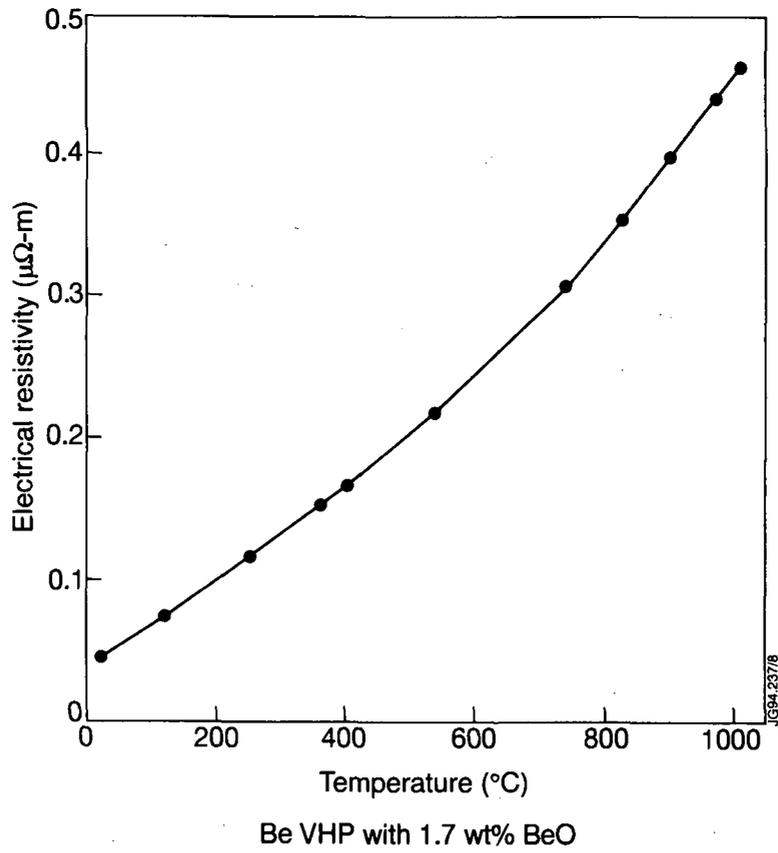
Fig. 9   Electrical resistivity VHP Be [16].
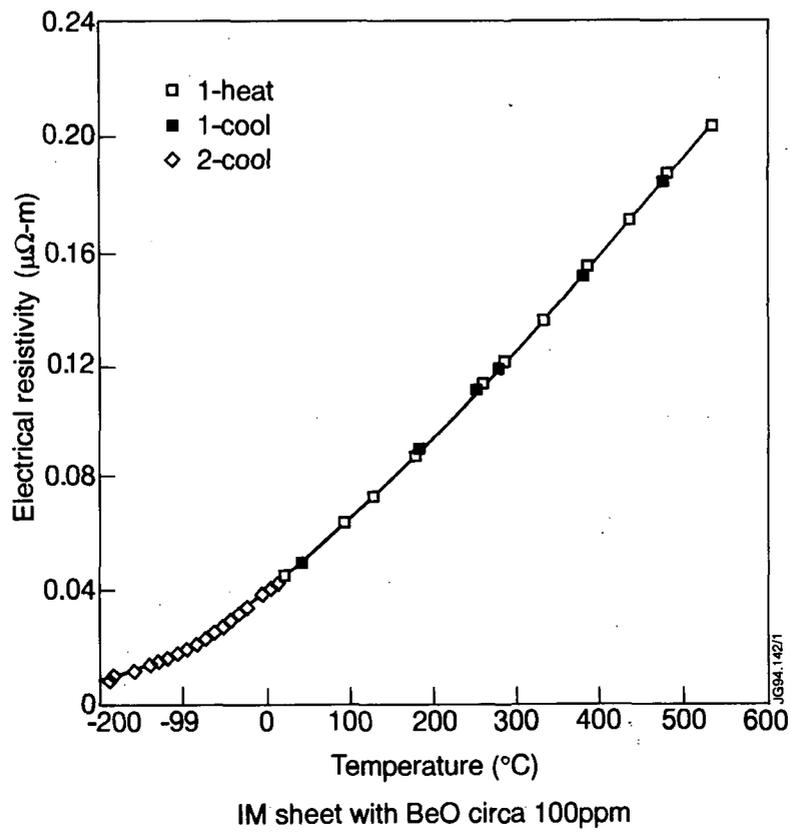
Fig. 10   Electrical resistivity of IM Be sheet [29].
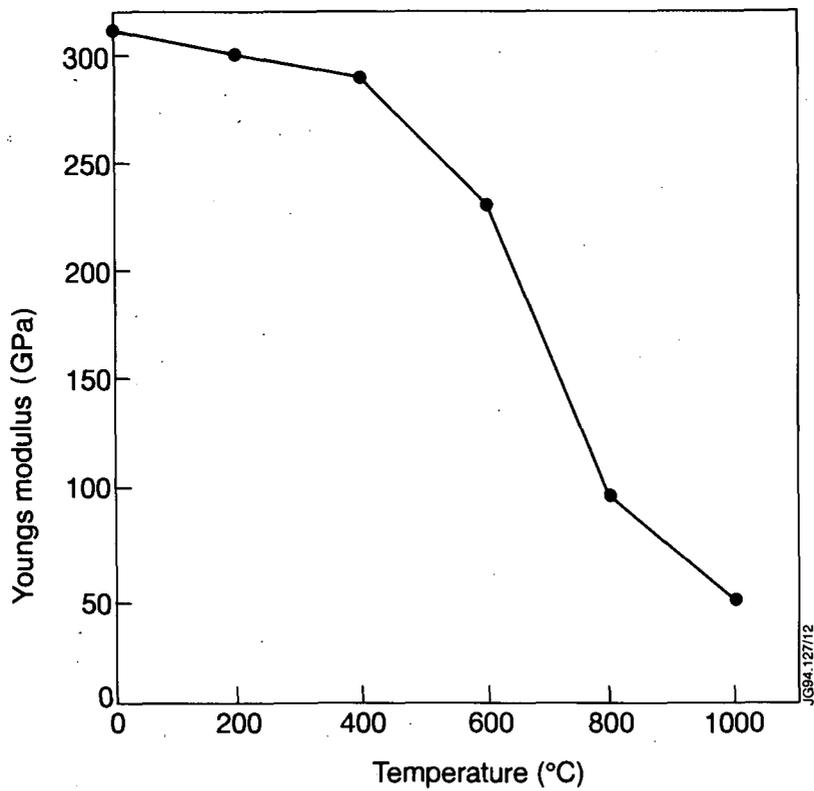
S-65B (VHP, 0.9wt% BeO)

Fig. 11   Tensile elastic modulus of S-65B VHP Be [21].
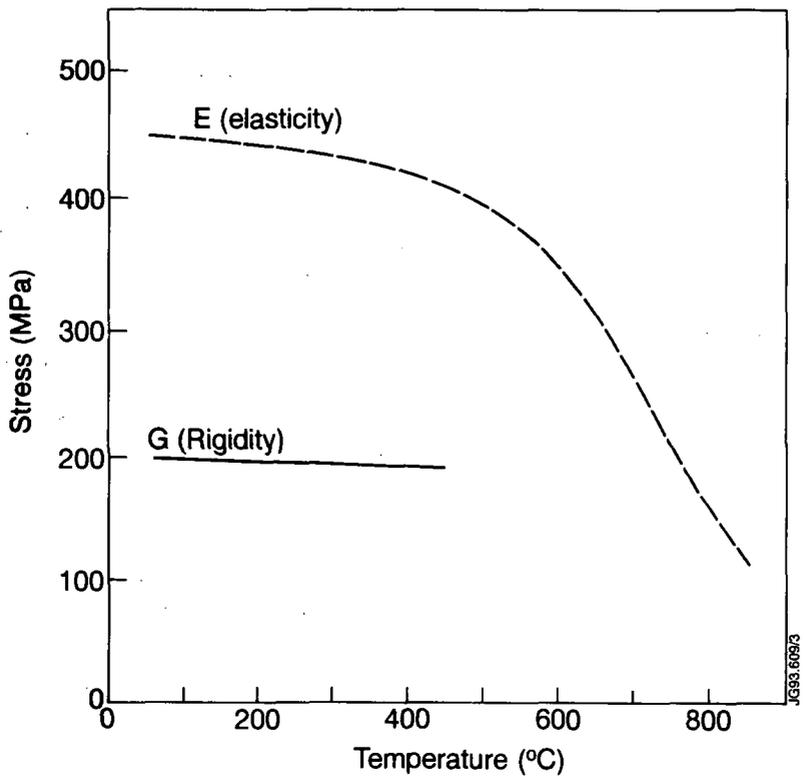
S200E up to 2.0 wt% BeO

Fig. 12   Elastic and shear moduli for S-200E VHP Be [36].

with 1.06% by weight of BeO measured values are reported of 311 GPa ± 6.9 GPa and 310 GPa ± 4.8 GPa for the tensile modulus in the longitudinal and transverse directions [19]. Variation with temperature of the tensile elastic modulus is shown for S-65B (VHP, 0.9wt% BeO) in Figure 11 and also in Table 6 below.

Table 6: Tensile Elastic Modulus S-65B [21].

Modulus GPa	310	300	290	230	97	48
Temperature °C	0	200	400	600	800	1000

6e   Shear modulus

Shear modulus of S-200F grade VHP beryllium was measured at room temperature by torsion according to the ASTM E-143 procedure. The average shear modulus was determined to be 135 MPa ± 4.8 MPa and 134 MPa ± 4.8 MPa for the longitudinal and transverse directions respectively [19]. Shear rupture modulus was determined from the maximum stress of the stress-strain curve to be 297 MPa ± 13 MPa in the longitudinal direction and 309 MPa ± 8.3 MPa in the transverse direction [19].

Figure 12 shows the variation of shear modulus with temperature for S-200E grade beryllium [36]. This grade is no longer produced.

6f   Poisson's Ratio

Table 7: Room Temperature Poisson's ratio for S-200F VHP Be with 1.06 wt% BeO.

Orientation	Stress Axis	Direction of Orthogonal Strain	Poisson's Ratio
LC	Longitudinal	Circumferential	0.102 0.064 0.072
LR	Longitudinal	Radial	0.102 0.080 0.105
TL	Transverse	Longitudinal	0.069 0.071 0.108
TR	Transverse	Radial	0.102 0.058 0.066

Table 7 above shows the only known published data on accurately measured room temperature Poisson's ratio for a modern grade of beryllium [37].
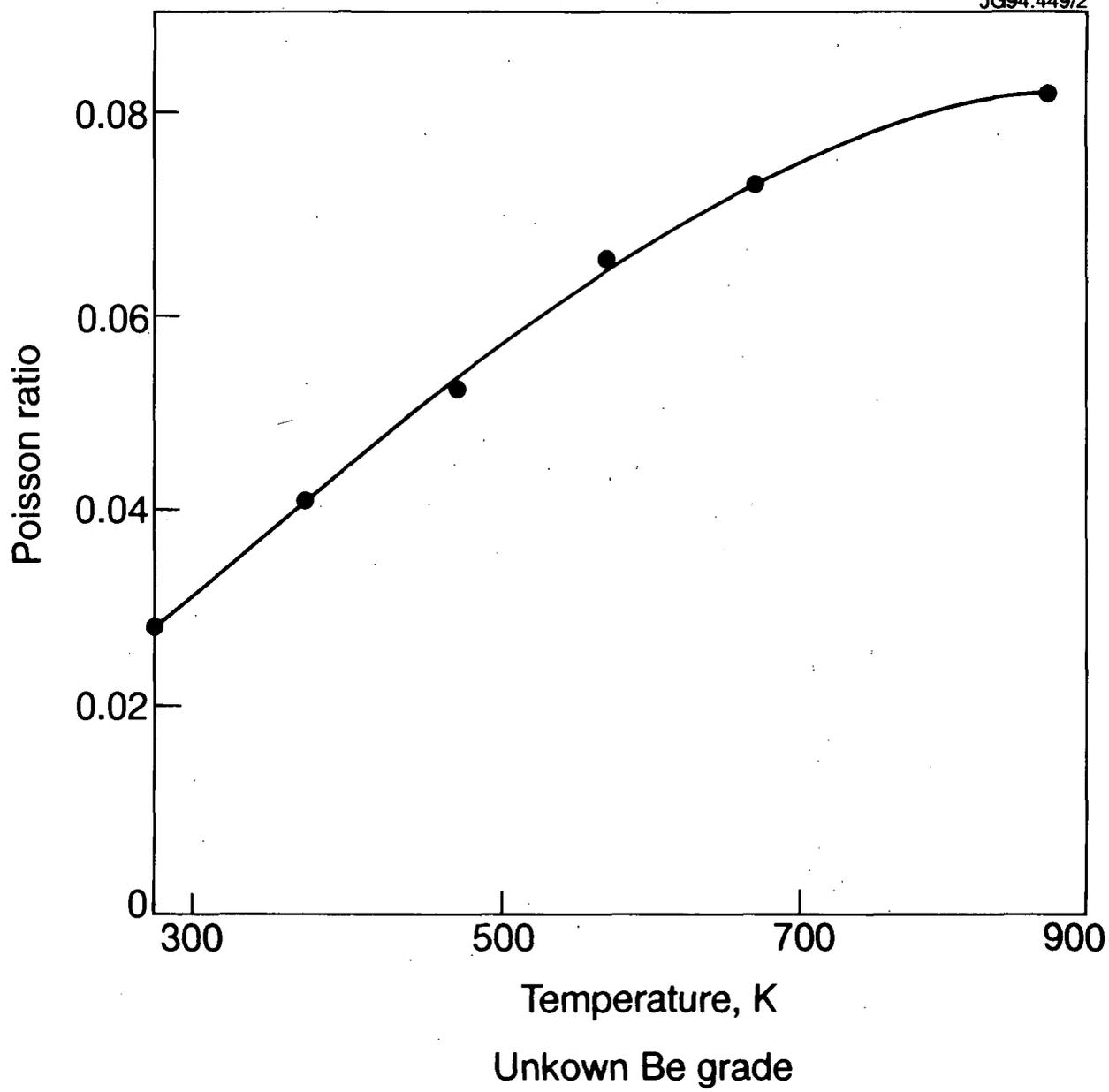
Fig. 13   Poisson's ratio for an unknown grade of Be [38].
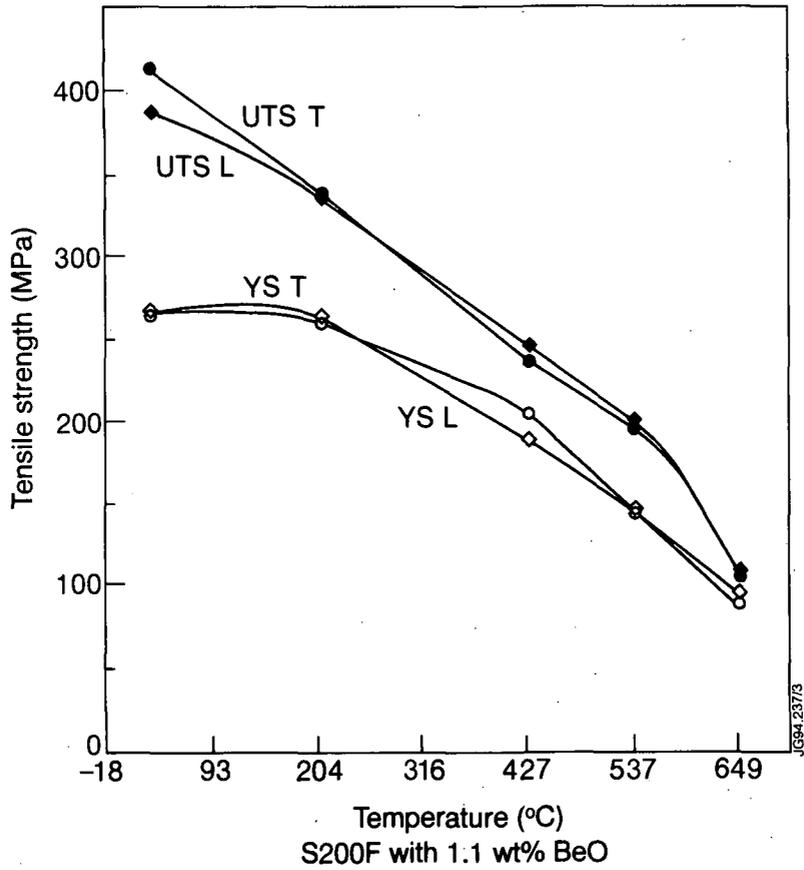
Fig. 14   Ultimate tensile strength and 0.2% offset yield strength
for S-200F grade VHP Be [19].
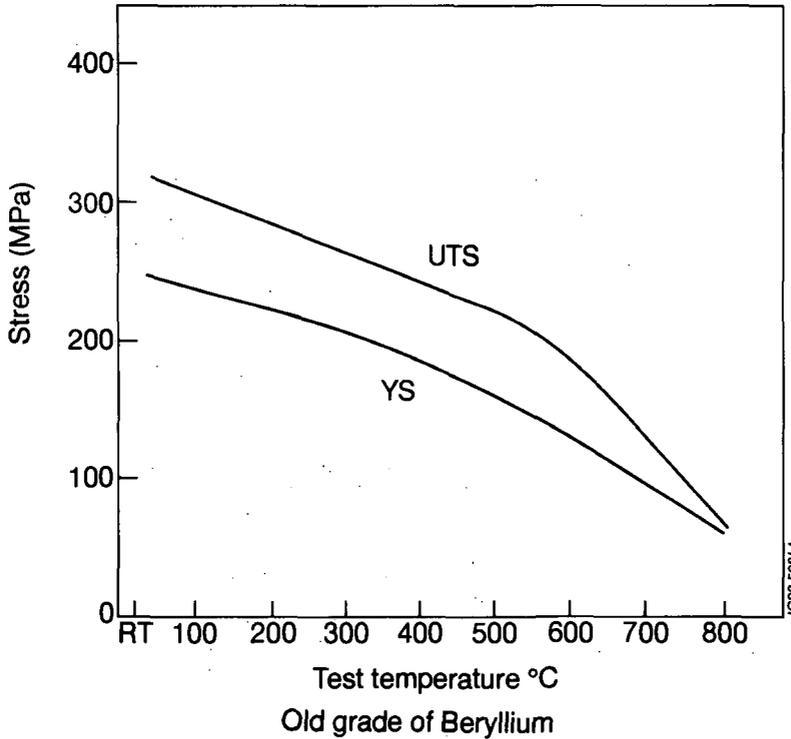
Fig. 15   Ultimate tensile strength and 0.2% offset yield strength
for earlier production grade of VHP Be [14].

44

Poisson's ratio was determined at room temperature according to ASTM standard E-132-61. The tests were performed using sheet geometry specimens that were machined from a piece of as-pressed beryllium; the sheet geometry was not produced by rolling. Specimens were tested in four orientations: LC, LR, TL, and TR. The first letter specifies the orientation of the stress axis of the specimen to the vacuum hot pressing direction: L or T. Longitudinal (L) signifies that the stress axis was parallel to the pressing direction, and transverse (T) signifies that the stress axis was perpendicular to the pressing direction. The second letter (R, C or L) compares the orientation of the orthogonal strain to the pressing direction. The strain was either in a radial (R) direction in the cylindrical billet compared to the pressing direction, circumferential (C), or longitudinal. There is significant scatter in the data. This is a low value that may be difficult to measure precisely.

No measurements of Poisson's ratio as a function of temperature have been reported for modern commercial PM grades of beryllium. However, by analogy for data presented for older forms of beryllium it is expected that the value of Poisson's ratio will increase with increasing temperature [13]. Figure 13 shows data for an unknown grade of beryllium [38]. However, the room temperature values therein are lower than measured e.g. Table 7 above. This data may have been derived from measurements of shear modulus. A different report on the variation of Poisson's ratio with temperature [39] appears to show a falling tendency with increasing temperature.

6g   Ultimate Tensile Strength

6g.1   VHP Block

Figure 14 shows ultimate tensile strength (UTS) versus temperature for S-200F grade Be (1.5% BeO, 98.5% Be, impact ground, VHP). Values range from 382 and 408 MPa at room temperature for longitudinal and transverse directions respectively to 108 and 107 MPa for longitudinal and transverse directions at 649°C [19]. Note that the data points are mean values from triplicate tests on the same lot of material. Testing was done in accordance with ASTM specifications E8, E4 and E21, with additional requirements specified by the Materials Advisory Board.

Figure 15 shows data to 800°C for grade that is no longer produced [14]. This particular grade had lower strength than S-200F, but the plot is useful because it indicates the
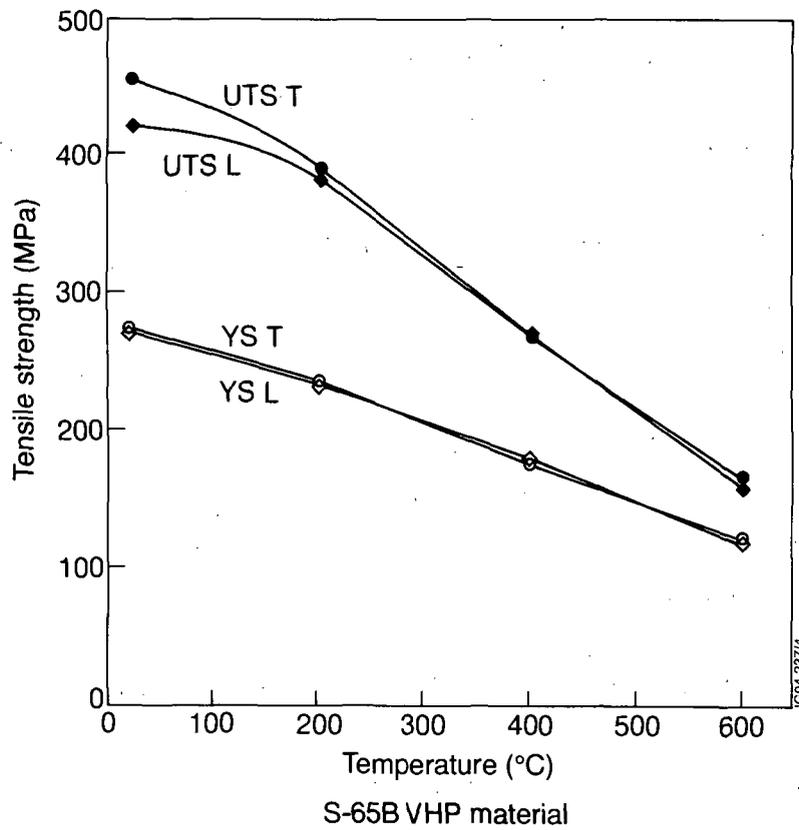
Fig. 16 Ultimate tensile strength and 0.2% offset yield
strength for S-65 VHP Be [21].
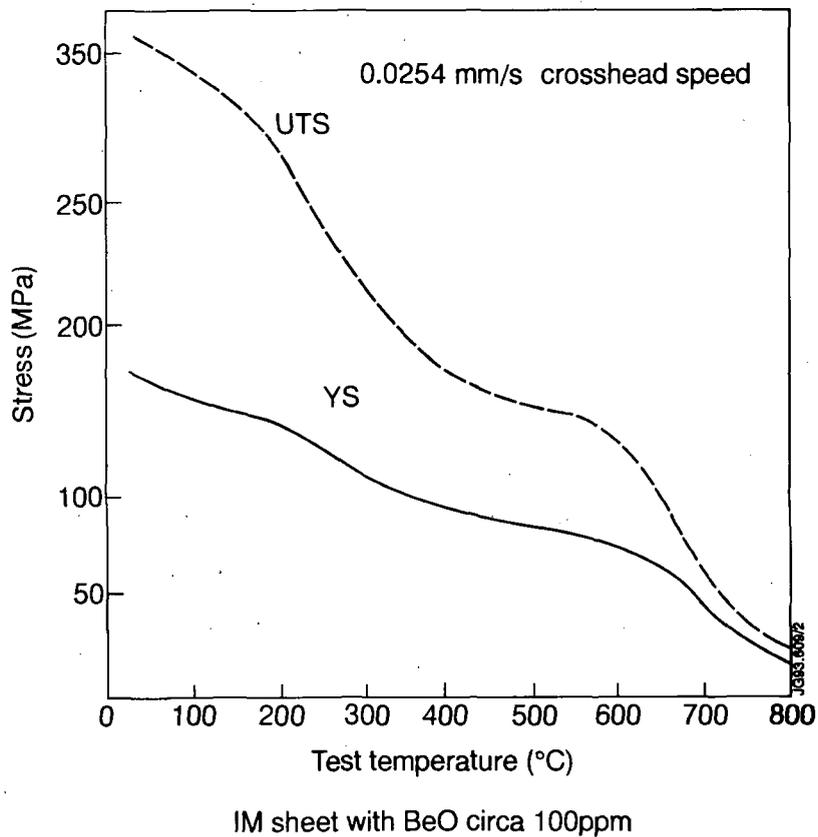
Fig. 17 Ultimate tensile strength and 0.2% offset yield
strength for IM Be sheet [24].

46

general trend of UTS at higher temperatures. Note that at 800°C UTS is only 18% of the UTS at room temperature.

Figure 16 shows ultimate tensile strength (UTS) versus temperature for S-65B grade Be (1.0% BeO, 99.0% Be, impact ground, VHP) [21]. Values range from 421 MPa and 454 MPa at room temperature for longitudinal and transverse directions respectively, to 160 MPa and 168 MPa at 600°C for the same directions. This grade of beryllium has an 11% greater UTS at room temperature than S-200F.

6g.2   HIP Block

S-200F-H is a grade (HIP, 1.5wt% BeO, impact ground) formed by HIP instead of VHP. Table 8 shows data for room temperature mechanical properties [40]. As expected for a HIP product, there is no statistically significant difference in mechanical properties between two orthogonal directions. This HIP grade has about 8 MPa greater UTS than the equivalent VHP grade transverse direction. The transverse direction is the stronger of the two directions in VHP material.

Table 8: Room Temperature Mechanical Properties of S-200F-H Block [40]

Orientation		No. of Samples	UTS (MPa)	0.2% YS (MPa)	Elongation (%)
Longitudinal	mean	67	438	343	4.6
	std.dev.		9.682	16.74	0.5601
Transverse	mean	66	447	346	5.3
	std.dev.		10.75	16.65	0.6105

UTS was measured for S-65B purity material made by cold pressing, then sintering and finally hot isostatic pressing (CP/Sinter/HIP) instead of vacuum hot pressing (VHP) [41]. The value at 370°C is 228 MPa and the value at 605°C is 123 MPa. S-65B has BeO content at or below 1.0 wt%.

Bulk ingot beryllium will generally have lower strength than PM billet due to the differences in grain size, BeO size, and BeO distribution. Sheet is the most notable ingot product because it has lower oxygen content than sheet derived by PM, and also shows greater ductility above 200°C. Recent measurements of UTS as a function of temperature for ingot sheet are shown in Figure 17 [29]. Although the BeO content was not measured, it was expected to be less than 100 ppm. Figure 18 also shows UTS versus temperature for SR-200 (sheet of PM origin) [36].

6h Yield Strength

6h.1 VHP Block

Figure 14 also shows the tensile yield strength (YS) versus temperature for S-200F grade Be (1.5% BeO, 98.5% Be, impact ground, VHP) [19]. Values range from 263 and 262 MPa at room temperature for longitudinal and transverse directions, respectively, to 90 and 95 MPa for longitudinal and transverse directions at 649°C. These data points are mean values from triplicate tests on the same lot of material.

Figure 15 shows data for temperature to 800°C for a grade no longer in production [14] which had lower strength than S-200F. The plot is useful because it indicates the trend of yield strength at higher temperatures. Note that YS for this grade at 800°C is about 22% of the YS at room temperature.

Figure 16 shows a plot of 0.2% YS versus temperature for S-65B grade Be (1.0% BeO, 99.0% Be, impact ground, VHP) [21]. Values range from 270 and 273 MPa at room temperature for longitudinal and transverse directions, respectively, to 119 and 122 MPa for longitudinal and transverse directions at 600°C.

6h.2 HIP Block

Table 8 above lists data for room temperature mechanical properties for a sample of S-200F-H. As expected for a HIP product, there is no statistically significant difference in mechanical properties between two orthogonal directions. This grade has a 0.2% YS that is 80 MPa greater than the YS for an equivalent VHP grade in the transverse direction. The transverse direction is the stronger of the two directions in VHP material.
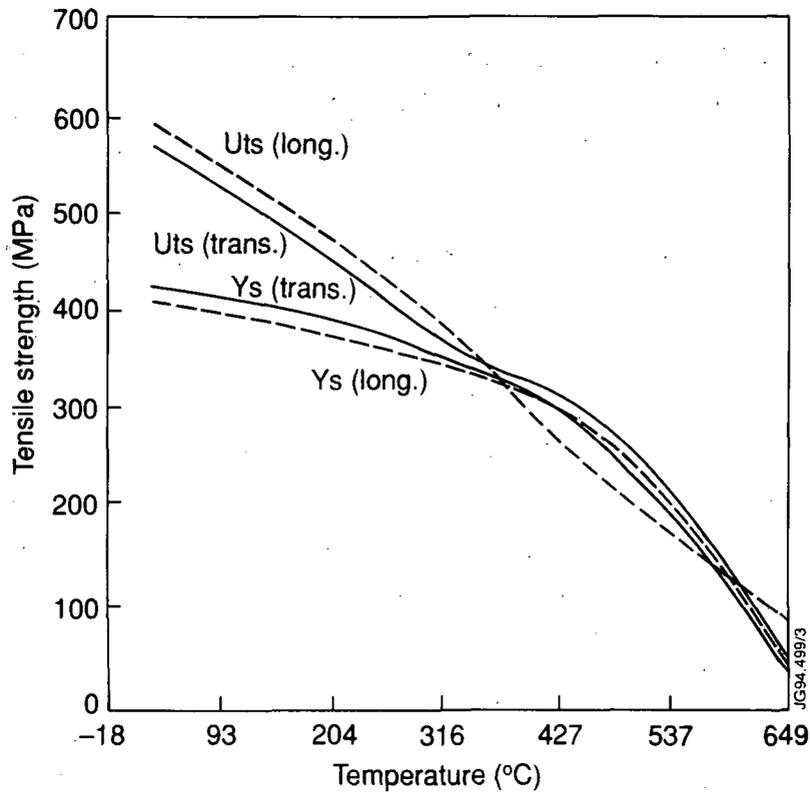
SR–200 Cross-rolled sheet

Fig. 18   Ultimate tensile strength and 0.2% offset yield strength
for SR-200E PM Be sheet [36].
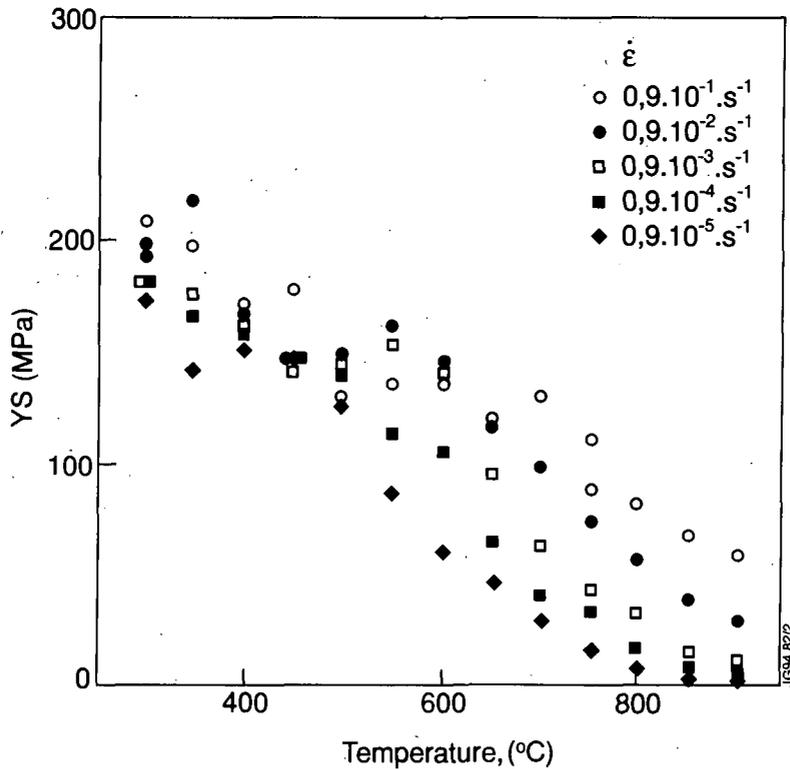
S65 Be VHP 0.6 wt % BeO

Fig. 19   0.2% offset yield strength as a function of temperature
and strain rate for S-65 VHP Be [42].

49

The behaviour of YS versus temperature was measured for S-65 purity material made by the (CP/Sinter/HIP) method instead of (VHP) [41]. The value at 370°C is 133 MPa and the value at 650°C is 80.7 MPa.

The effects of strain rate upon yield strength may be important particularly as the research aspects of the ITER programme require PFCs to sustain variable loadings in normal operating regimes and extreme loadings under upset (disruption) events. Usually YS values are quoted for strain rates, in particular tensile strain rates of 10^{-6}/sec. We have found only limited data for the effects of strain rate, cf. Figure 19 for a sample of S-65 (VHP, 0.6wt% BeO) [42]. Clearly the most extreme influence of strain rate on YS occurs at elevated temperatures i.e. nearly fivefold increase at 800°C for a strain rate change of five orders of magnitude.

6h.3 Ingot and Powder Metallurgy Sheet

Recent measurements of yield strength [29] as a function of temperature for ingot sheet are shown in Figure 17. Although the BeO content was not measured, it is expected to be less than 100 ppm. Yield strength versus temperature for cross-rolled sheet of PM origin [36] is shown in Figure 18.

6i   Uniform Elongation

Uniform elongation is the elongation at maximum load and immediately preceding necking in a tensile test. There is so little necking at room temperature that the tabulated data for room temperature percent elongation can be taken as uniform elongation. However, the reduction in area data discussed below shows that this approximation is not valid at higher temperatures.

6k   Total Elongation

Total elongation is the total amount of permanent extension of a test piece broken in a tensile test.

6k.1   VHP Block

Figure 20 shows a plot of total elongation versus temperature for S-200F grade Be (1.5% BeO, 98.5% Be, impact ground, VHP) [19]. Total elongation is expressed as

50
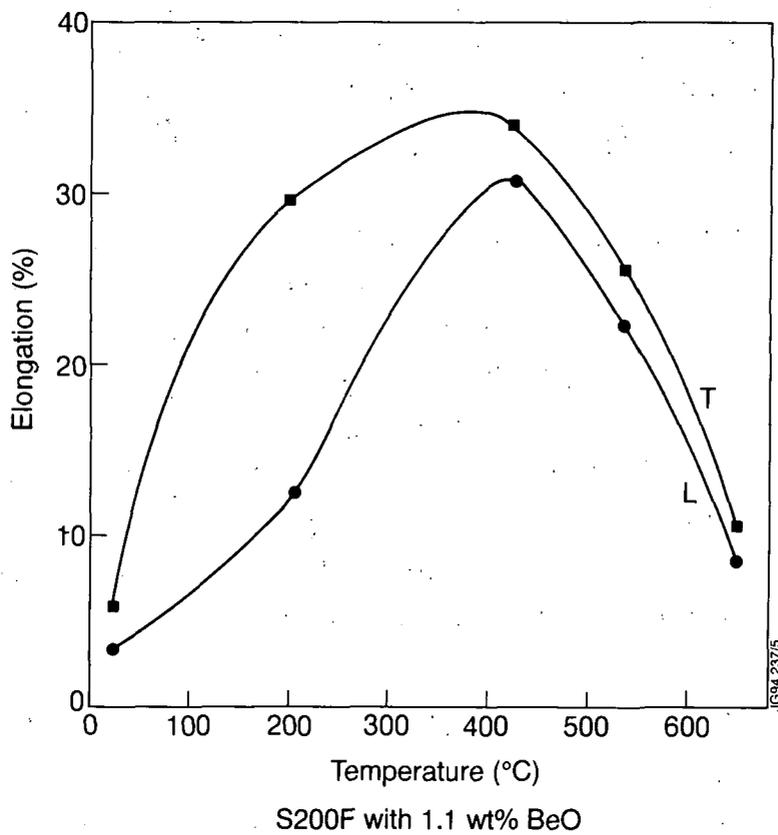
Fig. 20   Percent elongation for S-200F VHP Be [19].
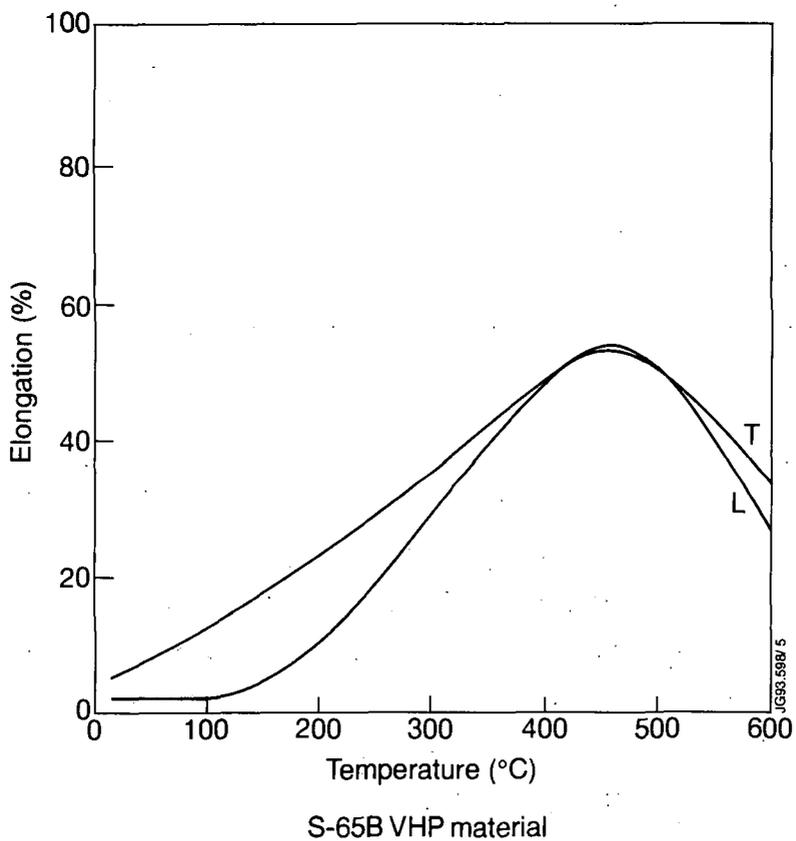

Fig. 21   Percent elongation for VHP S-65 Be [21].

percent elongation. Values range from 3.4 and 6.1 percent elongation at room temperature for longitudinal and transverse directions respectively to 30.4 and 33.8 percent elongation for longitudinal and transverse directions at 427°C. Percent elongation decreases as temperature increases from 427°C to 649°C. Note that the data points are mean values from triplicate tests on the same lot of material.

Figure 21 and Table 9 show the behaviour of percent elongation versus temperature for vacuum hot pressed S-65B grade Be (0.9% BeO, 99.0% Be, IG, VHP) [21]. Values range from 3.0 and 5.4 percent elongation room temperature for longitudinal and transverse directions respectively to 50.0 and 49.5 percent elongation for longitudinal and transverse directions at 400°C. Percent elongation decreases as temperature increases from 400°C to 600°C. The value of elongation at 400°C is a significant improvement over the values for S-200F grade material.

Table 9: Percent elongation versus temperature for vacuum hot pressed S-65B Be (1.0% BeO. 99.0% Be, impact ground, VHP) [21].

| Temperature (°C)	Orientation	Elongation (%)
20	L	3.0
20	T	5.4
200	L	10.2
200	T	23.4
400	L	50.0
400	T	49.5
600	L	25.2
600	T	31.9

6k.2   HIP Block

Percent elongation was measured for S-65B purity material made by the (CP/Sintering/HIP) method instead of (VHP) method [41]. These results are the average of four tests: at 370°C the elongation is 49.4%; the value at 650°C is 38.5%.

Table 8 above lists data for room temperature mechanical properties for S-200F-H for which there is no statistically significant difference in percent elongation between two orthogonal directions. This HIP grade has 4.9% elongation when longitudinal and transverse direction values are averaged together.

52

IM sheet with BeO circa 100ppm
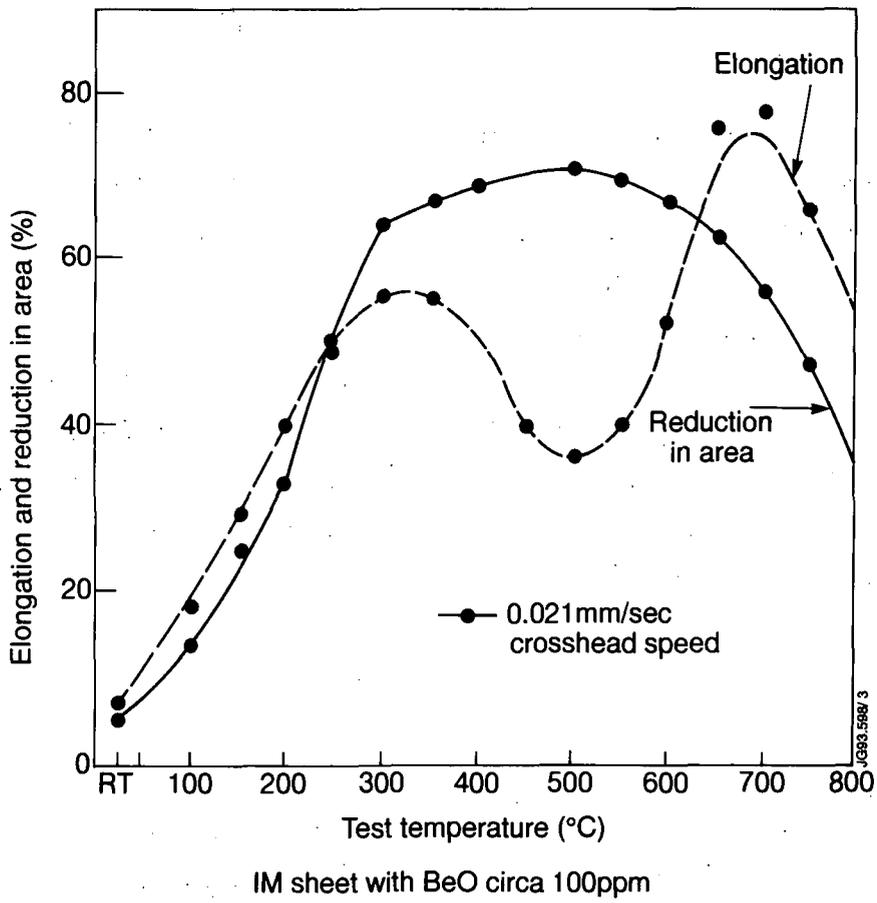
Fig. 22   Percent elongation and reduction in area for IM Be sheet [29].

SR-200E Cross–rolled sheet
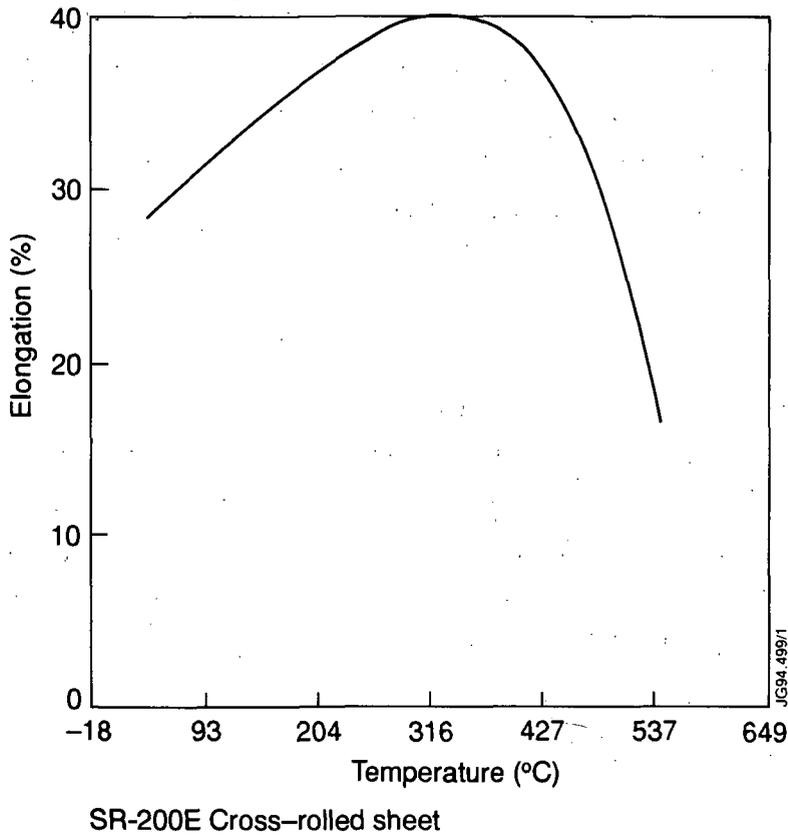
Fig. 23   Percent elongation for SR-200E PM Be sheet [36].

6k.3   Ingot and Powder Metallurgy Sheet

Figure 22 shows percent elongation as a function of temperature for ingot sheet and SR-200 powder metallurgy sheet [29]. Figure 23 shows percent elongation as a function of room temperature for SR-200 sheet (cross-rolled sheet of PM origin) [36]. Note that the in-plane elongation of IM sheet is lower than PM sheet up to 200°C, but that elongation for IM sheet is greater above that temperature. Out-of-plane elongation (or through-thickness elongation) is much lower than in-plane percent elongation for both types of sheet. For example, it is estimated that room temperature out-of-plane elongation for PM sheet is less than 1% [36]. Although there is no published data, IM sheet is thought to have greater out-of-plane elongation; it has performed better in elevated temperature bend formability tests [14].

6l   Reduction of Area

6l.1   VHP Block

Figure 24 plots the reduction in area versus temperature for S-200F (1.5% BeO, 98.5% Be, impact ground, VHP) [19]. Values range from 3.3 and 5.9 percent reduction in area at room temperature for longitudinal and transverse directions respectively to 52.5 and 54.0 percent reduction in area for longitudinal and transverse directions at 427°C. Percent reduction in area decreases as temperature increases from 427°C to 649°C. Reduction in area values at the latter temperature are 7.3 and 9.7 percent, for the longitudinal and transverse directions respectively. Note that the data points are mean values from triplicate tests on the same lot of material.

6l.2   HIP Block

Measurements were made of percent reduction in area for S-65B purity material made by the (CP/Sinter/HIP) method instead of VHP [41]. These results are the average of four tests. These reported values are greater than corresponding data for S-200F VHP material.   Reported values are 66.9% reduction in area at 370°C and 29.5% at 650°C.

6l.3   Ingot and Powder Metallurgy Sheet

Figure 22 shows the percent reduction in area as a function of temperature for ingot sheet (29).
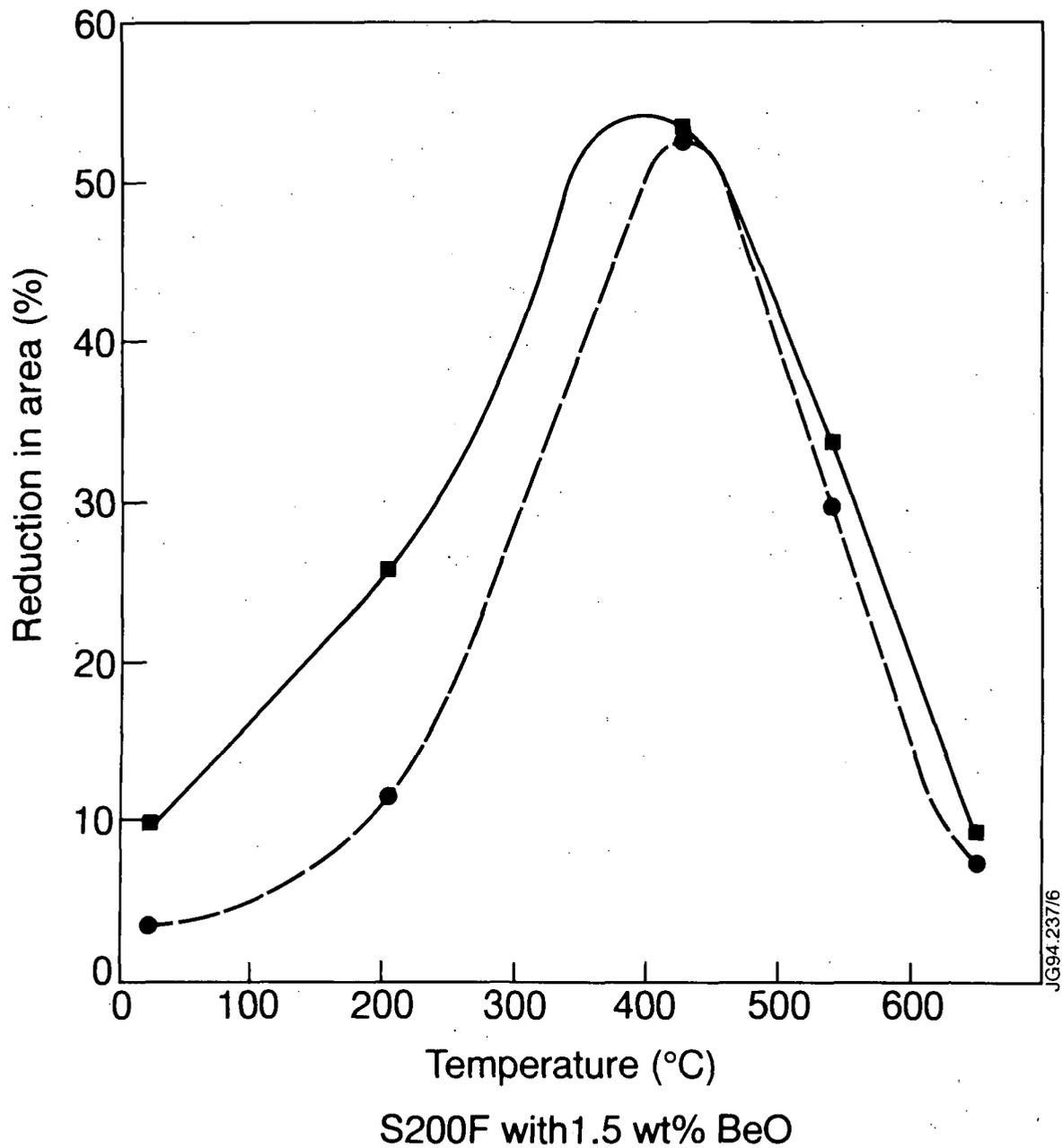
Fig. 24   Reduction in area for S-200F VHP Be [19].

6m   Creep

There is no published data on creep of modern grades of beryllium.

Webster and Crooks [43] published a study for Be grades of unknown origin. HIP, VHP and cast Be samples of various purity were evaluated. Figure 25 shows the creep rate as a function of stress for a HIP Be sample (RR243), which had 1.56 wt% BeO, 550 ppm Fe, 200 ppm C, 16 ppm Al, 30 ppm Mg, and 36 ppm Si. Figure 26 compares the creep stress needed to give a creep rate of 10^{-1} percent per second for annealed RR243 and a specimen labelled as commercial purity hot pressed Be (sample 5310). Sample 5310 had 1.70 wt% BeO, 900 ppm Fe, 500 ppm C, 300 ppm Al, 200 ppm Mg, and 200 ppm Si. Creep stress to get the same rate of deformation was approximately the same for both grades to about 800°C. The higher purity HIP grade had significantly higher creep resistance above that temperature. Creep rate is inversely proportional to grain size [43], e.g. rates for 3000 μm and 4 μm grain sizes differ by several orders of magnitude.

Webster and Crooks [44] state that the creep strength of beryllium is significantly improved when the concentrations of low melting point impurities (Al, Si, Mg) found at the grain boundaries are decreased. They also reported that creep strength dropped markedly when the BeO content was substantially reduced below one percent.

Larson-Miller plots describe the empirical relationship of the engineering stress and time to rupture as a function of temperature. The following relationship is assumed:

$$(T + 460) (\log t_r + C) = m$$

where T is the temperature in °F, t_r is the time to rupture, C is a constant that depends on the metal, and m is dependent on the initial engineering stress. Once C is determined, a master plot of engineering stress versus m allows one to predict rupture time for any combination of initial stress and temperature. Figures 27 and 28 show Larson Miller plots for S-200E grade VHP Be and SR-200E grade Be sheet [36]. Note that both materials are made from attrited powder whereas current Be grades are made from impact ground powder. The former have composition limits of 2.0 wt% BeO, 1800 ppm Fe, 1500 ppm C, and 1600 ppm Al.
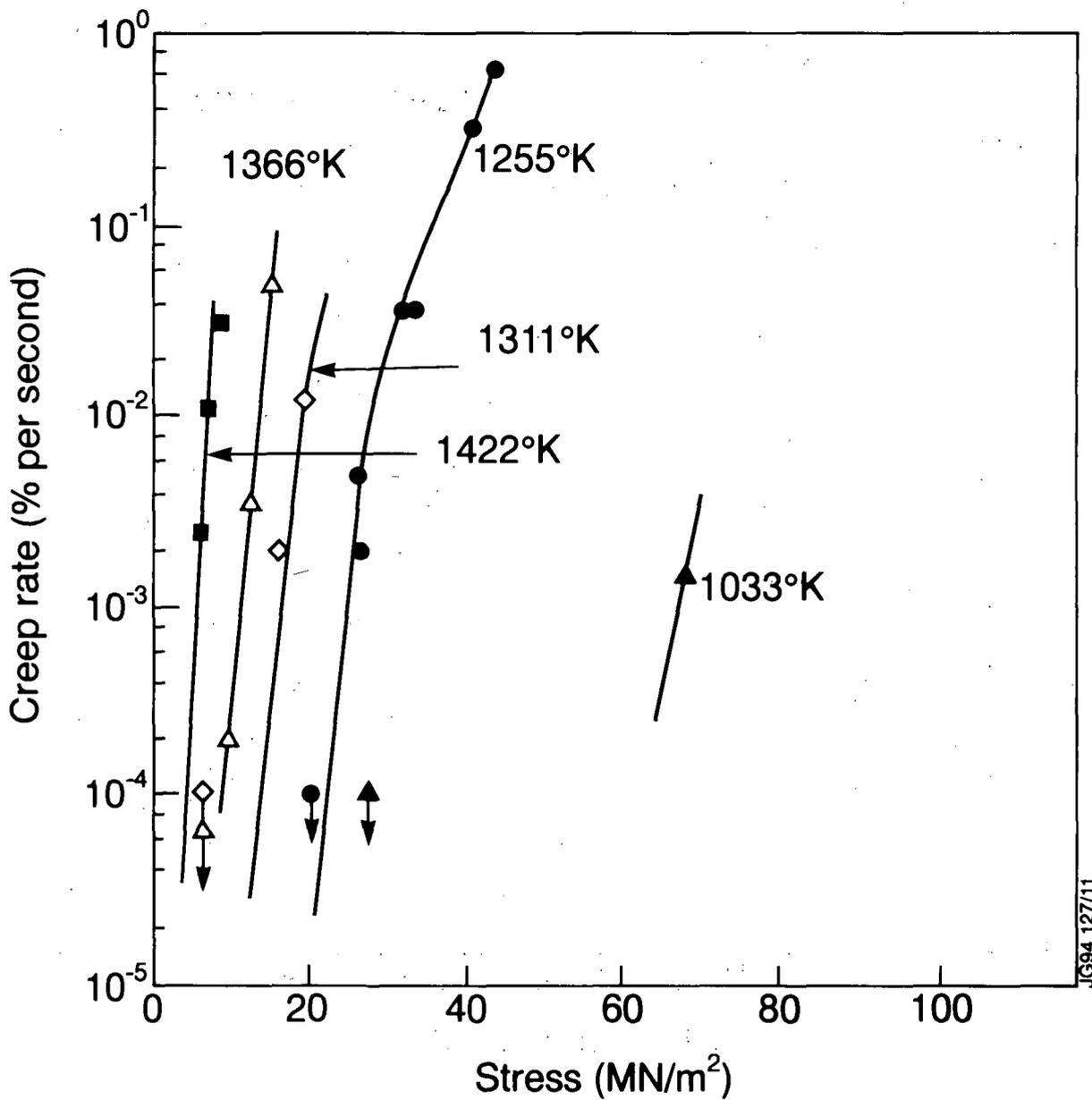
Fig. 25   Creep rate as a function of stress and temperature for sample
RR243 (HIP, 1.56 wt% BeO, 550 ppm Fe, 200 ppm C, 16 ppm Al, 30 ppm Mg,
and 36 ppm Si) [43].
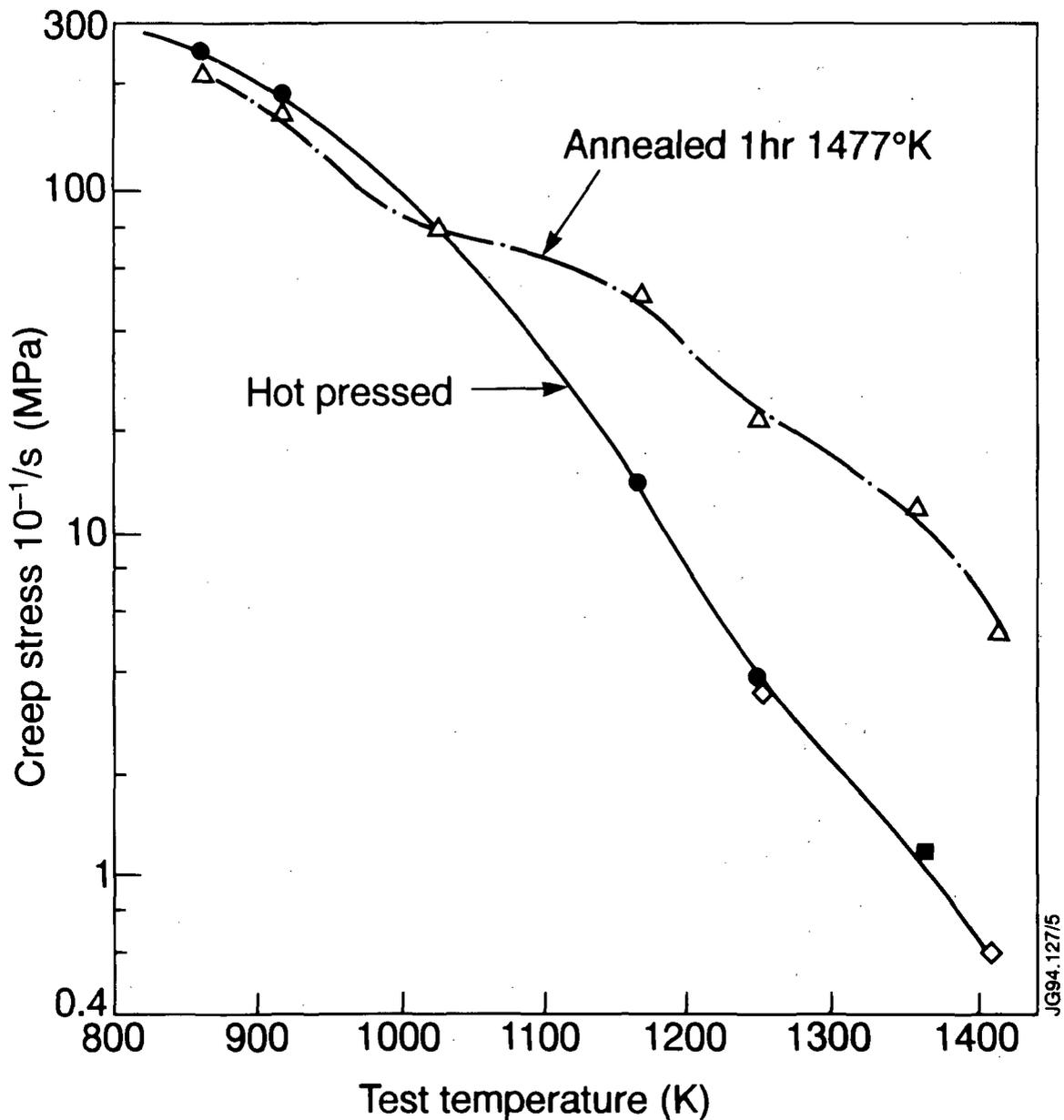
Fig. 26   Creep stress needed to give a creep rate of 10⁻¹ percent per second as a function of temperature for annealed RR243 (HIP, 1.56 wt% BeO, 550 ppm Fe, 200ppm C, 16 ppm Al, 30 ppm Mg, and 36 ppm Si) and sample 5310 (VHP, 1.70 wt%BeO, 900 ppm Fe, 500 pmm C, 300 ppm Al, 200 ppm Mg, and 200 ppm Si) [43].
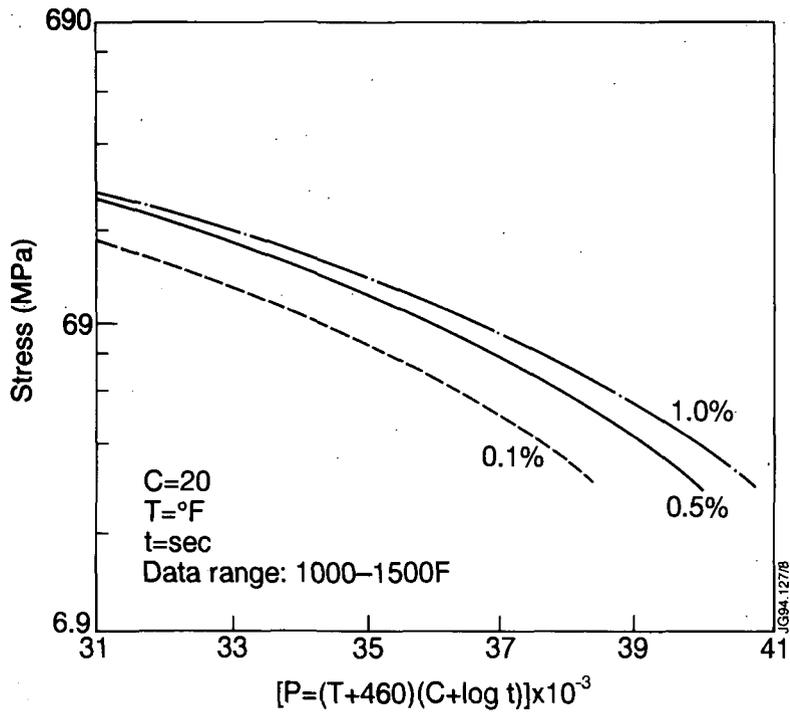
S-200E VHP block with 2 wt% BeO

Fig. 27 Larson-Miller parameter versus stress for S-200E VHP block [36].
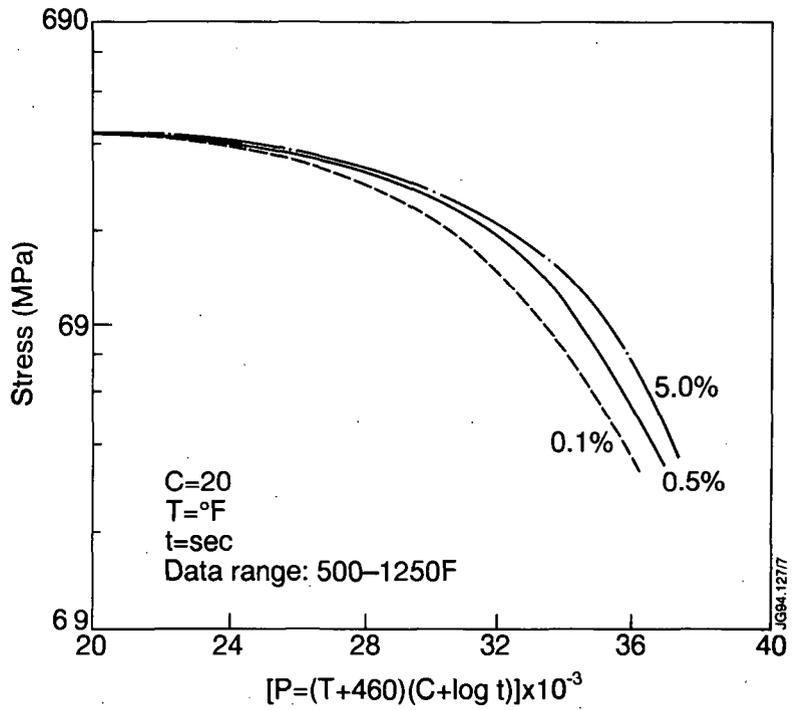
SR-200E sheet with 2 wt% BeO

Fig. 28 Larson-Miller parameter versus stress for SR-200E PM Be sheet [36].
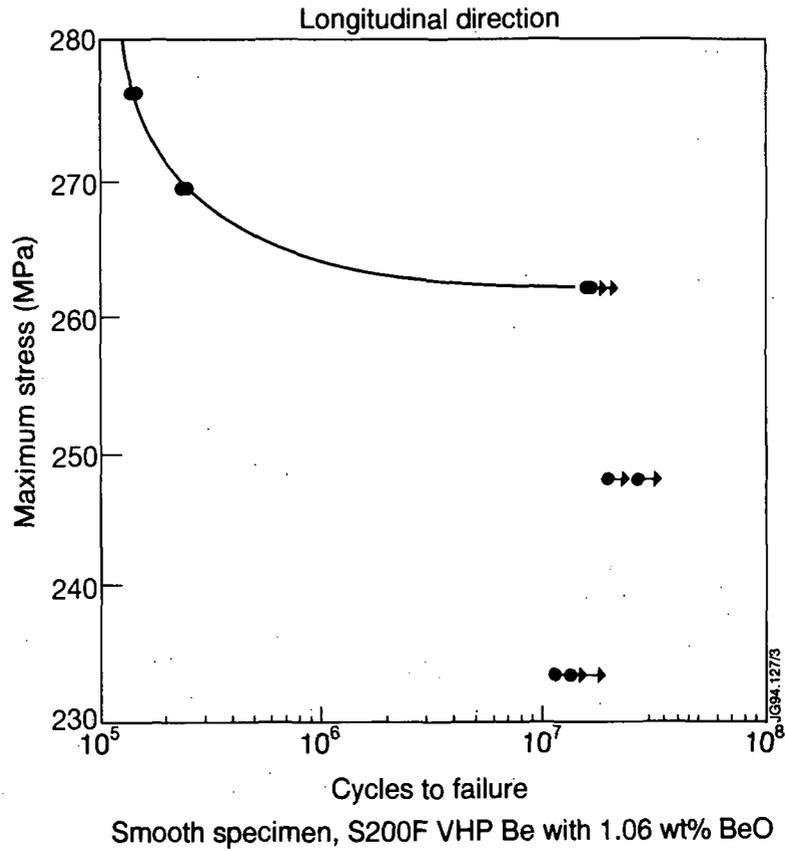
Smooth specimen, S200F VHP Be with 1.06 wt% BeO

Fig. 29   S/N curve for smooth specimen room temperature rotating beam fatigue
data at R = -1 for S-200F VHP Be [19].

Smooth specimen, S200F VHP Be with 1.06 wt% BeO
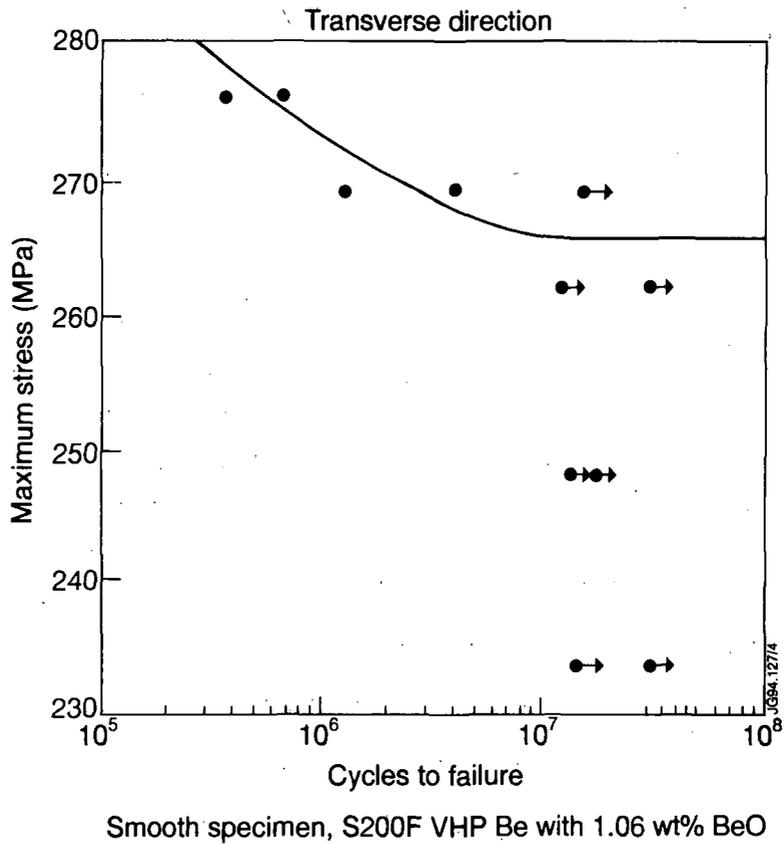
Fig. 30   S/N curve for smooth specimen room temperature rotating beam fatigue
data at R = -1 for S-200F VHP Be [19].

6n Fatigue

Haws [19] measured smooth room temperature fatigue for S-200F grade VHP Be with a Krouse rotating beam fatigue machine according to ASTM specification E-466. Transverse fatigue properties appear to be greater than longitudinal properties. Figures 29 and 30 show S/N curves for the longitudinal and transverse directions respectively. This data is for R values (ratio of minimum stress to maximum stress) of -1. Fatigue life (10^7 cycles) is 262 MPa and 266 MPa for the transverse and longitudinal directions respectively. The above tests are a case where the mean stress is zero.

6o Fracture Toughness

Fracture toughness testing is difficult in beryllium. The relatively brittle nature of the metal makes nucleation of a fatigue crack difficult using the ASTM E-399-83 standard. Fatigue cracks are successfully nucleated using compressive forces; a precracking stress ratio of R < 0 is successfully used rather than the value of +0.1 usually required by the ASTM standard. The ASTM fracture toughness committee E-24 now recommends in addendum A-2 to the ASTM E-399-83 standard a change in the testing procedure which would allow fatigue cracking to occur at up to 80% of the estimated K_{IC} value with a negative stress ratio.

Grensing et al. [27] measured room temperature fracture toughness of VHP consolidated attrition ground powder (S-200E grade Be) having 1.1 wt% BeO, VHP impact ground powder (S-200F grade Be) having 0.67 wt% BeO and VHP consolidated atomised spherical powder (ASP) having 0.37 wt% BeO according to ASTM standard E399-83 using a stress ratio of R = -2. Lemon and Brown [45] report fracture toughness for VHP S-65 grade Be having 0.7 wt% BeO using a stress ratio of R = -3. Haws [37] measured fracture toughness according to ASTM-399 for multiple samples taken from a single production lot of S-200F grade beryllium using an unspecified stress ratio. Production data for S-200F-H, a HIP version of S-200F, has also been reported [46].

A summary of results at room temperature for different grades is shown in Table 10 below.

Table 10: Room Temperature Fracture Toughness for VHP Beryllium from Different Powder Sources

Material	Specimen Orientation	Fracture Toughness K_{IC} (MPa-m$^{-1/2}$)	Std. Deviation	n	% BeO	Grain Size (μm)	Reference
VHP S-200E	L-T T-L	9.85[1] 11.05[1]	0.363 0.81	11 11	1.7	8.4	44
VHP S-200E	L-T T-L	10.3 12.3	0.468 0.230	5 3	1.1	NA	45
VHP S-200F	L-T T-L	10.62 12.31	-	1 1	0.67	8.7	20
VHP S-200F	L-T T-L	9.5 10.9	0.28 0.38	3 4	1.06	NA	35
VHP S-65	L-T T-L	10.6 10.9	0.77 0.72	3 3	0.7	11.4	44
VHP ASP2	T-L	13.59	-	1	0.37	13.2	20
HIP S-200F-H	L-T T-L	9.07 9.16	0.41 0.32	3 3	0.78	7.2	46

(1). These are K_q values because $K_{max} > 0.6K_{IC}$.
(2). Atomised Spherical Powder.
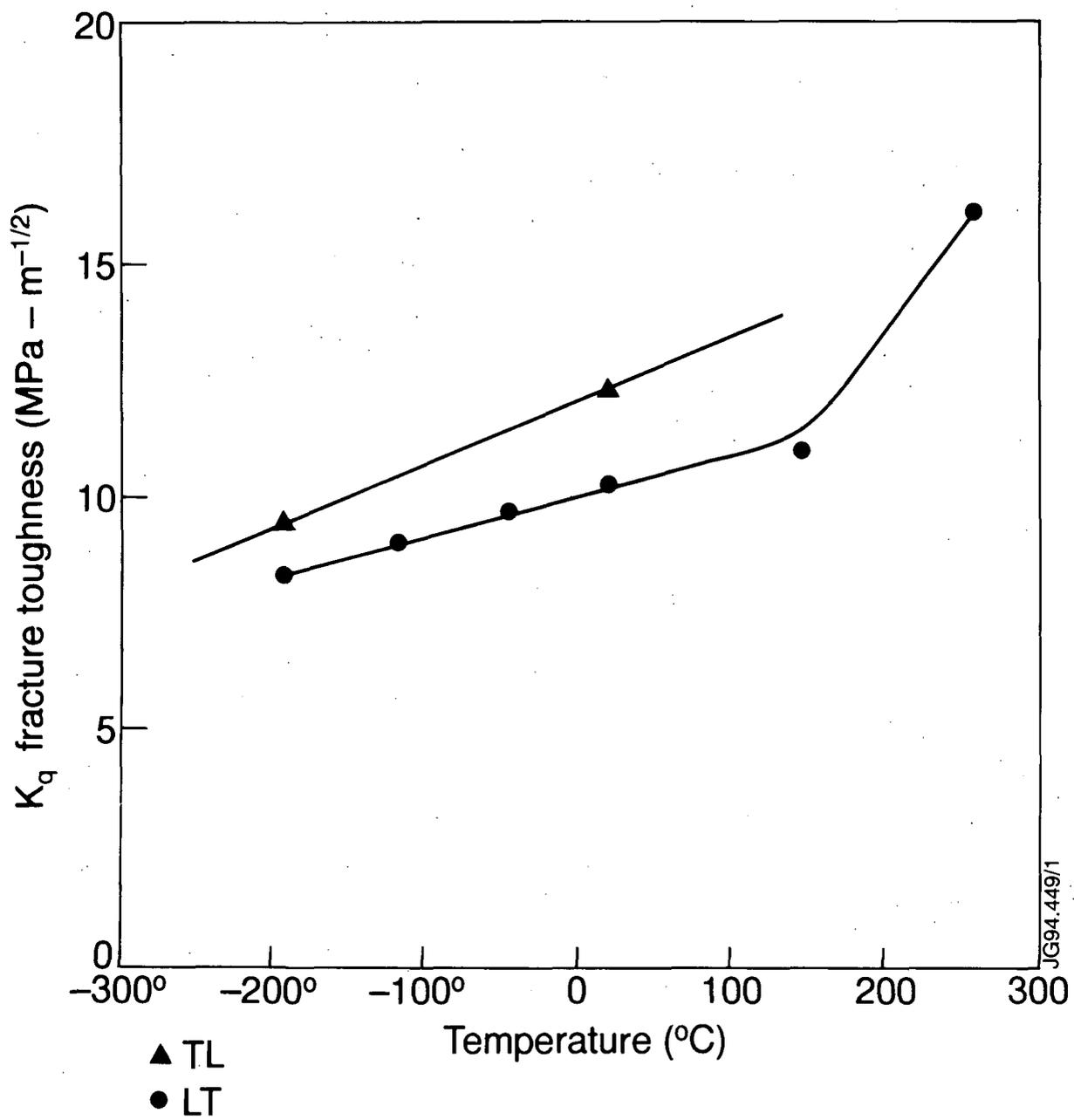
Fig. 31   Plane strain fracture toughness (K_q) for S-200E VHP Be [47].

Specimens labelled L-T were cut from a VHP billet so that the testing load was applied parallel to the longitudinal (L) or pressing direction, and the crack was propagated perpendicular to the pressing direction, transverse (T). In T-L specimens, the testing load was applied perpendicular or transverse (T) to the pressing direction, and the crack was propagated parallel to the pressing direction (L). Values for K_{IC} range from 9.9 to 13.59 MPa-m$^{-1/2}$. S-200F exhibits a slight improvement in fracture toughness compared to S-200E. There is insufficient data to show whether atomised spherical powder material consistently shows better fracture toughness than the other grades. Further testing is warranted.

Figure 31 shows the general trend of plane strain fracture toughness versus temperature for S-200E grade beryllium [47]. This testing was done with compact tension specimens according to ASTM E-399-72 using a stress ratio of R = -1. Fracture toughness ranges from approximately 8 to 16 MPa-m$^{-1/2}$ as temperature increases from -200°C to + 200°C.

7. PROPERTIES AFTER NEUTRON IRRADIATION

The effects of neutron irradiation on the thermomechanical properties of beryllium are very difficult to summarise because testing to date has been done for widely differing combinations of irradiation conditions (flux, fluence, temperature, time), post irradiation testing conditions (temperature, pre-test annealing) and beryllium grades [48]. Often the forms of beryllium tested were non-commercial specimens made in the laboratory and not characterised in the unirradiated condition. Irradiation temperatures often differed substantially from temperatures of post irradiation testing, which makes extrapolation of the data to ITER operating conditions problematic. None of the tests were conducted with 14 MeV neutrons such as ITER will produce. However, there is expected to be an overlap in energy spectrum between fission test reactor neutron spectrum and the neutron spectrum produced by reflection of 14 MeV neutrons from the ITER stainless steel supporting structure, so testing in existing fission test reactors may provide valuable baseline data.

Qualitative trends for beryllium thermomechanical properties after fission test reactor irradiation have been summarised by Gelles [48]. Beryllium structure is altered during neutron irradiation by displacement damage and by transmutation. Displacement damage generates a wide range of defects in the beryllium crystal structure. High

defect concentrations are also produced. Transmutation produces helium in the crystal structure which acts as defects and which produces swelling. The effect of defects and swelling on thermomechanical properties depends on the irradiation temperature and on the temperature during post irradiation testing. As noted above, widely differing combinations of these variables have been studied. The broad trends stated by Gelles generally refer to the highest of the two temperatures. At low temperatures (T < 400°C), defects from displacement damage and transmutation will block dislocation motion and thereby increase strength. Hardness follows the same trend as strength; the increase in hardness upon radiation is called radiation hardening. Percent elongation decreases upon irradiation at low temperature; this is called embrittlement. Fracture toughness is decreased by irradiation at low temperature. In general, increasing fluence (neutrons/cm^2) increases the effects on the above properties. However, once ductility has reached zero, strength will decrease with increasing fluence.

At high temperatures (T > 400°C), thermomechanical behaviour is a more complex function of fluence, time and temperature. The additional factors of defect annihilation, swelling of entrapped helium, and accumulation of helium as bubbles complicates behaviour as compared to low temperature irradiation. Gelles et al. state that above 280°C the functional dependence of strength on fluence may change from lower temperatures. Above 600°C there is considerable variation in the observed trends. Some data show decreases in strength with increased fluence and some data show increase in strength. There are generally less severe drops in percent elongation with increased fluence for T > 600°C.

It should be noted that the above results are largely for obsolete beryllium grades or beryllium manufactured in the laboratory. It is expected that commercial grades will perform much better [48]. This needs to be confirmed by experiment.

8.   CHEMICAL PROPERTIES

Beryllium has a strong affinity for oxygen which is usually present in all forms of beryllium exposed to air in the form of BeO. In a tokamak edge plasma beryllium has been shown to getter oxygen strongly.

Hydrogen does not normally dissolve to any great extent in beryllium metal.

However, the redeposition of beryllium atoms from the edge plasma onto PFC surfaces results in a co-deposition of hydrogen with beryllium. For DT pulsed and steady state devices the amount of tritium atoms trapped this way are crucial in respect of tritium inventory and accountability. For a burning DT fusion reactor precise data for this chemical/physical process would have a strong impact on the tritium handling system.

The flammability of beryllium, in particular porous beryllium under accident conditions where upon hot beryllium is exposed to air or a steam air mixture have been investigated [49, 50]. The types of beryllium used are not commercial grades of interest to fusion applications. Evidently these tests must be repeated using modern forms of Be. Mitigation of the risk of this accident scenario is evidently a system design problem.

Reactivity of beryllium with liquid metals such as sodium, potassium and lithium is low below 500° provided that the oxygen concentration of the metals is low [13]. Beryllium is attacked by hydrofluoric acid, hydrochloric acid, and alkali hydroxide solutions. It has acceptable corrosion properties in high purity cooling water at 100°C in the pH range 5.5 to 6.5, and has been used in that environment for over ten years in the Materials Testing Reactor [51]. In addition to high reactivity with oxygen, beryllium will react with carbon based materials to form beryllium carbide at temperatures as low as 750°C. Beryllium reacts with most refractory metals e.g. tungsten to form intermetallic compounds.

9. SUMMARY OF CHARACTERISATION NEEDS FOR PFC APPLICATIONS

The need of additonal characterisation of beryllium properties is coupled to the choice of operational scenarios for ITER and second to the level of analysis intended for design of PFC's. The ITER operational scenario has variously been described as 100-600°C and 100°C melting of the outer beryllium layers. Characterisation needs are respectively rather minimal or very extreme. This refers to unirradiated properties. There is insufficient data on radiation damage to beryllium.

The level of data available for most structural and other grades of beryllium is adequate for a decision to be made between the relevance of various grades to a design problem. Substantial additional characterisation is mandatory if it is intended to assess analytically lifetime of PFC's or analyse observed failure/fatigue of prototypes.

9a   Unirradiated Properties

The design of JET PFC and associated material development was based on prototypical tests, e.g. [5], [21]. The substantial thermomechanical database for various products based on S65 powders is a consequence, i.e. [21], [41]. Nevertheless some further work needs to be done for this grade of beryllium as well as for other grades.

Thermal conductivity versus temperature has been measured extensively yet needs to be more specifically defined for modern VHP grades.

The coefficient of thermal expansion (CTE) of block grades needs to be accurately measured over the whole temperature range of interest for fusion applications. Measurements of CTE for both VHP and HIP grades would be beneficial.

Electrical resistivity of block materials needs to be measured over the whole temperature range of interest for fusion applications. This needs to be done for grades with different impurity levels.

The temperature dependence of elastic modulus is described with a few data points. Additional data points may be needed.

Shear modulus needs to be measured as a function of temperature for modern beryllium grades.

There is significant scatter in room temperature Poisson's ratio and no definitive measurement of temperature dependence of this property. Thorough and precise characterisation is needed for practically all grades of beryllium.

Design of PFC may require precise stress versus strain curves for temperatures up to 1200°C. Characterisation of several grades with different BeO contents would be most useful. The relevant strain rates would also need to be considered.

Although there is sufficient data to see the trends of tensile properties with temperature, there is no complete coverage of the temperature range for all modern

grades. There is a good data set for IM sheet, and for VMP S-65 grade. It would be useful to obtain more data for S-65 grade, as it is the baseline grade for ITER. However, the above data is for aerospace relevant strain rates. A characterisation program using strain rates relevant to fusion is desirable.

There is a lack of systematic creep data and high temperature fatigue data for all beryllium grades presently in production. This may be one of the most critical deficiencies in the database, since beryllium will definitely be subjected to thermal cycles and has a design steady state operating temperature of 600°C.

A complete set of data is needed on the temperature dependence of fracture toughness, particularly for the S-65 grade. It is not possible to generate valid K_{IC} for sheet, but K_q values can be measured.

9b   Irradiated Properties

As discussed above in section 7 a complete set of property measurements of neutron irradiated commercial grade material is needed. This is the area of greatest need. The most critical properties are high temperature creep and thermal fatigue. Many authors e.g. Gelles [48] have suggested that optimizing Be for strength under unirradiated conditions may not be possible while simultaneously optimizing for high temperature resistance to radiation damage. In fact the authors know of no published data on the susceptibility of modern forms of beryllium to a well characterised thermal neutron fluence let alone to even a very low fluence of fast neutrons. Given that in a fusion reactor such as ITER thermal neutrons will certainly be present together with fast neutrons, it seems advisable to carry out measurements on specimens that are irradiated by thermal neutrons. The authors are aware of substantial efforts being made in this area. The database in this aspect of beryllium properties is as yet extremely sparse.

There is a critical need for a thorough, systematic characterisation of thermomechanical properties for commercial beryllium grades after neutron irradiation under ITER relevant fluxes, fluence and temperature. As noted above, no facilities exist for irradiation with the 14 MeV neutrons which will be produced in ITER. A characterisation program using existing fission test reactors would provide baseline data. Although previous characterisation emphasised tensile and

compressive strength testing, the ITER programme should include all the other thermomechanical properties in particular data on high temperature fatigue and creep.

The present use foreseen for beryllium is in the form of cladding. Swelling and embrittlement due to neutron irradiation are likely to be of great concern as one likely outcome would be flaking of coatings and delamination of cladding. These factors are likely to be important limitations on the life time of beryllium PFCs.

9c   Ductile Beryllium

The choice of beryllium grades by JET has been dictated by consideration of high temperature strength, ductility at 300°C and levels of high Z impurities. Fabrication techniques were developed to give several tons of materials with reproducible minimum properties. Clearly this grade has been chosen as a reference for ITER. Further developments for ITER have been foreseen to produce grades with maximum realistic ductility at low temperatures, i.e. 25-100°C. There were some references in the late 70's to a form of beryllium which had 10% elongation in three orthogonal directions [52] at room temperature, so-called "ductile beryllium" [14], [53], [54]. A wealth of scientific data shows this result to be improbable.

A single crystal of beryllium will have very different mechanical properties depending on which crystallographic direction is tested. Ductility of beryllium single crystal is virtually zero parallel to the crystallographic "c" axis. The limiting factor, therefore, in beryllium ductility is the ease of cleavage of the basal plane in the hcp structure. Stresses perpendicular to the basal planes are reduced by slip and cause cleavage.

Early work in the 60's and 70's was able to achieve ductility increases in beryllium products from 1% min. (2% typical) to the current 3% (4-5% typical) by a combination of lower oxide content, finer grain size and impurity control. Such improvements, unfortunately, have their limits since they are essentially second order effects rather than fundamental solid state changes. Selected beryllium products with 4% min. ductility may be available in the near term (at added expense) from current products. Further substantial increases in room temperature isotropic ductility are unlikely in a commercially feasible product from; i.e., it is unlikely that so-called ductile beryllium can ever be produced.

REFERENCES

[1] M. Keilhacker et al., Overview of JET Results Using a Beryllium First Wall, JET report JET-P(89)83, Dec. 1989.

[2] R.R. Parker and ITER Team, Progress in the Design of In-Vessel Components for ITER, SOFT Conference, August 1994, Karlsruhe, Germany.

[3] P. Mioduszewski et al., Joint JET-ISXB Beryllium Limiter Experiment, Final Report, ORNL, July 1986.

[4] P.H. Rebut et al., Experience in the Wall Materials in JET, JNM Vol. 167-164, pp. 172-183, 1990.

[5] E.B. Deksnis et al., Assessment of Water Cooled Beryllium Components for PFC, ICRFM-6, in print, October 1993.

[6] ITER Project, Preliminary Design Outline, March 1993.

[7] V.P. Itkin, C.B. Alcock, Phase Diagrams of Binary Beryllium Alloys, eds. H. Okamoto, L.E. Tanner, ASM International, Metals Park, Ohio, 1987, pp. 1-3.

[8] H. Altmann et al., Brazing of Beryllium to CuCrZr, SOFE 1993.

[9] L. Jacobson et al., Joining Methods for Beryllium, LLNL UCID-20750 (1986).

[10] L. Pertrizsi et al., Further neutronic analysis of European Ceramic BIT blanket for DEMO, 17th SOFT, pp. 1449-1553, London 1992.

[11] M. Billone et al., ITER Solid Breeder Blanket Materials Database, ANL/FPP/TM-263 (in press)

[12] Brush Wellman report TR-987 prepared for JET Joint Undertaking, April 1990.

[13]   Beaver and Lillie in The Reactor Handbook Volume I (Materials), C.R. Tipton Jr. edition Interscience publishers NY, 1960, pp. 897-942.

[14]   N.P. Pinto in Beryllium Science and Technology Volume 2, D.R. Floyd, J.N. Lowe editors, Plenum Press 1979, pp. 319-346.

[15]   E. Baur, R. Brunner, Dampfdruckmessungen hochsieden metallen, Helv. Chim. Acta, Vol 17, 1934, pg 958.

[16]   R.P. Tye and J.P. Brazel, Thermophysical Properties of Beryllium, Rev. Int. Hantes Temp. et Refract., t.7, 1970, pp 326-334.

[17]   F. Grensing, J. Marder, unpublished Brush Wellman report, July 1989.

[18]   R. Hultgren et al., Cited in Beryllium Science and Technology, Volume 1, ed. D. Webster and G. London, Plenum Press 1979.

[19]   W. Haws, Internal Brush Wellman Report, TM-778, 1985.

[20]   I.V. Milov et al., Izvestia Akad. Nauk, SSSR - Metaly, No. 4, 1969, pp. 82-83.

[21]   M.F. Smith et al., Thermo-Mechanical Testing of Beryllium for Limiters in ISX-B and JET, Fusion Technology, Vol. 8, July 1985, pp. 1174-1183.

[22]   J.M. Marder, Beryllium in Stress Critical Environments, J. Materials for Energy Systems, Vol. 8, June 1986 pp. 17-26.

[23]   Designing with Beryllium, Brush Wellman Catalogue of Beryllium Products.

[24]   Ingot Metallurgy Beryllium, Material Sciences Corporation Catalogue of Beryllium Products.

[25]   V. Barabash, Properties of Beryllium, ITER document, June 1994, Revision 2.

[26]   D. Hashiguchi, Brush Wellman Internal Report, TM-900, June 1988.

[27] F. Grensing et al., in 1990 Advances in Powder Metallurgy, Vol. 2, E.R. Andreolti and P.J. McGeehan eds. American Powder Metallurgy Institute, Princeton. USA 1990, pp. 27-30

[28] R. Castro, et al., Presentation at Sixth International Conference on Fusion Reactor Materials, September 27 - October 1, 1993, Stresa, Italy.

[29] D. Floyd, Thermo-Mechanical Properties of a New Ingot Metallurgy Beryllium Product Line, in Proceedings of Beryllium Technology Workshop, Clearwater, Florida, Nov. 1991, EGG Report EGG-FSP-10017, G.R. Linghurst ed.

[30] K. Sonnenberg et al., Damage to inner wall Inconel Tiles, JET Progress Report 1984, p. 38.

[31] Metals-Mechanical Testing: Elevated and Low Temperature Tests, Metallography Vol. 3.01, ASTM, Philadelphia 1992.

[32] Thermophysical Properties of Matter, Vol. 1, Thermal Conductivity of the Metallic Elements and Alloys, Y.S. Touloukian et al. IFI/Plenum Data Corporation, New York 1970, pp. 18-24.

[33] F. Grensing, Internal Brush Wellman Memo, April 17, 1991.

[34] W. Haws, Internal Brush Wellman Report, TM-894, 1988.

[35] W. Haws, Internal Brush Wellman Memo, July, 1983.

[36] Aerospace Structural Materials Handbook, US DOD Mechanical Properties Centre, 1990 Addendum.

[37] W. Haws, Internal Brush Wellman Report TM-890, 1988.

[38] M.P. Baldwin, AWRE report O-49/70 (1970), as cited by G. Petzow et al., "Beryllium and Beryllium Compounds" in Ullmans Encyclopaedia of Industrial Chemistry, 5th ed, VCH Verlagsgesellschaft, Weinheim, Germany 1985.

[39]   I.I. Papirov cited by V. Barabash op cit [25].

[40]   C. Skillern, Internal Brush Wellman Memo, December 1, 1992.

[41]   A.J. Stonehouse, J. Vac. Sci. Tech. (4) #4(3), May/June, 1986.

[42]   Th. Lieven, Private Communication.

[43]   D. Webster and D.D. Crooks, Met. Trans. A., Vol. 6A, November 1985, pp. 2048-2054.

[44]   D. Webster and D.D. Crooks, Met. Trans. A, Vol. 7A, September 1976, pp. 1307-1315

[45]   D.D. Lemon and W.F. Brown, Int. J. of Testing and Evaluation 1(2), 1973, pp. 152-161.

[46]   D. Barclay, Brush Wellman Internal Memo, June 8, 1993.

[47]   W.O. Shabbits and W.A. Logsden, J. of Testing and Evaluation, 1(2), 1973, pp. 110-118.

[48]   D. Gelles, ICFRM-6, Stresa, Italy, September 1993.

[49]   J. Blumenthal, M.J. Santy, Behaviour of Beryllium in Simulated Launch Pad Abort Environments, Semdia Rep SCDC-65-1637 (1965).

[50]   G.R. Smolik et al., Implications of Beryllium in Steam Reactions in Fusion Reactors, JNM, Volume 191-194 (1992) pp. 153-157.

[51]   W.E. Berry, Corrosion in Nuclear Applications, John Wiley and Sons, Inc., NY, NY, 1971, pp. 157-162.

[52]   V. Ivanov et al., Phys. Met. Metall. 47 (2), pp. 168-173 (1977).

[53]   F. Aldinger in "Beryllium Science and Technology" Vol. 1, D. Webster and G. London, eds., Plenum Press, 1979 pp. 7-114.

[54]   H.J. Saxten and G.J. London in "Beryllium Science and Technology" op. cit [53].

APPENDIX A

JET SAFETY EXPERIENCE

The principal hazard arising from the use of beryllium is injury or disease following the inhalation of beryllium dust or dust comprising various beryllium compounds. It is noted that beryllium oxide is used industrially due to its refractory properties (melting point 2570°C) and that safe handling procedures for beryllium and for components contaminated by beryllium/beryllium compound dust have been instigated in various manufacturing and research establishments. JET has had the most exhaustive experience in the use of PFC for fusion and the various handling procedures developed there are herein reported.

The internal surfaces of JET have been contaminated with beryllium either evaporated for density control or as a result of localised melting due to high heat loads. An extensive programme of safety has been successfully implemented on JET [1] based on WHO recommendations and UK Health and Safety Regulations [2].

JET practice is to limit the maximum airborne contamination due to beryllium to a beryllium-worker in a controlled access area without protection to 0.2 μgm/m^3 (1/10th the industrial standard of 2 μgm/m^3). Similarly surface contamination levels of 10 μg/m^2 are the maximum allowed (vs 100 μgm/m^2 industrial standard). The presence of beryllium either in the form of airborne dust or as surface contamination is detected by analysing filter or smear samples by the atomic absorption spectroscopic method. JET also has used laser induced emission spectroscopy as a detector for the presence of airborne beryllium dust without relying upon this method to determine concentrations.

JET has now had two major and lengthy interventions to the beryllium contaminated vacuum vessel, the most recent one lasting nearly two years. During the latter operation decontamination has reduced initial airborne beryllium concentration from values of up to 10^4 μgm/m^3 which required working in full biological protection suits to values which allow working without dust masks. For further details of the aggressive decontamination methods required to achieve this see Scott et al. [3].

It is felt by the authors of this review that safe working practices based upon the JET experience can readily be developed for any controlled fusion experiment to work with beryllium PFC's provided sufficient care is taken in demarcating those areas of

the device and of supporting laboratory that require special attention. In any experiment using DT for ignition studies and/or to investigate the burning of a DT plasma, tritium safety related issues and the need for handling irradiated components are likely to predominate in how safe working practice is to be implemented even allowing for remote handling of the most severely activated parts.

References for Appendix A

[1]   Code of Practice for the Safe Use of Beryllium at the JET Laboratory, JET report JET-SR (89)02, Issue 4, July 1992.

[2]   UK Health and Safety Executive Guidance Note EH/13 Beryllium: Health and Safety Precautions.

[3]   Scott et al., Decontamination of JET Vacuum Vessel from Beryllium and Tritium, 17th SOFE Proceedings, Vol. 2, pp. 1216-1219, Elsevier 1993.

MATERIALS PROPERTIES DATA FOR FUSION REACTOR PLASMA FACING CARBON-CARBON COMPOSITES

T. D. Burchell[1]
Metals and Ceramics Division
Oak Ridge National Laboratory
Oak Ridge, Tennessee,
United States of America

T. Oku
Faculty of Engineering
Ibaraki University
Hitachi 316
Japan

Abstract. A summary of materials properties data for fusion reactor plasma facing carbon-carbon composites is given. Data are reported for 1D, 2D and 3D carbon-carbon composites materials. Properties reported include: physical properties, mechanical properties, corrosion effects and tritium behavior. The effect of neutron irradiation on properties of carbon-carbon composites is discussed and available data are reported.

1. MATERIALS

Carbon fiber composites (CFCs) or carbon-carbon (C/C) composites are a class of carbon materials widely used in tokamak devices. Carbon-carbon composites are comprised of two components, carbon fibers and a carbon matrix. Generally, C/C composites used in plasma facing components (PFCs) are heat treated during their production to a sufficient temperature (>2500°C) to ensure that both the fiber and matrix are graphitized and the material is therefore actually a graphite/graphite composite. Carbon-carbon composites are stronger and tougher than graphites, yet retain the excellent machinability exhibited by graphites. Carbon-carbon composite materials are, however, significantly more expensive than graphites. Carbon-carbon composite materials are typically described as being uni-directional (1D), two-directional (2D), or three-directional (3D), indicating the number of fiber bundle directions that a composite may possess. In 2D C/C composites, the fibers, in the form of multi-filament tows, are woven into a cloth. Alternatively, carbon filaments may be sprayed from a spinneret to form a felt or mat. The felt (or woven cloth) is then layered to build a "thick" structure. In a 3D C/C composite the fiber bundles are usually mutually perpendicular, as shown in Fig. 1. Multi-directional C/C composites (4D, 5D) are also available. Carbon fibers derived from a vapor phase growth process which possess very high thermal conductivity are also available.

The crystal structure within a carbon filament depends upon the fiber precursor, i.e., pitch, polyacrylonitrile (PAN) or rayon, and the specific condition of manufacture such as pretreatment, spinning condition, and filament cooling rate. Recently, the microstructures of pitch derived carbon fibers have been reported [1]. PAN fiber structures have also been

described [2, 3]. Figure 2 shows a core-sheath model of a PAN fiber. In the well ordered sheath region of the fiber depicted in Fig. 2, the graphitic crystal planes can be considered to be stacked such that the crystallographic <c> direction is radially oriented and the two crystallographic <a> directions are axial and circumferential.
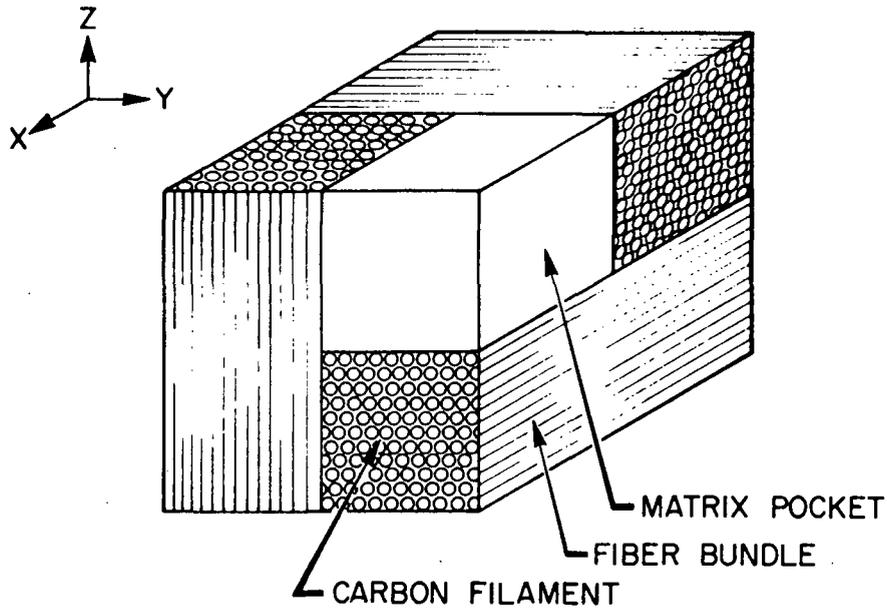

FIG. 1. The structure of an orthogonal carbon-carbon composite showing the three mutually perpendicular fiber reinforcement directions (X, Y, and Z).
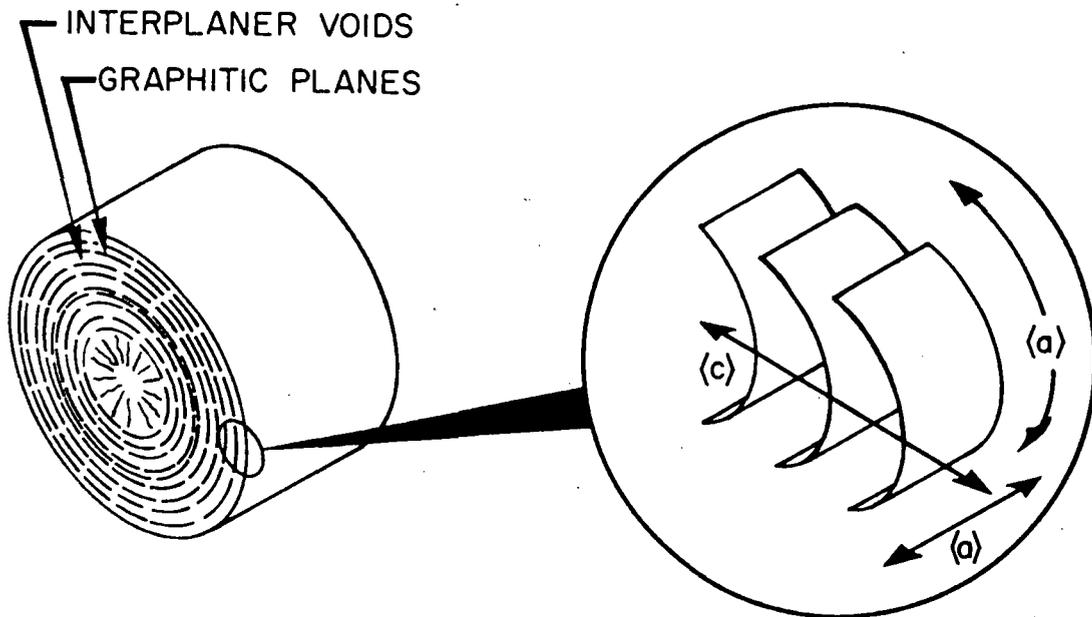
CORE-SHEATH MODEL

FIG. 2. The core-sheath model of PAN derived carbon fiber structure showing the crystallographic <a> and <c> directions in the well ordered sheath region of the fiber.

78

The manufacture of C/C composites involves two basic processing steps—preform production (weaving, lay-up, needling, piercing etc.) and preform densification. The preform is prepared from carbon fibers derived from either pitch, PAN, or rayon precursors and which generally have diameters in the range 7-15 μm. The woven preform is converted into a densified composite material by repetitive impregnations, using resins or pitch, followed by carbonization and graphitization. Alternatively, densification can be achieved using chemical vapor infiltration (CVI) or a combination of pitch or resin impregnation and CVI. Typically, final densities in the range 1.9-2.0 g/cm^3 can be attained by several reimpregnations, carbonizations, and graphitizations. Figure 3 shows flow diagrams for typical C/C production processes. The entire production process is lengthy, taking up to nine months from preform preparation through final machining. A typical finished 3D C/C composite would have a fiber volume fraction <50%, distributed in the three fiber axes, and additionally would contain approximately 35 percent impregnant derived matrix graphite. The balance of the composite volume is porosity, which is distributed in the fiber bundles, between the fiber bundles, and in the matrix pockets. A variation of the more typical processing routes is where the carbon-carbon composite is further impregnated with a metal, e.g., Cu or Ag. Such materials should offer improved thermal conductivities. However, no data has been published to date on such materials.
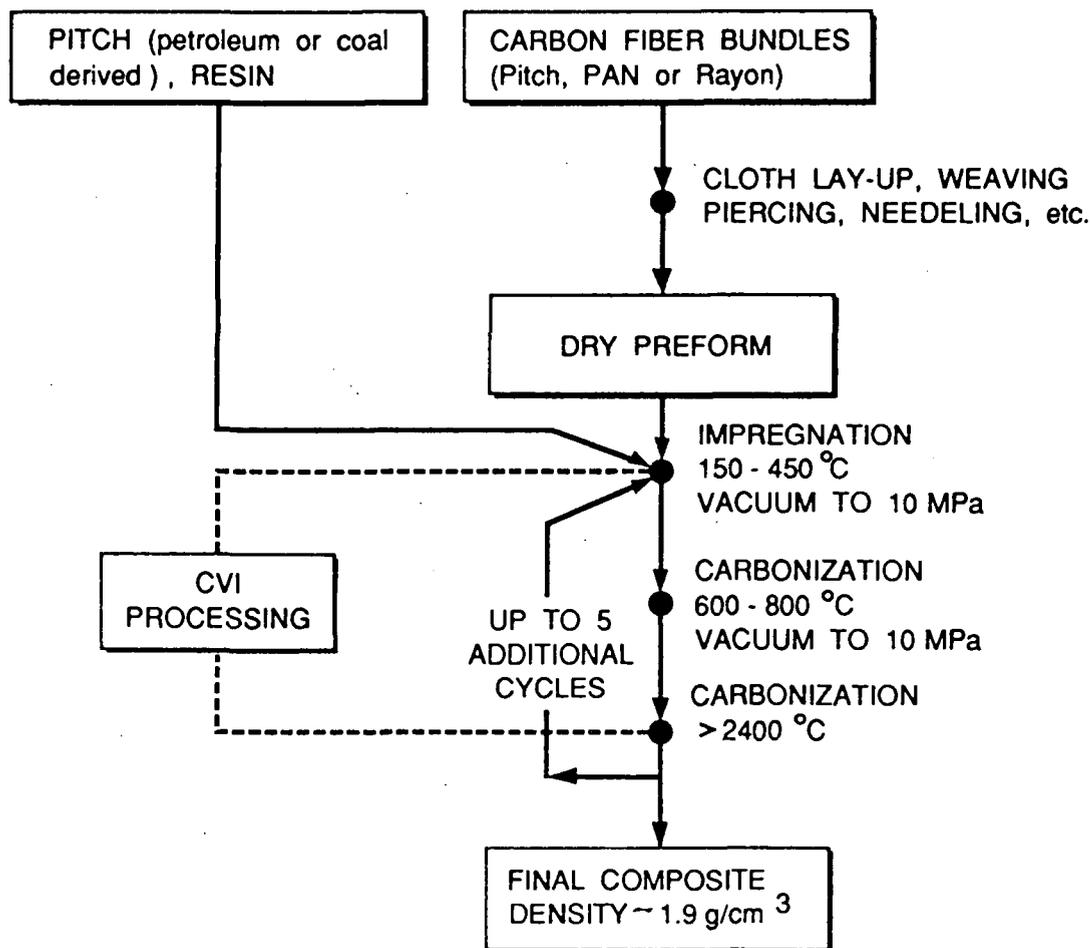

FIG. 3. Flow diagram for typical carbon-carbon composite manufacturing processes: (a) liquid impregnation route; (b) carbon vapor infiltration route.

Several factors will influence the properties of C/C composites, including fiber type, preform design, matrix precursor, and processing history. Consequently, different grades of C/C composites will possess markedly differing properties. The properties of graphite or C/C composites, particularly the electrical resistivity, thermal conductivity, strength and thermal expansivity will be strongly influenced by the final heat treatment temperature. The dependency of thermal conductivity of two C/C composites on final heat treatment temperature is reported in section 2, Physical Properties. The following property trends apply:

(i) strength increases with temperature due to thermal closure of microcracks,

(ii) the coefficient of thermal expansion is very small ($\sim$1.0 $\times$ 10^{-6} $°C^{-1}$) but increases with temperature, and

(iii) the thermal conductivity decreases with temperature above $\sim$50°C.

For fusion energy applications the low atomic number of carbon and its thermal stability (graphite sublimes at >3600 K) make C/C composites a strong candidate for ITER PFC applications.

2. PHYSICAL PROPERTIES

Physical properties of C/C composites are required for evaluating the behavior of the plasma-facing components under normal and disruption conditions of plasma in fusion devices. In particular, the temperature dependence of the thermal conductivity is very important to prediction of the surface temperature of plasma-facing components, and the amount of erosion. The coefficient of thermal expansion and the Young's modulus are used to calculate the thermal stresses. In order to reduce the surface temperature of the plasma-facing components (C/C), it is desirable that the C/C composite has higher thermal conductivity at high temperatures, such as 300 W/m·K at 1000°C.

The vapor pressure of the C/C composite should depend upon the degree of graphititzation. Generally the degree of graphitization of the C/C composite materials is smaller than that of graphite materials. Consequently, the vapor pressure of the C/C composite materials should be different from that of graphite. However, such differences are expected to be small. Bundy [4] has reported the vapor pressure of graphite as 1.3 $\times$ 10^{-5} Pa at 2000°C and 1.3 Pa at 2600°C. The following physical properties have been determined for graphite materials [4, 5]:

sublimation temperature: 39 15K
heat of vaporization: 600 kJ/mole
heat of sublimation: 588-714 kJ/mole

Some physical properties of two C/C composites (CX2002U, MFC-1-1992) are listed in Table I [6]. CX2002U and MFC-1 are used in JT-60U. Physical properties of PCC-1S and PCC-2S C/C composites are shown in Table II [7], PCC-2S has also been used in JT-60U. Physical and mechanical properties of three nuclear graphites and four C/C composites, which are candidate materials for plasma-facing components of JT-60U, are shown in Table III [8].

Recently, high thermal conductivity C/C composite development has been pursued worldwide. Improvements in fiber and composite technology are driving the thermal

TABLE I. PHYSICAL PROPERTIES OF C/C COMPOSITES AND METALLIC MATERIALS FOR PFCs* [3]

	CX2002U	MFC-1 (1992)
Ultimate tensile/compr./bend strength (MPa), at RT or higher	11/49/15 (min.) 50/54/50 (max.)	400/216/480 ($\parallel$) 3/16/5 ($\perp$)
Tensile elongation at RT	--	--
Young's Modulus (GPa)	$10^{1)}$, $8.1^{2)}$, $3.4^{3)}$	100 ($\parallel$), 0.8 ($\perp$)
Poisson ratio	0.19	0.15
Melt/sublim. temp. (°C)	3500	3500
Density (g/cm^3)	1.67	1.96
Thermal conductivity, 20°C (W/m·K) 300°C	$380.0^{1)}$ $240.0^{1)}$	640.0 ($\parallel$, 57°C) 442.0 ($\parallel$)
Specific heat at RT (J/gK)	0.71	0.71
Thermal expansion coeff. (10^{-6}/K)	$1.51^{1)}$, $1.7^{2)}$, $5.8^{3)}$	-0.9 ($\parallel$), 12.0 ($\perp$)

*Data measured, from literature and manufacturer's documentation, 1), 2), 3) are fiber directions, 1) and 2) in-plane and 3) perpendicular.
MFC-1 (1992): uni-directional pitch-type carbon-fiber-reinforced-carbon material, Mitsubishi Kasei, Japan.
CX2002U: two-directional felt-type carbon-fiber-reinforced-carbon materials, Toyo Tanso, Japan.

conductivity of C/C composites toward that of pyrolytic graphites. At the present time, C/C composites with thermal conductivities in excess of 300 W/m·K at room temperature have been manufactured. Thermal properties of the 3D-C/C composite, SEPCARB N112, are given in Tables IV through VII [9]. The thermal conductivity of C/C composites is controlled by that of the carbon fiber. The thermal conductivity of various carbon fibers is represented as a function of temperature in Table VIII [7] . Figure 4 shows the temperature dependence of thermal conductivity for a U.S. composite manufactured from VGCF, along with a U.S. pitch fiber composite. The thermal conductivity increases due to heat treatment. (Fig. 5 [10] and Fig. 6 [11], and Table IX [12].) The temperature dependencies of thermal conductivity for Japanese-made C/C composites are shown in Figs. 7 through 9 [6][13]. In the figures, the thermal conductivity values in the direction parallel and perpendicular to the fiber axis are given. Figure 10 [14] and Fig. 11 [15] indicate temperature dependencies of American-made C/C composites. Temperature dependence of thermal conductivity for C/C composites represents a typical T-1 dependence because of phonon conduction.

Thermal expansion data for 3D, C/C composite (FMI 223, PAN fiber) are shown in Figs. 12 through 15 [14].

TABLE II. PHYSICAL PROPERTIES OF C/C COMPOSITES, PCC-1S AND PCC-2S [7]

Material		PCC-1S	PCC-2S
Carbon Fiber		PA	Pitch
Density(g/cm^3)		1.86	1.83
Young's Modulus(GPa)		36.3	18.6
Bending Strength(MPa) ‖		79.5	38.3
⊥		24.8	12.0
Compressive Strength(MPa) ‖		77.0	45.5
⊥		69.3	37.3
Shore Hardness ‖		32	25
⊥		25	15
Electrical Resistivity ‖		425	335
($\mu\Omega \cdot$ cm) ⊥		778	678
Specific Heat(J/gK)		0.73	0.72
Thermal Conductivity ‖		223	280
⊥		128	150
Coefficient of Thermal ‖		0.6	1.0
Expansion(10^{-6}/K) ⊥		7.1	5.8
Ash Content(ppm)		<20	<20

The specific heat at a constant pressure will be expressed by

$$C_p = 0.54212 - 2.42667 \times 10^{-6}T^{-9}\ 0.2725T^{-1} - 43449.3T^{-2}$$
$$+ 1.5.3.9 \times 10^9T^{-3} - 1.43688 \times 10^9T^4 \qquad (1)$$

and it is applicable at 250-3000 K [16]. An example of the specific heat for POCO graphite is given in Fig. 16 [17].

82

TABLE III. PHYSICAL AND MECHANICAL PROPERTIES OF THE ISOTROPIC GRAPHITES (A-C) AND C/C COMPOSITES (D-G) [8]

Materials	Items	Density [g/cm³]	Electrical resistivity (mΩcm) ∥	⊥	Thermal conductivity [W/m·K] ∥	⊥	Coefficient of thermal expansion [10⁻⁶/K] ∥	⊥	Bending strength [MPa] ∥	⊥	Tensile strength [MPa] ∥	⊥	Compressive strength ∥	⊥
A	N	60	60	—	60	—	44	—	60	—	60	—	60	—
	mean	1.76	1.36	—	88	—	4.1	—	67.0	—	46.8	—	107.3	—
	SD	0.0155	0.0309	—	4.2	—	0.13	—	4.57	—	3.07	—	6.16	—
	max.	1.77	1.40	—	114	—	4.3	—	75.6	—	53.9	—	118.7	—
	min.	1.72	1.27	—	81	—	3.8	—	56.3	—	39.6	—	93.8	—
B	N	180	180	—	180	—	20	—	180	—	180	—	180	—
	mean	1.84	0.80	—	172	—	4.3	—	46.6	—	36.1	—	90.9	—
	SD	0.0127	0.0192	—	8.20	—	0.16	—	3.94	—	3.30	—	5.89	—
	max.	1.86	0.85	—	194	—	4.7	—	54.3	—	43.2	—	104.2	—
	min.	1.82	0.75	—	155	—	4.0	—	36.3	—	28.1	—	73.3	—
C	N	56	56	—	56	—	50	—	56	—	56	—	56	—
	mean	1.82	0.89	—	137	—	4.2	—	53.5	—	38.9	—	94.6	—
	SD	0.0147	0.034	—	5.08	—	0.17	—	3.96	—	2.89	—	4.93	—
	max.	1.85	0.98	—	148	—	4.5	—	61.2	—	45.3	—	106.7	—
	min.	1.80	0.83	—	128	—	3.9	—	45.0	—	33.6	—	85.8	—
D	N	30	30	30	5	5	5	5	30	30	30	30	30	88
	mean	1.92	0.44	3.54	339	58	0.12	10.2	151.8	10.33	83.2	3.37	78.1	110.3
	SD	0.0156	0.035	0.232	11.5	3.0	0.11	0.38	15.7	1.12	18.9	0.73	10.3	13.0
	max.	1.95	0.50	4.04	349	62	0.22	10.5	175.6	13.20	119.6	4.79	103.3	134.7
	min.	1.90	0.35	3.14	323	54	-0.06	9.6	119.3	8.16	43.5	1.22	57.2	73.4
E	N	6	6	—	4	2	2	1	6	—	—	—	4	4
	mean	1.71	0.34	—	332	171	1.8	5.8	42.8	—	—	—	45.0	42.7
	SD	0.041	0.0077	—	34.6	7.4	0.50	—	2.76	—	—	—	2.21	0.97
	max.	1.75	0.35	—	374	176	2.1	—	45.9	—	—	—	47.6	43.6
	min.	1.65	0.33	—	300	166	1.4	—	38.6	—	—	—	42.7	41.8
F	N	86	86	86	5	5	5	5	86	86	125	—	86	86
	mean	1.82	0.37	0.69	298	177	1.3	5.9	45.9	15.4	34.5	—	59.6	53.3
	SD	0.0148	0.016	0.035	10.7	5.89	0.16	0.18	5.07	1.30	4.11	—	5.72	6.65
	max.	1.85	0.41	0.76	310	184	1.5	6.1	58.3	18.6	44.4	—	73.4	70.0
	min.	1.78	0.34	0.62	281	171	1.1	5.6	37.9	12.8	21.3	—	45.7	38.2
G	N	108	108	—	12	12	9	9	108	—	108	—	108	108
	mean	1.83	0.43	—	318	124	0.69	8.9	93.7	—	74.3	—	82.7	82.4
	SD	0.0240	0.040	—	21.4	13.1	0.31	1.97	11.0	—	11.3	—	10.3	10.7
	max.	1.90	0.49	—	340	160	1.1	11.5	120.6	—	96.6	—	108.9	104.9
	min.	1.77	0.34	—	260	110	0.2	7.0	71.6	—	44.2	—	66.8	61.5

N = number of test pieces, SD = standard deviation.

83

TABLE IV. THERMAL EXPANSION UP TO 1500°C FOR X, Y, AND Z DIRECTIONS OF SEPCARB N112 C/C COMPOSITE [9]

Thermal Expansion (10^{-6} °C^{-1})			
	500°C	1000°C	1500°C
X	0.08	0.24	0.44
Y	0.08	0.24	0.44
Z	0.14	0.37	0.67

TABLE V. THERMAL DIFFUSIVITY UP TO 2000°C FOR X, Y, AND Z DIRECTIONS OF SEPCARB N112 C/C COMPOSITE [9]

Thermal Diffusivity (mm^2 s^{-1})						
Temperature (°C)	23	350	500	1000	1500	2000
X, Y	180	52	41	25	19	14
Z	135	43	32	20	15	12

TABLE VI. SPECIFIC HEAT VALUES USED FOR THE CALCULATIONS OF THERMAL CONDUCTIVITY VALUES [9]

Specific Heat (J kg^{-1} K^{-1})						
Temperature (°C)	23	350	500	1000	1500	2000
Cp (J kg^{-1} K^{-1})	780	1430	1580	1890	2030	2060

TABLE VII. THERMAL CONDUCTIVITY UP TO 2000°C FOR X, Y, AND Z DIRECTIONS OF SEPCARB N112 C/C COMPOSITE [9]

Thermal Conductivity (W m^{-1} K^{-1})						
Temperature (°C)	23	350	500	1000	1500	2000
X, Y	280	140	131	95	76	58
Z	210	123	105	76	62	52

TABLE VIII. CARBON FIBER THERMAL CONDUCTIVITY [7]

Temperature °C	P-55 W/m·K	P-100 W/m·K	P-120 W/m·K	P-130 W/m·K	VGCF W/m·K
25	120	520	640	1100	1900
100	92	501	598	1038	1500
300	57	311	370	643	900
500	42	228	272	473	650
700	34	182	218	377	550
900	28	152	181	314	450
1100	24	130	155	269	400
1300	21	113	135	234	350
1500	18	99	118	204	300
1700	16	88	105	183	250

TABLE IX. THERMAL CONDUCTIVITY AND DENSITY OF PREFORM AND C/C COMPOSITES [12]

Material	Density, ρ (g/cm^3)	Conductivity, κ (W/m·K)	κ/ρ
	As-Processed Heat Treated		
Preform	1.14 1.13	436 481	381 428
Composite			
CVI-2	1.64 1.62	476 590	290 364
CVI-3	1.59 1.60	470 568	296 355
PI-1	1.76 1.70	432 647	246 381
PI-2	1.79 1.79	602 736	337 411
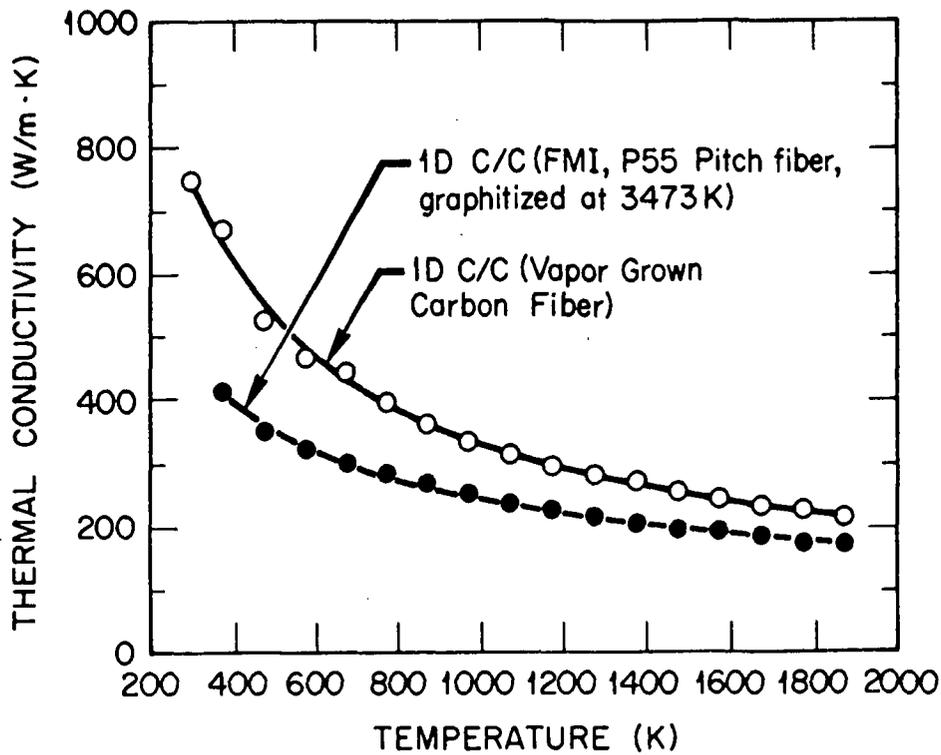
FIG. 4. The temperature dependence of thermal conductivity for pitch fiber and vapor grown fiber 1D C/C composites.
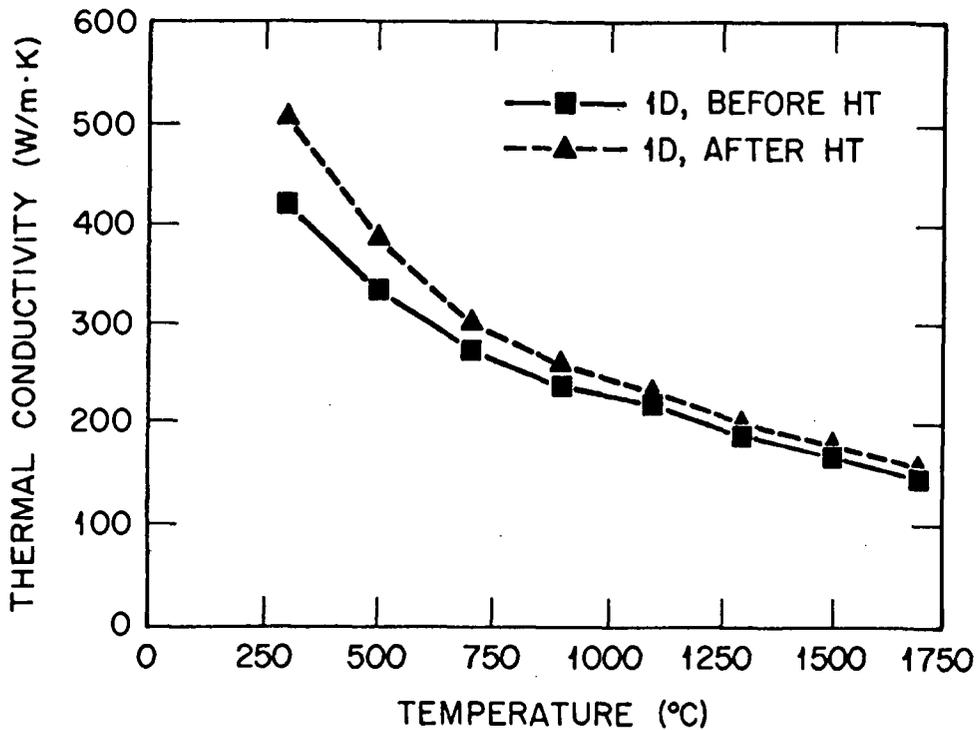
FIG. 5. Effect of heat treatment (HT) on the thermal conductivity of a 2D C/C composite [10].
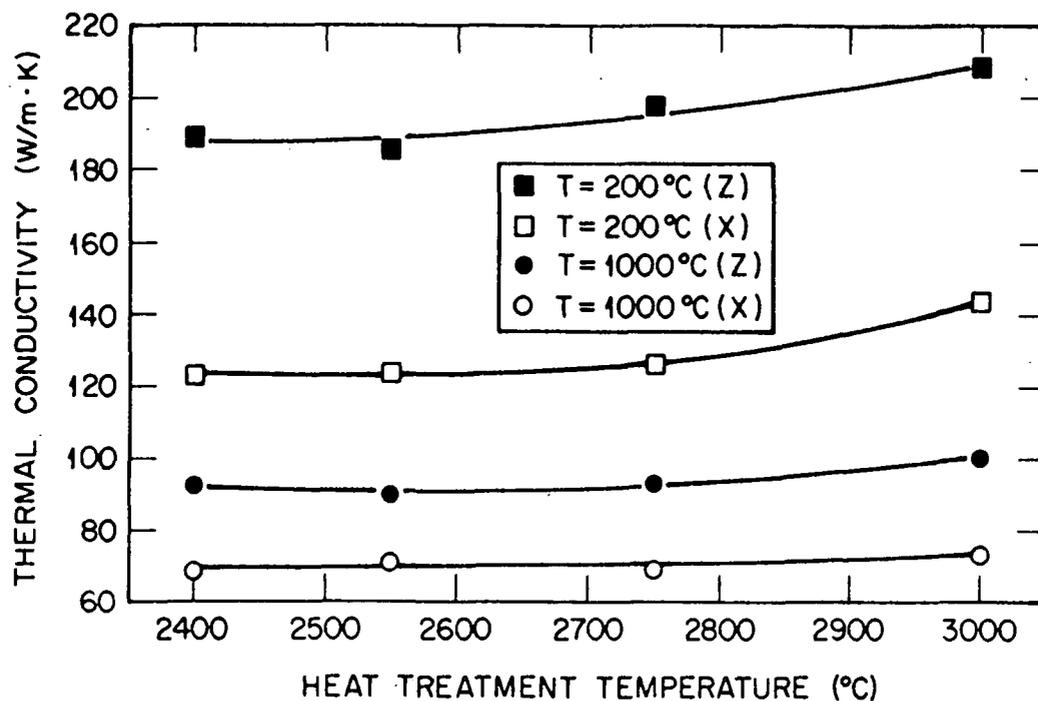
FIG. 6. Thermal conductivity at different measurement temperatures as a function of heat treatment temperature. Closed symbols represents data with heat flow in the Z direction and open symbols represents data with heat flow in the X direction [11].
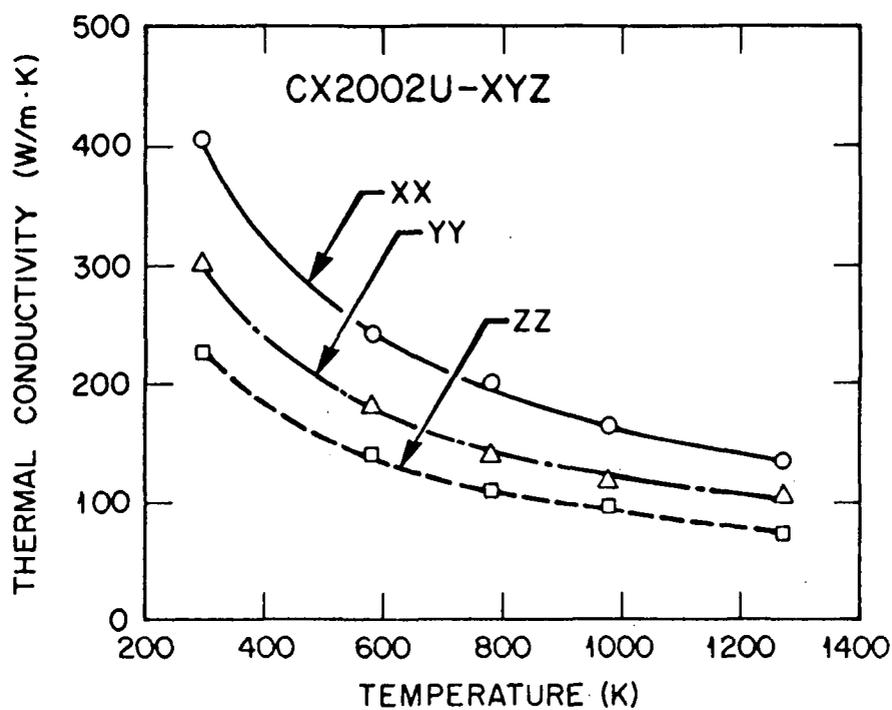
FIG. 7. Temperature dependence of thermal conductivity of CX-2002U C/C composite. XX: parallel to the fiber axis. YY, ZZ: perpendicular to the fiber axis [6, 13].
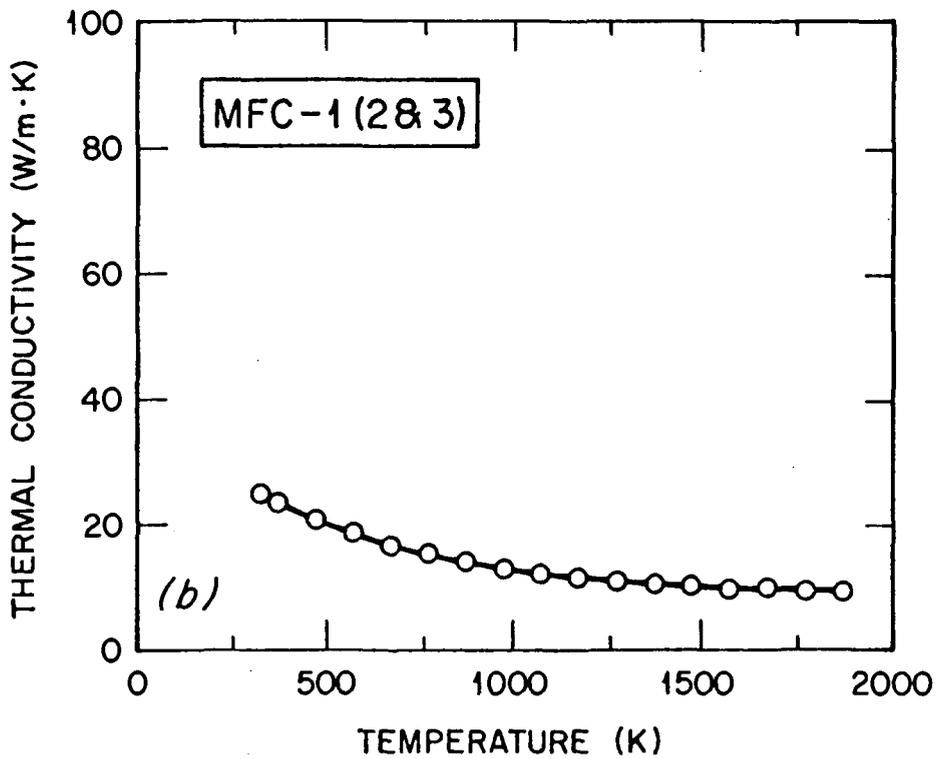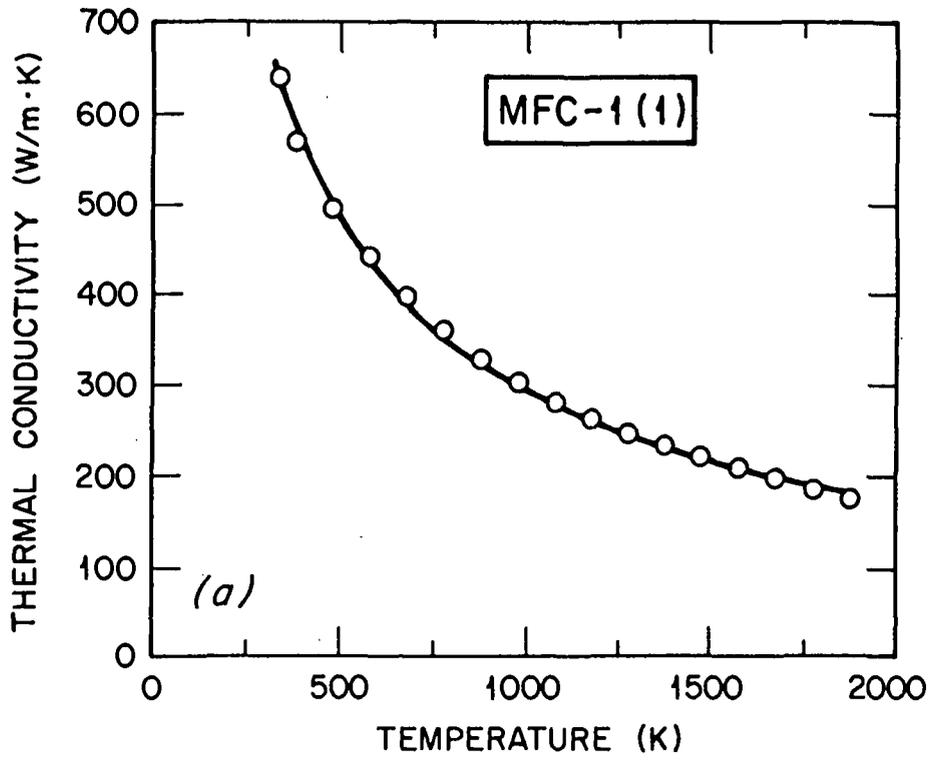
FIG. 8. The temperature dependence of thermal conductivity of MFC-1 C/C composite. (a) 1-direction, parallel to the fiber axis; (b) 2 & 3 direction, perpendicular to the fiber axis [3, 10].
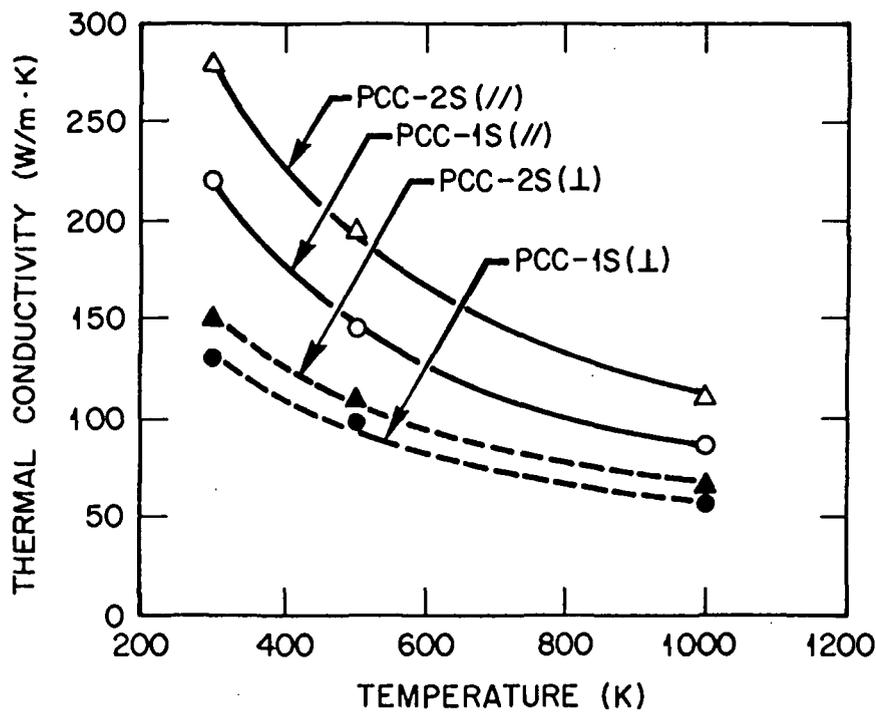
FIG. 9. The temperature dependence of thermal conductivity of PCC-1S and PCC-2S C/C composites [6, 13].
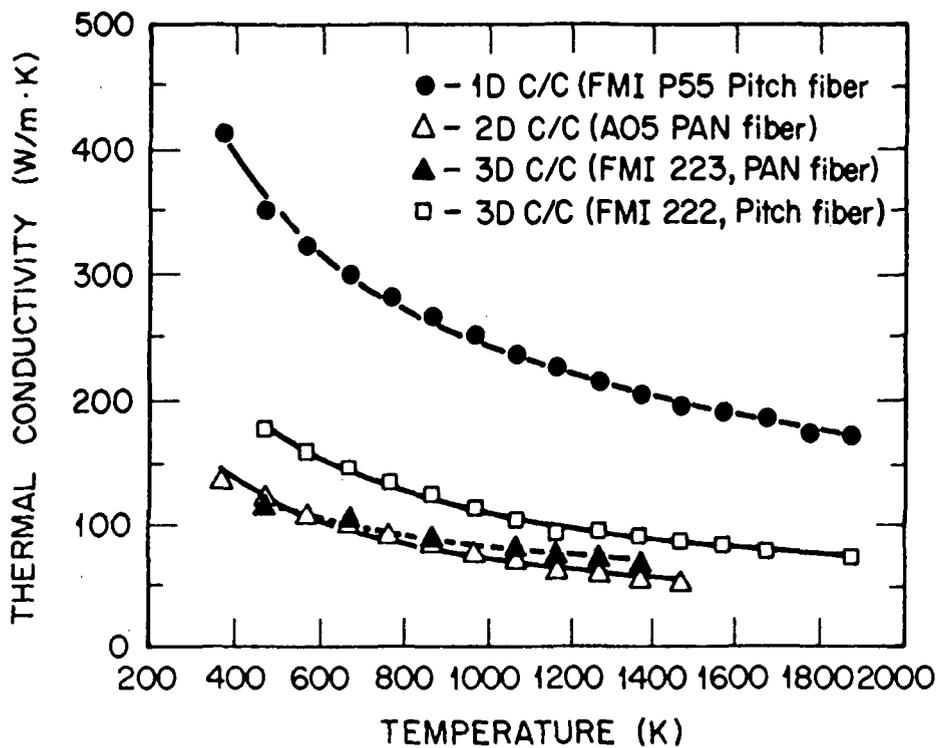
FIG. 10. The temperature dependence of thermal conductivity of 1D, 2D and 3D C/C composites from the USA (FMI, Fiber Materials, Inc.) and France (A05, Carbone Lorraine) [14].
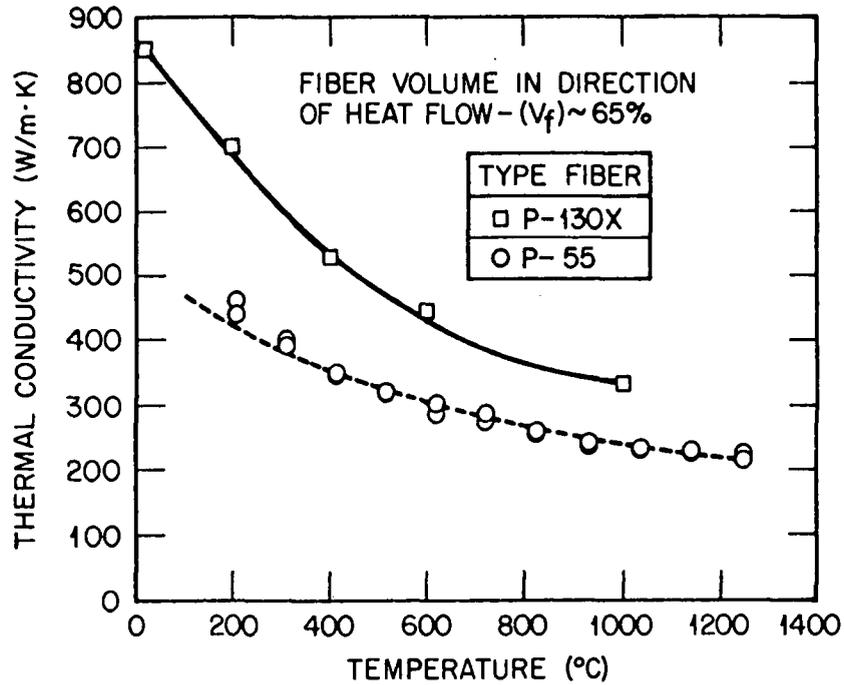
FIG. 11. The temperature dependence of thermal conductivity for P130X and P-55 pitch based carbon fibers [12].
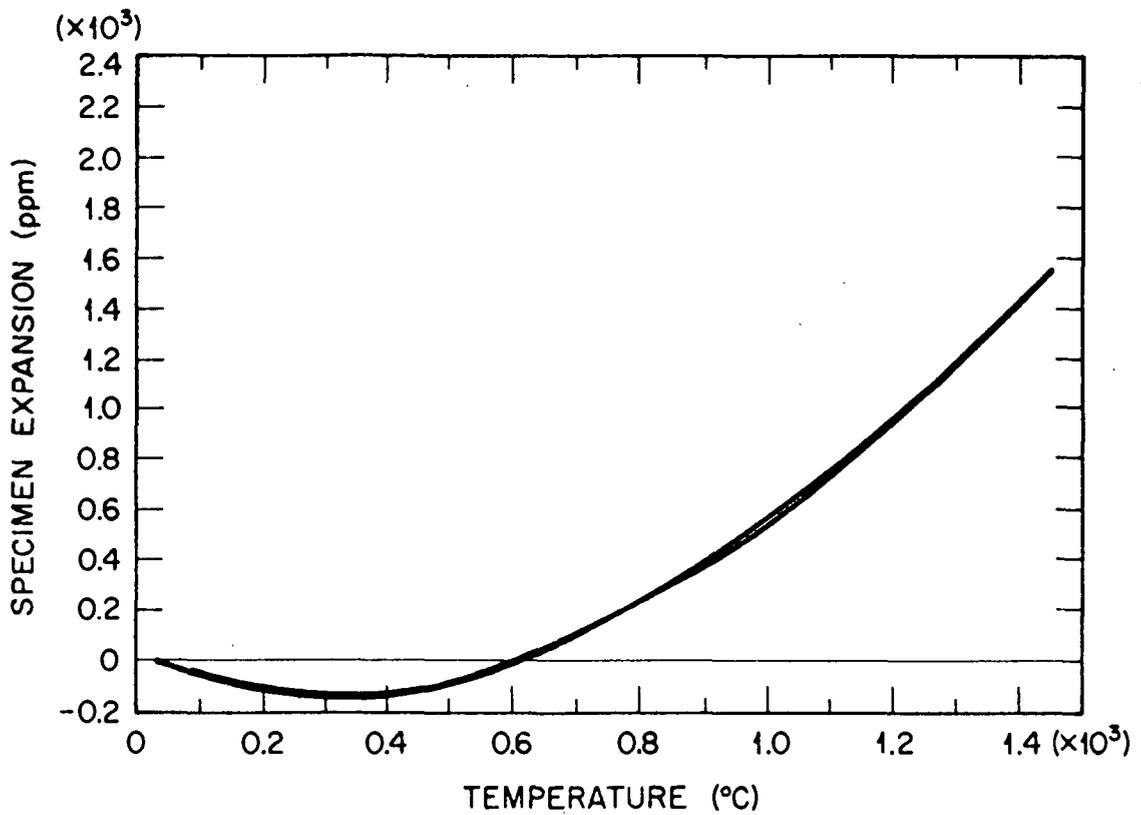
FIG. 12. The thermal expansion of a 3D C/C composite (FMI 223, PAN fiber) in the X or Y direction [14].
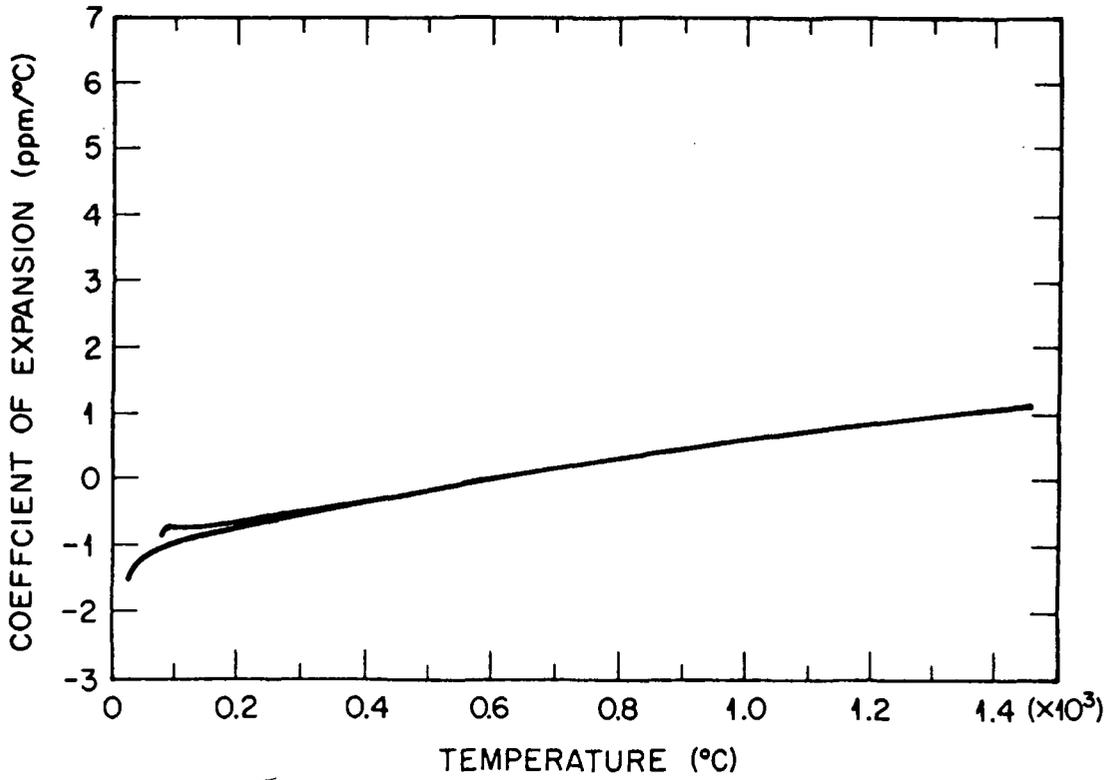
FIG. 13. The temperature dependence of the coefficient of thermal expansion of a 3D C/C composite (FMI 223, PAN fiber) in the X or Y direction [14].
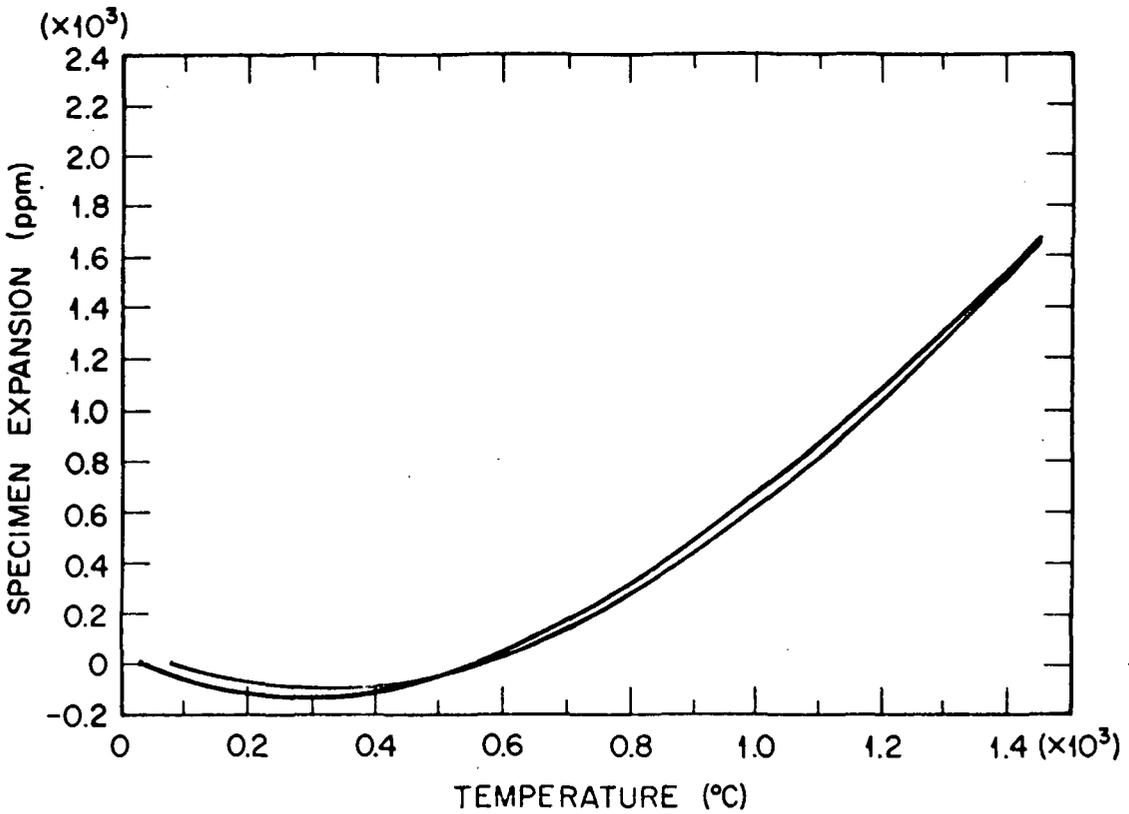
FIG. 14. The thermal expansion of a 3D C/C composite (FMI 223, PAN fiber) in the 2 direction [14].

FIG. 15. The temperature dependence of the coefficient of thermal expansion of a 3D C/C composite (FMI 223, PAN fiber) in the Z direction [14].
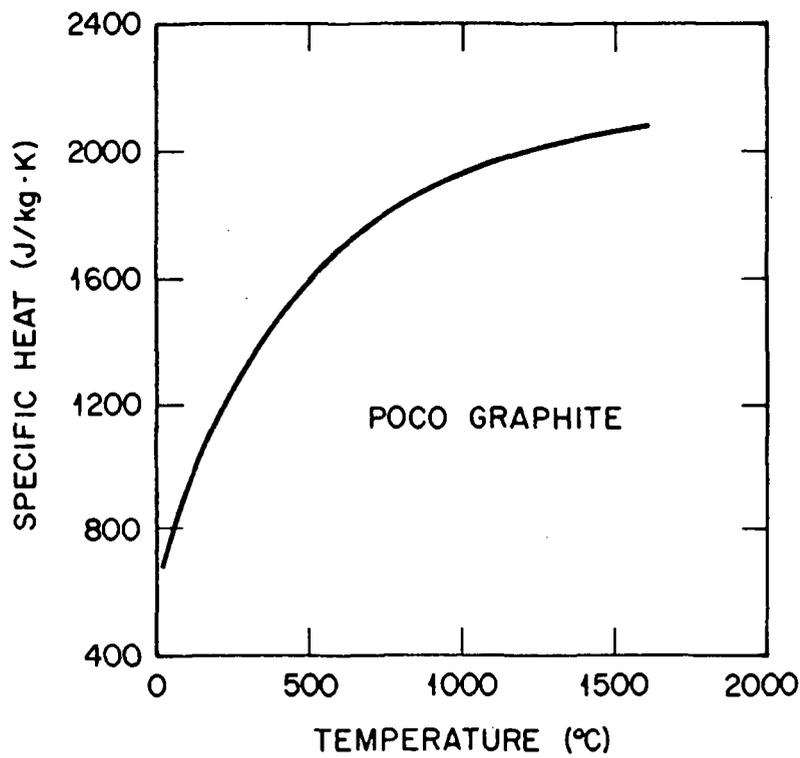
FIG. 16. The temperature dependence of the specific heat of graphite [17].

3. MECHANICAL PROPERTIES

Mechanical properties of C/C composites are required for evaluating stresses, e.g., thermal stresses or electro-magnetic mechanical stresses, induced in the plasma-facing components during disruption of the plasma (disruption stresses). Some mechanical properties of C/C composites, with fracture mechanics properties, are shown in Table X [18], where C/C-A and PCC-2S are pitch fiber, felt based composites, and C/C-B, CX-2002U and PCC-1S are PAN fiber, felt based C/C composites. The 2D-C/C is rayon fiber based, two-directional C/C composite. Tensile load-elongation curves for C/C-A and C/C-B materials, at four temperatures up to 2400°C, including room temperature, are shown in Fig. 17. The tensile stress-strain curve for the 3D-C/C composite SEPCARB N112 is shown in Fig. 18 [9]. No clear difference in the load-elongation curves was found between room temperature and 800°C. A definite increase in the maximum load of the load-elongation curve can be seen between 1600 and 2400°C.

TABLE X. MECHANICAL PROPERTIES OF C/C COMPOSITES [18].

Material	C/C-A	C/C-B	2D-C/C	CX-2002u	PCC-1S	PCC-2S
Density γ(g/cm^3)	1.58	1.75	1.74	1.72	1.86	1.83
Young's Modulus $\parallel$ E (GPa) $\perp$	13.5 -	26.0 -	23.8 -	11.3 -	36.3 5.9	19.6 5.9
Bending strength $\parallel$ σ_b (MPa) $\perp$	65.7 -	90.0 -	117 -	54,9 49.0	79.5 24.8	38.3 12.0
Compres. strength $\parallel$ σ_c (MPa) $\perp$	- -	80.0 -	44.1 -	61.7 52.9	77.0 69.3	45.5 37.3
Shore hardness $\parallel$ Hs $\perp$	- -	30 -	- -	35 30	32 25	25 15
Elec. resistance $\parallel$ ρ ($\mu\Omega$cm) $\perp$	- -	400 700	- -	440 -	425 778	335 678
Specific heat C(J/gK)	-	0.70	0.71	0.76	0.73	0.72
Thermal conduc. $\parallel$ k (W/m·K) $\perp$	- -	150 100	429 -	267 128	223 128	280 150
Thermal expan. $\parallel$ α(10^{-6}/K) $\perp$	- -	1.0 8.0	0.72 -	2.3 5.9	0.6 7.1	- -
Ash content (ppm)	<20	<20	-	<10	<20	<20
Carbon fiber	Pitch	PAN	Rayon	PAN	PAN	Pitch
Maker	Showa Denko	Showa Denko	-	Toyo Tanso	Hitachi Chemical	Hitachi Chemical

## PROPERTIES OF CARBON COMPOSITES
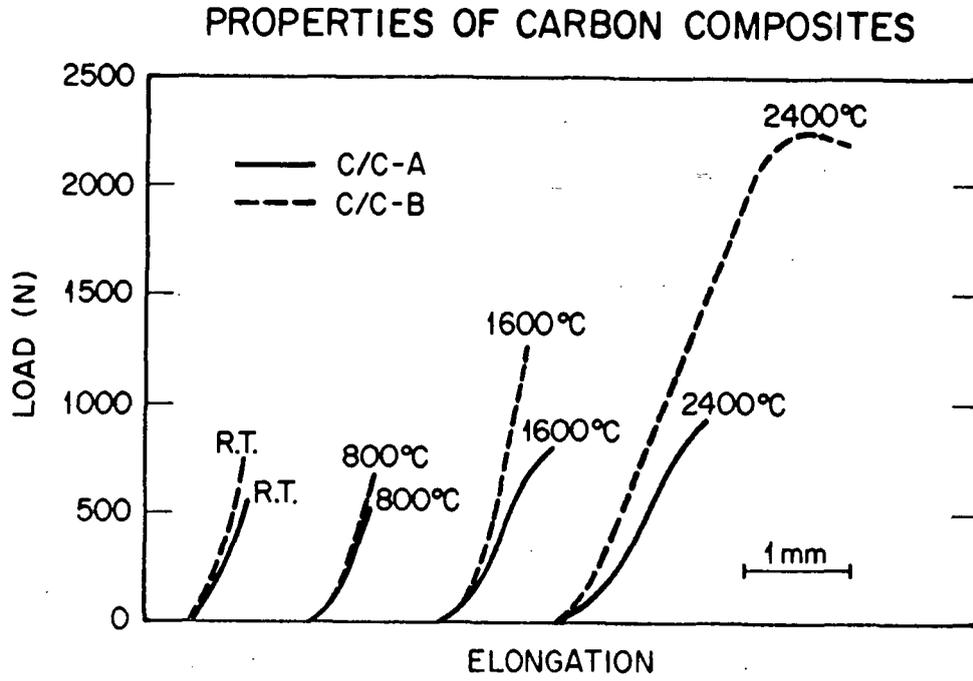
FIG. 17. *Tensile load elongation curves for C/C composites A and B at elevated temperatures [18].*
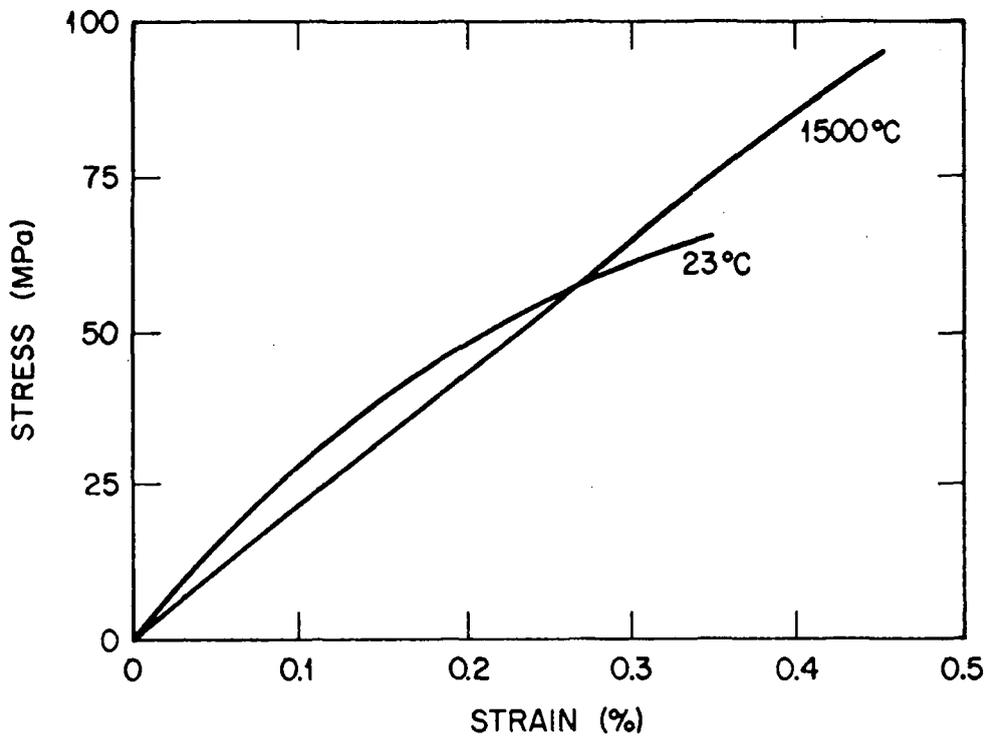

FIG. 18. *Tensile stress-strain curves at room temperature and 1500°C for SEPCARB N112 C/C composite in the X direction (X and Y are in fiber directions) [9].*

Temperature dependence of Young's Modulus for C/C composites and an isotropic high strength graphite are indicated in Fig. 19 [18]. Young's modulus increases up to 1500-2000°C with increasing temperature and decreases gradually above that temperature. Young's Modulus of UD-C/C (unidirectional C/C composite) increased, and then decreased with increasing heat treatment temperature, as shown in Figs. 20 and 21 [3]. The positive temperature dependence of Young's Modulus gradually decreased to nil with increasing heat treatment temperature and becomes negative after heat treatment at 2773K.

Temperature dependence of tensile strength for C/C composites and an isotropic graphite, IG-11, is shown in Fig. 22 [20]. This is different from that for Young's Modulus; the maximum tensile strength is seen above 2000°C for each C/C composite material.

Fracture toughness tests were performed at high temperatures using double notched tensile specimen for C/C composites and IG-11 graphite [20]. Load-elongation curves have been obtained as shown in Fig. 23. Temperature dependence of calculated fracture toughness values is given in Fig. 24. Clearly, fracture toughness values increase with increasing temperature.

Recently, a new process for manufacturing advanced C/C composites using hot isostatic pressing has been developed [21]. Figure 25 indicates the relationship between flexural strength and void fraction of the 3D-C/C composite manufactured by HIP. Tensile strength versus elastic modulus relations of 2D and 3D-C/C composites are shown in Fig. 26 [21].

The scatter of the C/C composite strength properties, and other properties, is larger than the isotropic graphites and the quality of the C/C composites depends strongly on the grade of the materials [22].
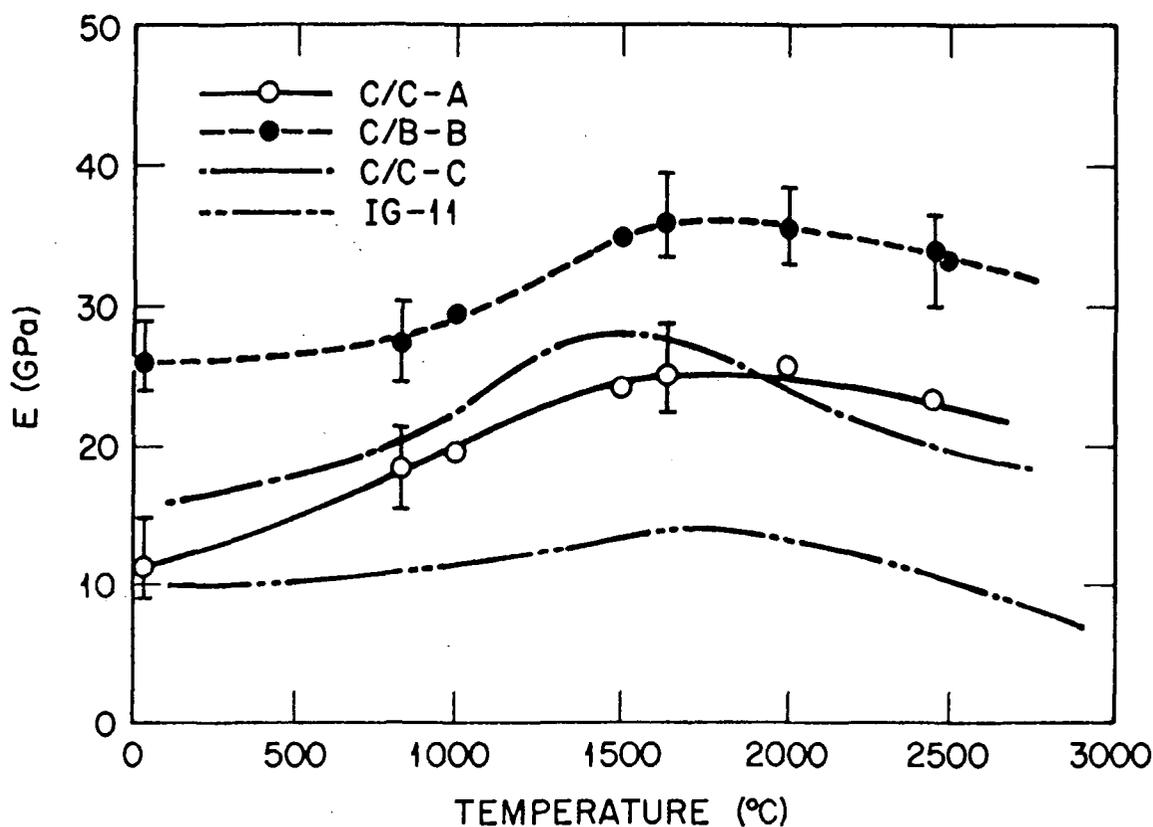
Fig. 19. Temperature dependence of Young's modulus of three C/C composites and graphite grade IG-110 [18].
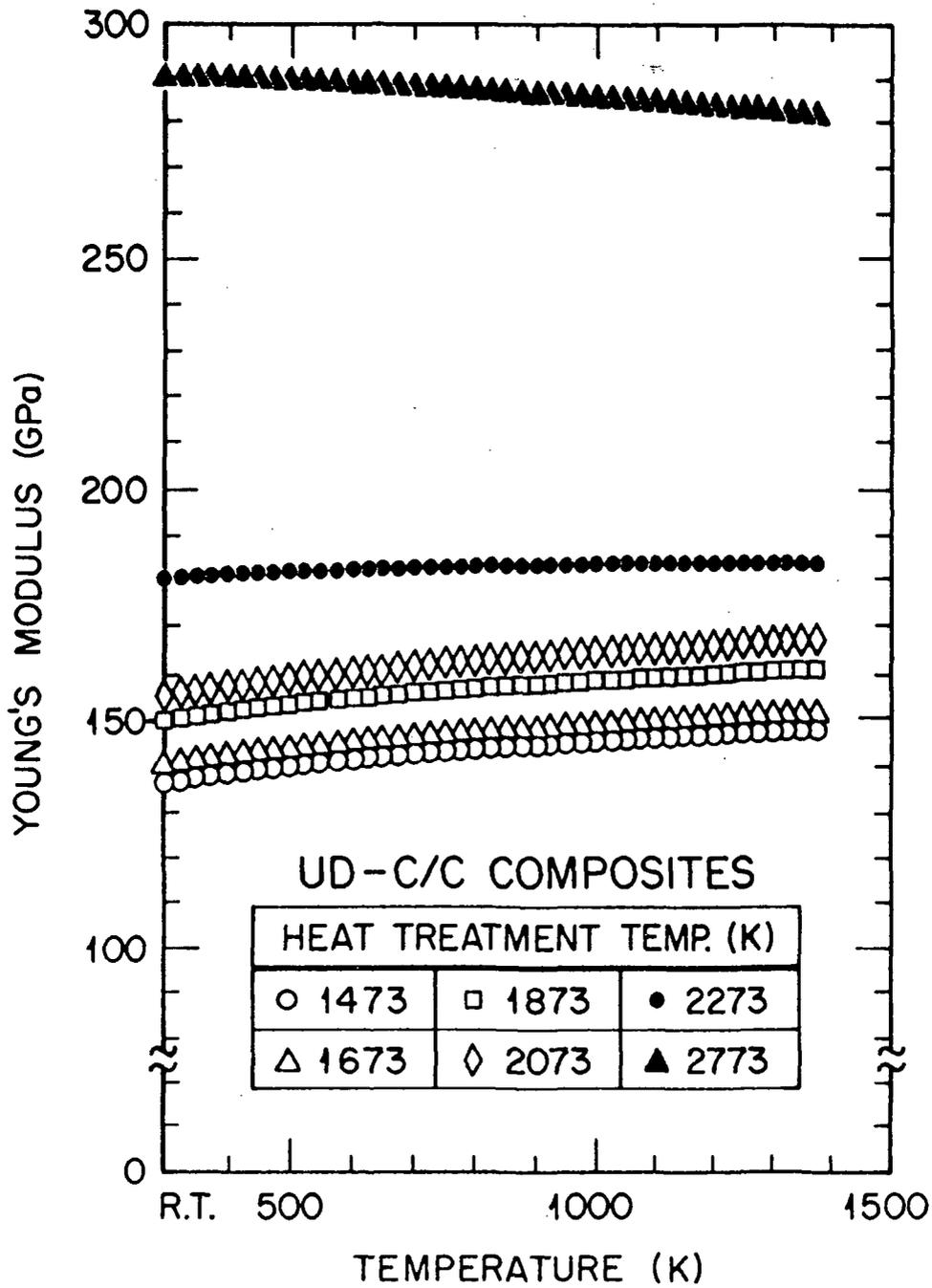
*FIG. 20. Temperature dependence of Young's modulus for UD-C/C composites [19].*
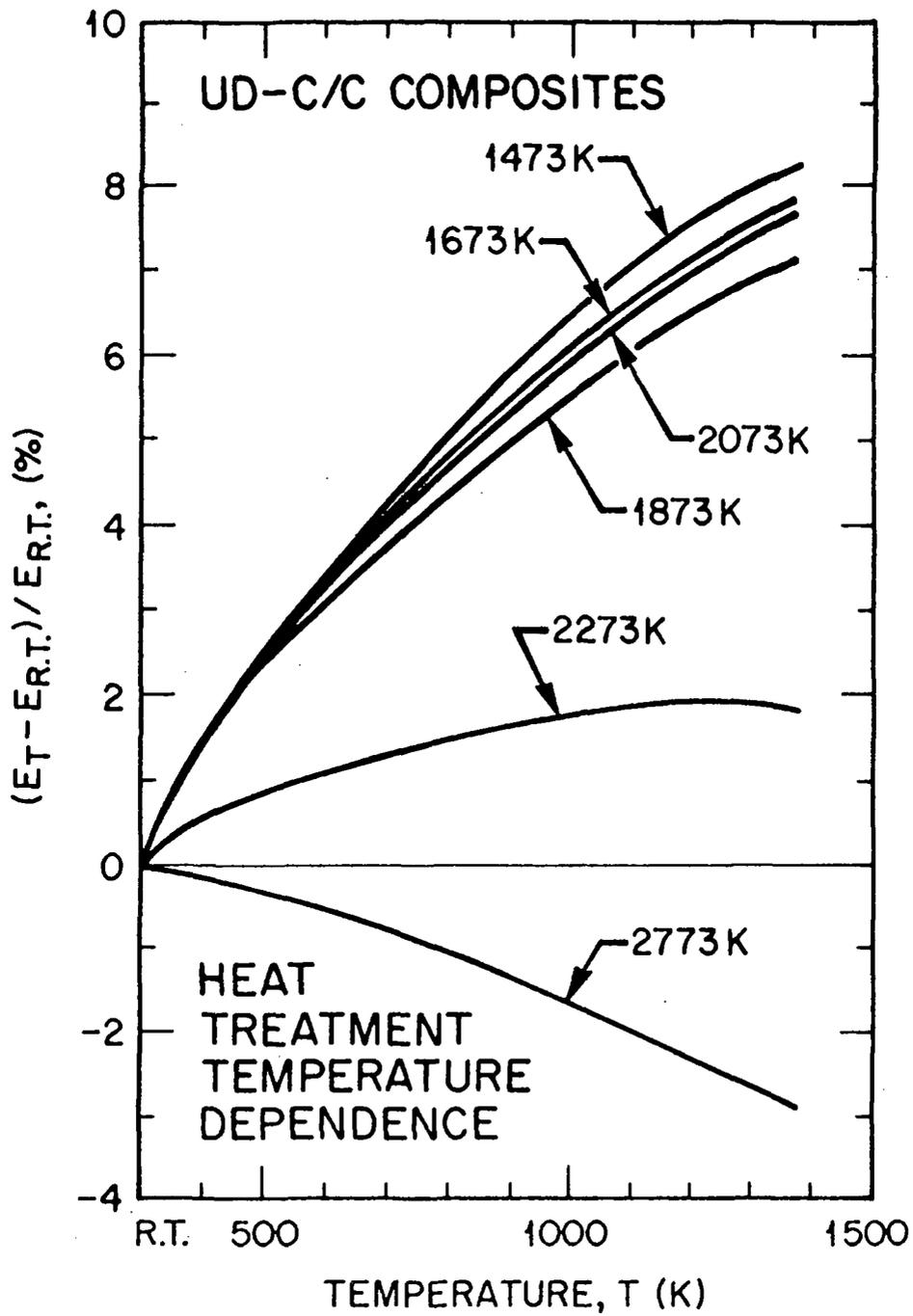
FIG. 21. Effect of heat treatment temperature on the temperature dependence of normalized Young's modulus for UD-C/C composites [19].
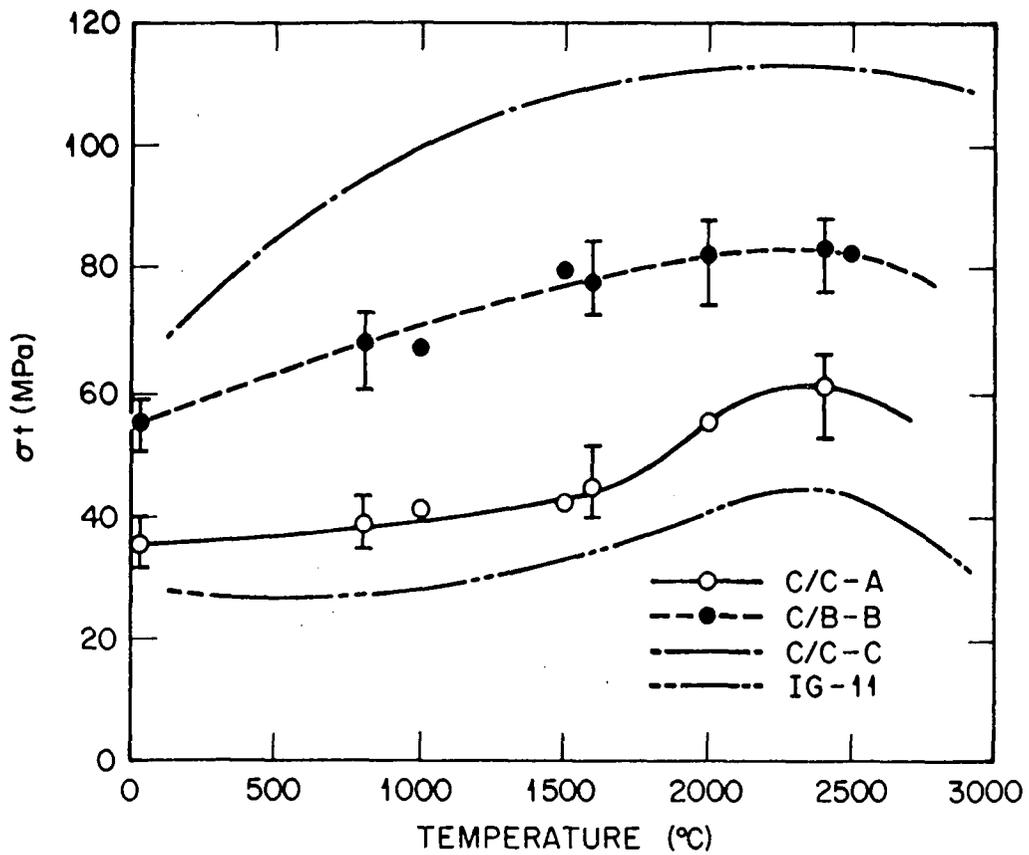
FIG. 22. Temperature dependence of tensile strength of three C/C composites and graphite grade IG-110 [20].
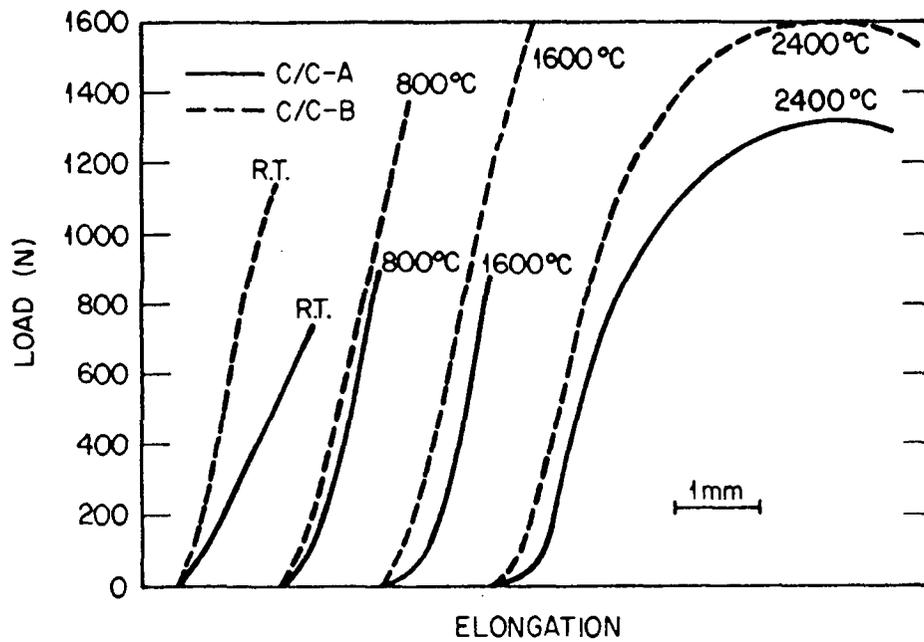
FIG. 23. Load-elongation curves from fracture toughness tests on C/C -A and -B at high temperatures [21].
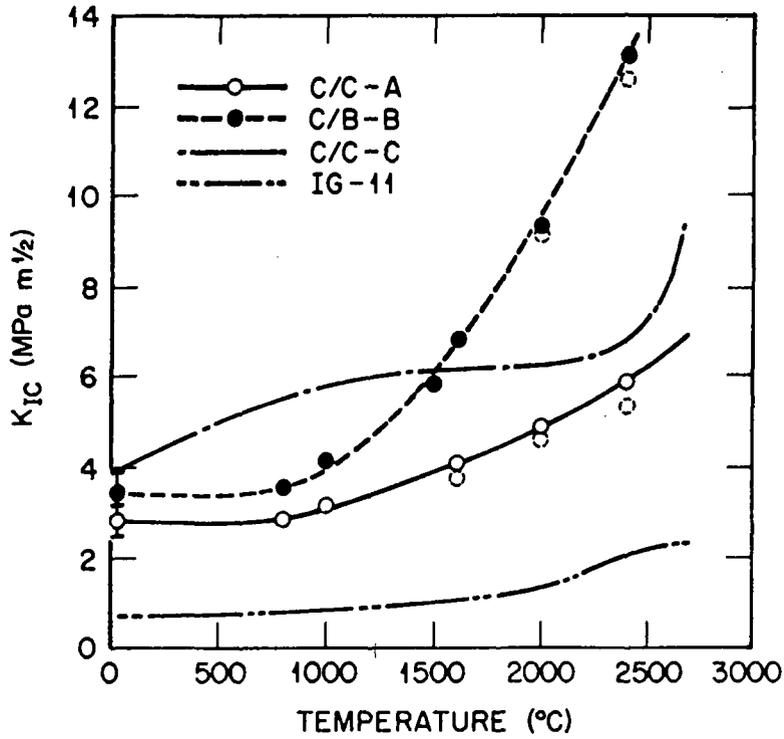
FIG. 24. Temperature dependence of fracture toughness of three C/C composites and graphite grade IG-110 [20].
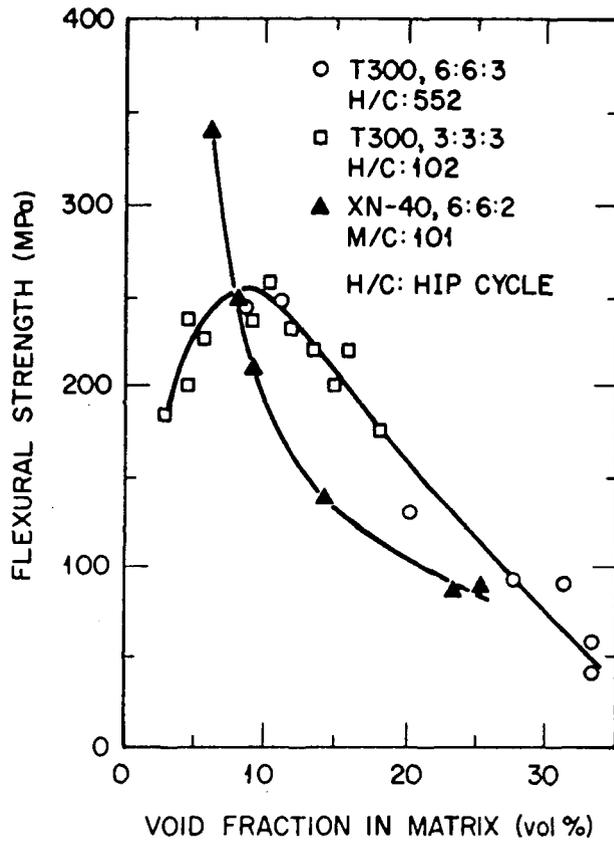
FIG. 25. The relationship between flexural strength and void fraction of 3D C/C composites [21].
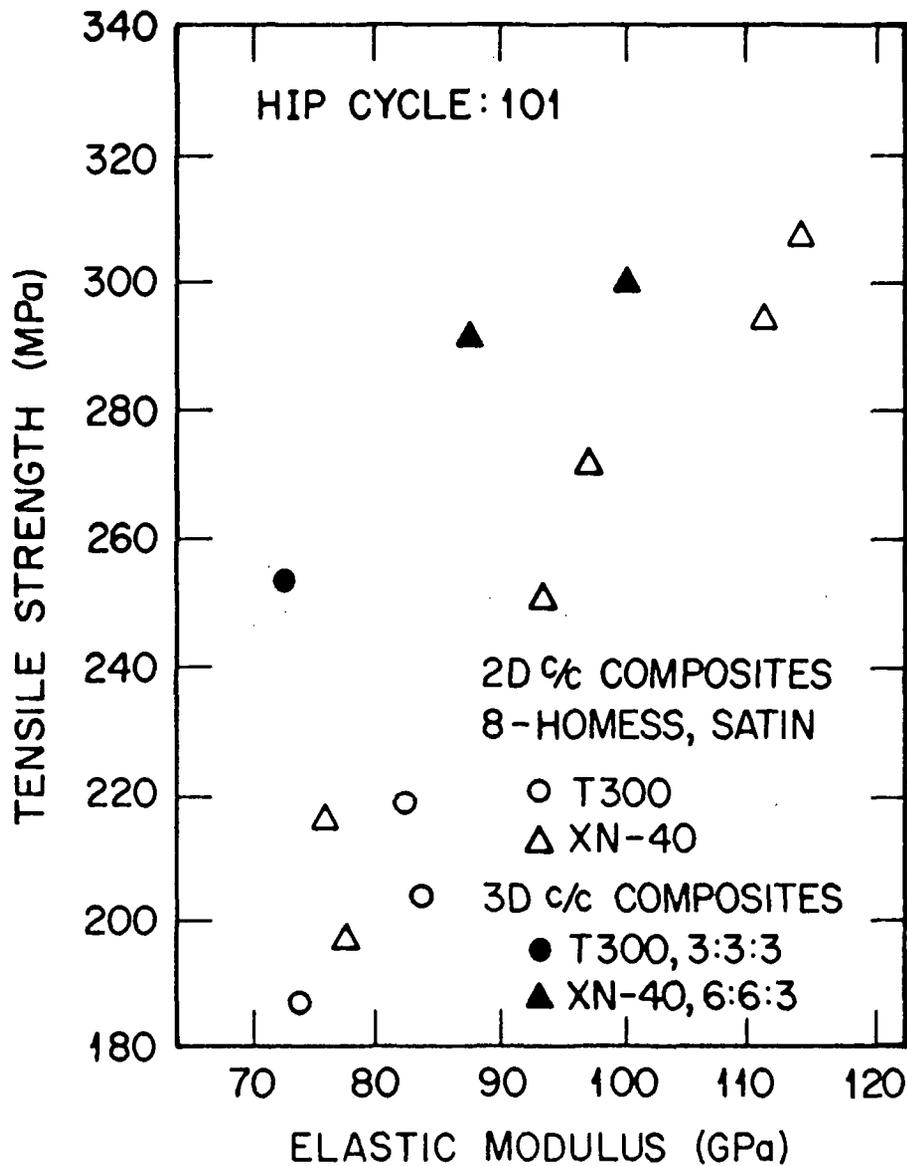
FIG. 26. Tensile strength versus elastic modulus of 2D and 3D C/C composites [21].

Mechanical properties of carbon materials, including C/C composites, were evaluated by means of a dynamic hardness test which yields a description of indented load versus indented depth [23]. The materials examined are listed in Table XI. The indented load-depth (L-h) curves for C/C composites are shown in Fig. 27. For example, the sign A in CC-312(A) means the axial direction of the carbon fiber in the composite. Figure 27 indicates the loading and unloading curves for each material. These curves were approximated by a parabola around the maximum load for both loading and unloading curves. If L/h is plotted as a function of depth (h), Fig. 28 is obtained. The slopes for the loading and unloading curves at the maximum load were denoted as parameters B and D, respectively. In the case of C/C composite material, the L/h versus h curves for the axial direction of the carbon fiber, the radial direction, and the matrix in the 3D-C/C composite material are given in Fig. 29. The correlations between the bending strength σ_B, the parameter B, the Young's Modulus E, and the parameter D were derived from data on different grades of carbon materials: $\sigma_B[\text{MPa}] = 10B[\text{GPa}]$, $E[\text{GPa}] = 0.826D[\text{GPa}]$.

TABLE XI. MECHANICAL PROPERTIES OF MATERIALS EXAMINED [23]

Properties Materials	App. Density kg/m³	Young's Modulus GPa	Bending Strength MPa
3D-C/C	1770	120/-	102/-
CC-312	1805	40.3/5.1	78/19
CX-2002U	1650	10.0/-	44/-
HBC-18S	1980	5.4	88.2
7447	1760	9.5/10.0	34.1/33.1
IM-2	1780	12/11.9	33.6/34.4
H-327	1780	14.8/6.7	25.5/14.6
ETP-10	1750	10.8	58.8
IG-11	1760	9.4/10.0	34.7/32.8
IG-15	1894	11.8/-	49.0/-
IG-43	1842	10.8/-	53.9/-
IG-56	1730	10.3/-	43.1/-
ISEM-3	1829	11.8/-	49.0/-
ISO-88	1915	12.8/-	93.1/-
SIC-6	1848	11.8/-	49.0/-

C/C: (axial direction of fiber)/(perpendicular to fiber axis)
GRAPHITE: (parallel to basal plane)/(perpendicular to basal plane)
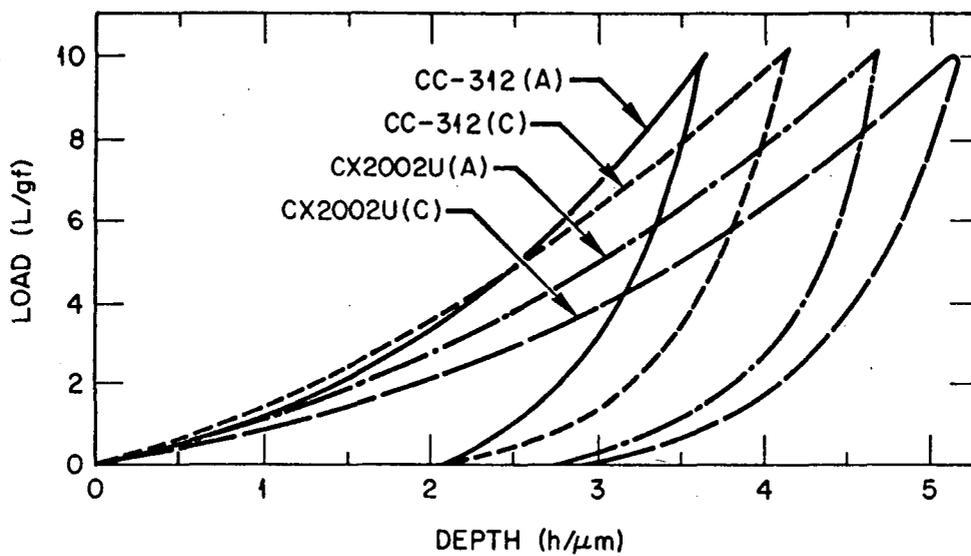
FIG. 27. L-h curves for two C/C composites [23].
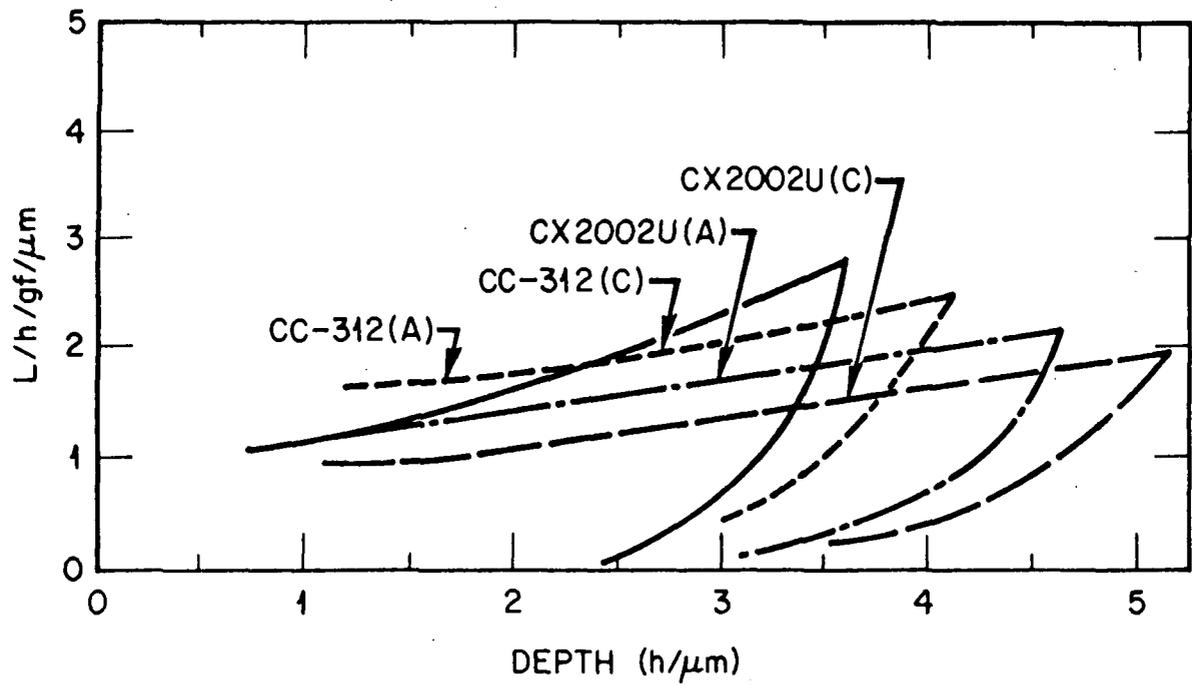
FIG. 28. L/h-h curves for two C/C composites [23].
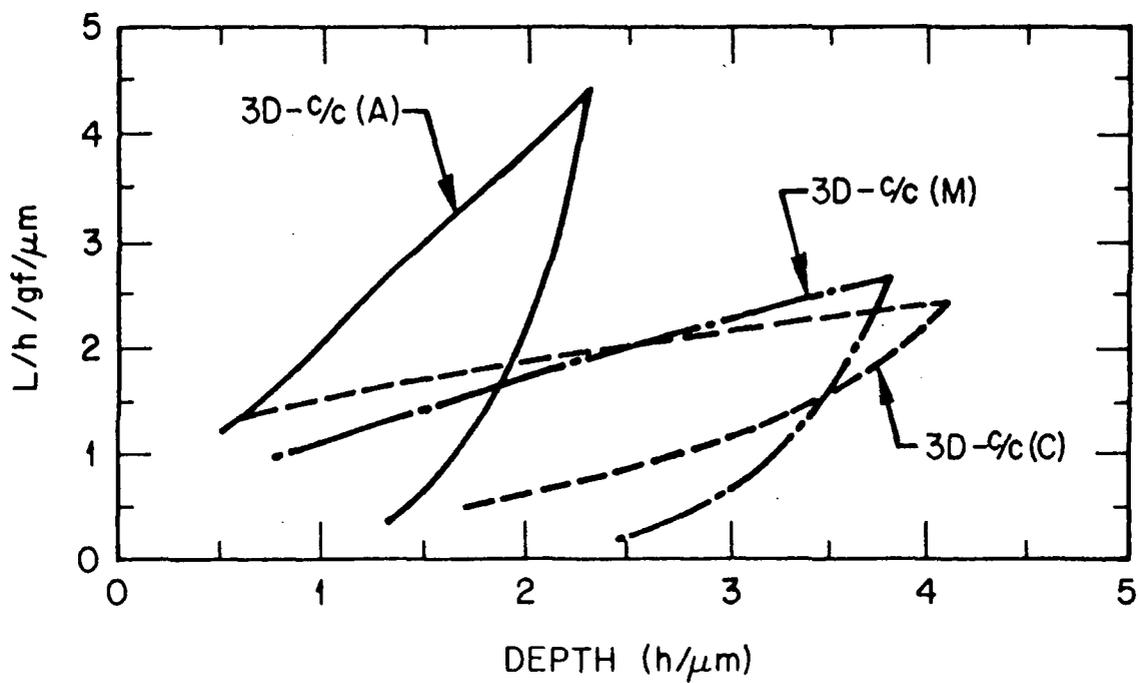
FIG. 29. L/h-h curves for two C/C composites [23].

102

4. RADIATION EFFECTS

4.1 Neutron Irradiation Damage Mechanism

The carbon atoms in carbon fibers and matrix carbon are arranged at the atomic level in the graphite crystal structure, consisting of layers of carbon atoms; the atoms being (sp^2) covalently bound in a hexagonal array within the graphite layer. The layers are stacked in an ABAB sequence with only weak secondary inter-layers bonding. The binding energy of a carbon atom in the graphite lattice is about 7 eV and the energy required to displace a carbon atom is ~ 25 to 60 eV.

The D-T reaction produces both 14.1 MeV neutrons and 3.5 MeV alpha particles. The majority of the alpha particles will deposit their energy in the plasma, but the neutrons will reach the first wall and displace carbon atoms. Moreover, the neutron energies are sufficient that transmutations such as $^{12}C(n,\alpha)$ ^9Be and $^{12}C(n, n')3\alpha$ will occur and cause additional carbon atom displacements. Displaced carbon atoms will recoil through the graphite lattice, displacing other carbon atoms and leaving vacant lattice sites (Fig. 30). Once moderated, the carbon atoms are able to diffuse interstitially between the graphite layer planes in two dimensions and a large fraction of them will recombine with lattice vacancies. Others will coalesce and eventually may form dislocation loops or new graphite planes. The interstitial clusters, on further irradiation, may themselves be destroyed by a fast neutron or displaced carbon atom—a phenomenon known as radiation annealing. The formation of interstitial clusters, dislocation loops, and new graphite planes will cause an expansion of the graphite crystal in the <c> direction (Fig. 30). Adjacent lattice vacancies in the same graphite layer are believed to collapse parallel to the layers and form sinks for other vacancies, causing a shrinkage in the graphite crystal in the two <a> directions, i.e., parallel to the graphite layers.
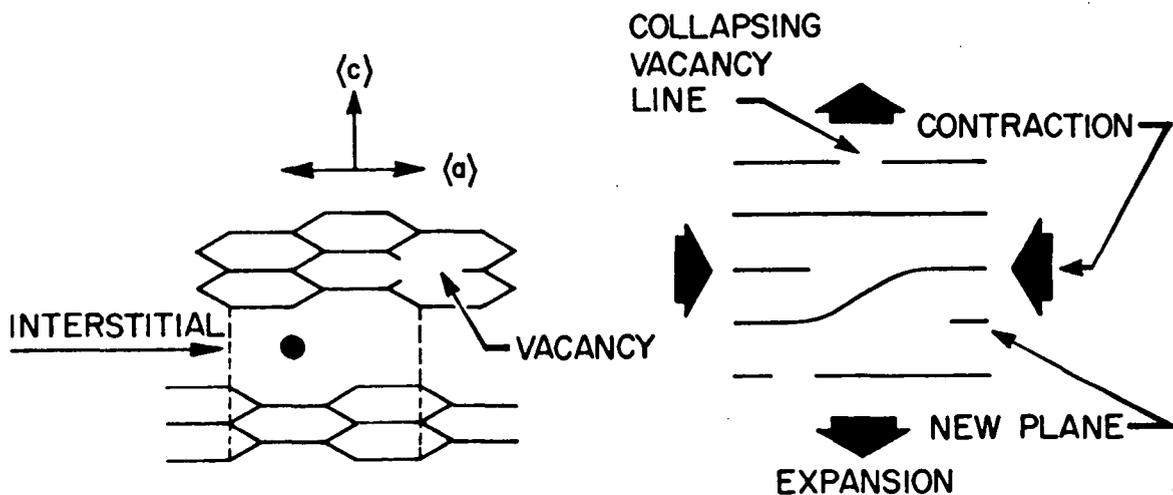
FIG. 30. The mechanism of radiation damage in the graphite crystal.

Graphite crystal neutron damage induced dimensional changes will cause dimensional changes in C/C composite materials. The nature of the dimensional changes in the composites will depend upon both the irradiation conditions (temperature, fluence) and the microstructure of the carbon fiber and architecture of the composite. The latter (structural) parameters are important because they control the amount and location of porosity which may accommodate the crystallographic <c>

axis expansion during neutron irradiation. The number of interstitial atoms and vacancies generated depends upon the neutron flux and energy, and the irradiation temperature controls the number of carbon atoms retained in the crystal lattice, and their distribution, because lattice vacancy mobility is temperature dependent. Moreover, the amount of available accommodating porosity within a carbon fiber or C/C composite will be reduced at higher temperatures by the thermal expansion of the material. Extensive studies of graphite crystal dimensional changes, performed on highly oriented pyrolitic graphite, have been published and are reviewed elsewhere [24, 25].

The formation of neutron irradiation induced defect structures in the graphite lattice will adversely affect a C/C composite materials physical properties. Phonons will be scattered by the defects, thus introducing additional thermal resistance and significantly reducing the thermal conductivity of an irradiated material. Similarly, electrons will be scattered by irradiation induced defects causing increased electrical resistivity. Pinning of dislocation lines by irradiation induced defects will increase the strength and elastic moduli of C/C composite materials. Data are presented here showing the influence of neutron irradiation on the dimensional change, physical and mechanical properties, and residual activity of C/C composite materials.

4.2 Irradiation Induced Dimensional Changes

Irradiation induced dimensional changes in fine-grained, fusion relevant graphites have been reviewed elsewhere [26]. The behavior of GraphNOL N3M [27, 28] is typical of many fine grained graphites and the irradiation induced dimensional changes are shown in Fig. 31. The solid lines in Fig. 31 are polynomial fits to the data. Data are shown for two temperatures (875 and 600°C) and two orientations (axial and radial) with respect to the forming axis of the graphite billet. The shrinkage rate initially increases and then decreases with increasing fluence. Turnaround (maximum shrinkage) occurs at lower fluences at 875°C compared to 600°C. The effect of temperature is more clearly demonstrated in Fig 32, where the volume change at minimum volume at 875°C is approximately 60% of that at 600°C, and occurs at 25% lower fluence, i.e., 15 displacements per atom (dpa) at 875°C cf. 21 dpa at 600°C. This effect is attributable to the thermally induced closure of a greater portion of the pores within the polygrannular graphite structure at the higher irradiation temperature, which reduces the internal "accommodation" for c-axis expansion, and accelerates the onset of pore generation (turnaround). Maximum dimensional shrinkages of several percent are typical, N3M for example has maximum shrinkages of ~2 and ~3% at 875 and 600°C and ~1 and ~2% at 875 and 600°C in the radial and axial directions, respectively. The dimensional change anisotropy is related to the texture in the molded N3M graphite billet. Most graphites exhibit isotropy in their radiation induced dimensional changes. However, fine grained isotropic graphites such as POCO AXF-5Q, or Toyo Tanso IG-110 are isotropic in their irradiation dimensional changes.

Data for the neutron irradiation induced dimensional changes of C/C composites have been reviewed elsewhere [26]. Burchell et al. [29, 30] have reported the dimensional changes of several C/C composite materials (Table XII). More recently Burchell [31] elucidated the mechanism of irradiation induced dimensional changes in C/C composites. Figure 33 shows the irradiation induced dimensional changes (diametral and longitudinal) of a unidirectional (UFC), two-directional (RFC) and three-directional (223) C/C composite irradiated at 600°C to a maximum fluence of ~5 dpa. The unidirectional C/C composite exhibited extremely anisotropic dimensional changes, undergoing rapid shrinkage in the fiber-axis direction (length). In the direction
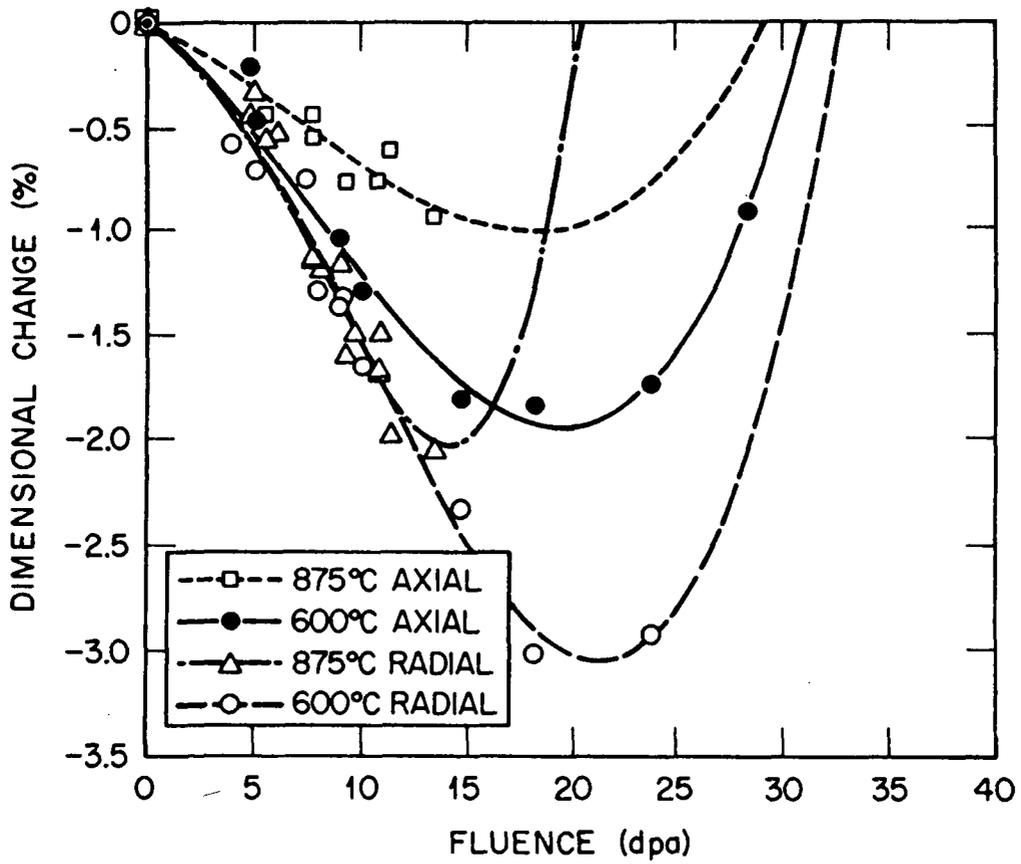
FIG. 31. Neutron irradiation induced dimensional changes in GraphNOL N3M [28].
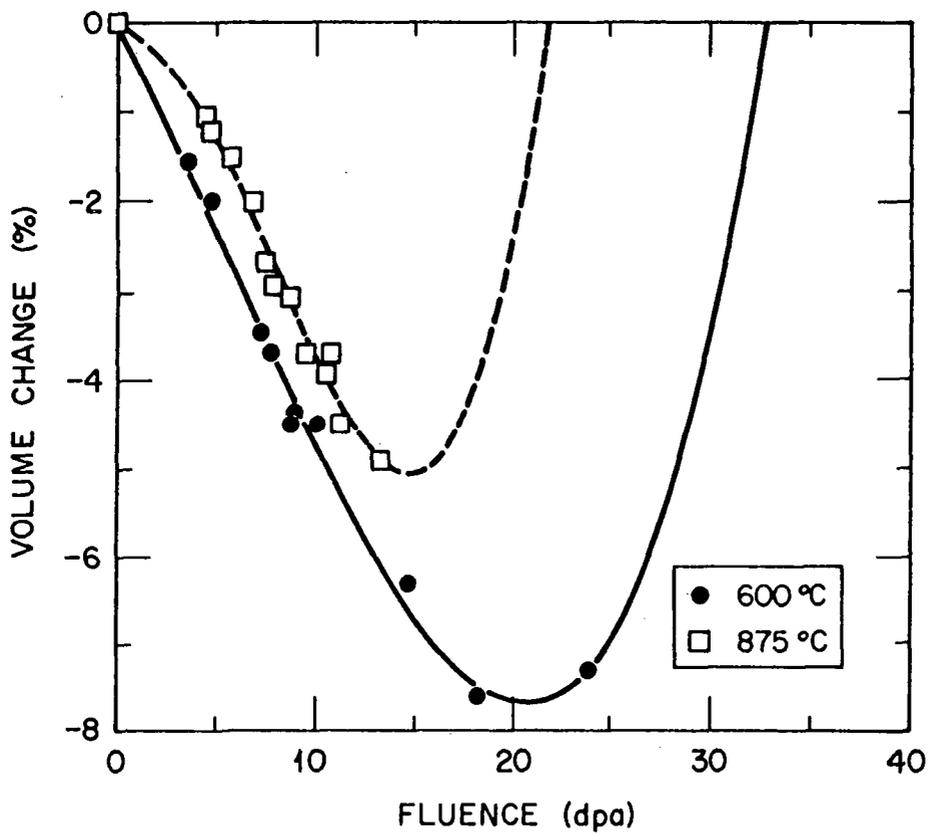
FIG. 32. Neutron irradiation induced volume changes in GraphNOL N3M [28].

perpendicular to the fiber axis (diameter) the composite first shrank up to a fluence of approximately 1 dpa, followed by a reversal to expansion, reaching the original diameter at about 2.5 dpa and continuing to expand at an increasing rate. Similar trends are observed for the two-directional, C/C composite (RFC), where the fiber axis is in the diametral direction. In the off-axis direction (length) the composite exhibited a slight contraction followed by expansion, returning to the original length at approximately 2 dpa. The diametral (fiber-axis) directions of the RFC specimen exhibited shrinkage, although the magnitude of the shrinkage was much less for the same fluence than in the case of the unidirectional composite. In contrast to the unidirectional and two-directional composites, the 3D PAN composite exhibited isotopic behavior at fluences up to approximately 2 dpa. At doses greater than 2 dpa the composite x direction (specimen length) continued to show shrinkage, whereas the fiber x-y (diameter) direction exhibited reversal and slight growth.

TABLE XII. SUMMARY OF MATERIALS IN IRRADIATED BY BURCHELL ET AL. [30, 31]

Designation	Description	Heat Treatment Condition
H-451	Near-isotropic nuclear graphite (reference material).	As received
A05	Carbone Lorraine. 2D C/C composite. PAN Fibers.	As received
UFC	Fiber Materials, Inc. 1D C/C composite. PAN Fibers.	3100°C
RFC	Fiber Materials, Inc. Random fiber composite. PAN Fibers (chopped).	2650 and 3100°C
223	Fiber materials, Inc. 3D C/C composite. PAN Fibers.	2650 and 3100°C
222	Fiber Materials, Inc. 3D C/C composite. Pitch Fibers (P55).	2650 and 3100°C

The influence of fiber structure and crystallinity on the irradiation-induced dimensional change of two three-directional, C/C composite materials is shown in Fig. 34. In Fig. 34(a), the dimensional changes of a pitch fiber (22) and a PAN fiber (23) three-directional composite in the z-fiber direction are shown. The pitch fiber composite exhibited less shrinkage for the same fluence than the PAN fiber composite. The superior behavior of the pitch-fiber composite is attributed to the greater degree of crystallinity in pitch fibers [32]. The data in Fig. 34(b) indicate that increasing the final graphitization temperature reduces magnitude of dimensional change in a three-directional PAN-fiber composite. The relationship between increased crystallinity or increased final heat treatment temperature and reductions in the magnitude of neutron irradiation-induced dimensional change has been clearly demonstrated in studies of the irradiation behavior of pyrolytic graphites [25]. It has been shown [29] that composites manufactured from more crystalline pitch fibers, or that are graphitized at high temperatures (>3000°C), exhibit less

106

dimensional change at a given fluence than C/C composites manufactured from less crystalline PAN fibers or graphitized at lower temperatures (<2700°C).
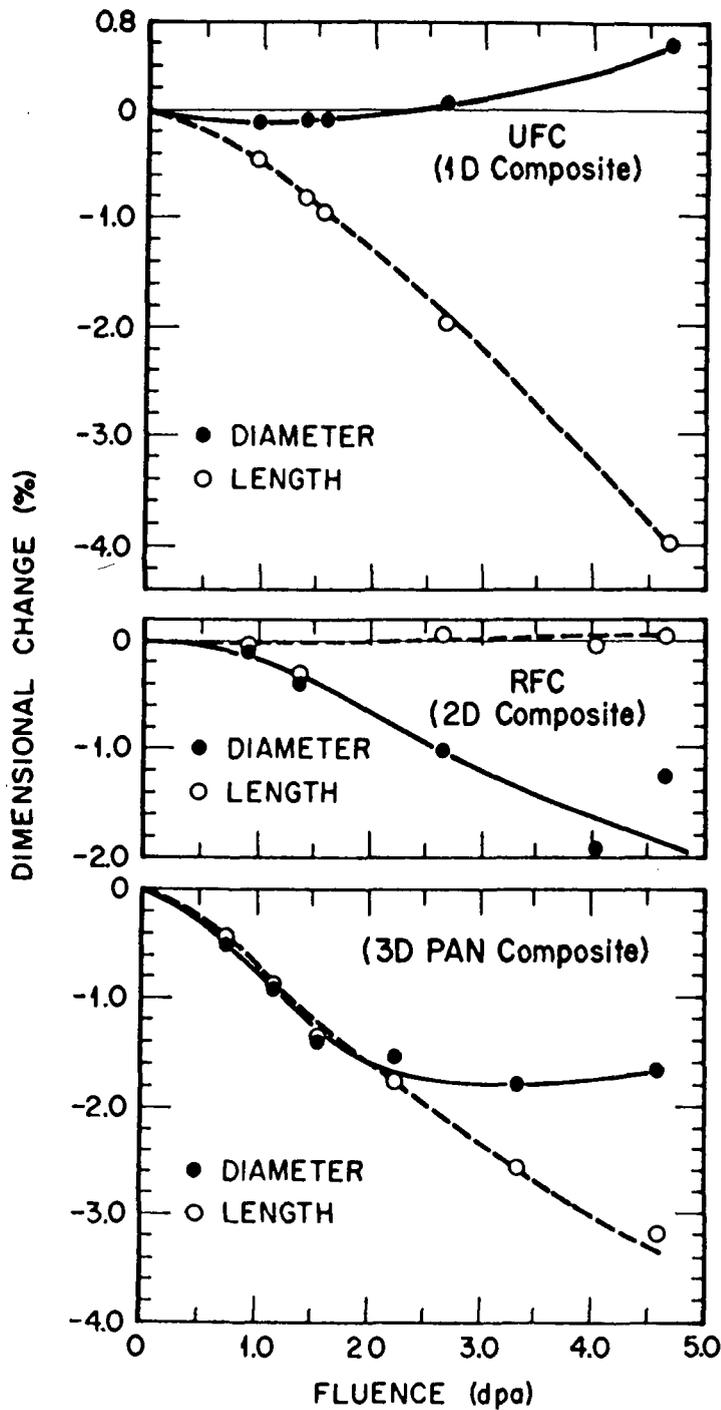

FIG. 33. Neutron irradiation induced dimensional changes of several carbon-carbon composites irradiated at 600°C [31].
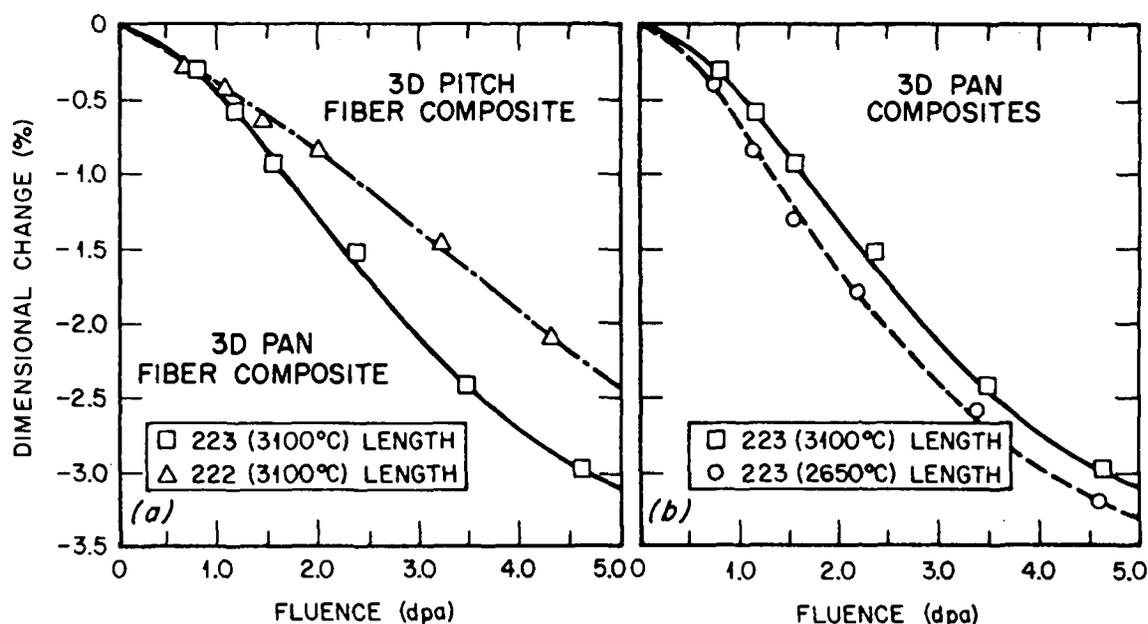
FIG. 34. Irradiation dimensional change in two 3D, C/C composites: (a) a comparison of pitch and PAN fiber composite behavior, and (b) the effect of heat treatment temperature on the dimensional change of a PAN (223) C/C composite [31].

The data in Figures 33 and 34 show that three-directional composites behave more isotropically than two-directional or unidirectional composites. Pitch fiber composites are more dimensionally stable than PAN fiber C/C composites and a higher final graphitization temperature is beneficial. At fluences of <5 dpa and irradiation temperatures of ~600°C shrinkages >3% can be expected. Turnaround to growth will occur rapidly for uni- and two-directional carbon-carbon composites in the direction perpendicular to the fiber axis. Dimensional change rates can be expected to be greater at elevated temperatures due to the reduced accommodation available within the composite structure.

4.3 Physical Properties

The effects of neutron irradiation on key physical properties of graphites are widely reported, for example Kelly [24], Engle and Eatherly [25], Nightingale [33] or Simmons [34]. Recently, Kelly and Burchell [35] reported on structure related property changes in polycrystalline graphite under neutron irradiation. Moreover, Kelly has recently summarized radiation effects in nuclear reactor moderator grade graphites [36]. Neutron irradiation produces defects in the graphite basal planes which act as phonon scattering centers, resulting in additional thermal resistance. The thermal conductivity of graphite and C/C composites will therefore be substantially reduced by irradiation. Figure 35 shows the degradation of thermal conductivity of several fine-grained, fusion relevant graphites irradiated at 600°C to damage doses in the range 0.005-0.1 dpa [37]. The thermal conductivity is reduced by 20% or more, even at these very low fluences. Similar data for C/C composites is given in Figure 36 [37], where large reductions in the thermal conductivity of the C/C composites are apparent. Data for the temperature dependance of the thermal conductivity of an irradiated C/C composite (CX2002U) are given in Figure 37 [38] for two irradiation temperatures (200 and 400°C). At the lower dose (0.01 dpa at 200°C) the damage is completely

108

annealed at 1200°C. However, at the higher dose of 0.9 dpa (400°C) thermal conductivity recovery is incomplete after annealing to 1200°C. The beneficial effects of post irradiation annealing on the thermal conductivity of a two-directional C/C composite (AO5) is shown in Figure 38 [26]. The thermal conductivity at 600°C of the unirradiated AO5 is approximately 84 W/m·K. After irradiation at 600°C to ~1 dpa the thermal conductivity (at the irradiation temperature) is only ~40 W/m·K. Thermal annealing to 1200°C restores the thermal conductivity to ~66 W/m·K. Figure 39 [31] shows data for FMI 222 material, a three directional pitch fiber C/C composite, in the unirradiated, irradiated (~4 dpa) and irradiated and annealed conditions (z-fiber direction). Data for the same C/C composite over the damage dose range 1-4.5 dpa has been reported [31] and is given in Figure 40. These data show that the radiation induced degradation is saturated over this dose range, but may be substantially recovered by thermal annealing to 1600°C.
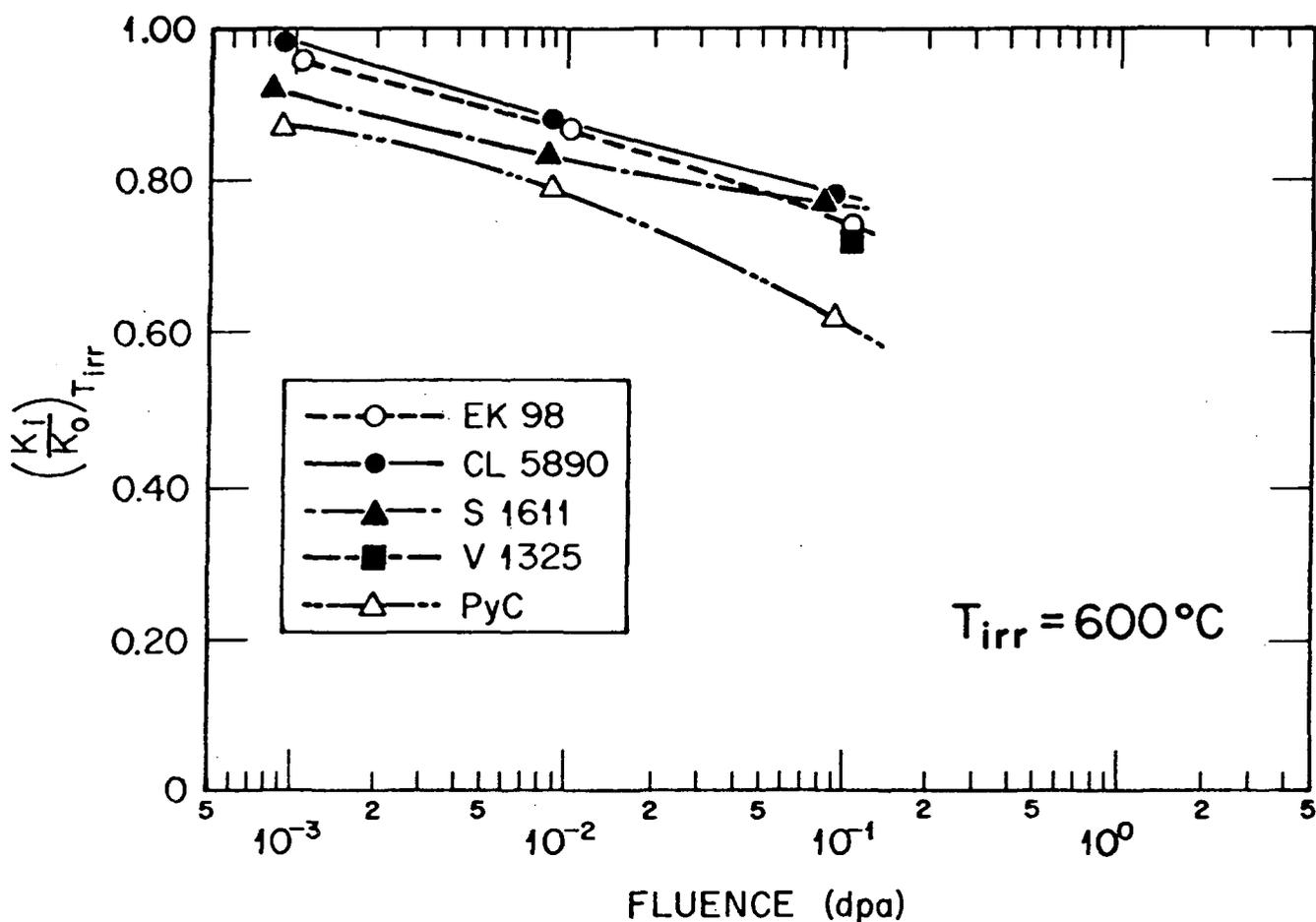
FIG. 35. The variation of normalised thermal conductivity $(K/K_o)_{irr}$ with neutron dose for pyrolitic carbon and several fine grained graphites [37].
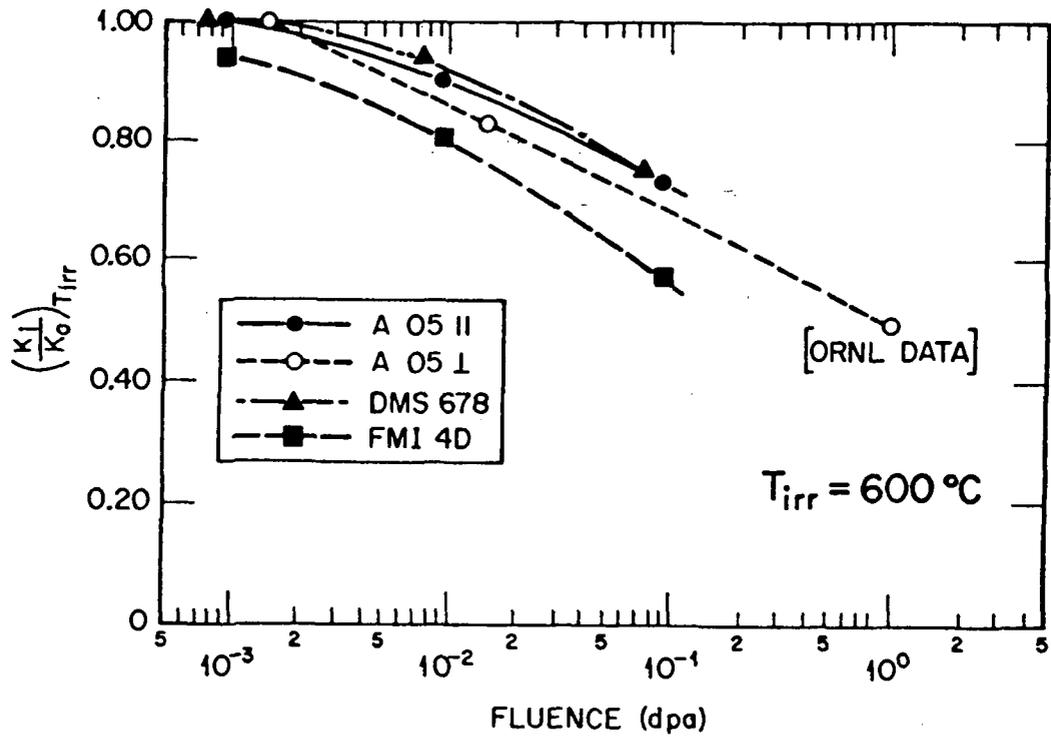
FIG. 36. The variation of normalised thermal conductivity $(K/K_o)_{irr}$ with neutron dose for several carbon-carbon composites [37].
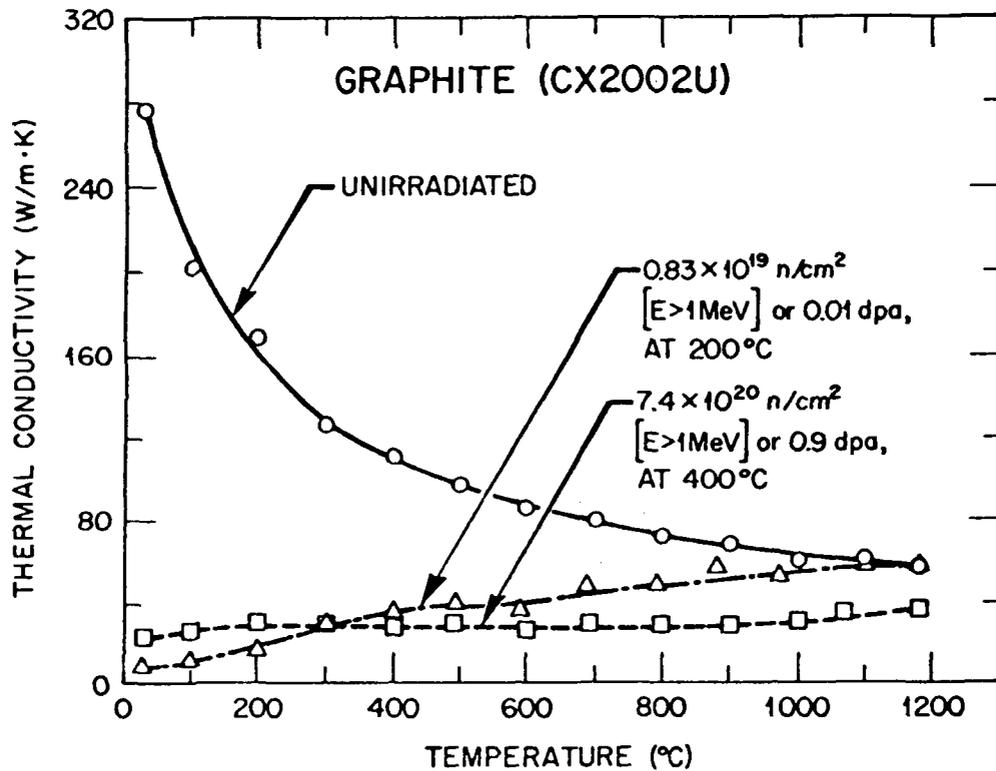
FIG. 37. The effects of neutron irradiation on the thermal conductivity of a two-directional carbon-carbon composite (CX2002U) [38].
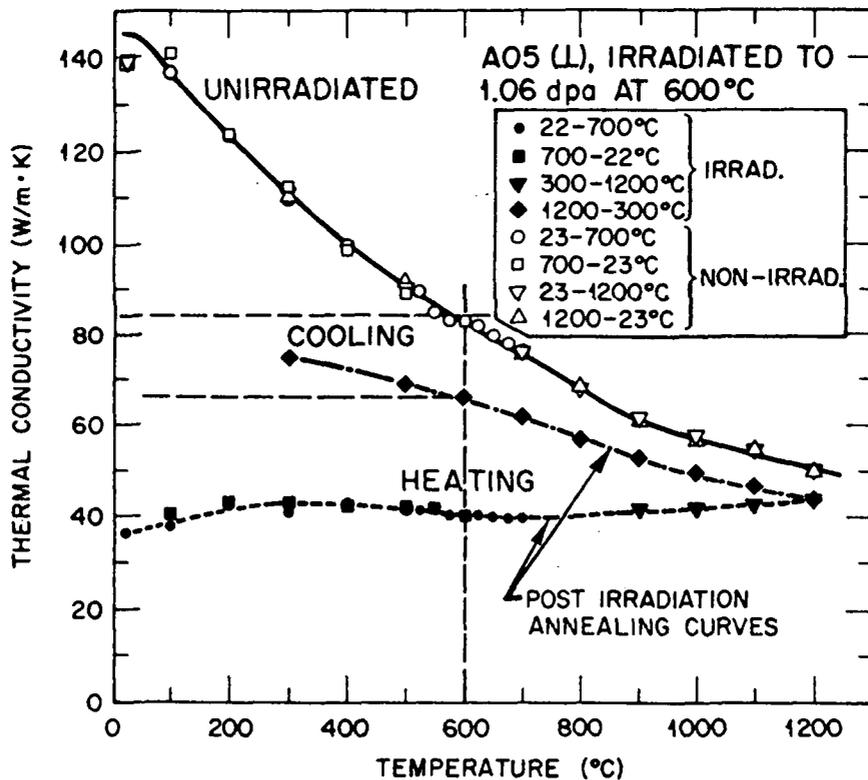
FIG. 38. The variation of thermal conductivity of a two-directional carbon-carbon composite (AO5) with temperature for three conditions: unirradiated, irradiated, and irradiated and annealed to 1600°C [31].
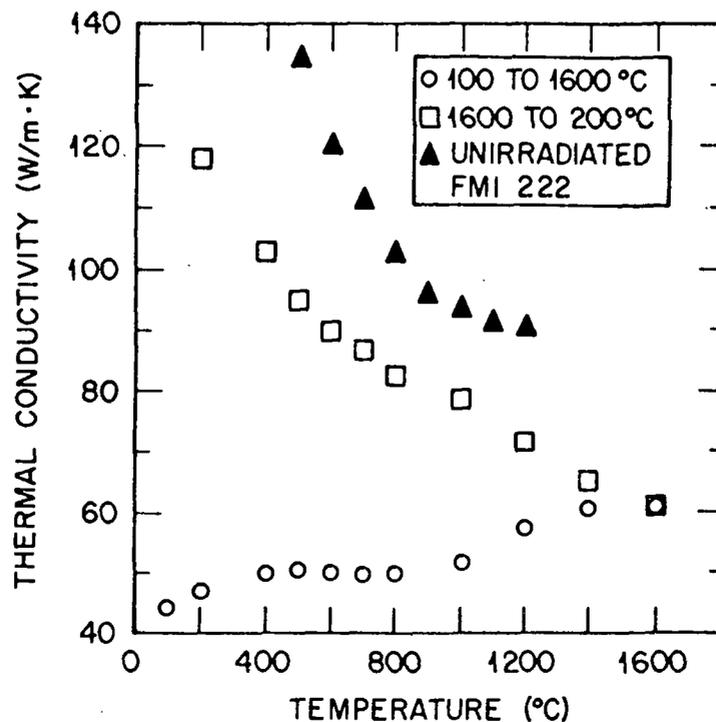

FIG. 39. The variation of thermal conductivity of a three-directional carbon-carbon composite (FMI 222) with temperature for three conditions: unirradiated, irradiated, and irradiated and annealed to 1600°C [31].
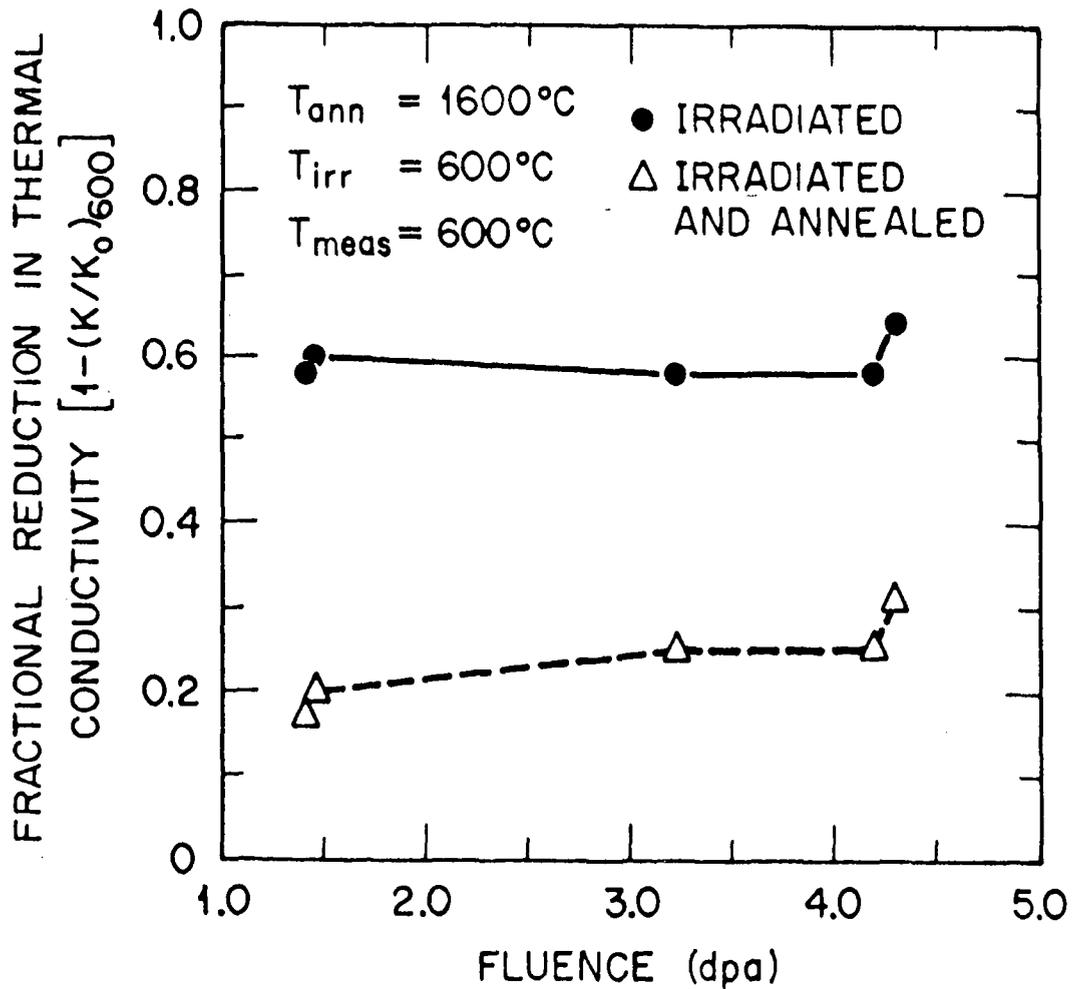
FIG. 40. The variation of the fractional reduction in thermal conductivity $[1-(K/K_o)_{600}]$ with irradiation dose for FMI 222 in the irradiated and irradiated and annealed conditions [31].

Data for the effects of neutron irradiation on the coefficient of thermal expansion (CTE) of C/C composites are extremely limited at the present time. Burtseva et al. [39] report the CTE of a multi-directional PAN fiber C/C composite was relatively unaffected after irradiation to 2×10^{20} n/cm^2 at irradiation temperatures of 200-400°C. Burtseva's C/C material had a initial CTE of 0.5×10^{-6} and a relatively low density (1.6 g/cm^3), which, in combination with the relatively low dose of ~0.3 dpa, may account for the negligible effect of irradiation on the CTE. Generally, C/C composite materials have low CTEs in the unirradiated condition, typically ~1×10^{-6} (section 2.). Based upon irradiation induced swelling data (section 4.2), irradiation to doses in the range 0.5-5 dpa can be expected increase the CTE of C/C composites, probably by no more than a factor of two. Extensive data exists for the effect of irradiation on the CTE of nuclear graphites [25, 26, 34, 35, 37]. Figure 41 shows the variation of the CTE of GraphNOL N3M graphite with neutron dose for an irradiation temperature of 600°C [28]. This behavior is typical of that off fine-grained, fusion relevant graphites, showing an initial increase in CTE followed by a significant decrease. The transition from increasing to decreasing CTE occurs at lower doses for higher irradiation temperatures. A similar pattern of irradiation behavior was reported by Kelly [24] for US POCO and UK Gilsocarbon graphites.
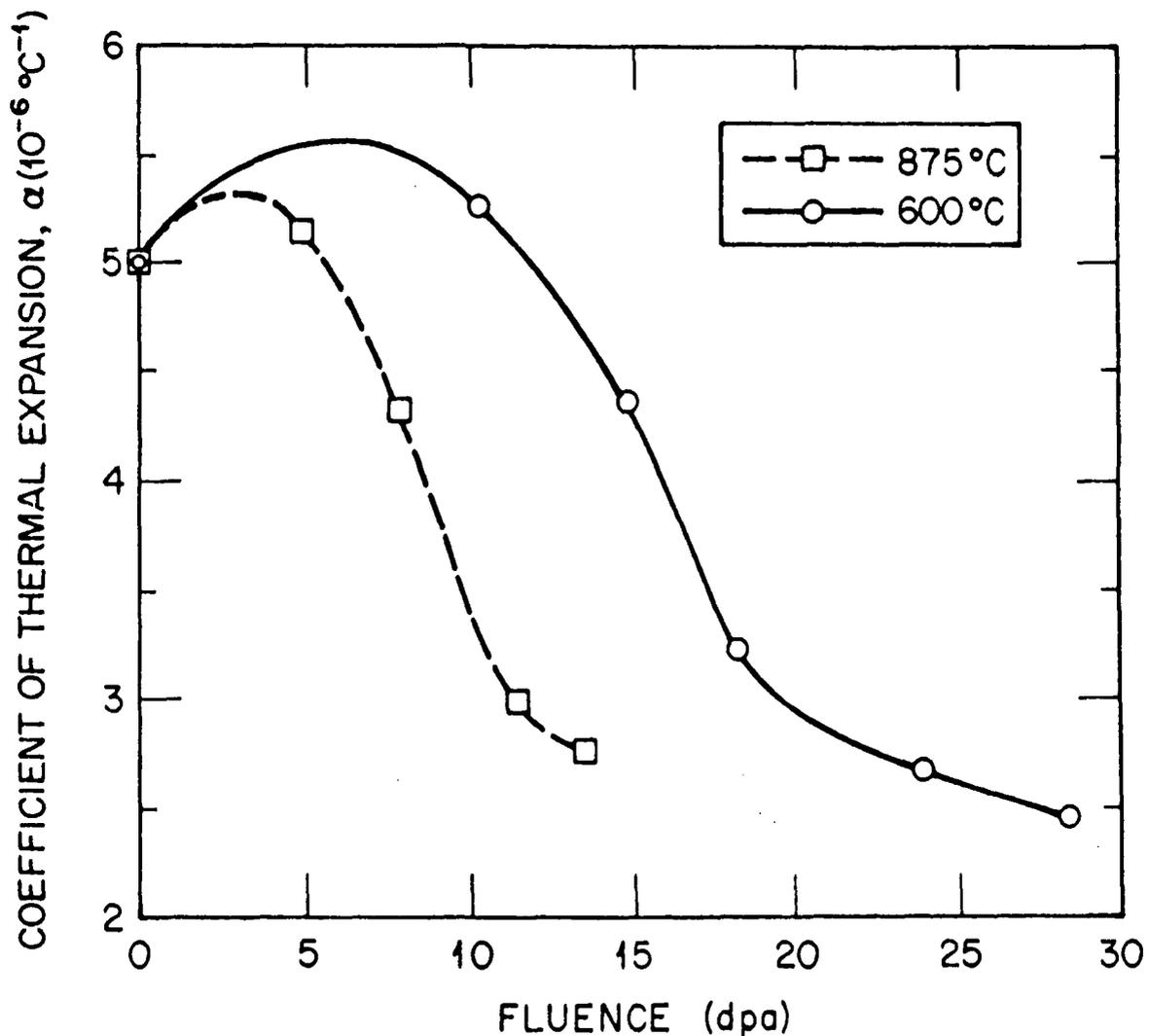
FIG. 41. The effect of neutron irradiation on the coefficient of thermal expansion of GraphNOL N3M graphite [28].

Very little data has been reported for the effects of neutron damage on electrical resistivity. Figure 42 shows the effects of neutron dose on the electrical resistivity of GraphNOL N3M graphite. Typically, the resistance increases rapidly to a saturation level 2-3 times greater than the unirradiated resistivity. Similar behavior can be expected for C/C composites. Data reported by Sato et al. [18] for two C/C composites (Table XIII) appears to support this supposition. Both C/C composites, irradiated at 650-810 °C to 1-1.7 dpa, exhibited increased electrical resistivity.

113
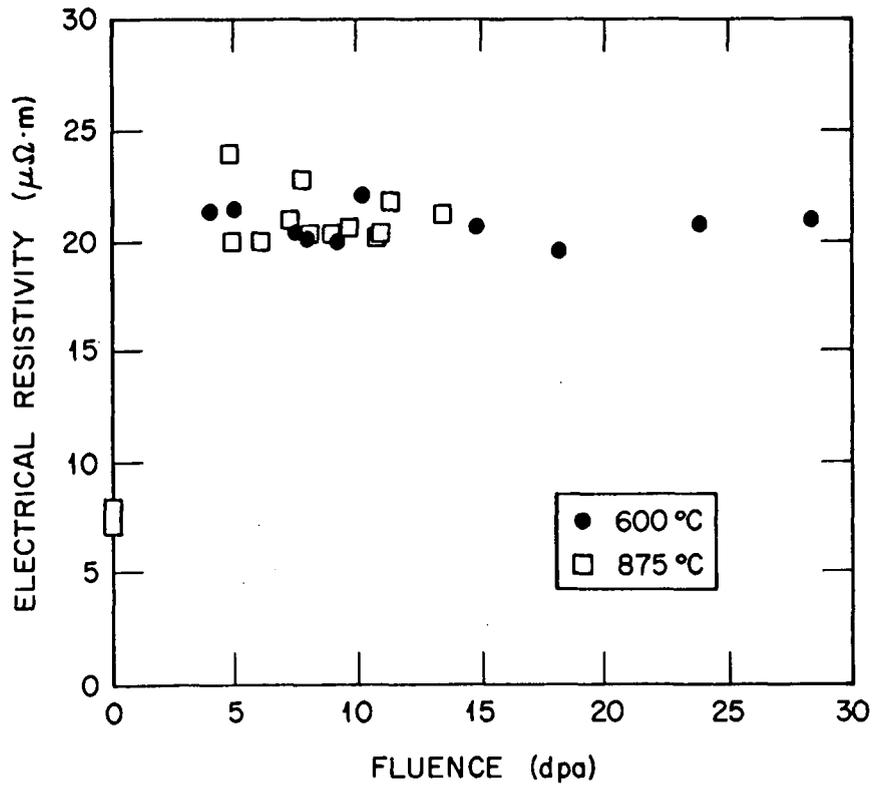
FIG. 42. The effect of neutron irradiation on the electrical resistivity of GraphNOL N3M graphite.

TABLE XIII. ELECTRICAL RESISTIVITY DATA AND IRRADIATION CONDITIONS FOR TWO C/C COMPOSITES [18]

Material	C/C B	2D C/C
Manufacturer	Showa Denka	-
Architecture & Fiber Type	2D felt, coal tar pitch binder, PAN fiber	2D cloth lay-up, rayon fiber
Irradiation Temperature (°C)	750-810	650-710
Fluence (x 10^{21} n/cm^2) [E>29fJ]	1.2	1.75-1.88
Damage Dose (dpa)	1.1	1.6-1.7
Unirradiated Electrical Resistivity (μohm.m)	4	12.17
Irradiated Electrical Resistivity (μohm.m)	5.8	23.23

114

4.4 Mechanical Properties

Sato et al. [18] have reported the effects of neutron damage on the mechanical properties of three C/C composite materials (Table XIV). The irradiation conditions for C/C-A were identical to those of C/C-B, and are shown along with the irradiation conditions for the 2D C/C in Table XIII. C/C-A was manufactured from a pitch based carbon fiber, and a coal tar pitch binder, by Showa Denka of Japan. The neutron dose received by the specimens was relatively low (1-1.7 dpa), yet was sufficient to significantly effect the mechanical properties of the C/C materials. Young's modulus increased by >30%, with the largest increase (42%) in the pitch fiber material (C/C-A). Compressive, bend and tensile strength data for the C/C materials are also presented in Table XIV. In all cases the strength increased on irradiation, typically by ~20%. The greatest strength gains were for the pitch fiber composite (C/C-A). Fracture toughness (critical stress intensity factors, K_{Ic}, K_{IIc}) increased after irradiation by 20-30% (Table XIV).

TABLE XIV. PRE- AND POST-IRRADIATION DATA FOR THE MECHANICAL PROPERTIES OF THREE C/C COMPOSITE MATERIALS [18]

Materials	C/C-A		C/C-B		2D C/C	
	Pre-Irr.	Post-Irr.	Pre-Irr.	Post-Irr.	Pre-Irr	Post-Irr
Young's Modulus, E (GPa)	13.5	19.2	26.3	34.2	23.8	31.6
Compressive Strength, σ_c (MPa)	44.9	58.4	66.6	81.2	-	-
Bending Strength, σ_b ($\parallel$) (MPa)	65.7	81.5	96.9	119.2	117	145
Bending Strength, σ_b ($\perp$) (MPa)	57.4	79.8	94.5	110.0	116	143
Tensile Strength, σ_t (MPa)	35.7	-	55.4	-	90.1	114
Critical Stress Intensity Factor K_{Ic} ($\parallel$) (MPa.m$^{1/2}$)	2.96	3.65	3.44	4.14	5.26	5.77
Critical Stress Intensity Factor K_{Ic} ($\perp$) (MPa.m$^{1/2}$)	2.14	2.65	3.03	3.94	-	-
Critical Stress Intensity Factor K_{IIc} (MPa.m$^{1/2}$)	3.79	4.85	4.39	5.56	-	-

Burchell et al. [30] irradiated several C/C composites, covering a range of fiber types and architectures (Table XII). The influence of neutron irradiation on the ring compression strength of these C/C composites is shown in Figures 43 and 44. The UFC, RFC and 222 composites showed increases in strength after irradiation to ~2.5 dpa at 600°C. The 223 C/C showed an initial rapid increase in strength up to ~0.8 dpa, followed by a decreasing strength. Tanabe et al. [40] have reported the mechanical properties of uni-directional, PAN fiber, C/C composites irradiated at 240 and 640°C to 0.64 and 0.87 dpa, respectively. Strength and failure strain both increased after irradiation. Poisson's ratio decreased from 0.2 to ~0.12. The fracture energy increased from a pre-irradiation value of ~6 kJ.m^{-2} to ~ 14 kJ.m^{-2} and 10 kJ.m^{-2} after irradiation to 0.64 dpa at

240°C and 0.87 dpa at 640°C, respectively. At the present time there are no data available for the irradiation creep behavior of C/C composites. A significant amount of data has been published for the irradiation creep behavior of graphites [21, 25, 33, 34, 41].
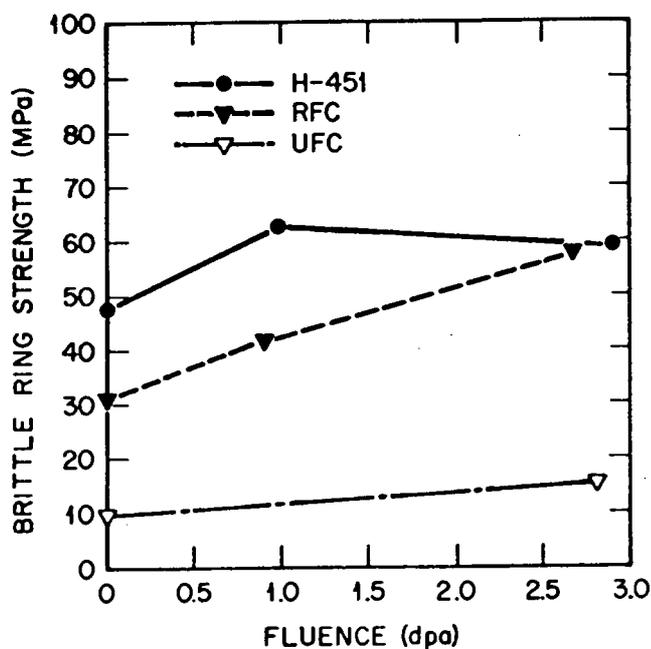

FIG. 43. The influence of neutron irradiation on the brittle ring strength of H-451 graphite, RFC and UFC carbon-carbon composites [30].
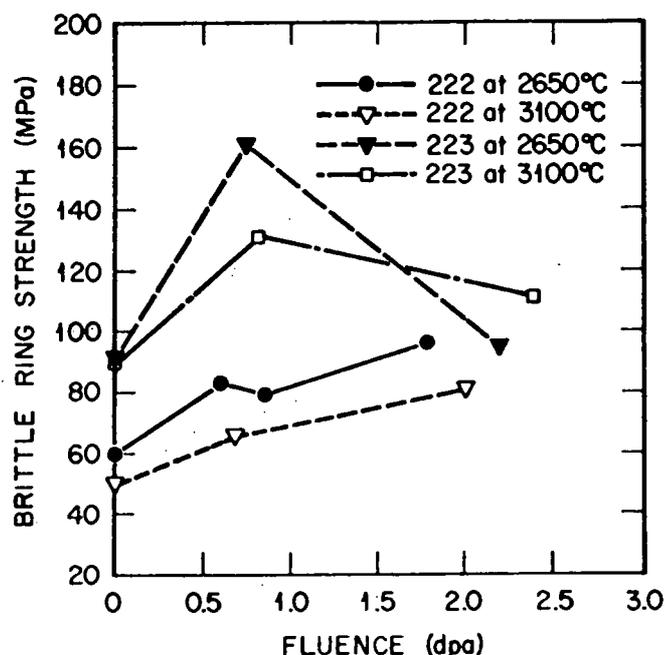
FIG. 44. The influence of neutron irradiation on the brittle ring strength of two 3D carbon-carbon composites [30].

4.5 Residual Activity

Snead [42] has reported the residual activity of three C/C composites irradiated to ~1.5 dpa at 600°C (Table XV). The radioactive elements detected are caused by: impurity levels of contaminants picked up during manufacture (eg. the Period IV elements); daughters of strong carbide formers (eg. ^{95}Nb, ^{46}Sc and ^{182}Ta); or impurities in the feed materials used for manufacture of the fibers, preforms or composites (eg. rare earths such as ^{154,155,156}Eu and ^{125}Te). Other radioactive isotopes are the unstable daughter products from the impurity elements identified. Among these major radioactive species, ^{60}Co and the rare earths such as ^{154,155}Eu have relatively long half lives and are transmuted mainly through reactions with thermal neutrons. Specific activities reported for fusion relevant graphites by Shikama et al. [43], are 10-100 times lower than those given by Snead [42] (Table XV). This very large difference can be attributed to the higher impurity contents of the C/C composites which, unlike the graphites reported by Shikama et al., were not halogen purified. For a purified graphite or C/C, maximum production rates for ^{60}Co and rare earth element are 4 and 40 nCi/g(thermal neutron fluence 10^{20}n/m^2), respectively [43].

116

TABLE XV. SPECIFIC ACTIVITIES OF THREE C/C COMPOSITE MATERIALS [42]

Isotope	Half Life [days (d), or years (y)]	Specific Activity (μCi.cm^{-3})		
		2D C/C (Pitch fiber)	3D C/C (PAN fiber)	3D C/C (Pitch fiber)
^{110m}Ag	249 d	1.82	0.053	0.158
^{109}Cd	62.3 d	-	-	0.159
^{58}Co/^{60}Co	71.3 d/5.26 y	0.17/1.65	0.262/2.06	-/2.08
^{134}Cs	2.1 y	0.008	0.026	0.040
^{154}Eu/^{155}Eu	8.5 y/5.0 y	0.067/0.041	0.22/0.158	0.026/0.006
^{192}Ir	74.0 d	2.54	0.317	0.132
^{54}Mn	312.2 d	0.66	0.026	0.265
^{95}Nb	35.1 d	3.46	-	1.165
^{46}Sc	83.8 d	71.11	27.3	8.7
^{182}Ta	114.5 d	0.25	33.86	11.19
^{160}Tb	72.4 d	2.57	0.30	0.18
^{125}Te	58.0 d	4.41	-	-
^{65}Zn	243.8 d	0.12	-	0.66
^{95}Zr	64.03 d	1.57	0.441	-

5. CORROSION EFFECTS

The property degradation due to oxidation of nuclear graphites and carbons is of importance in fusion reactors as well as in fission reactors. Long term oxidation influences the thermal and mechanical properties of carbon/carbon composite materials, just as it does graphite materials. The oxidation produces changes in the pore and micro structures of the materials: generally many new pores are generated in the structure due to oxidation and the bulk density decreases, that is the porosity increases. The oxidation occurs selectively in the binder part rather than in the crystalline (fiber) part. In graphite materials, an oxidation gradient can exist between the surface and the interior of the graphite block [44]. The oxidation of the surface of the specimen facing to the corrosive gas can be decreased by coating the surface with the materials such as oxide ceramics.

Two grades of 2D pitch matrix C/C composite material were used as an oxidation experiment [45]. The materials were made from carbon cloth in xy-plane pierced by fibers in the z-direction and a carbonized pitch matrix. Table XVI shows the preform characteristic and mechanical properties of the C/C composites. Figure 45 gives weight loss as functions of temperature and

time, measured in flowing air, at a constant temperature. The burn-off curves could be divided into three regimes, the weight loss is a parabolic function of time which means that the oxidation rate is a linear function of time in the zone III regime, whereas the weight loss is a linear function of time in the zone II regime. Differences in the reactivity of the different preform structures were also found, the faster losses were at temperatures above 650°C for material 1 and 683°C for material 2.

TABLE XVI. PROPERTIES AND PREFORM OF C/C COMPOSITES [45]

Materials		Carbon cloth harness	Z fiber bundles		Tensile	
			k	d (mm)	σ (MPa)	E (Gpa)
1	XY	5	6	1.2	45.5	32.6
	Z				100.5	106.
2	XY	8	8	1.4	146.7	70.5
	Z				132.7	53.3
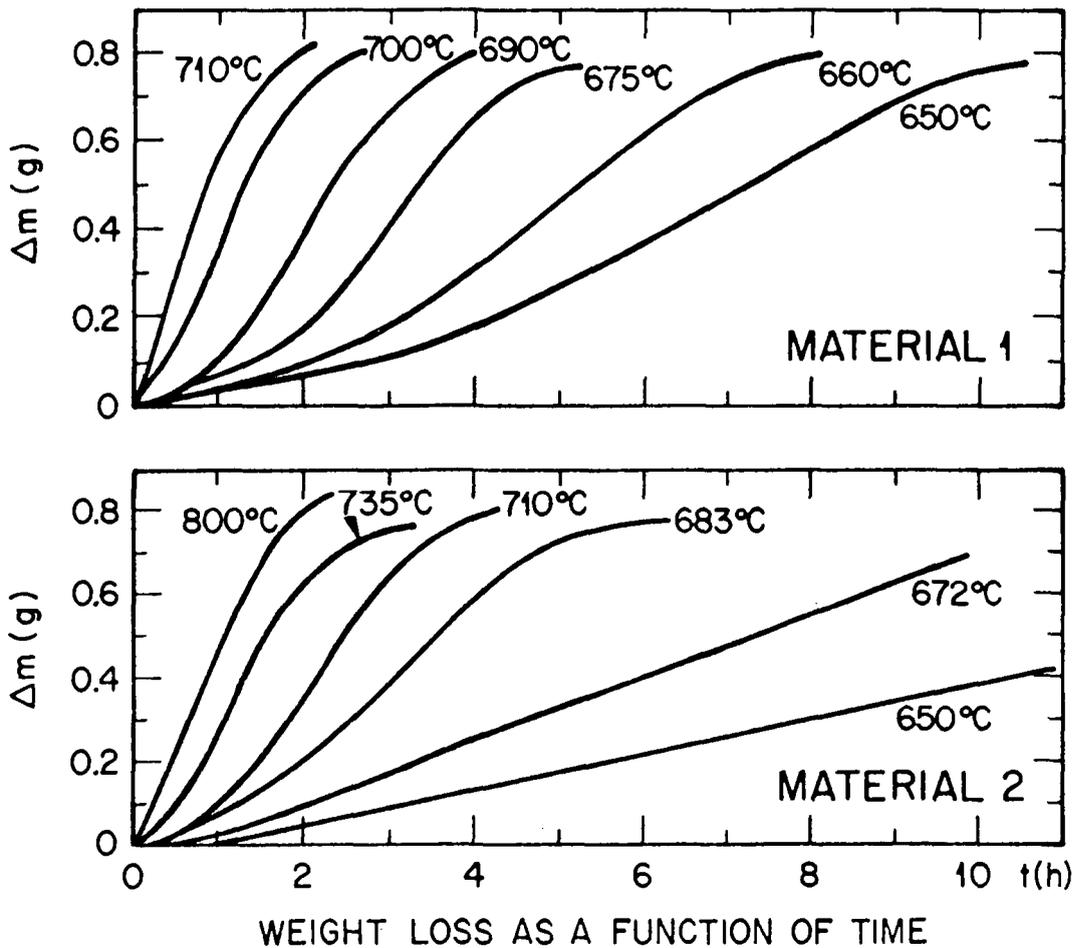
FIG. 45. Weight loss as a function of time for two grades of 2D C/C composite [45].

The oxidation rates of C/C composites were found to follow the Arrhenius type equation:

$$k = A \cdot \exp(-E_a/RT) \tag{2}$$

Figure 46 shows the logarithmic plots for the oxidation of material 2, there were marked differences in the oxidation characteristics of the various regimes. The C/C composites gave linear plots with apparent activation energy (E_a) of 87.5 kJ/mole for zone III and bilinear for zone II, low and high E_a are 55.0 kJ/mole and 249.0 kJ/mole, respectively, the two lines cross at the temperature of 720°C. Oxidation occurs in the zone I regime with rates controlled by the surface reaction of oxygen with active sites on the composite surfaces, and at the higher temperatures, the gasification rates were increasingly controlled by diffusion of gaseous oxygen into the pore network of the composites. In the zone II regime, the oxidation rate is attributed to the reaction between carbon and oxygen at low temperature (<700°C), the reactivity is controlled by both gas phase diffusion and reaction kinetics at high temperature (>700°C).
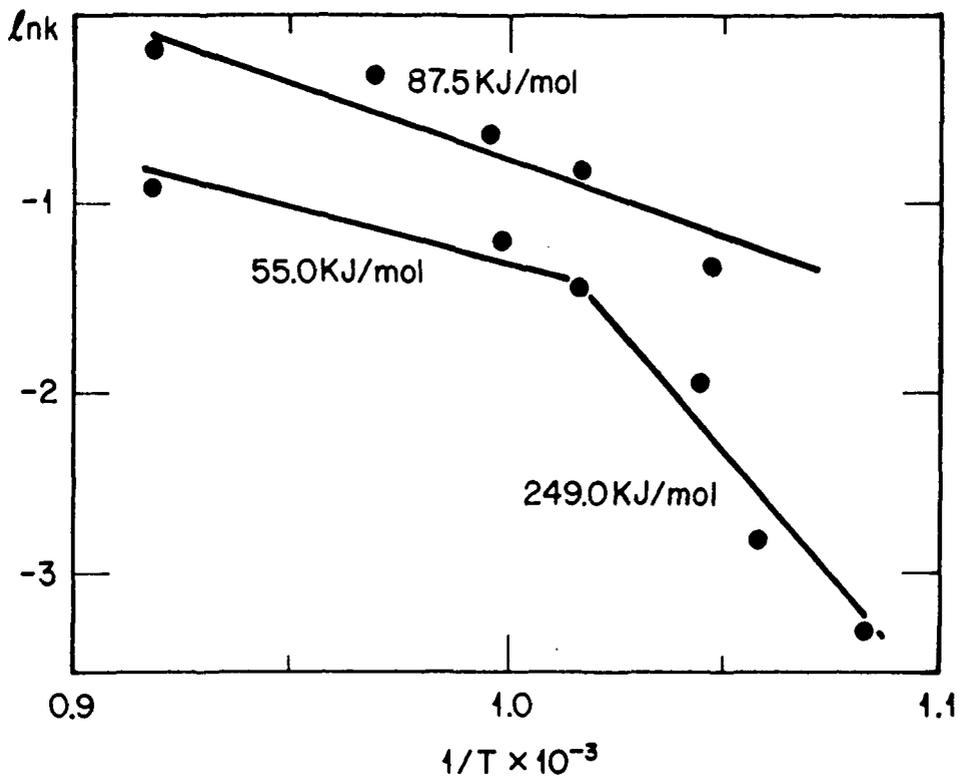
FIG. 46. Arrhenius plots of oxidation rate, K, as a function of reciprocal time for 2D C/C material 2 [45].

An example of the oxidation behavior of matrix inhibited C/C composites is shown in Fig. 47. The material was a 2D C/C composites containing approximately 18 wt.%B_4C in the matrix. The composite was fabricated using T-300 PAN fibers which were heat treated to 2473K and fabricated into a 2-D cloth. The laminate construction was a 0-90° lay-up. The matrix consisted of phenol formaldehyde resin containing 18 wt.% B_4C particulates. The composite was fabricated in a tape lay-up process. After the tape lay-up and carbonization, open pore volume was subsequently densified via CVI with pyrolytic carbon. An Arrhenius plot of reactivity of the C/C composite is indicated in Fig. 47 over the temperature range 1173 and 1673K in dry UHP O_2. In dry UHP O_2, there are two reaction mechanisms operative. In the relatively low temperature

range, up to ~1280K, the reaction is controlled by zone II (E_a=105.7kJ/mole) kinetics. At temperatures above 1280K (zone III), the reaction is controlled by diffusion through the boron oxide layer (E_a=19.6 kJ/mole). It is reported that the PAN fibers oxidize readily on all fiber surfaces and not just the fiber ends [47].
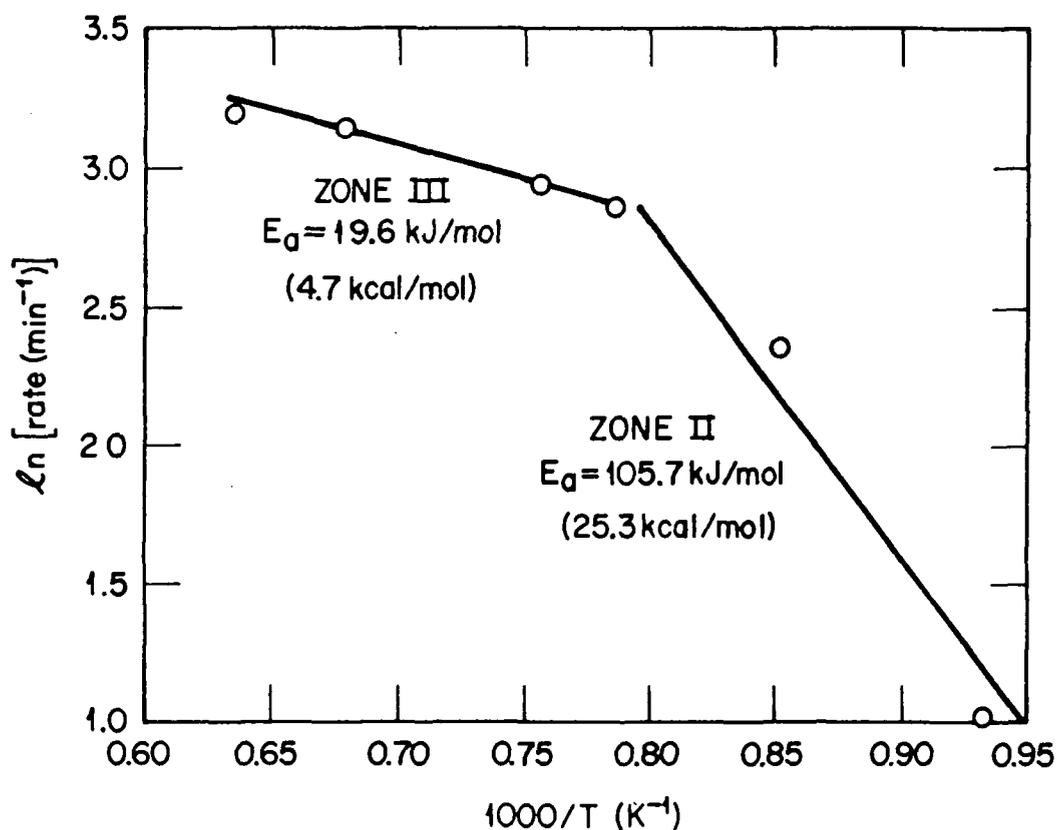

FIG. 47. *Arrhenius plot of the reactivity of inhibited C/C in dry UHP oxygen flowing at 20 cc/min over the temperature range 1173 to 1673 K [45].*

The PAN fiber felt type C/C composite (CX-2002U) was used to examine the effects of burn-off on the mechanical properties [48]. Figure 48 shows burn-off of CX-2002U by air oxidation as function of time. Young's modulus decreases with increasing burn-off: at 10% burn-off Young's modulus decreases to 60% of the original value (Fig. 49). Bend strength behaves similarly to Young's modulus, as shown in Fig. 50. Fracture toughness values give larger decrease with increase of burn-off. Figure 51 shows that 40% decrease in the toughness is seen at 5% burn-off level. In this experiment, it was observed that the fiber was oxidized at first, after that the matrix was attacked.
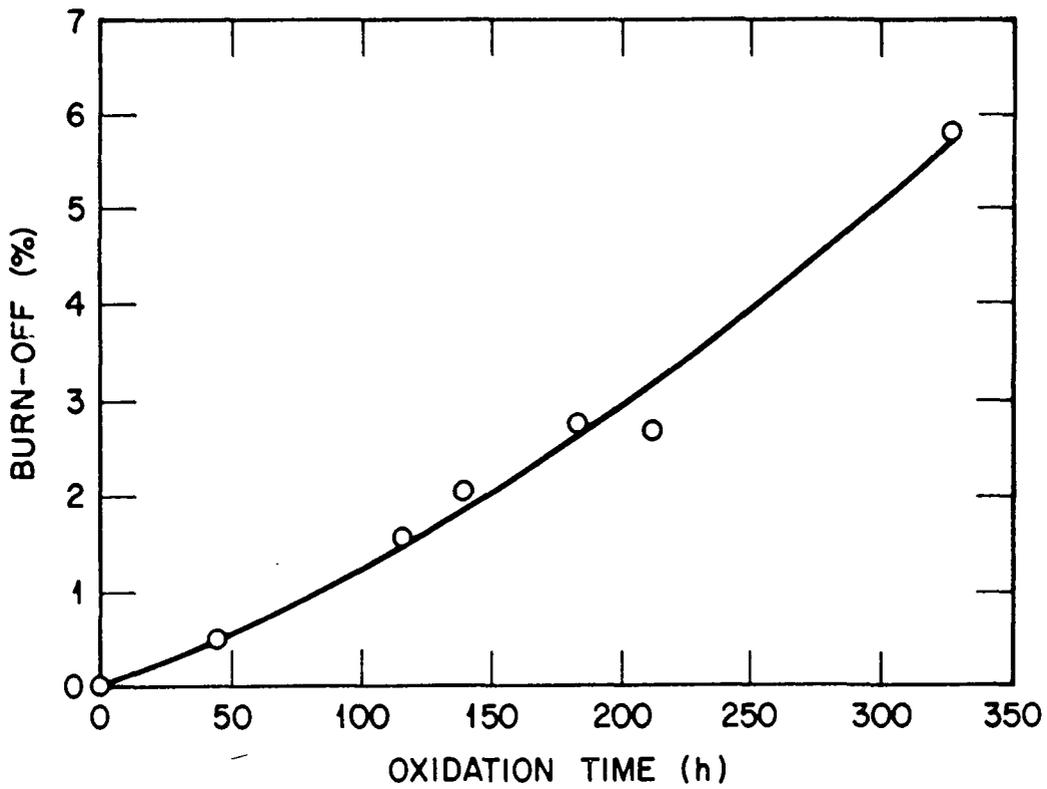
FIG. 48. The relationship between burn-off and oxidation time, h, of C/C composite grade CX-2002U [39].
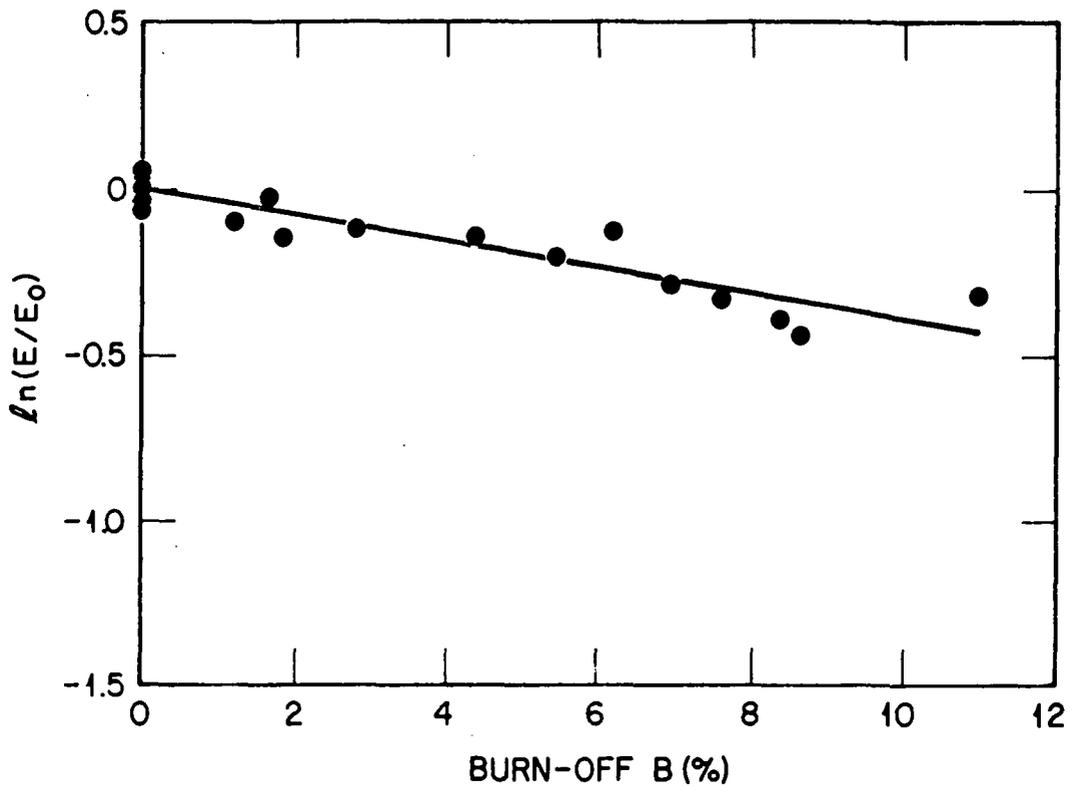
FIG. 49. The relationship between ln(E/E₀) and burn-off of C/C composite grade CX-2002U [48].
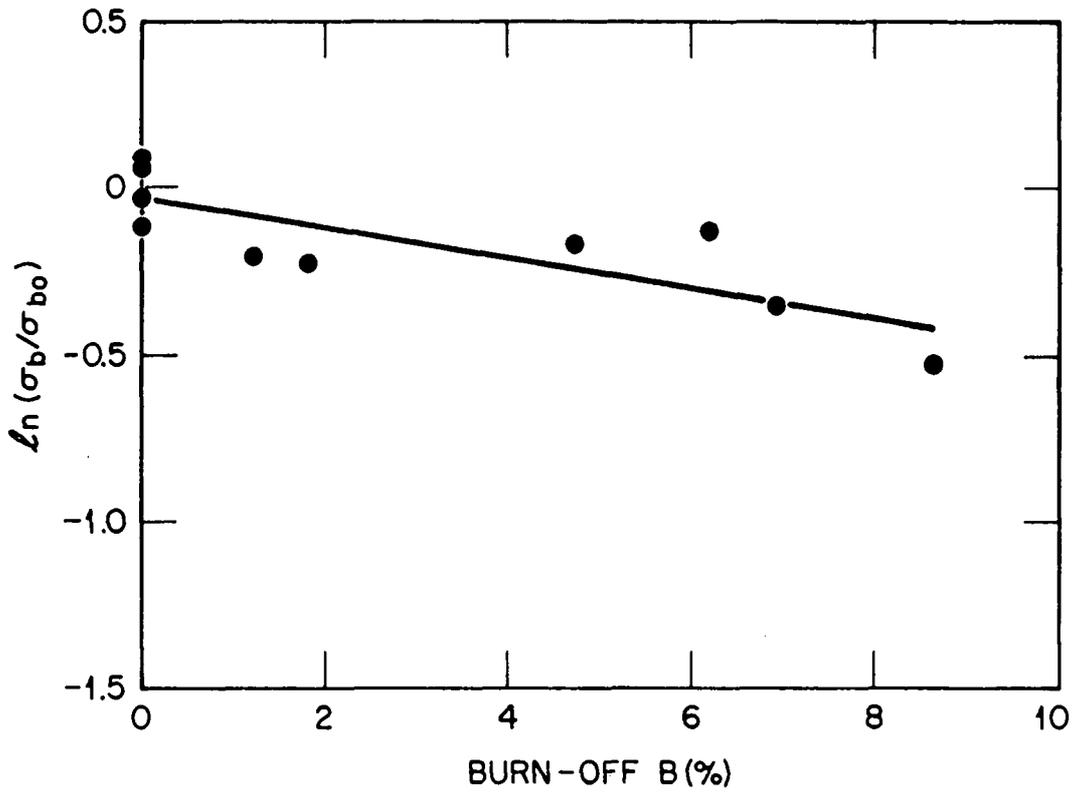
FIG. 50. The relationship between $ln(\sigma_b/\sigma_{bo})$ and burn-off of C/C composite grade CX-2002U [48].
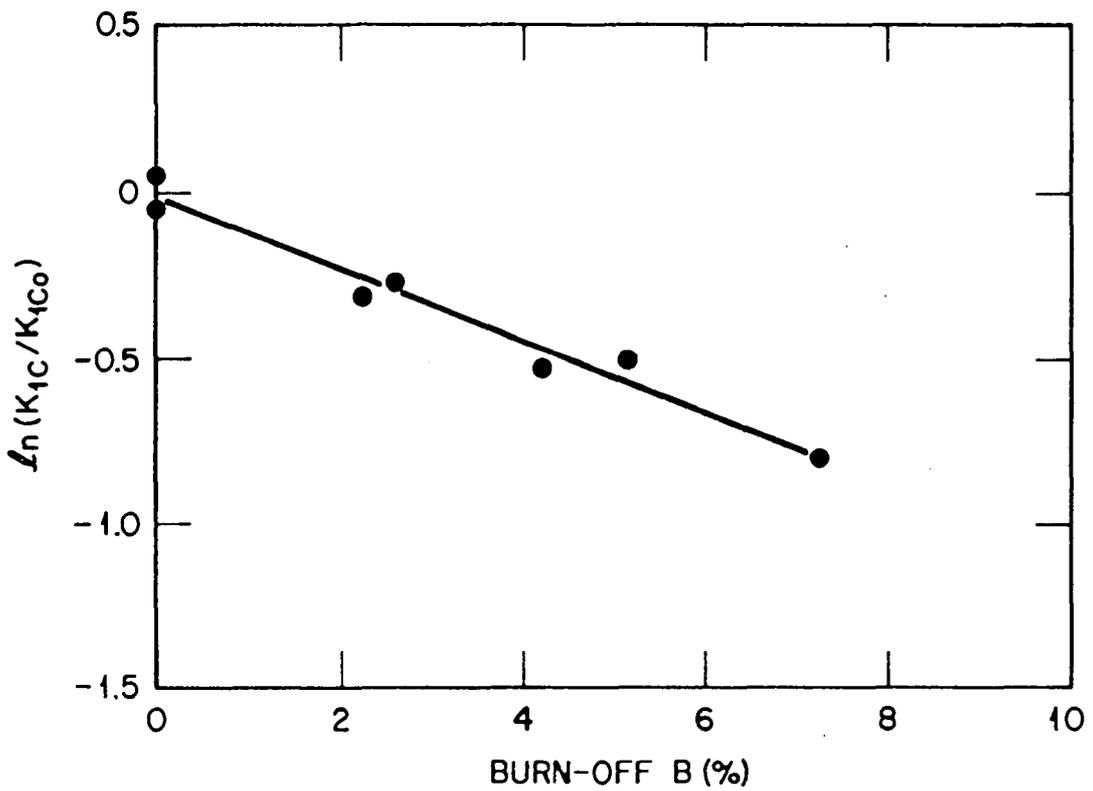
FIG. 51. The relationship between $ln(K_{1C}/K_{1Co})$ and burn-off of C/C composite grade CX-2002U [48].

6. TRITIUM BEHAVIOR

Graphite and C/C composites have very high specific surface areas, typically in the range 0.25 - 1 m²/g [49, 50]. Consequently, carbon materials can adsorb large quantities of gases, resulting in the possible retention of substantial amounts of hydrogen isotopes. This plays an important role in determining the recycling of fuel in the plasma-wall interface. Moreover, the adsorption of tritium may cause an unacceptably high tritium inventory for a fusion device during tritium operation. The interaction of tritium with graphite and C/C composites, and its impact on Tokomak operations has recently been reviewed by Causey [51]. There are four processes by which tritium can be retained in or on graphites and C/C composites: saturation of the implanted area; co-deposition with carbon on surfaces; adsorption on internal porosity, and transgranular diffusion with trapping. Pyrolytic graphites, which typically have densities >2.2 g/cm³, retain much less tritium than graphites or C/C composites [51]. Moreover, the tritium diffusion coefficients are significantly lower in pyrolytic graphite compared with C/C composites and graphites [52]. The lower tritium diffusion rate and significantly reduced retention are attributed to the absence of porosity in pyrolytic graphite [51]. Carbon-carbon composites are reported to behave similarly to graphites with respect to tritium behavior [51]. For present-day fusion reactors, the co-deposition process is likely to result in the greatest tritium inventory.

Causey has reported [51] the best estimates for the hydrogen isotope solubility and diffusivity in graphite are:

$$S = 6.44 \times 10^{-5} \exp (+0.2 \text{ eV/kT}) \text{ atom fraction/atom}^{\frac{1}{2}} \tag{3}$$

$$D = 0.93 \exp(-2.8 \text{ eV/kT}) \text{ cm}^2/S \tag{4}$$

Values of volumetric tritium retention are given in Table XVII for various graphites and C/C composites tested by Causey [51] at an ion energy of 100eV, (fluence of 2×10^{20} T/cm²) for 1.5 hours at 1273K.

Neutron irradiation has been shown to increase the amount of deuterium and tritium retained in graphite and C/C composites [53-55]. Crystal lattice damage, in the form of interstitial loops, vacancies and vacancy loops provide tritium trapping sites. Wampler et al. [55] studied the increase of deuterium trapping in graphite caused by displacement damage using 6 MeV C⁺ ions. Their data are summarized in Figure 52, which shows the D concentration increasing rapidly up to ~0.1 dpa, and then saturating at doses > 0.1 dpa. Several graphites were included in Wampler et al.'s study, and with the exception of highly oriented pyrolytic graphite (HOPG), all showed similar behavior. The HOPG saturated at a lower D concentration and at a lower dose. A parameterization for c, the concentration of retained D, as a function of damage dose, d was found to give [55]:

$$c = c_s (1 - \exp (-d/d_s)) \tag{5}$$

Fitting the data in Figure 52 yielded values of c_s = 650 appm and d_s = 0.035 dpa. The good agreement between D concentrations in ion damaged and neutron damaged graphites suggests that equation 5 may be useful for design studies of machines such as ITER. The close correlation of ion and neutron damage on trapping has also been reported for H-451 graphite by Causey et al. [53]. Their data, which are shown in Figure 53, clearly shows the amount of trapped tritium saturates in the dose range 0.1 - 1 dpa. Data for tritium behavior in neutron irradiated C/C

composites are very limited. Atsumi et al., reported hydrogen solubility in graphites and C/C composite CX-2002U after neutron irradiation to ~$2x10^{24}$ n/m^2 (E > 1 MeV) or 0.2 dpa. Significantly, the C/C composite showed less increase in hydrogen solubility than the graphites studied (Fig. 53). Additional data on tritium behavior in neutron irradiated C/C composites are clearly needed.

TABLE XVII. TRITIUM RETENTION AT 1273K IN DIFFERENT GRAPHITES AND C/C COMPOSITES [51]

Carbon Material	Tritium Volumetric Retention (10^{17} cm^{-3})
POCO AXF-5Q	12.0
ATJ 2000	6.7
K-KARB	6.5
B.F. Goodrich 2D	6.2
1G-11	5.2
Lorraine	4.0
FMI-4D	3.6
FE 1591	3.5
H-451	3.1
1G-110	3.0
POCO AXF-5Q-BG	2.8
HITCO	2.5
Pyrolytic Graphite	0.5
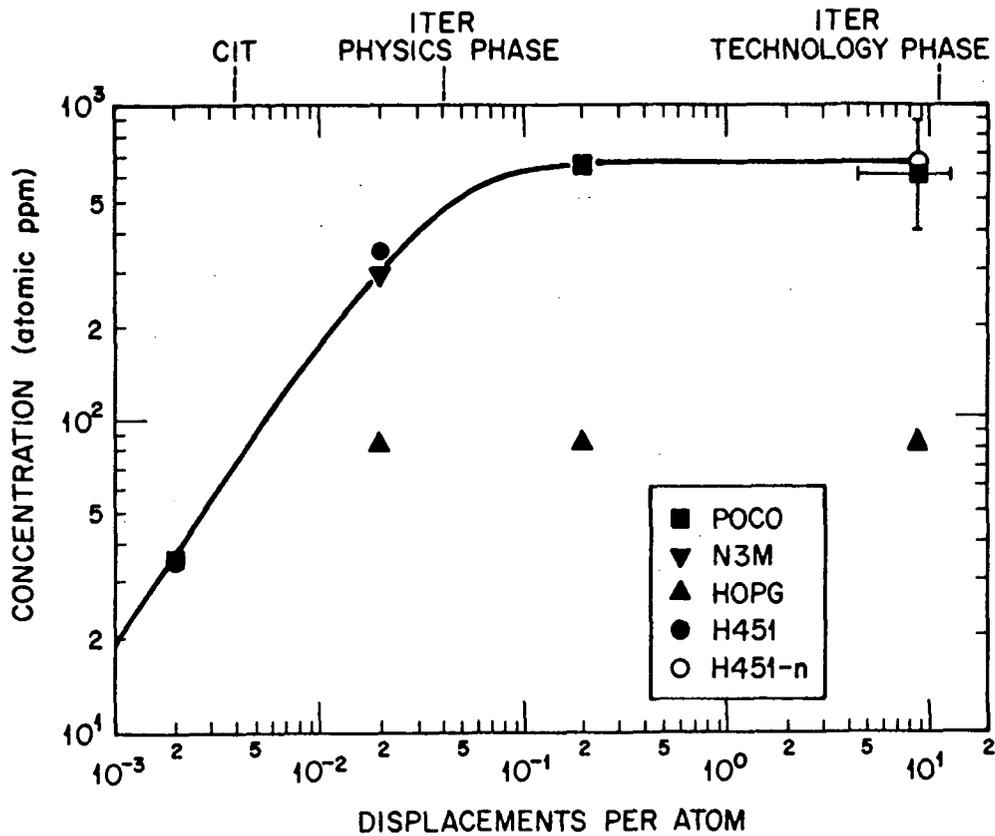
FIG. 52. D concentration versus damage in graphite irradiated with 6 MeV C^+ (filled symbols) and neutrons (open circle). Neutron and ion damage have similar effects on D retention. D retention increases with damage at low damage levels but saturates above about 0.04 dpa. The line shows the fit of equation 6.3 to the data for POCO, N3M and H-451 graphites which behave similarly [55].
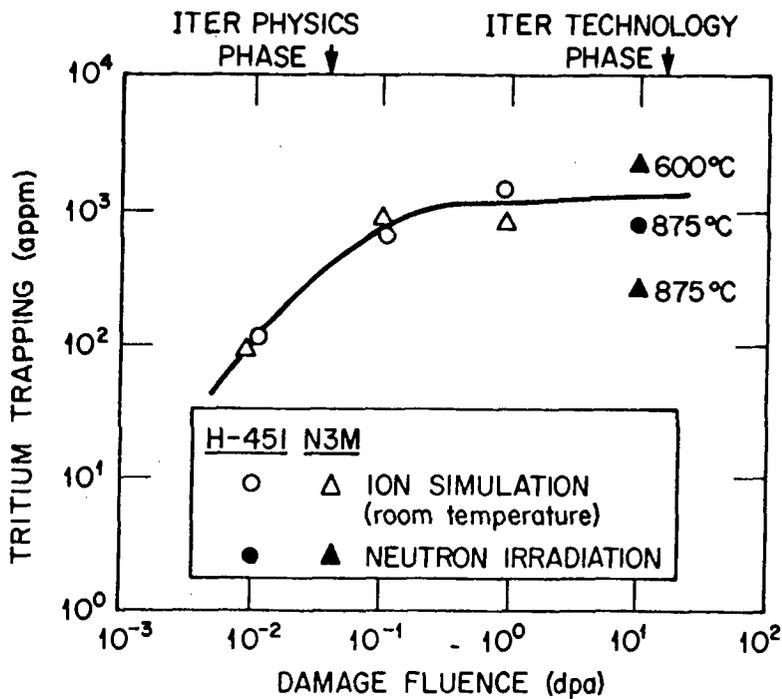

*FIG. 53. A comparison of Tritium Trapping in Ion and Neutron Irradiated graphite [53].*
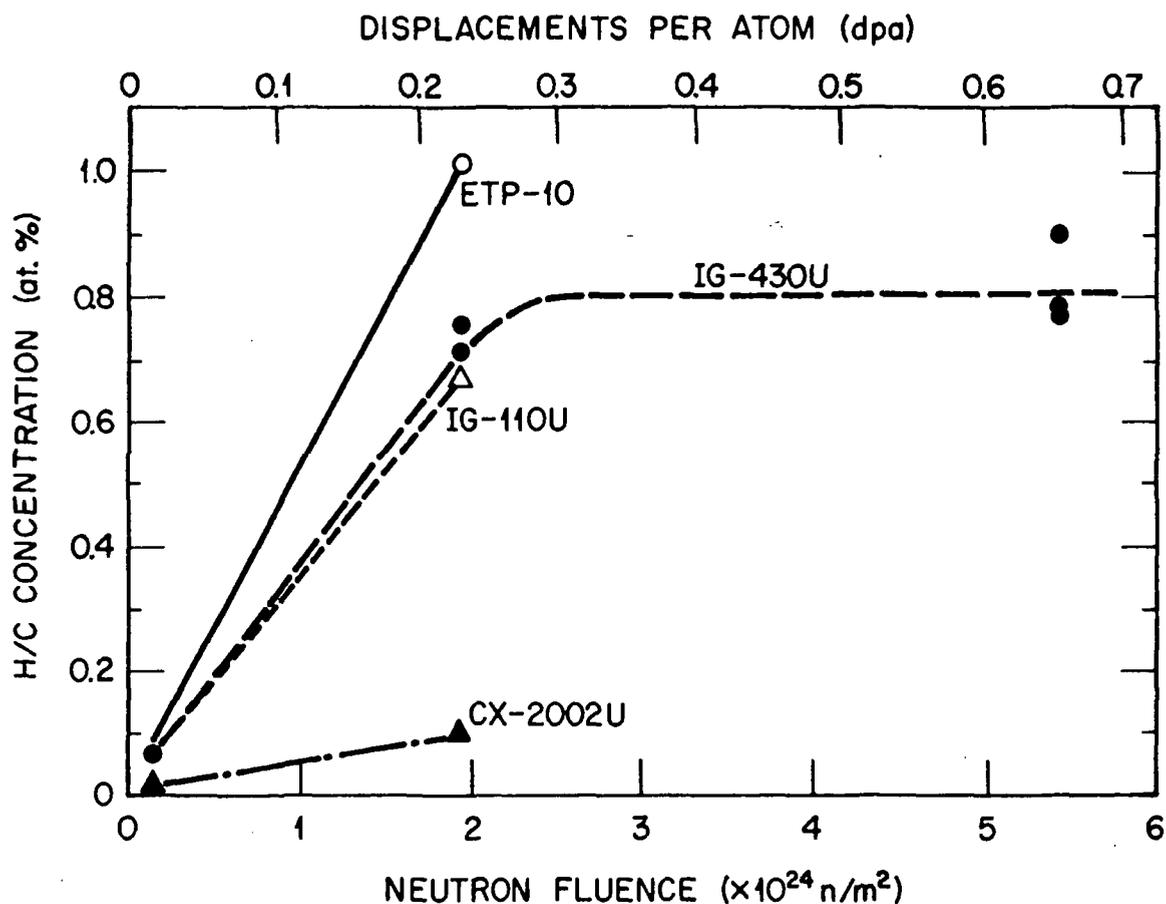
FIG. 54. Hydrogen solubility in graphite at 1000°C irradiated with neutron to various fluences (E > 1 MeV). The values of hydrogen concentration are normalized under 1 atm. of H_2 [54].

REFERENCES

[1]   PENNOCK, G.M., TAYLOR, G.H., and FITZ GERALD, J.D., Carbon, Vol. 31, No. 4, 591-609 (1993).

[2]   JOHNSON, D.J., "Carbon Fibers: Manufacture, Properties, Structure, and Applications," 199 in Introduction to Carbon Science, edited by Harry Marsh, Pub. Butterworths, London (1989).

[3]   DONNET, J.B., and BANSAL, R.C., Carbon Fibers, 2nd ed., Pub. Dekker (1990).

[4]   BUNDY, F.P., J. Chem. Phys. 38 (1963) 631.

[5]   LEIDER, H.R., Carbon 11 (1973) 555.

[6]   SMID, I., et al., JAERI-M 93-149 (July 1993).

[7]   SATO, S., et al., Fusion Eng. and Design 13 (1990) 159-176.

[8]   ANDO, T., et al., J. Nucl. Mater. 191-194 (1992) 1423-1427.

[9]   SUBRENAT, E., Carbon-carbon for Nuclear Fusion Application, MC-33395-91, Pub. SEP, Suresnes, France (1991).

[10] SAPP, J.W., et al., Extended Abstracts of 20th Biennial Conf. on Carbon, June 23-28 (1991) Santa Barbara, 644.

[11] DINWIDDIE, R.B., et al., Extended Abstracts of 20th Biennial Conf. on Carbon, June 23-28 (1991) Santa Barbara, 642.

[12] TING, J., LAKE, J.L., Extended Abstracts of 21st Biennial Conf. on Carbon, June 23-28 (1991) Buffalo, 42.

[13] OKU, T., HIRAOKA, T., Unpublished data.

[14] BURCHELL, T.D., Unpublished data.

[15] BAKER, C.F., Extended Abstracts of 21st Biennial Conf. on Barbon, June 23-28 (1991) Buffalo, 46.

[16] BUTLAND, A.T.D., et al., AEEW-R815 (1972).

[17] NBS Special Publication 260-89, Standard Reference Materials: A Fine Grained, Isotropic Graphite for use as NBS Thermal Physical Property RM's from 5 to 2500k.

[18] SATO, S., KURAMADA, A., KAWAMATA, K., ISHIDA, R., *Fusion Engineering and Design* 13 (1990) 159-176.

[19] SERIZAWA, H., KOHYAMA, A., SATO, S., Proc. the 9th Int. Conf. on Composite Mater. (ICCM/9), Madrid, 12-16 July (1993) vol. 2, 524-531.

[20] SATO, A., et al., *Carbon*, 27, No. 6, 791-801 (1989).

[21] FUJIOKA, J., et al., Proc. 1st Japan Int. SAMPE Symposium, Nov. 28-Dec. 1 (1989) 1160.

[22] ANDO, T., et al., *J. Nucl. Mater.* 191-194 (1992) 1423-1427.

[23] OKU, T., et al., TANSO (1983) [No.156] 15-21.

[24] KELLY, B.T., *The Physics of Graphite*, Applied Science Publisher, London (1981).

[25] ENGLE, G.B., EATHERLY, W.P., "*High Temperatures—High Pressures* 4," 119-158 (1972).

[26] BURCHELL, T.D., "Radiation Damage in Carbon Materials", in *Physical Processes of the Interaction of Fusion Plasmas with Solids* (HOFFER, W.O., ROTH, J., Eds.) To be published, Academic Press, Inc.

[27] KENNEDY, C.R., AND EATHERLY, W.P., in Proc 11th Biennial Conf. on Carbon (American Carbon Society, Gatlinburg, TN, USA, 1973), 131.

[28] BURCHELL, T.D., EATHERLY, W.P. , *Journal of Nuclear Materials*, Vol. 179-181, 205-208, (1991).

[29] BURCHELL, T .D., EATHERLY, W.P., ROBBINS, J.M., STRIZAK, J.P., *Journal of Nuclear Materials*, Vol. 191-194, 295-299 (1992).

[30] BURCHELL, T.D., EATHERLY, W.P., STRIZAK, J.P., "The Effect of Neutron Irradiation on the Structure and Properties of Carbon-Carbon Composite Materials," In: *Effects of Radiation on Materials: 16th International Symposium, ASTM STP 1175*, 1266-1282. (KUMAR, A.S., GELLES, D.S., NANSTAD, R.K., AND LITTLE, E.A., Eds.) American Society for Testing and Materials, Philadelphia (1994).

[31] BURCHELL, T.D., "Irradiation-Induced Structure and Property Changes in Tokamak Plasma-Facing, Carbon-Carbon Composites". In: *Proc. 39th International SAMPE Symposium*, Vol 39. 2423-2436, Pub. SAMPE (1994).

[32] BRIGHT, A.A., SINGER, L.S., *Carbon*, Vol 17, 59-69 (1979).

[33] NIGHTINGALE, R.E., *Nuclear Graphite*, Academic Press, New York (1962).

[34] SIMMONS, J.H.W., *Radiation Damage in Graphite*, Pergamon Press, Oxford (1965).

[35] KELLY, B.T., BURCHELL, T.D., *Carbon*, Vol. 32, No. 3, 499-505 (1994).

[36] KELLY, B.T., *Nuclear Reactor Moderator Materials*. In: *Material Science and Technology*, Vol. 10A, Nuclear Materials, Part 1, 365-417 (1994).

[37]　THEILE, B.A., BINKLE, L., KOZLICK, K., NICKEL, H., "The Effect of Neutron Irradiation on Thermal Conductivity of Carbon/Carbon Fiber Materials at 400 and 600°C in the Fluence Range 1×10^{22} to 1×10^{24} m^{-2}. In: *Effects of Radiation on Materials: 16th International Symposium, ASTM STP 1175*, 1304-1314 (KUMAR, A.S., GELLES, D.S., NANSTAD, R.K., LITTLE, E.A., Eds.) American Society for Testing and Materials, Philadelphia (1994).

[38]　MARUYAMA, T., HARAYAMA, M., *Journal of Nuclear Materials*, Vol. 195, 44-50 (1992).

[39]　BURTSEVA, T.A., et al., *Journal of Nuclear Materials*, Vol. 191-194, 309-314 (1992).

[40]　TANABE, Y., YASUDA, E., KIMURA, S., ISEKI, T., MARUYAMA, T., YANO, T., *Carbon*, Vol. 29, No. 7, 905-908 (1991).

[41]　KELLY, B.T., BURCHELL, T.D., *Carbon*, Vol. 32, No. 1, 119-125 (1994).

[42]　SNEAD, L.L., In: *Fusion Reactor Materials Semiannual Progress Report for the period ending Sept 30, 91.* DOE/ER-0313/11, 46-55, Pub. Oak Ridge National Laboratory, Oak Ridge (April 1992).

[43]　SHIKAMA, T., KAYANO, H., FUJITSUKA, M., TANABE, T., *Journal of Nuclear Materials*, Vol. 179-181, 209-213 (1991).

[44]　SATO, S., et al., Nuclear Eng. and Design 118 (1990) 227-241.

[45]　LIU, L.Y., HAN, J.C., HE, X.D., WAN, J., Extended Abstracts, 21st Biennial Conf. on Carbon June 13-18 (1993) 535-536.

[46]　SPERBER, D.M., JONES, L.E., Extended Abstracts, 21st Biennial Conf. on Carbon June 13-18 (1993) 32-33.

[47]　JONES, L.E., THROWER, P.A., *Carbon* 29[2], 251 (1991).

[48]　KURUMADA, A., OKU, T., et al., *Journal of the Faculty of Engineering*, Ibaraki University (1994) in press, "Influence of Burn-off on Strength and Toughness of Carbon Materials".

[49]　REYNOLDS, W.N., "Physical Properties of Graphite", published Elsevier, Amsterdam (1968).

[50]　NAKAYAMA, K., FUKUDA, S., HINO, T., and YAMASHINA, J., *J. Nucl. Mater.*, 145-147 (1987) 301.

[51]　CAUSEY, R.A., *J. Nucl. Mater.*, 162-167 (1989) 151-161.

[52]　CAUSEY, R.A., ELLEMAN, T.S., and VERGHESE, K., *Carbon 17* (1979) 323-328.

[53]　CAUSEY, R.A., WILSON, K.L., WAMPLER, W.R., and DOYLE, B.L. *Fusion Technology 19* (1991) 1585-1588.

[54]　ATSUMI, H., ISEKI, I., and SHIKAMA, T., *J. Nucl. Mater.*, 191-194 (1992) 368-372.

[55]　WAMPLER, W.R., DOYLE, B.L., CAUSEY, R.A., and WILSON, K., *J. Nucl. Mater.*, 176-177 (1990) 983-986.

HIGH Z CANDIDATE PLASMA FACING MATERIALS

T. TANABE
Faculty of Engineering
Osaka University
Osaka, Japan

ABSTRACT. High Z materials are very attractive as a plasma facing material because of their excellent thermo-physical properties. Nevertheless data for plasma materials interaction of the high Z materials are not enough and their potential risk of high radiation loss has been a serious concern. The paper gives a review of the materials properties of high Z materials for the application as a plasma facing materials. Their surface properties necessary for the application to the plasma facing materials are summarized. The behavior of the high Z materials under high heat load, and interaction with hydrogen and helium are discussed in detail. Referring recent high Z limiter and divertor experiments in tokamaks, future direction of the research and development of the high Z materials are suggested.

1. INTRODUCTION

### 1.1. Application of high Z materials as a plasma facing material
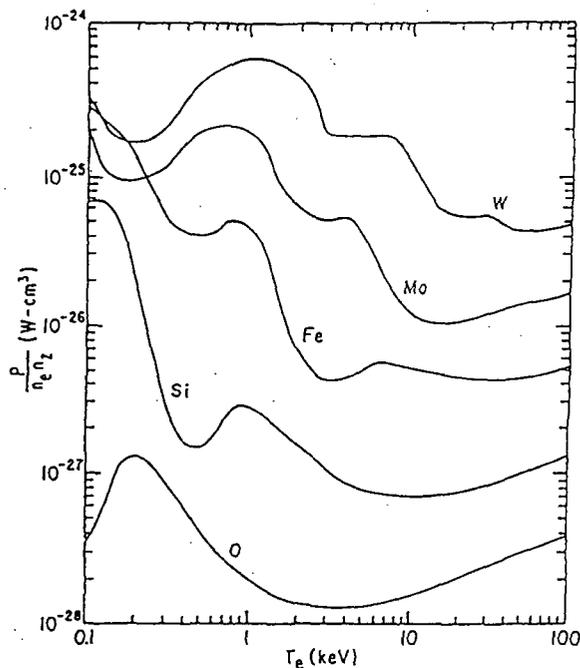
Fig. 1 Temperature dependence of radiation properties of various elements[4]

High Z materials such as Mo and W were once used as plasma facing materials(PFM) in early tokamaks[1,2] because of their refractory properties for future use in DT burning machines as well as enough experiences as vacuum high temperature materials[3]. Owing to their high radiation loss (see Fig.1), however, the plasma at that time was difficult to be heated and often collapsed by the accumulation of high Z impurities in the plasma center[2]. Instead of the high Z, introduction of carbon based low Z materials as PFM made plasma confinement much better and plasma parameters have advanced drastically in recent large tokamaks. Ironically, the advances of the plasma parameters result in extraordinary high heat load (over $20MW/m^2$) to the PFM. Hence evapora-

tion, erosion, and thermal stress (shock) of the PFM make the future usage of the low Z materials doubtful[5]. In addition neutron irradiation is found out to greatly deteriorate thermo-mechanical properties of the carbon based materials[6,7].

Thus high Z materials seem to come back into the consideration. However, most effort for the development of PFM has been paid to low Z materials and that for the high Z materials has been quite poor. Very recently some trial to use the high Z as the PFM is restarted in TEXTOR[8,9], ASDEX-U[10] and Alcator C-Mod[11], though the high Z materials still do not seem to be used as the PFM in the present large tokamaks for fear of the high radiation loss and less experiences.

For high temperature use of high Z materials as PFM, there are two important issues; (1) thermal response and thermal shock resistance to extraordinary high heat load in a very short period, and (2) recrystallization or thermal annealing for long term. Since most of the high Z materials are well known to be brittle at room temperature, there is some doubt about their thermal shock resistance especially for W. If they are used above ductile-brittle transition temperature (DBTT), however, they may tolerate the thermal stress. Therefore the response to the thermal shock or high heat load test should be examined in terms of operating temperature and temperature gradient in the material.

In addition, high Z materials mostly produced by powder metallurgy are in some sense under development, and advances of production techniques such as electron beam or arc melting improve materials properties very much. This in turn forces us to re-examine materials properties of those produced by the powder metallurgy.

1.2. Application of high Z materials as a structure (heat sink) material

Apart from the PFM use, high Z materials are also the candidate for heat sink or structure materials of plasma facing component(PFC), owing to their excellent thermal properties and capability of cooling. Especially, their higher melting temperature and higher thermal conductivity compared with stainless steels, the standard structure material, make a higher heat load as well as higher temperature operation possible.

For this application of the high Z, additional issues, which are thermal stress due to large temperature gradient between front surface to cooling channel and corrosion by coolant, should be taken into account. In this respect Nb and Ta, both of which do not seem suitable for PFM due to their potential risk of high tritium inventory, are very good candidates as appeared in their excellent performance under water cooling conditions in fission reactors[12].

One of the advantages of high Z metals as the PFC is that they can be used as a single component serving as both armor and structure with the cooling channel. However not only their poor ductility but also heavy mass make machining and handling very difficult. Further worse, neutron irradiation enhances the brittleness with the increase of DBTT. In most cases, therefore, the high Z armor should be brazed to the cooling channel and thus the brazing or adhesion is also a critical concern. Poor welderbility of the high Z materials needs much research and development.

This chapter is restricted to data of surface properties of the high Z materials, mainly Mo and W, for PFM applications. The bulk properties of Mo and Mo-alloys, and Nb and Nb-alloys as a structure material are given in Ref[13].

130

2. MATERIAL PROPERTIES

2.1. Characteristics of high Z refractory metals

High Z refractory metals have been widely used in vacuum technique as heaters, electrodes, electron emitters and so on. Most of the materials properties necessary for the vacuum use are nicely tabulated or summarized by Espe[3]. A comprehensive data book for physical and mechanical properties was published almost three decades ago[14]. It should be noted, however, those properties of high Z metals are quite dependent on metallurgical treatment (method of production, machining condition, temperature history, etc.) and impurities[3]. In addition, during in use at elevated temperatures high Z metals undergo large changes in their mechanical properties by release of occluded gases, evaporation of constituents and recrystallization. A metal which was originally work-hardened can fall below the permissible limit of mechanical strength. Hence it is important to know the properties of a material, not only as supplied, but after any heating process. Since high Z refractory metals have been produced mainly by powder metallurgy(PM), high temperature and prolonged heating results in a recrystallization or an enlargement of grains which deteriorates mechanical properties markedly because of low strength at the boundaries of the enlarged grains.

To avoid the recrystallization, one can use single crystal or make alloys. Recent advances in a sintering technique and electron beam or arc melting enable to make a large single crystalline possible as well as very pure materials. The mechanical properties of newly produced materials are sometimes significantly different from those for the materials produced by the PM. Hence some of data base referred here which are mostly for the PM materials must be reexamined with using the new materials. For example, one can see how differently behave a highly purified material and ordinary produced PM materials under high heat loading in Ref[15].

Until very recently such a high heat load as more than $50MW/m^2$ has never been injected to materials. Thus the response of high Z materials to the high heat load is one of the key issues for their application as PFM.

Alloying is a well-known technique to improve material properties and TZM and Mo-Re alloys are good examples. As a PFM the alloying elements to the high Z must be also refractory ones such like W-Re and W-Mo alloys. Otherwise the evaporation of the alloying elements at elevated temperatures not only deteriorates the material properties but also contaminates the plasma. Hence pure materials may be the first choice for the PFM. But it does not mean to exclude the alloys like TZM as a heat sink material. Concerning physico-chemical properties necessary for alloying and for high temperature usage one can refer special issues published by the IEAE for Nb[16], Mo[17] and Ta[18]. In the following only surface physical properties of elemental high Z materials necessary for the PFM use are summarized.

2.2. Thermo-physical properties

Temperature dependencies of thermal conductivity, thermal expansion, vapor pressure and evaporation rate for several high Z elements are compared in Figs. 2, 3, 4 and 5, respectively[3,14]. Because of the highest melting point, the lowest vapor pressure and evaporation rate, and the largest thermal conductivity, W is expected to be the best candidate as a PFM. Unfortunately, however, the poorest ductility of W makes the utili-
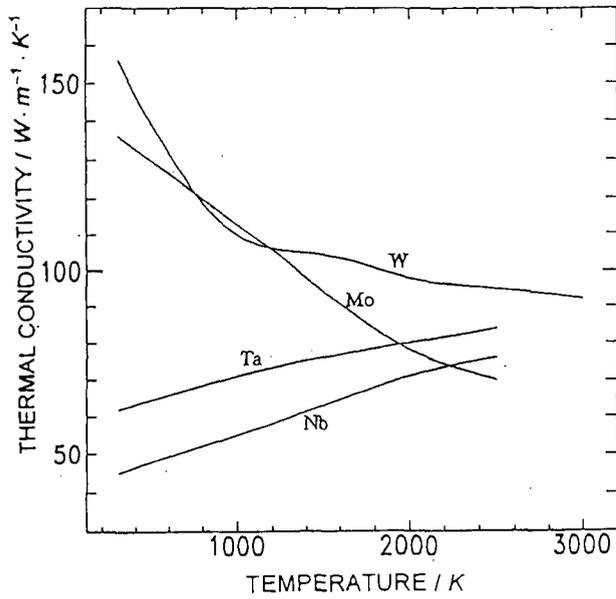
Fig. 2 Thermal conductivity[3,14]
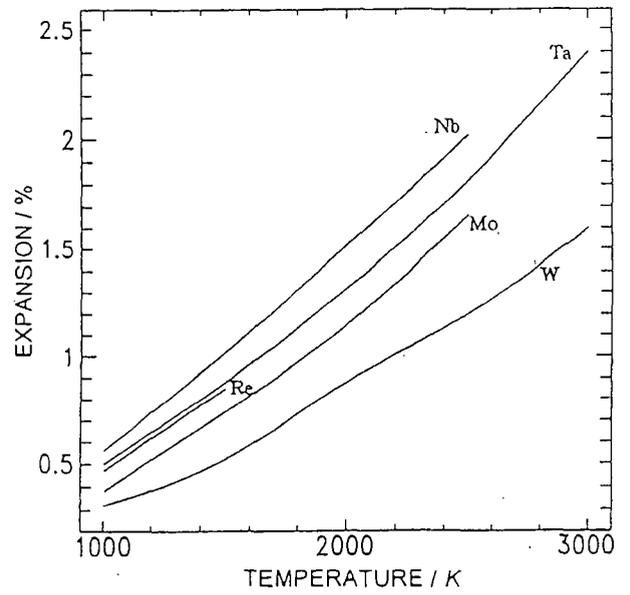

Fig. 3 Thermal expansion coefficient[3,14]
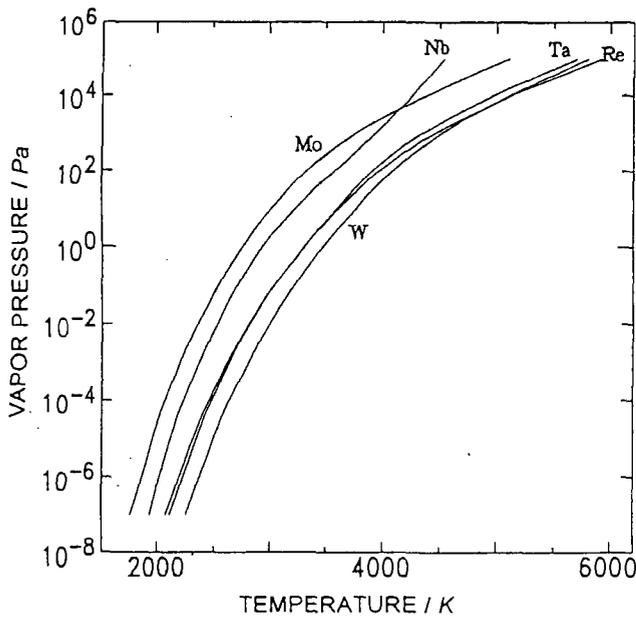

Fig. 4 Vapor pressure[3,14]
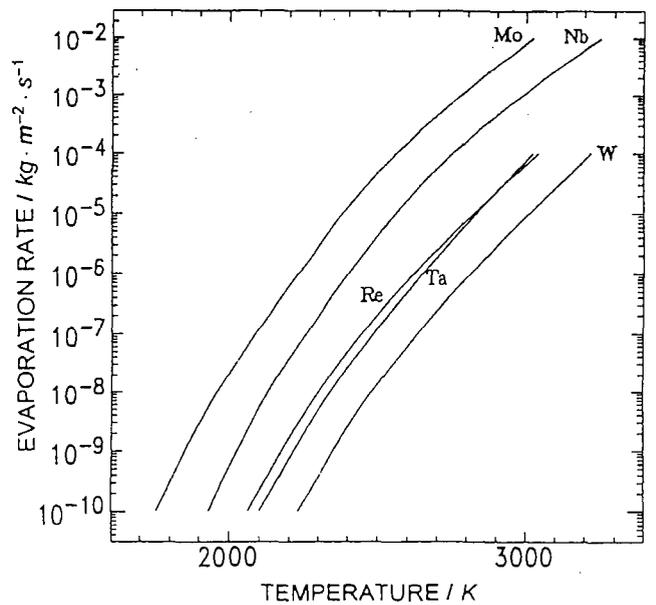
Fig. 5 Evaporation rate[3,14]

zation of W bulk very difficult.

Thermal radiation and emissivity, given in Figs. 6 and 7 respectively, are also important factors for the utilization of high Z materials at elevated temperatures. At very high temperatures, thermal radiation becomes large and important channel for surface cooling, though large differences are seen among the materials as seen in Fig. 7[14].

Determination of material temperature by optical emission is one of the most important technique. But the surface state (chemical and physical) influences the emissivity significantly and makes an accurate temperature measurement above 3000K difficult.
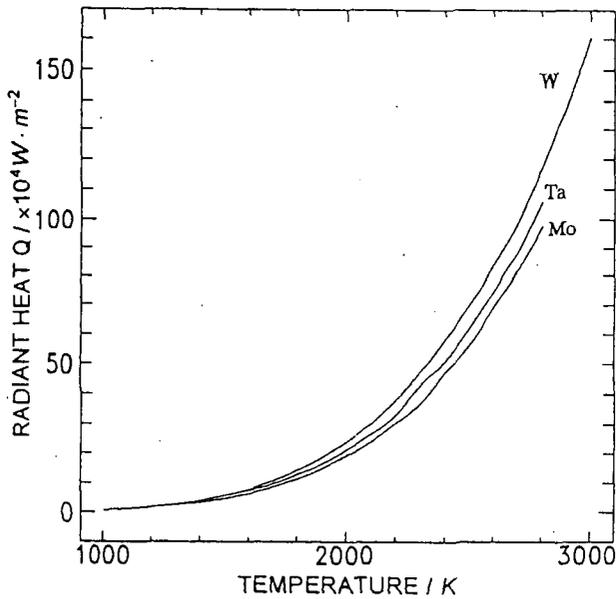
Fig. 6 Radiation heat[3,14]
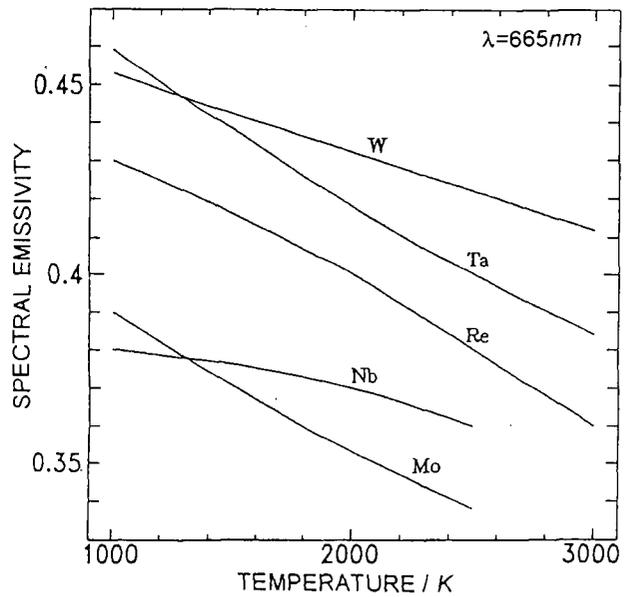
Fig. 7 Spectral emissivity[3,14]

2.3. Sputtering

Concerning physical sputtering, several comprehensive data books and reviews (see for example Ref[19-21]) as well as theoretical estimations [20,21] have been already published. Here only energy dependence of physical sputtering of Mo and W are given in Fig. 8. The high threshold

Target: Mo

Experimental Data

Target	Projectile	Angle	Symbol	$E_{iA}(eV)$	Q(atoms/ion)
Mo	H	0	□	199.	$0.800 \cdot 10^{-3}$
Mo	D	0	◊	87.0	0.0240

Calculated Data

Target	Projectile	Angle	Symbol	$E_{iA}(eV)$	Q(atoms/ion)
Mo	D	0	♦	83.0	0.0560
Mo	T	0	•	60.0	0.0940
Mo	Mo	0	►	55.1	16.0

Target: W

Experimental Data

Target	Projectile	Angle	Symbol	$E_{iA}(eV)$	Q(atoms/ion)
W	H	0	□	429.	$0.700 \cdot 10^{-3}$
W	D	0	◊	178.	0.0179
W	W	0	►	59.0	30.9

Calculated Data

Target	Projectile	Angle	Symbol	$E_{iA}(eV)$	Q(atoms/ion)
W	D	0	♦	201.	0.0345
W	T	0	•	129.	0.0654
W	W	0	►	63.0	32.2
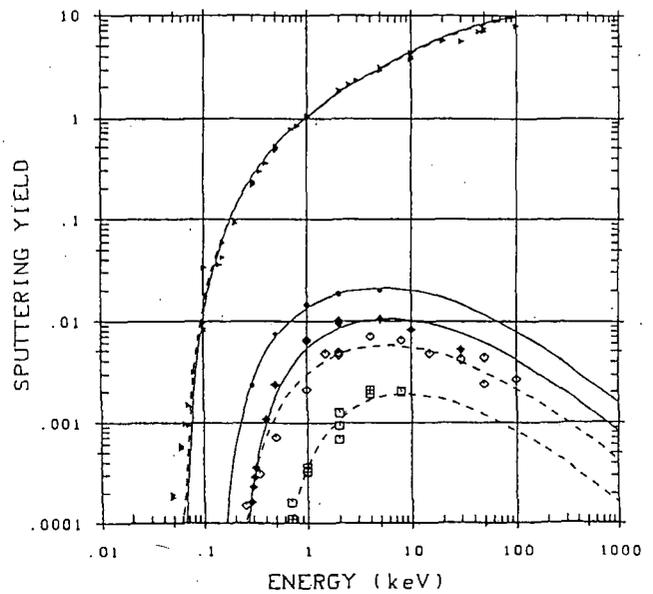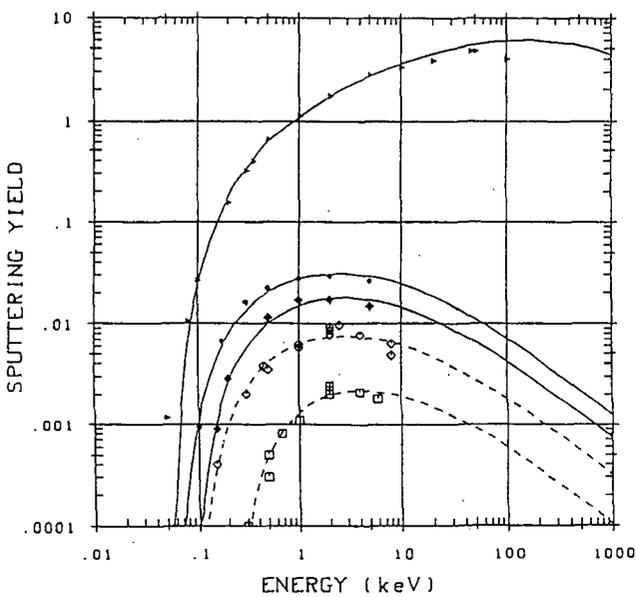
Fig. 8 Physical sputtering yields of Mo(a) and W(b) by hydrogen and self ions[20].

(a) Mo

(b) W
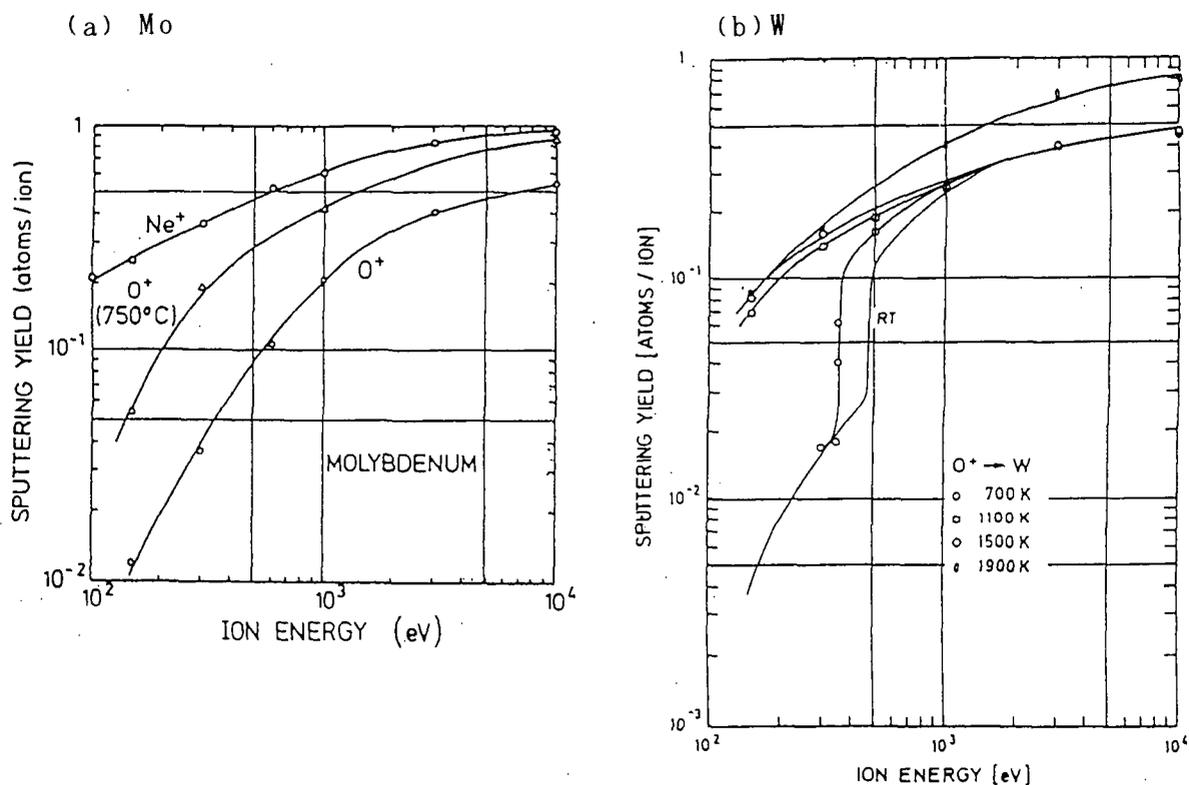
Fig. 9 Temperature dependencies of sputtering yield of
(a)Mo and (b)W by oxygen[24-26]

energy of hydrogen sputtering owing to their high mass is one of the advantages of high Z materials, whereas the low threshold energy by self-sputtering could cause impurity accumulation in a plasma center by sputter runaway. Control of plasma edge temperature below the self-sputtering threshold is a critical issue for the application of the high Z materials as PFM.

Different from the physical sputtering, chemical sputtering or erosion has basically no energy threshold but depends on the temperature of a target material. Since Mo and W are easily oxidized to form volatile oxides of MoO_3 and WO_3, enhanced erosion by the chemical sputtering of oxygen, the main impurity in plasma (several %), is one of the concerns like the chemical erosion of graphite by hydrogen producing CH_4[22]. Two institutions[23-28] have studied the oxygen sputtering of Mo and W. Figures 9(a) and 9(b) respectively show energy dependencies of the oxygen sputtering yields of Mo[24,25] and W[26] at various temperatures. As clearly seen the erosion of Mo and W by oxygen is enhanced at intermediated temperatures and high incident energies but does not exceed self-sputtering, different from carbon erosion by hydrogen[22]. Difference between OH and O sputtering is reported to be small[24].

At elevated temperatures oxygen does not remain on the surface and the oxygen sputtering yield at 1900K coincides with that of Ne(see Fig. 8). In addition, one should note that because hydrogen (even if it includes several % of oxygen) reduces the oxides of Mo and W producing volatile H_2O, hydrogen plasma does not allow oxygen to stay on the top surface of Mo and W. It is also important to note that carbides of Mo and W are thermodynamically more stable than their oxides at elevated temperatures. Since the impurity level of carbon in hydrogen plasma is nearly the same to that of oxygen and the fresh surface of Mo is reported to have a high gettering action for hydrocarbons[29], deposited carbon on the Mo and W surface does

not seem to allow the volatilization of their oxides as already pointed out by Miggie[30]. However no data for CO sputtering is available.

The chemical sputtering of Nb and Ta by oxygen is out of concern, because the oxides of Nb and Ta are not volatile. But one should keep in mind that reactions of these high Z metals with water or oxygen at elevated temperatures (may happen in the accident of cooling channels) result in an explosion reaction which is a very important safety concern as discussed in section 3-5.

2.4. Reflection

Particle reflection including electron reflection is also very important factor affecting a sheath potential in the boundary plasma as well as a heat load to the PFM from the plasma. In Figs. 10(a) and 10(b), reflection coefficients of deuteron on C and W are compared[31]. Reflection coefficients of electrons on W, Fe and C [32] are given in Fig. 11. Upon a high heat load test conducted by an ion beam or electron beam the deposited energy should be carefully calibrated considering the energy reflection carried by emitted particles from the surface. In the plasma machine, unfortunately, this effect has not been taken account and is left for a future work.

Recently heat loads to the limiter heads of Mo and graphite were compared in TEXTOR under similar discharge conditions[8]. But they did not show meaningful difference between the two, probably because the change of the limiter material also modified the plasma sheath due to the change of reflections of ions, electrons, secondary electron emission and so on.
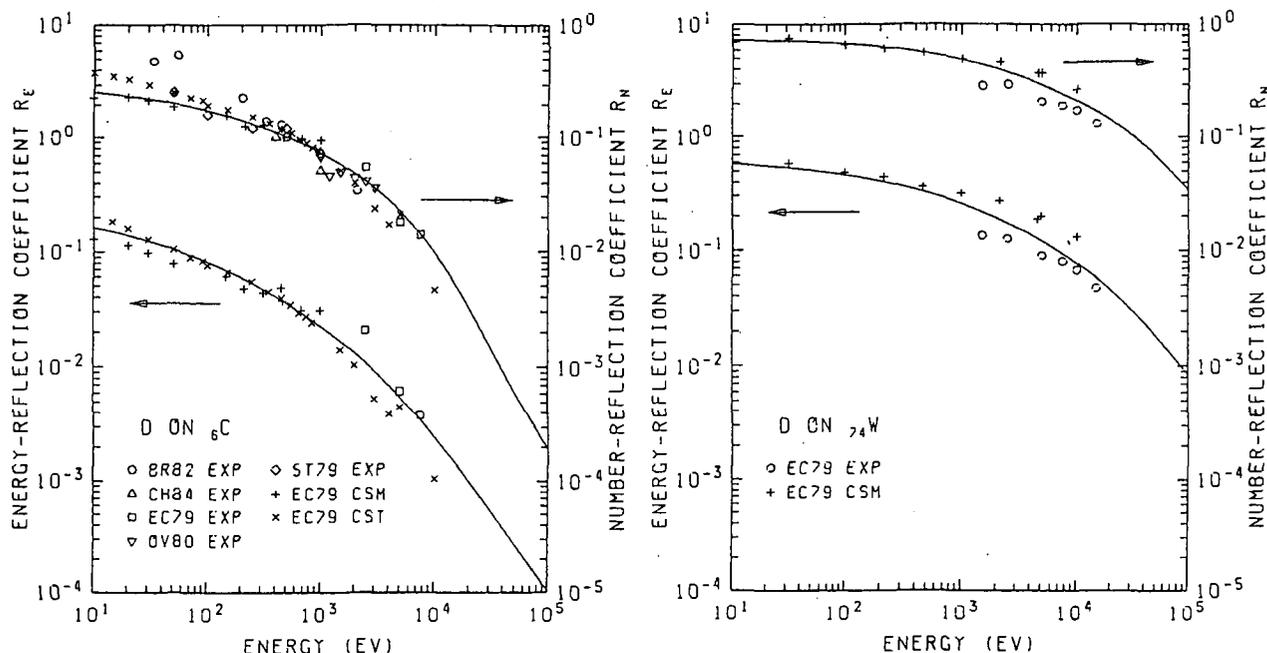

Fig. 10 Incident energy dependencies of particle and energy reflection coefficients for (a) carbon and (b) tungsten[31]

2.5. Electron emission

In respect of PMI, electron emissions, not only a secondary electron emission but also a thermionic emission, play an important role for producing a plasma sheath. Concerning the details of the secondary electron emission one can refer the previous review[33]. Here only data for the thermionic emission are given in Fig. 12. Recently such thermionic emission from graphite at elevated temperatures is attributed to the origin for production of a hot spot in tokamaks which results in a carbon bloom or carbon catastrophe [34]. If high Z refractory metals are used near their melting point, the thermionic emission becomes vary large (see Fig.12) and may influence the boundary plasma.

Under very high flux of plasma exposure, the secondary electron emission might be enhanced synergistically with the thermionic emission, but no experiment has been done so far.

PMI materials are exposed to various photons, X-rays, soft X-rays, and UV lines from impurities and strong visible lines from excited hydrogen atoms in the plasma. Therefore photo-electron emissions must be also taken into account. Since there have been no such strong sources of soft X-ray and UV as the plasma, dependence of the electron emission yield on the incident photon energy has not been examined well. Although surface impurities significantly influence the emission yield as seen in Fig.13[35], little systematic study has been done until now.
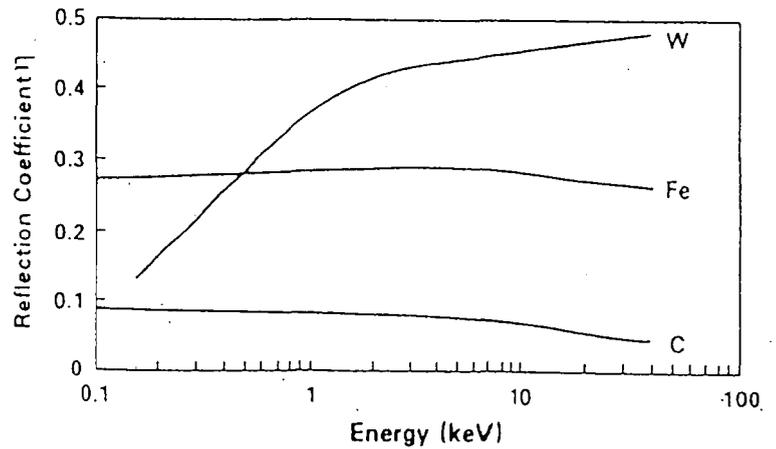

Fig. 11 Incident energy dependence of reflection coefficient of electrons for C, Fe and W[32]
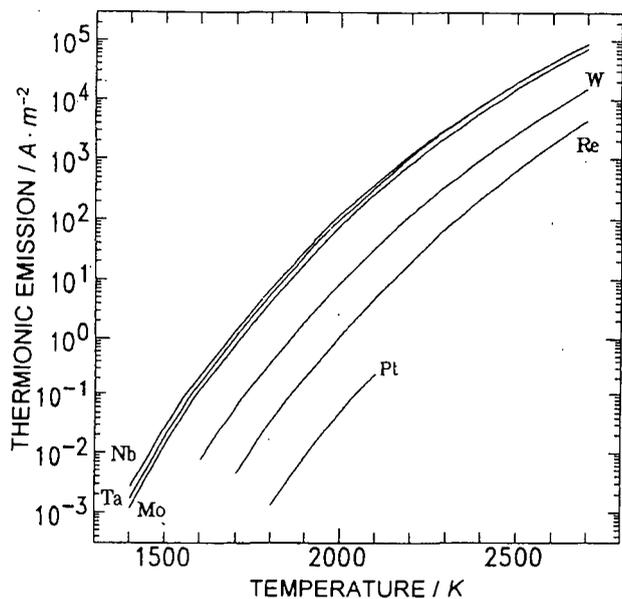
Fig. 12 Thermionic emission[3,14]
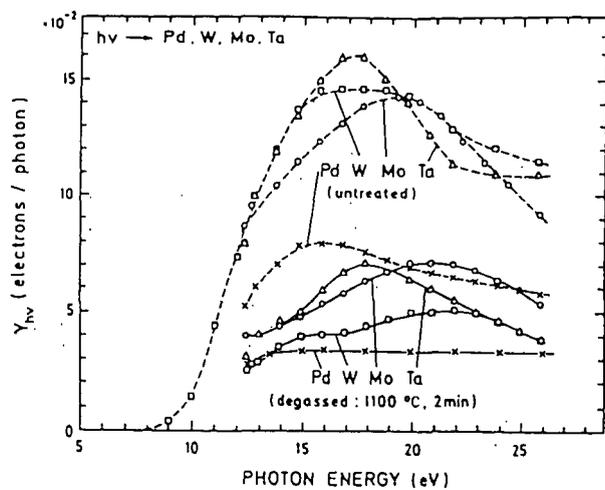
Fig. 13 Electron emission yield at photon bombardment for different surface conditions[35]

3. CHEMICAL EFFECTS/CORROSION

3.1. Interaction with hydrogen

Hydrogen adsorption on clean W surface is the one of the most extensively studied system in surface physics[36]. The adsorption sites and states of hydrogen on a clean surface of W single crystals are understood rather well. Surface adsorption states and energies in W are summarized in Table 1
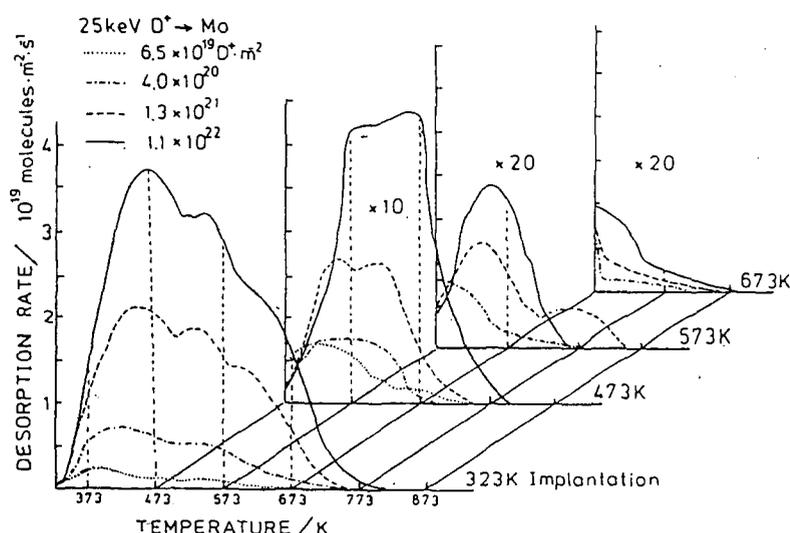

Fig. 14 Comparison of thermal desorption spectra taken immediately after the implantation at various temperatures [44]

Table 1. Surface adsorption states and energies along with hydrogen-vacancy (H-V) binding energies for W(After Ref [45] and references therein)

Temperature [K]/ heating rate [Ks^{-1}]	Peak/ site	Dissociation enthalphy [eV]	Attempt frequency [s^{-1}]
400/10	β_1	0.48	5×10^{11}
450/25	β_1	0.52	1×10^{12}
	β_1	0.49	1×10^{10}
/isothermal	β_1	0.45	1×10^9
450/10	β_1	0.76	1×10^{13}
450/25	β_1	0.58	1×10^{13}
500/10	β_2	0.60	1×10^{13}
550/25	β_2	0.92	1×10^{18}
	β_2	0.83	1×10^{17}
/isothermal	β_2	0.77	1×10^{16}
500/10	β_2	0.79	1×10^{17}
550/25	β_2	0.71	4×10^{13}
550/10	$\beta_2' \to DV$	1.43	1×10^{13}
450/10	HV	1.55	2×10^{14}
	HV	1.54	
400–550/10	$D_m V$	< 1.43	1×10^{13}
400	$H_2 V$	1.38	2×10^{14}
	$H_m V$	< 1.54	
580/10	DV		
400–700/10	$He_l D_m V_n$	1.2–1.8	1×10^{13}
550–850/4	$D_m V_n$		
600–700/10	voids created by MeV H^+	> 1.4 (TDS) 1.0–1.4 (PA)	

along with hydrogen-vacancy (H-V) binding energies[37]. Since most of those works have been done at temperatures below 700K and in ultrahigh vacuum with a very little amount of H_2 molecules as adsorbate, the results may not be directly applicable for fusion environment.

The first reemission experiment of hydrogen implanted in metals considering the fusion application appeared independently in Russia[38] for Ti, Ni, SS and Ta, and in England[39] for SS and Ti. McCracken and Erents [40] made the first detailed analysis on deuterium behavior implanted in Mo. Similarly to hydrogen behavior in bcc Fe where hydrogen migration is influenced significantly by trapping[41], a large amount of hydrogen is trapped by defects in Mo. Since the H-V binding energy in Mo is around 1.0eV[42], which is larger than that in Fe of about 0.6eV (see table 2), the trapping effect should alter hydrogen behavior very much. Reemission anomaly by the defect trapping in Mo is first demonstrated by Erents[43] and confirmed recently by Tanabe et al.[44]. In Fig. 14, one can see significant amount of hydrogen is trapped during the deuteron irradiation at temperature as high as 673K, which is noted as a dynamical hydrogen retention. Most part of the dynamic retention is, however, immediately released after the irradiation [44].

Hydrogen trapping in metals is reviewed by Myers et al.[45] and Moeller[47] taking account of the fusion applications. Myers et al.[45] summarized binding energies of hydrogen to vacancies (Table 2) and lattice location of deuterium trapped in vacancies determined by ion-channeling analysis as well as trapping energies in various metals. They also show that even He bubbles trap hydrogen as given in Table 3. Most of the work referred in these reviews are concentrated to low temperature trapping because of the detection limit of hydrogen by the ion beam technique utilized. Channeling can not be applied for movable hydrogen and very low concentration, too.

Thermal desorption of hydrogen adsorbed on a surface often obeys the first or second order desorption kinetics. Release kinetics of implanted hydrogen, however, include several process such as trapping-detrapping, diffusion, recombination and desorption. For analysis of hydrogen behavior implanted or subjected to the solid, several models considering these elemetnal processes have been proposed and they seem successful to describe the hydrogen behavior in fcc metals such like Ni as reviewed in Ref[47]. However, the recombination coefficients determined for a particular metal scatter very widely, sometimes more than several orders of magnitude, and the data scattering is mostly attributed to surface impurity effects.

For W, Anderl et al.[48] gave the recombination coefficient(K_r) of deuterium on W as,

$$K_r = 3.2 \times 10^{-15} \exp(-112kJ/mol/RT) \quad m^4/s.$$

However they noticed that the trapping affects significantly the transport of deuterium in W. Even fundamental constants of solubility, diffusivity and permeability for high Z metals are widely scattered as shown in the next section.

Recently Tanabe[49] has pointed out the importance of energy states of released hydrogen. In the recombination and trapping theory, hydrogen

Table 2. Binding energies of hydrogen to vacancies in metals at low occupancy (After [45] and references therein)

Host	Experiment (ion-beam analysis)	Theory (effective-medium)	Experiment (positrons)
Al	0.52	0.52	0.53
Fe	0.63	0.83	
Ni.	0.44	0.52	0.58, 0.44
Cu	0.42	0.37	≥ 0.4
Zr	0.28		
Mo	1.03	0.96	1.4
Pd	0.23	0.16	
Ta	0.42		≤ 1.2

molecules released after recombination at the surface are usually supposed to have the same temperature to the materials. And all theoretical estimations of the recombination coefficients have been done using hydrogen solubility and diffusivity in the bulk. But one should note that the surface trapping is sometimes so deep that most of the implanted hydrogen recombine without any influence of the surface trapped ones. In such case the implanted hydrogen is released at lower temperature than the desorption temperature of the surface trapped ones and the released hydrogen molecules have hyperthermal energy[50]. Therefore studies of the energy state or energy distribution of released hydrogen are highly desirable.

3.2. Diffusivity, permeability and solubility

Hydrogen diffusivity and solubility in Mo and W are summarized in Ref[47]. The permeability of Mo and W are shown in Figs. 15(a) and 15(b) respectively, and the recommended values of permeability(Φ), diffusivity(D) and solubility(S) are given by ;
For Mo,
$\Phi = 1.4 \times 10^{-7}$ exp(-60.3(kJ/mol)/RT) mol(H_2)m^{-3} Pa$^{-1/2}$
$D = 4.0 \times 10^{-8}$ exp(-22.3(kJ/mol)/RT) m^2/s
$S = 3.3 \times 10^3$ exp(-38.0(kJ/mol)/RT) mol/m^{-3}MPa$^{-1/2}$,
and for W
$\Phi = 1.1 \times 10^{-4}$ exp(-275(kJ/mol)/RT) mol(H_2)m^{-3} Pa$^{-1/2}$
$D = 4.1 \times 10^{-7}$ exp(-75(kJ/mol)/RT) m^2/s
$S = 2.7 \times 10^2$ exp(-200(kJ/mol)/RT) mol/m^{-3}MPa$^{-1/2}$.
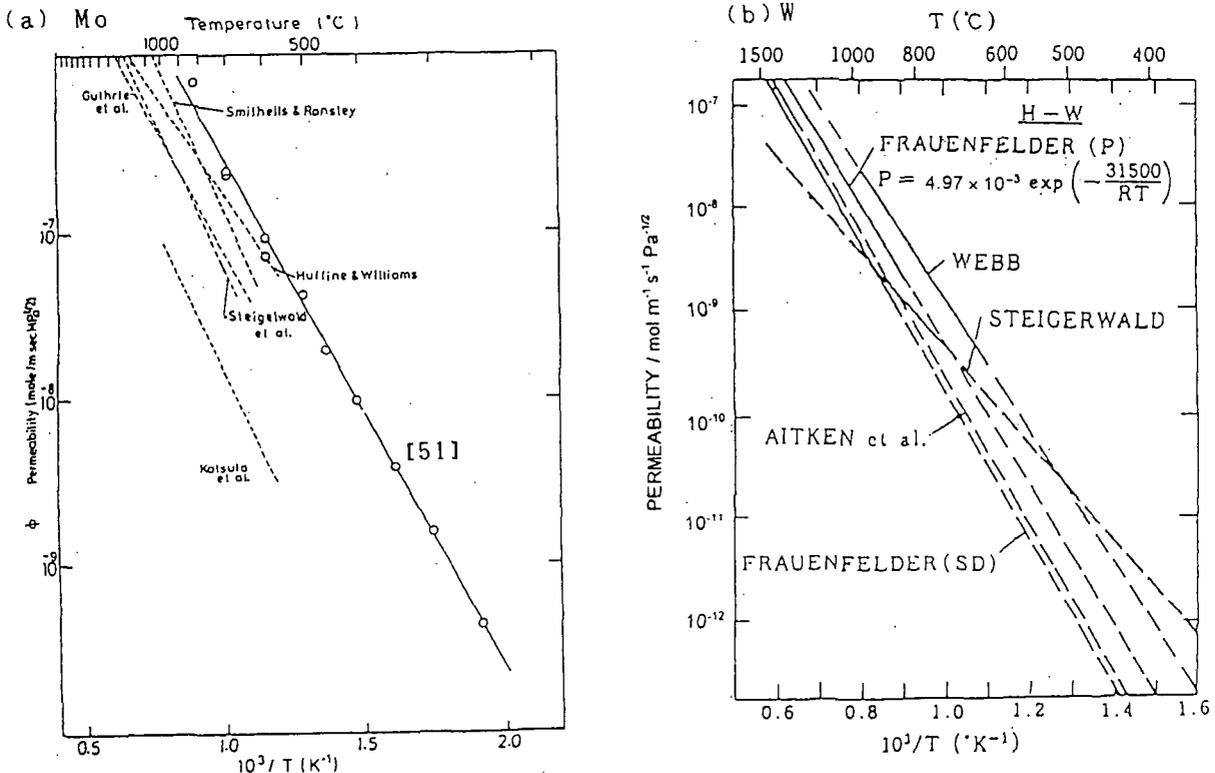
Fig. 15 Hydrogen permeation in (a) Mo and (b) W[47,51]

One should note that these values are determined mostly for the specimen produced by the powder metallurgy and are, therefore, possibly influenced by trapping at defects and impurities. In other words, the data scattering could be attributed to the difference of the material used. Only the permeation data for Mo is reliable showing small data scattering[51]. Both the activation energy of diffusion and the heat of solution of W given above seem too high compared with other BCC metals[52], and should be reexamined using a highly purified material.

For hydrogen behavior in Nb and Ta, Refs[41,53] give great details. Utilization of these metals as PFM was excluded because of their high hydrogen solubility. They could be used, if the operating temperature is high enough to avoid the precipitation of hydrides. Nevertheless hydrogen permeation could be very high, which is a serious concern from safety point of view.

Katsuta et al.[54] examined neutron irradiation effect on hydrogen permeation through Mo. The effect was not appreciable probably owing to rather low damage level compared with the data scattering or due to the surface effect and/or bulk trapping existing prior the irradiation. Comparing with carbon materials hydrogen trapping effect in metals, especially at higher temperatures, is believed to be much smaller.

3.3. Hydrogen embrittlement

For such metals in which hydrogen is dissolved exothermically (Zr, Nb, Hf, Ta ; often referred as exothermic hydrogen occluders or hydride formers), hydrogen embrittlement by the precipitation of hydrides is one of the main concern for their utilization in hydrogen atmosphere as described above. Since hydrogen diffusion in these metals is very rapid, hydrogen uptakes both from aqueous corrosion by the coolant and from the plasma should be taken into account[54].

Different from the hydride formers, Mo and W absorb hydrogen endothermically (endothermic hydrogen occluder) and hydrogen embrittlement by the precipitation of hydride has not been a serious concern. As mentioned before the recrystallization of Mo and W influence mechanical properties significantly, the effect of hydrogen (if there exists) may not be separated clearly. In addition, such a high temperature operation, where most of the trapped hydrogen are released, hydrogen embrittlement may not happen. However, owing to large trapping capability and neutron irradiation which produces additional trapping sites, the hydrogen embrittlement of Mo and W may have some influence via increase of DBTT synergistically with neutron irradiation after the plasma turn off or cooling phase. More detail of the irradiation effect will be given other issues of this volume.

3.4. Helium transport/trapping

Helium(He) implanted in high Z materials at lower temperatures is also studied well. And the lattice position of the implanted He is examined by channeling[56]. The channeling study is, however, limited to well crystallized materials and can not be applied to heavily damaged ones.

In the early stage of a fusion materials study, the surface blistering of the materials by He implantation had been extensively studied.(for instance see [57] and references therein). Unfortunately most of these works concentrated to the changes of surface morphology and little attention was

Table 3. Binding enthalpy for D trapping at He bubbles relative
to D in solution (After [45] and references therein)

Host	Gas-phase equilibrium (eV)	Temperature ramp (eV)	Effective-medium theory (eV)	Exp. chemisorption energy minus exp. solution energy (eV)
Al		≤ 0.52	0.52	
Fe	0.81	0.78	0.91	0.73
Ni	0.52	0.55	0.66	0.6
Mo		1.15	0.98	1.3
Pd		0.29	0.35	0.35–0.43
Ta		0.53	0.69	
Stainless steel		0.42		
Inconel		0.45		

paid on trapping and migration energies of He. Recently both particle and energy loads to the materials from plasma become so high that surface erosion or evaporation is more serious than the blistering. On the other hand, He atoms in metals which are injected from plasma, or produced by transmutation of tritium or nuclear reactions attract much attention, as they degrade materials properties very much. The influence of such He on plasma surface interactions is not studied. Only hydrogen release from graphite by helium ion bombardment is examined well, for the effect is utilized as helium discharge cleaning technique.

Dynamic behavior of He in metals is mostly studied by thermal desorption, though it is not analyzed nor understood well. Different from hydrogen which diffuses in metals interstitially, He strongly bounds to vacancies. After Chernikov[58], the binding (or trapping) energy of He-vacancy is 2.8 and 3.9 eV for Mo and W, respectively. Such high binding energies mean that He release under thermal desorption process automatically accompanies the modification of micro-structure and makes analysis very difficult[59]. During thermal desorption studies and/or reemission studies of implanted He with medium to low energy, burst-like He emission often appeared which is believed to be caused by the exfoliation of blisters (for example, see Ref[60]). Buters and Beukel[61] have claimed that shallowly implanted He, if trapped at dislocations, undergoes a rapid pipe diffusion to the nearest surface and vanishes without contributing to the measured desorption. Nevertheless, in thermal equilibrium at very high temperatures, predominant interstitial migration is to be expected. The effective migration energy in this case would be a rather low value and reported to be 0.2 to 0.3 eV for Mo and W[58,62].

One should note that He bubbles trap hydrogen as seen in Table 3. Hydrogen and helium may have synergistic effects on materials properties but this aspect has not been examined yet.

3.5. Corrosion by coolant

The application of high Z materials as heat sink materials is out of scope of this chapter and in Ref.[13] one can see data base for this application. Here only corrosion of the high Z by coolant is briefly reviewed. Since aqueous corrosion of Mo and W at high temperatures is serious concerns, water or water vapor does not seem suitable for coolant for both metals. And the coolant should be either He gas or liquid metals, otherwise Mo and W should be blazed to another heat sink material like Cu.

Comparing with stainless steels in which Cr, one of the main constituent

elements, is oxidized by impurity water or oxygen in helium coolant. Mo and W do not seem to be oxidized in very low oxygen potential owing to their rather unstable oxide.

Although binary phase diagrams for liquid metals (Li and Na) and high Z(Nb, Mo, Ta and W) are not fully available[63], most of the high Z materials seem compatible with the alkali metals. Utilization of Nb for tritium extraction in Li[64] relies on excellent compatibility of Nb with Li. It should be noted that dissolved oxygen-in alkali metals leads to considerable corrosion and mass transfer producing molybdates or tungstate of the alkali metals[65].

4. BEHAVIOR OF HIGH Z MATERIALS IN PLASMA AND HIGH HEAT LOAD TESTS

4-1. Results of high heat load tests

Recently extensive studies of high head load or thermal shock test have been done for high Z materials[15,66-69]. Owing to better thermal properties of the high Z materials, temperature increase is clearly lower compared with fine grain graphite (nuclear graphite) when subject to either neutral beam or plasma. Mo block is found to tolerate with 20MW/m^2 for several seconds without melting under a inertial cooling condition[15].

As mentioned earlier the crucial issue for the utilization of the high Z materials produced by the powder metallurgy(PM) is the recrystallization. In the PM-Mo once subjected to high heat load, the recrystallization and crack propagating the boundary between the recrystallized columnar grain zone and remaining granular grain region clearly appeared as shown in Ref[15]. In addition, cyclic heating will enhances the crack propagation due to thermal stress during the cooling phase. The brittleness of the high Z materials, i.e. intergranular fracture[70], might be avoided if the operating temperature is kept above 800K[71], which is very realistic condition for the first wall or divertor plates under the normal operation condition of ITER.

Weight Loss of Molybdenum
under 10 cycle EB Heating

Fig. 16 Comparison of surface erosion
between PM-Mo and AM-Mo under neutral
beam heating[73]. (AM means argon
arc melting)

In this respect a single crystal seems very attractive and one can not see recrystallization nor crack propagation even after surface melting[15]. However, the large single crystal of W can not be easily produced. Recently Hiraoka et al.[72] have developed a new technique to make a large crystal by sintering even for W.

Gaseous impurities also influence the response of the high Z materials to high heat load. One can clearly see surface craters due to gas release from PM-Mo, but not on electron beam melted Mo(EB-Mo) and single crystal of EB-Mo (see Fig. 2 in Ref[15]). Even surface erosion of arc-melted Mo (AM-Mo) is lower than that of the PM-Mo under the same neutral beam heating condition [73] as seen in Fig. 16.

One of the disadvantages of the high Z is their heavy weight. Although the high Z material can be used as a mono-block PFC serving both as plasma facing material and structure or heat sink material with cooling channel, the utilization only as armor tiles is much sense than the mono-block if considering their heavy weight, difficulty of machining and lack of ductility. Then the high Z armor should be blazed or welded to the cooling channel and the blazing or welding becomes the critical concern. Recently blazing of W to Cu is very successfully done and found to satisfy the ITER conceptual design[68,74]. Poor welderbility of the high Z materials needs much R&D efforts[75,76].

4.2. Behvior of high Z materials in plasma

In early tokamak experiments, high Z impurity accumulation in plasma center often resulted in hollow temperature profiles as shown in Fig. 17 due to their strong radiation[1,76]. This has been one of the most important reasons for excluding high Z elements as PFM. Nevertheless ITER designers request high Z materials as PFM for their attractive thermo-physical properties. Accordingly, re-examinations of the high Z as PFM are started in TEXTOR[9,10], ASDEX-U[11], ALCATOR C-Mod[12], and other small machines. Here some recent results from TEXTOR are reported[9,10,78]. These results clearly indicate that the high Z could be used as PFM if they do not accumulate in the center. In the high Z experiments of TEXTOR, electron beam melted Mo and W were used as a small limiter(10cm long 6cm broad and 5 cm high) and inserted to the plasma. In a high density ohmic discharged plasma, accumulation of high Z impurities in the plasma center was observed and accompanied the increase of central radiation as shown in Fig.18. At the high density limit it resulted in minor disruptions. This observation is very similar to the results reported in earlier experiments such as shown in Fig.17.

In a neutral beam heated plasma, in contrast, Mo limiter did not influence the plasma very much and no anomalies were found in the plasma characteristics such as electron density, temperature, radiation, etc. and even Z_{eff} stayed constant. A maximum power flux of about 20MW/m^2 could be loaded on the Mo limiter which led to the maximum surface temperature
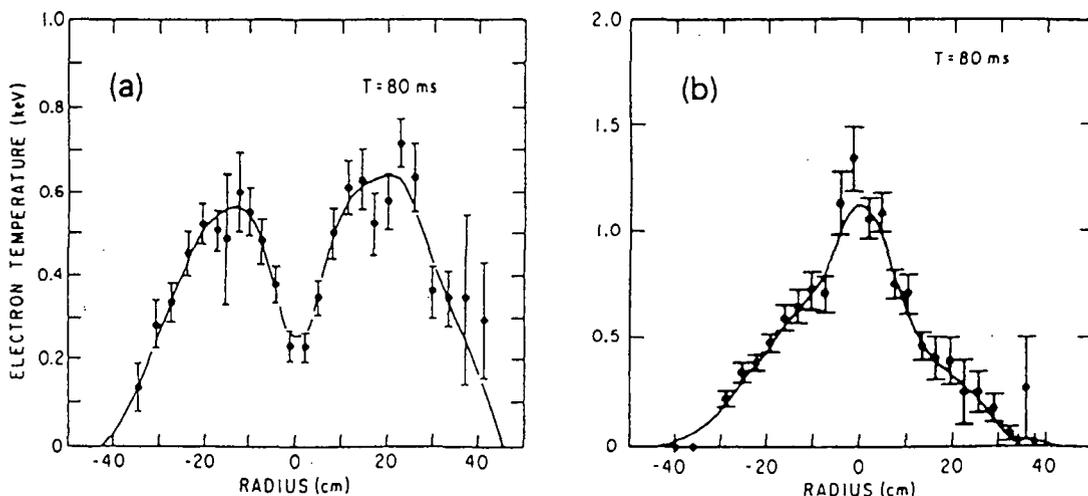

Fig. 17 (a) Hollow temperature profile due to W accumulation and
(b) disappearance with controlled gas puffing[75]
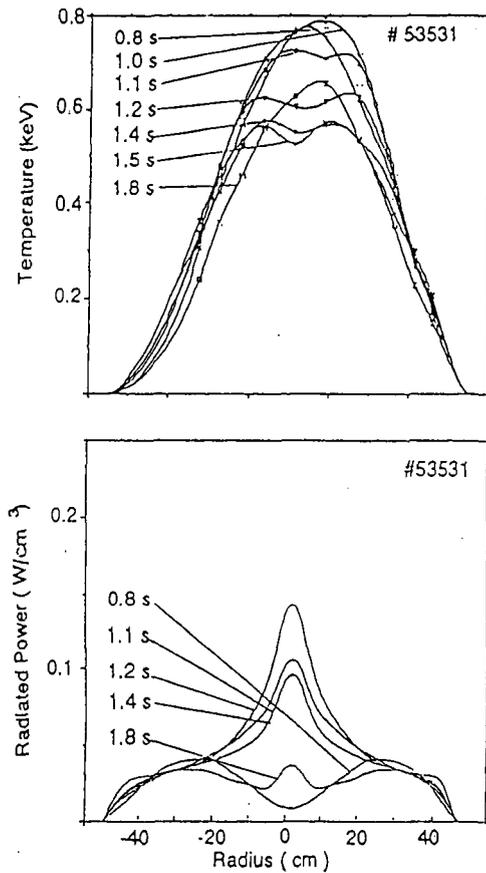
Fig. 18 Appearance of hollow temperature
profiles and accompanied central
peaked radiation in ohmic heated
TEXTOR plasma[76].
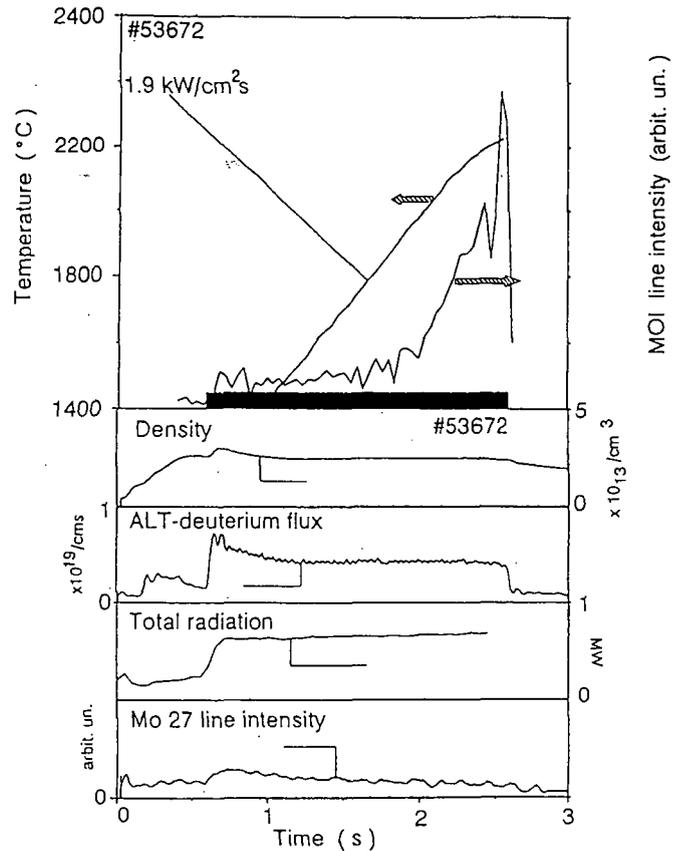
Fig. 19 Effect of melting of Mo limiter
on TEXTOR plasma parameters[8]

over 2800K. As a result the Mo limiter exhibited local melting leaving a very thin
molten layer without any cracks or serious damage. The heat load is very
similar to the critical heat load of Mo melting observed in a NBI heat load
test described in the previous section[15]. Although a large amount of Mo
was evaporated during the melting, the main plasma did not influenced very
much as seen in Fig. 19. This is a good indication that released high Z
impurities from the limiter with thermal or very low energies hardly enter
the main plasma due to the impurity screening effect in front of the
limiter[78]. The screening effect is tentatively attributed to the smaller
radius of gyromotion of the high Z elements under magnetic field than
ionization length, that is, before ionized to highly charged states and enter-
ing into the main plasma, the released high Z impurities are redeposited to
the limiter head by their gyromotion[78].

Recent experiments in Alcator C-Mod[11] which uses a Mo divertor have
indicated that Mo does not accumulate in the main plasma, too. Since impu-
rity transport is highly related to density and temperature profiles of
plasma, more detailed experiments are necessary to clarify the utilization
condition of high Z as PFM.

144

5. CONCLUSIONS

Materials properties of high Z materials for the application as PFM are reviewed. Although PMI data for the high Z are not enough and their potential risk of high radiation loss has been a serious concern, the high Z are very attractive because of their excellent thermo-physical properties.

It is no doubt that for the application of the high Z as PFM plasma edge temperatures should be below the threshold energy of self-sputtering. In addition, low Z impurities like C and O should be reduced, not only because both are main impurities in the current tokamaks but also most of the medium to high Z impurities in the present plasma are produced by the sputtering by these low Z impurities.

When high Z materials produced by powder metallurgy are subjected to an extraordinary high heat load, the recrystallization, cracking by thermal shock and thermal fatigue by cyclic thermal stresses are main concerns. The application of a single crystal can avoid the recrystallization problems but the manufacturing of a large single crystal is very difficult. The alloying may also reduce the recrystallization but it automatically introduces an upper limit of operation temperature. The brittleness of the high Z could be avoided under high temperature operation.

Recent advances in a sintering technique and electron beam or arc melting enable to make highly purified materials as well as a large single crystal. The mechanical properties of the newly produced materials may differ from those of the materials produced by powder metallurgy. Hence, data base referred here, which is mostly for the PM materials, must be revised.

Data concerning hydrogen behavior in Mo and W are not enough available nor fully reliable. Mo and W trap large amount of hydrogen and the hydrogen may cause an embrittlement below 800K. Nevertheless these disadvantages do not restrict the utilization of the high Z materials as PFM above 800K.

Effects of neutron irradiation from PMI aspects are unclear but they may not influence the PMI strongly, in contrast to the significant increase of DBTT. He injected from plasma or produced by nuclear reaction and transmutation also enhances the increase of DBTT. Unfortunately, neutron irradiation data are mostly for PM materials and more or less nothing exists for the highly purified ones. Hence, neutron irradiation effects must be re-examined for newly produced materials.

In most cases the high Z armor should be blazed to the cooling channel or the low Z armor to high Z structure materials. Therefore, the blazing is also an important issue. Poor welderbility of the high Z materials needs much more R&D efforts.

According to recent high Z limiter experiments in TEXTOR, accumulation of high Z impurities in the center of the ohmically heated plasma was observed, very similar to the results reported in earlier tokamak experiments. The NBI heated plasma, in contrast, was not influenced very much showing no anomalies in the plasma parameters (electron density, temperature, radiation, etc.) Even upon the melting of the Mo limiter the plasma was not disturbed by the Mo vapor. This is attributed to the impurity screening effect owing to the smaller radius of gyromotion of the high Z elements than their ionization length. This is a good indication for the utilization of high Z materials.

In conclusion, although from material aspects high Z materials are much more attractive than low Z one, the high radiation properties of the high Z materials can not be eliminated. Therefore much more efforts to reduce

the temperature of the boundary plasma and to study how the main plasma to withstand the power loss due to the high Z impurities are urgently needed.

<div align="center">REFERENCES</div>

[1] Tanabe, T., Nakamura, H., Noda, N., J. Nucl. Mater., 96-198(1992)11.
[2] Whitley, J.B., Wilson, K.L. and Buchernaur, D.A., J. Nucl. Mater., 155-157(1988)82.
[3] Espe, W., Materials of High Vacuum Technology (Pergamonn Press, 1966)
[4] Jensen, R.V., Nuclear Fusion, 17(1977)1187.
[5] Miyahara, A. and Tanabe, T., J. Nucl. Mater., 155-157(1988)49.
[6] Birch, M. and Brocklehurst, J.E., ND-R-1434(S), 1987.
[7] Maruyama, T. and Harayama, M., J. Nucl. Mater., 195(1992)44.
[8] Tanabe, T., Philipps, V., Ueda, Y., et al., J. Nucl. Mater., 212-215(1994) 1370.
[9] Philipps, V., Tanabe, T., Ueda, Y. et al., J. Nucl. Fusion in press.
[10] Roth, J., Naujoks, D., Krieger, K., et al., Proc. 11th PSI, J. Nucl. Mater. to be published.
[11] Kurz, C., Lipshultz, B., McCracken, G.M., et al., Proc. 11th PSI, J. Nucl. Mater. to be published.
[12] Lupton, D.. Aldinger, F. and Schulze, in Niobium, Proc. Int. Sympos. (The Metal. Soc. AIME. Warrendale, PA, 1981)p.533.
[13] Smith, D. L., Altovsky, I.V., Barabash, V.R., et al., ITER Material Evaluation and Data Base, ITET Documnet Series, (IAEA/ITER/DS/No.29), 1993
[14] Kotelnikov, R.B., Bashilikov, S.N., Galiakbarov, Z.G. and Kashitanov, A.I., Basic refractory elements and compounds Reference book (Moscow, 1969) (in Russian).
[15] Tanabe, T. Fujine, M. Noguchi, H. et al., J. Nucl. Mater., 200(1993)120.
[16] Lavrentev, V.I., et al., Niobium : Physico-chemical properties of its compounds and alloys, Kubaschewski, O. Ed., Atomic Energy Review Special Issue, No. 2, (IAEA,1968).
[17] Brewer, L., Molybdenum : Physico-chemical properties of its compounds and alloys, Kubaschewski, O. Ed., Atomic Energy Review Special Issue, No. 7, (IAEA,1980).
[18] Gerassimov, T.I., et al., Tantalum: Physico-chemical properties of its compounds and alloys, Kubaschewski, O. Ed., Atomic Energy Review Special Issue, No. 3, (IAEA,1972).
[19] Eckstein, W., Bohdansky, J. and Roth ,J., Physical Sputtering, Suppl. J. Nucl. Fusion, 1(1991)51.
[20] Eckstein, W., Garcia-Rosales, C., Roth, J. and Ottenberger, W., Sputtering Data, Repts. IPP Garching, IPP 9/82(1993).
[21] Yamamura, Y., Itikawa, Y. and Itoh, N., Repts. IPP Nagoya, IPPJ-AM-26(1983).
[22] Roth, J., Vietzke, E. and Haasz, A.A., Erosion of Graphite due to Particle Impact, Suppl. J. Nucl. Fusion, 1(1991)63.
[23] Bohdansky, J., Nucl. Instr. Methods, B2(1984)587.
[24] Hechtel, E., Eckstein, W., Roth, J. and Laszlo, J., J. Nucl. Mater., 179-181(1991)290.
[25] Hechtel, E., Bohdansky, J. and Roth, J., J. Nucl. Mater., 103&104(1981)333.
[26] Hechtel, E., and Bohdansky, J., J. Nucl. Mater., 122&123(1984)1431.
[27] Saidoh, M., Gnaser, H. and Hoffer, W. O., Nucl. Inst. Methods, B28(1987)540.
[28] Saidoh, M. and Yamada, R., Nucl. Instr. Methods, B39(1989)599.
[29] Kyoh, B., Uchida, K. and Imoto, S., Koongakkaishi, 16(1990)164 (in Japanese).
[30] Miggie, M., Proc. Int. Symps. Plasma Wall Interaction, Julich Germany, 1976, p.275.

146

[31] Ito R., et al., Data on the Backscattering Coefficient of Light Ions from Solids, Rep. IPPJ-AM-18(1981); At. Data Nucl. Data Tables 28(1983)493.
[32] Eckstein, W., Reflection, Suppl. J. Nucl. Fusion, 1(1991)17.
[33] Thomas, E.W., Particle induced electron emission, Suppl. J. Nucl. Fusion, 1(1991)79.
[34] Philipps, V., et al., Nuclear Fusion, 33(1993)953.
[35] Weissler, G.L., Handbuch der Physik 21, Springer-Verlag Berlin (1956) p.342
[36] Christman, K., Surf. Sci. Repts., 9(1988)1.
[37] Elevled, H. and Van Veen, A., J. Nucl. Mater., 191-194(1992)430.
[38] Borovik, E.S., Katrich, N.P. and Nikolaev, G.T., Atomn. Energia 18(1965), and ibid, 21(1966)339.
[39] Freeman, N.J., Latimer, I.D. and Daly, N.R., Nature, 212(1966)277.
[40] McCracken, G.J. and Erents, S.K., Radiation damage and gas diffusion in molybdenum under deuterium bombardment, in Application of ion beam to metals (Plenum, NY, 1974) p.585.
[41] Alefeld, G. and Volkl, J., Hydrogen in metals Vol.1 & 2 (Springer Verlag, 1978) and Volkl, J. and Alefeld, G., Diffusion in Solids, ed. Nowick, A.S. and Burton, J.J., (Academic Press, 1975) pp.231-301.
[42] Myers, S.M. and Basenbacher, F., J. Appl. Phys., 60(1986)3499.
[43] Erents, S.K., Vacuum, 24(1974)445.
[44] Tanabe, T., Hachino, H. and Takeo, M., J. Nucl. Mater., 176&177(1990)666.
[45] Myers S.M., Richards, P.M., Wampler, W.R. and Basenbacher, F., J. Nucl. Mater, 165(1989)9.
[46] Moeler W., Nucl. Instr. Methods, 209/210(1983)773.
[47] Wilson K.L., Bastasz, R., Causey, R.A., Brice, B.K., Doyle, B.L., Wampler, W.R., Moeller, W., Scherzer, B.M.U., Tanabe, T., Trapping, detrapping and release of implanted hydrogen isotopes, Supplement J. Nuclear Fusion, 1(1991)31.
[48] Anderl, R.A. et al., Fusion Technol., 21(1992)745.
[49] Tanabe, T., presented in IAEA Specialists' Meeting on "Tritium retention in fusion reactor plasma facing components" held in IAEA Headquarters Vienna, Austria, 17-18 June 1993.
[50] Chorkendorff, I., Russell, J.N., Jr., and Ates. J.T., Jr. Surface Sci., 182(1987)375.
[51] Tanabe, T. Yamanishi, Y. and Imoto, S., J. Nucl. Mater., 191-194(1992)439.
[52] Katsuta, H., McLellan, R.B. and Furukawa, K., J. Phys. Chem. Solids,43 (1982)553.
[53] Meller, W.M., Blackledge, J.P. and Lobowitz, G.G., Metal Hydride, (Academic Press, 1968).
[54] Katsuta, H., Iwai, T., Ohno, H., J. Nucl. Mater., 115(1983)208.
[55] Peterson, D.T., Hull, A. B. and Loomis, B. A., J. Nucl. Mater., 191-194(1992)430.
[56] Vook, F.L. and Picraux, S.T., Lattice Location Studies of Gases in Metals, in Radiation Effects on Solid Surface, ed. M. Kaminsky, (ACS, 1976) pp.308-324.
[57] Das, S.K. and Kaminsky, K., Radiation Blistering in Metals and Alloys, in Radiation Effects on Solid Surface, ed. Kaminsky, M.,(ACS, 1976)pp.112-170.
[58] Chernikov, V.N., and Zhakharov, A.P., J. Nucl. Mater., 165(1989)89.
[59] Jung, P. and Schhroeder, K., J. Nucl. Mater., 155-157(1988)1137.
[60] Bauer, B.W. and Thomas, G.J., J. Nucl. Mater., 53(1974)127.
[61] Butters W.Th.B. and Van den Beukel, A., J. Nucl. Mater., 144(1987)71.
[62] Amano, J. and Seidman, D.N., J. Appl. Phys., 56(1984)983.
[63] Massalski, T.B., et al., Binary alloy phase diagrams, Vol. 1&2 (ASM, 1986).
[64] Alire, R.H., UCRL-52455(1978).
[65] Gnanasekaran, T., Mahendran, K.H., Kutty, K.V.G. and Mathews, C.K., J, Nucl. Mater., 165(1989)210.
[66] Bolt, H., Kiuchi, K., Araki, M. and Seki, M., Fusion Technology, (1988)919.
[67] Kny, E., Kneringer, G., Koizlik, K. and Nickel, H., Fusion Eng. and Design, 9(1989)271.
[66] Ogawa, M., Seki, M., Fukaya, K., et al., Fusion Eng. and Design,9(1989)277.
[69] Rigon, G., Moretto, P. and Brossa, F., Fusion Eng. and Design, 5(1987)299.
[70] Kimura, H., Trans. Japan Inst. Metals, 29(1988)521.

[71] Akiba, M., private communication.
[72] Hiraoka, Y., Fujitsuka, M. and Fujii,T., J. Nucl. Mater., 179-181(1991)275.
[73] Nakamura, H. Private communication.
[74] Kitamura, K., Shibutani, Y., Shibui M., et al, Fusion Eng. and Design, 9(1989)283.
[75] Moorehead, A. J. and Slaughter, G. M., The Welding Journal, 53(1974)185S.
[76] Kohyama, A. and Igata, N., J. Nucl. Mater., 122&123(1984)767.
[77] Hawryluk, R.J., Nuclear Fusion, 19(1979)1307.
[78] Ueda, Y., Tanabe, T., Philipps, V., et al., Proc. 11th PSI, J. Nucl. Mater., to be published.

RECOMMENDED PROPERTY DATA FOR MO, NB, AND V-ALLOYS

R. F. MATTAS
Argonne National Laboratory
Argonne, IL 60439 USA

Abstract: A report summarizing the properties of Mo, Nb, and V-alloys is given. The properties include baseline physical properties, baseline mechanical properties, and irradiated mechanical properties.

1. INTRODUCTION

Refractory metal alloys are candidate structural materials for fusion components; in particular for high heat flux components. They generally exhibit low thermal expansion and high thermal conductivities with high melting points that are desirable to minimize thermal stresses and allow for high heat load compatibility.

This paper describes property data for pure Mo, Nb, and V and a number of alloys. The alloys chosen to report upon are TZM (Mo), Nb-1Zr, and V-5Cr-5Ti (and V-4Cr-4Ti) which are alloys that have previously received the considerable attention for fusion applications. The database for the thermo-physical properties is relatively complete for these materials, whereas the database for baseline mechanical properties is moderate, and the databases for irradiation effects is relatively sparse for specific properties. Section 2 describes the thermophysical properties; Section 3 describes the baseline mechanicial properties; and Section 4 describes the irradiated mechanical properties.

2. THERMO-PHYSICAL PROPERTIES

The physical properties of Mo, Nb, and V are given in Table 1 [1-6].

Table 1 - Physical Properties of Refractory Metals

Property	Mo	Nb	V
Melting Point (K)	2890 (1)	2740 (1)	2199 (1)
Boiling Point (K)	5833 (2)	4927 (2)	3682 (3)
Heat of Fusion (KJ/Kg)	270 (2)	290 (2)	410 (3)
Heat of Vaporization (KJ/Kg)	5123 (2)	7490 (2)	8870 (3)
Poisson's Ratio @ 20 C	.33 (TZM)(4)	.38 (Nb-1Zr)(4)	.37 (5)
Density @ 20 C	10.2 (TZM) (4)	8.46 (Nb-1Zr) (4)	6.2 (V-5Cr-5Ti) (6)

The variation in vapor pressure with temperature is given in Fig. 1 which indicates properties are given in Figs. 2-6 [2,7-11]. The low thermal expansion of Mo coupled with high thermal conductivity tends to favor this element for high heat load applications. This advantage, however, is offset by the high value of elastic modules such that the thermal stresses in Mo and Nb are comparable. Vanadium would be expected to be able to accomodate the lowest heat load of these three elements, although it would be considerably better than iron based alloys, either ferritic or austenitic steels.
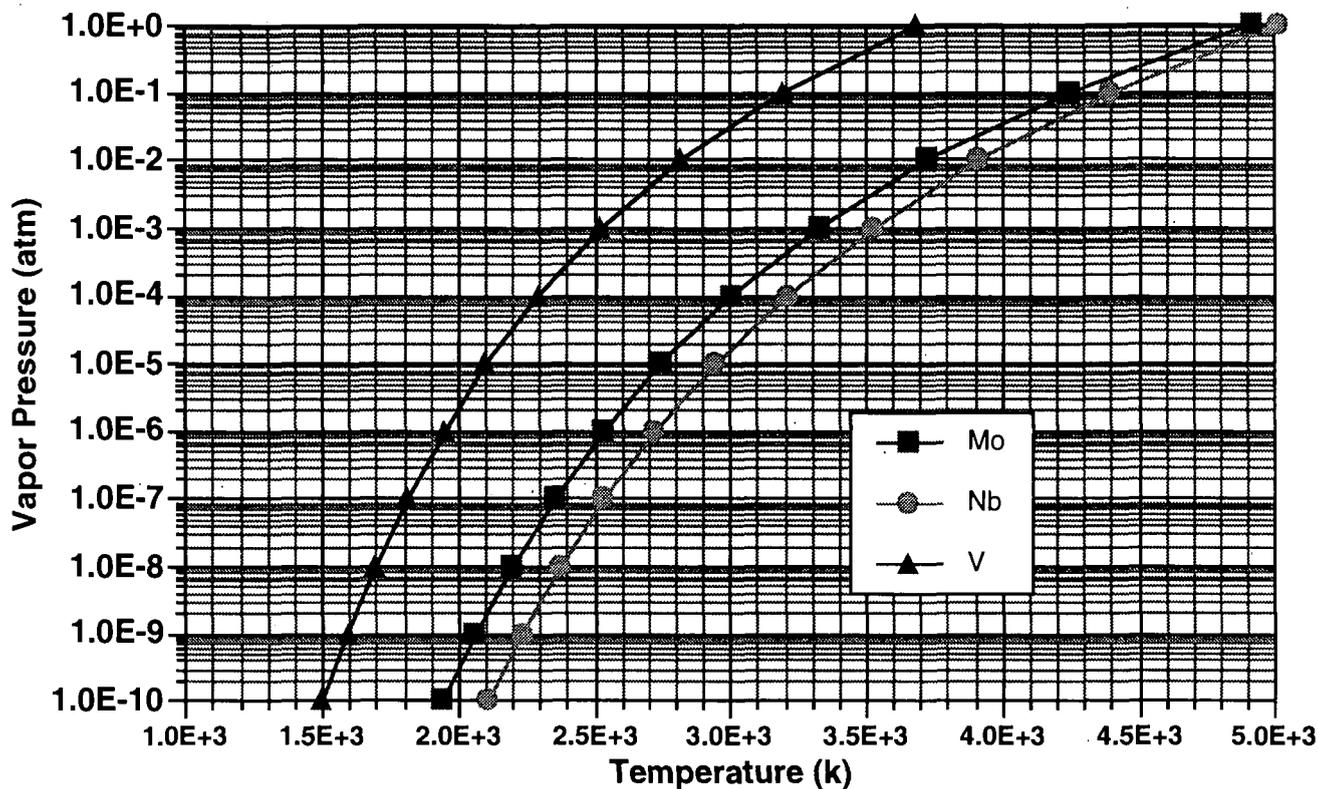
FIG. 1. Vapor pressure of Mo, Nb, and V as a function for temperature[1].

150
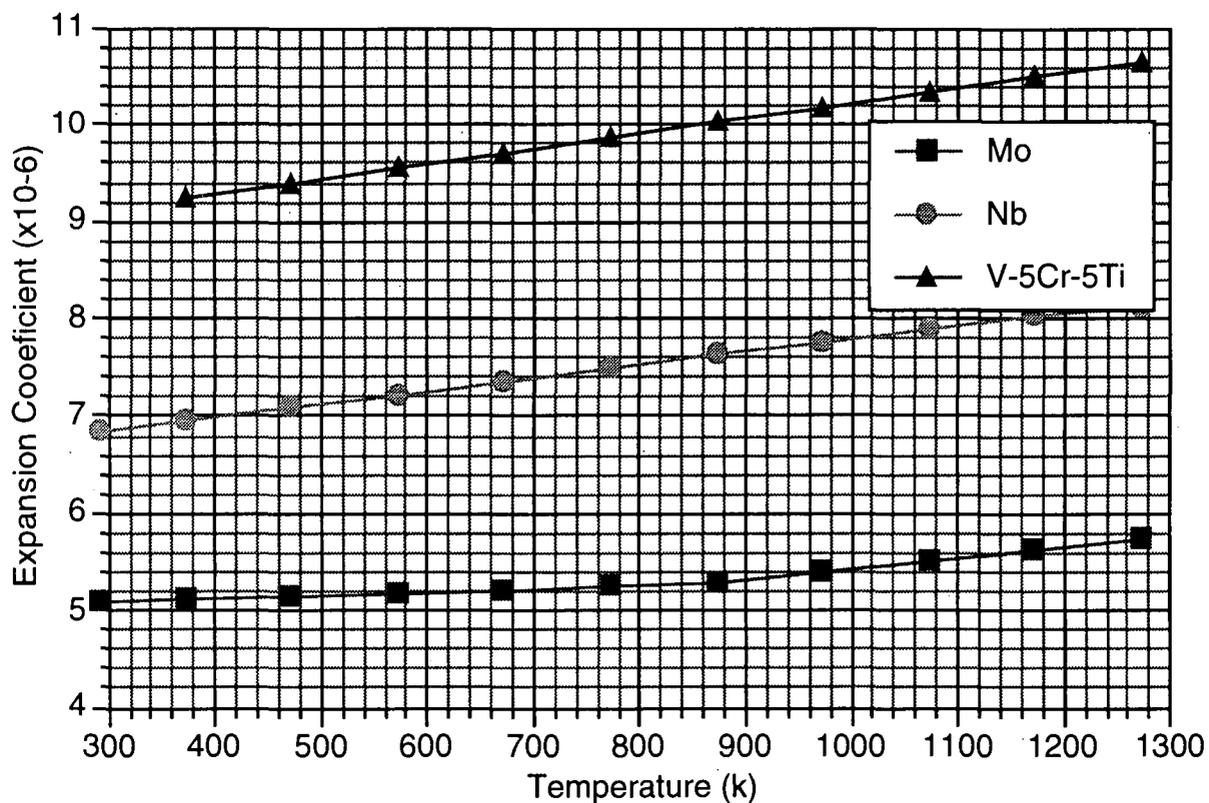
FIG. 2. Thermal exp[ansion coefficient of Mo, Nb, and V as a function of temperature [7,8,9]
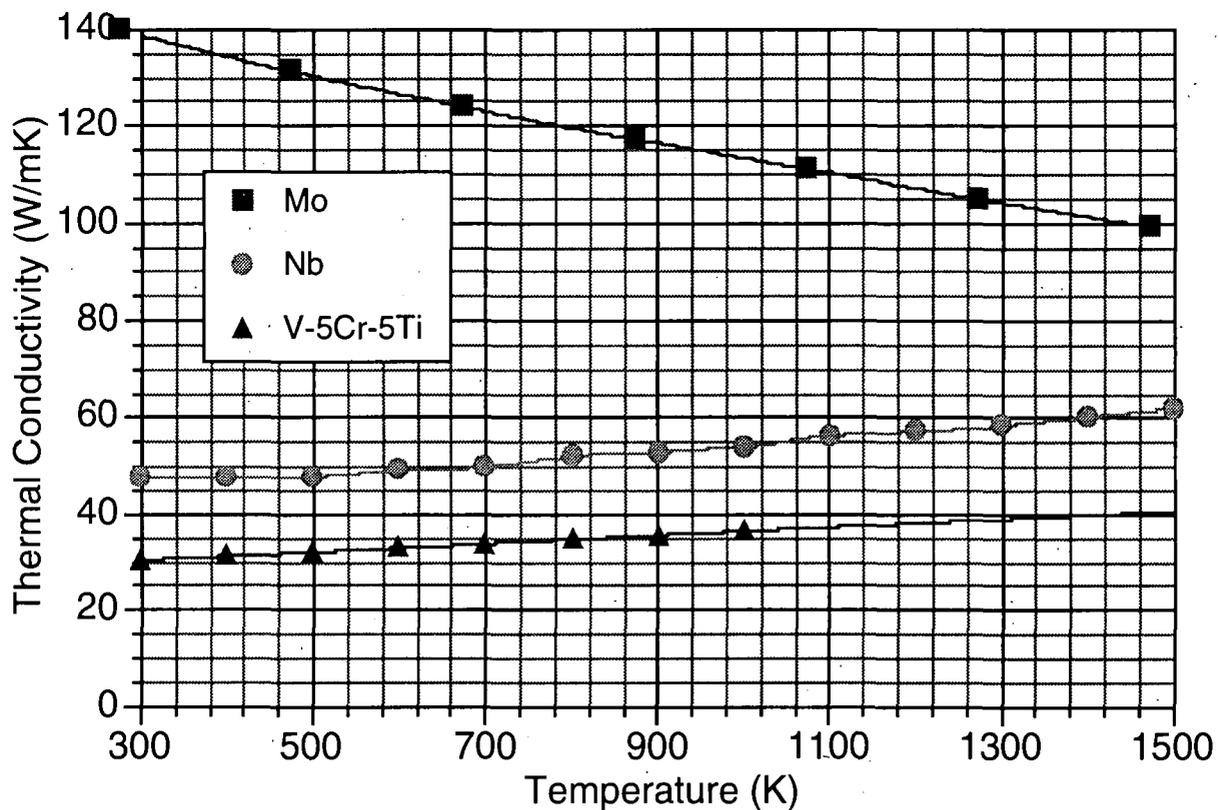
FIG. 3. Thermal conductivity of Mo, Nb, and V-5Cr-5Ti as a function of temperature [7,8,9].
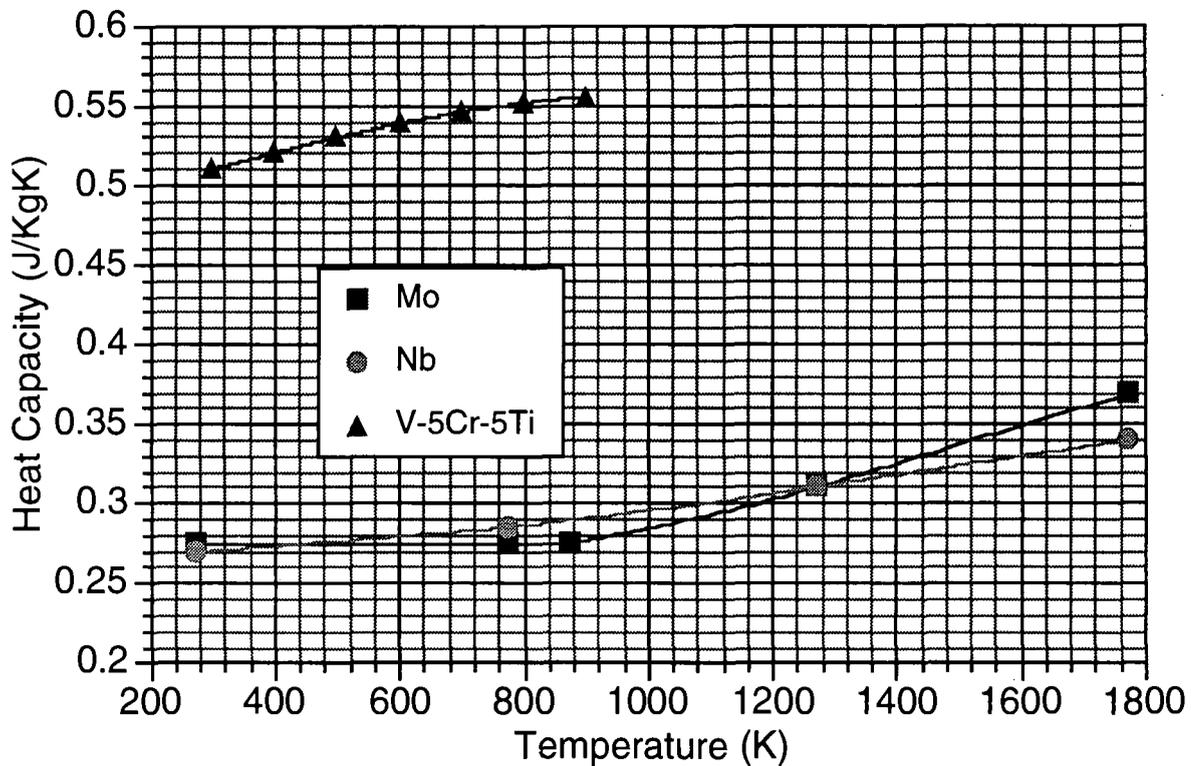
FIG. 4. Specific heat of Mo, Nb, and V-5Cr-5Ti as a function of temperature [7,8.9].
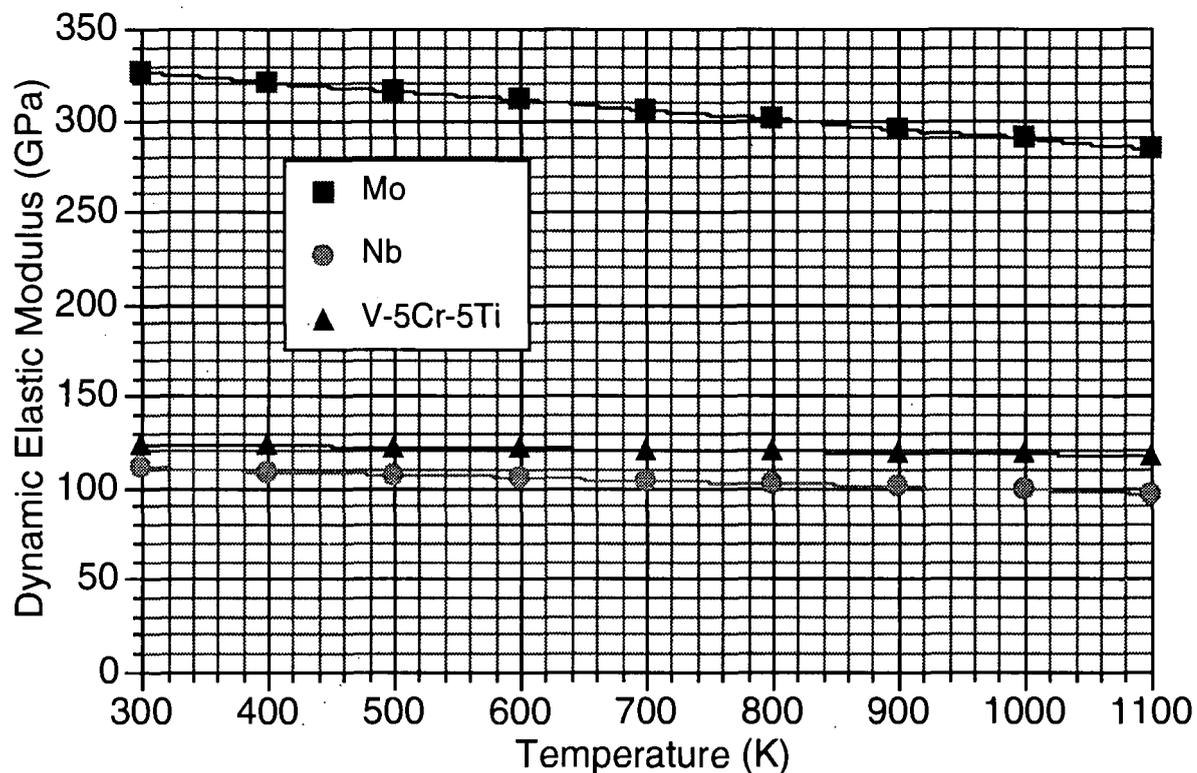
FIG. 5. Dynamic elastic modulus of Mo, Nb, and V-5Cr- 5Ti as a function of temperature [4,5,7,10,11].
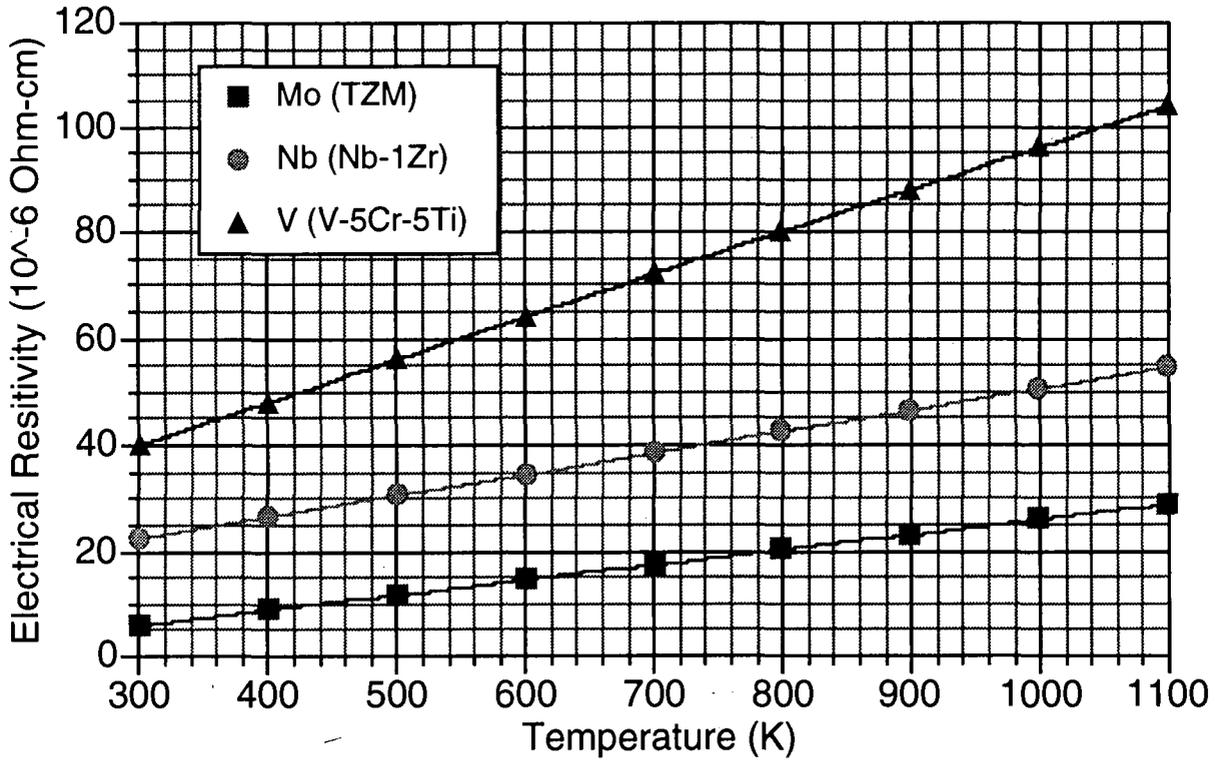
FIG. 6. Electrical resistivity of Mo, Nb and V-5Cr-5Ti as a function of temperature [2,9].
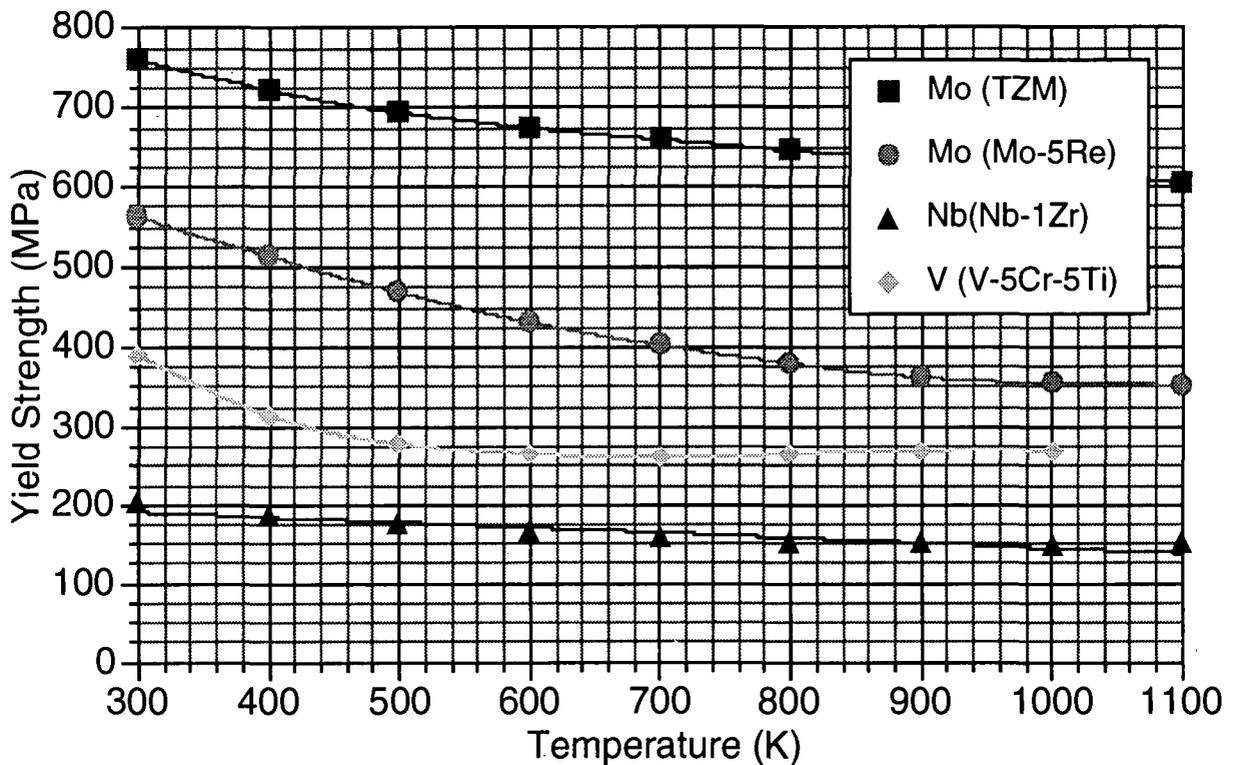
FIG. 7. Yield strength of TZM, Mo-5Re, Nb-1Zr, and V-5Cr-5Ti [4,7,12].
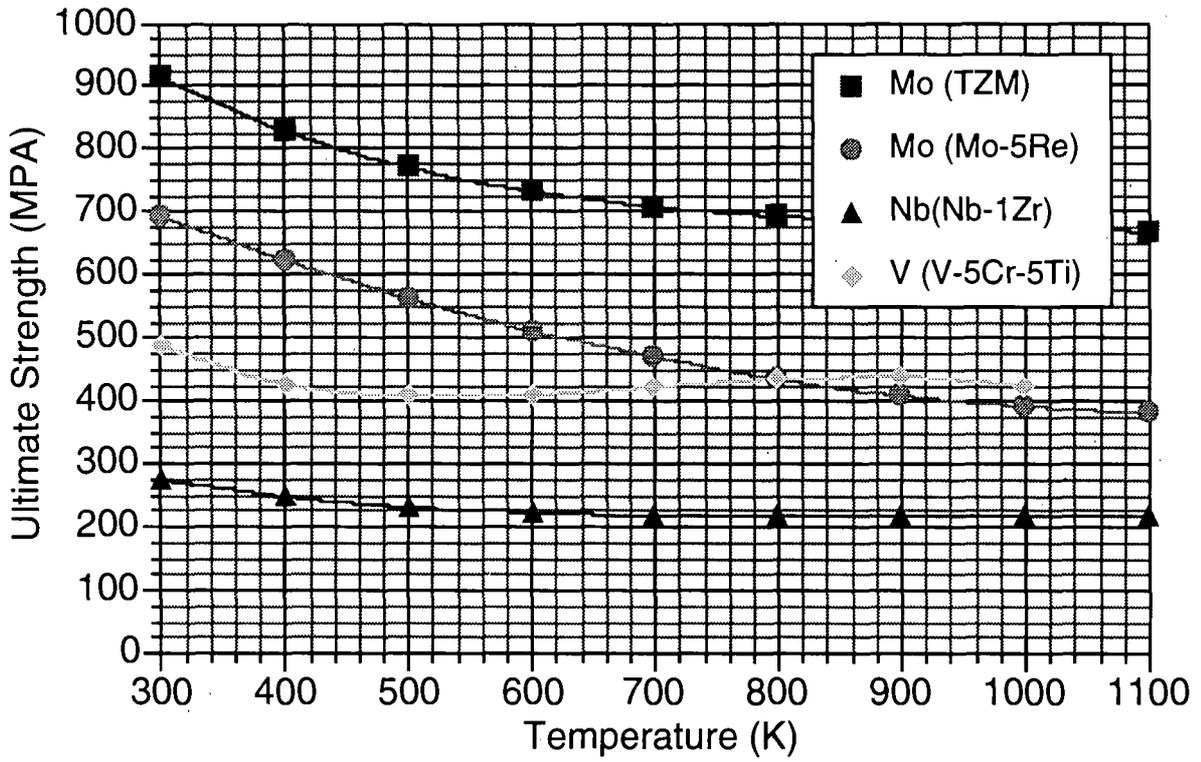
FIG. 8. Ultimate strength of TZM, Mo-5Re, Nb-1Zr, and V-5Cr-5Ti [p4,7,12].

3. BASELINE MECHANICAL PROPERTIES

The baseline tensile properties are shown in Figs. 7-10 [4,7,12]. The Mo alloys are the strongest materials but also exhibit the lowest ductibility. The fatigue properties of vanadium alloys are shown in Fig. 11 [13,14]. The fatigue properties of powder metallurgy molybdenum, stress relieved, are shown in Fig. 12 [15] and the fatigue properties of Nb-1Zr are shown in Fig. 13 [16]. Overall, the vanadium alloys exhibit superior fatigue strength. Fatigue crack growth rates of vanadium and Nb are given in Fig. 14 [17,18] which indicates crack growth rates are comparable for the different materials.
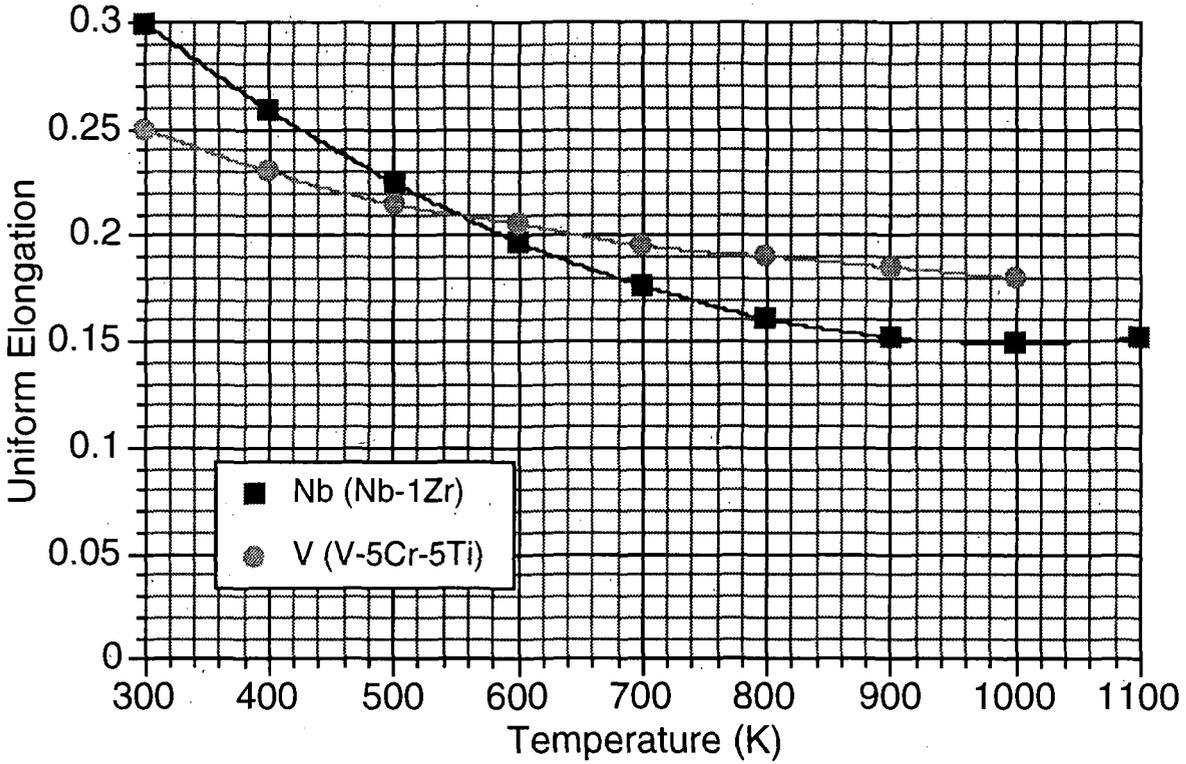
FIG. 9.   Uniform elongation of Nb-1Zr and V-5Cr-5Ti [4,7,12].
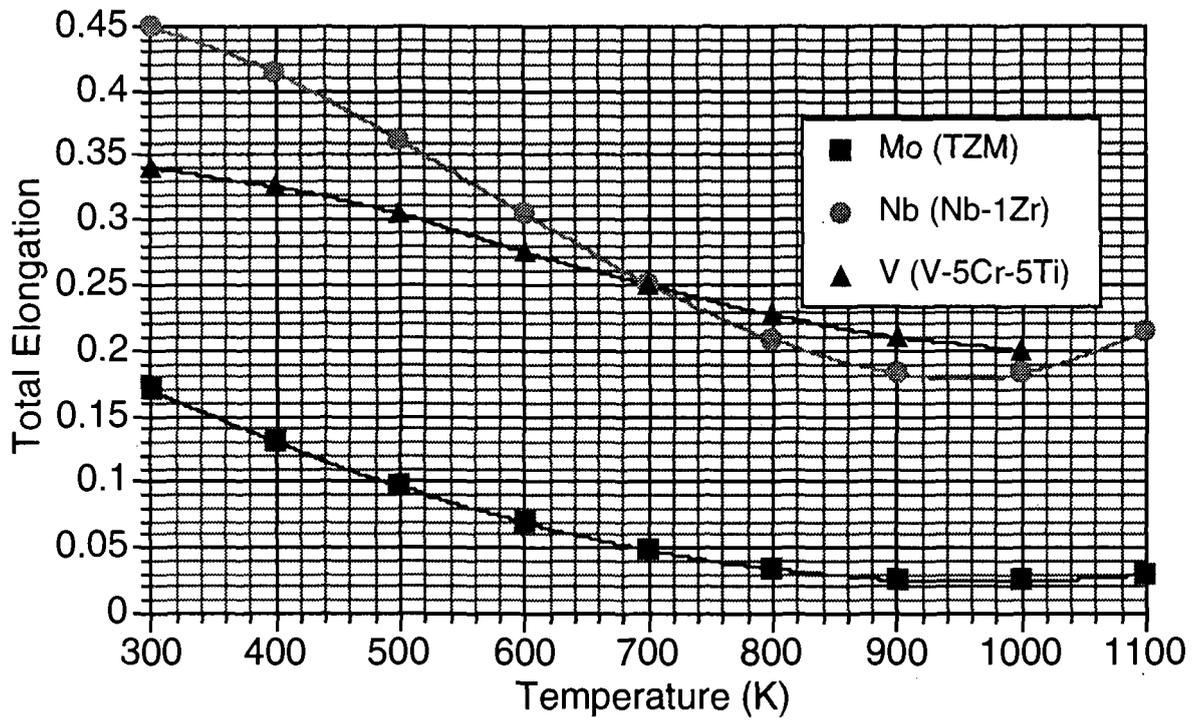
FIG. 10.   Total elongation of TZM, Nb-1Zr, and V-5Cr-5Ti [4,7,12].
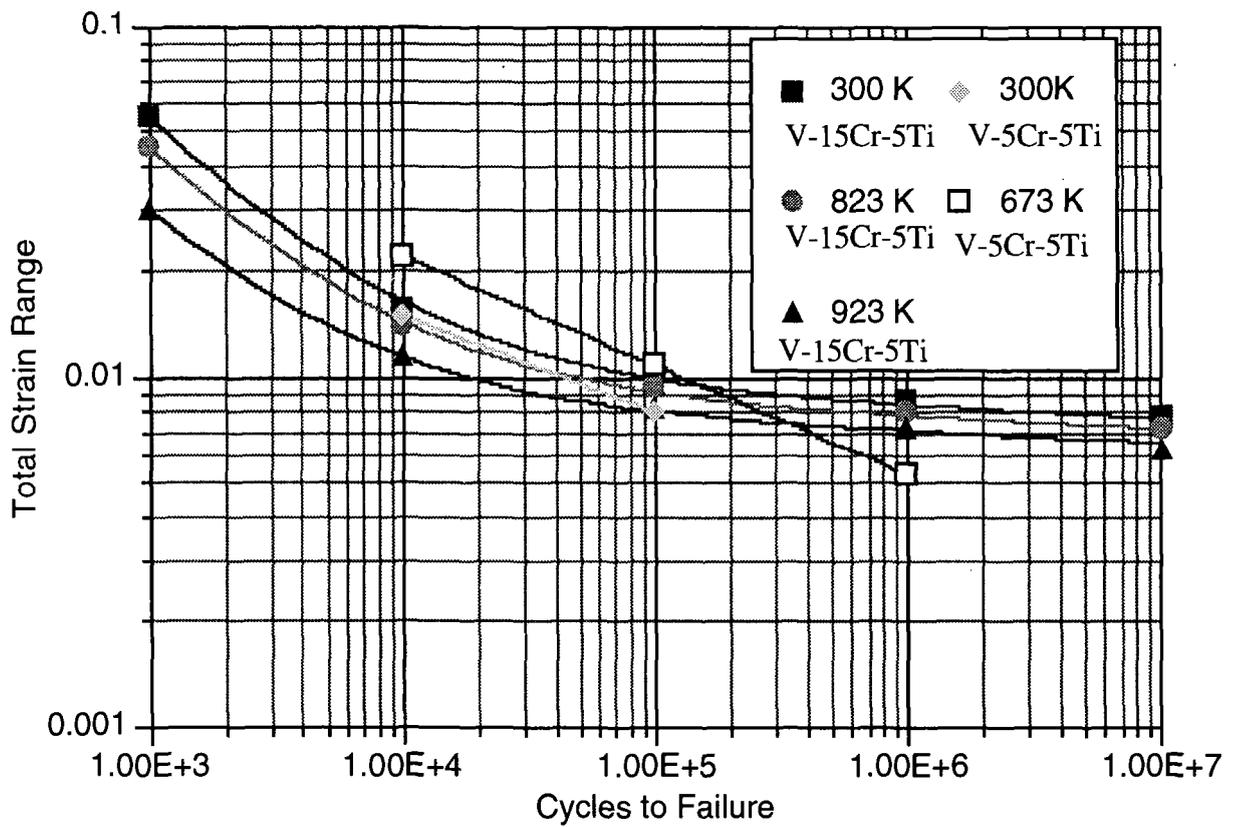
FIG. 11.   Fatigue behavior of V-15Cr-5Ti and V-5Cr-5Ti [13,14].

156
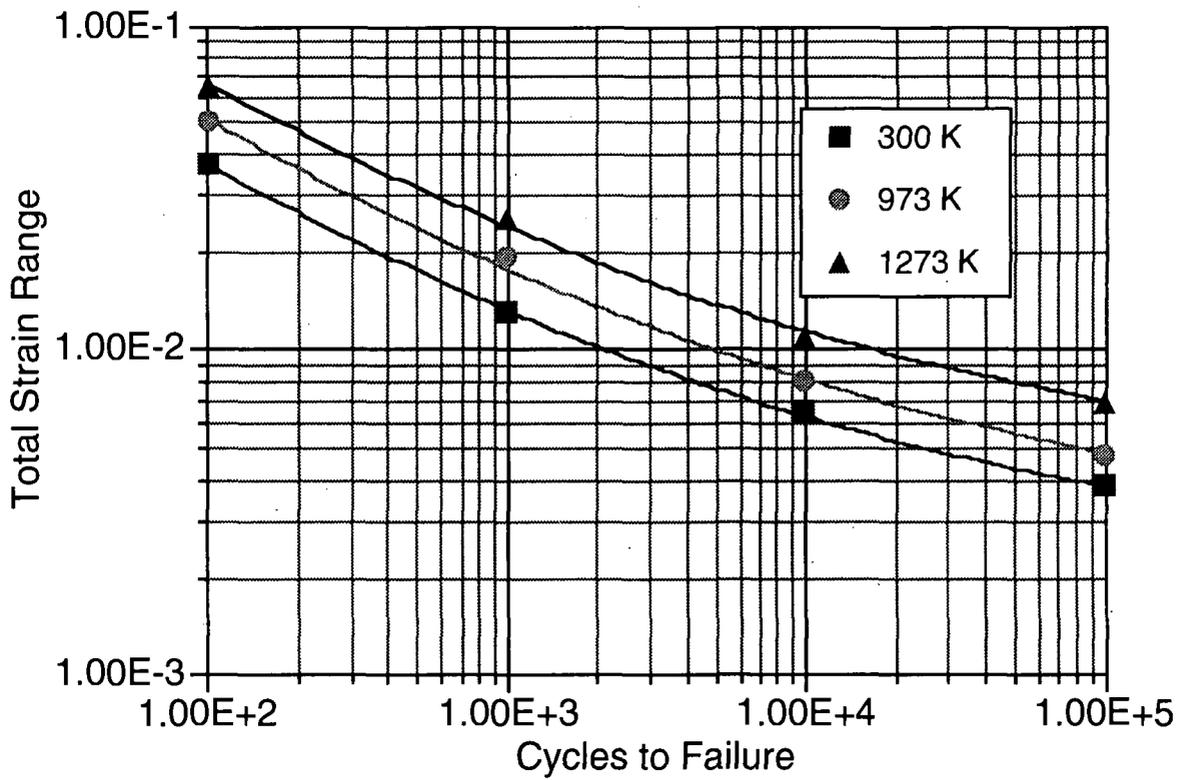
FIG. 12. Fatigue behavior of powder metallurgy Mo, stress relieved [15].
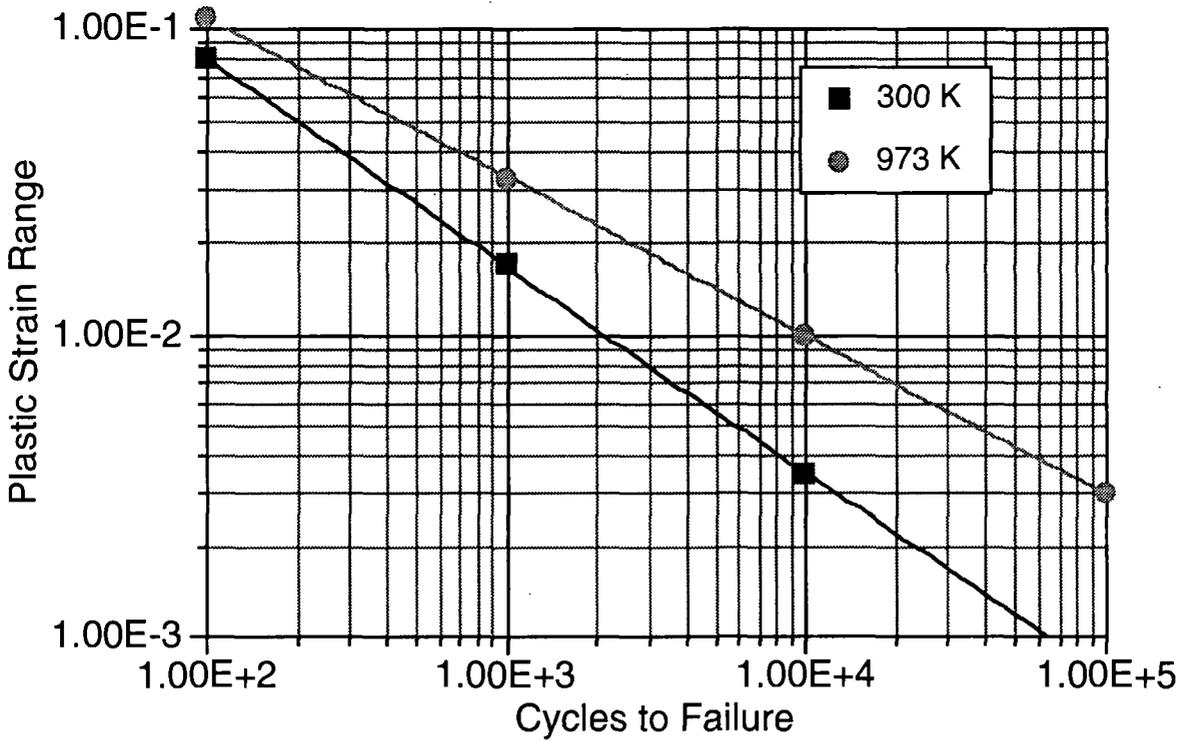

FIG. 13. Fatigue behavior of Nb-1Z Note - plastic strain range rather than total strain range [16].
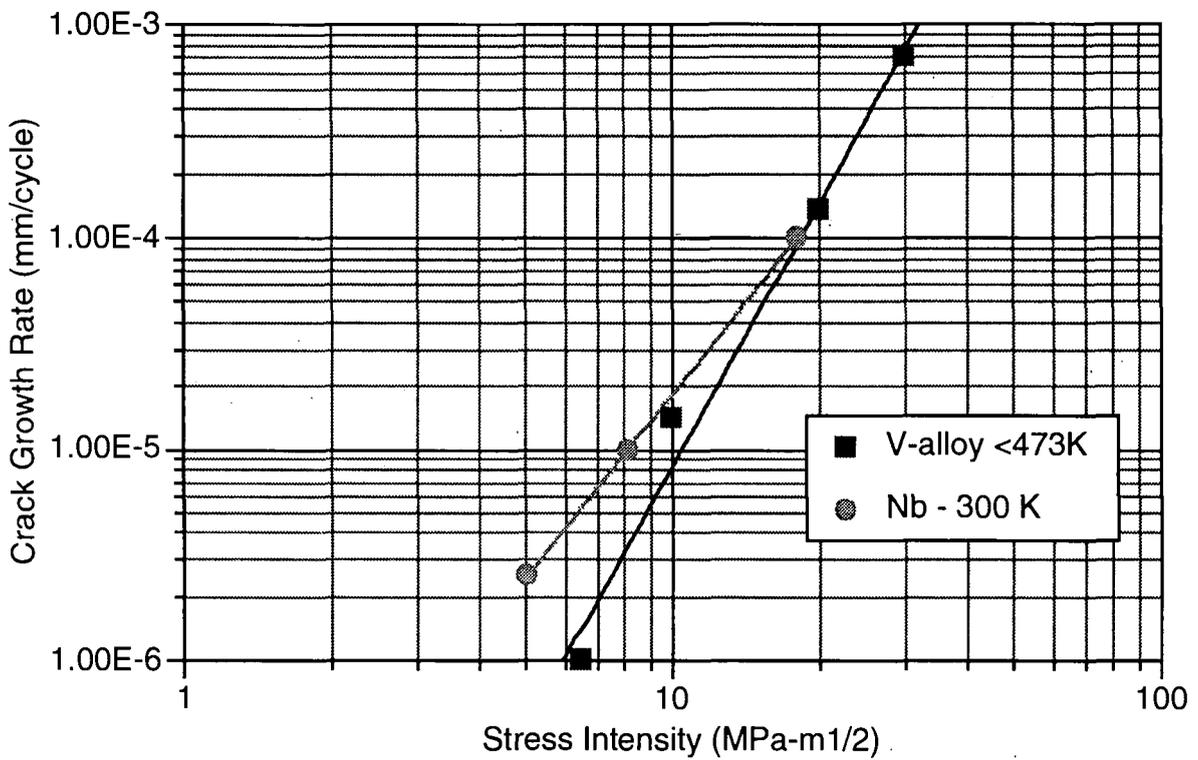
FIG. 14. Fatigue crack growth in Nb and vanadium alloys at low temperatures [17,18].

The creep behavior of Mo, Nb-1Zr, and vanadium alloys are shown in Figs. 15 to 17 [19,20].

$P=T(13.7+\log(tR)) \times 10^{\wedge}-3$ (T in K and t in h)
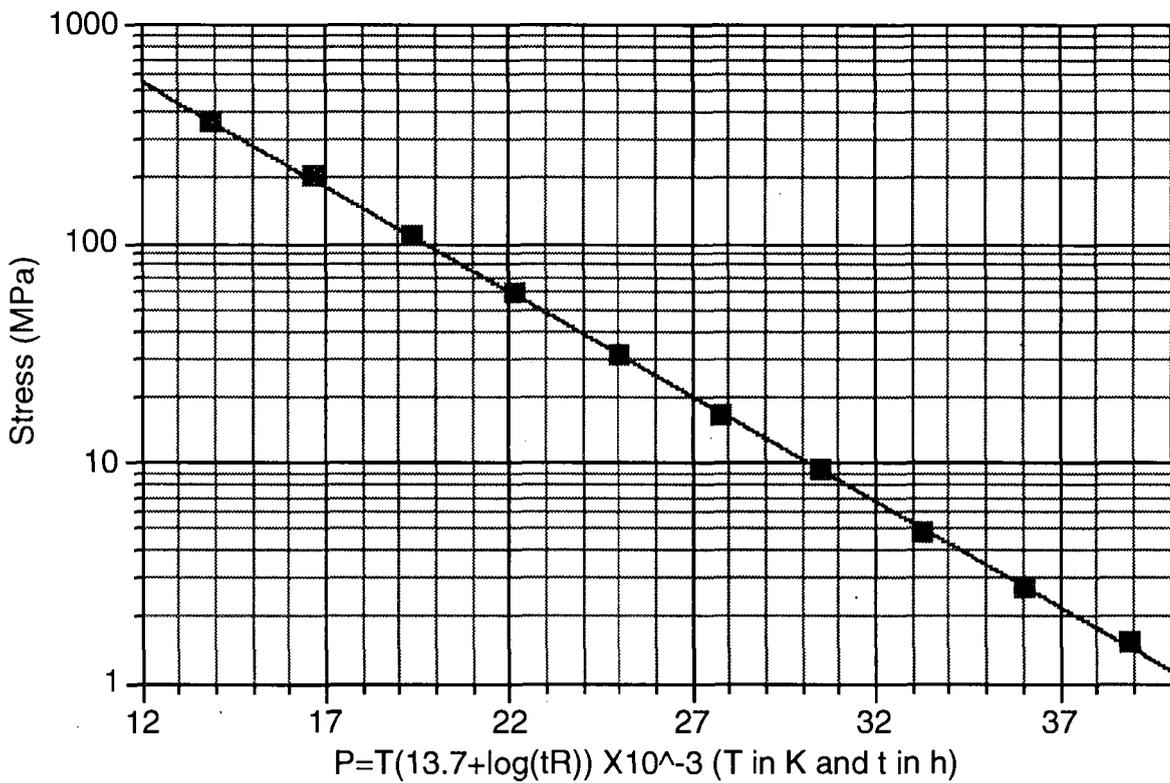
FIG. 15. Larson-Miller curve for pure Mo [19].
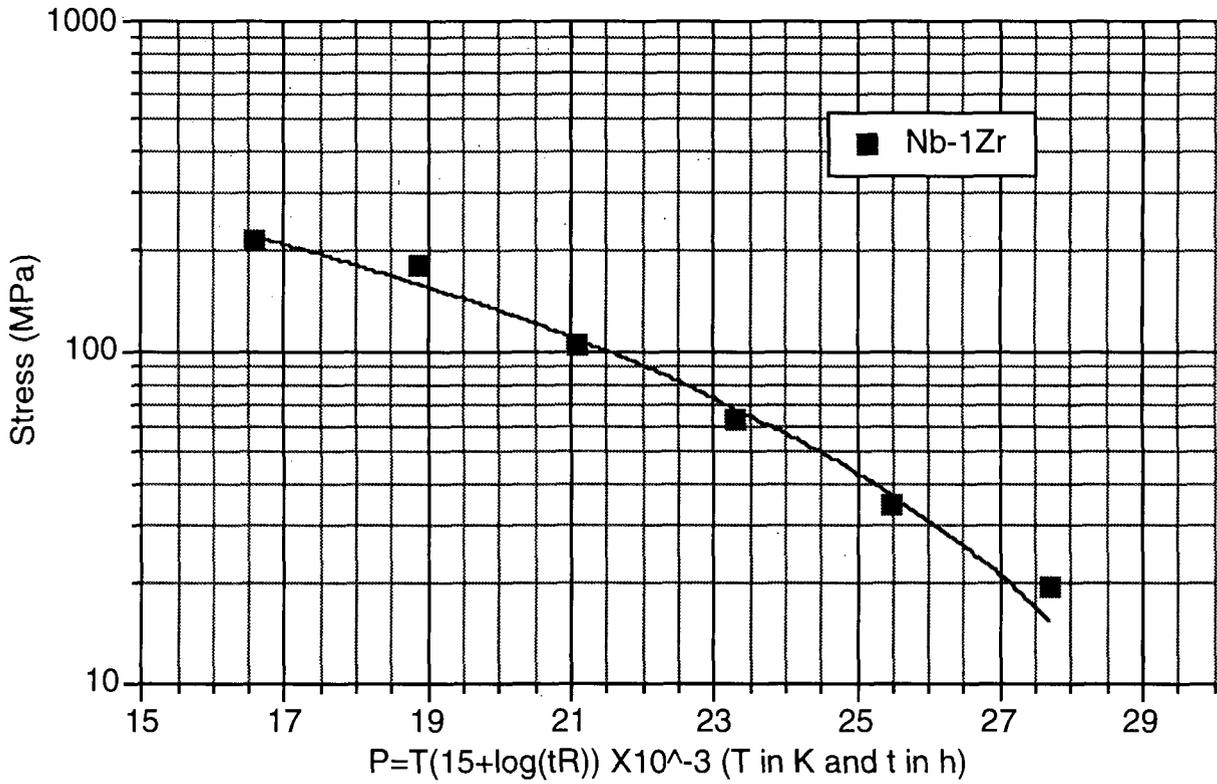
FIG. 16. Larson-Miller curve for Nb-1Zr [19].
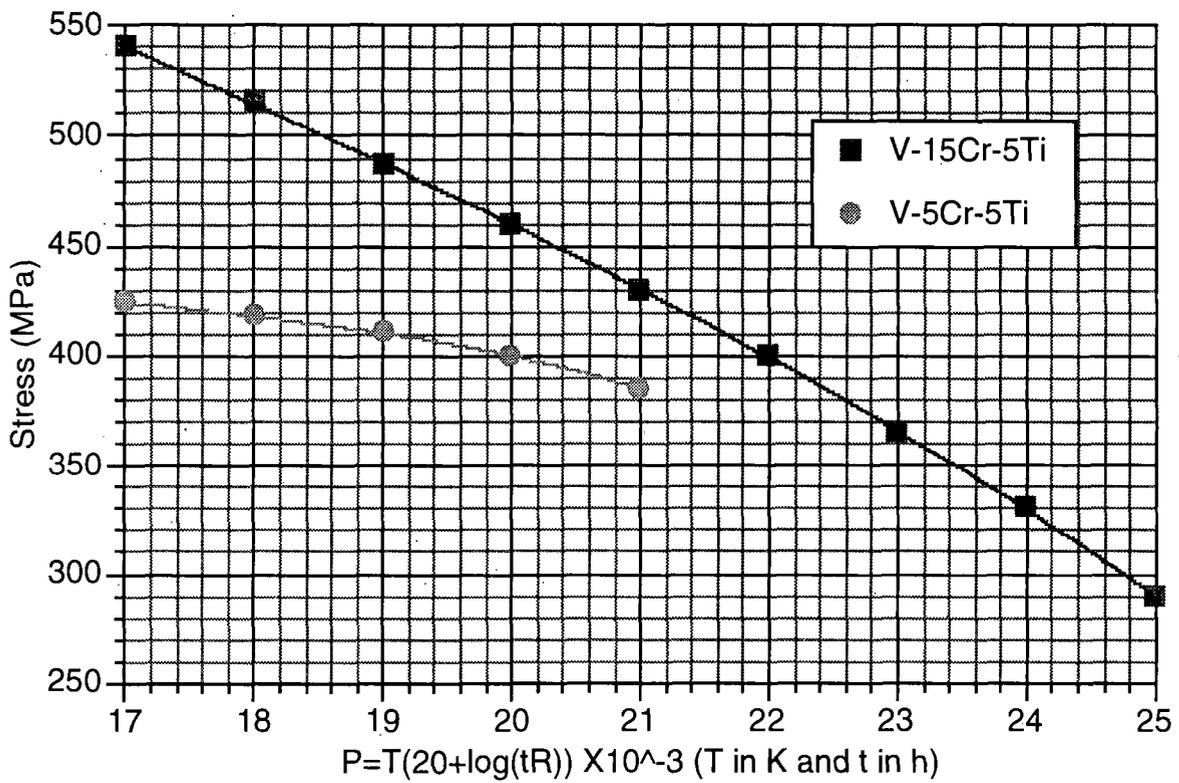
FIG. 17. Larson-Miller curves for V-15Cr-5Ti and V-5Cr-5Ti [20].

159

4. IRRADIATED MECHANICAL PROPERTIES

There is limited information available on irradiation effects on mechanical properties making it difficult to draw definite conclusion concerning irradiation behavior. In general, these materials will increase in strength and lose ductibility during irradiation, but there is considerable scatter in the data. The most complete information available is for the vanadium alloys. The changes in tensile properties tend to saturate by about 20-30 dpa. The saturation values of tensile properties for V-5Cr-5Ti are shown in Figs. 18 and 19 [21]. It should be noted that the uniform elongation saturates at a value of over 8% which means that this alloy will have considerable work hardening capability even after high levels of irradiation.
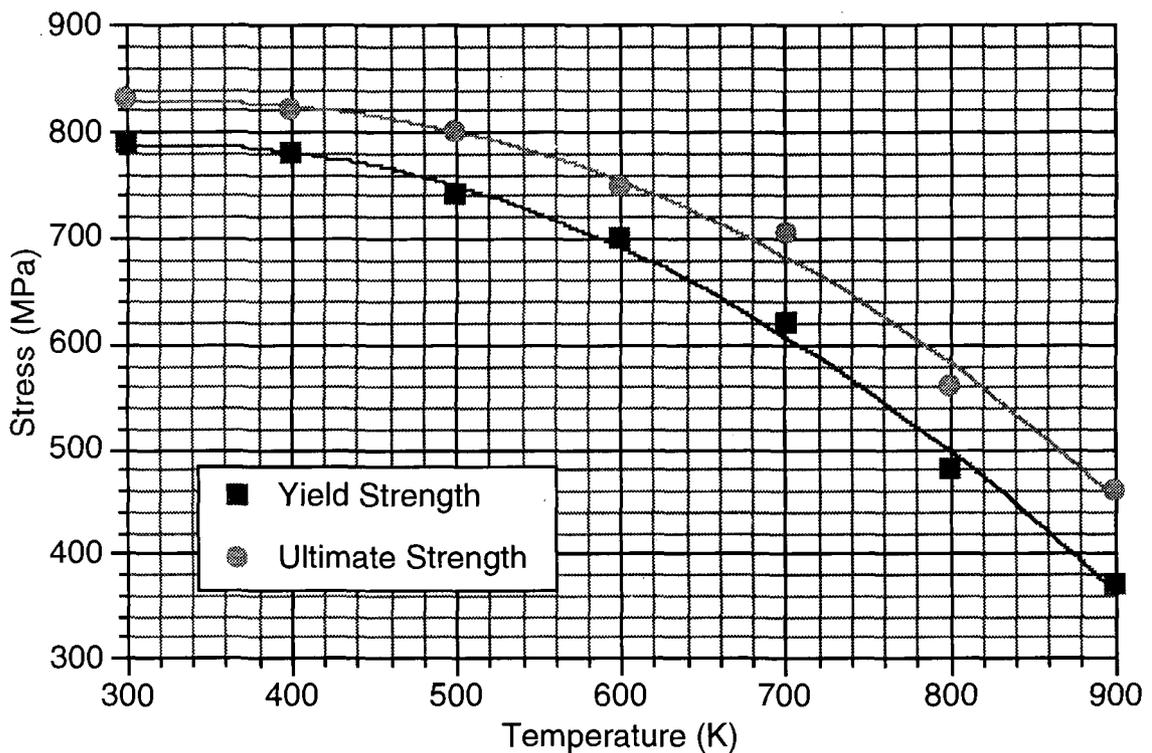

FIG. 18. Saturation strength of V-5Cr-5Ti (~30 dpa) [21].

160
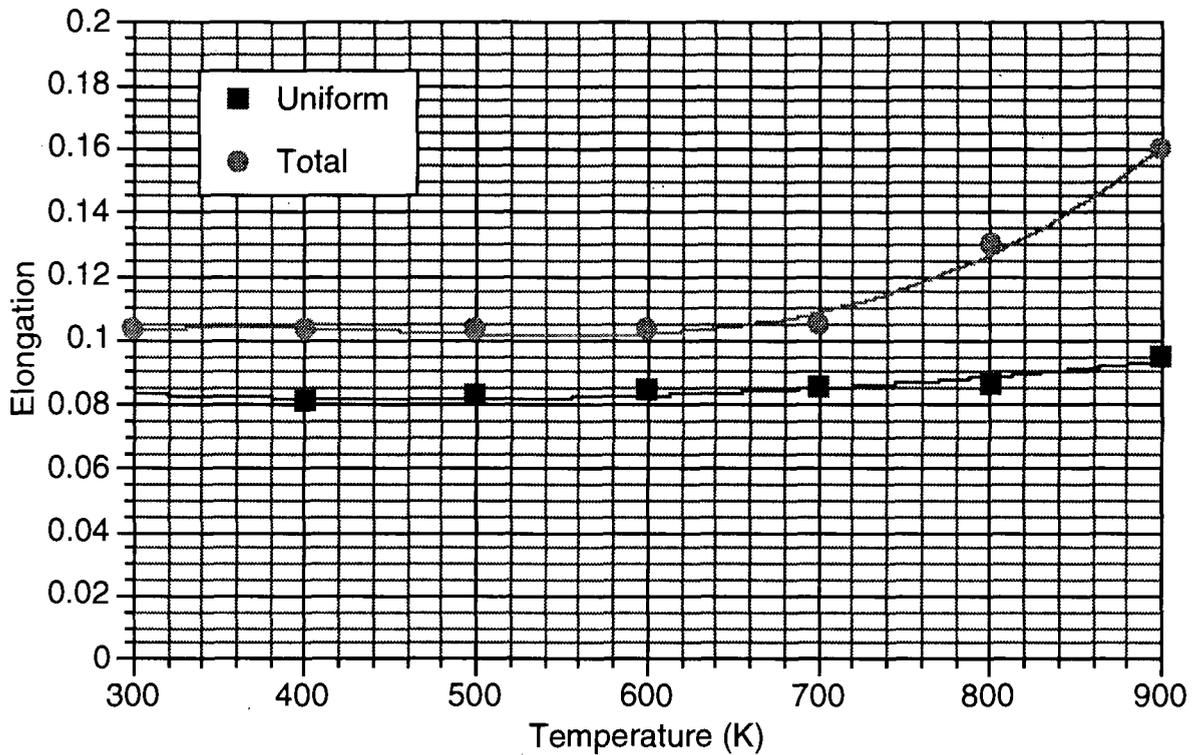
FIG. 19. Saturation ductility of V-5Cr-5Ti (~ 30 dpa) [21].

REFERENCES

(1) HULTGREN, R., ET. AL., Selected Values of the Thermodynamic Properties of the Elements, American Society For Metals, Metals Park, Ohio (1973).

(2) METALS HANDBOOK, Ninth Edition, Vol. 2, Properties and Selection: Nonferous Alloys and Pure Metals, American Society For Metals, Metals Park, Ohio (1979).

(3) AMERICAN INSTITUTE OF PHYSICS HANDBOOK, Third Edition, McGraw-Hill Book Company, New York, (1972).

(4) SMITH, D.L., ET. AL., ITER Blanket, Shield, and Material Data Base, International Atomic Energy Agency, Vienna (1991).

(5) TECHNICAL ASSESSMANT OF VANADIUM BASE ALLOYS FOR FUSION REACTOR APPLICATIONS, FINAL REPORT, Vol. 2, Review of Properties: Vanadium and Vanadium Base Alloys, Westinghouse Electric Corporation (1976) COO-4540-1 (Vol. 2).

(6)   SMITH, D.L., J. Nucl. Mater. (1984) 122 & 123, 51-65.

(7)   TIETZ T.E., WILSON, J.W., Behavior and Properties of Refractory Metals, Stanford University Press, Stanford, CA (1965).

(8)   PORTER, W.D., DINWIDDLE, R.B., GROSSBECK, M.L., "Thermophysical Properties of V-5Cr-5Ti," Fusion Materials Semiannual Progress Report for Period Ending March 31, 1994, DOE/ER-0313116 (1994) P260.

(9)   TOULOUKIAN, Y. S., ed., Thermophysical Properties of High Temperature Solid Materials, The Mae Millan Company, New York (1967).

(10)   FARRARO, R. J., MCLELLEN, R. B., Met. Trans., 10A, P260 (1979) 1701.

(11)   BILLONE, M., Argonne National Laboratory personal communication (1993).

(12)   LOOMIS, B. A., NOWICKI, L. G., SMITH, D. L., "Dependence of YS and UTS on Temperature and Ti Concentration for Vanadium Alloys," Fusion Materials Semiannual Progress Report for Period Ending March 31, 1991, DOE/ER-0313110 (1991) pp145-156.

(13)   LIU, K.C., J. Nucl. Mater. 103 & 104, (1981) 913.

(14)   GROSSBECK, M.L., ET. AL., "Physical Properties and Processing of Vanadium Alloys" presented at IEA Workshop on Vanadium Alloys for Fusion Applications, Salem, OR, (1994).

(15)   FURUYA, K., NAGOTA, Y., WANTANABE, R., YOSHIDA, H., "Effect of Low Cycle Fatigue on the Ductile-Brittle Transition of Molybdenum", personal communication.

(16)   NAGOTA, Y., FURUYA, K., WANTANABE, R., J. Nucl. Mater., 85 & 86 (1979) 839.

(17)   VAN WITZENBURG, W., DEBRUYNE, H.J., Radiation Effects in Materials, ASTM STP 1175, pp1201-1214.

(18)   STOLOFF, N.S., J. Nucl. Mater., 85 & 86 (1979) 855-859.

(19)   CONWAY, J.B., FLAGELLA, P.Y., Creep Rupture Data for the Refractory Metals to High Temperatures, Gordon and Breach Science Publishers, New York (1971).

(20)   CHUNG, H.M., LOOMIS, B.A., SMITH, D.L., J. Nucl. Mater., 212-215, (1994) 790-793.

(21)   LOOMIS, B.A., NOWICKI, L.J., SMITH, D.L., J. Nucl. Mater. 212-215 (1994) 790-793.

COPPER ALLOYS FOR HIGH HEAT FLUX STRUCTURE APPLICATIONS

S.J. ZINKLE
Metals and Ceramics Division
Oak Ridge National Laboratory
P.O. Box 2008
Oak Ridge, TN 37831-6376, USA

S.A. FABRITSIEV
D.V. Efremov Scientific Research Institute of Electrophysical Apparatus
189631 St. Petersburg, Russian Federation

ABSTRACT: The mechanical and physical properties of copper alloys are reviewed and compared with the requirements for high heat flux structural applications in fusion reactors. High heat flux structural materials must possess a combination of high thermal conductivity and high mechanical strength. The three most promising copper alloys at the present time are oxide dispersion-strengthened copper ($Cu-Al_2O_3$) and two precipitation-hardened copper alloys (CuCrZr and CuNiBe). These three alloys are capable of room temperature yield strengths > 400 MPa and thermal conductivities up to 350 W/m-K. All of these alloys require extensive cold working to achieve their optimum strength. Precipitation-hardened copper alloys such as CuCrZr are susceptible to softening due to precipitate overaging and recrystallization during brazing, whereas the dislocation structure in $Cu-Al_2O_3$ remains stabilized during typical high temperature brazing cycles. All three alloys exhibit good resistance to irradiation-induced softening and void swelling at temperatures below 300°C. The precipitation-strengthened alloys typically soften during neutron irradiation at temperatures above about 280°C and therefore should only be considered for structural applications operating at temperatures <280°C. Dispersion-strengthened copper may be used up to temperatures in excess of 500°C. Based on the available data, dispersion-strengthened copper ($Cu-Al_2O_3$) is considered to be the best candidate for high heat flux structural applications.

1. INTRODUCTION

High-strength copper-based alloys with high thermal conductivity are considered to be a promising class of materials for fusion reactor components which must withstand high levels of heat flux. Recent engineering design studies for the International Thermonuclear Experimental Reactor (ITER) have proposed copper alloys for the divertor structure and first wall regions. Relatively thick walls can be accommodated in the heat sink structure of the divertor or first wall if high-conductivity copper alloys are used instead of low-conductivity materials such as stainless steel; the temperature drop across a 10 mm plate of a high-conductivity copper alloy exposed to a heat flux of 1 MW/m^2 would be ~30°C. Copper alloys are well known for their high electrical and thermal conductivity, excellent resistance to corrosion, ease of fabrication, and good strength and fatigue resistance [1]. The manufacturing infrastructure for copper alloys is well established. The worldwide annual production (and consumption) of copper exceeds 10^{10} kg, with pure copper accounting for more than 50% of the applications. The annual production of specialized high strength, high conductivity alloys such as CuCrZr and $Cu-Al_2O_3$ is greater than 10^6 kg.

Reviews on the unirradiated and irradiated properties of copper alloys are available from several different sources [1-6]. The general criteria for selection of a high heat flux structural material are summarized in a companion paper in this volume [7]. In the present paper, we will first summarize the physical and mechanical properties of copper alloys. Most of the remaining review concentrates on several high-strength, high-conductivity copper alloys which have the best mechanical and physical properties for fusion reactor high heat flux applications. Critical issues such as fabricability, joining, corrosion resistance and radiation effects are discussed. Property data quoted by the manufacturers of high-strength, high-conductivity copper alloys have generally been excluded from

the present compilation, unless there was insufficient data from independent researchers to establish trend lines.

2. FABRICATION AND PROPERTIES OF COPPER ALLOYS

Table I summarizes the physical properties of pure copper [1,8,9]. The high thermal conductivity of copper ($k_{th}{\sim}380$ W/m-K) is maintained over a wide range of temperatures, making this material very useful for high heat flux applications. Since the free electrons in copper are mainly responsible for conduction of both thermal and electrical currents, the thermal conductivity and electrical resistivity (ρ_e) are conveniently related by the Wiedemann-Franz law, $k_{th}\,\rho_e = L\,T$, where T is the absolute temperature and L is the Lorentz number, which has a theoretical value of 2.45×10^{-8} W-Ω/K^2. Experimental measurements of the Lorentz number for copper indicate that it is slightly less than the theoretical value, ranging from 2.23×10^{-8} at 0°C to 2.38×10^{-8} at 500°C [8]. Electrical resistivity measurements can often be performed on specimens designed for another purpose (e.g., on neutron irradiated tensile specimens), and the Wiedemann-Franz relationship allows the thermal conductivity of copper and copper alloys to be estimated from the resistivity data without making a direct measurement of k_{th}.

Whereas pure copper exhibits very high thermal conductivity, the intrinsic strength of copper is relatively low. Solid solution additions are generally not effective in increasing the strength of copper by a significant amount, and cause a concomitant decrease in thermal conductivity. Two general categories of high-strength, high-conductivity copper alloys are commercially available, namely precipitation-strengthened and dispersion-strengthened alloys. Since all of the copper alloys under consideration for high strength, high conductivity applications contain <3% solute additions, their thermophysical properties are the same as those listed for pure copper in Table I to within a few percent (except for k_{th} and ρ_e). Table II summarizes the chemical composition of several commercially available high-strength, high-conductivity copper alloys.

TABLE I. Thermophysical properties of pure copper [1,8,9].

Melting temperature	1083°C	
Boiling temperature	2567°C	
Heat of fusion	2.05×10^5 J/kg	
Heat of vaporization	4.80×10^6 J/kg	
Vapor pressure	1.0×10^{-4} Pa @ 850°C	0.015 Pa @ 1050°C
	0.15 Pa @ 1150°C	
density	8950 kg/m^3 @ 20°C	
coefficient of thermal expansion (α)	17.0×10^{-6} @ 20°C	20.0×10^{-6} @ 500°C
Poisson's ratio (υ)	0.345 @ 20°C	0.351 @ 500°C
Young's modulus of elasticity (E)	117 GPa @ 20°C	108 GPa @ 500°C
specific heat (C_p)	385 J/kg-K @ 20°C	431 J/kg-K @ 500°C
thermal conductivity (k_{th})	391 W/m-K @ 20°C	370 W/m-K @ 500°C
electrical resistivity (ρ_e)	17.1 nΩ-m @ 20°C	49.7 nΩ-m @ 500°C

TABLE II. Chemical composition of commercial high-strength, high-conductivity copper alloys.

Alloy tradename & manufacturer	Alloy type*	Composition (wt%)
Cu-Cr-Zr	PH	
MZC (AMAX Copper, Inc.)		Cu - 0.8%Cr - 0.15%Zr - 0.04%Mg
ELBRODUR G (Kabelmetal)		Cu - 0.65%Cr - 0.10%Zr
Cu-Ni-Be	PH	
C17510 (Brush Wellman, Inc.)		Cu - 1.4 to 2.2%Ni - 0.2 to 0.6%Be
Oxide dispersion-strengthened Cu	DS	
GlidCop AL-15 (SCM Metals)		Cu - 0.15% Al as oxide particles (0.28%Al$_2$O$_3$)
GlidCop AL-25 (SCM Metals)		Cu - 0.25% Al as oxide particles (0.46%Al$_2$O$_3$)
GlidCop AL-60 (SCM Metals)		Cu - 0.60% Al as oxide particles (1.12%Al$_2$O$_3$)
MAGT 0.05 (Ultram-Golden)		Cu - 0.1%Al - 0.01%Hf - 0.03%Ti as oxide particles
MAGT 0.2 (Ultram-Golden)		Cu - 0.1 to 0.4%Al - 0.01 to 0.1%Hf -0.03 to 0.14%Ti as oxide particles

*precipitation-hardened (PH) or dispersion-strengthened (DS)

2.1 Room temperature strength and thermal conductivity

The thermal stress parameter (M) is a useful figure of merit for evaluating the suitability of candidate high heat flux structural materials:

$$M=\sigma_y k_{th}(1-\upsilon)/\alpha E \qquad (1)$$

where σ_y is the yield strength, k_{th} is the thermal conductivity, υ is Poisson's ratio, α is the linear coefficient of thermal expansion, and E is Young's modulus. The values of σ_y and k_{th} are strongly dependent on the particular alloy and thermomechanical processing. Figure 1 shows the range of room temperature strengths and conductivities that can be achieved in various copper alloys and Type 316 stainless steel [1,2,4,5,6,10-21]. The range of possible strengths for a given alloy is due to different thermomechanical treatments: cold-worked (CW), cold-worked & aged (CWA), and solutionized & aged (SA) conditions. The high strength CuNiBe datum labeled TMT was obtained on thin sheet specimens of a high purity laboratory heat [12-14] and may not be achievable in large commercial heats. The wrought Cu-Al$_2$O$_3$ datum refers to hot extruded (M30 temper) GlidCop AL-25 plate of 13 cm thickness [1,15].

Cold working can greatly increase the room temperature strength of copper without any significant change in the thermal conductivity. However, pure cold-worked copper softens due to recovery and recrystallization at temperatures above 100 to 200°C [22,23] and is therefore not suitable for applications above room temperature. The strength of copper alloys can be significantly increased by suitable combinations of heat treatment and cold working. Since the average amount of deformation that can be achieved in a thick plate or rod is less compared to a thin strip or wire, the strength of these alloys also depends on the product form [1]. For example, the as-consolidated yield strength of GlidCop AL-25 Cu-Al$_2$O$_3$ alloy varies from 345 MPa for 1 cm plate to 296 MPa for 13 cm plate thickness [15]. Similarly, the room temperature yield strength of solution quenched and aged (TF00 temper) Cu-Cr alloys can vary between 250 and 450 MPa depending on the product form and heat treatment conditions [1].

Figure 2 compares the room temperature thermal stress parameters of high-strength, high-conductivity copper alloys and stainless steel. Conventional precipitation-strengthened alloys such as Cu-2%Be have high strength but very low thermal conductivity compared to copper, resulting in a relatively low thermal stress parameter M. The highest combined strength and conductivity is
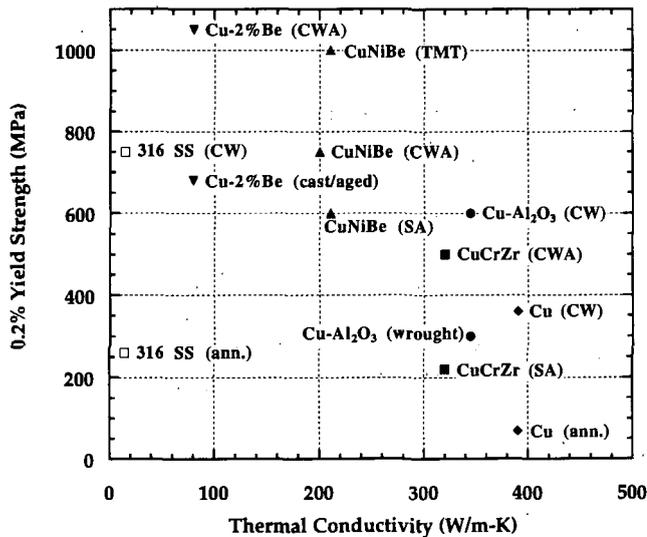
FIG. 1. Room temperature strength and thermal conductivity of copper [1], Cu-Cr-Zr [1,5,10,18-20], CuNiBe [1,12-14], Cu-Be [1,17], Cu-Al$_2$O$_3$ [1,11,15-18], and stainless steel [21].
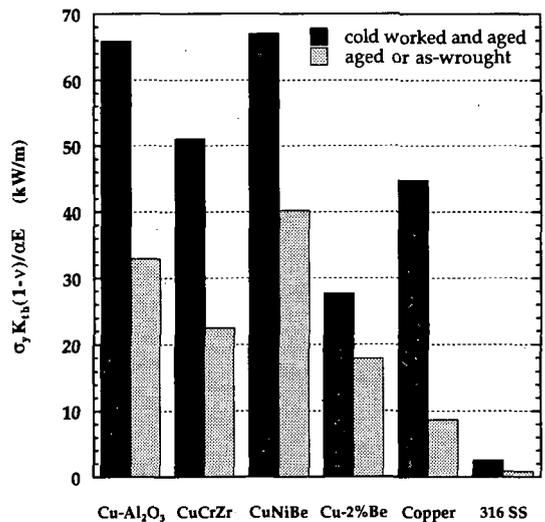
FIG. 2. Comparison of the room temperature thermal stress parameter for copper alloys and stainless steel. The copper alloy data were taken from Table I and Fig. 1.

achieved in cold-worked copper alloys that contain a uniformly distributed second phase of small particles. This is achieved in both precipitation-strengthened (e.g., CuCrZr and Cu-Be-Ni) and dispersion-strengthened (e.g., Cu-Al$_2$O$_3$) alloys. It can be seen from Fig. 2 that the room temperature thermal stress parameter of these copper alloys is more than an order of magnitude higher than the corresponding value for stainless steel.

It is worthwhile at this point to consider in more detail the influence of thermomechanical processing on the strength and conductivity of copper alloys. Several studies have shown that the yield strength in CuCrZr alloys which have been heat treated for maximum precipitation hardening (without cold working) is about 50 to 70% of the peak cold-worked and aged strength [10,24,25]. For example, the maximum yield strength in solution quenched and aged CuCrZr is about 350 MPa [20,25], whereas cold-worked and aged CuCrZr can have room temperature yield strengths up to at least 600 MPa [26]. Figure 3 compares the room temperature tensile curves of AMAX-MZC CuCrZr foil in the solutionized & aged condition (SA) and in the solutionized, cold worked & aged condition (CWA) [10]. The CWA treatment consisted of solution annealing at 950°C for 0.75 h, water quench, 90% cold roll, and aging at 400°C for 0.5 h. The SA alloy was annealed at 930°C for 0.75 h, water quenched, and aged at 500°C for 1 h. It can be seen that precipitation hardening in the absence of cold work produced yield strengths that were only about half of the cold-worked and aged strength. The room temperature thermal conductivities deduced from electrical resistivity measurements were 210 and 230 W/m-K, respectively for the SA and CWA conditions [10].

Thermomechanical processing can produce a wide range of strengths and conductivities in precipitation-hardened copper alloys [1,2,10,13,14,24,25]. Cold working can produce large increases in the alloy strength with only minor degradation in the thermal conductivity. Heat treatments which increase the alloy strength generally cause a concomitant decrease in the thermal conductivity. Figure 4 shows an example of the variation in room temperature yield strength and thermal conductivity that is achievable in Cu-2%Ni-0.4%Be subjected to different schedules of heat treatment and cold work [13,14]. The standard cold-work and aging (CWA) treatment produced lower strengths than thermomechanical treatment (TMT) consisting of preaging, cold work, and reaging. The thermal conductivity in Fig. 4 was estimated from electrical resistivity measurements using the Wiedemann-Franz law. Heat treatments which increased the thermal conductivity produced corresponding decreases in the alloy strength. Similar tradeoffs between yield strength and thermal

166
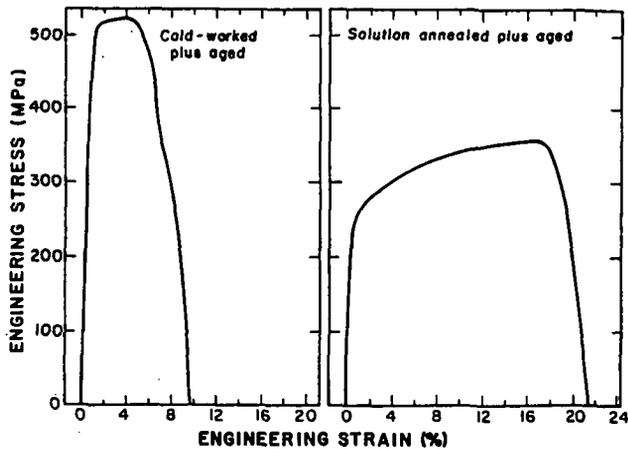
FIG. 3. Room temperature load-elongation curves for AMAX MZC Cu-Cr-Zr-Mg alloy [10].
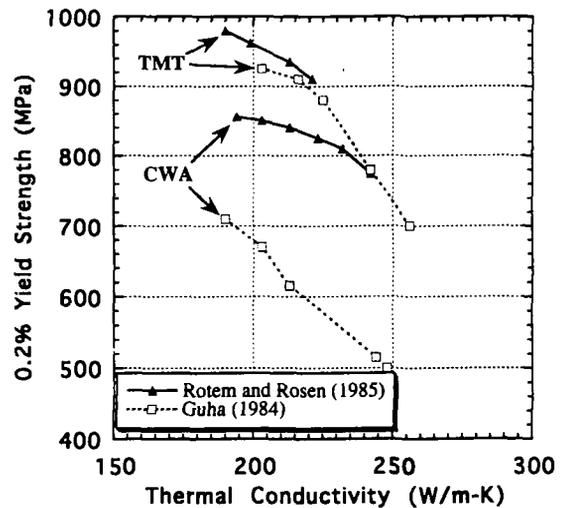
FIG. 4. Room temperature yield strength and thermal conductivity of Cu-2%Ni-0.4%Be thin sheet specimens subjected to different combinations of cold working and heat treatment [13,14].

conductivity occur for all precipitation-hardened copper alloys. The maximum in the thermal stress parameter (which is proportional to the product of the yield strength and thermal conductivity) in precipitation-hardened alloys can occur for either high-conductivity or high-strength heat treatments, depending on the alloy system.

Since the copper matrix is intrinsically weak compared to more traditional structural materials such as iron- and nickel-based alloys, high-strength, high-conductivity copper alloys are generally produced in wrought form. The high dislocation density associated with wrought alloys can be pinned by precipitates or oxide particles, thereby producing high strengths. Precipitation-hardened alloys can in principle be cast and subsequently heat treated, which is advantageous for structural components with complex geometries that would be difficult to machine [20]. However, it must be recognized that the strength of the cast and aged alloy will be significantly less than the same alloy in wrought form (e.g. Fig. 3). Dispersion-strengthened alloys cannot be cast, since the oxide particles would not remain uniformly dispersed in the liquid phase. The wrought alloys can be produced in a variety of forms. For example, sheets of dispersion-strengthened copper ($Cu-Al_2O_3$) are routinely available in cross-section sizes up to 6.3 x 50 cm [15], and moderately complex geometries can be produced by using suitable dies. It is worth emphasizing that many of the high strengths reported for precipitation-hardened and dispersion-strengthened copper alloys were obtained on thin strips which had been heavily cold-worked. These very high strengths (>500 MPa) generally cannot be achieved in large structural components fabricated from copper alloys, because large components cannot be heavily cold-rolled.

2.2 Effects of annealing and test temperature on the tensile properties

The remainder of this review concentrates on the three copper alloys that have the best room temperature thermal stress resistance (Fig. 2), namely the precipitation-hardened alloys CuCrZr and CuNiBe and oxide dispersion-strengthened copper (primarily $Cu-Al_2O_3$). The optimum mechanical properties for the CuCrZr and CuNiBe alloys are produced by aging at temperatures of 320 to 500°C for 0.5 to 2 h [10,12,14,24,27]. Therefore, it can be anticipated that these alloys will be susceptible to softening after extended exposure to temperatures above 400°C due to precipitate coarsening (overaging) and recrystallization. On the other hand, the oxide particles in dispersion-strengthened

167
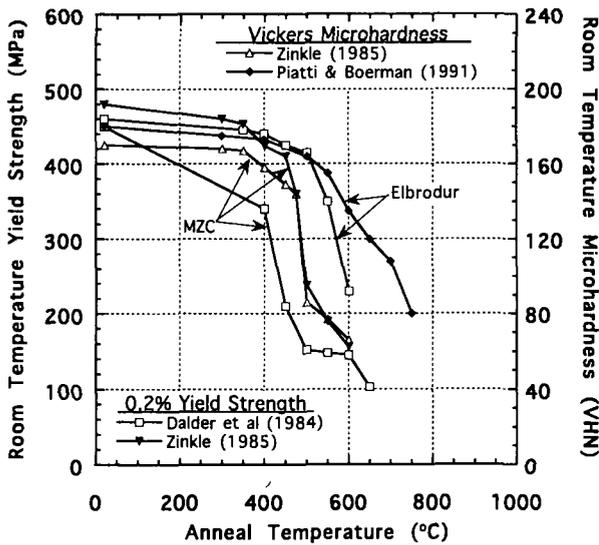
FIG. 5. Effect of annealing on the room temperature yield strength of MZC [10,29,30] and Elbrodur [19,30] CuCrZr alloys. The annealing times varied between 0.5 and 10 h.
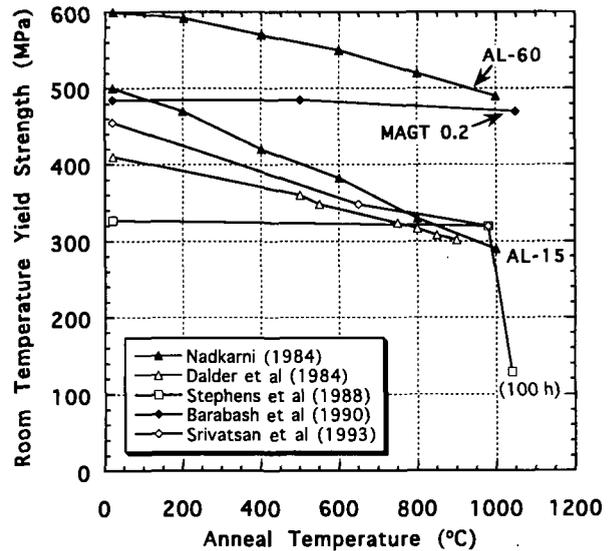
FIG. 6. Effect of annealing on the room temperature yield strength of GlidCop AL-15 and AL-60 [11,30-32] and MAGT [33] oxide dispersion-strengthened copper alloys. With the exception of the data point labeled 100h, the annealing times varied between 0.25 and 10 h.

copper are thermally stable up to the melting point of the copper matrix and therefore this type of copper alloy is inherently resistant to softening [28].

Figure 5 shows the room temperature yield strength of CuCrZr alloys following short term (0.5 to 1 hour) annealing at temperatures between 300 and 750°C [10,19,29,30]. Significant softening begins to occur after exposure to temperatures above 400 to 500°C. Similar results have been reported for CuCrZr alloys by other researchers using Brinell hardness measurements [25], and this alloy has been shown to soften dramatically when aged for 1 h at temperatures above 500°C [e.g., 24,27]. Vandermeulen et al. [26] reported that annealing at 700°C for 15 minutes reduced the room temperature yield strength of CuCrZr from 595 MPa to 210 MPa. According to the data presented in Fig. 5, Elbrodur CuCrZr appears to have somewhat better resistance to softening than MZC CuCrZr. There is not sufficient annealing data on CuNiBe to determine its softening temperature. However, due to the similarity between CuCrZr and CuNiBe regarding precipitation hardening treatment temperatures, CuNiBe may be expected to behave similar to the softening trend shown in Fig. 5. The observed softening temperature for CuCrZr of 400 to 500°C is significantly higher than that of cold-worked copper: the corresponding softening temperature for high purity copper is only about 100°C [22,23], although small amounts of impurities can increase the softening temperature to 200°C or higher [1,22]. Unfortunately, the softening temperature of CuCrZr is too low to prevent significant loss of strength during joining by conventional furnace brazing or welding techniques. Conventional furnace brazing of copper alloys is performed at temperatures between 600 and 1000°C with typical hold times between 5 and 15 minutes. Some of the strength loss induced by the exposure to high temperatures can be recovered by subsequent heat treatment. The maximum room temperature yield strength that can be expected in a conventional furnace brazed or welded CuCrZr joint following heat treatment is the solutionized and aged value of 300 to 350 MPa [10,20,25].

The ultimate tensile strength (UTS) of CuCrZr alloys follows a similar softening behavior as the yield strength following exposure to temperatures above 400 to 500°C [10,26,30]. The room temperature UTS of the as-fabricated alloy is typically 5 to 20% higher than the yield strength, with the lowest ratios of ultimate to yield strength occurring in heavily cold-worked (high strength) alloys. Following annealing at temperatures above 500 to 600°C, the room temperature UTS is generally

~50% higher than the room temperature yield strength. Typical room temperature ultimate strengths of the annealed CuCrZr alloys are 300 to 350 MPa [10,26,30]. The total elongation to failure (e_{tot}) of the CuCrZr alloys increases after high-temperature annealing. Typical as-fabricated values of e_{tot} are 5 to 15%, with the lowest elongation occurring in the highest strength alloys [10,19,20,26, 30]. The room temperature elongation to failure in annealed CuCrZr alloys is generally >25% [10,26,30]. The measured reduction in area was >50% for cold-worked & aged MZC CuCrZr [25], which is indicative of a very ductile material.

Figure 6 shows the room temperature yield strength of commercial oxide dispersion-strengthened copper alloys following short-term annealing at elevated temperatures [11,30-33]. It can be seen that these Cu-Al_2O_3 alloys are resistant to softening up to temperatures close to the melting point of copper. Grant and coworkers [28] have found that the room temperature hardness of oxide dispersion-strengthened copper alloys remained within 5% of its original value following 1 h anneals at temperatures as high as 1000°C. Since these alloys do not recrystallize during exposure to temperatures as high as 1000°C, the room temperature ratio of the ultimate to yield strength remains nearly constant [11,30-33]. The room temperature UTS is typically 10 to 20% higher than the yield strength, depending on the amount of cold work induced during fabrication. The measured elongation to failure at room temperature in the dispersion-strengthened alloys generally ranges between 10 and 20% for the as-fabricated alloys and between 15 and 25% for the annealed alloys [11,30-33]. The reduction in area at room temperature is >50% in both the as-fabricated and annealed alloys [11,31].

Figure 7 shows the yield strength of CuCrZr alloys measured at elevated temperatures [19,20, 26,34-36]. The room temperature yield strength varied between 350 and 600 MPa, due to different thermomechanical fabrication procedures for the alloys. The lowest room temperature strength occurred in a cast and aged alloy [20], and the highest strength was produced in an alloy that was cold rolled after aging to achieve a 63% reduction in foil thickness [26]. The yield strength of all alloys decreased steadily with increasing test temperature, reaching a value of about 250 MPa at 500°C. Additional elevated temperature results, which are in good agreement with the average of the data shown in Fig. 7, have been obtained on MZC and Elbrodur CuCrZr alloys over the limited temperature range of 20 to 200°C [37]. Hot microhardness measurements obtained on CuCrZr alloys also exhibit a similar temperature dependence [27]. The typical strength of cast-and-aged Elbrodur plate is apparently lower than cast-and-aged tube or block moulds, with reported yield strengths of 300 and 165 MPa at test temperatures of 20 and 500°C, respectively, for plate material [20]. It is worth noting that high amounts of cold work are effective at increasing the room temperature strength of CuCrZr alloys. However, these cold-worked alloys suffer the largest decrease in strength with increasing test temperature, which may be attributed to the accelerated rate of recrystallization (and accompanying softening) that occurs with increasing amounts of initial cold work [22].

The ultimate tensile strength of CuCrZr alloys shows a similar dependence on test temperature as that shown for the yield strength in Fig. 7 [19,20,26]. The ratio of ultimate to yield strength depends on the thermomechanical treatment given to the alloy. For cold-worked alloys, the UTS is about 5% higher than the yield strength at room temperature and about 10% higher than the yield strength at 500°C [19,26]. For cast and aged alloys, the UTS is about 25 to 35% higher than the yield strength at room temperature and about 15 to 20% higher at 500°C [20]. Various studies on cold-worked CuCrZr alloys have reported either a decrease [18,19] or slight increase [26] of the total elongation to failure (e_{tot}) with increasing test temperature between 20 and 500°C. Typical values for the uniform and total elongation in the cold-worked alloys for this temperature range are 1 to 5% and 5 to 15%, respectively [18,19,26]. The typical e_{tot} for cast and aged CuCrZr over this temperature range is ~18% [20].

The yield strength of oxide dispersion-strengthened copper alloys measured at elevated temperatures is shown in Fig. 8 [16,31,33,38-40]. Most of the data were obtained on GlidCop AL-15 and AL-20, which have lower strengths compared to the AL-25 and AL-60 alloys [11,15]. The room temperature yield strength varied between 300 and 600 MPa, mainly due to different amounts of cold work present in the alloys. The lowest room temperature strengths were obtained from as-wrought plates [16] and from an alloy consolidated from coarse particles that was cold worked 31% [39]. The highest strengths were obtained on 80%CW AL-20 [38], 86%CW AL-15 consolidated from fine particles [39], and the higher strength MAGT 0.2 alloy [33]. The yield strength of all of the
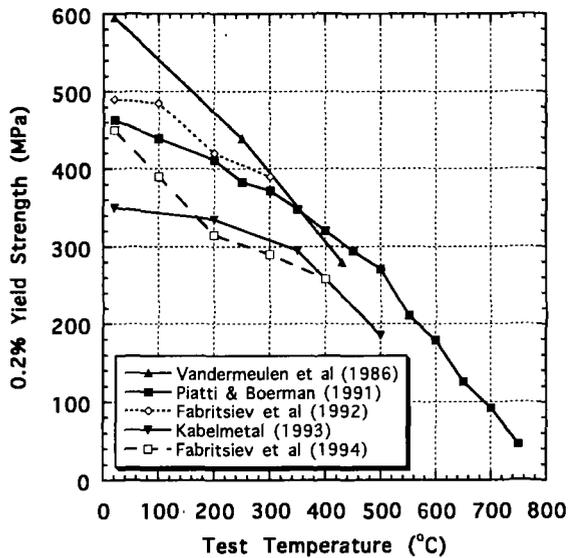
FIG. 7. Yield strength of Elbrodur [19,20,26] and Russian [34-36] CuCrZr alloys measured at elevated temperatures.
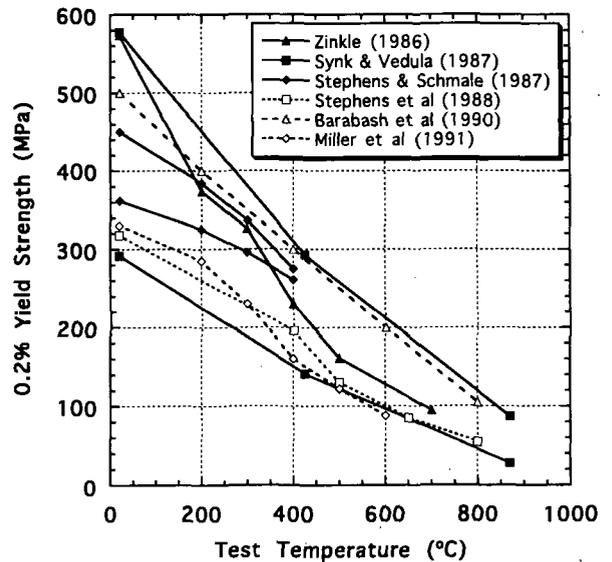

FIG. 8. Yield strength of GlidCop AL-15 [16,31,39,40] and AL-20 [38] and MAGT 0.2 [33] oxide dispersion-strengthened copper alloys measured at elevated temperatures.
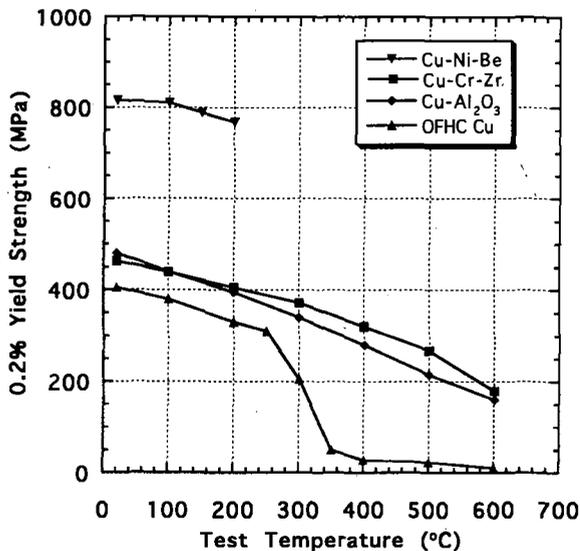

FIG. 9. Comparison of the elevated temperature yield strength of cold-worked copper and copper alloys. The data were obtained from Figs. 7 and 8 and refs. [1,41] for pure copper and refs. [37,42] for CuNiBe.

dispersion-strengthened alloys decreased steadily with increasing test temperature. The average measured yield strength was about 200 MPa at 500°C. Additional tensile results on GlidCop dispersion-strengthened copper that agree with the average of the data shown in Fig. 8 have been reported for the temperature range of 20 to 200°C [37].

The ultimate tensile strength of the dispersion-strengthened alloys has been measured by several researchers at elevated temperature [16,31,33,38-40], with results that are similar to the yield strength behavior shown in Fig. 8. The UTS is about 5 to 15% higher than the yield strength at all test temperatures. Typical values of the uniform and total elongation are 1.5 to 5% and 5 to 15%, respectively, over the temperature range of 20 to 500°C. The total elongation has been observed to either decrease [39], increase [38], or remain roughly constant [16,31] with increasing test temperature. The reduction of area has been observed to decrease from ~70% at room temperature to 10-50% at temperatures between 200 and 800°C for tests performed in air and high-purity argon environments [31,40]. The reduction of area at elevated temperatures in these non-vacuum environments was very sensitive to the strain rate, with the lowest reduction in area occurring at low strain rates [31,40].

Figure 9 summarizes the effect of test temperature on the yield strength of cold-worked copper and the high strength copper alloys CuNiBe, CuCrZr and Cu-Al2O3. The data for pure copper were taken from refs. [1,41], and the data for CuCrZr and Cu-Al2O3 were obtained from an average of the

data shown in Figs. 7 and 8, respectively. There are only limited data on the elevated temperature tensile properties of CuNiBe alloys, with no known data available at test temperatures above 200°C [12,37,42]. The most extensive results were presented by Rosenwasser and coworkers [37,42], and their data on conventional cold-worked and aged CuNiBe are shown in Fig. 9. Some caution should be exercised with these data, since their results are about 100 MPa higher than the yield strength data at 20 and 150°C reported by Mollard et al [12] for a similar high-purity alloy. From the data trends summarized in Fig. 9, it can be surmised that CuNiBe has superior strength compared to the other alloys, at least over the temperature interval of 20 to 200°C. However, it should be kept in mind that the relatively low thermal conductivity of this alloy does not yield a superior resistance to thermal stress. The elevated temperature yield strength of CuCrZr and dispersion-strengthened copper is very similar over the temperature range of 20 to 600°C for these short term (< 1 h) exposures. The elevated temperature UTS, e_{tot}, and uniform elongation of CuCrZr and dispersion-strengthened copper measured during short-term exposures are also comparable.

2.3 Creep and fatigue properties and fracture toughness

The maximum stress that can be safely applied to high-strength copper alloys during extended operation at elevated temperatures is less than the yield strength measured during short term exposures (Figs. 7-9), due to the phenomena of creep and fatigue. Figure 10 compares the mechanical stresses which produce creep failure within 100 hours in copper, CuCrZr and Cu-Al$_2$O$_3$ during exposure at elevated temperatures [1,11,23,39,43]. Both alloys have significantly higher rupture strengths than pure copper. The 100 hour rupture strength of both MZC CuCrZr [23,43] and GlidCop AL-15 Cu-Al$_2$O$_3$ [11] is approximately 300 MPa at 300°C. However, the rupture strength of CuCrZr decreases rapidly with increasing temperature above 300°C. Oxide dispersion-strengthened copper has superior 100 h rupture strengths at temperatures above 400°C. The higher-strength grades of dispersion-strengthened copper such as GlidCop AL-60 have particularly good stress-rupture strengths. For example, the rupture strengths shown in Fig. 10 for GlidCop AL-60 and AL-15 at 400°C are about 360 and 240 MPa, respectively [11,39]. The impressive creep-rupture strengths of oxide dispersion-strengthened copper alloys such as GlidCop at elevated temperatures is due to the uniform dispersion of thermodynamically stable particles of ~7 nm diameter, which is close to the optimum size for high creep strength [44].
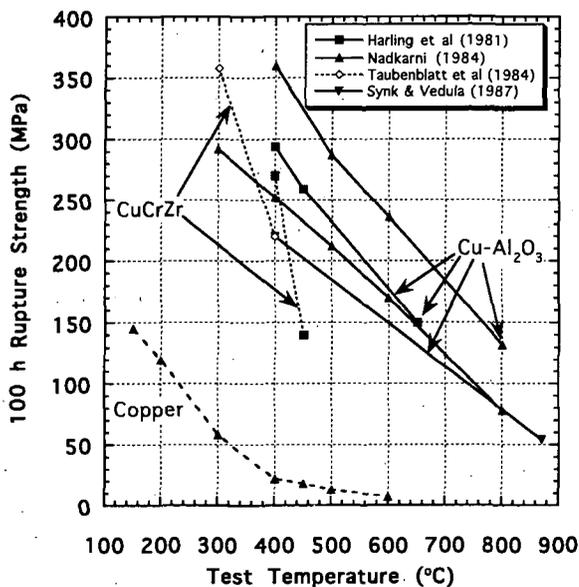

FIG. 10. Elevated temperature stress-rupture strength of copper [1,11], MZC CuCrZr [23,43], Cu-3.5 vol.% Al$_2$O$_3$ [43], and GlidCop AL-15 [11,39] and AL-60 [11].
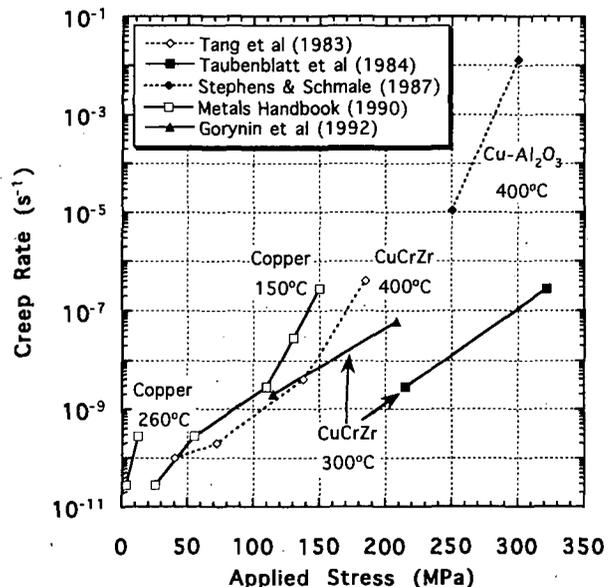

FIG. 11. Thermal creep rate in copper and copper alloys [1,18,23,40,45].

The steady-state thermal creep rate in copper, CuCrZr and Cu-Al$_2$O$_3$ at temperatures between 150 and 400°C is shown in Fig. 11 [1,18,23,40,45]. Pure copper creeps readily at low applied stress levels. For example, the creep rate of copper at 400°C is nearly 10^{-4}/s for an applied stress of 100 MPa, and about 10^{-8}/s for an applied stress of only 15 MPa [46]. CuCrZr and oxide dispersion-strengthened copper alloys can be subjected to much higher stresses at elevated temperature without suffering excessive creep. The available data indicate that creep rates of ~5×10^{-9}/s are produced in CuCrZr [23] and oxide dispersion-strengthened copper [33] with applied stresses of about 200 MPa at 300°C. Unfortunately, there are not enough data to quantitatively compare the creep behavior of the various high-strength copper alloys over the ITER-relevant temperature range of 20 to 400°C. High strength copper alloys generally have a threshold stress below which creep deformation is negligible [44]. Further study is needed to determine the value of the threshold stress for the various copper alloys at temperatures between 20 and 400°C. The creep data reported by Nadkarni [11] suggest that the threshold stress at 650°C is about 130 and 190 MPa for cold-worked GlidCop AL-15 and AL-60, respectively. The data by Tang et al. [45] indicate that the threshold stress is about 100 MPa for MZC CuCrZr tested at 400°C.

A further factor which must be considered for the precipitation-hardened alloys is that their softening behavior at elevated temperatures due to overaging and recrystallization depends on both the exposure time and temperature. For example, extrapolation of short-term (0.25 to 100 h) annealing results on MZC CuCrZr indicates that the softening temperature is about 410°C for a 100 h exposure, but decreases to ~330°C for a 10 year exposure [10,29]. Therefore, although the creep rate or rupture strength of precipitation-hardened copper alloys such as CuCrZr may be acceptable at temperatures above 300°C during short-term tests, the alloy could become unacceptably soft during extended exposure (>>100 h) at these temperatures due to overaging and recrystallization. The softening at elevated temperatures is accelerated by irradiation or the presence of stress [47].

The cyclic fatigue strength of copper alloys generally increases with increasing tensile strength, i.e., metallurgical changes which increase the tensile strength of copper alloys also increase the fatigue strength. Figure 12 shows the room temperature cyclic fatigue strength of cold-worked pure copper, CuCrZr and CuNiBe [1,16,48]. The high-cycle fatigue strength of copper at room temperature is about 100 MPa [1,16,49], which is about 1/3 of the yield strength of the starting material (250 to 300 MPa). The corresponding high-cycle fatigue strength of MZC CuCrZr, with a yield strength of about 550 MPa, was reported to be 170 MPa [50]. There is a lack of fatigue data on CuCrZr and CuNiBe alloys, particularly at high cycles. The room temperature fatigue strengths of Elbrodur CuCrZr and Brush-Wellman CuNiBe alloys at intermediate (10^5) cycles are ~280 and 400 MPa, respectively [48]. The fatigue strengths of normal and overaged CuNiBe were found to be comparable (~400 MPa) at 10^5 cycles, whereas the initial yield strengths were 770 and 570 MPa, respectively [48]. Additional low-cycle ($<3 \times 10^4$) fatigue data on CuNiBe have been reported by Rosenwasser and coworkers [37,42] using a minimum to maximum stress ratio of R=0. Their fatigue strengths were 200 to 250 MPa higher than the data reported by Bushnell and Ellis (Fig. 12) for a stress ratio of R=-1 [48].

The room temperature cyclic fatigue strength of GlidCop Cu-Al$_2$O$_3$ is shown in Fig. 13 [16,32, 48,51,52]. The fatigue data from refs. [48,52] were obtained under stress-controlled conditions, whereas the remaining data were obtained under strain-controlled conditions and converted to equivalent stress. All of the data were obtained on GlidCop AL-15 except for Singhal et al. [51], who examined GlidCop AL-25. The fatigue strengths of AL-15 and AL-25 appear to be comparable at intermediate (10^4 to 10^6) cycles. The high-cycle fatigue strength of Cu-Al$_2$O$_3$ with a yield strength of 330 MPa is about 175 MPa [16]. Nadkarni [11] reported somewhat higher fatigue strengths for GlidCop AL-15 and AL-60 compared to the data shown in Fig. 13 over the range of 3×10^4 to 2×10^7 cycles. His rotating-bending cantilever beam fatigue measurements indicated fatigue strengths at 2×10^7 cycles of about 205 and 230 MPa for AL-15 and AL-60, respectively. As discussed elsewhere [16], this discrepancy may be due to dynamic hysteresis effects associated with the rotating-bending beam measurements, or to the higher frequency (167 Hz vs. 1 to 10 Hz) of these measurements compared to the intermediate-to-high cycle data shown in Fig. 13. Alternatively, the higher fatigue strength may be due to a higher initial yield strength of Nadkarni's material (470 MPa for AL-15).

172
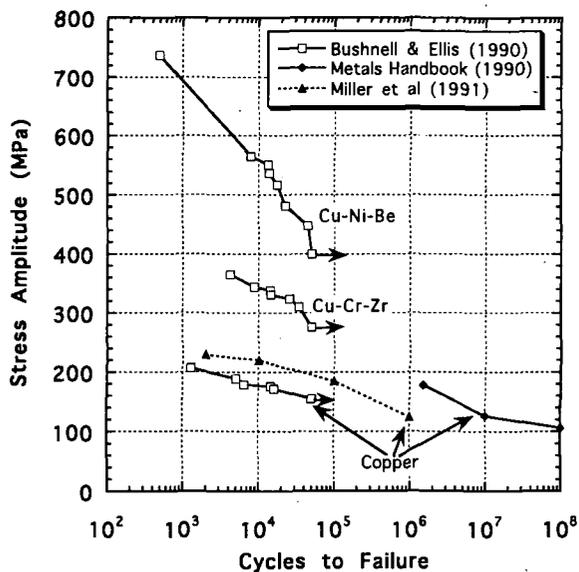
FIG. 12. Room temperature cyclic fatigue strength of copper [1,16,48], Elbrodur CuCrZr [48] and CuNiBe [48]. Fully reversed stress amplitude (R=-1). All data except for refs. [1,16] were stress-controlled. The data points with arrows denote specimens which did not fail during the test lifetime.


FIG. 14. Strain-controlled cyclic fatigue behavior of copper alloys [18,32,37,42,51].

FIG. 13. Room temperature cyclic fatigue strength of Cu-Al$_2$O$_3$ [16,32,48,51,52]. All of the data was obtained under fully reversed (R=-1) stress conditions except for ref. [16], which used a minimum to maximum stress ratio of R=0.

The limited amount of data obtained on CuCrZr (Fig. 12) indicates that the room temperature fatigue behavior of this alloy is comparable to that of Cu-Al$_2$O$_3$ (Fig. 13).

There have only been a few studies of the fatigue behavior of CuCrZr [18,45,53,54], CuNiBe [37,42], and oxide dispersion-strengthened copper [16,18] at elevated temperatures. The high-cycle (>10^6) fatigue strength of GlidCop AL-15 was measured to be about 75 MPa at 600°C [16]. Figure 14 summarizes the fatigue results obtained on high-strength copper alloys under strain-controlled conditions at temperatures between 20 and 300°C [18,32,37,42,51]. Additional low-cycle strain-controlled data have been obtained on MZC CuCrZr at 400°C, with the results reported only in terms of the plastic strain range [45,53]. The low-cycle strain-controlled fatigue behavior of CuCrZr and oxide dispersion-strengthened copper appears to be very similar over the temperature range of 20 to 300°C.

The results by Rosenwasser and coworkers [37,42] suggest that CuNiBe has superior low-cycle fatigue properties compared the other copper alloys. There does not appear to be a strong dependence on temperature between 20 and 300°C when the data are evaluated according to strain amplitude. All of the alloys have comparable or better fatigue properties than pure copper. For example, the fatigue lifetime of pure copper tested in the temperature range of 20 to 300°C decreases from about 10^5 cycles to 10^3 cycles as the total strain amplitude increases from about 0.15% to 0.6% [55,56].

173

We are not aware of any published measurements of the fracture toughness or fatigue crack growth behavior of CuCrZr, CuNiBe, or commercial oxide dispersion-strengthened copper. The room temperature fracture toughness of a medium-strength (σ_y=250 MPa) Cu-Zr alloy that should be comparable to CuCrZr was measured to be an impressive 420 MPa√m, and the tearing modulus was 440 [57]. The fatigue crack growth rate was also found to be much better than pure copper. On the other hand, unpublished measurements on a cold-worked GlidCop AL-15 alloy (σ_y=330 MPa) indicate that the room temperature fracture toughness was only 20 to 50 MPa√m [52,58], which is similar to values for high strength aluminum alloys [59].

3. IRRADIATION EFFECTS

Exposure to radiation generally produces small (<1%) changes in most of the copper alloy physical properties such as the specific heat and coefficient of thermal expansion. On the other hand, large radiation-induced changes can be produced in the density (void swelling), thermal conductivity, and mechanical properties. The radiation stability of high-strength, high-conductivity copper alloys is directly linked to the stability of the precipitates or oxide particles. The interface between the particles and the copper matrix promotes the recombination of vacancies and interstitials, thereby imparting good resistance to void swelling. In addition, the particles are needed to stabilize whatever dislocation structure is present and to maintain high strength levels in the alloy.

Several studies have been performed to investigate the stability of the second phase particles in irradiated CuCrZr [60-65], CuNiBe [61,66] and oxide dispersion-strengthened copper [60,61,63,66-69]. These studies are not in complete agreement regarding the structural stability of copper alloys. For example, either precipitate shrinkage [62,63,65] or coarsening [60] has been reported for the Cr precipitates in CuCrZr, and other studies [61,64] have found that the precipitates are not affected by irradiation. The most detailed studies of particle stability have been performed on irradiated oxide dispersion-strengthened copper [63,68,69]. These studies have found that a gradual reduction in oxide particle size occurs after irradiation to high doses (>10 displacements per atom) due to ballistic dissolution. However, the overall structural stability of the oxide dispersion-strengthened alloys remains very good even after damage levels in excess of 100 dpa [65,69,70]. The published investigations suggest that the oxide particles in dispersion-strengthened copper have somewhat better stability against radiation-induced dissolution than the precipitates in CuCrZr and CuNiBe.

3.1 Swelling

Copper alloys are susceptible to radiation-induced swelling due to microscopic void formation at temperatures between 180 and 550°C [6,71-74]. Figure 15 shows the temperature-dependent void swelling that occurred in copper and a dilute Cu-B alloy following fission neutron irradiation to a damage level of about 1.2 dpa ($\sim$1.2x10^21 n/m^2, E>0.1 MeV) at a damage rate of $\sim$2x10^-7 dpa/s [71,72]. Void swelling in copper is maximized at intermediate temperatures of 275 to 325°C for this damage rate, which is comparable to the damage rate at the first wall of ITER. It can be seen from Fig. 15 that significant levels of volumetric swelling ($\sim$0.5%) occur in pure copper at a damage level as low as $\sim$1 dpa. High dose studies performed on pure copper at temperatures near 400°C indicate that the steady-state swelling rate is about 0.5%/dpa [74], although even higher swelling rates have been reported [75]. Hence, it is obvious that pure copper is not suitable for high fluence (>1 dpa) applications at temperatures between $\sim$200 and 500°C due to unacceptable amounts of void swelling. Similar steady-state swelling rates have also been observed in simple copper alloys such as Cu-5%Ni [76].

The CuCrZr, CuNiBe and oxide dispersion-strengthened copper alloys have superior void swelling resistance compared to pure copper [4-6,17,18,36,61,67,70,74,76-79]. Figure 16 summarizes some of the swelling data obtained on these alloys following neutron irradiation to high damage levels [74,76,79]. Whereas irradiation to a damage level of 50 dpa near 400°C produces radiation-induced density changes near 25% in pure copper and simple copper alloys such as Cu-5%Ni [74,76], the corresponding density changes in CuCrZr and Cu-Al2O3 alloys are generally less
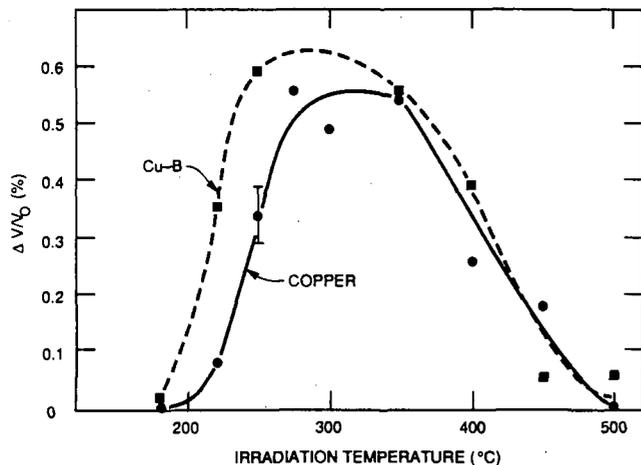
FIG. 15. Temperature-dependent cavity swelling in copper and Cu-100 appm [10]B irradiated with fission neutrons to ~1.2 dpa at ~2x10^-7 dpa/s [71,72]. The irradiation produced ~0.2 and 100 appm He in the pure copper and Cu-B alloy, respectively.
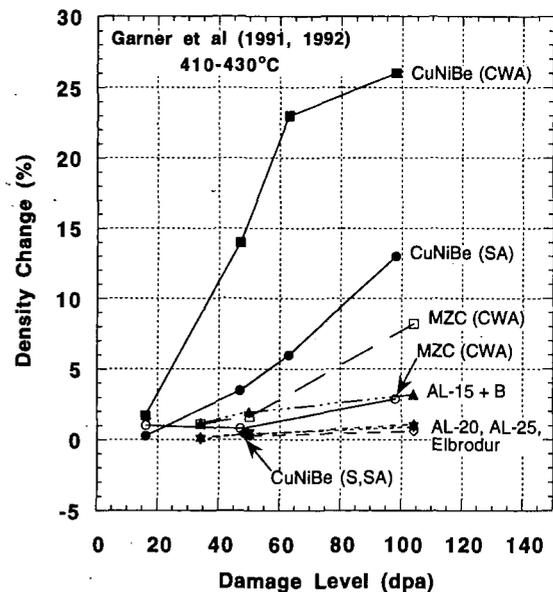

FIG. 16. Swelling behavior of CuCrZr, CuNiBe and Cu-Al$_2$O$_3$ alloys irradiated with neutrons at 400 to 430°C [74,76,79]. The materials were irradiated in solutionized (S), solutionized & quenched (SA) and cold-worked & aged (CWA) conditions.

than 2%. Swelling levels below 2% have been maintained in some CuCrZr and Cu-Al$_2$O$_3$ alloys irradiated with fast fission neutrons up to a damage level of 150 dpa at 410 to 415°C [74,78]. The CuNiBe alloy shows a widely varying swelling behavior, depending on the initial thermomechanical treatment [74,79]. The measured swelling in CuNiBe after irradiation to ~50 dpa at 410 to 430°C varied from about 0.4% for solutionized and solutionized & aged alloys [79] to 3.5 to 14% for solutionized & aged and cold-worked & aged alloys [74]. The CuCrZr alloys exhibit a similar, although less pronounced, dependence on thermomechanical treatment [74]. Swelling levels between 0 and 2% have been observed in CuCrZr alloys after irradiation to 50 dpa at ~410°C, depending on the detailed manufacturing procedure [74]. Ion irradiation studies performed over a wide range of temperatures and damage levels provide further evidence for the good swelling resistance of the precipitation- and dispersion-strengthened alloys [10,47,65,66]. Void formation was not observed in CuCrZr or MAGT 0.2 dispersion-strengthened copper alloys during ion irradiation up to 150 dpa at temperatures between 260 and 600°C [66]. Unfortunately, there are no high dose (>5 dpa) neutron irradiation swelling data on CuCrZr, CuNiBe or oxide dispersion-strengthened copper alloys at ITER-relevant temperatures of 50 to 350°C. Swelling levels between 0.2 and 3% have been reported for CuCrZr alloys after neutron irradiation to moderate damage levels of about 4 dpa at 300 to 350°C [18,36].

The good swelling resistance of precipitation- and dispersion-strengthened copper alloys may be attributed to their high dislocation and particle densities, which promote recombination and annihilation of the point defects created by neutron irradiation [6]. The best swelling resistance occurs in cold-worked alloys which retain their high dislocation density during irradiation. During high-fluence ion [66] or neutron [61,67,80] irradiation, void formation is initiated in regions of the matrix that have recrystallized (leaving a low defect sink density). Unfortunately, the precipitation-strengthened alloys are susceptible to radiation-enhanced recrystallization [47,81], which is due to a combination of radiation-enhanced precipitate overaging and dislocation recovery processes. The dislocation recovery and sweeping-up of precipitates by migrating grain boundaries during recrystallization can produce a relatively sink-free matrix that is susceptible to void swelling. The

susceptibility to radiation-enhanced recrystallization increases with increasing amount of cold work. Since solutionized & aged alloys do not have a cold-worked dislocation structure, they will not suffer the dramatic microstructural changes associated with recrystallization. Therefore, in some cases solutionized & aged alloys may have lower levels of swelling than cold-worked & aged alloys which recrystallize during the irradiation. A large part of the swelling resistance of dispersion-strengthened copper alloys is due to their thermally stable particles, which impart superior resistance to recovery and recrystallization. Since precipitate overaging does not occur in the oxide dispersion-strengthened alloys, they are very resistant to radiation-enhanced recrystallization.

Further work is needed to determine if the precipitation- and dispersion-strengthened copper alloys remain swelling resistant in the presence of fusion-relevant levels of helium transmutation products. The helium generation rate in copper irradiated in fission reactors is ~0.2 appm/dpa, which is more than one order of magnitude smaller than the ITER first wall generation rate of ~7 appm He/dpa. Spitznagel et al. [66] observed that dispersion-strengthened copper had about four times higher swelling (0.8% after 20 dpa) following dual-ion beam irradiation at 30 appm He/dpa compared to specimens irradiated without helium coimplantation. The somewhat higher amounts of swelling that occurred in the GlidCop AL-15 alloy compared to AL-20 and AL-60 during high-dose neutron irradiation (Fig. 16) may be partially due to helium generated via $^{10}B(n,\alpha)$ reactions with residual boron (<200 wt. ppm) in the AL-15 alloy [6,80].

3.2 Mechanical properties

The general effect of neutron irradiation on the mechanical properties of copper can be divided into two temperature regimes [6,34,82]. At irradiation temperatures below about 300°C, radiation hardening usually occurs along with a reduction in ductility. Radiation-enhanced softening generally occurs at irradiation temperatures above 300°C. The radiation hardening at low temperatures is due to the creation of a high density of small (<10 nm) dislocation loops and stacking fault tetrahedra. These so-called "black spot" defect clusters can increase the room temperature yield strength of annealed copper (unirradiated σ_y~60 MPa) to more than 350 MPa [6,83]. The radiation hardening associated with these small defect clusters approaches a saturation level after doses of ~0.1 dpa [6,84,85]. The stacking fault tetrahedra are thermally unstable at temperatures above about 150°C [6,86]. Therefore, the radiation hardening in copper and copper alloys becomes progressively smaller with increasing irradiation temperature above ~150°C, and generally becomes insignificant above ~300°C.

Figure 17 summarizes the available data on the elevated-temperature yield strength of CuCrZr following neutron irradiation at temperatures between 100 and 420°C [26,34-36,77,82]. All of the yield strength data shown in Fig. 17 were obtained at or near the irradiation temperature on cold-worked & aged specimens which had initial room temperature yield strengths between ~400 and 500 MPa. The yield strength steadily decreased with increasing irradiation and test temperature, reaching a value of about 300 MPa at 300°C and ~100 MPa at 400°C.

It is instructive to compare the temperature-dependent strengths of irradiated and unirradiated alloys. Radiation-enhanced recrystallization can produce significant softening in cold-worked copper and copper alloys at irradiation temperatures above ~280°C [6,17,18,26,34-36,67,74,77,81,87-90]. Figure 18 shows the measured change in yield strength in cold-worked & aged CuCrZr alloys following neutron irradiation at temperatures between 100 and 500°C [17,26,34-36,74,77,82,89,90]. The figure includes some alloy screening experiments that were tested at room temperature rather than at the irradiation temperature. The initial room temperature yield strengths of the CuCrZr alloys varied from ~400 to 500 MPa, and the irradiation damage levels were between 1 and 150 dpa. Fabritsiev et al. [36] have shown that most of the radiation hardening or softening in CuCrZr occurs at relatively low neutron doses (<1 dpa). The CuCrZr yield strength was increased by ~5 to 25% after irradiation at temperatures below 260°C. Conversely, radiation softening occurred and became progressively more significant as the irradiation temperature was increased above 280°C. Approximately 80% of the initial alloy yield strength was lost after irradiation at temperatures above ~400°C. Similar radiation softening has been observed in CuNiBe alloys irradiated at temperatures above 400°C [17,74,89]. However, there are insufficient data on CuNiBe at irradiation temperatures below 400°C
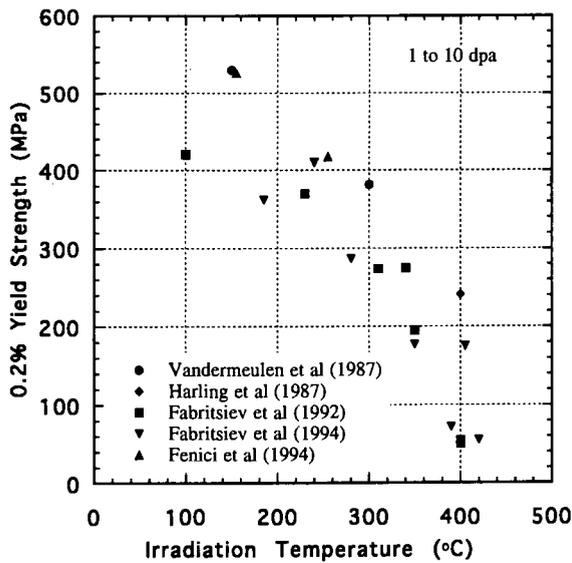
FIG. 17. Effect of irradiation temperature on the yield strength of neutron-irradiated CuCrZr alloys [26,34-36,77,82]. The tensile tests were performed at or near the irradiation temperature.
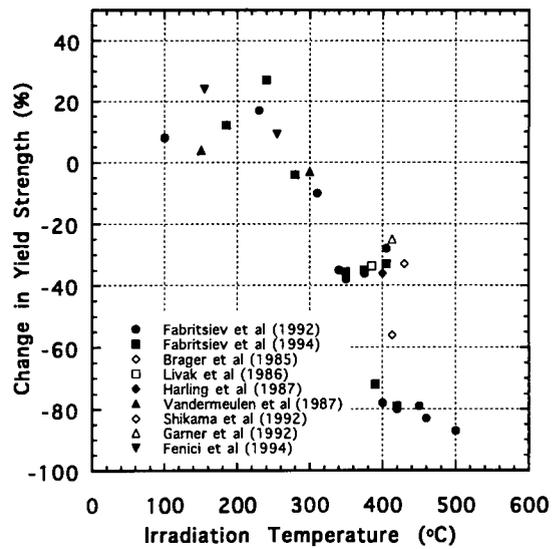

FIG. 18. Change in the yield strength of CuCrZr alloys following neutron irradiation at 100 to 500°C [17,26,34-36,74,77,82,89,90]. The filled symbols denote measurements made at or near the irradiation temperature, whereas the open symbols refer to room temperature tensile measurements.
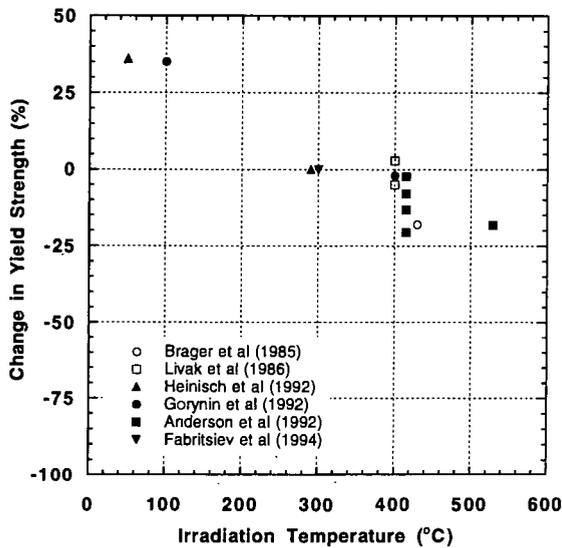

FIG. 19. Change in the yield strength of oxide dispersion-strengthened copper alloys after neutron irradiation at 50 to 530°C [17,18,36,78,80,90,92]. All of the tensile data except for refs. [18,36] were obtained at room temperature.
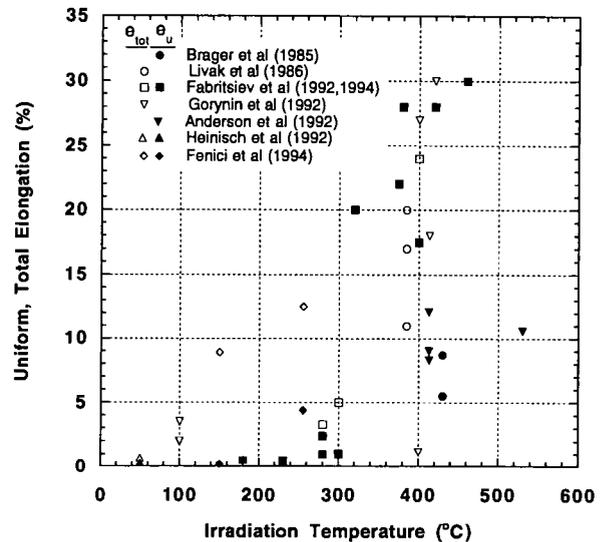

FIG. 20. Effect of irradiation temperature on the uniform (e_u) and total (e_tot) elongation of CuCrZr and oxide dispersion-strengthened copper alloys [17,18,34-36,80,82,90,92]. The tensile data from refs. [18,34-36,82] were made at or near the irradiation temperature, with the remaining data obtained from room temperature tests.

[91], so the overall temperature-dependent radiation softening behavior cannot be quantified at this time.

The oxide dispersion-strengthened alloys are very resistant to radiation softening compared to the precipitation-hardened alloys. Figure 19 shows the measured change in yield strength in oxide dispersion-strengthened copper following neutron irradiation at temperatures between 50 and 530°C [17,18,36,78,80,90,92]. The initial room temperature yield strengths ranged from 340 to 500 MPa, and the irradiation damage levels were between 1 and 150 dpa with the exception of the 0.04 dpa data of Heinisch et al. [92]. The available data are consistent with the CuCrZr results that radiation hardening occurs for irradiation temperatures below ~300°C, and radiation softening occurs above ~300°C. However, the magnitude of radiation softening was much less pronounced in the oxide dispersion-strengthened alloys compared to CuCrZr. The radiation softening in oxide dispersion-strengthened copper was less than 25% even after irradiation at 410 to 430°C to a damage level of 150 dpa [78] or irradiation at 530°C to a damage level of 32 dpa [80].

A loss of ductility is associated with the radiation hardening that occurs at irradiation temperatures below about 300°C. The uniform and total elongation of pure copper and Cu alloys are strongly reduced after neutron irradiation at temperatures below 250°C [6,18,34,36,82,92,93]. Cold-worked specimens appear to be particularly susceptible to radiation embrittlement. For example, Makin [93] found that 20% cold-worked copper had a total elongation of only ~1 to 2% following irradiation near room temperature to an E>1 MeV neutron fluence of 4×10^{23} n/m^2 (~0.04 dpa). The corresponding total elongation in copper irradiated without any initial cold work was ~16%. Figure 20 summarizes the uniform and total elongation measured in CuCrZr and oxide dispersion-strengthened copper alloys following irradiation at temperatures between 50 and 530°C [17,18,34-36,80,82,90, 92]. Similar temperature-dependent trends have been observed for irradiated CuNiBe [17,89,91], but only a few scattered results are available. Both classes of alloys exhibit very low uniform elongation (<1%) after irradiation at temperatures below 250°C to damage levels in excess of ~1 dpa. The corresponding total elongation in this radiation hardening temperature regime varied from ~1 to 10%, depending on the initial thermomechanical treatment given to the alloy. Irradiation at temperatures above 300°C generally produced high uniform and total elongation (>10%). The transition temperature between the low- and high-ductility regimes at 275 to 300°C corresponds to the transition between radiation hardening and radiation softening (Figs. 18,19).

The relatively low ductility of the high strength (cold-worked) copper alloys in the ITER-relevant temperature range of 50 to 300°C may limit the applicability of these alloys for structural components. Unfortunately, there are no known published data on the important engineering properties of fracture toughness, fatigue strength, and fatigue crack growth rates in irradiated copper alloys. Conflicting results have been obtained on the fatigue properties of pure copper after low dose (~0.001 dpa) neutron irradiation near room temperature [94,95], although the overall effect of radiation on the fatigue strength was small due to the low damage level in these studies. There are no known published fatigue results on copper or copper alloys irradiated to damage levels >1 dpa. A recent unpublished study indicates that the fracture toughness of GlidCop AL-15 is severely reduced following irradiation to ~3 dpa at 250°C [58]. Based on the observation that radiation embrittlement in the temperature range 50 to 250°C apparently becomes more severe with increasing cold work level [93], future irradiation studies should include the medium-strength as-wrought and cast & aged alloys. Whereas these alloys have less attractive unirradiated strengths compared to cold-worked alloys, it is possible that their irradiated properties may be superior to the cold-worked alloys due to higher ductility and work hardenability.

The presence of insoluble helium generated by transmutation reactions can produce additional embrittlement in copper and copper alloys [36,96-98]. However, helium embrittlement is generally most pronounced at elevated temperatures, where the overall ductility of irradiated copper and copper alloys is high. The threshold temperature for observable helium embrittlement decreases with increasing helium concentration [36,98]. For pure copper, the threshold temperature is about 500°C for a helium concentration of 2 appm and ~350°C for a He concentration of 60 appm. Alloys containing precipitates or oxide particles exhibit a significantly higher threshold temperature for observable He embrittlement compared to pure copper. For example, the threshold temperature for

178

MAGT 0.2 dispersion-strengthened copper containing 60 appm He is ~900°C [98]. The increased resistance to helium embrittlement in the alloys is presumably due to effective partitioning of the helium among the numerous particle-matrix interfaces.

There are only a few published studies of radiation creep in copper [99,100], with no known studies on high-strength copper alloys. The magnitude of radiation creep in copper is comparable to other FCC metals such as Ni and austenitic stainless steel [99]. An irradiation-creep compliance of $\dot{\epsilon}/\sigma P = 6.2 \times 10^{-11}$/Pa-dpa was obtained on 20% cold-worked copper irradiated with light ions at 150°C [99], where P is the displacement damage rate and σ is the applied stress.

3.3 Transmutation effects and thermal conductivity degradation

The high energy neutrons produced in fusion reactors will produce significant concentrations of solid and gaseous transmutation products in copper, in addition to causing displacement damage. Table III summarizes the calculated displacement damage [101-103] and major transmutation products [5,102-106] for copper exposed to typical fusion reactor first wall irradiation spectra. For purposes of comparison, the corresponding values for copper irradiated in the EBR-II or FFTF fast fission reactors are also included in Table III [102,106]. The displacement damage calculations summarized in Table III used the recommended [107] average displacement energy of 30 eV for copper. The dominant transmutation products in both fusion and fission reactor spectra are nickel and zinc. The transmutation rates (appm/dpa) are lower in the fast fission spectrum for all of the major transmutation products. Water-cooled fission reactors produce significantly higher transmutation rates of copper to Ni and Zn (up to ~5000 and 2000 appm/dpa, respectively) due to thermal neutron reactions, but produce similar amounts of Co, Fe, H and He as fast fission reactors [108,109]. Since fast fission reactors operate with liquid metal coolants, it is generally not possible to obtain irradiation data at temperatures below ~350°C. Water-cooled reactors can provide irradiation data in the ITER-relevant temperature range of 50 to 350°C, but spectral shielding of the thermal neutron flux is required for high-dose investigations (>1 dpa) to reduce the Ni and Zn transmutation rates to a level comparable to the fusion condition. As discussed in the following, the thermal conductivity of copper alloys is very sensitive to variations in the solid transmutation rate. Therefore, fission reactor thermal conductivity data must be corrected for solid transmutation differences before it can be applied for fusion design purposes.

The transmutation rates in CuCrZr, CuNiBe and oxide dispersion-strengthened copper will generally be very similar to the pure copper values given in Table III. The one notable exception is CuNiBe, where the Be will transmute during exposure to high energy neutrons (E> 2 MeV) via a threshold (n,2n) reaction and subsequent decay to produce two helium nuclei. Transmutation calculations indicate that this reaction will produce an additional 7 appm He/dpa in CuNiBe exposed to a fusion first wall spectrum and ~5 appm He/dpa in a fission reactor spectrum [109].

TABLE III. Calculated displacement damage [101-103] and transmutation products [5,102-106] for copper in first wall fusion and fast fission reactor spectra. The dpa calculation for the fusion reactor is normalized to a neutron wall loading of 1 MW-yr/m² = 1 full power year (FPY) .

Spectrum	Damage rate (dpa/FPY)	Transmutation rate (appm/dpa)					
		Ni	Zn	Co	Fe	H	He
Fusion 1st wall	15	190	90	7	0.02	40	7
Fast fission	54 to 73	51	46	0.1	---	7	0.1

TABLE IV. Experimental and calculated energies for hydrogen and helium migration (E_m), formation (E_f), binding energy to vacancies (E_{vB}) and vacancy-solute mutual diffusion (E_{vm}) in copper.

Solute	E_m (eV)	E_f (eV)	E_{vB} (eV)	E_{vm} (eV)	Reference
H	0.40	0.40	0.4	---	[113,114,116]
He	0.6	>2.0	2.1	2.1	[118-120]

Numerous studies have been performed on the solubility and diffusivity of hydrogen [110-117] and helium [118-120] isotopes in copper. Copper and its alloys are an effective barrier to tritium permeation compared to other metals such as austenitic stainless steel, due to the very low solubility of hydrogen in copper [121]. The solubility of hydrogen in copper is <100 appm at the melting point of copper, and ~0.1 appm at 300°C for an external hydrogen partial pressure of one atmosphere [112, 117]. The combination of low tritium solubility and high tritium diffusivity in copper alloys produces a low tritium inventory, which is advantageous for accident scenarios. Table IV summarizes the diffusion and solubility data for hydrogen and helium in copper [110-120]. The solubility of hydrogen in copper obeys Sieverts Law, i.e. the solubility is proportional to the square root of hydrogen pressure. The pre-exponential factor for H diffusion is $D_0=1.06 \times 10^{-6}$ m^2/s [113]. The activation energy for bulk permeation of hydrogen through copper is given by $E_\phi = E_m + E_f = 0.80$ eV, with a pre-exponential factor of 8.4×10^{-7} mol/(m-s-$\sqrt{Pa}$) [114]. Similar bulk permeation constants are obtained for tritium, with the exception that the pre-exponential factor is 4.9×10^{-7} [114]. In practice, the permeation of hydrogen isotopes through copper at temperatures below 400°C is even lower than the bulk permeability [115]. The rate limiting step for low temperature hydrogen permeation is adsorption of molecular hydrogen at the surface of copper [115].

Although the hydrogen and helium produced by transmutation reactions are both insoluble in copper, their diffusion behavior creates two different responses. Hydrogen has a low migration energy, and its binding energy to traps such as vacancies and voids is ~0.4 to 0.6 eV (Table IV and ref. [116]). Therefore, hydrogen can diffuse rather easily at temperatures above room temperature and generally does not produce observable precipitation. On the other hand, helium has a somewhat higher migration energy and is strongly trapped by monovacancies and vacancy clusters. This behavior promotes the formation of cavities containing He in irradiated copper. Hydrogen generally does not produce any serious alterations in the mechanical properties of oxygen-free copper. Hydrogen embrittlement occurs in copper containing excess amounts of oxygen (>0.01%) in the form of copper oxide during exposure to hydrogen at temperatures >400°C [38].

The solutes created by neutron transmutation reactions (Table III) produce a degradation in the electrical and thermal conductivity of copper. Additional radiation-induced processes such as void formation and precipitate dissolution can cause further decreases in the conductivity [122-124]. However, these contributions in radiation resistant copper alloys are generally small compared to the transmutation effects. The overall degradation in the thermal conductivity can be estimated by invoking Matthiesson's rule [125] and the Wiedemann-Franz law given in Section 2. Table V summarizes experimental measurements of the specific resistivity of the principal solutes produced in neutron-irradiated copper, along with theoretical and experimental specific resistivity values for other radiation-induced defects [123,125,126]. According to Matthiesson's rule, the individual resistivity components can be independently summed to determine the overall resistivity degradation:

$$\rho = \rho_0 + \rho_{Ni} X_{Ni} + \rho_{Zn} X_{Zn} + \rho_{Co} X_{Co} + \dots \qquad (2)$$

TABLE V. Room temperature electrical resistivity contributions to pure copper (atomic fractions) [123,125,126]. The solute resistivities are valid for solute concentrations up to 30%, 3%, 1% and 1% for Ni, Zn, Co and Fe, respectively.

Solute resistivity (10^{-8} Ω-m)				Dislocation resistivity (Ω-m^3)	Stacking fault resistivity (Ω-m^2)	Frenkel pair resistivity ($\mu\Omega$-m)
Ni	Zn	Co	Fe			
1.12	0.30	6.4	9.3	1.6×10^{-25}	1×10^{-19}	1.9

where ρ_0 is the electrical resistivity of pure copper (17.1 nΩ-m at 20°C), and ρ_i and X_i are the specific resistivity and atomic concentration of solute i. Similar terms can be written for the resistivity contribution from dislocation loops and network dislocations [123], but these terms typically produce less than a 1% increase in the resistivity of irradiated copper. Figure 21 shows the calculated degradation in the thermal conductivity of copper due to solid transmutations produced by exposure to a fusion reactor first wall neutron spectrum (Table III). The largest contribution to the thermal conductivity degradation is due to Ni, followed by Co and Zn. The accumulation of solid transmutation products alone causes the thermal conductivity of copper to be reduced to 66% of its initial value after 2 MW-yr/m^2 (30 dpa). Figure 21 also shows the calculated change in the thermal conductivity of copper alloys with an initial thermal conductivity of 340 W/m-K (comparable to unirradiated CuCrZr and oxide dispersion-strengthened Cu, Fig. 1) and 210 W/m-K (comparable to


FIG. 21. Effect of solid transmutations on the thermal conductivity of copper at a fusion reactor first wall. The calculations were performed for three different initial conductivities, expressed in terms of percent International Annealed Copper Standard (IACS).

unirradiated CuNiBe). The degraded thermal conductivity due to transmutation product formation after 2 MW-yr/m^2 in these two cases are 237 and 165 W/m-K, respectively.

Void swelling produces an additional degradation in the thermal conductivity of copper and copper alloys [17,18,77,122,124]. Experimental studies [122,124] have confirmed that the void swelling contribution to conductivity loss can be described by a simple mixing rule (originally derived by Maxwell), $\rho/\rho_m = [(1+0.5 \, \Delta V)/(1-\Delta V)]$, where ρ_m is the matrix resistivity and ΔV is the volume fraction of cavities. This relationship is valid when the average cavity size is larger than the electron mean free path in the matrix material, which is ~30 nm for pure copper at room temperature. Assuming a design limit for radiation-induced swelling of 5%, the corresponding degradation in the thermal conductivity beyond that due to solid transmutation effects is 8%. Therefore, void swelling produces relatively minor changes in the thermal conductivity of swelling-resistant copper alloys.

A final factor that influences the thermal conductivity of irradiated copper alloys is the stability of the precipitate structure and its interaction with transmutation-produced solute. Experimental measurements have shown that the conductivity of neutron-irradiated copper alloys can be larger or

smaller than the preirradiation value [17,18,74,77,122,124]. The conductivity increases occur in some alloys with initial thermal conductivities below ~250 W/m-K, or in precipitation-strengthened alloys which were not heat treated to produce maximum conductivity. Radiation-enhanced precipitation and aging is the likely mechanism responsible for the conductivity increases in these low- to medium-conductivity alloys. It has been suggested that complex solute redistribution processes may occur in some irradiated alloys, involving the transmutation solute atoms and solute ejected from pre-existing precipitates (ballistic dissolution) [70,74,78]. These processes can produce decreases in the thermal conductivity of neutron-irradiated CuNiBe that are larger than predicted by Eq. 2 [74]. Large decreases in conductivity may occur if a high density of small precipitates are formed during irradiation, since this type of microstructure is very effective in reducing the conductivity [127].

Several studies have examined the radioactivation characteristics of copper and copper alloys exposed to a fusion first wall neutron spectrum [5,105,128]. The overall radiological hazard of copper is comparable to other structural materials such as Type 316 austenitic stainless steel [5,128]. The alloying elements in the high-strength, high-conductivity copper alloys under consideration for fusion reactor applications (Table II) generate a radiation hazard that is similar to pure copper [105].

4. JOINING

Copper alloys can be joined by a variety of techniques, including welding, brazing and diffusion bonding [1,129]. Welding is generally not used for joining high-strength copper alloys, however, for several reasons. The precipitates in high-strength alloys such as CuCrZr and CuNiBe are subject to partial or complete dissolution in the melt layer of the weld joint. Therefore, the entire welded component must be solutionized and aged to recover some of the initial precipitation hardening in the joint. In addition, very high strengths generally cannot be achieved in the joint region after welding since the precipitation-strengthened copper alloys require cold working to attain their optimum strength. In some cases it is possible to design the joint region so that it can be cold worked after welding [130]. Oxide dispersion-strengthened copper cannot be welded by conventional techniques due to aggregation of the oxide particles in the melt layer, which destroys the uniform particle spacing that is needed to produce high strength. Recrystallization would also occur in the melt layer. Welded GlidCop alloys have been shown to have very poor radiation resistance [70,78,80].

Brazing is the most common method for joining copper alloys. Copper alloys are typically brazed at temperatures between 600 and 950°C with hold times at the brazing temperature ranging from ~10 seconds (torch, resistance, or induction brazing) to ~10 minutes (furnace brazing). The most common brazing filler metals are Cu-, Ag- and Au-base alloys [129]. Oxide dispersion-strengthened copper has been successfully joined using torch [131,132], furnace [131], resistance [134] and induction [133,135] brazing. Due to the high recrystallization temperature of dispersion-strengthened copper, significant softening does not occur in the base metal at the brazing temperature (see, e.g. Fig. 6). On the other hand, precipitation-hardened copper alloys typically soften during furnace brazing (ref. [129] and Fig. 5). The amount of softening in the base metal of precipitation-hardened alloys can be minimized by using torch, resistance or induction brazing, which limit the time that the base metal is at high temperature to less than one minute. Alternatively, the brazed component can be aged following furnace brazing to recover some of its initial strength. Complete recovery of high strength after furnace brazing by heat treatment is rather difficult in practice since the component must be heated to a temperature greater than typical brazing temperatures and rapidly quenched to create a supersaturation of solute prior to aging. For example, the strength of solutionized & aged CuCrZr alloys exposed to a solution anneal temperature of 900°C before aging is about 90% of the strength of alloys given a solution anneal at 1000°C [27]. As mentioned previously, the precipitation-hardened copper alloy would require cold working following furnace brazing in order to achieve the optimum strength.

The fine grain structure of wrought oxide-dispersion-strengthened copper creates problems when trying to furnace braze with Ag-base braze alloys [131]. The grain boundary diffusion coefficient of Ag in copper is much larger than the bulk diffusion coefficient. Therefore, excessive diffusion of silver along grain boundaries can occur during furnace brazing of dispersion-

strengthened copper. The rapid grain boundary diffusion of Ag can cause the formation of small voids in the braze region and poor joint strength. Cold-worked precipitation-hardened alloys have a fine grain structure that is similar to dispersion-strengthened copper. However, the precipitation-hardened alloys suffer recrystallization during the typical furnace braze cycle (with accompanying loss of strength). The resultant increase in the grain size during recrystallization minimizes the number of grain boundaries available for Ag diffusion, and effectively inhibits Ag depletion in the braze joint of precipitation-hardened alloys. The excessive diffusion of Ag from the braze region in furnace brazed dispersion-strengthened copper can be prevented by electroplating the joint surfaces with 10 to 50 μm of copper or nickel prior to brazing [131,135]. The large grain boundaries in the plated layer act as a barrier for grain boundary diffusion of silver. Alternatively, joints with satisfactory shear strength can be obtained in dispersion-strengthened copper with Ag-base braze alloys by torch [131,132] or induction [133,135] brazing.

The highest mechanical strength braze joints in alloys such as oxide dispersion-strengthened copper are produced using Au-base braze alloys [131]. The grain boundary diffusion coefficient of gold in copper is low enough to prevent excessive depletion of Au from the joint region during furnace brazing. Therefore, fine-grained high-strength copper alloys can be furnace brazed using Au-based alloys without prior electroplating. The measured room temperature shear strength of GlidCop AL-15 and AL-25 brazed with Au-Cu filler metals was 200 to 240 MPa [131]. The typical shear strength of GlidCop alloys brazed with Ag-base filler metals was 150 to 200 MPa [131,133, 135]. A room temperature tensile strength of 380 MPa was measured for a torch-brazed GlidCop AL-15 joint prepared with Ag-base foil, and the joint did not fail during fatigue testing up to 80,000 cycles at a stress amplitude of 276 MPa [132]. The fatigue strength of brazed copper joints is generally comparable to the base metal strength [55,56,132], although lower braze joint fatigue strengths have also been reported [133,134]. The ductility of the braze joint is generally much lower than the base metal [131,133-135]. Neutron irradiation studies on brazed GlidCop joints are in progress. Transmutation calculations indicate that significant burnup of the Ag and Au used in many braze alloys would occur in a fusion first wall neutron spectrum [136], which could affect the mechanical properties of the braze joint. The calculations indicate that approximately 40% of Ag and 55% of Au would be burned up by exposure to a first wall fluence of 2 MW-yr/m^2 (30 dpa).

Joints with high mechanical strength can be produced in dispersion-strengthened copper alloys by diffusion bonding. Shear strengths comparable to that of the base metal (~300 MPa) have been obtained by applying 5 to 100 MPa pressure for ~1 hour at 900 to 930°C [131,137]. These diffusion-bonding conditions are similar to the conditions normally employed for the hot isostatic pressure consolidation of GlidCop powder billets [131]. Diffusion bonding cannot be used to produce high strength joints in precipitation-hardened alloys, since unacceptable softening of the base metal occurs during exposure to the high temperatures necessary for effective solid state bonding. An attempt to diffusion bond precipitation-hardened Cu-Zr at 500°C produced a low hydrostatic bond strength of <17 MPa [138].

5. CORROSION

Copper and its alloys are widely known for their excellent corrosion resistance in water and other environments [1,139-141]. Surface corrosion rates below 10 μm/yr (~1 mg/dm^2-day) occur in copper exposed to water containing less than 1000 ppm oxygen at room temperature [139]. Pitting occurs in copper exposed to water containing high concentrations of CO$_2$. The presence of aqueous ammonia causes preferential attack at grain boundaries [139] and stress corrosion cracking in copper alloys [140,141]. The corrosion behavior of the three high-strength copper alloys considered to be most promising for fusion applications (CuCrZr, CuNiBe and oxide dispersion-strengthened copper) should be similar to that of pure copper. However, residual stresses associated with cold working are known to increase the susceptibility of copper alloys to stress corrosion cracking [140].

Very little is known about the effect of irradiation on the corrosion of copper and copper alloys [18,139]. Satisfactory corrosion resistance was observed for several high strength copper alloys that were exposed to flowing water (~0.5 m/s) during neutron irradiation near 90°C to a damage level of

~1 dpa [18]. The weight loss was about 5 times less in a CuCrZr alloy compared to MAGT 0.05 and MAGT 0.2 dispersion-strengthened copper. The possibility of irradiation-assisted stress corrosion cracking apparently has not been investigated in copper or copper alloys.

6. CONCLUSIONS

Most of the mechanical and physical properties of high-strength copper alloys needed for a qualitative evaluation of their suitability for high heat flux structural applications have been measured. Three types of copper alloys are commercially available which appear to have suitable properties for fusion reactor high heat flux applications: CuCrZr, CuNiBe, and oxide dispersion-strengthened copper. Due to the dependence of the physical and mechanical properties of these alloys on thermomechanical processing, additional property measurements would be required on specific prototypic heats in order to develop a comprehensive set of engineering design data for ITER. There are few available data on thermal fatigue, creep, fracture toughness, and near-threshold fatigue crack growth rates in high-strength copper alloys. In addition, there is a general lack of data on the effect of neutron irradiation on the properties of high-strength copper alloys at ITER-relevant temperatures of 50 to 350°C. The effects of irradiation on creep, fatigue, fracture toughness and corrosion of base metal and joints needs further study. In particular, the ductility reductions associated with neutron irradiation at 50 to 250°C needs to be quantified in cold-worked, wrought, and solutionized & aged alloys.

The precipitation-hardened CuCrZr and CuNiBe alloys are susceptible to significant radiation-enhanced softening during operation at temperatures above ~275°C. Both alloys appear to be promising for high heat flux structural applications if the operating temperature can be maintained below 275°C. The solutionized & aged strengths should be used for engineering design purposes rather than the more commonly quoted cold-worked & aged strengths of these two alloys, since joining operations will likely cause recrystallization with accompanying softening. The data base on CuNiBe is very limited compared to CuCrZr and dispersion-strengthened copper, which makes it difficult to evaluate its suitability for ITER.

Dispersion-strengthened copper and precipitation-hardened CuCrZr have similar mechanical and physical properties at temperatures between 20 and 300°C. Oxide dispersion-strengthened copper has a considerable advantage over all precipitation-hardened copper alloys in terms of high temperature creep resistance and strength retention after exposure to elevated temperatures. The main disadvantages associated with dispersion-strengthened copper are that it is only available in wrought form and it cannot be welded. Dispersion-strengthened copper can be satisfactorily joined by brazing or diffusion bonding. Considering the published data on mechanical properties (base metal and joints), thermal conductivity, and radiation stability, oxide dispersion-strengthened copper appears to be the most promising high strength copper alloy for high heat flux structural applications.

REFERENCES

[1] ASM Metals Handbook, 10th ed., Vol. 2 , Properties and Selection: Nonferrous Alloys and Special-Purpose Materials, ASM International, Metals Park, OH (1990) 216-427.

[2] E. Ling and P.W. Taubenblat (Eds), High Conductivity Copper and Aluminum Alloys, The Metallurgical Society of AIME, Warrendale, PA (1984).

[3] S.J. Zinkle and R.W. Knoll, A Literature Review of Radiation Damage Data for Copper and Copper Alloys, UWFDM-578, Univ. Wisconsin Nucl. Eng. Dept., Madison, WI, June 1984.

[4] K.R. Anderson and D.S. Gelles, ITER Materials Data Base for Irradiation Effects on the Design Properties of CuNiBe and Cu-Al$_2$O$_3$ Alloys, Fusion Reactor Mater. Semiann. Prog. Report DOE/ER-0313/5, April 1989, pp. 268-279.

[5] G.J. Butterworth and C.B.A. Forty, J. Nucl. Mater. **189** (1992) 237.

[6] S.J. Zinkle, in Effects of Radiation on Materials: 15th Int. Symp., ASTM STP 1125 (R.E. Stoller, et al., Eds.), American Soc. for Testing and Materials, Philadelphia (1992) 813-834.

[7] W.B. Gauster, At. Plasma-Mater. Interact. Data Fusion (this volume).

[8] CRC Handbook of Chemistry and Physics, 59th Ed. (R.C. Weast, Ed.), CRC Press, Boca Raton, Florida (1978).

[9] G. Simmons and H. Wang, Single Crystal Elastic Constants and Calculated Aggregate Properties: A Handbook, MIT Press, Cambridge, MA (1971) p. 181.

[10] S.J. Zinkle, Effects of Thermal Annealing and Ion Irradiation on the Properties and Microstructures of Copper Alloys, Ph.D. Thesis, Univ. Wisconsin-Madison Nucl. Eng. Dept. report UWFDM-642, May 1985.

[11] A.V. Nadkarni, in ref. [2], pp. 77-101.

[12] F.R. Mollard, K.G. Wilke and A.R. Chaudry, in ref. [2], pp. 147-168.

[13] A. Guha, in ref. [2], pp. 133-145.

[14] A. Rotem and A. Rosen, Metall. Trans. A **16** (1985) 2073.

[15] SCM Metal Products, Inc., technical data brochure on GlidCop® dispersion-strengthened copper

[16] T.J. Miller, S.J. Zinkle and B.A. Chin, J. Nucl. Mater. **179-181** (1991) 263-266.

[17] H.R. Brager, H.L. Heinisch and F.A. Garner, J. Nucl. Mater. **133&134** (1985) 676-679.

[18] I.V. Gorynin, S.A. Fabritsiev, V.V. Rybin et al., J. Nucl. Mater. **191-194** (1992) 401-406.

[19] G. Piatti and D. Boerman, J. Nucl. Mater. **185** (1991) 29-38.

[20] KM-Kabelmetal, technical data brochure on Cu alloy moulds for continuous casting (Elbrodur® CuCrZr alloys).

[21] Materials Handbook for Fusion Energy Systems, DOE/TIC-10122, McDonnell Douglas, St. Louis, Missouri (1991).

[22] R.E. Reed-Hill, Physical Metallurgy Principles, 2nd ed., Brooks/Cole-Wadsworth, Inc., Monterey, California (1973) pp. 267-325.

[23] P.W. Taubenblat, W.E. Smith and A.R. Graviano, in ref. 2, pp. 19-29.

[24] H. Suzuki, M. Kanno and I. Kawakatsu, J. Japan Inst. Metals **33** (1969) 628-633.

[25] A.K. Lee and N.J. Grant, Mater. Sci. and Engineering **60** (1983) 213-223.

[26] W. Vandermeulen, V. Massaut, J. Van de Velde and W. Hendrix, in Proc. 14th Symp. on Fusion Technology, Pergamon Press, New York (1986) pp. 1031-1035.

[27] H. Suzuki, I. Kawakatsu and H. Kitano, J. Japan Inst. Metals **31** (1967) 342-346.

[28] N.J. Grant, A. Lee and M. Lou, in ref. [2], pp. 103-117.

[29] S.J. Zinkle, D.H. Plantz, A.E. Bair, R.A. Dodd and G.L. Kulcinski, J. Nucl. Mater. **133&134** (1985) 685-689.

[30] E.N.C. Dalder, W. Ludemann and B. Schumacher, in Proc. Workshop on Copper and Copper Alloys for Fusion Reactor Applications (F.W. Wiffen and R.E. Gold, Eds.), CONF-830466, National Tech. Information Service, Springfield, Virginia (1984) pp. 251-307.

[31] J.J. Stephens, R.J. Bourcier, F.J. Vigil and D.T. Schmale, SAND88-1351, Sandia National Laboratories (1988).

[32] T.S. Srivatsan, S. Anand and J.D. Troxell, Eng. Fracture Mechanics **46** (1993) 183-198.

[33] V.R. Barabash, G.L. Saksagansky, Y.F. Shevakin et al., ITER Specialist Meeting on Materials Data Base, ITER-IL-NE-1-0-3 (Feb. 1990).

[34] S.A. Fabritsiev, V.V. Rybin, V.A. Kasakov, A.S. Pokrovskii and V.R. Barabash, J. Nucl. Mater. **195** (1992) 173-178.

[35] S.A. Fabritsiev, V.V. Rybin, V.A. Kasakov, A.S. Pokrovskii and V.R. Barabash, J. Nucl. Mater. **195** (1992) 179-183.

[36] S.A. Fabritsiev, V.R. Barabash, Y.G. Prokofiev and A.S. Pokrovsky, "Neutron Spectrum and Transmutation Effects on the Radiation Damage on Copper Alloys", Proc. 6th Int. Conf. on Fusion Reactor Materials, J. Nucl. Mater., in press (1994).

[37] S.N. Rosenwasser, in ref. [30], pp. 309-329.

[38] S.J. Zinkle, in Alloy Development for Irradiation Performance Semiann. Progress Report for period ending March 31, 1986, DOE/ER-0045/16, pp. 163-167.

[39] J.E. Synk and K. Vedula, Mater. Sci. and Technology **3** (1987) 72-75.

[40] J.J. Stephens and D.T. Schmale, SAND87-1296, Sandia National Laboratories (1987).

[41] G. Piatti and H.A. Weir, J. Nucl. Mater. **150** (1987) 1-9.

[42] S.N. Rosenwasser, R.D. Stevenson, G. Listvinsky, D.L. Vrable, J.E. McGregor and N. Nir, J. Nucl. Mater. **122&123** (1984) 1107-1120.

[43] O.K. Harling, G.P. Yu, N.J. Grant and J.E. Meyer, J. Nucl. Mater. **103&104** (1981) 127.

[44] J. Groza, J. Mater. Eng. and Performance **1** (1992) 113-121.

[45] N.Y. Tang, D.M.R. Taplin and G.L. Dunlop, in Proc. 6th Int. Conf. on Strength of Metals and Alloys, Vol. 2 (R.C. Gifkins, Ed.), Pergamon Press, New York (1983) pp. 665-670.

[46] W.D. Nix and J.C. Gibeling, in Flow and Fracture at Elevated Temperatures (R. Raj, Ed.) Amer. Soc. for Metals, Metals Park, Ohio (1985) p. 50.

[47] S.J. Zinkle, R.A. Dodd and G.L. Kulcinski, in 12th Int. Symp. on Effects of Radiation on Materials, Vol. 1, ASTM STP 870 (F.A. Garner and J.S. Perrin, Eds.) Amer. Soc. for Testing and Mater., Philadelphia (1985) 363-382.

[48] C. Bushnell and R. Ellis, Princeton University reports F-900216-PPL-04 (GlidCop AL-15), F-900403-PPL-03 (Brush-Wellman CuNiBe), F-900404-PPL-03 (Elbrodur CuCrZr), F-900430-PPL-03 (Brush-Wellman overaged CuNiBe), and F-900518-PPL-04 (OFHC Cu), 1990.

[49] A.J. Kennedy, Processes of Creep and Fatigue in Metals, John Wiley & Sons, Inc., New York (1963) pp. 289-313.

[50] P.W. Taubenblat, W.R. Opie and Y.T. Hsu, Met. Eng. Quarterly 12 (1972) 41-45.

[51] A. Singhal, J.F. Stubbins, B.N. Singh and F.A. Garner, Proc. 6th Int. Conf. on Fusion Reactor Materials, J. Nucl. Mater., in press (1994).

[52] B.G. Gieseke, Oak Ridge National Laboratory, private communication (1994).

[53] A.L.W. Collins, D.M.R. Taplin and V. Singh, 2nd Int. Conf. on Mechanical Behavior of Materials, Amer. Soc. for Metals, Metals Park, Ohio (1976) pp. 871-875.

[54] V. Singh and D.M.R. Taplin, Bull. Electron Microsc. Soc. India 2 (1978) 17-18.

[55] K.C. Liu and C.M. Loring, Jr., J. Nucl. Mater. 122&123 (1984) 783-788.

[56] M. Seki, T. Horie, T. Tone et al., J. Nucl. Mater. 155-157 (1988) 392-397.

[57 W.A. Logsdon and P.K. Liaw, J. Mater. Eng. 9 (1987) 63-69.

[58] D.J. Alexander, Oak Ridge National Laboratory, private communication (1994).

[59] J.G. Kaufman and J.S. Santner, in Application of Fracture Mechanics for Selection of Metallic Structural Materials (J.E. Campbell, W.W. Gerberich and J.H. Underwood, Eds.), Amer. Soc. for Metals, Metals Park, Ohio (1982) pp. 169-211.

[60] T-S Lee, L.W. Hobbs, G. Kohse et al., J. Nucl. Mater. 141-143 (1986) 179-183.

[61] H.R. Brager, J. Nucl. Mater. 141-143 (1986) 163-168.

[62] N. Wanderka, C. Ramachandra, R.P. Wahi, and H. Wollenberger, J. Nucl. Mater. 189 (1992) 9-13.

[63] N. Wanderka, Y. Yuan, L. Jiao, R.P. Wahi and H. Wollenberger, J. Nucl. Mater. 191-194 (1992) 1356-1359.

[64] E.V. Nesterova, V.V. Rybin, S.A. Fabritsiev and V.R. Barabash, J. Nucl. Mater. 191-194 (1992) 407-410.

[65] V.R. Barabash, A.A. Gervash, A.V. Naberenkov et al., J. Nucl. Mater. **191-194** (1992) 411.

[66] J.A. Spitznagel, N.J. Doyle, W.J. Choyke et al., Nucl. Instr. Meth. B **16** (1986) 279-287.

[67] R.J. Livak, T.G. Zocco and L.W. Hobbs, J. Nucl. Mater. **144** (1987) 121-127.

[68] S.J. Zinkle, E.V. Nesterova, V.R. Barabash, V.V. Rybin and A.V. Naberenkov, J. Nucl. Mater. **208** (1994) 119-127.

[69] D.J. Edwards, F.A. Garner, J.W. Newkirk and A. Nadkarni, Proc. 6th Int. Conf. on Fusion Reactor Materials, J. Nucl. Mater., in press (1994).

[70] D.J. Edwards, J.W. Newkirk, F.A. Garner et al., in Effects of Radiation on Materials: 16th Int. Symp., ASTM STP 1175 (A.S. Kumar et al., Eds.), American Soc. for Testing and Materials, Philadelphia (1994) 1041-1060.

[71] S.J. Zinkle and K. Farrell, J. Nucl. Mater. **168** (1989) 262-267.

[72] S.J. Zinkle, K. Farrell and H. Kanazawa, J. Nucl. Mater. **179-181** (1991) 994-997.

[73] B.N. Singh, A. Horsewell, D.S. Gelles and F.A. Garner, J. Nucl. Mater. **191-194** (1992) 1172-1176.

[74] F.A. Garner, M.L. Hamilton, T. Shikama, D.J. Edwards and J.W. Newkirk, J. Nucl. Mater. **191-194** (1992) 386-390.

[75] K. Yamakawa, I. Mukouda and Y. Shimomura, J. Nucl. Mater. **191-194** (1992) 396-400.

[76] F.A. Garner, H.R. Brager and K.R. Anderson, J. Nucl. Mater. **179-181** (1991) 250-253.

[77] O.K. Harling, N.J. Grant, G. Kohse et al., J. Mater. Res. **2** (1987) 568-579.

[78] D.J. Edwards, K.R. Anderson, F.A. Garner et al., J. Nucl. Mater. **191-194** (1992) 416-420.

[79] F.A. Garner, D.J. Edwards, B.N. Singh and H. Watanabe, in Fusion Reactor Materials Semiann. Prog. Report DOE/ER-0313/13, Sept. 1992, pp. 253-254.

[80] K.R. Anderson, F.A. Garner, M.L. Hamilton and J.F. Stubbins, in Effects of Radiation on Materials: 15th Int. Symp., ASTM STP 1125 (R.E. Stoller, et al., Eds.), American Soc. for Testing and Materials, Philadelphia (1992) 854-874.

[81] S.J. Zinkle, G.L. Kulcinski and L.K. Mansur, J. Nucl. Mater. **141-143** (1986) 188-192.

[82] P. Fenici, D.J. Boerman, G.P. Tartaglia and J.D. Elen, in Proc. 6th Int. Conf. on Fusion Reactor Materials, J. Nucl. Mater., in press (1994).

[83] J.C. Wilson, in Proc. 2nd UN Int. Conf. on Peaceful Uses of Atomic Energy, Vol. 5, United Nations, Geneva (1958) pp. 431-445.

[84] I.A. El-Shanshoury, J. Nucl. Mater. **45** (1972/73) 245-257.

[85] H.G. Mohamed, A.M. Hammad and F.H. Hammad, Trans. Ind. Inst. Metals **35** (1982) 258.

[86] S.J. Zinkle, A. Horsewell, B.N. Singh and W.F. Sommer, in Proc. 6th Int. Conf. on Fusion Reactor Materials, J. Nucl. Mater., in press (1994).

[87] S.J. Zinkle and W.C. Oliver, J. Nucl. Mater. **141-143** (1986) 548-552.

[88] M. Appello and P. Fenici, J. Nucl. Mater. **152** (1988) 348-350.

[89] T. Shikama, F.A. Garner, M.L. Hamilton and K.R. Anderson, in Effects of Radiation on Materials: 15th Int. Symp., ASTM STP 1125 (R.E. Stoller, et al., Eds.), American Soc. for Testing and Materials, Philadelphia (1992) 846-853.

[90] R.J. Livak, H.M. Frost, T.G. Zocco, J.C. Kennedy and L.W. Hobbs, J. Nucl. Mater. **141-143** (1986) 160-162.

[91] H.L. Heinisch and C. Martinez, J. Nucl. Mater. **141-143** (1986) 883-887.

[92] H.L. Heinisch, M.L. Hamilton, W.F. Sommer and P.D. Ferguson, J. Nucl. Mater. **191-194** (1992) 1177-1182.

[93] M.J. Makin, in Radiation Effects (W.F. Sheely, Ed.), Gordon & Breach, New York (1967) 627-669.

[94] R.B. Adamson, Trans. Metall. Soc. AIME **239** (1967) 714-720.

[95] F.C. Strible and J.R. Cady, J. Appl. Phys. **43** (1972) 417-424.

[96] S.H. Goods, in Effects of Radiation on Materials: 14th Int. Symp., ASTM STP 1046, Vol. I (N.H. Packan et al., Eds.) American Soc. for Testing and Materials, Philadelphia (1989) 340-352.

[97] S.H. Goods, Scripta Met. **20** (1986) 565-569.

[98] S.A. Fabritsiev, V.R. Barabash, Y.G. Prokofiev and A.S. Pokrovsky, "The Neutron Irradiation Induced 400 C Embrittlement of Copper Alloys", Proc. 6th Int. Conf. on Fusion Reactor Materials, J. Nucl. Mater., in press (1994).

[99] P. Jung, J. Nucl. Mater. **200** (1993) 138-140.

[100] Sh. Sh. Ibragimov, E.S. Aitkhozhin and Yu.S. Pyatiletov, in Influence of Radiation on Material Properties: 13th Int. Symp., Vol. II, ASTM STP 956 (F.A. Garner et al., Eds.) American Soc. for Testing and Materials, Philadelphia (1987) 5-10.

[101] L.R. Greenwood and R.K. Smither, ANL-FPP/TM-197 (Argonne National Lab., Argonne, IL, 1985).

[102] T.A. Gabriel, B.L. Bishop and F.W. Wiffen, ORNL/TM-6361 (Oak Ridge National Lab., Oak Ridge, TN, 1979).

[103] R.L. Hagenson and R.A. Krakowski, in ref. [30], 87-128.

[104] L.J. Perkins, J. Nucl. Mater. **122&123** (1984) 1371-1375.

[105] G.J. Butterworth, J. Nucl. Mater. **135** (1985) 160-172.

[106] F.A. Garner, L.R. Greenwood and F.M. Mann, in Fusion Reactor Materials Semiann. Prog. Report DOE/ER-0313/13, Sept. 1992, pp. 42-47.

[107] Standard Practice for Neutron Radiation Damage Simulation by Charged Particle Irradiation, E521-89, Annual Book of ASTM Standards, Vol. 12.02, American Soc. for Testing and Materials, Philadelphia (1990).

[108] F.A. Garner, H.L. Heinisch, R.L. Simons and F.M. Mann, Rad. Effects Def. Solids 113 (1990) 229-255.

[109] R.A. Lillie, Oak Ridge National Laboratory (1984, 1990) private communication.

[110] E. Fromm and E. Gebhardt, Eds., Gase und Kohlenstoffe in Metallen, Springer-Verlag, New York (1976).

[111] G.R. Caskey, Jr., A.H. Dester, M.L. Holzworth, M.R. Louthan, Jr. and R.G. Derrick, Corrosion-NACE 32 (1976) 370-374.

[112] W.R. Wampler, T. Schober and B. Lengeler, Phil. Mag. 34 (1976) 129-141.

[113] D.B. Butrymowicz, J.R. Manning and M.E. Read, Diffusion Rate Data and Mass Transport Phenomena for Copper Systems, INCRA Series on The Metallurgy of Copper, National Bureau of Standards, Washington, DC. (1977); also J. Phys. Chem. Ref. Data 4 (1975) 177-249.

[114] S.A. Stewart, UCRL-53441. Lawrence Livermore National Lab., Livermore, California (1983)

[115] T.N. Kompaniets and A.A. Kurdyumov, Prog. Surf. Sci. 17 (1984) 75.

[116] F. Besenbacher, S.M. Myers and J.K Nørskov, Nucl. Instr. Meth. B 7/8 (1985) 55-66.

[117] W.A. Swansiger, Fusion Technol. 14 (1988) 631-636.

[118] W.D. Wilson and C.L. Bisson, Rad. Effects 19 (1973) 53-58.

[119] M.I. Baskes and C.F. Melius, Phys. Rev. B 20 (1979) 3197-3204.

[120] W.Th.M. Buters, A. van Veen and A. van den Beukel, Phys. Stat. Sol. (a) 100 (1987) 87-94.

[121] T. Tanabe, Y. Yamanishi, K. Sawada and S. Imoto, J. Nucl. Mater. 122&123 (1984) 1568.

[122] H.M. Frost and J.C. Kennedy, J. Nucl. Mater. 141-143 (1986) 169-173.

[123] S.J. Zinkle, J. Phys. F: Met. Phys. 18 (1988) 377-391.

[124] D.J. Edwards, F.A. Garner and L.R. Greenwood, Proc. 6th Int. Conf. on Fusion Reactor Materials, J. Nucl. Mater., in press (1994).

[125] C.Y. Ho, M.W. Ackerman, K.Y. Wu et al., J. Phys. Chem. Ref. Data 12 (1983) 183-320.

[126] K. Schroeder, CRC Handbook of Electrical Resistivities of Binary Metallic Alloys, CRC Press, Boca Raton, Florida (1983).

[127] A.J. Hillel and P.L. Rossiter, Phil. Mag. B 44 (1981) 383-388.

[128] S.J. Piet, E.T. Cheng and L.J. Porter, Fusion Technol. **17** (1990) 636-657.

[129] M.M. Schwartz, Brazing, ASM International, Metals Park, Ohio (1987).

[130] H. Kimoto, H. Kojima, S. Hioki et al., Proc. 12th Symp. on Fusion Technology, Vol. 2, Pergamon Press, New York (1983) 1045-1050.

[131] P.K. Samal, Brazing and Diffusion Bonding of GlidCop® Dispersion Strengthened Copper, SCM Metals, Research Triangle Park, North Carolina, in The Metal Science of Joining, The Minerals, Metals and Materials Society, Warrendale, PA (1992) 295-305.

[132] T.J. McManamy, R.D. Benson, R.L. Brown, et al, Design and Fabrication of a Prototype Solenoid for the Spherical Torus Experiment, Oak Ridge National Lab. Oak Ridge, Tennessee (1987)

[133] C-K Lee, B.A. Chin, S.J. Zinkle and R.C. Wilcox, in Effects of Radiation on Materials: 16th Int. Symp., ASTM STP 1175 (A.S. Kumar et al., Eds.), American Soc. for Testing and Materials, Philadelphia (1994) 1026-1040.

[134] S.F. Chen, J.Y. Liu and B.A. Chin, Proc. 6th Int. Conf. on Fusion Reactor Materials, J. Nucl. Mater., in press (1994).

[135] A.A. McFayden, R.R. Kapoor and T.W. Eagar, Welding J. **69** (1990) 399s-407s.

[136] F.A. Garner, L.R. Greenwood and D.J. Edwards, in Fusion Reactor Materials Semiann. Prog. Report DOE/ER-0313/16, April 1994, in press.

[137] H. Nishi, Y. Muto and K. Sato, Proc. 6th Int. Conf. on Fusion Reactor Materials, J. Nucl. Mater., in press (1994).

[138] C. Logan, J. Dini, W. Ludemann et al., J. Nucl. Mater. **103&104** (1981) 1551-1556.

[139] P.T. Gilbert, in Copper: The Science and Technology of the Metal, its Alloys and Compounds, (A. Butts, Ed.), Reinhold Publ., New York (1954) 379-409.

[140] H. Leidheiser, Jr., The Corrosion of Copper, Tin and Their Alloys, Wiley & Sons, New York (1971) .

[141] J.A. Beavers, in Stress Corrosion Cracking (R.H. Jones, Ed.), ASM International, Metals Park, Ohio (1992) 211-231.

EROSION OF PLASMA-FACING MATERIALS DURING A TOKAMAK DISRUPTION*

Ahmed Hassanein
Argonne National Laboratory
Argonne, Illinois 60439 USA

Isak Konkashbaev
Troitsk Institute for Innovation and Fusion Research
Moscow Region, 142092 Russia

ABSTRACT

The behavior of divertor materials during a major disruption in a tokamak reactor is very important to successful and reliable operation of the device. Erosion of material surfaces due to a thermal energy dump can severely limit the lifetimes of plasma-facing components and thus diminish the reactor's economic feasibility. A comprehensive numerical model has been developed and used in this analysis, which includes all major physical processes taking place during plasma/material interactions. Models to account for material thermal evolution, plasma/vapor interaction physics, and models for hydrodynamic radiation transport in the developed vapor cloud above the exposed surface are implemented in a self-consistent manner to realistically assess disruption damage. The extent of self-protection from the developed vapor cloud in front of the incoming plasma particles is critically important in determining the overall disruption lifetime. Models to study detailed effects of the strong magnetic field on the behavior of the vapor cloud and on the net erosion rate have also been developed and analyzed. Candidate materials such as beryllium and carbon are considered in this analysis. The dependence of divertor disruption lifetime on disruption physics and reactor conditions is analyzed and discussed.

In addition, material erosion from melting of plasma-facing components during a tokamak disruption is also a serious problem that limits reactor operation and economical reactor lifetime. In particular, metallic low-Z components such as Be will be subjected to severe melting during disruptions and edge localized modes (ELMs). Loss of the developed melt layer will critically shorten the lifetime of these components, severely contaminate the plasma, and seriously inhibit successful and reliable operation of the reactor. In this study mechanisms responsible for melt-layer loss during a disruption are also modeled and evaluated. Implications of melt-layer loss on the performance of metallic facing components in the reactor environment are discussed.

1. INTRODUCTION

Disruption damage to plasma-facing materials (PFMs) in a magnetic fusion reactor is a major concern for safe, successful, and reliable reactor operation. The intense deposition of energy (10-200 MJ/m^2) over short periods (0.1-3 ms) will cause severe surface erosion and melting of these components. If all of the incident energy were to be deposited entirely in the PFM, extensive ablation would severely limit the lifetime of the divertor plate and critically diminish the economic feasibility of the reactor. The exact amount of eroded material is critically important to reactor design and component lifetime analysis. In current tokamak machines, Demo and ITER-like heat loads and disruption conditions are not achievable. It is therefore necessary to develop a comprehensive model that includes all major physical processes occurring during a disruption in order to correctly simulate plasma/material interaction in reactor environments and conditions. It is expected, however, that the initial wave of the ablated material due to the sudden energy deposition will form a vapor cloud in front of the incoming plasma particles, thereby reducing the energy flux to facing-material surfaces. This vapor shielding effect would then significantly reduce the eroded thickness of these materials and consequently prolong its lifetime substantially. Several analyses of this vapor shielding effect have been performed [1-7]. Some previous work focused on one or two separate areas of the various processes involved during plasma-material interaction. Other work has focused separately on issues such as radiation transport [8], simulation experiments [9,30], and magnetic field effects [10]. Modeling the detailed and the dynamic interaction of plasma particles with the initial ablated material is then quite important because the ablated material provides a much-needed shielding layer that protects the PFM from the incident plasma particles.

A recently developed comprehensive model [11-13] has been extensively used in the analysis to evaluate PFMs response to disruptions. In this model, three major modeling stages of plasma/material interaction were developed with sufficient detail to accurately simulate a disruption effect on PFM. Initially, the incident plasma particles from the disrupted plasma will deposit part of their energy on the PFM surface. Models for particle deposition and material thermal evolution that take into account phase change, moving boundaries, and temperature-dependent thermophysical properties, etc., were developed to predict the behavior of these components. This initial burst of energy delivered to PFM surfaces from the direct impact of plasma particles will cause sudden ablation of these materials. As a result, a vapor cloud will be formed in front of the incoming plasma particles. Shortly thereafter, the plasma particles will be completely stopped in this vapor cloud. Continuous heating of the vapor cloud will ionize, excite, and generate photon radiation. The initial plasma particle kinetic energy is therefore transformed into radiation energy. Comprehensive models for the hydrodynamics and heating of the vapor cloud that shields the original surface were developed for the second stage of disruption modeling. Finally, models for radiation transport throughout the vapor cloud were developed to estimate the net heat flux transmitted to the facing material. It is therefore the dynamics and evolution of this vapor cloud that will finally determine the net erosion rate at the end of a disruption. Figure 1 is a schematic illustration of the various interaction zones and processes during the plasma/material interaction that follows a disruption under the influence of a strong magnetic field. This problem requires the solution of three moving boundaries: the vapor front, the receding target surface, and the solid/liquid interface. These three moving boundaries are

interdependent, and a complete solution should link them dynamically and simultaneously.
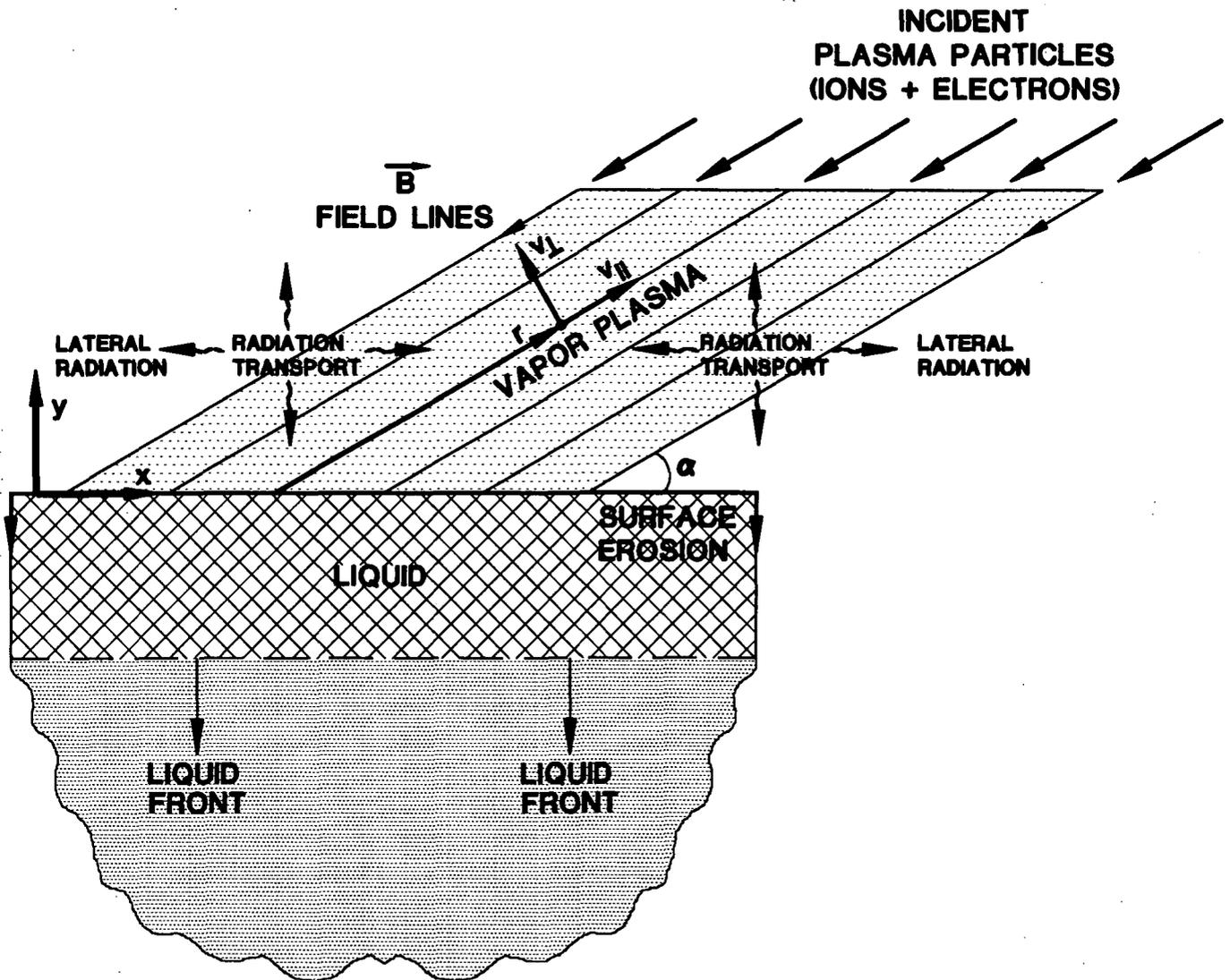

Fig. 1. Schematic illustration of various interaction zones during a reactor plasma disruption.

The detailed effects of the strong reactor-environment magnetic field on the magnetohydrodynamics of the vapor cloud and on the resulting erosion rate were also examined. A two-dimensional (2-D) magnetohydrodynamic model was developed to include effects such as magnetic field diffusion, friction forces, and Joule heating of the vapor material [12]. Previous analysis of the effect of a strong magnetic field on the dynamics of plasma/material interaction were mainly qualitative, used simple assumptions, and were not integrated dynamically with other physical processes [1,4,15]. Candidate PFMs such as beryllium and carbon were considered in this analysis. Disruption lifetime of these materials have been calculated, and dependence on characteristics of the plasma/vapor interaction zone and disruption parameters were

analyzed. In addition, to evaluate laboratory simulation experiments, a two-dimensional radiation transport model has been developed, integrated, and numerically perfected in a self-consistent way and with sufficient detail to realistically simulate the effect of small size samples on the vapor-cloud dynamics [13].

Material erosion from melting of plasma-facing components during a tokamak disruption is also a serious problem that limits reactor operation and economical reactor lifetime. In particular, metallic low-Z components such as Be will be subjected to severe melting during disruptions and edge localized modes (ELMs). Loss of the developed melt layer will critically shorten the lifetime of these components, severely contaminate the plasma, and seriously inhibit successful and reliable operation of the reactor. Mechanisms responsible for melt-layer loss during a disruption are also modeled and evaluated [14]. Implications of melt-layer loss on the performance of metallic facing components in the reactor environment are discussed.

2. MODEL SUMMARY

2.1 Plasma/material Interaction

The thermal response of the PFM is calculated by solving a time-dependent heat conduction equation in one-or two-dimensions [16]. For simplicity, the heat conduction equation in the one-dimensional form (y being the direction perpendicular to the surface) can be given by:

$$\rho c_p \frac{\partial T}{\partial t} = \nabla \cdot (K \nabla T) + \dot{q}(y, t) \tag{1}$$

where T is temperature, ρ is density, c_p is specific heat, K is thermal conductivity, and $\dot{q}$ is the volumetric energy deposition rate of the energetic plasma ions and electrons. All thermophysical properties are assumed to be a function of local temperature. The surface temperature is determined by both the boundary conditions and the evaporation process. Specifying the correct boundary condition at the surface requires that the incident energy be partitioned into conduction, melting, and evaporation. The boundary condition at the surface can then be given by:

$$-K \frac{\partial T}{\partial y}(0,t) = q_{gas} + q_{rad} - q_{evap} \tag{2}$$

where q_{gas} is the net heat flux from the near-wall vapor zone; q_{rad} is the radiation heat flux absorbed at the material surface; and q_{evap} is the evaporated heat flux, as determined by the enthalpy of evaporation. The evaporation flux leaving the surface is calculated in detail from models developed under nonequilibrium conditions [2,17]. Several boundary conditions can be used at the back surface of the material. The developed model can also be used to analyze the response of various layers of materials such as coating, substrate, and intermediate layers, with each layer having its own boundary conditions. This is important in studying the effect of disruption on substrate structural materials under certain disruption conditions [18].

The volumetric energy deposition function $\dot{q}$ (y,t) is calculated, in the condensed target material, with detailed models that include the slowing-down physics of plasma particles (both ions and electrons) in various target materials [5]. Phase change of metallic materials, when temperature exceeds their melting points are calculated using previously developed models [19].

The net heat flux q_{gas}, due to particle transport from the near-surface vapor to the target, is described by a free-streaming energy transport term according to [20,21]:

$$q_{gas} = \alpha \frac{1}{4} n_i v_i \frac{3}{2} k (T_i - T_s)$$

(3)

where v_i is ion thermal velocity, T_i is ion temperature, T_s is the target surface temperature, and α is a collisional modification factor (known as the accommodation coefficient $\alpha \approx 0.2$) of the free-streaming energy transport. The free-streaming term is more important for higher Z-materials such as tungsten, where the vapor near the target is quite dense [6]. The electron free-streaming term is neglected because a negative potential is assumed at the target surface.

2.2 Plasma/vapor Interaction

As direct heating of the PFM continues by the impinging plasma particles, the surface temperature rises to the point at which significant ablation begins. The produced vapor leaving the surface will accumulate, expand, and interact with incoming plasma particles. The continuous deposition of energy in the vapor layer by plasma particles will produce intense bulk vapor heating and vapor ionization. The ionized vapor will interact with the strong magnetic field, which then limits expansion of the vapor mainly to along field lines. Additional heating of the original exposed PFM surface is only from vapor thermal radiation, vapor thermal conduction, free-energy streaming, and other enhanced plasma radiation losses [11].

Vapor expansion into the vacuum vessel under the influence of a strong magnetic field is determined by solving the vapor magnetohydrodynamic equations for conservation of mass, momentum, and energy:

$$\frac{\partial \rho}{\partial t} + \nabla \cdot (\rho V) = 0 ,$$

(4)

$$\rho \frac{\partial V}{\partial t} + \nabla P = 0 ,$$

(5)

and

$$\frac{\partial E}{\partial t} + \nabla \cdot (EV) + P \nabla \cdot V = \nabla \cdot [K \nabla T + Q_r + Q_b] ,$$

(6)

where **V** is vapor velocity, ρ is vapor density, E is energy, P is pressure, K is vapor conductivity, Q_r is radiation flux, and Q_b is the incident particle-energy flux from the disrupting plasma. All variables of these equations are both time- and space-dependent. The vapor plasma, once ionized, is assumed to move freely along magnetic field lines (r-direction), as shown in Fig. 1. One needs to solve the vapor equation of motion in two directions; along and perpendicular to the divertor surface. The radiation transport equations are not directly affected by the magnetic field and can be solved in one or two dimensions.

The vapor equation of motion in a strong magnetic field environment can be written as:

$$\rho \frac{d^2 r}{d t^2} = -\nabla P + \mathbf{J} \times \mathbf{B} ,$$

(7)

where r is distance along field lines, **J** is vapor current density, and **B** is magnetic flux density. The induced magnetic force **J** x **B** acts as a retarding force to vapor expansion. This force mainly acts in the perpendicular direction to magnetic field lines. The magnetic force is assumed to be composed of a magnetic pressure force, $\mathbf{F_m}$, and a friction force, $\mathbf{F_c}$, due to the curvature of the magnetic field lines, where:

$$\mathbf{F_m} = \frac{1}{\mu_o} \nabla B^2 ,$$

(8)

and

$$\mathbf{F_c} = \frac{1}{\mu_o} \frac{B^2}{R_c} ,$$

(9)

where μ_o is free-space permeability and R_c is the radius of curvature of magnetic field lines. The current density, **J**, is given by:

$$\mathbf{J} = \frac{1}{\mu_o} \nabla \times \mathbf{B} .$$

(10)

The solution of the magnetohydrodynamic vapor equation of motion takes into account magnetic field diffusion in the vapor cloud. The variation of the magnetic field with time can be written as:

$$\frac{\partial \mathbf{B}}{\partial t} = -\frac{1}{\mu_o} \nabla \times \{\mathbf{\varepsilon} + \mathbf{V} \times \mathbf{B}\} ,$$

(11)

and

$$\mathbf{\varepsilon} = \frac{\mathbf{J}}{\sigma} ,$$

(12)

where $\mathcal{E}$ is the induced electric field and σ is vapor conductivity. For a weakly ionized low-temperature, high-density vapor-plasma, the conductivity is given by:

$$\sigma = \frac{4\pi\, n_e e^2}{m_e}\, \tau \tag{13}$$

where n_e is density, e is charge, m_e is mass of the electron, and τ is the vapor plasma collision time. The above equations are solved in 2-D coordinates, i.e., along and across the magnetic field lines. The solution is then transformed to the x (along divertor surface) - y (normal to divertor surface) coordinates, as shown in Fig. 1. Joule heating of the vapor cloud, which is given by J^2/σ, is also taken into account in these calculations.

2.3 Radiation Transport

After enough vapor accumulates in front of the incoming plasma particles, the plasma particles are then completely stopped in the vapor cloud, heating and ionizing it. Continuous deposition of incident plasma energy in the vapor will cause the vapor to radiate photons. The transport of these photons in the vapor layer is very important in determining the fraction of plasma energy transmitted to the PFM and subsequently determining the final erosion rate and lifetime of these components. It is then quite important to correctly model the radiation transport for a wide range of vapor conditions. For quasistationary conditions, the transport equation for the radiation has the form:

$$\Omega \nabla I_\upsilon = \varepsilon_\upsilon - k_\upsilon I_\upsilon , \tag{14}$$

where I_υ is radiation intensity, υ is frequency, ε_υ is vapor emissivity, Ω is the solid angle, and k_υ is the absorption coefficient. Several methods are available for solving radiation transport equations. The most appropriate, however, is the so-called forward-reverse method [22]. This method is more appropriate in treating and describing both optically thick and optically thin plasma conditions. Other popular methods, such as the diffusion approximation are valid only for optically thick plasma and should not be where the vapor is optically thin, particularly for low-Z PFMs. The forward-reverse method treats the photon flux moving to the right (forward) I_υ^+ separately from the photon flux moving to the left (reverse) I_υ^-. For simplicity, in the one-dimensional (1-D) case the radiation fluxes in the forward and reverse direction are calculated for each vapor zone as:

$$\frac{1}{2}\frac{d I_\upsilon^\pm}{d y} = \varepsilon_\upsilon - I_\upsilon^\pm , \tag{15}$$

where y is the perpendicular distance in the vapor zone above the surface. In the two-dimensional (2-D) case, the magnitudes of the forward and reverse photon fluxes for each vapor zone are controlled by the solid angle subtended by the exposed disrupted area and the distance from this area to this vapor zone. Lateral escaping radiation fluxes can be quite high and can affect both vapor hydrodynamics and the resulting erosion rates particularly for smaller exposed surfaces.

In these calculations, the radiation fluxes are composed of two separate components, the continuum radiation flux I_{c_υ} and line radiation flux I_{ℓ_υ}, so that:

$$I_\upsilon^\pm = I_{c_\upsilon}^\pm + I_{\ell_\upsilon}^\pm \ . \tag{16}$$

Therefore, the most intense lines are treated separately using the Collisional Radiative Equilibrium (CRE) method. A set of rate equations is solved for the populations of each individual atomic level. The less intense lines are combined with the continuum radiation. The most intense lines are usually <100 lines for each of the beryllium and carbon materials. Each line is approximated by about 10-20 photon energy groups, depending on line shape and width. Doppler and Stark broadening of the lines of radiation are taken into account as a function of vapor temperature and density for each vapor zone. Multigroup approximations (1000-4000 photon groups) were used for the continuum solution of the above equations. Plank averaging was used for the optically thin regions, whereas Rosseland averaging was more preferred for the optically thick regions [23]. Opacity and emissivity data are provided in the form of tables for a wide range of expected vapor densities and temperatures. The rate of energy loss due to radiation Q_r in each vapor zone can then be given by:

$$Q_r = \frac{1}{\rho} \sum_\upsilon \nabla \cdot (I_\upsilon^+ + I_\upsilon^-) \ . \tag{17}$$

3. VAPORIZATION EROSION

The models described above, including that for the effect of a strong magnetic field on vapor cloud hydrodynamics, are implemented in a new optimized version of the computer code A*THERMAL-S [2,13]. Thermal quench time during the disruption is assumed in this analysis to be 100 μs. Other disruption times can easily be used. Calculations for radiation transport and vapor magnetohydrodynamics are extended up to 10 μs beyond the disruption time to realistically simulate a situation where the vapor and the radiation flux cannot immediately disappear just after the disruption. Disruption energy densities of 10-100 MJ/m^2 are used in this analysis. The effect of both plasma electrons and ions, with different kinetic energies, on the net erosion rate was investigated [11]. The effect of a strong magnetic field on the vapor magnetic hydrodynamics and on the resulting erosion rate was also studied [12]. Detailed effects of radiation transport in the vapor-cloud such as lines and continuum radiation spectra as well as 2-D effect of the radiation transport in the vapor cloud on vapor hydrodynamics and on net erosion were discussed [13]. The main results of these studies are summarized below.

3.1 Effect of Plasma Parameters

Figure 2 shows the time evolution of beryllium surface temperature, melt layer thickness, and eroded thickness for a disruption with 20 keV plasma electrons and 10 MJ/m^2 energy density. The sudden early rise in surface temperature is due to direct electron energy deposition in beryllium. The following decrease in the beryllium surface temperature was caused by the shielding effect of the eroded material above the beryllium surface. The flat temperature behavior during the rest of the disruption was

mainly due to the low generated radiation heat flux in this case. The net ablation erosion rate for the given disruption conditions is about 4 μm, which is substantially lower (more than 25 times lower) than that without the shielding effect [19].
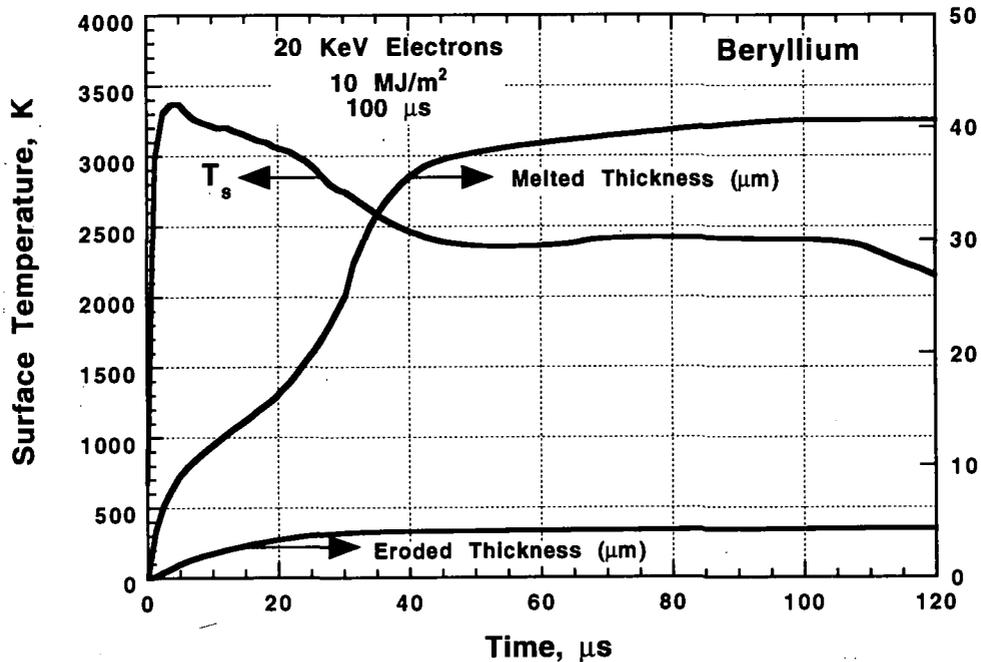
Fig. 2. Change in beryllium surface temperature, melt layer, and eroded thickness with time, following exposure to plasma electrons.

Figure 3 shows the relationship of beryllium solid-liquid-vapor temperatures to distance at two times, i.e., 10 μs and 100 μs, during the disruption. At an early time (10 μs) the solid temperature was higher than at later times because of the direct deposition of plasma electrons. The temperature of the vapor layer at that time was relatively low (≈1 eV) and the vapor layer only expanded to about 3-4 cm above the surface. At longer times, towards the end of the disruption, the solid-liquid temperature was lower because only a small fraction of the radiation energy was deposited on the surface. The vapor had then expanded to distances up to 70 cm above the surface and reached a temperature of ≈ 4 eV.

It is still uncertain, however, what the plasma-particle kinetic energy will be at the divertor plate during a disruption. Estimates range from several keV down to a few hundreds eV. Figure 4 shows the effect of plasma-electron kinetic energy on the erosion rate. Particles with higher kinetic energy usually penetrate the target to a greater depth and result in more erosion rate. However, because more material is eroded by high-energy particles, the vapor, being optically thick in this case, will have a lower temperature and, consequently, emits less radiation flux toward the PFM. This is evident from the slope of ablated thickness in Fig. 4. Particles with lower kinetic energy erode less material and, for the same energy density, result in higher vapor temperatures and thus higher radiation fluxes. The effect of plasma-particle kinetic energy is, however, less of a factor in the case of an oblique and a strong reactor magnetic field.
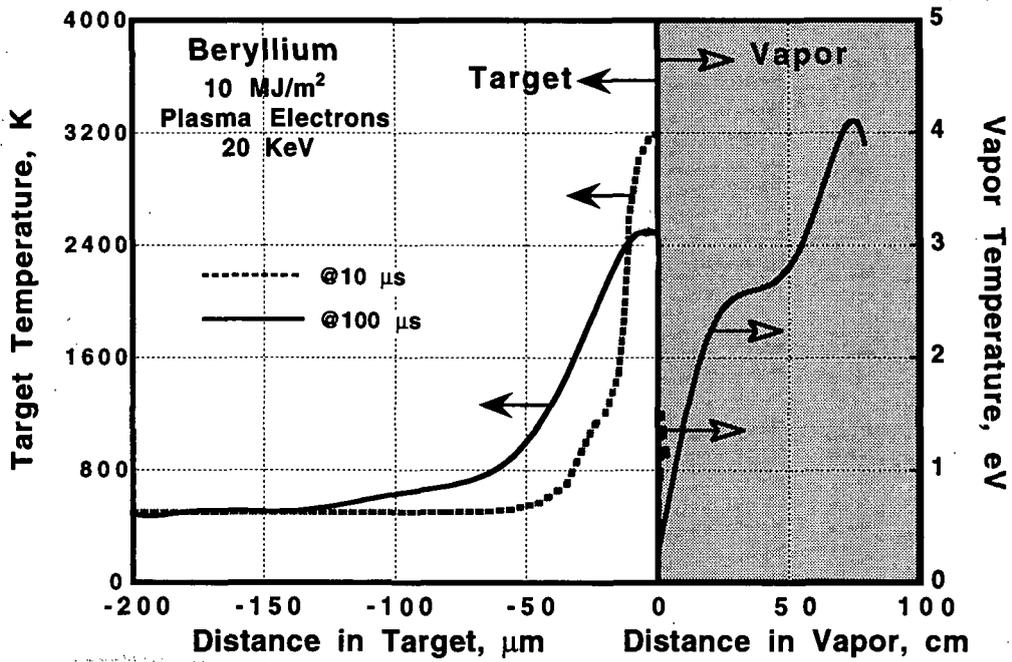
Fig. 3. Relationship of target and vapor temperature to distance at different times during disruption.
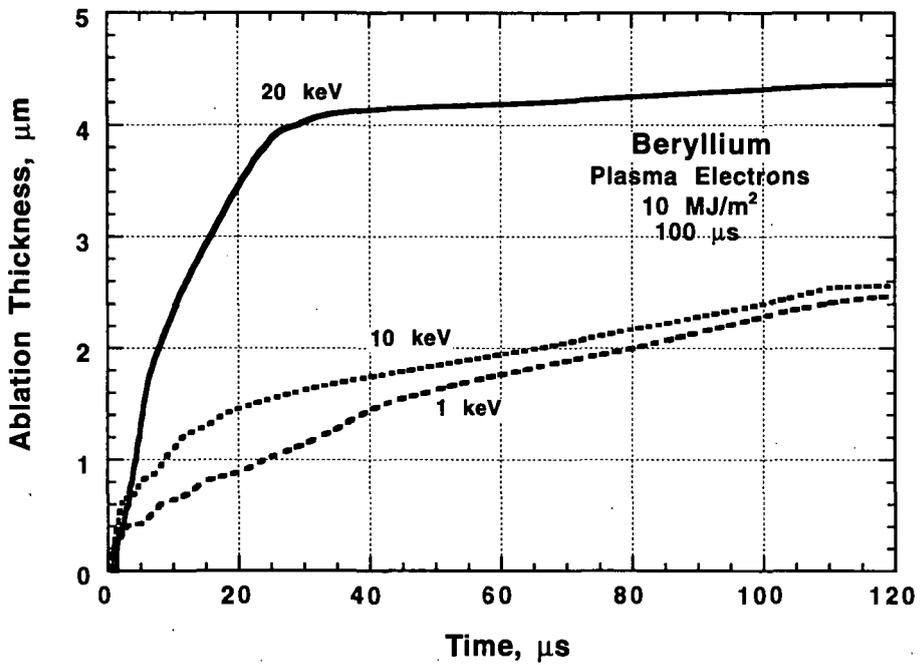
Fig. 4. Effect of plasma-electron kinetic energy on beryllium erosion thickness.

Figure 5 shows the change in temperature of the beryllium vapor front. It can be seen that, in the case of 20 keV plasma electrons, because of both the long range and the large mass of the eroded material, the temperature of the front vapor is only ≈ 3 eV. Particles with lower kinetic energy deposit their energy near the vapor front which results in higher front vapor temperature. This means that the vapor ionization rate is higher. Higher ionization rate means more free vapor electrons, which, in turn, result in a much shorter range of plasma electrons in the vapor because of their additional stopping power, etc. This is the main reason why the 1 and 10 keV incident plasma electrons exhibit the same front vapor temperature, of ≈ 15 eV, halfway through the disruption.
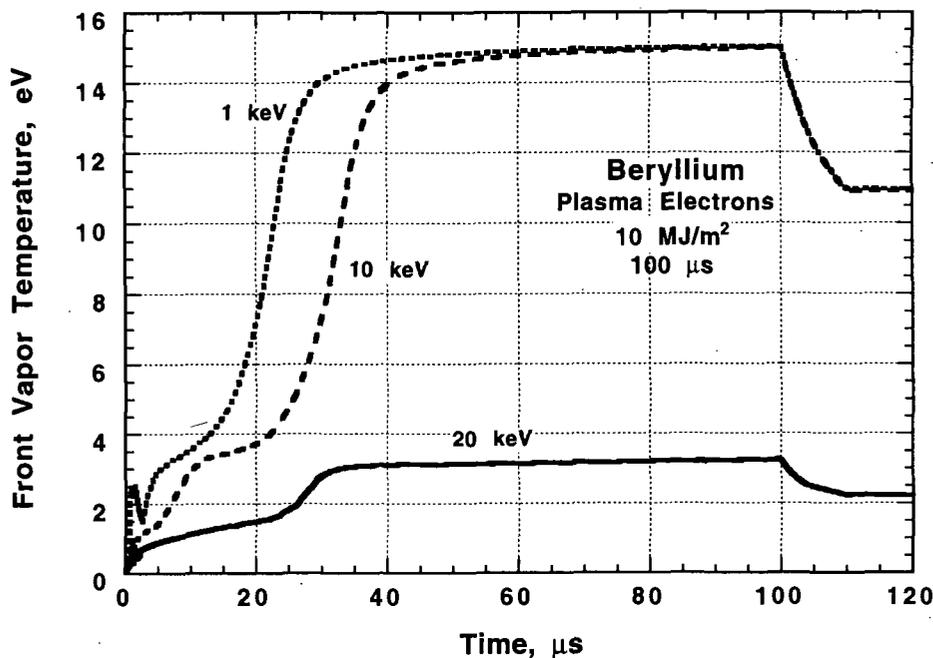
Fig. 5. Change in beryllium-vapor front temperature with time.

The difference between the effect of plasma electrons and plasma ions, with similar kinetic energy on the beryllium erosion rate is also studied. Basically, ions with higher kinetic energy (20 keV) behave in a manner similar to that of electrons with lower kinetic energy (1 keV), where the front vapor zone is heated to higher vapor temperatures and results in some radiation flux reaching the PFM surface. This is due to the fact that ions have a much shorter range than electrons with the same kinetic energy. Ions then produce less erosion than electrons with similar kinetic energy as clearly shown in Fig. 6. However, plasma ions exhibit a much larger momentum than electrons, a circumstance that tends to confine the vapor plasma closer to the PFM surface.

The energy density reaching the divertor plate during a disruption can be much higher than 10 MJ/m² because of the high plasma-energy content. This can also occur if the plasma deposits its energy only on parts of the toroidal divertor plate. Figures 7 and 8 show the effect of higher energy densities (up to 100 MJ/m²) on the erosion rate of carbon and beryllium respectively. An order of magnitude increase in energy density results in an increase of only ≈ 30 - 40% in erosion rate. This is mainly because most of the incident plasma-energy heats only the front regions of the vapor, as shown in Figs. 9

and 10 for carbon and beryllium respectively. This means that most of the radiation flux is emitted in a direction away from the PFM. It can also be seen that, for the same heat flux, carbon erodes more than beryllium; this is because carbon radiates energy more than beryllium which results in more net radiation flux to the PFM and higher free-streaming energy flux from the near-wall vapor zone. In addition, the lower thermal conductivity of carbon has the effect of keeping the surface temperature higher which tends to increase the erosion.
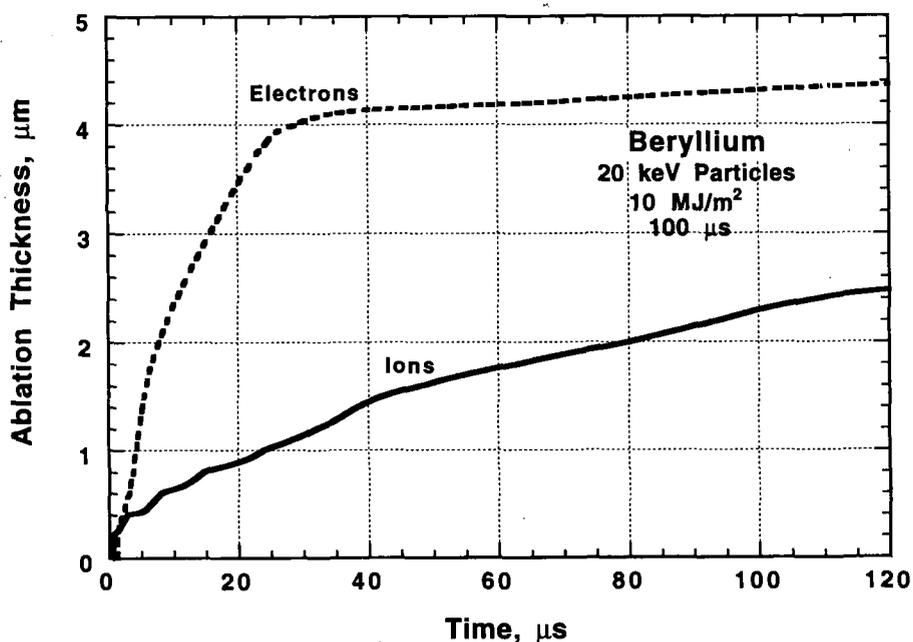
Fig. 6.   Effect of plasma ions and electrons on beryllium erosion thickness.
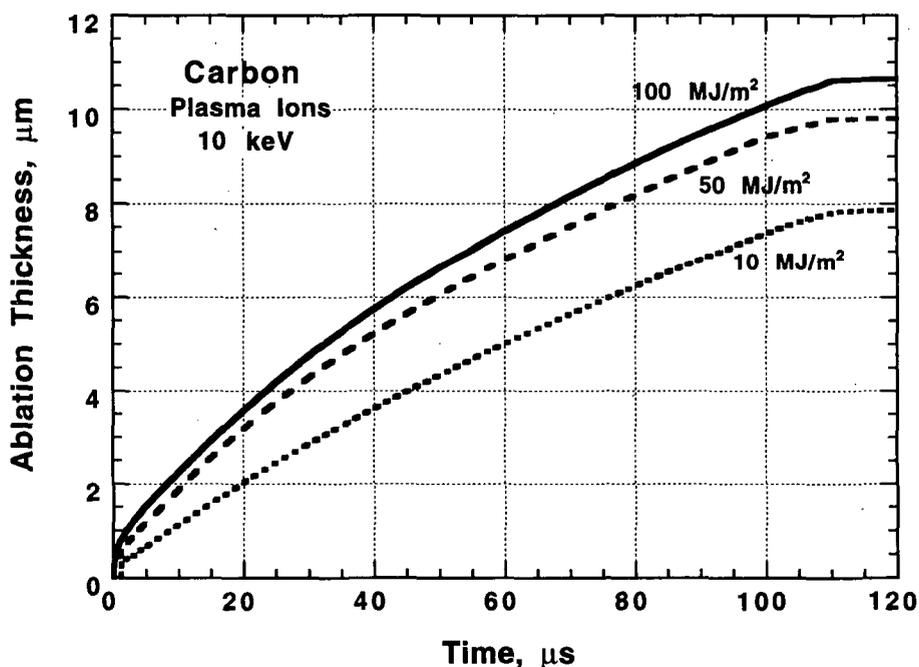
Fig. 7.   Effect of higher disruption energy densities on carbon erosion thickness.
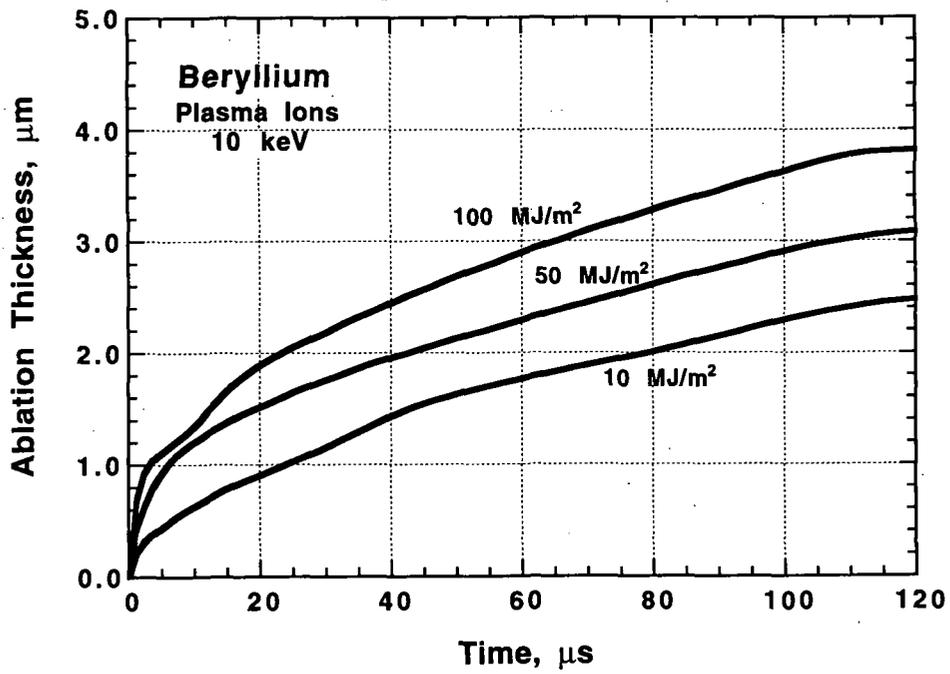
Fig. 8. Effect of higher disruption energy densities on beryllium erosion thickness.
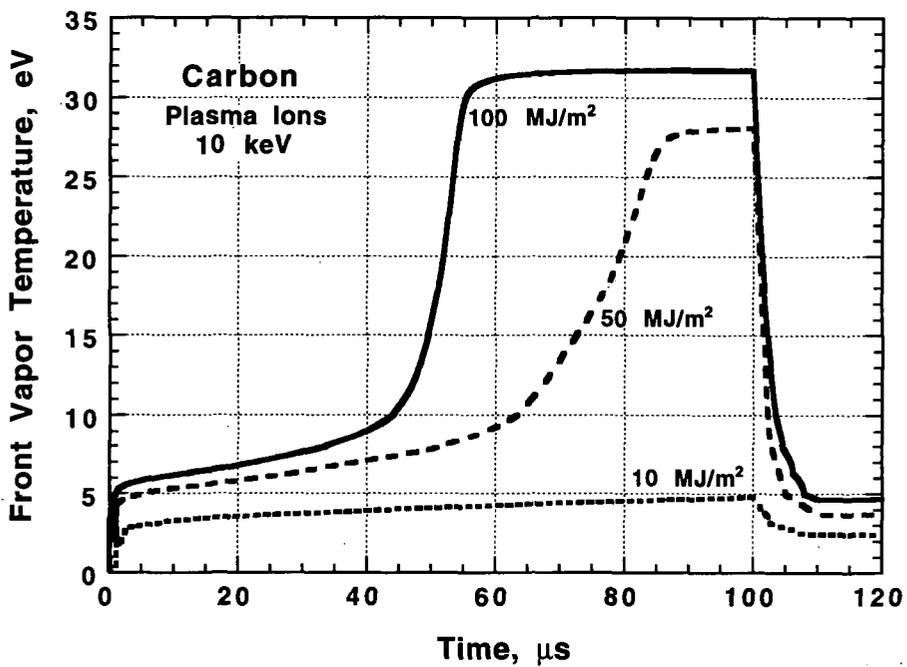
Fig. 9. Effect of higher disruption energy densities on carbon vapor-front temperature.

Beryllium
Ions
10 keV

100 MJ/m²

50 MJ/m²

10 MJ/m²

Front Vapor Temperature, eV

30

25

20

15

10

5

0

0   20   40   60   80   100   120

Time, μs
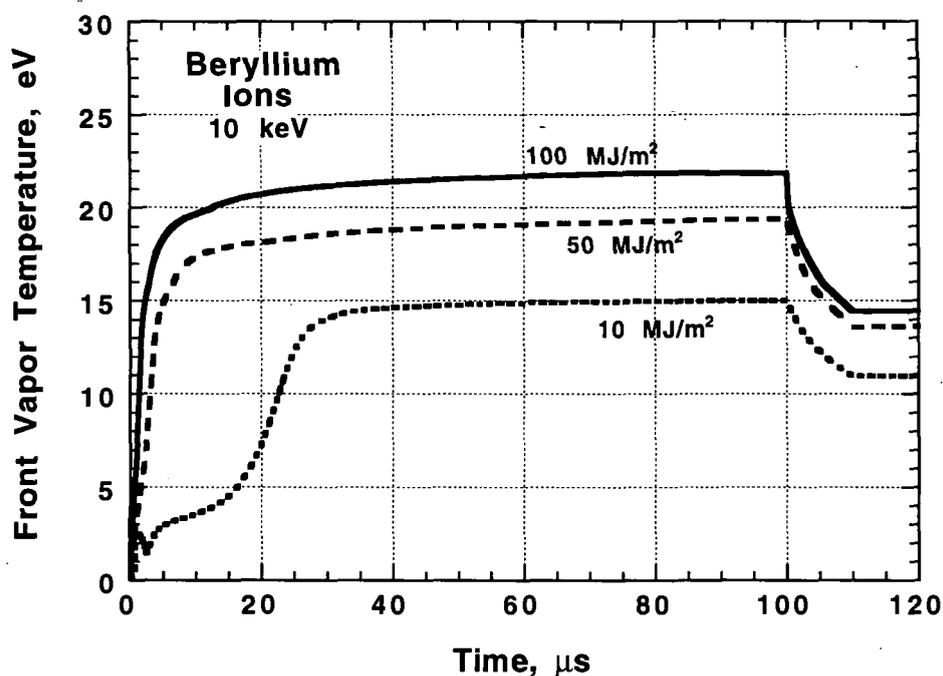
Fig. 10. Effect of higher disruption energy densities on beryllium vapor-front temperature.

3.2 Effect of Line Radiation

Line radiation in the vapor is particularly important for the low-Z and high-temperature vapor-cloud. In most beryllium vapor cases, more than 90% of radiation from the front vapor zone is attributed to line radiation. Figure 11 shows the calculated photon spectrum with and without line radiation from a beryllium vapor during a 50 MJ/m² disruption energy density. Excluding line radiation results in a significant overestimation of the continuum radiation spectrum. Figure 12 shows that excluding line radiation can result in very high vapor temperatures that can significantly affect plasma-vapor interaction and vapor hydrodynamics. However, excluding line radiation has less impact on the resulting overall erosion rate in this case.

3.3 Effect of a Strong Magnetic Field

Figure 13 shows the effect of a 5-T magnetic field on the carbon erosion rate during a 100-μs disruption with an energy density of 10 MJ/m². The inclined magnetic field reduced the erosion rate in this case by about 30%. The magnetic field keeps the vapor cloud more dense and closer to the surface, thus more radiation is absorbed in the vapor and less radiation is transported to the PFM surface. A similar effect is predicted for a disruption on beryllium, as shown in Fig. 14. In this case the magnetic field reduced both erosion rate and melt layer thickness by a factor of 2. The resulting melt layer thickness is much greater than the ablation thickness, which causes a serious concern if the melt layer is lost during the disruption from the various forces acting on the melt layer, as discussed later. The magnetic field is found to be more effective in reducing disruption erosion of beryllium than that of carbon. In fact, where disruption energy density is very high, the magnetic field can slightly increase the carbon erosion rate. This is mainly

because carbon is a better radiative material than beryllium which means that more energy is emitted from a carbon vapor compared to that of a beryllium vapor for the same energy content.
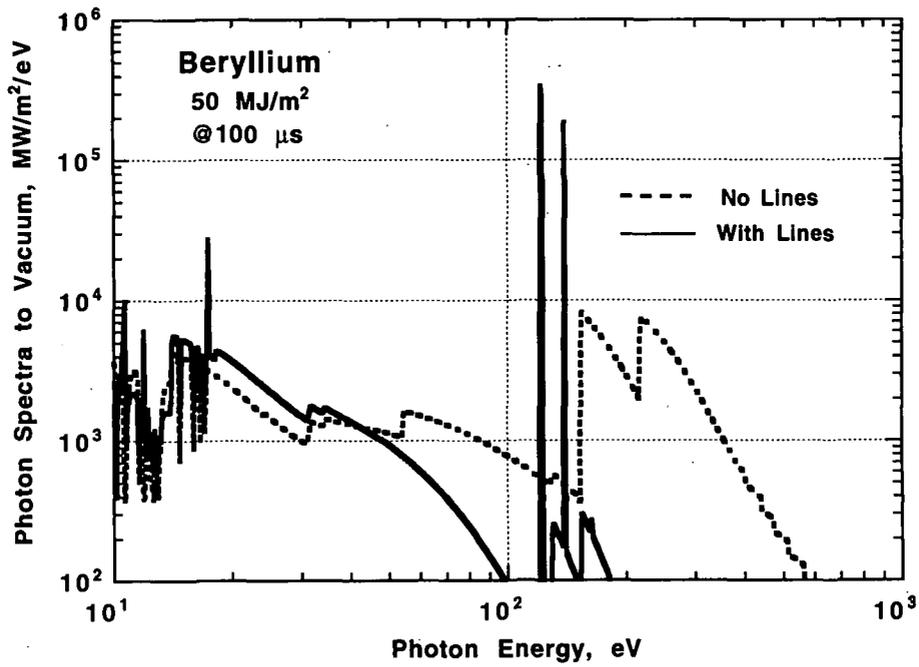
Fig. 11. Photon radiation spectra with and without line radiation.
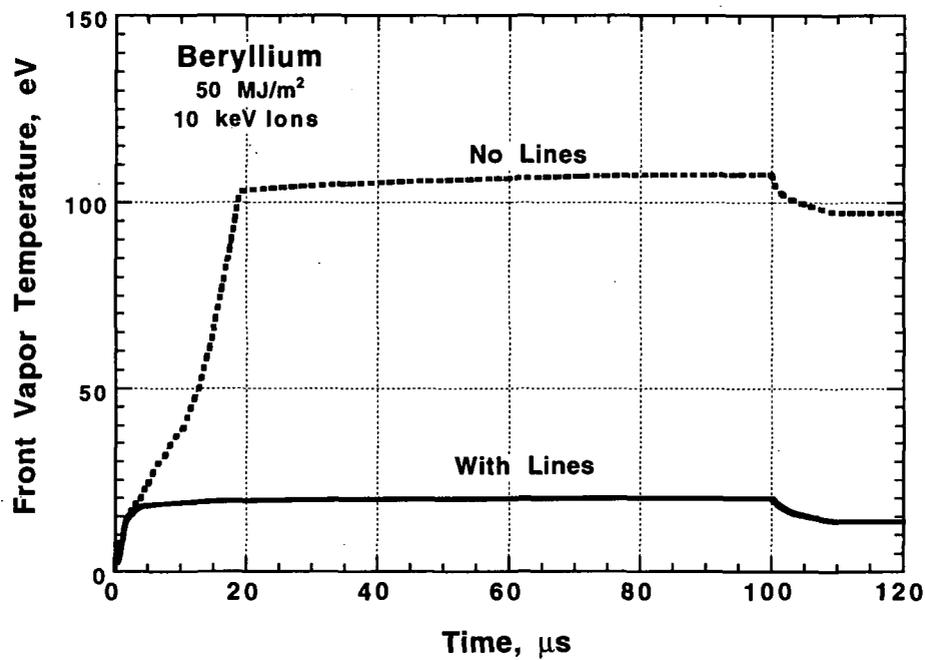
Fig. 12. Effect of line radiation on beryllium front vapor temperature.
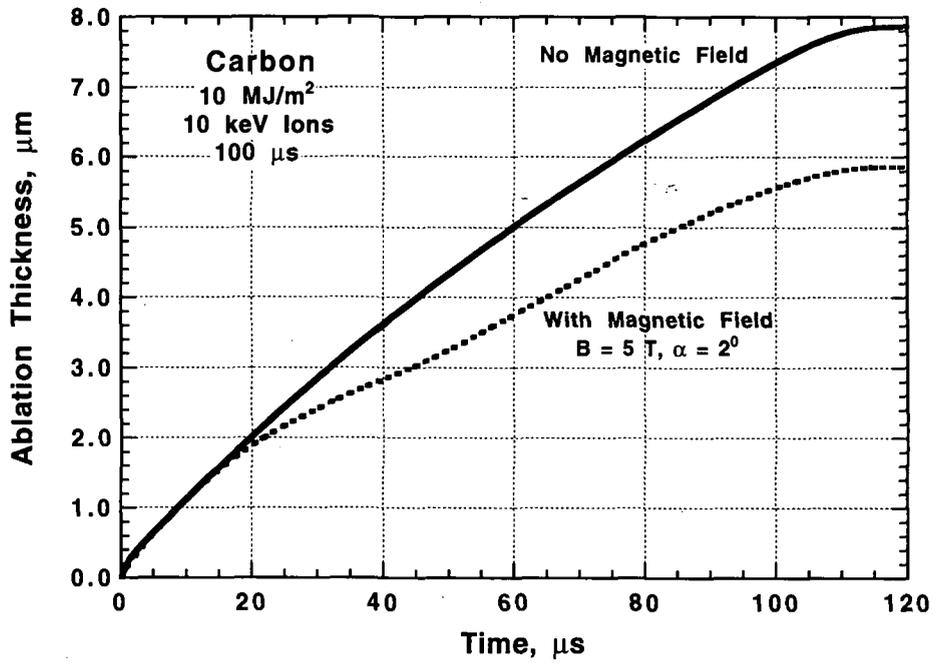
Fig. 13. Carbon erosion rate with and without magnetic field effect during a disruption.
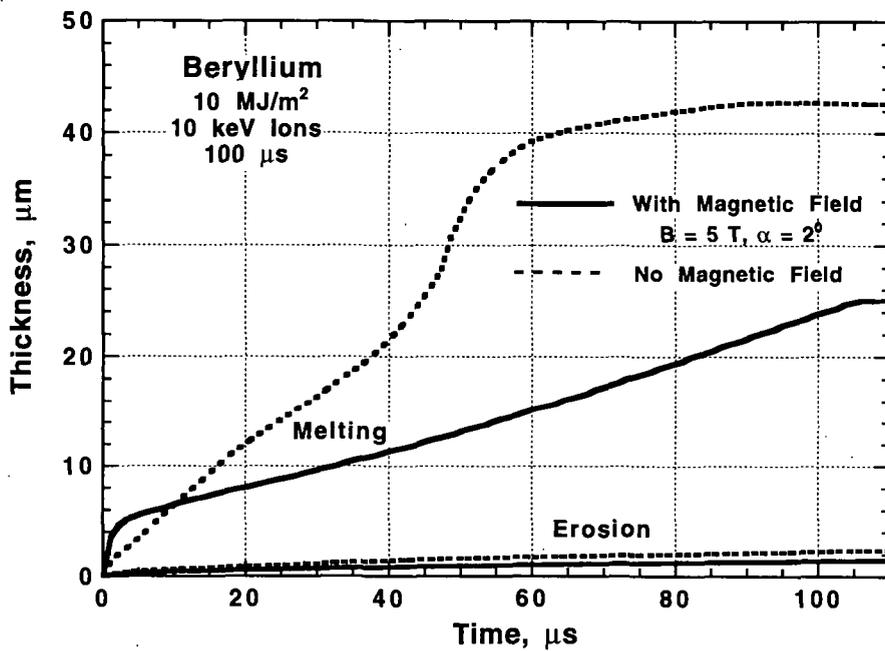

Fig. 14. Beryllium erosion rate and melting thickness with and without magnetic field effect during a disruption.

Figure 15 shows the vapor front temperature of both beryllium and carbon vapor during a disruption. Carbon, being a higher-Z material, radiates more energy than beryllium, which results in a lower vapor temperature at these disruption parameters. At higher disruption power densities, however, the carbon vapor front temperature can exceed that of beryllium due to different radiation physics properties. The higher radiation rate of carbon (radiation cooling) causes more radiation flux to be emitted toward the PFM, which in turn causes more material to be ablated. For the same disruption conditions given in this case, the carbon ablation rate is about two to three times that of beryllium. Vapor shielding is generally expected to be more effective in reducing net energy flux to lower-Z PFM materials than to higher-Z materials.
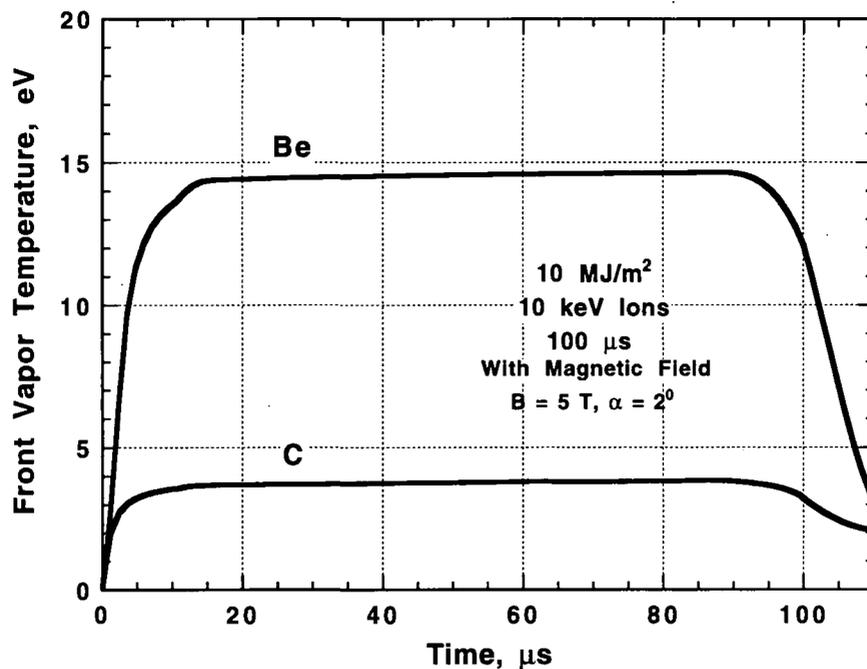
Fig. 15. Front vapor-cloud temperature for both beryllium and carbon during a disruption.

Figure 16 shows the beryllium vapor density and temperature in relationship to the normal distance above the divertor plate with and without a magnetic field. In the absence of a magnetic field, the ablated material expands freely - opposed only by plasma particle momentum - in the normal direction. Once the vapor is ionized in a magnetic field environment its motion follows field lines. Because of the oblique angle of the field lines, vapor expansion normal to the surface is substantially reduced. As a result, vapor density near the divertor plate is much higher which tends to provide better shielding to the PFM surface. However, this higher vapor density tends to increase processes such as vapor conduction, turbulence, and instabilities that can substantially increase the erosion rate. Figure 17 shows the expansion velocity components in the x and y directions under the influence of a 5-T magnetic field. Vapor expansion along the divertor surface is much higher ($\approx$40 times) than in the normal direction. Initially, the normal velocity is higher because the ablated material leaves the surface as neutrals in the normal direction and is not affected by the magnetic field until it is ionized.
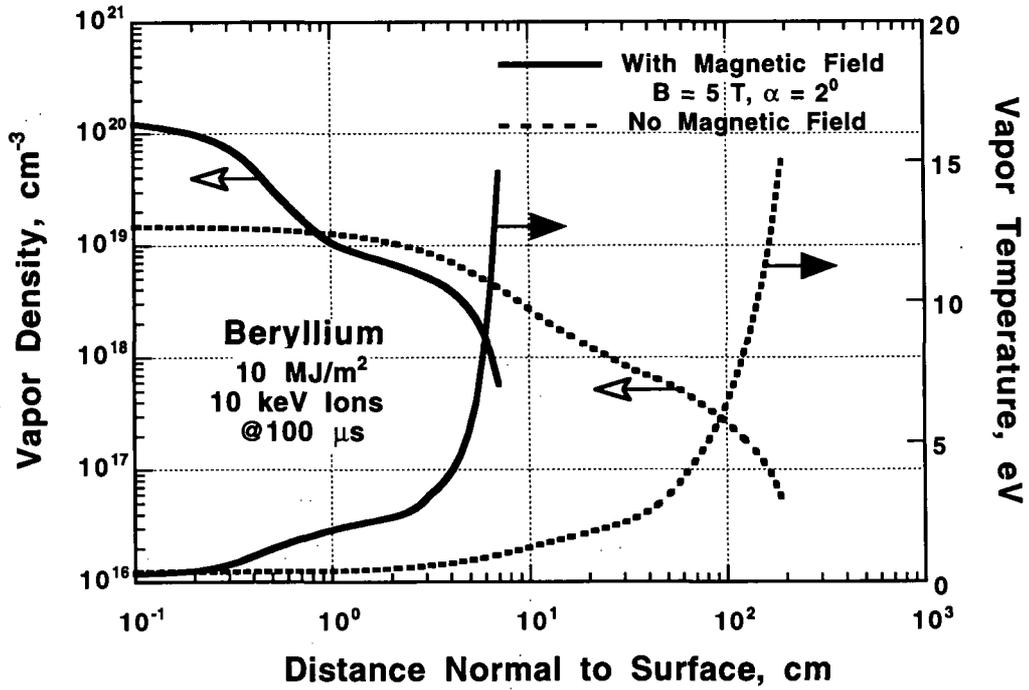
Fig. 16. Effect of magnetic field on beryllium vapor temperature and density.
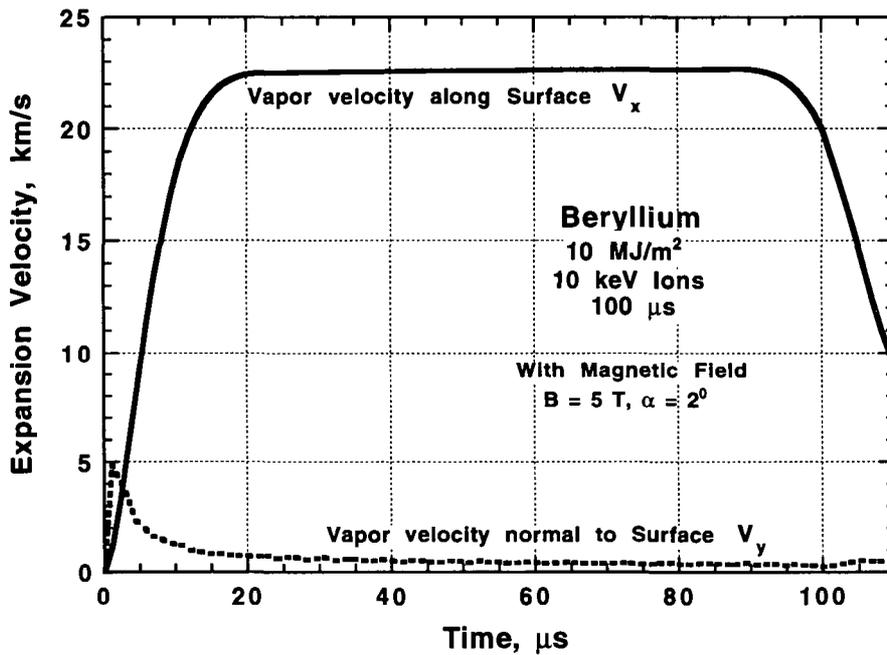
Fig. 17. Beryllium vapor expansion velocities along (V_x) and normal (V_y) to the divertor surface.

210

Figure 18 compares beryllium and carbon vapor density and temperature as a function of normal distance above the divertor plate for the same disruption conditions. Carbon vapor has a higher density and lower temperature, and expands farther in the normal direction, than beryllium. The higher normal expansion is due mainly to the more powerful pressure gradient of the ablated carbon. The lower temperature is mainly due to the increased radiation emitted from the higher-Z carbon vapor. Because of this lower temperature, carbon vapor expansion along the divertor surface is lower than that for beryllium [12].
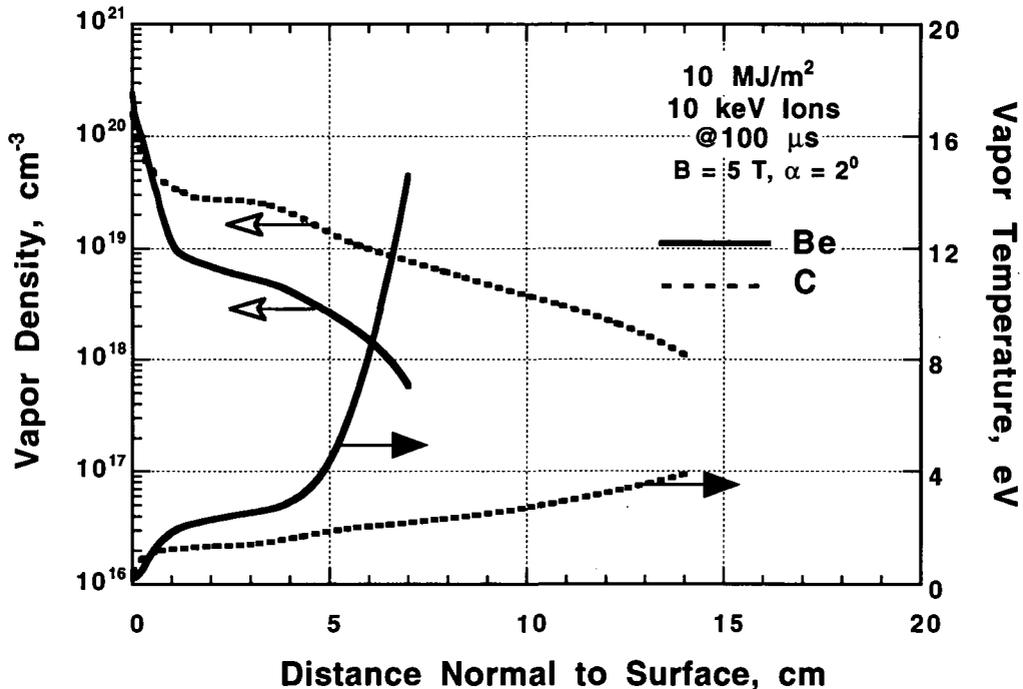
Fig. 18. Beryllium and carbon vapor density and temperature as a function of distance normal to the surface.

4. SIMULATION EXPERIMENTS

Laboratory experiments to simulate plasma disruptions have been actively pursued with several reactor candidate materials and different high-intensity power sources. Among these sources are laser light, electron and ion beams, and plasma guns [24-29]. The majority of these experiments have reactor-relevant disruption parameters (i.e., heat loads of 10-20 MJ/m^2 and deposition time of <1 ms). The erosion results from these experiments, however, do not agree. In particular, recent plasma gun experiments have yielded much lower erosion rates than in previous laser and electron beam experiments. One reason can be the very low particle kinetic energy used in the gun experiments (E < 100 eV). An attempt has been made to evaluate the key factors and differences among these experiments, including the effect of particle kinetic energy, particle type, beam momentum, and multidimensional effects of radiation transport. Because of the small size of the test samples, a two-dimensional multigroup radiation transport model (for both line and continuum radiation) has been developed [13]. In some disruption experiments

211

and conditions, a large fraction of the incident energy is lost and radiated away from the specimen surface, resulting in lower erosion rates.

This analysis is intended to show the effect of particle kinetic energy, the importance of line radiation, the 2-D effects of radiation transport, and the effect of high beam momentum in some simulation experiments on the erosion rate of candidate materials such as carbon and beryllium [13]. In the 2-D calculations, the diameter of the disrupted area is assumed to be 2 cm, a typical size for a disruption simulation experiment.

Figure 19 shows carbon erosion rates from 10 keV ions and 100 keV electrons calculated by both the 1- and 2-D models. The 100 keV electrons case is used because of the relevance to disruption-simulation experiments with high-energy electron beams. The 10 keV ions case is more relevant to a reactor condition. The plasma ions usually have much shorter range in the PFM than do electrons with the same kinetic energy. Shorter range usually means higher surface temperature and thus higher erosion rate. Shorter range in the PFM also means shorter range in the developed vapor material, which means heating the front vapor zone to higher temperatures. Higher vapor temperature, in turn, usually means fast vapor expansion and high radiation fluxes. Both of these factors help substantiate 2-D lateral radiation losses that tend to reduce the net erosion rate, as shown in Fig. 19. However, for the 100 keV electrons, energy deposition inside the PFM is extended over a large mass and the resulting surface temperature in this case is much lower than in the ion case. This results in a much lower erosion rate. Because the high-energy electrons also have a long range in the vaporized material, the electrons do not heat the vapor to higher temperatures, as shown in Fig. 20. Therefore, the vapor will not have enough energy to emit significant photon radiation. This is the main reason that the erosion rate for the electrons is practically the same in both the 1- and 2-D cases. The vapor front temperature in this case remains below 1 eV, resulting in a very low emitted radiation flux.
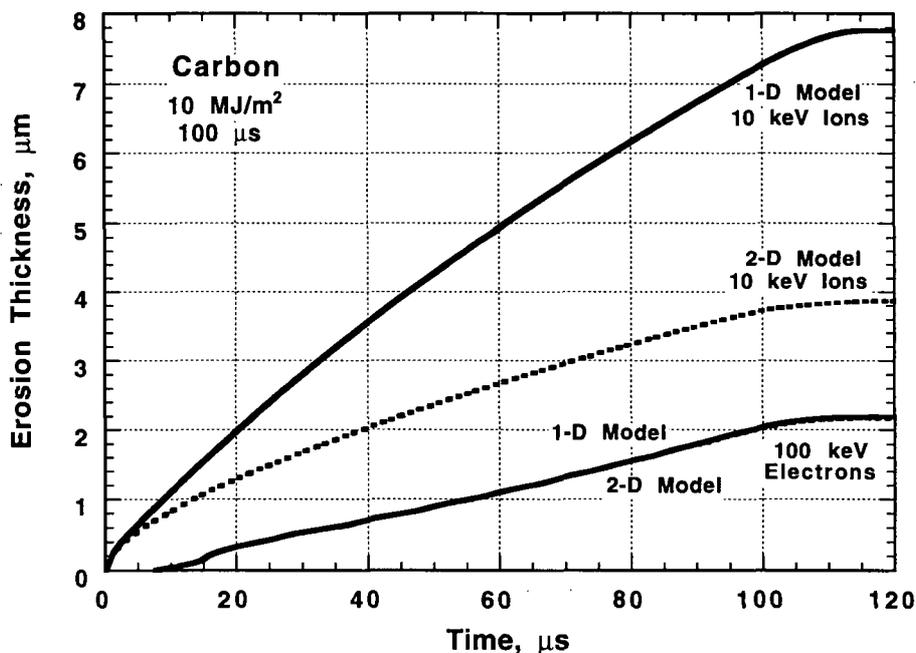

Fig. 19. Effect of particle type and energy on carbon erosion thickness.

212
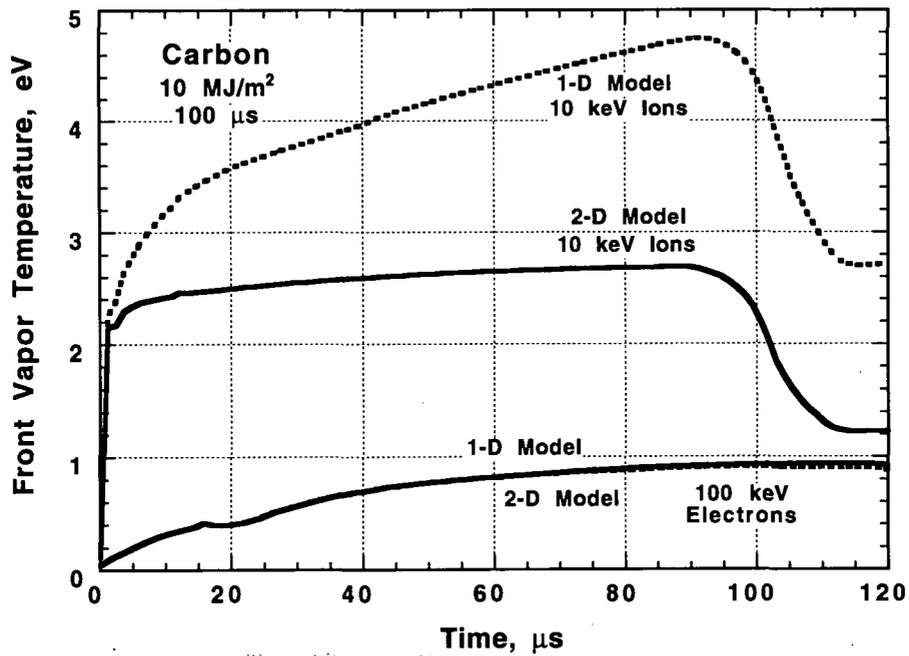
Fig. 20. Front carbon-vapor temperature for different particle types and kinetic energies.

Figure 21 shows the relationship of carbon vapor temperature to distance into the vapor layer above the PFM surface. The higher the vapor temperature, the farther it expands away from the material surface. Again, because of the lower vapor temperature (< 1 eV) in the case of high-energy electron disruption, the carbon vapor only expands to about 20 cm above the surface. Because of escaping lateral radiation in the 2-D model for ions, the vapor temperature is reduced and so is vapor expansion above the surface.
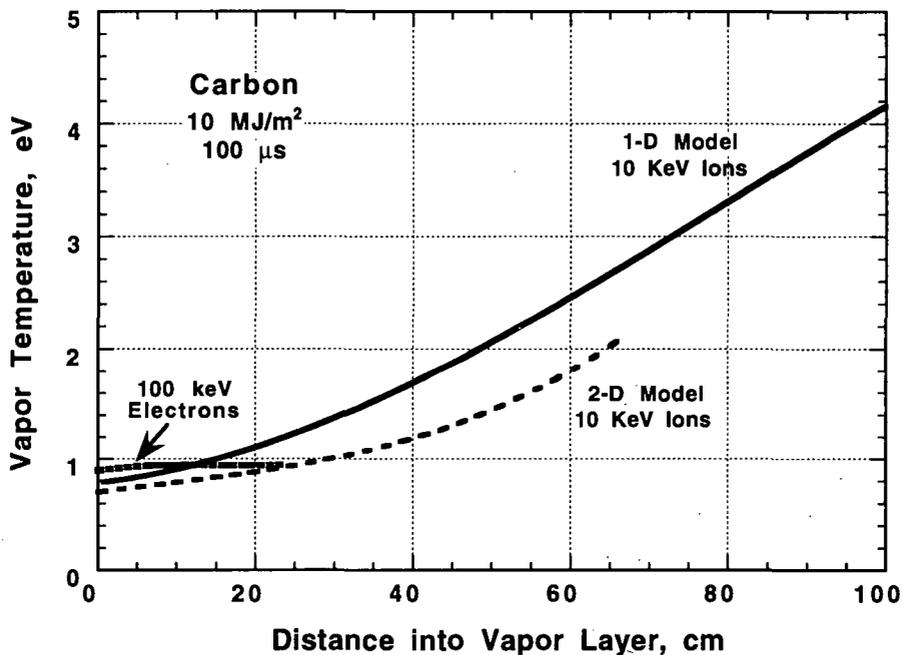
Fig. 21. Relationship of carbon-vapor temperature to distance into vapor layer.

Plasma gun experiments used to simulate disruption have mainly used low-energy hydrogen ions (E < 100 eV). For the same energy density, plasma guns will have high particle momentum (tens of atmospheres). Figure 22 shows the effect of low-energy, high-momentum, plasma gun disruption simulation on carbon erosion rate. Ideally, the high plasma pressure associated with the plasma gun will confine the ablated material closer to the surface, thus reducing 2-D radiation losses, therefore, increasing the erosion rate. However, many uncertainties are associated with plasma gun experiments, including high energy reflection coefficient from the low particle-kinetic energy, plasma-source radiation, and high Z-impurities, that make modeling of such experiments extremely difficult [30]. Nevertheless, these results are in good agreement with recent plasma gun simulation experiments [28].
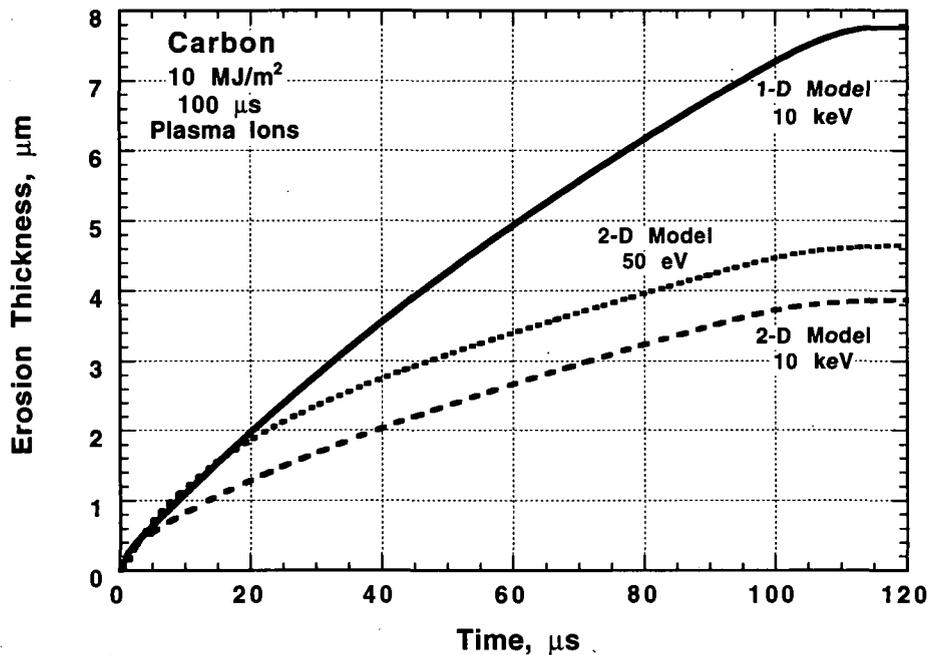
Fig. 22. Effect of low kinetic-energy plasma ions on carbon erosion thickness.

Figure 23 compares beryllium and carbon erosion rates for electron kinetic energies of 10 and 100 keV. At the lower electron kinetic energy, the higher energy density deposited near the PFM surface causes rapid vaporization. Incident energy is then deposited in the front vapor zone heating it to high temperatures. For beryllium, most of the radiation is emitted away from the PFM surface near the high-temperature zone, while for carbon, with its higher Z, more radiation is emitted in general and a higher fraction is directed toward the PFM surface resulting in more net erosion. At higher electron kinetic energy, more energy is initially deposited deep inside the PFM, resulting in lower surface temperature and lower initial erosion rates. However, because of beryllium's higher thermal conductivity, more heat is then diffused from the bulk to the surface, causing significant erosion and melting as shown in Fig. 24. This may explain the high erosion rates of metallic targets in high-energy electron-beam simulation experiments as discussed later. Loss of the resulting thick melt layers from various forces and as a result of melt-layer instabilities during the experiments can significantly contribute to such high erosion rates [25,31].
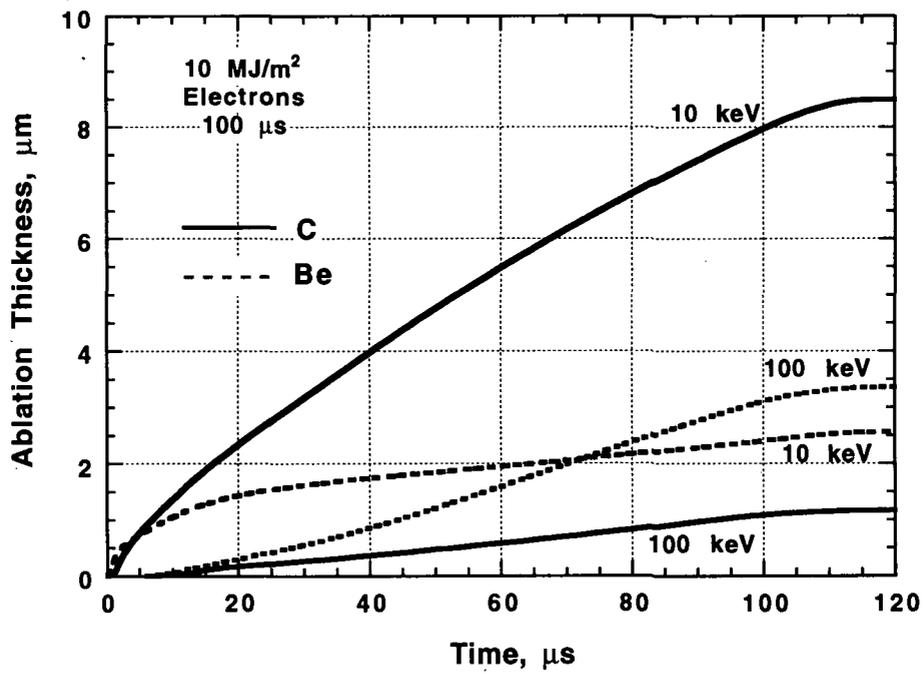
Fig. 23. Beryllium and carbon ablation thickness at different electron kinetic energies.
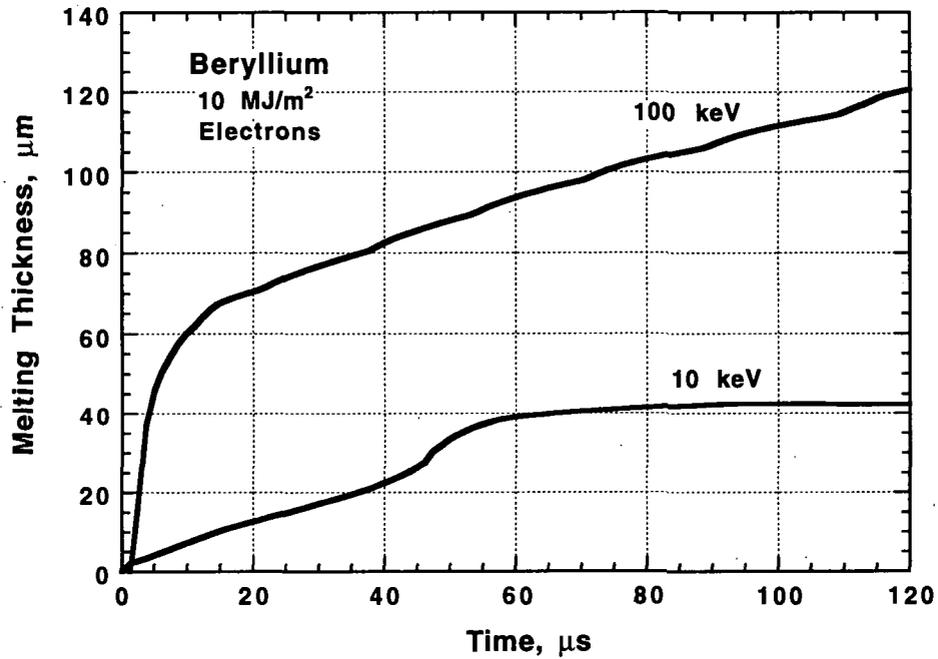

Fig. 24. Beryllium melt-layer thickness at different electron kinetic energies.

215

Laser beam simulation experiments usually produces higher erosion rates from vaporization, mainly because vapor shielding is significantly less important in these experiments [24]. Because of the very small size of the laser beam (diameter ≈ 1 mm) and the high expansion velocity of the vapor, the beam penetrates through the expanded vapor cloud basically unattenuated, thus delivering most of its energy to the target material.

5. MELT-LAYER EROSION

Most previous modeling studies that predict PFM erosion lifetime during disruptions have considered surface ablation losses as the main erosion mechanism. This is partly because carbon-based materials (CBMs), which usually do not melt, were once the favorite choice as PFMs in most reactor design studies. However, because of many potential problems associated with CBMs (including tritium inventory, chemical sputtering, radiation-enhanced sublimation, and neutron irradiation effects), metallic PFMs are now becoming serious candidates for the near-term tokamak machines.

Metallic PFMs, however, will be subjected, to severe melting during disruptions and ELMs. The lifetime estimates of these metallic components should also take into account the potential loss of the melt layer. Erosion of melt layers can critically shorten the lifetime of PFMs, severely contaminate the plasma, and consequently prevent reliable reactor operation.

Previous analysis of disruption erosion has mainly focused on modeling the self-protection of PFM by its own ablated material. It was shown that vapor shielding can significantly reduce vaporization losses of PFMs during reactor disruptions. Also determined was that the resulting Be melt-layer thickness during a typical disruption (10 MJ/m^2 energy density and 100 μs disruption time) is more than one order of magnitude greater than ablation erosion loss. During a disruption, the melt layer will be subjected to various forces such as electromagnetic, gravitational, mechanical, plasma-particle momentum, ablation recoil, and surface tension as shown in Fig. 25 [31]. Detailed interaction of these forces with the melt layer during the disruption will determine the net erosion rate and consequently the lifetime of these components [31]. Recent disruption simulation experiments on Be and on Al targets have shown erosion losses up to 4-5 times greater than those of CBMs for similar disruption simulation conditions [30]. It was evident from postexperimental evaluation that parts of the melted layer had been splashed and lost.

Two important mechanisms that can cause melt-layer loss during a thermal quench disruption are modeled and discussed [14]. One mechanism which can contribute to melt layer loss at high disruption heat loads is melt splashing due to the formation and boiling of volume bubbles. This may result from continuous heating and overheating of the liquid layer during disruptions and ELMs. Another mechanism of melt-layer loss of particular importance is due to instabilities that develop in the liquid layer because of the various existing forces on the melt layer during a disruption. Models to study melt-layer erosion are implemented in the SPLASH computer code [36]. The implications of melt-layer erosion during these abnormal events on the overall performance and lifetime of metallic PFMs are discussed below.
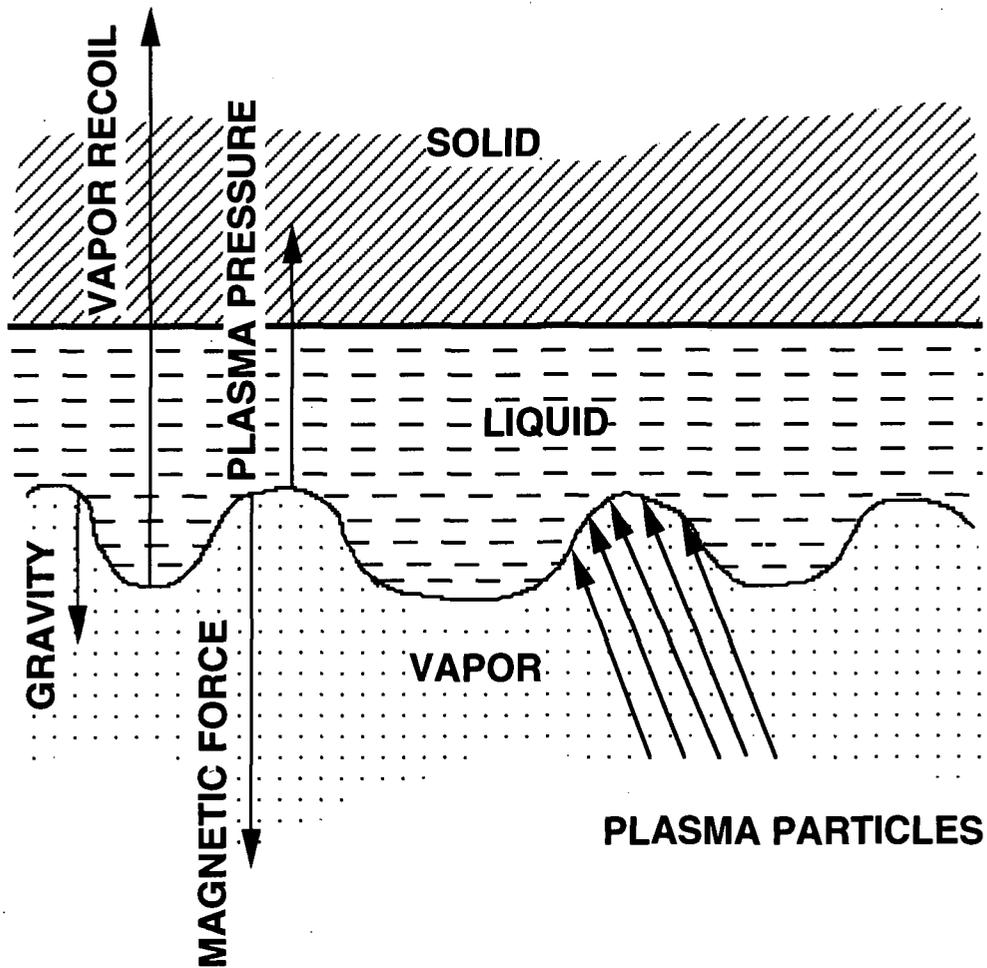
Fig. 25. Various forces acting on the melt layer during a disruption.

5.1 Melt-layer Splashing

During the thermal quench ($\tau_d \approx 100$ μs) of a disruption, energetic plasma ions and electrons will deposit energy densities of 10-100 MJ/m^2 on PFMs, causing surface melting and ablation. The ablated material will form a protective vapor cloud in front of the incoming plasma particles, thereby reducing net energy flux, S_{in}, to PFM, to $S_{in} \leq 0.5$ MW/cm^2 [13]. The surface temperature, T_s, will exceed the equilibrium vaporization temperature, T_v, during parts of the disruption as shown earlier . This overheating $\delta = (T_s - T_v)/ T_s > 0$, along with other factors, will result in the formation of bubbles and bubble growth; and consequently, bubble volume vaporization can occur, leading to ejection and loss of parts of the melt layer, as shown in Fig 26 [14]. Two conditions are necessary for bubbles to grow:

$$S_{in} > S_k + S_v , \tag{18}$$

$$P > 2\sigma/R_o , \tag{19}$$

where

$$S_V = nv \, (5/2 \, kT + q_v) \, , \tag{20}$$

and S_k is heat conduction flux to the bubble surface, P is bubble vapor pressure, σ is bubble surface tension, R_0 is initial bubble radius, nv is vapor flux, and q_v is heat of vaporization. The probability of bubble origination depends on many factors, such as initial material inhomogeneity, injected impurities, and diffusion of defects. Bubble growth and fate can be defined by an energy balance such that:

$$S_k > S_\sigma + S_L + S_V \, , \tag{21}$$

where S_σ is surface energy flux and S_L is kinetic energy of the surrounding liquid. For a typical disruption energy density of 10 MJ/m^2 and a disruption time $\tau_d = 100$ μs, the overheating degree for liquid Be is estimated to be $\delta \approx 0.1$. The maximum bubble radius, R_{max}, can be obtained indirectly from Eq. 21 as $R_{max} \approx 15 \, \delta = 1.5$ μm. An embryonic bubble forming at a depth $h < R_{max}$ can burst and produce liquid drops (splashes), as shown in Fig. 26. To estimate melt-splatter erosion, it is assumed that the erosion has the form of a stationary splashing wave with a velocity, V_s, given by:

$$V_s = dh/dt \approx S_{in}/(q_m + C_v T_v) \, , \tag{22}$$

where q_m is heat of fusion and C_v is specific heat. Numerical simulations of a typical disruption case on Be PFM predicted that $S_{in} \approx 0.2$ MW/cm^2, thus $V_s \approx 0.2$ $\mu m/\mu s$. For $\tau_d = 100$ μs, the splattered melt depth is $h_m \approx 20$ μm. This is much greater than the calculated ablation loss $h_v \approx 2\text{-}3$ μm. These high erosion estimates due to melting are consistent with recent experimental data [30,35].
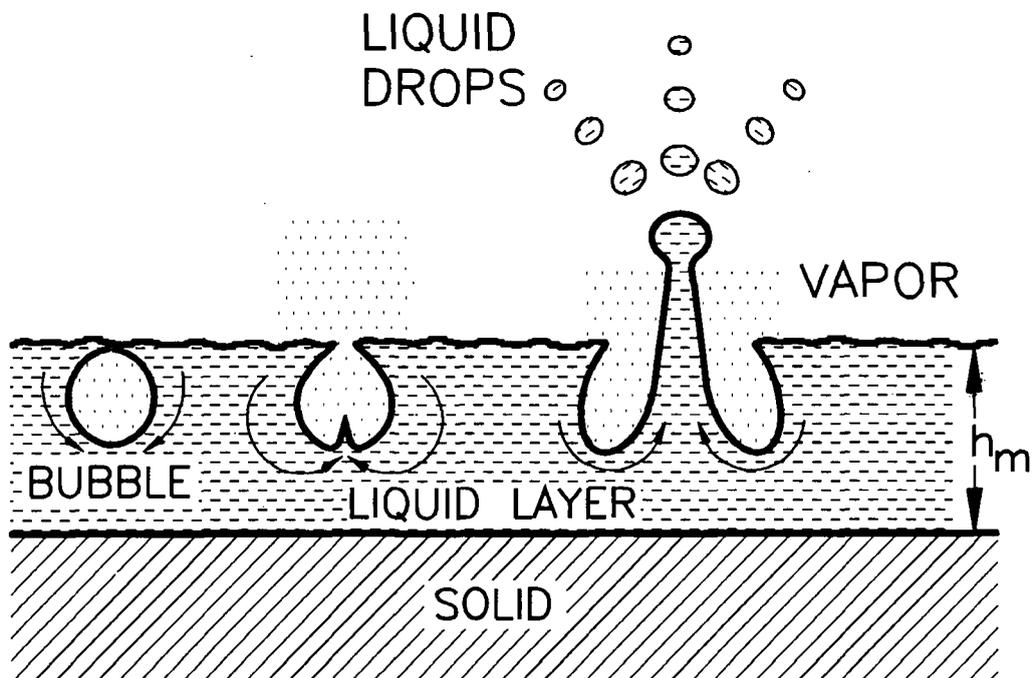

Fig. 26. Melt-layer splashing due to bubble growth and explosion.

This model can also be extended and used to explain the high erosion rates of metallic targets exposed to a high-energy electron beam [25]. At higher electron kinetic energy, more energy is deposited deep inside the target material, causing substantial melting volume. For example at 100-keV electron energy (usually used in simulation experiments), the resulting melt layer is about three times thicker than that for 10-keV electron energy (more relevant to reactor conditions) as previously shown in Fig. 24. In this case, the model discussed above predicts erosion losses > 100 μm, which is in good agreement with the experimental results.

5.2 Melt-layer Instabilities

Another possible mechanism for loss of a melt layer subjected to external forces is the development and growth of hydrodynamic instabilities. At locations where the normal components of these forces, $F_\perp$, act on the liquid surface, Rayleigh-Taylor instabilities may develop [32,33]. Normal components can be produced by a magnetic force, a vapor recoil force, a gravitational force, and by a force due to plasma-particle impact. The interplay of these forces and the dynamics of melt-layer evolution during a disruption will determine the extent of the melt layer loss [31].

The tangential forces during the thermal quench phase, $F_\parallel$ mainly result from plasma impact momentum "plasma wind" into the liquid surface due to the oblique magnetic field. This momentum, M, can be given by [14]:

$$M = \int \rho \; V_\parallel \; V_\perp \; dt \approx P_o \tau_d \; \text{Sin} \; \alpha \; , \tag{23}$$

where $V_\parallel$ and $V_\perp$ are plasma flow velocity components, P_o is plasma pressure, and α is the angle between the magnetic field lines and the divertor plate surface. The liquid metal then moves as a result of absorbing this momentum, as shown in Fig. 27, with a velocity given by:

$$V(x,t) = V_o(t) \; \text{erfc} \, (x \, / \sqrt{4 v \tau}) \; , \tag{24}$$

where x is distance from the surface, ν is kinematic viscosity, and V_o is the velocity at the liquid surface determined by disruption parameters. For a typical disruption, the characteristic depth of the liquid flow $h_u < 5$ μm, much less than melt layer depth ($h_m \approx$ 40 μm). The liquid flow is then unstable and is subject to a Kelvin-Helmholtz instability. The time constant, γ_{max}, for such instability to develop can be estimated from the Orr-Sommerfeld equation for this frictional boundary layer where:

$$\gamma_{max} \approx 0.1 \; V_o/h_u \; . \tag{25}$$

For time $t = 1/\gamma_{max} \approx 10^{-8} << \tau_d$, the unstable wave has enough time to grow and its amplitude, A, can increase to high values. This leads to a very unstable wave (kA >>1), where the liquid drops originate due to capillarity, as shown in Fig. 28. This time is usually estimated as $\tau^* = 100 \; C/\gamma_{max}$, where $C \approx 1$. In time τ^*, the plasma momentum

diffuses to depth h_u. For $\alpha = 6°$, $v = 5 \times 10^{-4}$ cm^2/s, one can show that $h_u \approx 0.6$ μm and $V_0 \approx 3 \times 10^3$ cm/s. Using the same assumption as for the stationary splashing wave, the erosion rate from this instability can be estimated as:

$$U = dh/dt = h/\tau^* = 0.33 \,. \tag{26}$$

The Be erosion depth from this instability can be estimated as $h = U \cdot \tau_d \approx 33$ μm, which is also comparable to recent simulation experiments [30].
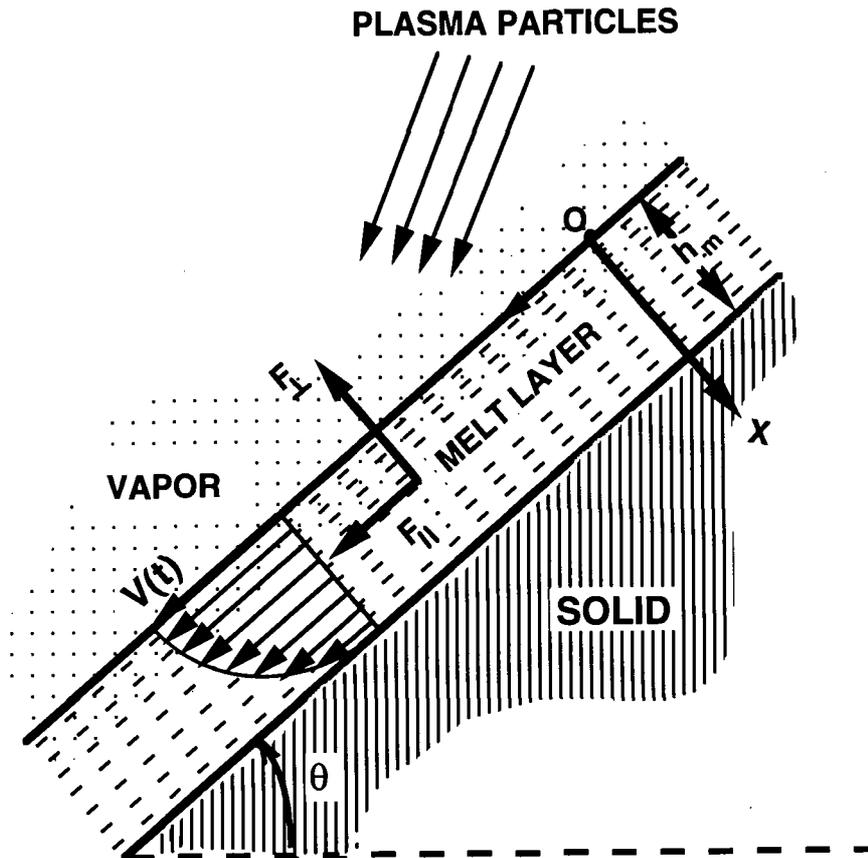

Fig. 27. Melt-layer motion and erosion due to tangential forces.

The interaction of various forces during the disruption and the existence of the vapor cloud above the liquid surface may affect the stability and splatter behavior of the melt layer. Surface rippling and roughening can also result from the vapor pressure above the surface depressing the liquid layer [34]. Magnetic forces generated from current decay during the current quench phase of disruption can also cause instabilities and loss of the melt layer [31]. Mechanical vibrations associated with reactor disruption can shake-off parts of the liquid layer causing surface erosion. In addition, if the melt layer is lost as soon as it develops, particularly at longer disruption times, PFM lifetime can be further reduced, and successful reactor operation may not be achievable.
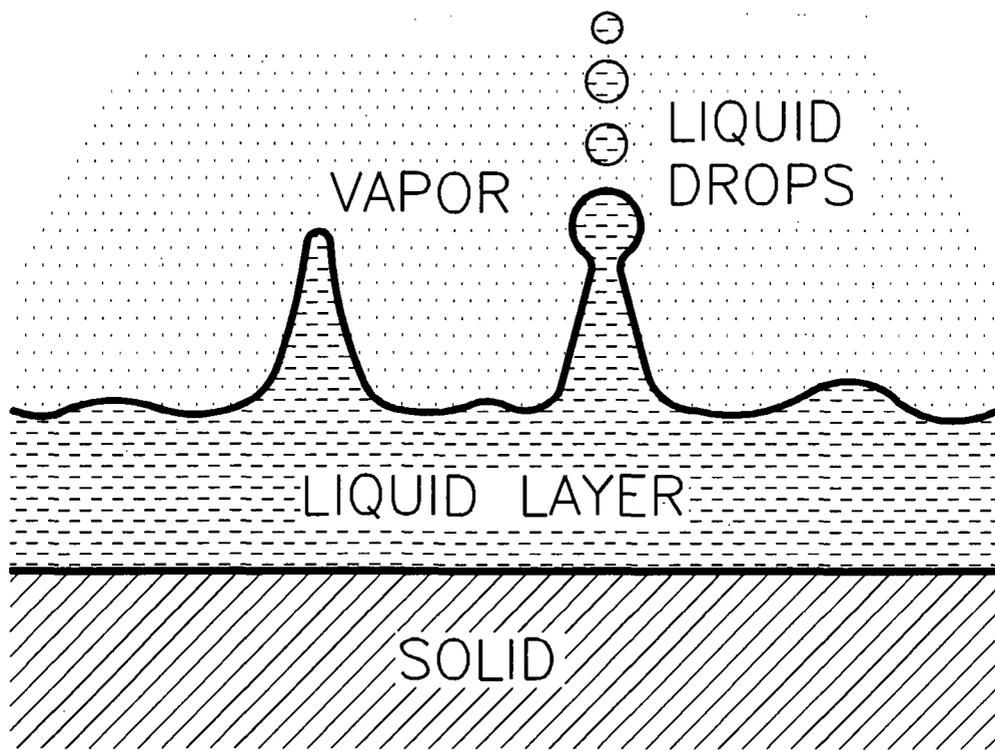
Fig. 28. Melt-layer erosion due to developed hydrodynamic instabilities.

6. LIFETIME ESTIMATES

Because of the high heat load expected during normal operations, and due to design limitations on the maximum allowable surface temperature, it is assumed in this study that typical initial thicknesses of beryllium coating and carbon tiles are 5 and 10 mm, respectively. It is further assumed that 50% of this initial thickness can be sacrificed to disruption erosion before repair of the beryllium coating or replacement of the carbon tiles becomes necessary. Figure 29 shows the maximum allowable number of disruptions for beryllium and carbon materials at various incident plasma energy densities. If the beryllium melt layer is lost during the disruption, the beryllium disruption lifetime is only limited to less than 100 disruptions. If the melt layer is lost as soon as it develops, however, disruption lifetime can be severely shortened. A one-order-of-magnitude increase in energy density reduces the disruption ablation lifetime by a factor of only ≈2. This is because higher incident plasma energy densities are mainly used to heat the front regions of the vapor and only a small fraction of this energy is transmitted to and deposited on the PFM surface as it was shown earlier.

The effect of plasma particle kinetic energy on erosion thickness is less important in a magnetic field environment. This is due to the oblique angle of incidence of the magnetic field lines (≈ 2°-5°) to the divertor plate surface. This substantially shortens the range of the plasma particles in both the PFM and the ablated material, resulting in more surface energy deposition rather than volumetric deposition. However, if a sheath potential is developed during disruption, plasma particles can be accelerated to much higher energies. The magnetic field helps reduce the 2-D radiation transport losses

221

because it confines the vapor cloud near the surface of the divertor plate. However, this tends to increase the erosion rate because less radiation escapes to the vacuum chamber away from the PFM surface [13].
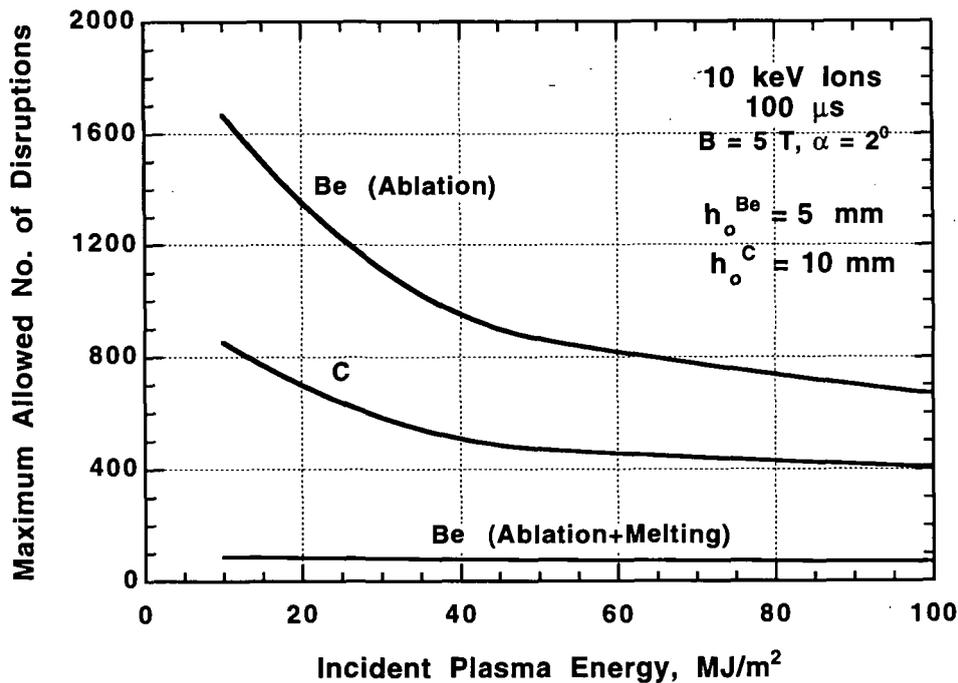

Fig. 29. Maximum allowable number of disruptions for various incident energy densities.

Additional detailed analysis is required for several important issues that can affect net erosion rate and consequently the lifetime of the divertor plate. Uncertainties in disruption parameters such as incident energy density and disruption time are very important in determining ablation rate, melt-layer thickness, development of melt-layer instabilities, and potential loss of the melt layer. Vapor thermal conduction with turbulence, as well as development of vapor instabilities, may significantly increase heat flux to the PFM, resulting in a large increase in erosion rate. Magnetic field edge effects should be investigated where the ablated material is not fully ionized and can escape confinement by the magnetic field, resulting in much less shielding for the PFM. In addition, vapor diffusion across the magnetic field lines can be quite high particularly at low vapor temperatures near the PFM surface which tends to significantly reduce the protection from the vapor-cloud.

7. CONCLUSIONS

A two-dimensional magnetohydrodynamic and radiation transport model recently developed to take into account detailed interaction physics of the vapor cloud with the reactor magnetic field was used to study PFMs response to a plasma disruption. Included are fine-detailed effects such as magnetic field diffusion, induced electric field, vapor conductivity, Joule heating of the vapor, and 2-D lateral radiation transport for both line and continuum radiation spectra. This model is integrated with a recently developed comprehensive model that realistically solves the problem of three moving boundaries,

i.e., vapor expansion, surface recession, and liquid metal propagation front. Models for material thermal evolution with phase change, vapor magnetohydrodynamics, and radiation transport are then dynamically linked, integrated, and numerically optimized for realistic evaluation of disruption effects in reactor environment.

The reactor magnetic field may help reduce erosion rates during a disruption at lower energy densities. The inclined field, however, will reduce 2-D radiation transport losses which have the effect of increasing erosion rates particularly for higher energy densities. Edge effects due to oblique incidence of the magnetic field as well as vapor diffusion across field lines may reduce vapor accumulation in front of the incoming plasma, which has the effect of increasing erosion rates. In addition, higher vapor density due to magnetic field confinement enhances processes such as vapor conduction, turbulence, and instabilities which all tend to increase erosion rates.

Models and preliminary calculations have also been presented to study the potential loss of the melt layer during disruptions and ELMs. Hydrodynamic instabilities, as well as melt-layer splashing due to bubble vaporization, can lead to melt-layer erosion. Melt-layer loss during a disruption can significantly reduce PFM lifetime and critically diminish the economic feasibility of the reactor. More-detailed modeling and simulation experiments are required to accurately predict melt-layer erosion during such abnormal events.

REFERENCES

[1]   A. Sestero and A. Ventura, J. Nucl. Mater. 128 & 129 (1984) 828.
[2]   A. Hassanein et al., Nucl. Eng. Design/Fusion 1 (1984) 307.
[3]   B.J. Merrill and J.L. Jones, J. Nucl. Mater. 111 & 112 (1982) 544.
[4]   H. Bolt et al., J. Nucl. Mater. 196-198 (1992) 948.
[5]   A. Hassanein and D. Ehst, J. Nucl. Mater. 196-198 (1992) 680.
[6]   B. Goel et al., Fusion Technology (1992) 272.
[7]   W. Höbel et al., J. Nucl. Mater. 196-198 (1992) 537.
[8]   R.R. Peterson, Radiative Heat Transfer in Self-Shielding Vapor Layer During Tokamak Disruptions, UWFDM-357 (1983).
[9]   A. Hassanein , Fusion Technology Vol. 19 (1991) 1789.
[10] J. Gilligan et al., J. Nucl. Mater. 162-164 (1989) 957.
[11] A. Hassanein and I. Konkashbaev, "Comprehensive Model for Disruption Erosion in a Reactor Environment," presented at the 11th International Conference on Plasma-Surface Interactions, Mito, Japan, May 22-27, 1994. To be published in J. Nucl. Mater.
[12] A. Hassanein and I. Konkashbaev, "An Assessment of Disruption Erosion in the ITER Environment," presented at the 3rd Int. Symp. on Fusion Nuclear Technology (ISFNT-3), Los Angeles, CA, June 27-July 1, 1994. To be published in Fusion Engineering/Design.
[13] A. Hassanein, "Plasma Disruption Modeling and Simulations, " invited paper presented at the 11th Topical Meeting on the Technology of Fusion Energy, ANS, June 19-23, 1994. To be published in Fusion Technology.
[14] A. Hassanein et al., "Erosion of Melt Layers Developed during a Plasma Disruption," presented at the 18th Symposium on Fusion Technology (SOFT), Karlsruhe, Germany, August 22-26, 1994. To be published in Fusion Technology.
[15] J. Gilligan and D. Hahn, J. Nucl. Mater. 145-147 (1987) 391.

[16] A. Hassanein, J. Nucl. Mater. 122 & 123 (1984) 1453.
[17] S.I. Anisimov and A.Kh. Rakhmatulina, Sov. Phys. JETP, Vol. 37 (1973) 441.
[18] A. Hassanein and D. Smith, J. Nucl. Mater. 191-194 (1992) 503.
[19] A. Hassanein, ASME, 88-WA/NE-2.
[20] R.J. Procassini and C.K. Birdsall, Phys. Fluids B3 (8) (1991) 1876.
[21] Y.L. Igitkhanov et al., Sov. J. Plasma Phys. 12 (1) 1986.
[22] B.N. Chetverushkin, Mathematical Modelling of the Radiative Gas, Nauka, Moscow (1986).
[23] I.V. Nemchinov, "The Averaging of the Radiation Transport Equations for the Radiation Transport in Gas," VINITI, N1721-83, Moscow, 1983.
[24] J.G. Van der Laan et al., J. Nucl. Mater. 196-198 (1992) 612.
[25] J. Linke et al., J. Nucl. Mater. 196-198 (1992) 607.
[26] M. Akiba et al., J. Nucl. Mater. 191-194 (1992) 373.
[27] V.R. Barabash et al., J. Nucl. Mater. 187 (1992) 298.
[28] J. Gahl et al., J. Nucl. Mater. 191-194 (1992) 454.
[29] M. Bourham and J. Gilligan, 15th IEEE/NPSS Symp. on Fusion Engineering, Vol. I (1994) 23.
[30] A. Hassanein et al., J. Nucl. Mater. 212-215 (1994) 1272.
[31] A. Hassanein, Fusion Technology 15 (1989) 513.
[32] S. Feldman, J. Fluid Mech. 6 (1959) 131.
[33] W. Wolfer and A. Hassanein, J. Nucl. Mater. 111 & 112 (1982) 560.
[34] H. Cline and T. Anthony, J. Appl. Phys. 48 (1977) 3895.
[35] V. Kozhevin, private communication.
[36] A. Hassanein, to be published.

RUNAWAY ELECTRON EFFECTS

H.-W. BARTELS
Max-Planck-Institut für Plasmaphysik, EURATOM-IPP Association
Boltzmannstr. 2, D-85748 Garching
Germany

T. KUNUGI
Japan Atomic Energy Research Institute
Tokai-mura, Naka-gun
Ibaraki, 319-11
Japan

A.J. RUSSO[1]
Sandia National Laboratories
Albuquerque, NM 87185
United States of America

ABSTRACT. One of the possible consequences of tokamak operation is the generation of runaway electrons which can impact plasma facing components and cause damage due to high local energy deposition. This problem becomes more serious as the machine size and plasma current increases. Since large size and high currents are characteristics of proposed future machines, control of runaway generation is an important design consideration. The impact of runaway electrons on plasma facing components can be quantitatively studied with Monte Carlo codes which simulate the various processes leading to energy losses of the electrons. Some of these codes (GEANT3 and EGS4) originate from high energy physics where they have been used for many years to model detector responses. The accuracy of the codes is estimated to be better than 20%. Another code package (PTA) was developed specially for fusion purposes, and electron beam experiments were used to validate it. It is important to include the magnetic field in the analysis. It causes bending back of reflected charged particles and reduced penetration depth of the electrons due to gyration of the electrons around the magnetic field lines. Cooling tubes covered with 1 cm of graphite will melt at about 50 (25) MJ/m^2 if molybdenum (copper) is used. A bare metallic wall is prone to melting at about 15 MJ/m^2.

1 Introduction

Among many other design restrictions on plasma facing components, runaway electrons (RE) are of serious concern since some of the first wall damage to existing tokamaks has been caused by generation of a beam of high energy electrons during thermal quench of a disruption. The electrical resistance of electrons in a plasma decreases with energy. Therefore, it is possible to have some electrons in the high energy part of the thermal Gaussian spectrum which gain more energy in an electric field than they lose by friction. Subsequently their friction decreases further and the electrons run away [1]. The maximum energy of an electron for a given constant loop voltage in the plasma chamber is limited either by the synchrotron radiation (radiated energy per loop less than or equal to the gain from the loop voltage) or by the time available for acceleration (volt-seconds).

A wide range of signatures of RE in tokamaks has been observed. The most unpleasant signature is some localized damage of first wall components [2]. More quantitative information has been deduced from the neutron production measured during RE – first wall impact, where bremsstrahlung triggered (γ,n) reactions [3]. Either the neutrons can be measured directly or the resultant activation in the first wall materials can be examined. Many activation products are formed by threshold reactions which need electron energies above 30 MeV. The

---

spatial distribution of the RE impact can also be determined from the distribution of activation products. Another sign of RE in tokamaks is hard X-ray bursts produced by the interaction of RE and first wall material, as observed in JT60 [4]. During disruptions in JET direct observation of RE was performed by measuring hard X-rays generated by interaction of RE with the background plasma [5].

For next step fusion experiments the expected occurrence rate of RE's is quite uncertain and is dependent on plasma operation and first wall design. It was observed in JET that both divertor operation and beryllium coating lead to a strongly reduced generation rate of RE compared with carbon limiter operation, this being consistent with recent modelling of RE generation in tokamaks [6], [7], [8]. For the ITER-CDA designs RE energies of up to 300 MeV and surface heat load of about 30 MJ/m^2 were considered possible [9]. The time scale of the RE – first wall interaction is of the order of 1 ms [3].

An important difference to most disruption induced heat loads on plasma facing materials is the large penetration depth of RE leading to significant heating of cooling tubes covered with a thick coating. Possible consequences are melting or material damage induced by steep temperature gradients [10]. The RE are thus a potential initiator of in-vessel loss of cooling accidents (LOCA's).

The next section gives an overview of RE generation processes. One section describes the most important physics processes involved in the energy loss of relativistic electrons penetrating material. Since it is not possible to calculate the energy distribution analytically, two computer codes (GEANT3 [11] and EGS3 [12]) are introduced which are widely used in high energy physics for quantitative simulation of the interaction of high energy particles with matter. Another code package (PTA [13]) was developed specially for fusion purposes and electron beam experiments were used to validate it [13]. The first analysis of the impact of RE on plasma facing components was performed by McGrath [14] for 20 MeV electrons. Calen et al. [15] made the first RE calculations in the 300 MeV region using the GEANT3 code. The importance of including the magnetic field in the analysis was stressed by Bartels [16], [17] and Kunugi [18]. It causes bending back of reflected charged particles and reduced penetration depth of electrons due to gyration of the electrons around the magnetic field lines. Generally, these codes can be used to describe the heat distribution in various plasma facing design options to predict the maximum tolerable RE surface heat load. The accuracy of these codes is better than 20% .

2 Physics of Runaway Electrons in Tokamaks

2.1 Generation

In the presence of an electric field, the electrons in a plasma ordinarily drift in the electric force direction until the dynamic friction due to collisions and the electric force are in equilibrium. When the dynamic friction is due to Coulomb interactions it decreases as the electron energy increases. When the energy acquired from the field in one self collision time approximately equals its thermal energy, W_t, the electron can run away. The self collision time is proportional to $W_t^{3/2}$, therefore as the electron temperature goes up, the electron acquires more energy per collision time, and smaller fields are able to produce runaway electrons (RE). Equating the collisional friction with the electric field force, the critical electric field, E_c, to achieve runaway was calculated for a singly ionized plasma by Dreicer as [19],

$$E_c = \frac{e}{4\pi\epsilon_o\lambda^2}\ln(\Lambda) = 3.1 \times 10^{-13}\frac{n_e\ln(\Lambda)}{T_e} \tag{2.1}$$

where λ is the Debye length$=\left(\epsilon_o kT_e/ne^2\right)^{1/2}$, e the absolute value of the electronic charge, ϵ_o the permittivity of space, k the Boltzmann constant, n_e the electron density, T_e the temperature and $\ln(\Lambda)$ the Coulomb logarithm.

Subsequent calculations, reviewed in [1], including the effect of multiple ionic species with effective charge number, Z, showed that the critical electron velocity, v_c, parallel to the electric field, E, for RE to form was

$$v_c = [(2 + Z)\frac{E_c}{E}]^{1/2}. \tag{2.2}$$

Even for small values of E, electrons in the tail of the distribution can run away (unless of course v_c is $\geq$ the speed of light,c). The corresponding critical energy is $W_c = (1/2)m_e v_c^2$.

More recently numerical integration of the 2-D Fokker-Planck equation has shown that while the condition of Equation (2.2) is sufficient for RE, electrons with velocities less than v_c can also become RE [20]. This is because while they are slowing down in the parallel direction, due to collisions, these collisions may also be accelerating them in the perpendicular direction. The curve of $\dot{v}_\parallel$, the time derivative of the parallel velocity component, extends upward into the $(v_\parallel, v_\perp^2)$ phase plane. If the phase trajectory of the electron crosses this curve while its perpendicular velocity is increasing it can also run away. Similar statements hold for high energy electrons travelling in a direction opposite to the field force.

The rate at which RE are generated has been studied by a number of authors [21], [22], [23], [24], [25], [26]. All assume a spatially uniform electric field, E, and solve a form of the Fokker-Planck equation by perturbation or numerical methods for the distribution function, in the $v_\parallel = v_c$ region, to determine the flux of particles crossing that boundary. One of the most complete of these solutions, given in [26], yielded the approximation for the runaway generation rate, λ_g (in RE/s), that is commonly accepted.

$$\lambda_g = C \left(\frac{E_c}{E}\right)^{(3(Z+1)/16)} n_e \nu \exp\left[-\frac{E_c}{4E} - \sqrt{(Z+1)\frac{E_c}{E}}\right] \tag{2.3}$$

where C is weak function of Z estimated to range between 0.13 and 0.43 for Z values between 1 and 10, and ν is the electron collision frequency. A relativistic correction to this equation has been given in [27]. Because of approximations inherent in this equation, e.g. the Coulomb logarithm appearing in E_c has been approximated at the electron temperature, and appears in the dominating exponential term, fine tuning of this expression is not likely to improve its accuracy. Equation (2.3) is useful in simple models where ohmic heating is used and spatial gradients can be neglected.

Harvey and McCoy have reported calculations with a 2-D momentum-space Fokker-Planck code, suitable for toroidal geometry, and which can include the effects of auxiliary heating, radial diffusion and synchrotron radiation [28]. Calculations for an ohmic heated plasma at r/a=0.65, with and without radial diffusion, showed that the number of electrons in the RE tail increased by more than two orders of magnitude when diffusion of hot electrons from the core was included. Radial transport reduced the RE rate at the center of the plasma and increased it toward the edge.

Another mechanism for RE generation has been proposed by Jayakumar et al. [29]. Once an existing RE current has been established, the interaction between these RE and the surrounding thermal electrons is small, but non-zero. The surrounding electrons can be scattered by Coulomb collisions, usually in a direction perpendicular to the beam, so that their energy increases to, or above, a critical value for runaway. The rate for secondary RE generation, λ_s is estimated to be

$$\lambda_s = n_r n_e \frac{e^4}{8\pi\epsilon_o m_e v_r} \frac{1}{a(Z)W_c}$$

where n_r and v_r are the RE density and velocity, and $a(Z)$ is a function of order 1. Using this relation for typical tokamak plasma conditions it was estimated that in the 10-20 MeV range, each RE generates an additional RE for every $\delta W = a(Z)(10 - 20 \; MeV)$ increment in energy acquired from the field. This can lead to an avalanche-like exponential growth of RE. Although the arguments for this effect are plausible, no experimental verification of it has been reported yet. The effect may be masked by the rapid rise rates predicted by Eq.(2.3) when E is large, and cancelled by other compensating effects when E is small.

When auxiliary energy sources are used to heat the plasma the generation rate of RE can be greatly enhanced. The use of RF heating raises the electron temperature and produces a superthermal tail which permits rapid acceleration into the RE regime [30], [31], [32], [33]. The use of neutral-beam heating can have a similar effect [34].

2.2 Synchrotron Radiation

When an electron orbiting in a magnetic field is accelerated to relativistic velocities, the radiation emitted from it changes from the discrete cyclotron frequency, and its harmonics, to a broad band, forward directed, beam [35], [36]. An expression for the power emitted by a single electron in all directions and polarizations per unit wavelength, λ (W/m), has been given in [37], [38] as

$$P_\lambda = \frac{4\pi}{\sqrt{3}} \frac{m_e c^3 r_e}{\gamma^2 \lambda^3} \int_w^\infty K_{5/3}(x)dx \tag{2.4}$$

where

$$w = \frac{4\pi R_{cur}}{3\lambda\gamma^3}$$

$r_e = 2.82 \times 10^{-15}$ m is the classical electron radius, $K_{5/3}$ is the modified Bessel function, and R_{cur} is the instantaneous radius of curvature of the electron trajectory. When Eq. (2.4) is integrated over all wavelengths, the total power radiated in Watts per electron is [37], [39],

$$P = \frac{e^2 c}{6\pi\epsilon_o} \frac{\gamma^4}{R_{cur}^2} \left(\frac{v}{c}\right)^4 \approx 4.61 \times 10^{-20} \frac{\gamma^4}{R_{cur}^2} \tag{2.5}$$

In a tokamak the radius of curvature is continually changing and a rough approximation to its average value is

$$R_{cur} = [(1 - f^2)/R + eBf/(mc\gamma)]^{-1}$$

where f is the sine of the pitch angle and R is the major radius of the machine. As the average pitch angle changes from zero to $\pi/2$, R_{cur} varies from the machine radius to the Larmor radius. Since from Eq. (2.5) the power radiated is proportional to R^{-2}, which can change by a factor of 10^6, the synchrotron losses can be a significant determinant of the limiting energy that a RE can attain, depending on what values of perpendicular energy the RE has [40], [41].

There has been some success in fitting synchrotron radiation spectra from RE generated in a low density steady tokamak plasma with values of f of less than 0.1 [42]. Observations of photoneutron production and post facto residual activation analysis of stainless steel components have also suggested that small values (< 0.1) of f were present on at least some RE [43]. There are, however many processes which can rapidly increase the perpendicular energy of RE (see next section) and it is likely that in most cases of interest these will play a major role in determining the RE energy.

2.3 Instability Mechanisms

It might be thought that once the electric field strength exceeded the critical field (Eq. (2.1)), that most of the electrons would become RE and the effective conductivity of the plasma would approach infinity. This is not the case. In fact as the value of E/E_c increases the value of the conductivity decreases. This is due to current-induced-turbulence which scatters the RE and prevents unimpeded acceleration. An extensive review of these turbulence phenomena is given in [44]. Of particular significance are the two-stream or beam instabilities which occur when $|\frac{\partial f_e}{\partial v_\parallel}| < |\frac{\partial f_e}{\partial v_\perp}|$. Resonant oscillations involving particles which meet the condition $\omega - n\omega_{ce} - k_z v_z = 0$ can grow and transfer energy from the beam. A value of $n = 0$ corresponds to Cerenkov resonance, and n=-1 corresponds to the "anomalous Doppler" resonance which increases the pitch angle of the RE [45]. The "fan" instability, which is a relaxation oscillation that rapidly ($< 100~\mu$s) isotropizes the RE beam can occur when the beam velocity exceeds $3\left(\frac{\omega_{ce}}{\omega_{pe}}\right)^{3/2} v_c$ [45], [46], [47]. Reference [48] identifies four stability regimes in $(E/E_c, \omega_{pe}/\omega_{ce})$ space and concludes that for values of $E < 0.1E_c$ and $\omega_{pe} < \omega_{ce}$ the runaway tail should be stable. Except at the start of disruptions tokamaks are usually operated in that regime.

In addition to the direct effect of these instabilities on the RE, magnetic turbulence, which is produced, increases the diffusion coefficient of the RE and also can increase the pitch angle [49], [50]. Increased pitch angle causes increased synchrotron radiation losses and also increases the possibility of RE being trapped in any magnetic mirrors present in a tokamak. Once trapped, the RE can move inward toward the magnetic axis, due to $\vec{E}_\parallel \times \vec{B}_\perp$ drift until they become untrapped [51].

2.4 Disruption Generated Runaways in Tokamaks

Although RE can be generated at start-up [51], [52], [53], and during steady state operation [1], [42], [55], [56], [57] the RE with most damaging potential occur during disruptions due to the large loop voltages present, and the likelihood of rapid deposition when the plasma moves. Runaway electrons are generated during a disruption as follows. At the start of a disruption there is a rapid cooling of the plasma. During this period there is a redistribution of current in the plasma which usually flattens the profile and reduces the plasma internal inductance. This leads to a slight increase in current and a short lived negative spike in the external loop voltage [58]. The drop in temperature causes the plasma resistance to rise and the plasma loop voltage rises to high values (up to kilovolts) from its normal value of less than a volt. This causes the current to fall and the collapsing poloidal magnetic field inductively sustains the high loop voltage. An electron circling the machine gains energy approximately equal to the loop voltage every cycle and can reach MeV values in a few ms.

The mechanisms that limit electrons from acquiring more energy are the following: radiation by the electron, which removes energy at higher rates as the electron energy increases; impact with a solid barrier as its orbit changes (increase in energy is accompanied by an outward shift of the RE trajectory [1], [45], and the inability of the control circuits to respond quickly usually results in an inward motion of the flux surfaces); or some instability or resonant interaction which increases its energy perpendicular to the magnetic field to the point where it can be trapped in a magnetic well. If a sufficient number of electrons run away, the high energy, low resistance portion of the current can approach the total current, and the loop voltage will fall as the current stabilizes at a plateau which is some fraction of its initial value [58]. This effect can also limit the maximum attainable energy of an electron. Another parameter of high significance for runaway generation rate is the impurity content of the plasma at the time of disruption and current decay. If the plasma temperature can be maintained at the low thermal quench level by radiation of the energy deposited in it by the collapsing magnetic field, the current decay will be rapid and the loop voltage will be large enough to generate large runaway currents. If the impurity radiation is low, however, particularly at low temperatures (<20 eV), the current decay would be retarded and fewer runaways will be generated and their energy will also be reduced [59], [8].

3 Interaction of Fast Electrons with Matter

A comprehensive review of the interaction of high energy particles with matter can be found in [60]. Here the most relevant physics processes of relativistic electrons traversing matter should be summarized. Electrons penetrating matter lose their energy by two processes:

1. ionization loss,

2. bremsstrahlung.

The electron energies of interest vary from 20 to 300 MeV, i.e. the relativistic γ-factor (ratio of particle energy to energy of the rest mass) varies from 40 to 600 and $\gamma \gg 1$ is thus always fulfilled. In this case the ionization loss is essentially independent of the particle energy and is just a function of the density ρ [g/cm^3]:

$$\left(\frac{dE}{dx}\right)_{ion} \simeq -2 \cdot \rho \quad \frac{MeV}{cm} \tag{3.1}$$

This kind of energy loss results in the formation of ion pairs (positive ions and electrons) in the medium and is responsible for the heat generated in the material.

The situation is different for bremsstrahlung. Here the electrons lose energy in radiative collisions with atomic nuclei:

$$e^- + nucleus \rightarrow e^- + nucleus + \gamma$$
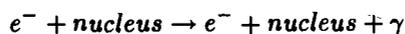
where γ in this case is the generated photon. The nuclear electric field decelerates the electron and the energy change appears in the form of a photon. The photon spectrum has the approximate form dE'/E', where E' is

Table I. Radiation length X_0 and E_c in various materials

Material	Z	X_0 in cm	E_c in MeV
beryllium	4	35.3	150
carbon	6	22.6	100
water	7.2	36.1	72
iron	26	1.74	24
molybdenum	42	0.98	17.5
tungsten	74	0.35	11

the photon energy. Integrated over the spectrum, the total radiation loss of an electron traversing a medium of thickness dx is

$$\left(\frac{dE}{dx}\right)_{rad} = -\frac{E}{X_0} \tag{3.2}$$

where X_0 is called the radiation length of the material. The radiation length is inversely proportional to the density and the atomic number Z, which indicates the very good absorption property of high Z, high density metals such as tungsten. From Eq. 3.2 it follows that the average energy of a beam of electrons of initial energy E_0, after traversing a medium of thickness x, will be

$$\langle E \rangle = E_0 \cdot exp\left(-\frac{x}{X_0}\right) \tag{3.3}$$

Thus, the radiation length X_0 may be simply defined as the thickness of the medium which reduces the mean energy of a beam by a factor e.

Since the rate of ionization energy loss for fast electrons $(dE/dx)_{ion}$ is approximately constant, while the average radiation loss is $(dE/dx)_{rad} \sim E$, it follows that at high energies radiation loss dominates. The critical energy E_c is defined as that at which the two are equal. It can be roughly given as a function of Z:

$$E_c \simeq \frac{600}{Z} \; MeV \tag{3.4}$$

Values of X_0 and E_c in various materials are given in Table I.

The photons generated via bremsstrahlung lose their energy by three processes:

1. photoelectric absorption,

2. Compton scattering,

3. pair production.

The photoelectric absorption dominates at γ-energies below 0.5 MeV (cross section $\sim 1/E^3$ where E is the photon energy). Here the whole energy is transferred to an atomic electron. In Compton scattering (cross section $\sim 1/E$), which is important in the energy range from 0.5 to 5 MeV, just a fraction of the γ-energy is transferred to an electron:

$$\gamma \rightarrow \gamma' + e^-$$

At energies larger than 5 MeV the process of conversion of a high energy photon to an electron-positron pair (in the field of a nucleus to conserve momentum)

$$\gamma \rightarrow e^+ + e^-$$

is closely related to that of electron bremsstrahlung (cross section independent of energy). The attenuation of a beam of high energy photons of intensity I_0 by pair production in an absorber of thickness x is described by

$$I = I_0 \cdot exp\left(-\frac{7}{9}\frac{x}{X_0}\right)$$ (3.5)

where X_0 is the above defined radiation length. Positrons (e^+), the anti-particles of the electron (e^-), lose their energy similarly to the electrons with the exception that the ultimate fate of a positron will be annihilation with an electron, releasing the energy of the rest mass of an e^+e^- system (1 MeV) in the form of two or three photons.

For high energy electrons ($E_0 \gg E_c$), a dramatic result of the combined phenomena of bremsstrahlung and pair creation is the occurrence of cascade showers, so-called electromagnetic showers. A parent electron will radiate photons, which convert into pairs, which radiate and produce fresh pairs in turn, the particles increasing exponentially with depth in the medium. This process continues until the energy of the shower particles is comparable to or lower than E_c. For electrons with an initial energy $E_0 \gg E_c$ the maximum energy deposition occurs at a depth

$$d_{max} = X_0 \cdot \frac{\ln(E_0/E_c)}{\ln 2}$$ (3.6)

increasing logarithmically with the primary energy E_0, and thus the shape of the energy deposition is roughly independent of E_0. Because of Coulomb scattering, a shower spreads out laterally. This spread is described by the Moliere radius

$$R_m = 21 \cdot \frac{X_0}{E_c}, \quad E_c \text{ in MeV}$$ (3.7)

Single particles undergo numerous transverse Coulomb scattering processes with the atomic nuclei. The resultant distribution in the net scattering angle follows a Gaussian distribution. The root-mean-square (rms) deflection in a layer x of a medium with the radiation length X_0 is given by

$$\Theta_{space}^{rms} = \frac{20 \ MeV/c}{p}\sqrt{\frac{x}{X_0}} \quad (radians)$$ (3.8)

A small fraction of large-angle scattering processes is underestimated by this formula. For a 100 MeV electron traversing 1 mm of tungsten the width of deflection angles is 3°. The transverse displacement y from a straight path due to multiple scattering can be written in the form

$$y_{plane}^{rms} = \frac{1}{\sqrt{6}} \cdot x \cdot \Theta_{space}^{rms} \sim x^{3/2}$$ (3.9)

Runaway electrons are expected to hit the plasma facing surface at small incident angles in the range from 1 to 5°. It is mainly the effect of multiple scattering which can lead to substantial reflection of electrons hitting material at small angles. A magnetic field parallel to the surface such as is present in all runaway events in tokamaks counteracts this reflection of electrons, since it bends the particles back into the plasma facing components.

4   Codes for Runaway Electron Heating Calculation

Given the discussion of the preceding section, it is clear that an analytical approach to the heat deposition of fast electrons hitting plasma facing components at small incident angles seems to be impossible, since one has to follow a lot of secondary particles produced, whose history is determined by probabilistic (quantum-mechanical) laws. The simulation of such events can be achieved in computer codes which follow the primary particle in small steps, computing for each step the energy loss, multiple scattering and generation of secondary particles according to the distribution functions of the probabilistic laws. When the particle has lost all its energy, the

231

code follows all secondary particles produced, which can again generate new particles etc. An example of such a code is GEANT3 [11] which was developed at CERN, the large European center of high energy physics, and is widely used in that area. It is a typical application of the 'Monte-Carlo' method, where random generators are used to take decisions at every step according to the distribution functions. For complicated problems this method has by far the best convergence properties, which always goes like $1/\sqrt{n}$, where n is the number of trials (statistical behaviour). In our case this means that the accuracy of the energy distribution of electrons hitting the plasma facing components converge to the correct result with $1/\sqrt{n}$ of electrons simulated with the computer code.

The geometry has to be built up by the user and consists typically of boxes or tubes nested in each other. Magnetic fields can be considered too. The user has to set up the starting conditions for the space point and momentum of the primary particle. The code then provides the user with the full information about the track of the particle and secondary particles generated.

The EGS system [12] is also a general purpose package for the Monte Carlo simulation of coupled transport of electrons and photons originating from SLAC, the high energy center in California. The most recent and enhanced version of the EGS system is called EGS4. The EGS4 system can simulate electromagnetic processes, and the transport of electrons and photons in arbitrary geometry for particles above a few keV up to several TeV. The Fortran preprocessor called MORTRAN3 is used to write the user code which specifies the energy and angular distribution of source particles, detectors and geometries. This allows greater flexibility and applicability for general purposes, such as the realistic simulations of RE's which impact with plasma facing components with complex geometrical shapes.

The PTA code package [13] including ITS is a three dimensional, time dependent computational code package developed at Sandia National Laboratories to predict energy deposition, temperature rise and damage of first wall materials from RE impact. ITS is a set of coupled electron/photon Monte Carlo transport codes. ITS includes several electron/photon transport codes, such as TIGER (1-dimensional geometry), CYLTRAN (2-dimensional geometry) and ACCEPT (3-dimensional combinatorial geometry). These codes are based on ETRAN [61] and are designed for transport at primary source energies from a few tens of MeV down to 1 and 10 keV for electrons and photons, respectively.

A comparison of the results with GEANT3 and EGS3 was performed by Kunugi et al. [62] for energy deposition distributions in a 10 mm thick carbon layer on top of a 50 mm thick molybdenum layer. The incident electron energies ranged from 10 to 300 MeV and the incident angles from 0.5 to 25 degrees. The quantities

$$D = \frac{E_{GEANT} - E_{EGS}}{E_{GEANT}}$$

where E is energy deposition and

$$\Delta D = \sqrt{< D^2 > - < D >^2}$$

can be taken as measures of the relative differences of the two calculations. In Table II the average values of D and ΔD from all calculations presented are listed. For both code systems the results for the peak deposited energy densities and the deposited energy fraction in carbon and molybdenum are compared. The calculations of GEANT3 and EGS4 agree better than 20% . This accuracy was also estimated by detailed studies of the systematic errors due to the finite steps used in the Monte Carlo codes [17].

Table II. Relative difference of the GEANT3 and EGS4 code results for runaway electron impact on 10 mm carbon on top of 50 mm molybdenum

| code result	D [%]	ΔD [%]
peak energy density in molybdenum	15.6	6.4
peak energy density in carbon	-4.1	14.7
fraction of energy in molybdenum	-7.3	5.3
fraction of energy in carbon	-9.0	9.5

232
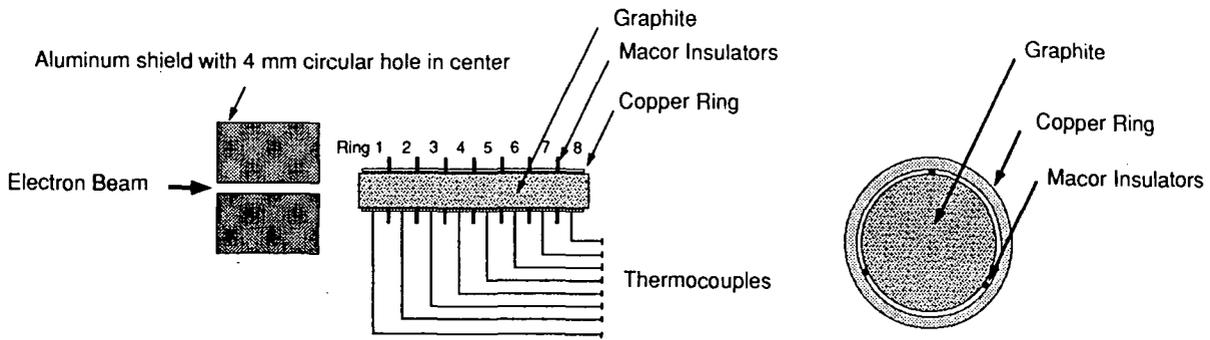
Figure 1: *Experimental setup of runaway electron simulation experiments carried out with the linear electron accelerator of Osaka University [62].*

5 Experimental Results

Experiments were conducted with the linear electron accelerator of the Institute of Scientific and Industrial Research of Osaka University [10]. The beam energy was varied between 20 and 30 MeV and an input power of about 1.2 kW was applied to various materials for up to 60 s. The specimens were subjected to normal beam incidence. Post experimental examinations were carried out to determine the damage caused by high energy electron impact. Graphite, SiC, stainless steel, molybdenum and tungsten were tested as bulk materials. In relative comparison, graphite and SiC showed the highest structural resistivity to electron impact due to the low density and stopping power. Among metals stainless steel suffered severe damage such as grain growth and melting. The molybdenum samples in the experiment underwent high thermal loads due to deposition of the beam energy in small volumes caused by the high density of the molybdenum. The thermally induced damage was less severe than for stainless steel due to the high melting point and hence the threshold for grain growth initiation in molybdenum was also high. The irradiation of tungsten led to grain growth and microcracking at the surface.

To investigate RE impact on actively cooled components brazed layer systems were tested. Small droplets were observed after electron irradiation which may originate from the braze used for bonding a 5 and 10 mm graphite layer on a Mo-Cu-Mo substrate. On the other hand only a few conclusions can be drawn from these experiments since the electron beam incidence was perpendicular to the specimen surface, whereas a tokamak RE impact is expected to be almost tangential to the first wall surface.

To simulate the grazing incidence angle, more sophisticated specimens were developed [63]. The experimental setup can be seen from figure 1. Graphite rods of different diameter were used with 8 copper rings of slightly larger diameter around the graphite rods. The geometry was chosen to simulate the case of RE impact on first wall components in which the high energy electrons are scattered through the graphite protection to the structural components of the first wall. The electron beam was directed through an aluminium block with a circular hole in the center to reduce the oval beam to a circular beam.

The thermal response of the experimental setup was modelled with the PTA code package [13]. Figure 2 shows the temperature rise in the copper rings as measured experimentally and calculated by PTA. The large temperature rise in the first ring is due to energy deposition from X-rays, generated when electrons hit the aluminum shield. The experimental data of 6 graphite rods of different diameter could be successfully modelled with the PTA code system. The beam power and the graphite-copper slit conductance (filled with air) were used as free parameters to match the computer results to the experimental data.

Long pulses of 10 to 60 s were needed to obtain measurable results. In contrast, RE in tokamaks interact with first wall materials on a ms time scale [3], which leads to significant differences in the temperature distribution for
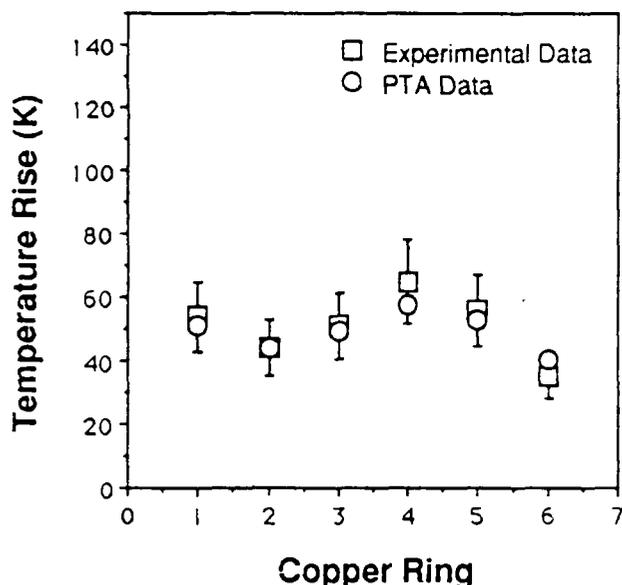
Figure 2: *Temperature rise in copper rings after 10 s electron irradiation using a 13 mm diameter graphite rod: comparison of experimental data and PTA results. Electron beam energy: 30 MeV per electron.*

the same energy input. In addition, the beam and sample geometry can vary significantly between the simulation experiments and the RE events in tokamaks. The magnetic field inherently coupled to tokamak operation also influences the RE impact (see next section). Some attention should thus be given to the extrapolation of electron simulation events to RE events in tokamaks, which can instead be analyzed with appropriate computer models. The accelerator experiments provided a basis for validation of the PTA computer code. In addition material damage such as grain growth and microcracking have been observed. This kind of material damage occurs at energy depositions well below those needed for melting or sublimation of test samples.

6 Energy Deposition on Various Types of PFC

Various types of plasma facing component (PFC) designs have been investigated for their resistance to RE impact. The generation of runaway electrons in tokamaks is inherently coupled with the presence of a strong magnetic field which is roughly parallel to the surface of the plasma facing components. This has two main consequences:

1. Reflected charged particles will be bent back into the material.

2. Charged particles will be forced to gyrate around the magnetic field lines inside the material.

The first effect leads to a substantial increase of the energy deposition into the plasma facing components by the runaway beam and the second effect leads to a reduced penetration depth of the electrons. To quantify these findings, GEANT3 simulations of energy deposition of electrons ($\theta_i = 1^\circ$) on a simple two layer model with 1 cm carbon on 1 cm molybdenum (see figure 3) was performed without magnetic field ('no B'), a magnetic field just in the vacuum ('B-vac') to demonstrate the effect of the reflection power, and finally a magnetic field everywhere ('B-all') to show the effect of decreasing penetration depth. The energy deposition in carbon and molybdenum is plotted in figure 4 as a function of the incident electron energy is plotted [16]. Neglect of the magnetic field can lead to underestimation of the integral heat deposition by a factor of up to 3 and the peak energy deposition in the metal substrate can be overestimated by a factor of up to 8 when the shielding effect of the magnetic field inside the material is neglected [65]. The energy deposition in the materials was observed to be independent on the incident angles and energies over 100 MeV [18].
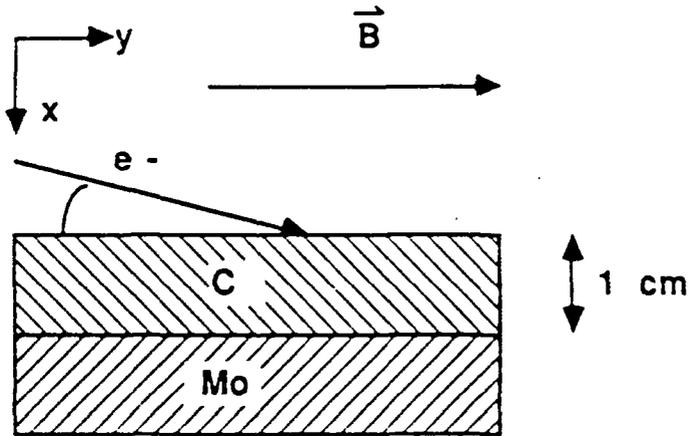
Figure 3: *Geometrical setup of a simple model for a plasma facing component (1 cm graphite on 1 cm molybdenum).*
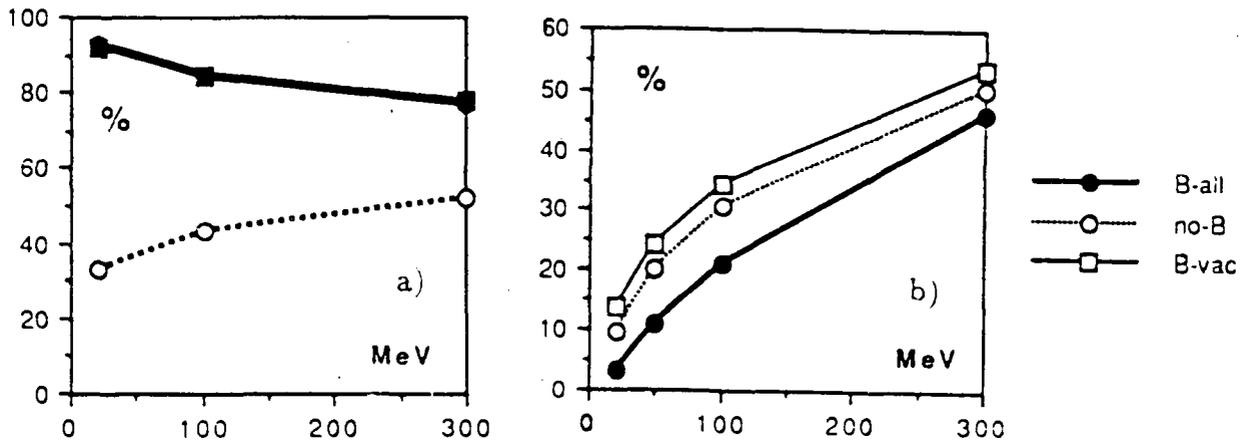
Figure 4: *The fraction of the runaway electron beam dumped a) into the whole setup (incident angle 1°) and b) into the molybdenum (incident angle 5°) for different assumptions concerning the magnetic field.*
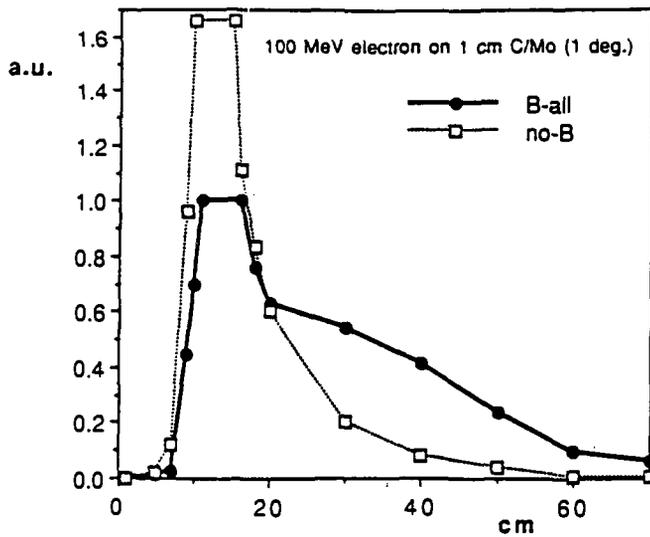
Figure 5: Lateral (y-direction, see figure 3) spread of the energy deposition in a molybdenum surface protected by 1 cm of graphite with and without magnetic field. The maximum energy deposition with magnetic field served as normalization point.

It has been argued [65] that the reflected part of the energy, which is bent back by the magnetic field, will not contribute to the volumetric heating, since the point of second entry into the material may be far away from the beam impact point. To investigate this question the spread of the beam in the y-direction (see figure 3) is shown in figure 5. Starting with a uniform distribution of 100 MeV electrons ($\theta_i = 1^\circ$) with a width of 2 cm, the width of the beam impact is shown for the first 250 μm in molybdenum [66]. One can clearly observe the effect of the magnetic field leading to a long tail of the initial peaked distribution. About 60% of the dumped electron energy is spread over 10 cm, and about 90% over 50 cm. It is worth mentioning that the position of the peak of the lateral energy distribution at the molybdenum surface is not at the place where it would be expected for a straight path of the electrons, but rather is shifted due to multiple scattering. The horizontal (z-direction, see figure 3) spread is shown in figure 5. Starting with no beam spread in the z-direction, one ends up with a typical width of 2 cm (root mean square) after penetration of 1 cm of graphite.

EGS4 calculations [18] of energy depositions from RE's were performed for the three types of carbon/copper based divertor targets shown in figure 7. Type A represents a monoblock concept proposed for the physics phase
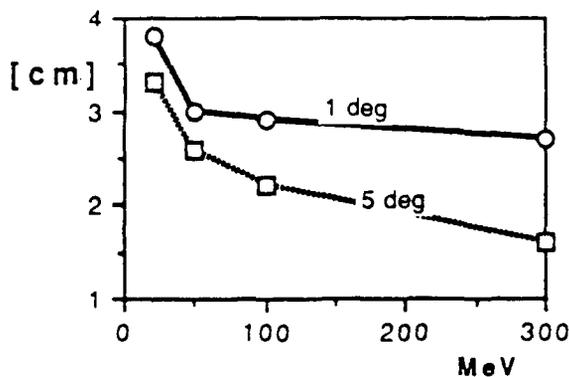
Figure 6: Perpendicular (z-direction, see figure 3) spread of the runaway electron beam after penetration of 1 cm of graphite. Twice the root mean square of the spatial distribution is plotted versus the electron energy.

236
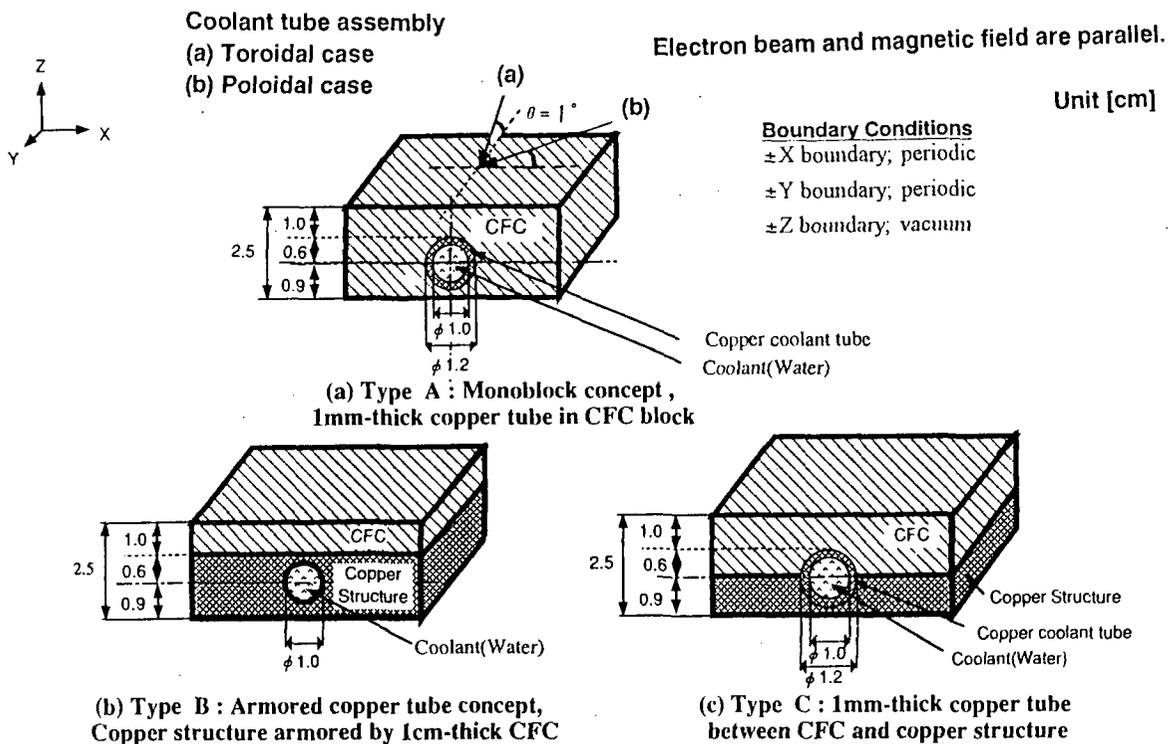
Figure 7: *EGS4 model for the calculation of energy deposition from runaway electrons on various types of divertor targets.*

of ITER-CDA [9]. Type B represents an armoured metallic tube concept with carbon fiber composite (CFC) tiles and copper structure. Type C represents a concept with a coolant pipe centered at the interface between CFC and copper structures. The thickness of the CFC above coolant pipes was 10 mm for all types. The incident electron energy was assumed to be 300 MeV and the incident angle to the surface 1 degree because the RE's will have very small incident angles. Figure 8 shows the deposited energy pattern for the three different design solutions. The most crucial parameter, viz. the peak energies deposited in the copper and CFC components was almost the same for all divertor targets. In this calculation there is no dependence on the geometrical shape of the metallic components, but the thickness of the carbon armour affects the peak energy in the metallic component. For toroidal coolant assembly and 1 cm graphite protection the damage threshold is about 30 MJ/m^2 for all designs. Figure 9 shows the deposited energy contour for the type A divertor with 6 T magnetic field.

The steps in the distribution of the energy density correspond to the density changes when going from one material to the other, which reflects the proportionality of the ionization loss to the density. Structural material can be very effectively protected by thick carbon tiles. To quantify the thickness effect, a simple case was considered [66]: 10 cm thick graphite hit by 300 MeV electrons at an incident angle of 1°, as shown in figure 10. Between 0.3 and 4.0 cm the distribution is roughly exponential, with the energy deposition decreasing by a factor of 2 for every cm. Since a steel structure at any depth would yield a roughly 4 times higher energy density ($\rho_{steel}/\rho_{carbon} \approx 4$), it can be generally stated that 1 cm of carbon increases the runaway protection by a factor of 2. Another conclusion can be drawn: the end of life conditions of the plasma facing components might show substantial erosion of the C tiles, implying their reduced potential in affording protection against runaway electrons.

The peak energy deposition in a monoblock design with molybdenum tubes is shown in figure 11 [67] for various incident angles and single electron energies. A uniform RE heat flux of 30 MJ/m^2 was assumed as in the ITER-CDA [9]. The results of the peak energy deposition in the coolant tubes are rather independent of
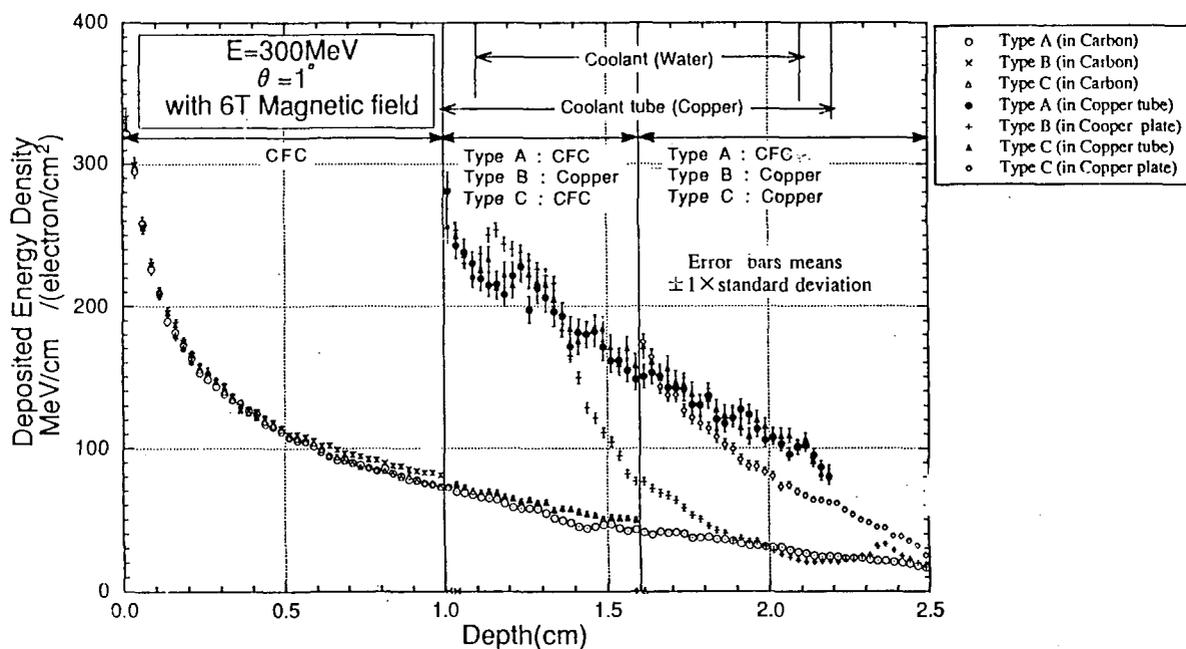
Figure 8: *Deposited energy densities in three types of divertor tagets. Incident beam angle (θ) = 1°, electron energy (E) = 300 MeV. The deposited energy density is an average of deposited energy per unit volume in each 0.025 cm thick layer.*
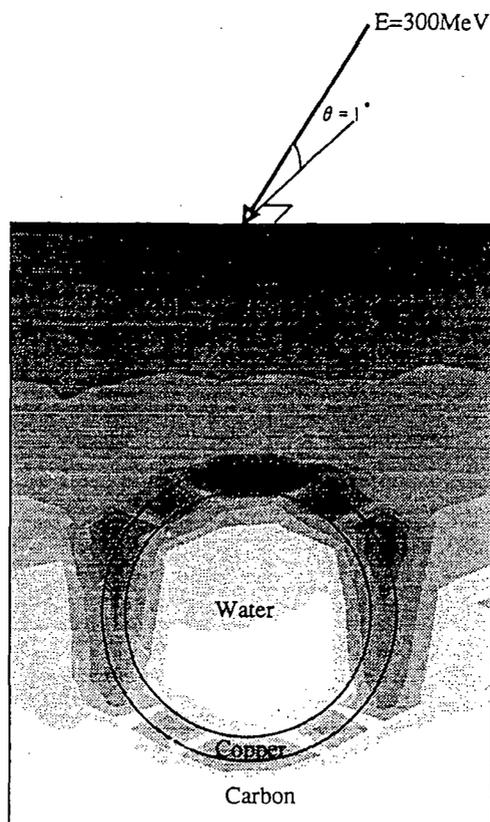

Figure 9: *Deposited energy contour for the Type A divertor with 6 Tesla magnetic field.*
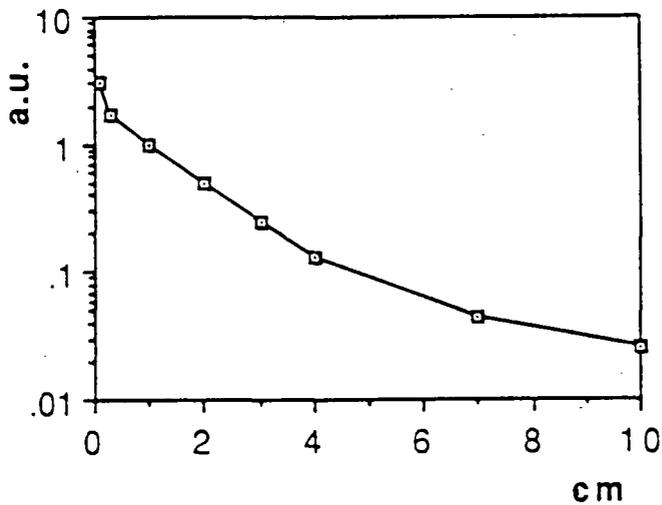
Figure 10: *Energy deposition by runaway electrons in a thick graphite block. Between 0.3 and 4 cm the energy density in graphite decreases roughly exponentially, i.e. every cm of graphite thickness doubles the runaway protection of structures behind it.*
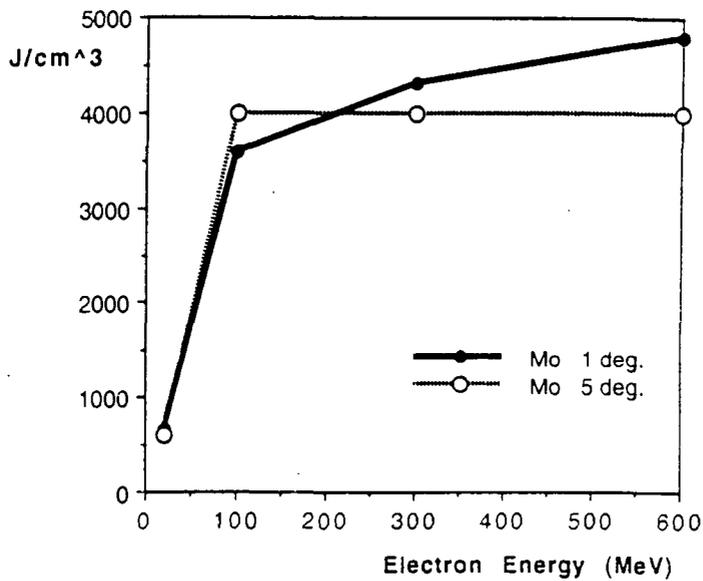
Figure 11: *Peak energy depositions in the molybdenum tube of the monoblock divertor due to 30 MJ/m^2 runaway electron impact.*
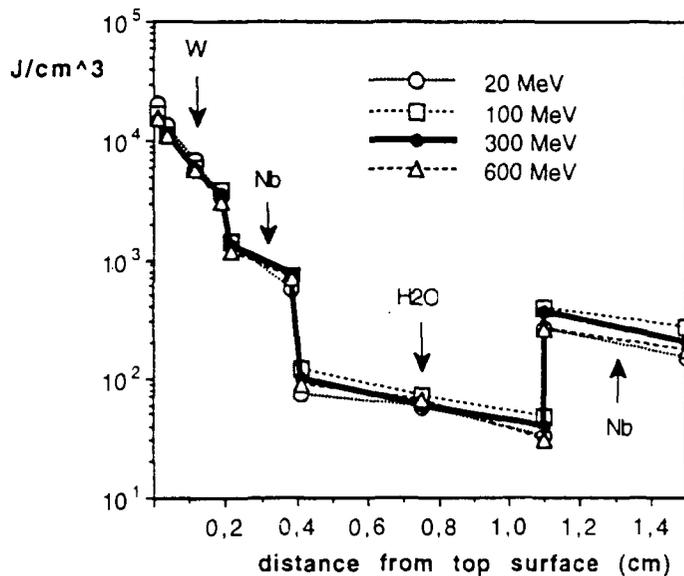
Figure 12: *Energy deposition of a 30 MJ/m² runaway electron beam (incident angle 1°) into a W-Nb divertor.*

the initial electron energy (for energies > 100 MeV) and incident angle. The explanation for this behaviour is the smearing of the incident angle by multiple scattering and the very small dependence of the shape of electromagnetic showers on the initial electron energy (see section 3). Thus the most important parameter in the RE impact studies is the RE surface heat flux. Melting of the cooling tubes must be expected for RE heat fluxes of about 50 (25-30) MJ/m² for molybdenum (copper) cooling tubes [18], [17].

Figure 12 shows results of an extremely different design solution for the plasma facing components that is based on high-Z coating material, viz. tungsten. In this case one has roughly no dependence on incoming electron energies above 20 MeV, which is due to the fact that electromagnetic shower development is already the dominant process above an electron energy of 10 MeV. The high 'stopping power' of tungsten would lead to melting of the structure above 15 MW/m². On the other hand, the structure behind the tungsten coating is very well protected.

The first wall of ITER is loaded by concentrated α-particle bombardment and therefore local damage can be produced during normal plasma burn. A possible solution to this problem is the use of local limiters [68]. A parametric study has been performed to investigate the required carbon tile thickness for local limiters covering 10 and 20% of the first wall [17].

In the first case the heat load imposed on the carbon surface was assumed to be 300 MJ/m² since the toroidal coverage of the limiters is a factor 10 smaller than the coverage of a continuous first wall. For the 20% coverage the load was again 300 MJ/m², but in this instance striking only half of the toroidal extent. This would be expected with a 'roof-shaped' local limiter angled in two directions to the magnetic field ripple. The incident angle was assumed to be 1° and the individual electron energy was 300 MeV. Tiles incorporating tungsten filaments, corresponding to 1 mm effective tungsten thickness, are considered as a third case.

Figure 13a shows the maximum energy deposition in a cooling tube, the steel component nearest to the plasma for all three cases, as a function of tile thickness. For comparison, the full carbon coverage case is also shown. A tile thickness of 3 cm provides a safety factor of three against melting if tungsten filaments are used, whereas the same factor would require 4 cm of pure carbon. If tungsten filaments are used, care should be taken to ensure that their temperature is maintained below the melting point to prevent damage to the tiles.

The peak energy deposition in the local limiters by runaway impact shows up at the surface of graphite and does not vary with thickness. The first 3 mm of the carbon tiles will be subject to a heat load of 33 kJ/cm³, which is certain to result in at least partial erosion (see figure 13b)
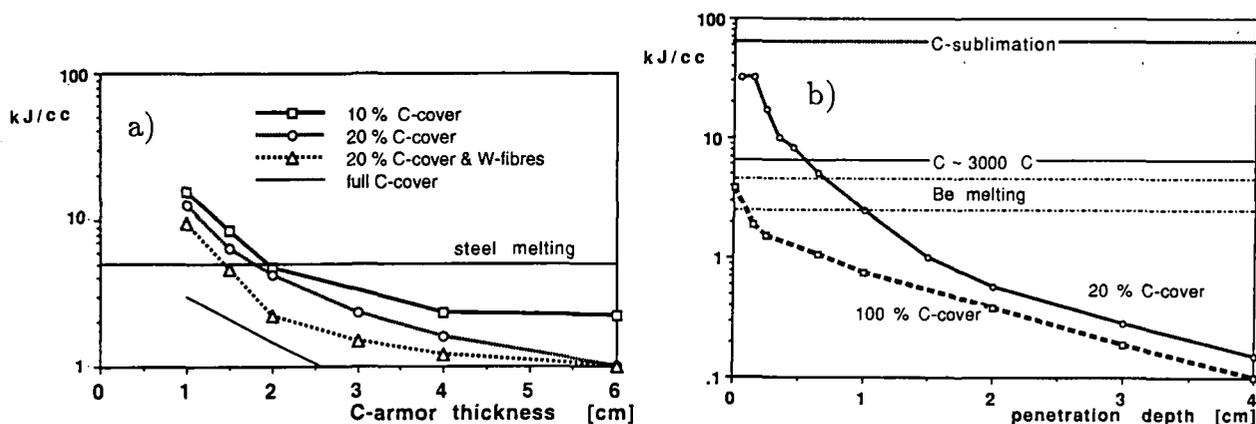
Figure 13: *Peak energy deposition in the first wall steel(a) and carbon protection (b) for the local limiter design. A runaway electron beam with 300 MJ/m² surface heat load on the limiter surface and a single electron energy of 300 MeV were assumed (incident angle 1°).*

7 Conclusion

The production of runaway electrons during disruptions has already caused some damage in existing tokamaks. Consequently, the next step device ITER will try to avoid operational scenarios which are prone to runaway production. It is also being attempted to include runaway electron protection in the design criteria of the plasma facing components. The exact prediction of the maximum heat flux envisaged is uncertain owing to the large variation of runaway generation with electron density and temperature at the end of thermal quench of a disruption. A rough estimation yields a 100 MJ beam energy of up to 300 MeV electrons, leading to about 30 MJ/m² heat flux to the plasma facing components if they are properly aligned and the magnetic field ripple is small.

Monte Carlo codes either originating from high energy physics or developed for fusion research can be used for quantitative modelling of the energy deposition that includes the magnetic field. The overall uncertainty of the modelling is estimated to be smaller than 20%.

Structural components (e.g. cooling channels) are best protected by thick carbon tiles, e.g. a thickness of 1 cm prevents melting of molybdenum below 50 MJ/m². For a bare metallic first wall or divertor, melting has to be expected at about 15 MJ/m². On the other hand, a thin tungsten layer (2 mm) affords considerable protection of the structures behind it. The use of beryllium and copper could lead to component damage at about 10 MJ/m², but in JET a significant reduction of runaway electron generation has been observed with beryllium coating.

For reactors working at high water temperatures, the additional heating by runaway electrons may lead to overpressurization of the cooling channels and subsequent loss of coolant accidents.

In some machines (DIIID), no disruption generated runaway electrons have been observed, which gives rise to the hope that a proper understanding of the suppression mechanism might solve the problem.

References

[1] H. Knoepfel and D.A. Spong, Nuclear Fusion, 19:6 (1979) 785.

[2] K.J. Dietz, J. Nucl. Mat. 155-157 (1988) 8-14.

[3] O.N. Jarvis, G. Sadler and J.L. Thompson, Nuclear Fusion, 28:11 (1988) 1981.

[4] T. Kimura, I. Yonekawa, M. Takahashi and N. Hosogane, 'Disruption-Induced Hard X-Ray in JT-60', ITER-IL-PH-8-0-23, Garching, 1990.

[5] R.D. Gill, 'Generation and Loss of Runaway Electrons following Disruptions in JET', JET-P(93)28, Abingdon, UK. (1993), submitted to Nuclear Fusion.

[6] G.R. Harris, 'An Assessment of Major Disruption Characteristics', Final Report of NET Contract 398/89-9 UK, NET Team Garching, Germany, Dec. 1990.

[7] G.R. Harris, 'Comparisons of the Current Decay During Carbon Bounded and Beryllium Bounded Disruptions in JET', JET Report, JET-R(90)07, Abingdon, Oxon, UK, Dec. 1990.

[8] A.J. Russo, 'A Model for Disruption Generated Runaway Electrons' submitted to Nucl. Fusion, (1993).

[9] International Atomic Energy Agency, 'ITER Conceptual Design Report', ITER Documentation Series No. 18.,Vienna, 1991.

[10] H. Bolt, A. Miyahara, M. Miyake et al., J. Nuclear Materials, 151 (1987) 48.

[11] R. Brun, F. Bruyant, M. Maire, A.C. McPherson, and P. Zanarini, GEANT3, CERN Data Handling Division (1987).

[12] W.R. Nelson, H. Hirayama and D.W.O. Rogers, 'The EGS4 code system', SLAC-265, US. (1985).

[13] K.A. Niemer, C.D. Croessmann, J.G. Gilligan et al., 'Computational and Experimental Modeling of Runaway Electron Damage', Sandia National Lab., SAND89-2304 (1990).

[14] R.T. McGrath, 'Runaway Electron Analysis for TORE SUPRA', Proc. of Japan-U.S. workshop P-92 on plasma material interaction, Chikusa-ku, Nagoya 464, Japan, January 1987.

[15] H. Calen, S. Kullander and A. Mörtsell, 'Energy Deposition in Tokamaks by Impact of Runaway Electrons', Department of Radiation Science, Uppsala University, UU267 (1989).

[16] H.-W. Bartels, 'Runaway Electrons on Plasma Facing Components', Proc. 17th Symp. Fusion Technol., Rome, 1992.

[17] H.-W. Bartels, 'Impact of Runaway Electron', accepted for publication in Fus. Eng. Design (1993).

[18] T. Kunugi, 'Effects of Runaway Electrons on Plasma Facing Components', accepted for publication in Fus. Eng. Design (1993).

[19] H. Dreicer, Physical Review 115 (1959) 28.

[20] V. Fuchs, R.A. Cairns, and C.N. Lashmore-Davies, Phys. Fluids 29:9 (1986) 2931.

[21] H. Dreicer, Physical Review 17:2 (1960) 329.

[22] A.V. Gurevitch, Soviet Physics JETP 12:5 (1961) 904.

[23] M.D. Kruskal and I.B. Bernstein, Physics of Fluids 7:3 (1964) 904.

[24] A.N. Lebedev, Soviet Physics JETP 21:5 (1965) 931.

[25] R.M. Kulsdrud, Y.C. Sun, N.K. Winsor and H.A. Fallon, Physical Rev. Lett. 31:11 (1973) 690.

[26] R.H. Cohen, Physics of Fluids 19:2 (1976) 239.

[27] J.W. Connor and R.I. Hastie, Nucl. Fus. 15 (1975) 415.

[28] R.W. Harvey and M.G. McCoy, 'The CQL3D Fokker-Planck Code', General Atomics Report GA-A20978, 1992.

[29] R. Jayakumar, H.H. Fleishmann and S.J. Zweban, Physics Lett. A 172 (1993) 447.

[30] N.J. Fisch and C.F.F. Karney, Phys. Rev. Lett. **54:9** (1985) 897.

[31] C.F.F. Karney and N.J. Fisch, Physics of Fluids **29:1** (1986) 180.

[32] V.S. Chan, C.S. Liu, and Y.C. Lee, Physics of Fluids **29:6** (1986) 1900.

[33] K. Ogura, H. Tanaka, S. Ide, et al., Nucl. Fus. **30:4** (1990) 611.

[34] G. Taylor, C.W. Barnes, A. Cavello, et al., Plasma Physics and Controlled Fus. **31:13** (1989) 1957.

[35] C. Kunz, ed., 'Synchrotron Radiation,' in Topics in Current Physics V10, Springer Verlag, N.Y. (1979).

[36] G. Margaritondo, Introduction to Synchronous Radiation, Oxford Univ. Press (1988).

[37] J. Schwinger, Physical Rev. **75:12** (1949) 1912.

[38] D. Rusbuldt, and K. Thimm, Nucl. Instrum. Methods **116** (1974) 125.

[39] W.K.H. Panofsky and M. Phillips, Classical Electricity and Magnetism, Addison-Wesley, Reading, MA, p.307 (1955).

[40] A.J. Russo, Nucl. Fus. **31:1** (1991) 117.

[41] L. Laurent and J.M. Rax, Europhysics Lett. **11** (1990) 219.

[42] K.H. Finken, J.G. Watkins, D. Rusbuldt, et al., Nucl. Fus. **30:5** (1990) 859.

[43] M. Chatelier, A. Geraud, P. Joyer, et al, 'Runaway Electron Dynamics and Confinement in Tore Supra', in Controlled Fusion and Plasma Physics (Proc. 16th Eur. Conf. Venice, 1989) V13B:1 Eur. Physical Soc. (1989) 19.

[44] H. de Kluiver, N.E. Perepelkin, and A. Hirose, Physics Reports **199:6** (1991) 283.

[45] V.V. Parail and O.P. Pogutse, Reviews of Plasma Physics, ed. M.A. Leontovich, **11** (1986) 1.

[46] TFR Group, Nucl. Fus. **16** (1976) 476.

[47] A.A. Oomens, L.Th.M. Ornstein, R.R. Parker et al., Phys. Rev. Lett. **36:5** (1976) 255.

[48] E. Moghaddam-Taaheri, U. of Maryland, College Park Ph. D. Thesis, 1986 (U. Microfilm Order 87-12,258), also Phys. of Fluids **28:11** (1985) 3356.

[49] A.V. Gurevich, K.P. Zybin, Ya.N. Istomin, Nucl. Fus. **27:3** (1987) 453.

[50] J.R. Myra, P.J. Catto, A.J. Wootton, et al., Phys. Fluids B **4:7** (1992) 2092.

[51] A.A. Ware, Physical Rev. Lett. **25:1** (1970) 15.

[52] A.S. Sharma and R. Jayakumar, Nucl. Fus. **28:3** (1988) 491.

[53] A. Raicu, T. Ionescu-Bujor, A. Pantea, et al., Czech. J. of Physics B **B37:7** (1987) 850.

[54] H. Knoepfel and S.J. Zweban, Phys. Rev. Lett. **35** (1975) 1340.

[55] Z. Yoshida, Nucl. Fus. **30:2** (1990) 317.

[56] T.K. Chu, R. Bell, A. Cavallo, et al., Nucl. Fus. **26:10** (1986) 1319.

[57] T. Fujita, Y. Fuke, Z. Yoshida, et al., J. exit of the Physical Soc. of Japan **60:4** (1991) 1237.

[58] Wesson, J.A., Gill, R.D., Hugon, M. et al., Nucl. Fusion **29** (1989) 641.

[59] G.R. Harris, JET Report JET-R(90)07, Dec. (1990).

[60] D.H. Perkins, 'Introduction to High Energy Physics', 3rd edition, Addison-Wesley Publishing Company Inc., (1987).

[61] M.J. Berger, Methods in Computational Physics, Academic Press, New York, 1 (1963) 133.

[62] T. Kunugi, M. Akiba, M. Ogawa et al., 'The Simulation of the Energy Deposition from Runaway Electrons in Plasma Facing Components with EGS4', Fusion Technology, 21 (1992) 1868.

[63] H. Bolt, A. Miyahara, M. Miyake et al., J. Nuclear Mat. 155-157 (1988) 256.

[64] K.A. Niemer, C.D. Croessmann, J.G. Gilligan and H.H. Bolt, 'Modeling of Runaway Electron Damage for the Design of Tokamak Plasma facing Components', Sandia Report, SAND89-2405 (1990).

[65] H. Bolt, E. Zolti, H. Calen and A. Mörtsell, 'Effects of Runaway Electron Energy Deposition on Plasma Facing Components', Proc. 16th Symp. Fusion Technol., London (1990).

[66] H.-W. Bartels, 'Interaction of Relativistic Electrons with Plasma Facing Components', Max-Planck-Institut für Plasmaphysik, Garching b. München, IPP-1/269 (1992).

[67] R. Toschi, F. Engelmann, E. Salpietro et al., Fus. Eng. Des. 21 (1993) 1.

[68] R. Shaw, H.-W. Bartels and G. Vieider et al., 'Conceptual Design of a Local Alpha-Particle Limiter for NET', Proc. 17th Symp. Fusion Technol., Rome, 1992.

Data Bases for Thermo-hydrodynamic Coupling with Coolants

M. Araki[a], M. Akiba[a], R. D. Watson[b], C. B. Baxi[c], D. L. Youchison[b]

[a]   Japan Atomic Energy Research Institute, 801-1, Naka-machi, Naka-gun, Ibaraki, 311-01 Japan
[b]   Sandia National Laboratories, Albuquerque, NM 87185-1129 United States of America
[c]   General Atomics, San Diego, CA 92138-5608 United States of America

ABSTRACT

Since high heat flux removal in fusion reactors such as plasma facing components, in particular divertor plates, is subjected to high heat loads from their one side, comprehensive and promising databases are required.   This database summarizes thermal and mechanical properties of various materials including newly developed carbon based materials.   Thermal-hydraulics including heat transfer data and many critical heat flux data under one sided heating conditions are also summarized for water and helium gas.

1. INTRODUCTION

As the second stage of research and development (R&D) for fusion experimental reactors, recent three large tokamaks, i.e., JET in the European Community, JT-60 in Japan, and TFTR in the United States of America, were designed and constructed.   Break-even plasma condition which is defined that an output fusion power produced by D-T reaction is equal to an input power have been achieved in JET.   Equivalent break-even plasma condition in hydrogen plasma operation has also been achieved in JT-60.   These promising positive results lead the importance of R&D efforts on the next stage of fusion experimental reactors such as the International Thermonuclear Experimental Reactor (ITER) program [1], which is a collaborative enterprise between the European Community, Japan, the Russian Federation, and the United States of America.

Since next fusion experimental reactors will be designed to handle the nuclear fusion power, reactor engineering R&D issues are very important.   In particular, development of plasma facing components which will be subjected to severe heat loads not only during steady state normal operation but also during off-normal events such as plasma disruptions becomes one of the key issues to be overcome.   Divertor plates are the most important plasma facing components.   To minimize impurities into the plasma, it is necessary to use low-Z plasma facing materials such as high performance carbon- or beryllium-based materials with high thermal conductivity and strong mechanical properties.   Furthermore, to facilitate the conduction of heat from the armor to the actively cooled heat sink structure, the armor tile must be well-bonded to the heat sink structure.   Therefore, it is very important to develop the bonding technology because of poor compatibilities of thermomechanical properties.   Since the ITER is also designed for high plasma current and steady state operation, the plasma facing components will be subjected to more severe heat loads than those for the existing fusion experimental machines such as the JET, JT-60, and TFTR.   As summarized in table 1 [1], the steady state heat flux on the surface of the divertor plate is expected to be 15 to 30 $MW \cdot m^{-2}$.

For developing the plasma facing components such as the divertor plate, R&D issues can be

categorized into three developmental items: 1) the armor, 2) the heat removal structure, and 3) the braze technology.

With regard to developing the armor materials, there are some experimental results [2-10]. The most important issue is erosion damage by the tokamak plasma at normal and off-normal operations. Evaluations of the damage of divertor plates under disruption heat loads reveal that the surface of the armor material is enormously damaged. Essentially undamaged are the interface and the substrate of the divertor plate during a disruption. However there are large discrepancies of the material erosion data on the thermal shock heat loads between the experiments [2-10]. Therefore, only thermal and mechanical properties of carbon based materials and metals are presented in this paper.

The second issue is development of heat removal structures for the divertor plates under one-sided heating condition. In ITER, the divertor plate is exposed to stationary heat flux as high as 15 to 30 MW•m^{-2} described above. Since little developmental study of heat removal structure under one-sided heating conditions is available, high performance cooling structure is needed for the ITER divertor plates. The following thermal characteristics becomes important; critical heat flux (CHF) of the cooling structure, critical heat flux (CHF) correlations, and heat transfer around the circumference.

Since the third issue, i. e., brazing and fabricating technologies, are described and reported in Ref. 11, this R&D issue is skipped.

2. MATERIAL PROPERTIES

Tables 2 to 5 and figures 1 and 2 show thermal and mechanical properties of various carbon based materials and metals [1, 12, 13]. For carbon based materials, carbon fibers are used for improving thermal conductivity and reinforcing the bulk material compared with the graphite. One, two, and

Table 1 Required Performances for ITER PFCs.

Operation Phase		Physics		Technology	
Components		First Wall	Divertor	First Wall	Divertor
Normal Operation - Average neutron wall load	MW/m^2	1	0.5	0.8	0.4
- Peak/Average Surface Heat Flux	MW/m^2	0.6/0.15	15~30	0.6/0.15	15~30
- Peak Volumetric Heat Load in Structure	MW/m^3	20	5	15	4
- Number of Pulses (full load)		1		2~5	
- Total Burn Time	H	400		$10^4 \sim 3 \times 10^4$	
-Peak Neutron Damage (steel)	dpa	0.7	0.3	12~36	5~15
- Incident DT-Ions:					
• Peak Flux	10^{20}/m^{2}s	1	4000	1	4000
• Energy	eV	10~100	50~100	10~100	60~200
- Allowed water leak	g/s	10^{-8}		10^{-8}	
Disruptions - Number (at full load)	10^4	500		200~500	
- Thermal Quench					
•Time	ms	0.1~3		0.1~3	
• Peak energy depos.	MJ/m^2	2	10~20	2	10~20
- Current Quench					
•Time	ms	5~100		5~100	
• Radiative energy depos.	MJ/m^2	2		2	
• Run-away electron energy depos. (< 300MeV)	MJ/m^2	30		30	

three directional carbon fiber reinforced carbon composites (CFCs) are commercially available for fusion applications. Since fibers are highly oriented in the CFCs, these materials have anisotropic properties as shown in table. In general, one-directional CFCs have high thermal conductivities over 500 W•m⁻¹•K⁻¹ at room temperature parallel to the fiber, while fairly low perpendicular to the fiber. Their thermal expansion coefficient are almost zero in the fiber direction and around 10^{-5} K⁻¹ parallel to the fiber. From viewpoint of the residual stress from brazing, it is very important to match their thermal expansion coefficients. In this case, copper based materials are much better selection for one directional CFCs. Although their suitable thermal properties and thermal expansion coefficients as an armor tile for divertor plates, one directional CFCs have fairly low ultimate strengths in perpendicular to the fiber. From viewpoint of thermal stress and fatigue of the bonds, higher ultimate strength in this direction is required to withstand cracking and fracturing problems induced by high heat loads during manufacturing process and operation under one sided heating conditions. On the other hand, two or three directional CFCs have higher mechanical properties and relatively high thermal conductivities. In particular, newly developed three directional CFCs have thermal conductivities around 100 W•m⁻¹•K⁻¹ at 1000 °C. For design of divertor plates, further databases such as thermal and mechanical properties after neutron irradiation are required.

Table 2 Thermal conductivities of varoius carbon based materials as a function of temperature

Unit : W•m⁻¹•K⁻¹

Temp./°C	IG-430U	P-130 [1]	MFC-1 [2]	CX-2002U [3]	3DCC/s [4]	SEP112 [4]
20.0		850.0			247.0	280.0/210.0
27.0	155.0			381.0/320.0/215		
57.0			640.0/25.0		230.0	
100.0			570.0/23.5			
127.0	142.0			299.0/251.3/180		
200.0		700.0	495.0/21.0			
227.0	128.0			254.0/213.5/150	186.4	
300.0			442.1/19.0		.	140.0/123.0
350.0					157.1	
400.0		525.0	397.3/17.0			
427.0	100.0			193.0/161.7/117	145.0	
500.0			359.7/15.5		125.4	131.0/105.0
600.0		440.0	328.3/14.2			
627.0	80.0			153.0/127.1/94	116.5	
700.0			302.1/13.1			
800.0			280.3/12.3		106.0	
900.0			261.9/11.6		105.6	
1000.0	63.0	325.0	246.3/11.1	120.0/100.0/74		95.00/76.00
1100.0			232.6/10.7		107.9	
1200.0			220.2/10.3		104.0	
1300.0			208.5/10.1			
1400.0			196.8/9.8		.	
1500.0	52.0		184.8/9.6	104.0/85.0/65		76.00/62.00
1600.0			176.0/9.4			
2000.0	44.7					58.00/52.00

[1] : P-130 is bulk fiber material, not composite. Thermal conductivity is measured in fiber direction.

[2] : MFC-1 is felt type unidirectional carbon fiber reforced carbon composite. In the table, the first value corresponds to the thermal conductivity in the fiber direction and the second value in perpendicular to the fiber, respectivily.

[3] : CX-2002U is felt type two-directional carbon fiber reforced carbon composite. In the table, the values in each direction are measured.

[4] : 3DCC/S is three-directional carbon fiber reforced carbon composite. In the table, these data are measured by area method.

Table 3 Thermal conductivities of varoius metals as a function of temperature

Unit : $W \cdot m^{-1} \cdot K^{-1}$

Temp./°C	Mo	TZM	Mo5Re	Mo41Re	Nb-1Zr	OF-Cu	DS-Cu	W	W3Re	W5Re	W10Re	W26Re	W30Cu
20.0		125.0			47.5		350.0						
27.0						398.0		178.0					
57.0													
100.0	137.0		118.0	50.9			340.0		118.0			39.5	293.0
127.0													
200.0	136.0		115.0	54.3	50.2		325.0		115.0			47.6	285.0
227.0										88.5			
300.0	134.0		114.0	57.4			315.0		116.0			51.9	276.0
327.0						383.0		139.0					
400.0	131.0		113.0	61.5			300.0		113.0			55.3	267.0
427.0													
500.0		115.0	112.0	63.2	54.5		290.0		110.0			59.2	258.0
527.0						371.0		128.0			90.0		
550.0											68.9		
600.0	124.0			64.3					108.0			60.9	
650.0											70.1		
700.0				57.5									
727.0						357.0		121.0					
750.0											71.8		
800.0													
850.0		100.0									73.2		
900.0													
927.0						342.0		115.0					
950.0											74.4		
1000.0												66.7	
1050.0		87.0									75.3		
1500.0		75.0										64.1	
2000.0												62.8	

DS-Cu : dispersion strengthened copper, 0.5 % Al2O3, "GridCop"
W30(wt%)Cu : copper-infiltrated W-Cu (pseudo-) alloy.

Table 4 Thermal expansion coefficients

Unit : $10^{-6} \cdot K^{-1}$

Temp./°C	MFC-1 (1/2,3)	CX-2002U (1,2/3)	SEPN112 (1,2/3)	IG-430U	Mo	TZM	W	W5Re	W30Cu	Nb-1Zr	Cu	DS-Cu
	-0.9/12.0	1.6/5.8		4.7		5.3			11.5			
20.0												16.9
27.0					4.8	4.4				7.0	15.4	
100.0								4.35				17.0
200.0												17.3
300.0										7.3	16.6	17.7
327.0					5.3							
350.0			1.5/2.7									
400.0											18.3	18.0
500.0			1.7/2.9				4.5	4.45		7.8	19.1	18.5
527.0					5.7							
600.0											20.0	19.0
700.0										8.1		
800.0											21.6	
927.0					6.7							
1000.0			2.4/3.8			4.7						

W30(wt%)Cu : copper-infiltrated W-Cu (pseudo-) alloy.
DS-Cu : dispersion strengthened copper, 0.5 % Al2O3, "GridCop"

Table 5 Density, elastic moduli, yield and ultimate strength, and Poisson ratio

	MFC-1	CX2002	SEP N112	IG430U	OF-Cu	DS-Cu	TZM	W5Re	W-30Cu
density at RT, g/cm3	1.96	1.67	1.95	1.81	8.9	8.9	10.2	19.4	14.0
elastic modulus, GPa	100. (//) 0.8 (⊥)	10.7 (1) 8.1 (2) 3.4 (3)	28.0 (//) 24.0 (⊥)	9.5	82.4 (20°C) 78.5 (100°C) 73.5 (200°C) 65.7 (500°C) 58.8 (800°C)	134. (20°C) 121. (200°C) 106. (400°C) 91. (600°C) 75. (800°C)	300. (20°C) 260. (500°C) 220.(1000°C) 140.(1500°C)	400. (27°C) 382. (527°C)	218.
yield strength, MPa.(%)-°C at 20° and 400°C					44.1(.2)-20. 103.(4.)-20. 34.3(.2)-400. 66.7(4.)-400.	462.(.2)-20. 516.(10)-20. 228.(.2)-400. 270.(4.)-400.	710.(.2)-20. 1150(17)-20. 550.(.2)-400. 970.(15)-400.		
ultimate strength at RT, MPa, tensile/compressive	400./216(//) 3./16.(⊥)	35./49.(1) 31./50.(2) 11./54.(3)	65./160(//) 35./180(⊥)	42./94.	245.	516.	1150.	1100.	520.
Poisson ratio	0.15	0.19	0.11	0.18	0.33	0.3	0.32	0.3	0.3
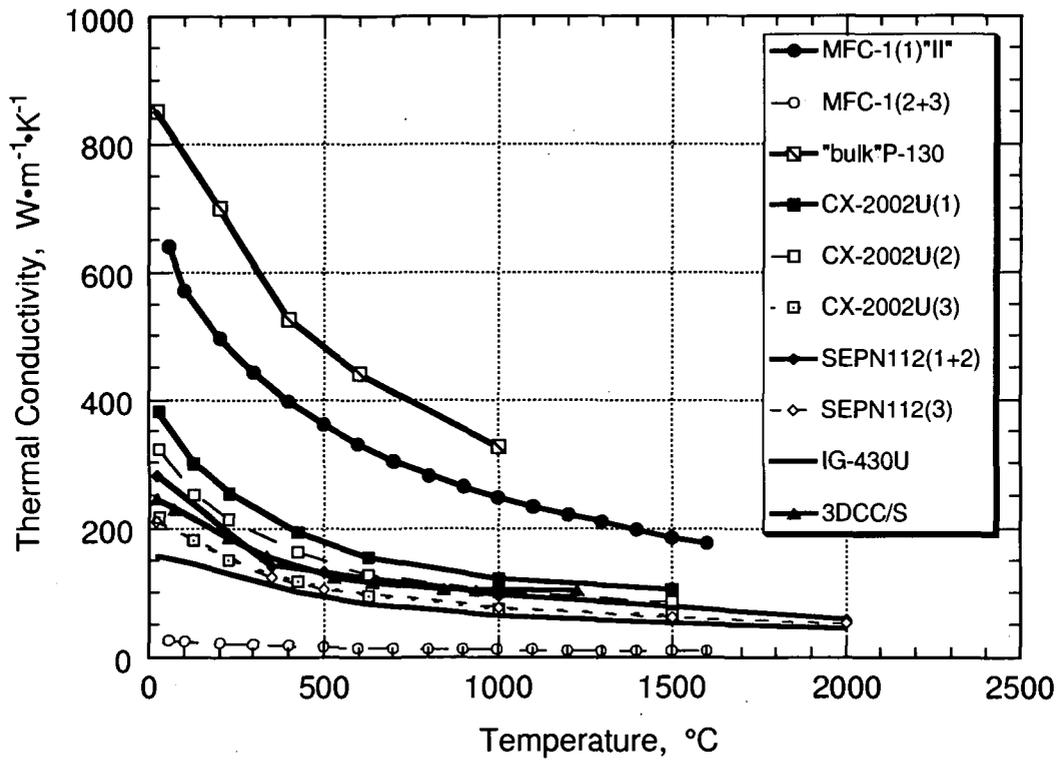
Figure 1   Thermal conductivities of various carbon based materials
as a function of themperature
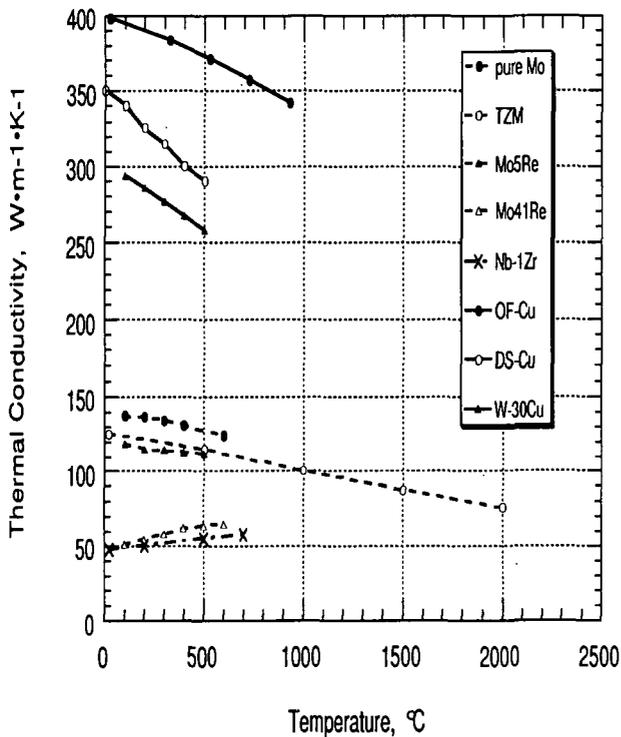
Figure 2a   Thermal conductivity of the candidate materials
for divertor plate cooling structure (I)
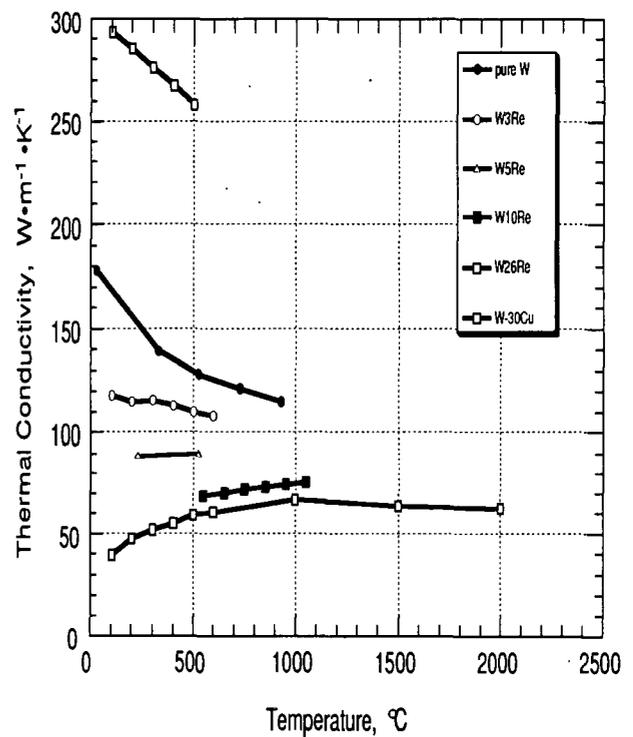
Figure 2b   Thermal conductivity of the candidate materials
for divertor plate cooling structure (I)

3. THERMAL-HYDRAULICS

Since divertor plates are subjected to high heat loads under their one side, characteristics of thermal-hydraulics such as critical heat fluxes and heat transfer coefficient of the cooling channel are required. In this paper, critical heat fluxes and heat transfer coefficients based on the experiments under one sided heating conditions are summarized and are compared with existing correlations based on the uniform heating condition.

3.1 Critical heat flux

Under one sided heating conditions, various kinds of cooling channel elements for high heat flux and steady state heat removal have been investigated so far [14-21]. There are two types of the cooling elements, i. e. either a tube or a panel structures. In this section, critical heat flux of the tube structure, straight tube, internally-finned tube, and swirl tube, is described first and performance of hypervapotron as the panel structure is discussed second.

3.1-1 Straight tube

Figure 3 shows a typical example of incident critical heat flux of various cooling channels performed in hydrogen ion beam facility at Japan Atomic Energy Research Institute (JAERI) [20]. In the figure, vertical axis indicates incident critical heat flux (ICHF) which is defined as heat flux applied at outer surface of the cooling structure. Inlet water pressure and flow velocity range from 0.44 to 0.96 Mpa and from 2.2 to 15 $m \cdot s^{-1}$, respectively. All data were measured at the subcooling from 55 to 100 K. As seen in Fig. 3, ICHFs of tubes without internal fins or a twisted tape under one sided heating condition increase with flow velocity. However, ICHF saturates if flow velocity increases for more than 10 $m \cdot s^{-1}$. For example, ICHF of straight tube is around 20 $MW \cdot m^{-2}$ for flow velocities from 10 to 16 $m \cdot s^{-1}$. In this experiment, major dimensions of the straight tube were 10 mm outer diameter and 7 mm inner diameter. To investigate the outer diameter dependence, JAERI has also performed identical experiments for different outer diameter straight tube. At smaller tube (OD/ 7mm), ICHFs were slightly higher under identical cooling conditions. On the other hand, ICHFs of larger tube (OD/15 mm) were similar values compared with those of 10 mm outer diameter straight
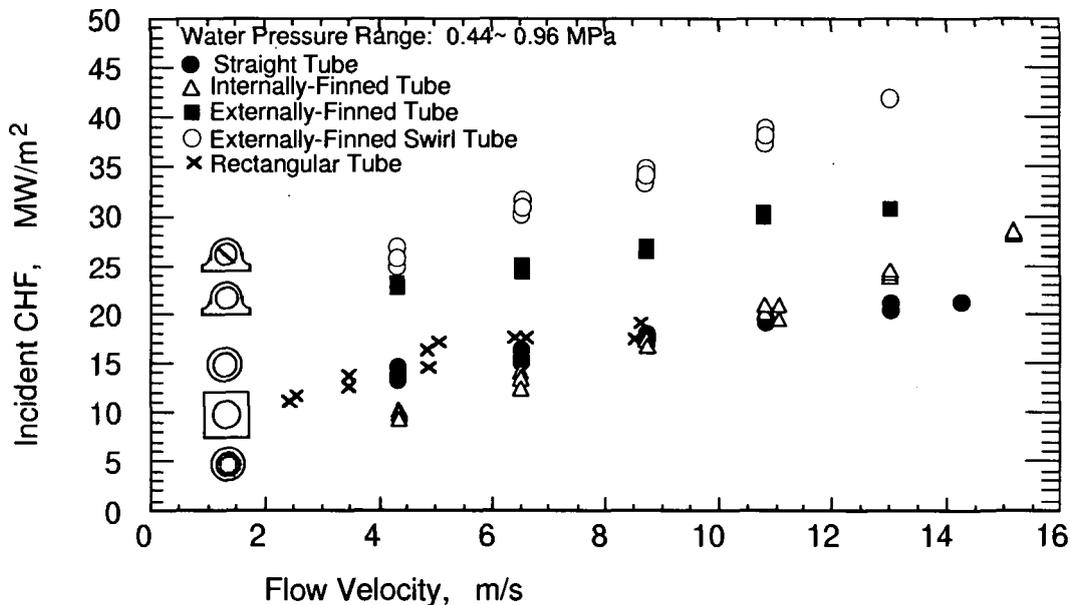
Figure 3   Experimental CHF Data as a Function of Flow Velocity.

It is noted that the ordinate shows CHF at the tube outer surface, but not that at the tube inner surface.

tube. For the evaluation of the dimension dependence of ICHF, further experiments will be required. Dependence of ICHFs on the inlet pressure was also evaluated and was small in the experiments. These results are very consistent with the previous experimental results [16].

3.1-2 Internally-finned tube

There are some kinds of tubes with an internal fin, namely internally-finned tube. In general, tubes with helixed internal fins are used for high heat flux removal to enlarge cooling area and to promote small vortex flow along the flow direction at the boundary layer. In Oak Ridge National Laboratory (ORNL) and the JAERI experiments, number of fins and helix angle were selected to 16 and 5°. Experimental results of the internally-finned tube have also indicated in figure 3. Major dimensions were 10 mm outer diameter, 7 mm inner diameter, and about 1 mm fin height. ICHFs of the internally-finned tube linearly increase with the flow velocity. At lower flow velocities (up to 9 $m \cdot s^{-1}$), ICHFs, however, are lower than those of the straight tube due mainly to large flow stagnation area around the internal fins. At higher flow velocities (more than 9 $m \cdot s^{-1}$), ICHFs are higher. It means that much larger flow rate will be necessary to obtain the identical ICHF up to 20 $MW \cdot m^{-2}$. Dependence of ICHFs on the inlet pressure was also measured and was confirmed to be small which is similar tendency of the straight tube.

3.1-3 Swirl tube

Up to now, swirl tube has been tested in many laboratories [18 -21], and has confirmed its high performance. In general, a thin tape around 0.5 mm made of Inconnel-625 or stainless steel 304 is twisted, and then this twisted tape is inserted and fixed to a smooth tube inner wall by cold working or brazing. To obtain strong extraction force between the tape and the tube wall (i. e. force needed to pull out the tape, normalized to the unit length of tape), cold working and/or brazing are applied, resulting in the extraction force per length at least 600 $N \cdot m^{-1}$ even if only cold working is applied [20]. Furthermore, both ends of the twisted tape are also fixed to the tube wall with sleeves. Advantages of twisted tape are not only to increase heat transfer coefficient but also to mix hot and cold water under one sided heating conditions. During boiling, the resultant centrifugal force radially accelerates the denser water and displaces the lighter vapor bubbles more efficiently.

To minimize the thermal deformation during heating, JAERI proposed to add an external fin at the rear of the swirl tube as shown in Fig. 4 [20]. Consequently, the plastic thermal deformation measured drastically decreased as shown in Fig. 5. The abscissa is defined by vertical thermal deformation length at the tube length of 1 m. Although only one point for each tube in the figure is
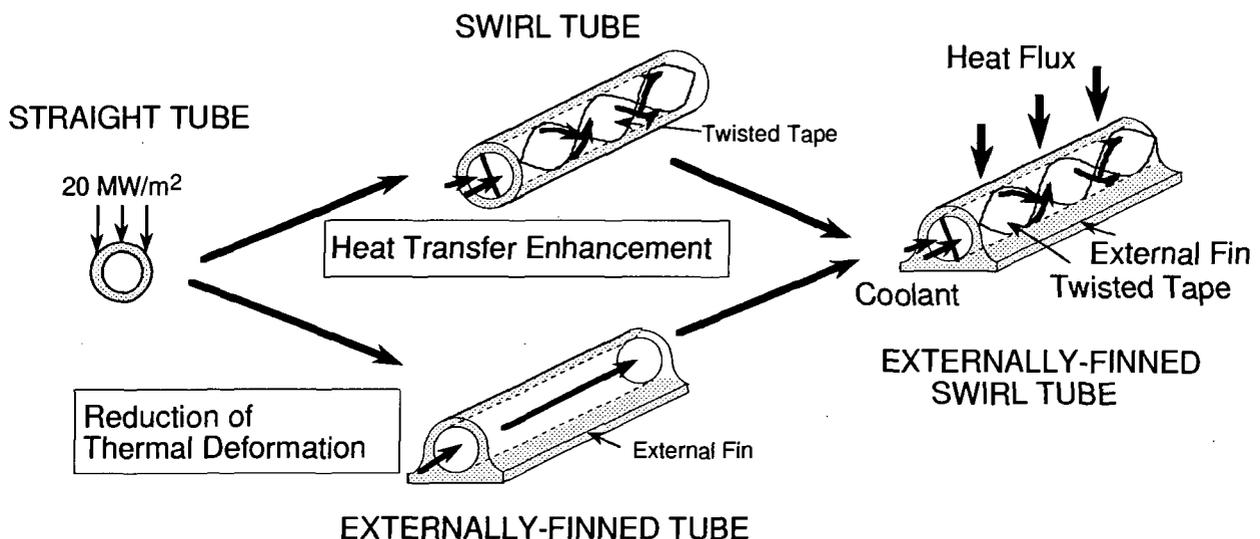
Figure 4   Schematic of the externally-finned swirl tube.

measured with micrometer after testing, it is confirmed that thermal deformation behavior of the tube is similar tendency during heating. This type of tube, namely an externally-finned swirl tube, has great performances on not only ICHFs, but also thermal deformation compared with other type of tubes. It is noted that at the flow velocity of 10 m•s⁻¹ ICHF as high as 38 MW•m⁻² was obtained in the externally-finned swirl tube.

Effect of the pressure on ICHFs are also indicated in Fig. 3. Its dependence on the inlet water pressure of from 0.5 to 0.9 MPa, which corresponds to saturation temperature difference of about 25 K, seems to be small. For evaluation of ICHF on the pressure, further experiments will be necessary for relatively wide pressure ranges up to 4 MPa.

Other important issue for the design of the divertor plate, ICHF dependence on the subcooling, should be evaluated. Figure 6 shows ICHF of swirl tube as a function of the subcooling for different flow velocities performed in electron beam test system at Sandia National Laboratories as the collaborative experiment between US and Japan [22]. Strong dependences of ICHFs on the subcooling are observed. ICHF-dependence on subcooling is nearly linear, ranging from as low as 20 MW•m⁻² at 30 K subcooling, to 60 MW•m⁻² at 150 K subcooling. From the figure, a proportionality constant is expected to be around 0.3 MW•m⁻²•K⁻¹. For example, ICHF at the subcooling of 80 K decreases by a factor of 0.6 at the 130 K. Even if such high dependence on the subcooling, swirl tube has ICHF as high as 40 MW•m⁻² at a cooling condition for subcooling, flow velocity, and inlet pressure to be 80 K, 10 m•s⁻¹, and 1MPa. Swirl tube has already been applied as a cooling tube element of an ion beam dump for neutral beam injector at ORNL. This ion beam dump can handle a total power of 2.7 MW, in particular surface heat flux as high as 54 MW•m⁻² for 30 s [18]. An ion beam dump which consists of an array of 16 externally-finned swirl tubes was also installed in JT-60 NB test bed (PBEF). This ion beam dump have been operated for long periods under large number of high-heat-flux environments, which typical beam condition is 20 to 35 MW•m⁻² for several seconds. For more than 5 years operation, no fatal damages including erosion by sputtering and water corrosion induced by high flow velocity around 10 m•s⁻¹ have been confirmed. Furthermore, for neutral beam injector based on negative-ion-beam of JT-60 the externally-finned swirl tube is applied for a cooling tube element of a negative and positive ion dumps, based on the successful experimental results. Each ion dump is designed to be able to handle residual deuterium beams at an beam energy of 500 keV and a total power of 4.2 MW for 10 s with a peak heat flux around 15 MW•m⁻² under the design velocity of 10
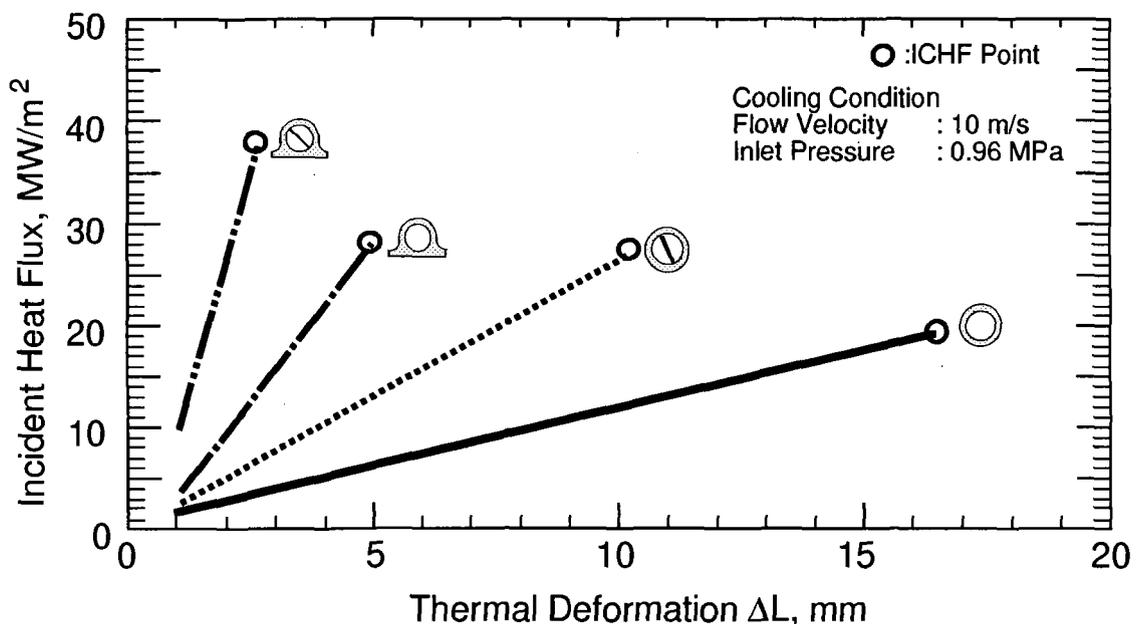
Figure 5   A comparison of thermal deformation for various cooling tubes.
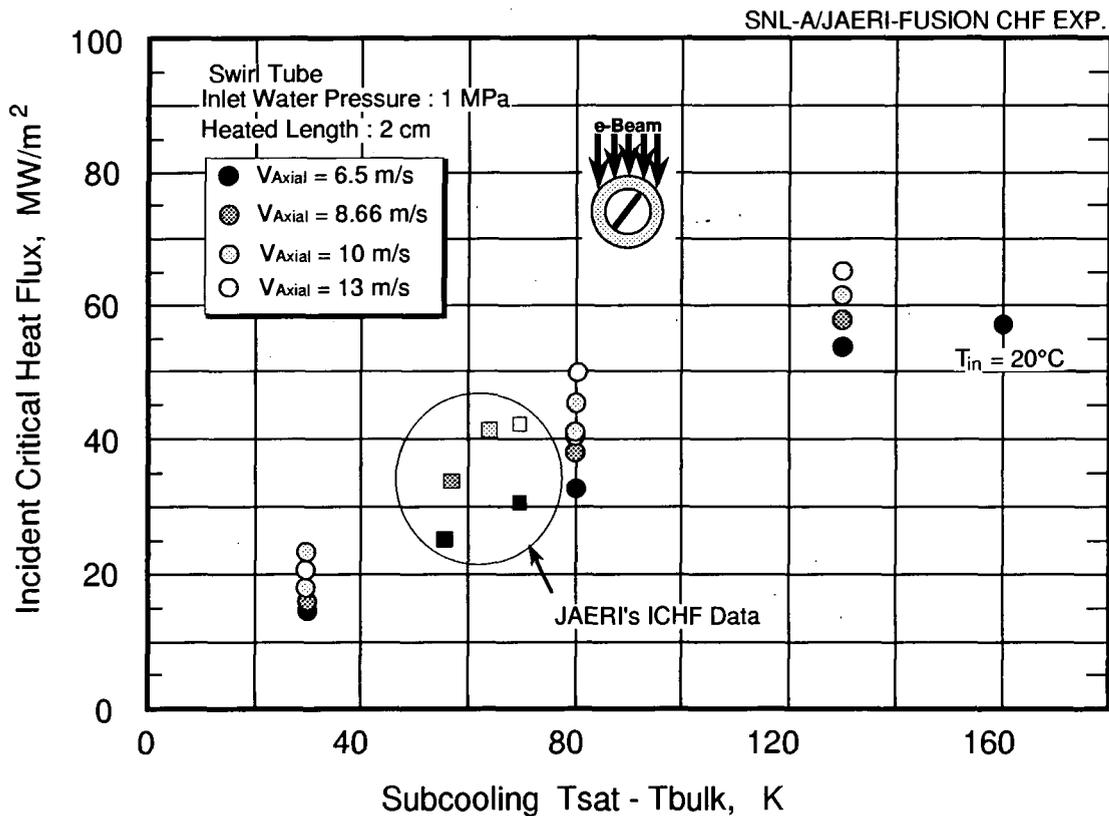
Figure 6   ICHF of Swirl Tube for Diffierent Subcooling

In the figure, symbols ■, ▨ , ▦ , and □   show JAERI ICHF data obtained under the subcooling of from 75 to 90 K.

$m \cdot s^{-1}$ for 1 MPa [23].

3.1-4 Hypervapotron

Hypervapotron (HV) as shown in Fig. 7 is device of finned panel structure with flow direction perpendicular to the fins. To be effective, HV is made from a high thermal conductivity material such as copper. Coolant is subcooled water at a velocity of 3 to 10 $m \cdot s^{-1}$. The device operates in a " hypervapotron" mode at velocities less than 3 $m \cdot s^{-1}$ if the heat flux is high enough [24]. During this mode, the space between the fins starts filling up with water vapor. Once the space is completely filled with steam, the steam is expelled in the main stream and the space filled with cold water. Thus the device operates in a transient (pulsating) mode. At higher velocities (above 5 $m \cdot s^{-1}$), the device operates in a steady state mode.   Figure 8 shows some of the experimental results obtained at JET test bed by Falter [25] for a water cooled copper HV. These results show that, at low values of incident heat flux the heat transfer is by forced convection only. As the heat flux is increased some of the heat transfer surface reaches incipient boiling temperature. After further increase in the incident heat flux, due to high thermal conductivity of the copper, and large conduction areas, heat transfer by forced convection, nucleate boiling and film boiling can simultaneously occur in HV. Peak surface heat fluxes greater than 25 $MW \cdot m^{-2}$, which are adequate for fusion divertors, have been achieved in HVs without burnout at a subcooling of about 100 K. Further experiments such as subcooling dependence will be necessary for the evaluations. A comparison of HV and swirl tube under identical heat flux and cooling conditions, has shown that, HV has a 50 % pressure drop and about 33 % pumping power compared to swirl tube. During the coolant pressure was about 1 MPa, the subcooling for swirl tube was 134 K and subcooling for HV was 114 K, respectively. The peak surface temperatures were approximately equal at the peak heat flux of 25 $MW \cdot m^{-2}$.

A method to analytically predict the performance of HV described in Ref. 26, shows good agreement between analysis and experiments for variety of geometries, for two different materials and a range of flow conditions as shown in Fig. 9. The analytical method consists of using the standard thermal hydraulic correlations in different heat transfer regimes (forced convection, incipient boiling, nucleate boiling etc.) to obtain a continuous relation describing heat transfer coefficient as a function of local heat transfer surface temperature. The relation depends on the flow geometry, flow velocity, coolant pressure and subcooling. This relation is then used in a finite element analysis with the prescribed incident heat flux to calculate the temperature distribution in the HV geometry.

HV can be rectangular or cylindrical in geometry as shown in Fig. 7. Therefore, HVs can be possible for cooling of ITER (peak heat flux = 5 MW•m⁻²) and TPX (peak heat flux = 7.5 MW•m⁻²) divertors. In addition it can be used for other fusion applications with high heat flux where water is acceptable as a coolant, such as NB dump plates, Gyrotrons and ECH dummy loads. Main advantages of hypervapotron is the ability to operate at lower velocities and pressure, for same heat transfer performance and safety margin.
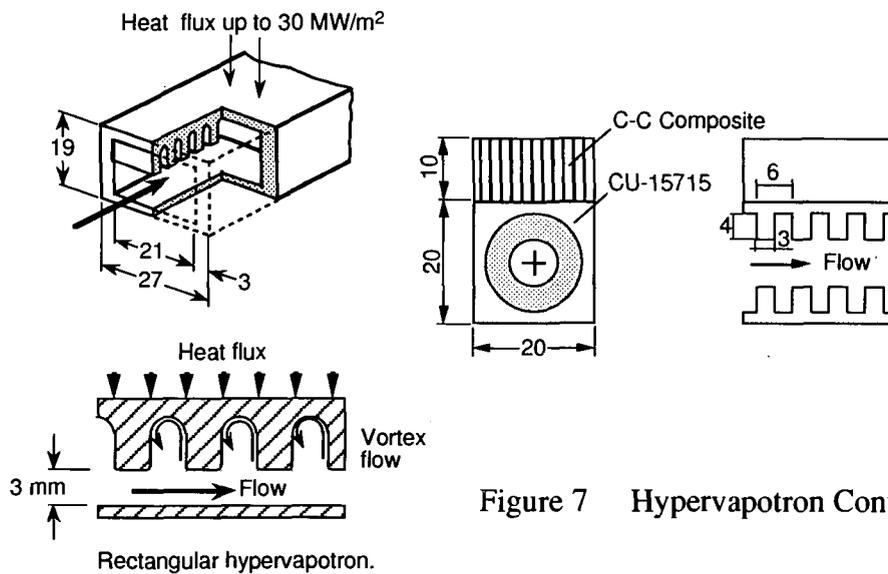
Figure 7   Hypervapotron Configurations.

Heat transfer in a vapotron with a water inlet
temperature of 15, 40 and 50 °C and 7.5 bar.

Heat transfer in a vapotron with a water inlet
temperature of 15 and 50 °C and 3.5 bar.
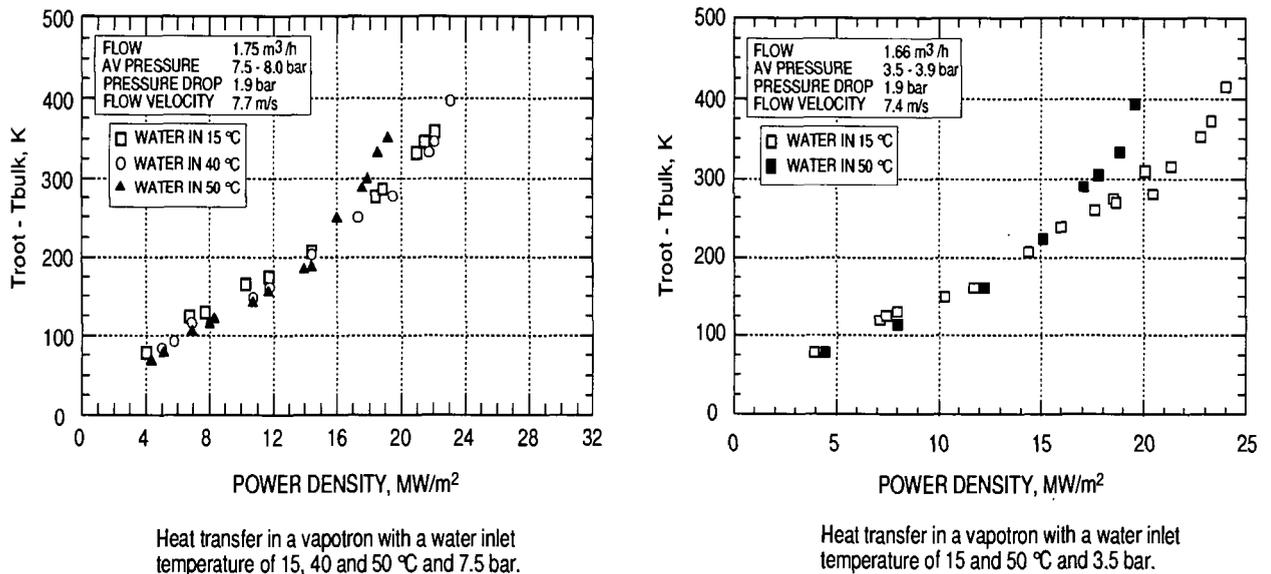
Figure 8   Experimental Results and Different Regimes

254
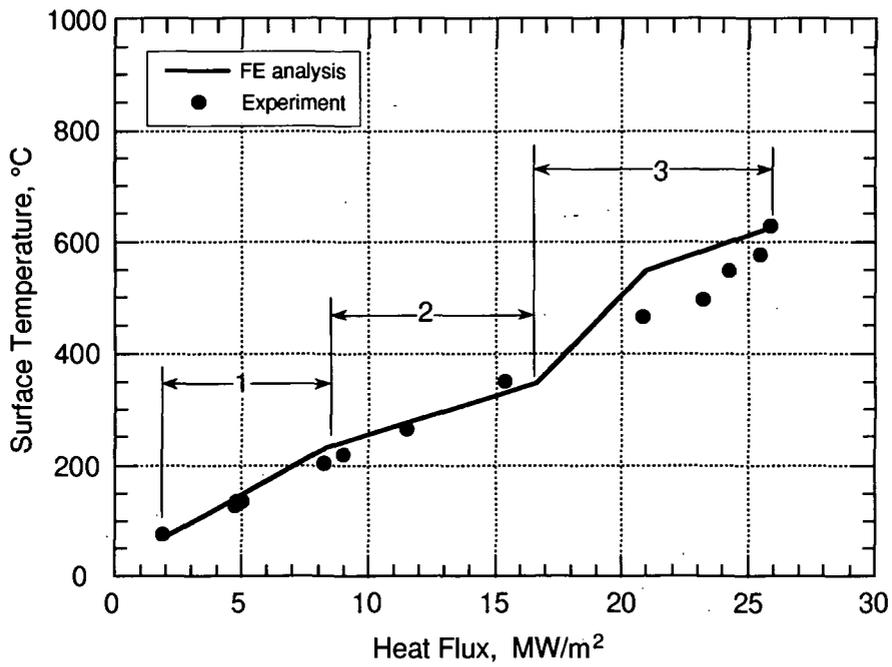
Rectangular copper hypervapotron; V=8.4 m/s, P=6.8 bar; Tin=20 °C
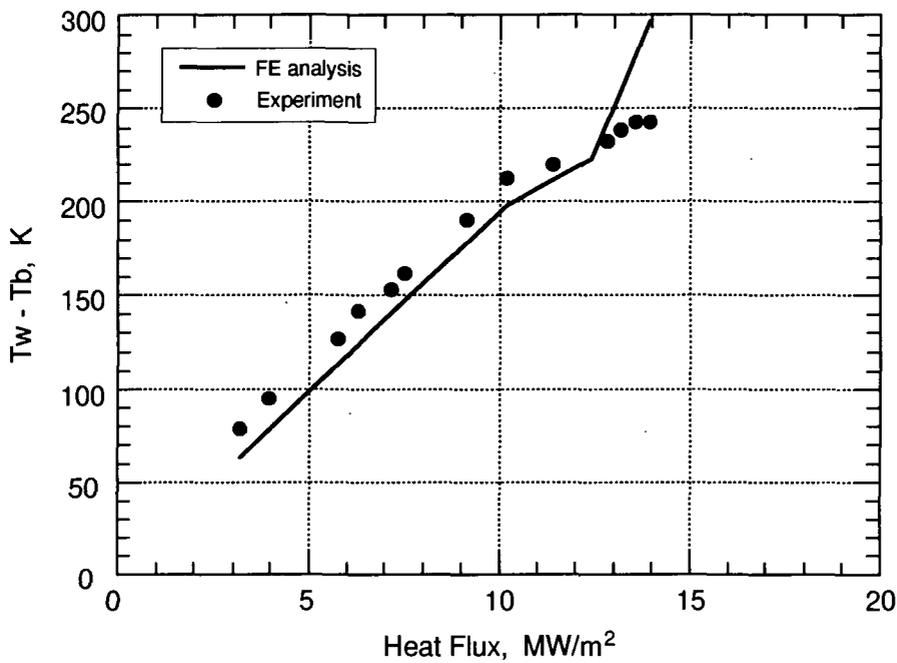
Comparison of analysis with experiment for cylindrical hypervapotron.

Material: Moly, Velocity=9.2 m/s, Pressure= 0.93 MPa, Subcooling= 91°C

Figure 9   Comparison of Analysis with Experiments for Cylindrical Hypervapotron.

3.2 CHF comparison [27]

3.2-1 Tube without heat transfer enhancement

Before the comparison between the experimental CHF data and the existing CHF correlations, experimental ICHFs have been translated into critical heat flux at the tube inner surface (CHF) by applying heat transfer coefficient proposed by Thom [28] or Shah [29]. Since none of correlations for CHF under one sided heating conditions do not yet exist, experimental CHF data have been compared with some existing CHF correlations [30-34] obtained under the uniform heating condition. It is noted that these correlations predict CHF values with a discrepancy as large as around ± 40 % at the
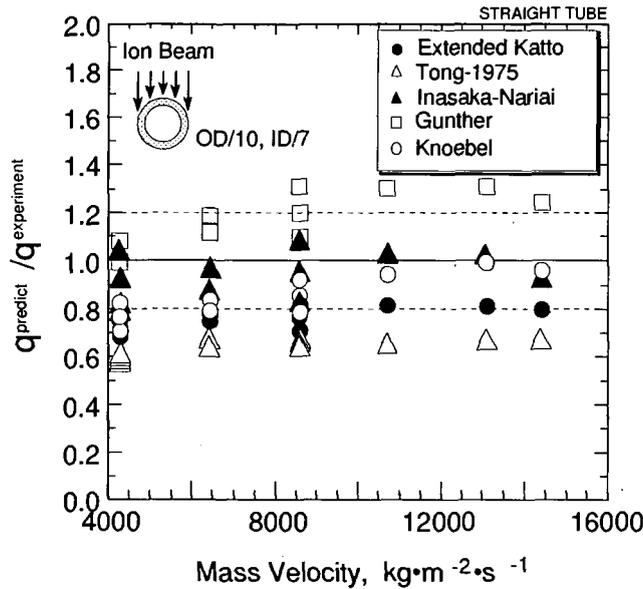
Figure 10   Comparison of experimental CHF data with predicted CHF for straight tube.
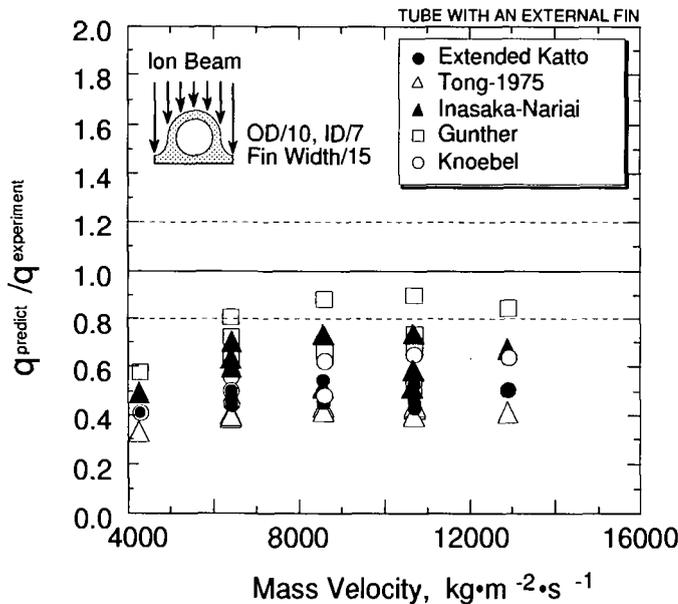
Figure 11   Comparison of experimental CHF data with predicted CHF for externally-finned tube.

256
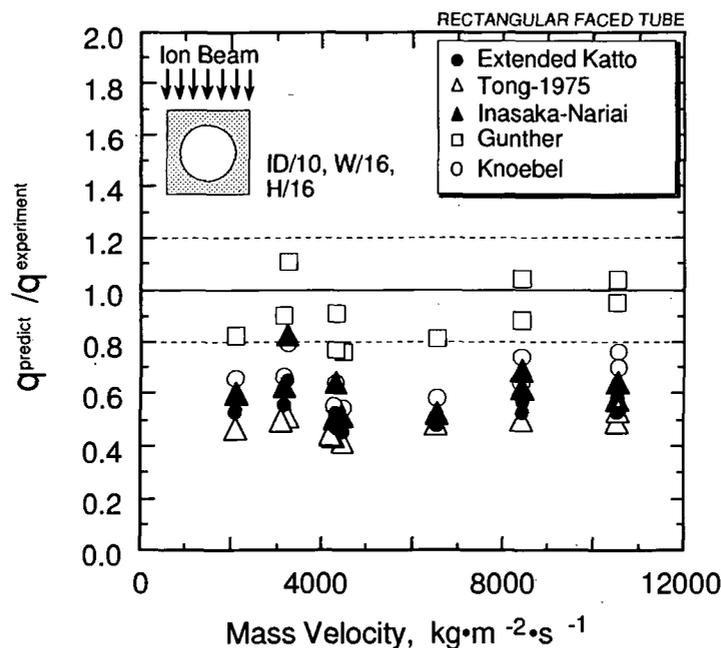
Figure 12   Comparison of experimental CHF data with predicted CHF
for rectangular faced circular tube.

same flow condition due mainly to different data bases. Figures 10, 11, and 12 show comparison results of the experimental CHF data under one sided heating conditions with the existing correlations. The ordinate indicates the ratio of the experimental CHF value to that predicted by each correlation. For straight tube, the experimental data show relatively good agreement with the some correlations proposed by Inasaka-Nariai, Knoebel, and Katto with an accuracy of -20 to +10 %. On the other hand, for a tube with an external fin or a rectangular faced circular tube, correlations except for Gunther's correlation systematically underestimate CHF values for over the range of mass flows investigated in the present experimental conditions described above. It might be for two reasons; 1) applied heat transfer coefficient along the circumference of the tube is slightly different compared with the actual phenomenon and 2) the existing correlations strongly depend on the inner diameter and the pressure, while in the experiments a small difference for different inner diameter and the pressure. To evaluate the applicability of the existing correlations for one sided heating conditions, further experiments at the wide ranges of the pressure, dimension and subcooling are necessary.

3.2-2 Swirl tube

For swirl tube, there are a few investigations on a comparison of the experimental results with the existing correlation. Koski [19] and Schlosser [21] reported that modified Tong-75 has been shown to be reasonable for their experimental results under one sided heating conditions performed in different test facilities. Though they measured ICHFs from the experiments, CHF at the tube inner wall have been analyzed with using the existing heat transfer correlations based on the uniform heating condition described above. However they have not investigated whether or not the existing heat transfer correlations are applicable for one sided heating conditions. From the experimental results on heat transfer under one sided heating conditions described in next section, it is noted that an additional error about ± 10 % between the correlations and the experimental results includes in their evaluations when their existing correlations are simply applied. Furthermore, a few experimental data was used for their evaluations and experimental conditions ranged very small. For the evaluation of the applicability of the existing CHF correlations on CHF under one sided heating conditions, further experiments are strongly required. It is also very important to evaluate heat transfer coefficient along the circumference of the tube because of one sided heating conditions.
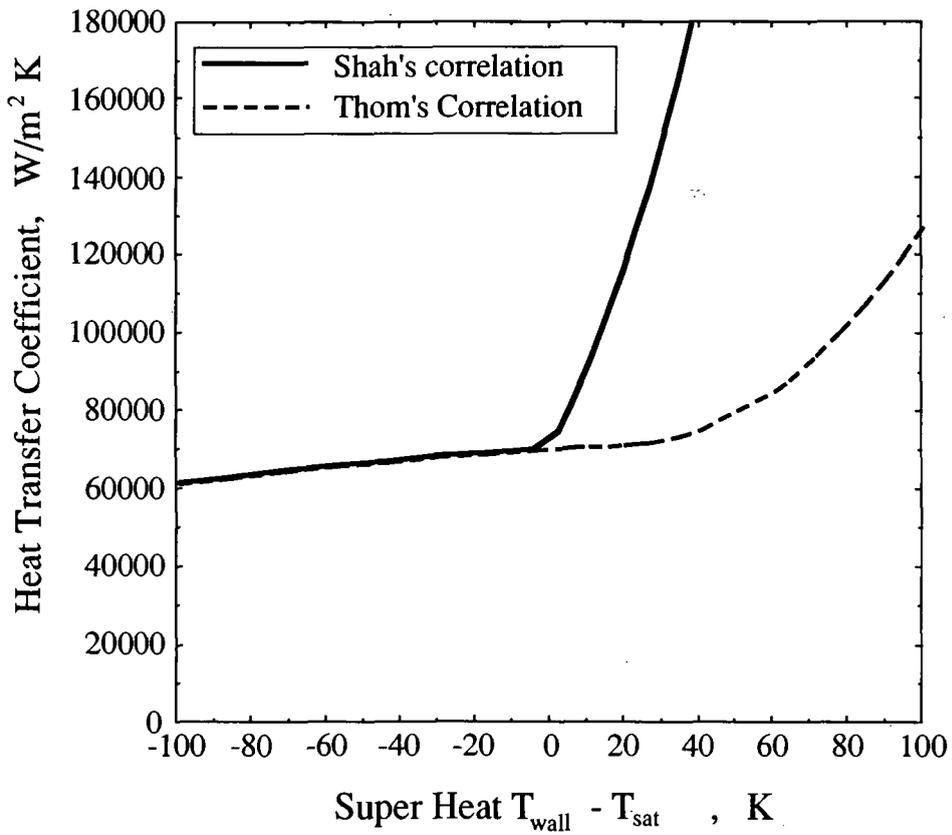
Figure 13 A comparison of existing heat transfer correlations for subcooled flow boiling.
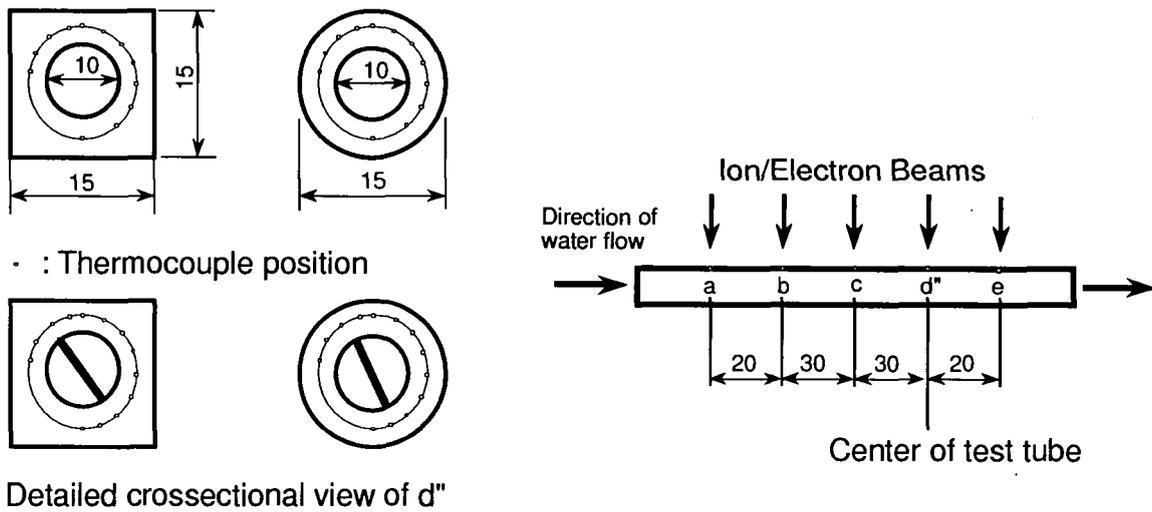
Figure 14 Test tubes for heat transfer experiment.
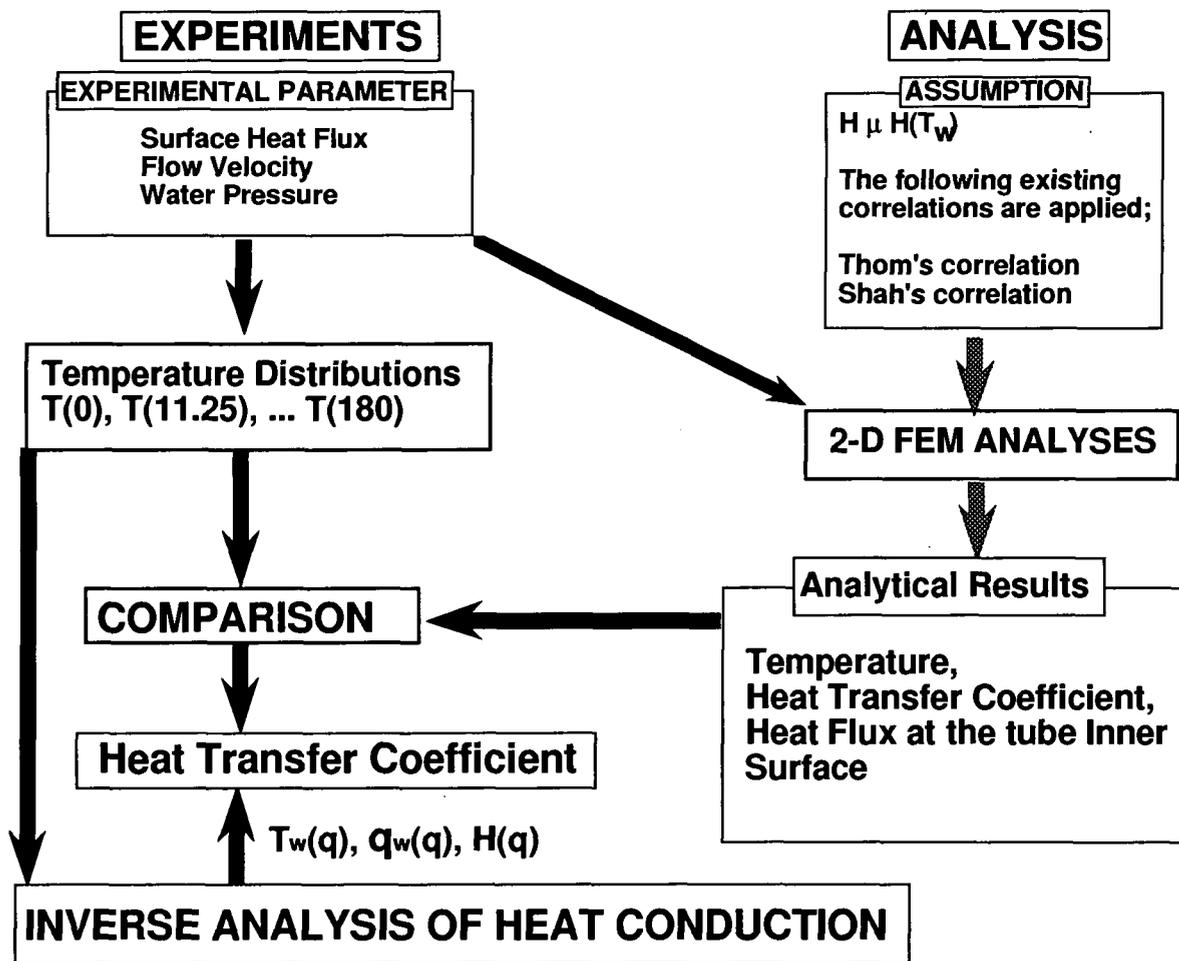
Figure 15 Evaluation procedure for the prediction of heat transfer coefficients.

3.3 Heat transfer

3.3-1 Water cooling

For prediction of heat transfer under one-sided heating conditions, none of literatures and experimental results, however, have led us whether or not existing correlations based on uniform heating condition, i. e., Thom and Shah (Jens-Lottes) correlations, can be applied. Furthermore, their predictions are also scattered as shown in Fig. 13 even if the same analytical condition is applied. This reason is attributable mainly to 1) lack of database, 2) small range of super heat up to 20 K, and 3) wide extrapolation. In the cooling channel of the divertor plates, nucleate boiling with super heat more than 20 K will be expected due to high heat flux environment. To systematically evaluate heat transfer phenomenon under one sided heating conditions, JAERI has performed heat transfer experiments of four kinds of cooling test tubes as shown in Fig. 14 at JT-60 NB test bed [35]. In the test tube, many thermocouples are buried along the circumference and flow direction to measure temperature responses at different positions. Figure 15 shows the evaluation procedure for the prediction of heat transfer coefficients under one sided heating conditions. Experimental conditions are as follows;

water flow velocity   ; 4.2 ~ 16 m/s
Local pressure   ; 0.5 ~ 1.3 MPa
Incident heat flux (peak)   ; 2 ~ 40 MW/m^2
Heat flux profile ; Gaussian
e-holding at half maximum   ; 175 mm

259
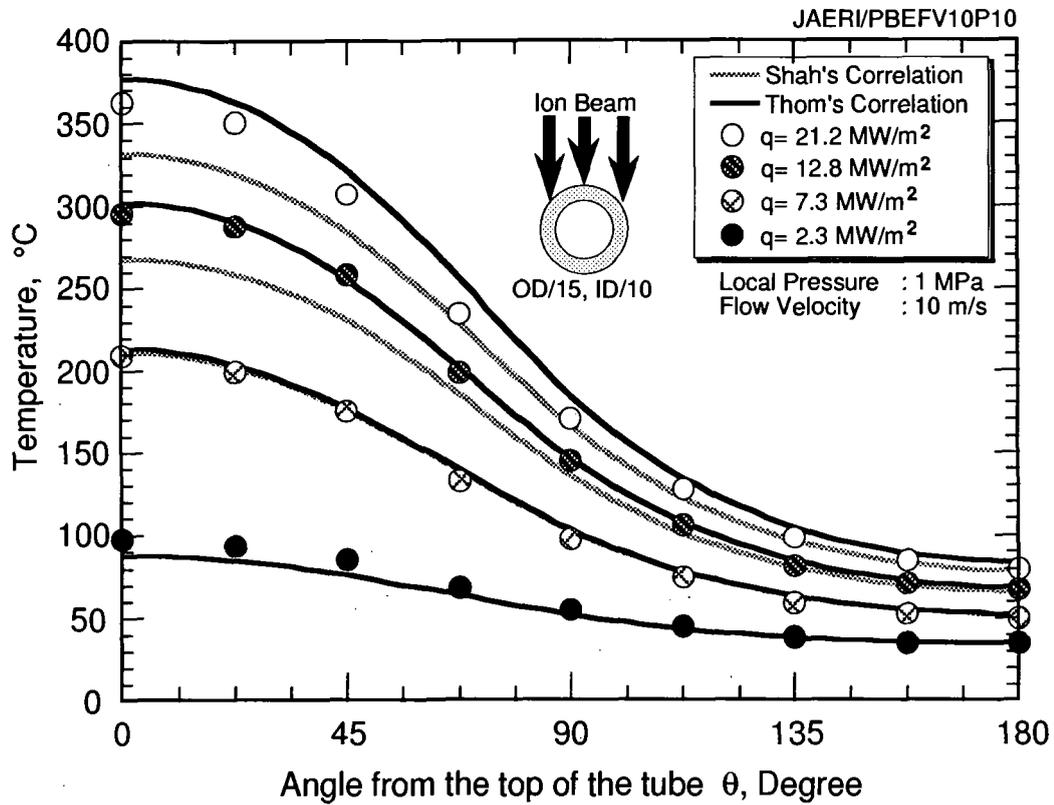
Figure 16   Temperature distributions at the thermocouple positions.
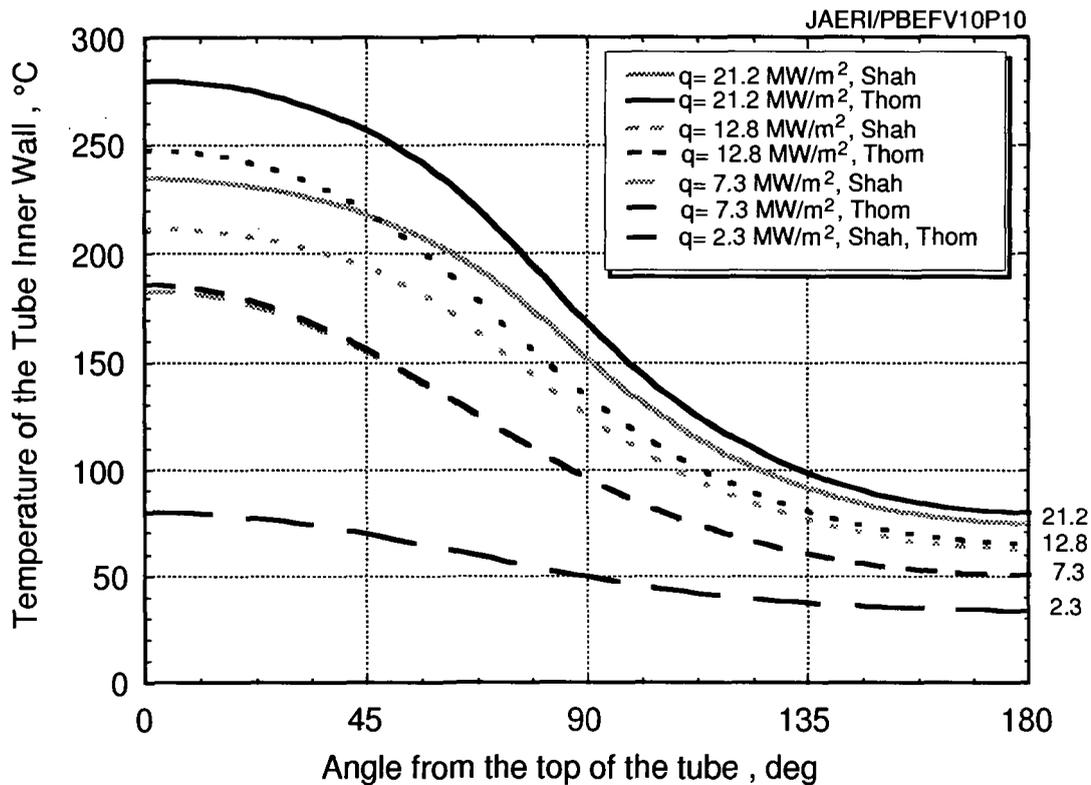
Figure 17   Temperature distributions at the tube inner wall.

260

At the first step, finite element analysis using ADINA has been performed applying the experimental conditions to predict the temperature distributions at the thermocouple positions and has been compared with the experiments. Typical results in the tube without a twisted tape are shown in Figs. 16, 17, and 18. Figure 16 shows an example of temperature distributions at the thermocouple positions for different surface heat fluxes ranged from non boiling to nucleate boiling close to burnout. The abscissa shows the angle from the top of the tube. This figure also shows analytical results predicted by Thom and Shah(Jens-Lottes) correlations. At forced convection cooling (none boiling) regime, analytical results show relatively good agreement with the experimental results. On the other hand, at transition to boiling and nucleate boiling regimes it is found that experimental data position among lines predicted by their correlations within an error of -10 % to + 30 % as shown in Fig. 16, where Thom correlation overpredicts the temperatures, while Shah correlation underpredicts. It means that experimental data can roughly be predicted within a band between their predicted lines. Based on these results, temperature distributions at the tube inner wall and inner surface heat fluxes are analyzed as shown in Figs. 17 and 18, respectively [35]. In particular inner surface heat flux can be predicted within an accuracy of ± 10 % by applying their correlations even if relatively large temperature differences between their correlations are observed. Therefore, for tubes without a twisted tape, existing heat transfer correlations introduced by Thom and Shah are roughly applicable for the heat transfer prediction under one sided heating conditions with an accuracy of ± 30 %, although a small discrepancy between the experiments and the analyses is found. To determine the heat transfer coefficients under one sided heating conditions, further evaluations such as inverse analyses of heat conduction are necessary. Figure 19 shows a preliminary result of inverse analysis of heat conduction [36].
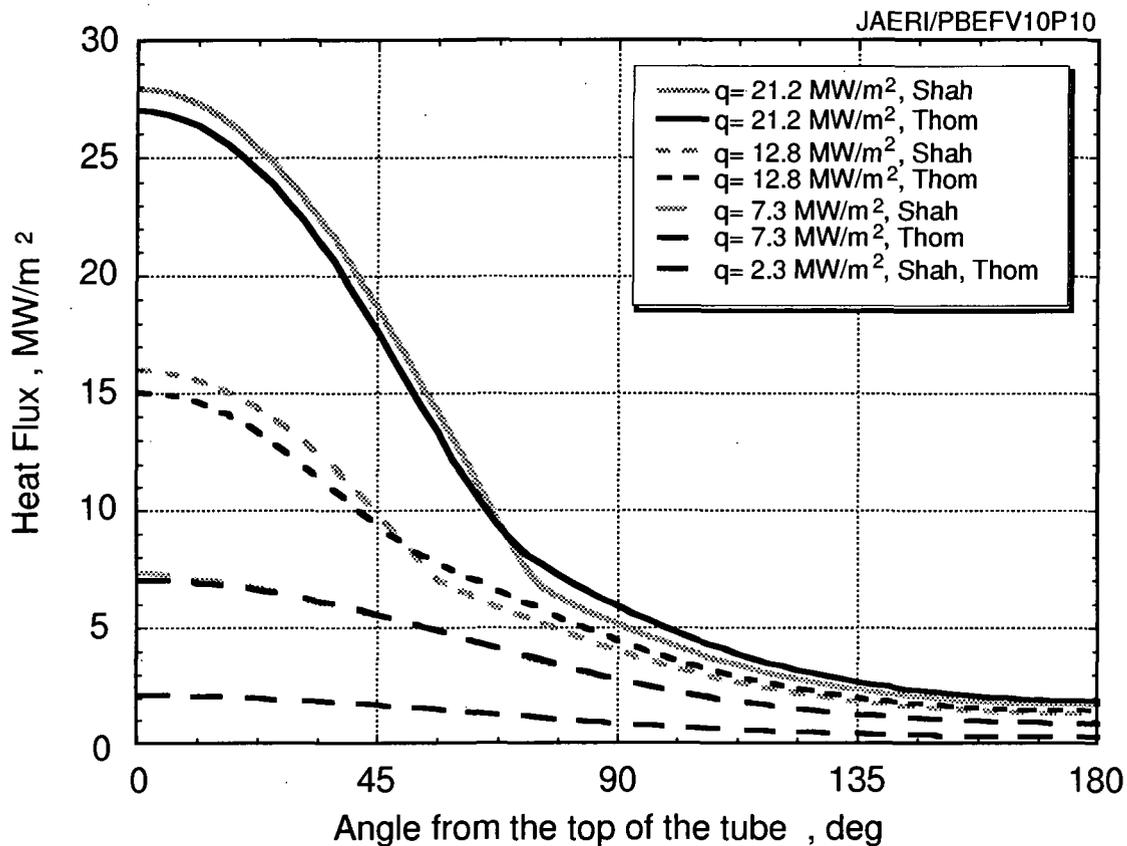
Figure 18   Heat flux distributions at the tube inner wall.
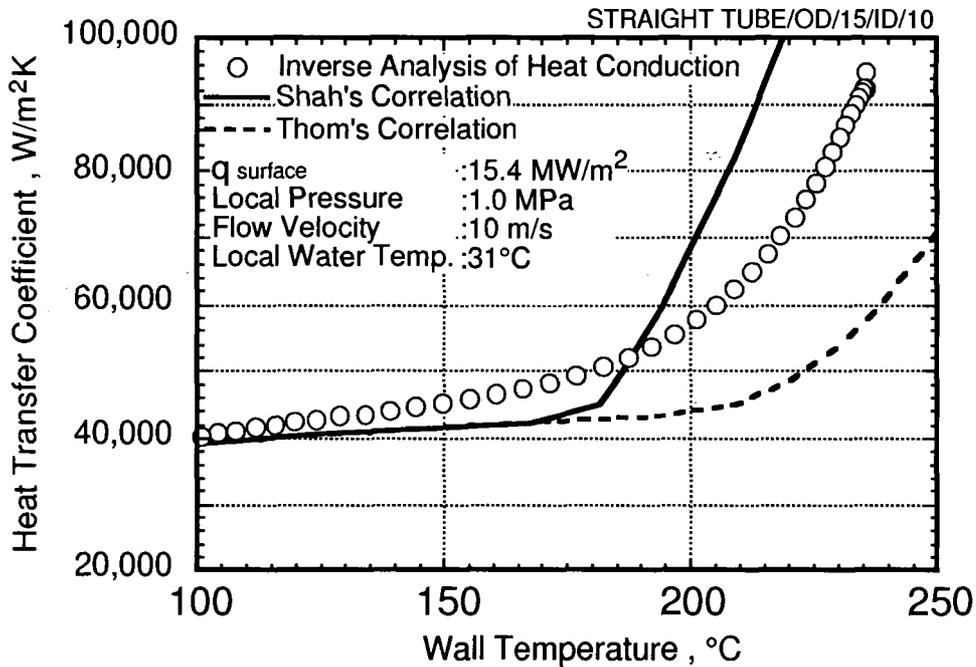
Figure 19   Predicted heat transfer coefficients under one sided heating condition.

For the tube with the twisted tape inserted, similar evaluation procedure has been applied to predict heat transfer coefficients under one sided heating conditions [36]. In this case, large heat transfer enhancement is expected due to vortex flow. At the first step for the evaluations, Gambill correlation [37] for heat transfer enhancement factor at non boiling regime has simply been applied for all regimes. Figure 20 shows a comparison of experimental and analytical temperature distributions at the thermocouple positions for different incident heat fluxes. Experimental data also roughly position among the predicted lines as the similar to the results of the tube without the twisted tape, leading us to conceive prospect for the prediction of heat transfer coefficients under one sided heating conditions. Therefore, heat transfer coefficients over the entire temperature range at this time can be predicted by applying the following correlations within an accuracy of ± 30%;

- Non boiling regime

$$Nu = 0.023 \cdot Re^{0.8} \cdot Pr^{0.4} \cdot (\frac{\mu^{0.14}}{\mu_w^{0.14}}),$$
Dittus-Boelter equation [38]   ..... (1)

$$Nu_s = Nu \cdot \frac{2.18}{y^{0.09}};$$
Gambill equation for swirl flow [37] .... (2)

- Transition to nucleate boiling

$$\frac{q}{q_{con}} = \left[1 + \left(\frac{q_{boil}}{q_{con}}\left(1 - \frac{q_{bi}}{q_{boil}}\right)\right)^2\right]^{0.5};$$
Bergles-Rohsenow equation [39] .... (3)

- Nucleate boiling

$$T_{wall} - T_{sat} = 0.022 \cdot \frac{q^{0.5}}{exp\left(\frac{p}{8.6}\right)};$$
Thom correlation [28]   .... (4)

262
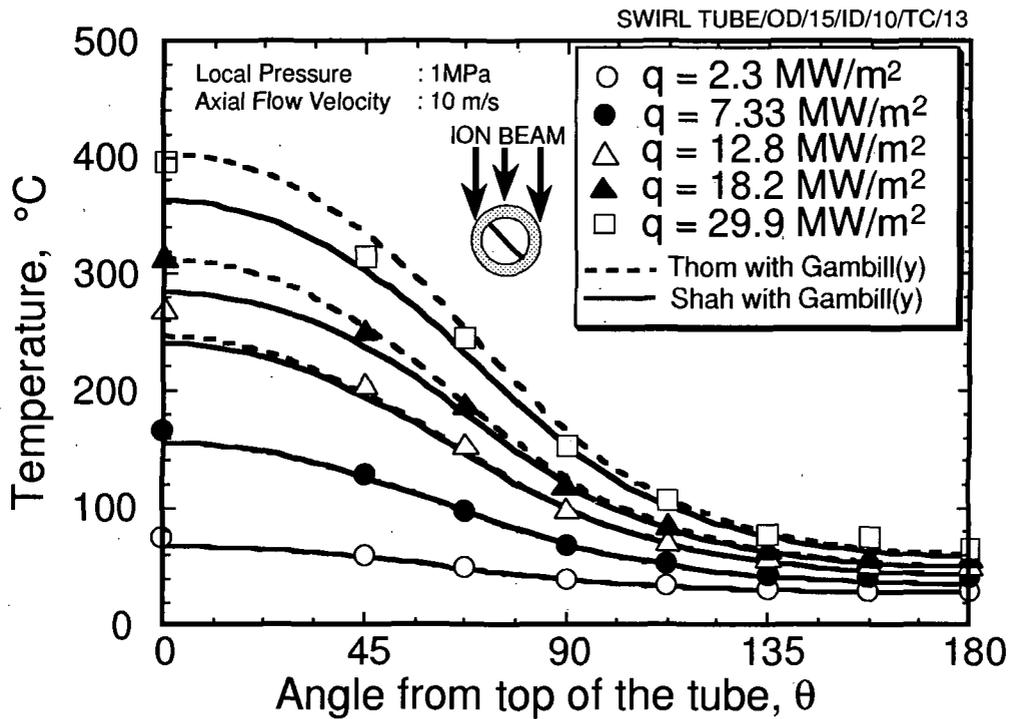
Figure 20 Temperature distributions of the swirl tube at the thermocouple positions.

or

$$T_{wall} = \frac{1}{\psi}\left((\psi - 1.0)\cdot(T_{sat} - T_L) + \left(\frac{q}{h_L}\right)\right) + T_L. \qquad \text{Jens-Lottes correlation [40]} \qquad \text{......... (5)}$$

$$\psi = 230.0\cdot\left(\frac{q}{(G\cdot H_g)}\right)^{0.5}. \qquad \text{......... (6)}$$

where,

Nu	: Nusselt number (-),
Nu$_s$	: Nusseld Number for swirl flow (-),
Re	: Reynolds Number (-),
Pr	: Prandtl Number (-),
μ	: Dynamic viscosity of liquid (Pa•s),
μ_w	: Dynamic viscosity of liquid at wall temperature (Pa•s),
y	: Tape twist ratio (=L$_{180}$/Di),
q	: Total heat flux (MW•m^{-2}),
q$_{con}$	: Heat flux predicted at forced convection flow (MW•m^{-2}),
q$_{boil}$	: Heat flux for boiling (MW•m^{-2}),
q$_{bi}$	: Fully developed boiling heat flux at incipient boiling (MW•m^{-2}),
T$_{wall}$	: Wall temperature (K),
T$_{sat}$	: Saturation temperature (K),
p	: Local water pressure (MPa),
T$_L$	: Mixed-mean temperature of liquid (K),
h$_L$	: Heat transfer coefficient at non-boiling regime (W•m^{-2}•K^{-1}),
G	: Mass flow rate (kg•s^{-1}),
H$_g$	: Latent heat of vaporization (J•K^{-1}).

3.3-2 Performance of helium gas cooling

To investigate performances of helium gas cooling, the EBTS helium flow loop (HeFL) at Sandia National Laboratories has successfully been used to test three types of helium-cooled divertor mock-ups in 1993. All three mockups were manufactured of Glidcop dispersion-strengthened copper alloy. The first heat exchanger was manufactured by Creare, Inc. and makes use of microfin technology and helium flow normal to the heated surface. This technology provides for enhanced heat transfer at relatively low flow rates and much reduced pumping requirements. The Creare sample was tested to a maximum heat flux of 4.0 MW•m^{-2} in the 30 kW electron beam test system (EBTS) using 7.3 g•s^{-1} of helium mass flow and produced a pressure drop of only 3.4 kPa at 1.4 MPa. The second helium-cooled divertor mock-up was designed and manufactured by General Atomics. It consisted of millimeter-size axial fins and flow channels machined in Glidcop Al-15. This design used low pressure drops and high mass flow rates to achieve good heat removal. The GA specimen was tested using 22 g•s^{-1} of helium mass flow which produced a 5 kPa pressure drop at 4.0 MPa. It attained a maximum heat flux of 9 MW•m^{-2} while maintaining a surface temperature below 400 °C. This temperature was selected to be compatible with a 2 mm thick beryllium tile at the plasma interface, where the maximum surface temperature must be below 700 °C. The third specimen was an Glidcop Al-15, axial flow, helium-cooled divertor mock-up filled with a porous metal wick designed and manufactured by Thermacore, Inc. The internal porous metal wick effectively increases the available heat transfer area. This divertor module was characterized by low mass flow, ~1g•s^{-1}, and high pressure drop operation near 66 kPa at 4.0 MPa. It survived a maximum heat flux of 16 MW•m^{-2} and reached surface temperatures of 740 °C.

References

[1] T. Kuroda, G. Vieder, M. Akiba, et al., ITER Documentation Series, No. 30, IAEA (1991).

[2] C. D. Croessmann, J. of Nucl. Matr., 128 & 129 (1984).

[3] K. Koizlik, H. Bolt, H. Hoven, et al., in Proc. of 15th Symp. on Fusion Technology, Utrecht, (1988) 1066.

[4] M. Akiba, M. Araki, M. Dairaku, et al., in Proc. of IEEE 13th Symp. on Fusion Engineering, Knoxville, (1989) 529.

[5] J. Linke, M. Akiba, M. Araki, et al., in Proc. of 16th Symp. on Fusion Technology, London, (1990) 428.

[6] J. G. van der Laan, H. Th. Klippel, R. C. L. van der Stad, et al., Fusion Technology, 19, (1991) 2070.

[7] M. Seki, M. Akiba, M. Araki, et al., Fusion Engineering and Design, 15, (1991) 59.

[8] M. Araki, M. Akiba, M. Seki, et al., Fusion Engineering and Design, 19, (1992) 101.

[9] R. C. L. van der Stad, H. Th. Klippel, G. J. Kraaij, in Proc. of 17th Symp. on Fusion Technology, Rome, (1992) 401.

[10] S. Suzuki, J. F. Crawford, J. T. Bradley III, et al., J. Nucl. Mater. 200, (1992) 265.

[11] M. Akiba and R. D. Watson, Atomic and Plasma-Material Interaction Process in Controlled Thermonuclear Fusion, (1993) 455.

[12] I. Smid, M. Akiba, M. Araki, et al., JAERI-M 93-149, Japan Atomic Energy Research Institute (1993).

[13] T. Baba and T. Tanamura, private communication (1993).

[14] R. Haange, in Proc. of 9th Symp. on Engineering Problems of Fusion Research, Chicago, (1981) 1356.

[15] J. A. Paterson, G. Koehler and R. P. Wells, in Proc. of 9th Symp. on Engineering Problems of Fusion Research, Chicago, (1981) 1666.

[16] H. Horiike, M. Kuriyama and H. Morita, Nuclear Technology/Fusion Vol. 2, (1982) 637.

[17] D. J. McFarlin, A. E. Betz, C. C. Tompson, et al., in Proc. of 10th Symp. on Fusion Engineering, Philadelphia, (1983) 526.

[18] S. L. Milora, S. K. Combs and C. A. Foster, ORNL-TM-9183, Oak Ridge National Laboratory (1986).

[19] J. A. Koski, A. G. Beattie, J. B. Whitley, et al., ASME 87-HT-45 (1987) and also see J. A. Koski, in 7th of Proc. Nucl. Thermal Hydraulics, 1991 ANS Winter Meeting, San Francisco (1991) 7.

[20] M. Araki, M. Dairaku, T. Inoue, et al., Fusion Engineering and Design Vol. 9, (1989) 231.

[21] J. Schlosser, in Proc. of 17th Symp. on Fusion Technology, Rome (1992) 367 and also see J. Schlosser, A. Cardella, P. Massmann, et al., in 7th of Proc. Nucl. Thermal Hydraulics, 1991 ANS Winter Meeting, San Francisco (1991) 26.

[22] M. Araki and R. D. Watson, (in preparation).

[23] M. Kuriyama, N. Akino, M. Araki, et al., in Proc. of IEEE 15th Symp. on Fusion Engineering, Hyaniss (Oct. 1993).

[24] A. Cardella, G.P. Celata, G. P. Gaspari, " Tests On the Hypervapotron , " 1990 SOFT, London

[25] H. Falter, et al , SPIE, San Diego, 1992.

[26] C. B. Baxi and H. Falter, in Proc. of Fifth Int. Meeting on Nuclear Thermal Hydraulics, (Sept. 1992).

[27] M. Araki, M. Ogawa, and M. Akiba, Fusion Technology, 21 (1992) 1835.

[28] J. R. S. Thom, in Proc. Int. Mech. Engrs. Pt. 3C, 180 (1966) 226.

[29] M. M. Shah, Heat Transfer Engng., 4 (1983) 24.

[30] F. C. Gunther, Trans., ASME, 73-2 (1951) 115.

[31] D. H. Knoebel, USAEC DP-1306, E. I. Dupont de Nemours & Company (1973).

[32] L. S. Tong, ASME, 75H68 (1975).

[33] F. Inasaka and H. Nariai, JSME Int. J., 30, (1987) 1595.

[34] Y. Katto, Japanese Heat Mass Transfer, 28, B-144 (1991).

[35] S. Ikeda, M. Araki, M. Ogawa, et al., JAERI-M 93-070, Japan Atomic Energy Research Institute Report (1993).

[36] M. Araki, S. Ikeda, M. Ogawa, et al., in Proc. of 3rd Specialists' Workshop on High Heat Flux Components Thermal-Hydraulics, Cadarache (1993) 3-1 and in preparation.

[37] W. R. Gambill, et al., ORNL-2911, Oak Ridge National Laboratory (1960).

[38] F. W. Dittus and L. M. K. Boelter, Univ. Calf. Publs Engrs., 2, (1930) 443.

[39] A. E. Berges and W. M. Rohsenow, J. of Heat Transfer, (1964) 365.

[40] W. H. Jens and P. A. Lottes, A. N. L. Report, (1951) 4627.

[41] C. B. Baxi, and GA Divertor Team, General Atomics Report GA-A21448, Sept. 1993.

Contents of previous volumes of
Atomic and Plasma–Material Interaction Data for Fusion

INFORMATION FOR AUTHORS

General

Atomic and Plasma–Material Interaction Data for Fusion (APMIDF) publishes papers, letters and reviews which deal with elementary atomic collision processes in fusion plasmas, collision processes of plasma particles with surfaces and plasma–material interaction phenomena, including the thermophysical and thermomechanical response of candidate fusion reactor plasma facing materials. Each contribution submitted to APMIDF should be highly fusion relevant and should contain a significant amount of quantitative data information in one of the above fields. Review articles are normally prepared on invitation of the Scientific Editor or with his prior consent. APMIDF is a regular Supplement to the journal NUCLEAR FUSION (NF) and its abbreviation for the purpose of referencing is: At. Plasma–Mater. Interact. Data Fusion.

Manuscripts, which may be submitted in Chinese, English, French, Russian or Spanish, will be published in English. For a manuscript submitted in a language other than English, a translation into English of technical terms should be provided. Manuscripts must be submitted in triplicate and typewritten double spaced on good quality standard size paper. All copies should include the main text, an abstract, tables, references, figures, captions and appendices, as appropriate. One set of glossy prints or reproducible transparencies of the figures should also be provided. Final manuscript versions may be submitted in camera ready form or on diskettes (see NF's Note for Authors, available on request from the NF Office).

Every manuscript submitted must be accompanied by a disclaimer stating that the paper has not been published and is not being considered for publication elsewhere. If no copyright is claimed by the authors, the IAEA automatically owns the copyright of the paper.

Authors will receive proofs of the text of accepted manuscripts. Proofs of figures are sent only if requested. Rejected manuscripts will not be returned unless this is expressly requested within six weeks of rejection.

Fifty reprints are provided free of charge; additional reprints may be ordered at the time the author returns the proofs. Manuscripts and correspondence should be addressed to: The Editor, NUCLEAR FUSION (A+M Supplement), International Atomic Energy Agency, Wagramerstrasse 5, P.O. Box 100, A-1400 Vienna, Austria.

Manuscript preparation

Authors are referred to any recent issues of APMIDF or NF for examples of format and style.

All submitted articles should be concise and written in a clear style. The description of the methods used for obtaining the presented original data information should be kept to a reasonable minimum. The review papers should provide a critical analysis of a broader class (or classes) of data or processes together with a set of recommended data of specified accuracy.

Titles should be as concise as possible but sufficiently informative to describe the subject of the paper.

Abstracts must briefly summarize the contents of the article. They should state the principal objectives, mention the methodology employed, summarize the results (emphasizing the new findings) and present the main conclusions. They should be concise and self-contained so that they can be used by the International Nuclear Information System (INIS) and other abstracting systems without changes. General, well known information should be avoided in the abstract and accommodated in the introduction.

Letters to APMIDF are short communications of net sets of data obtained with a standard, highly accurate method. As a rule, they should be not longer than ten typewritten double spaced standard pages, including references and figures.

Guidelines for bibliographical citations can be found in issues 2, 3 and 4 of NF 28 (1988). In short, references should be accurately described in sufficient detail for easy identification. In the text, they should be indicated consecutively by Arabic numerals in square brackets. All references should be listed on a separate page at the end of the text. In this list, the names of all authors (or, if there are more than six, of the first three authors plus 'et al.') should be given. All unpublished material, e.g. laboratory reports, doctoral theses or papers in proceedings that have not yet been published, should be cited with full titles, place and year; citations of reports should also contain the laboratory prefix and number, date of issue, etc. References to periodicals should contain the name of the journal, volume number, page number and year of publication; the title of the article is not needed. References to books should contain the full title of the book, names of editors (if any), name and location of the publisher, year of publication and page number (if appropriate). References to personal communications should be avoided if possible. For journal citations use the list of abbreviations given in "IAEA-INIS-11, INIS: Authority List for Journal Titles".

Russian names should be transliterated according to "IAEA-INIS-10, INIS: Transliteration Rules for Selected Non-Roman Characters". Examples of the style followed by NF for references are:

REFERENCES

[1] SHAH, M.B., GILBODY, H.B., J. Phys., B (Lond.). At. Mol. Phys. **14** (1981) 2361.

[2] WILSON, K.L., BASTASZ, R.A., CAUSEY, R.A., et al., At. Plasma–Mater. Interact. Data Fusion **1** (1991) 31.

[3] BRANSDEN, B.H., Atomic Collision Theory, 2nd edn., Benjamin, New York (1982).

[4] MÄRK, T.D., DUNN, G.H. (Eds), Electron Impact Ionization, Springer-Verlag, Berlin, Heidelberg, New York, London (1985).

[5] MÖLLER, W., ROTH, J., in Physics of Plasma–Wall Interactions in Controlled Fusion (POST, D.E., BEHRISCH, R., Eds), Plenum Press, New York (1986) 45.

[6] McGRATH, R.T., Thermal Loads on Tokamak Plasma Facing Components During Normal Operation and Disruptions, Rep. SAND89-2064, Sandia National Laboratories, Albuquerque, NM (1990).

[7] TRUBNIKOV, B.A., in Problems of Plasma Theory, Vol. 1 (LEONTOVICH, M.A., Ed.), Gosatomizdat, Moscow (1963) 98 (in Russian). (English translation: Reviews of Plasma Physics, Vol. 1, Consultants Bureau, New York (1965) 105.)

[8] HUBER, B.A., Zum Elektronentransfer zwischen mehrfach geladenen Ionen und Atomen oder Molekülen, PhD Thesis, Ruhr-Universität, Bochum (1981).

[9] de HEER, F.J., HOEKSTRA, R., KINGSTON, A.E., SUMMERS, H.P., Excitation of neutral helium by electron impact, to be published in At. Plasma–Mater. Interact. Data Fusion.

[10] MOORES, D.L., Electron impact ionisation of Be and B atoms and ions, submitted to At. Plasma–Mater. Interact. Data Fusion.

All figures should be on separate sheets and numbered consecutively with Arabic numerals, e.g. Fig. 1. A separate list of captions must be provided (see also General above).

Tables must carry a heading and be numbered consecutively with Roman numerals in the order in which they are mentioned in the text, e.g. Table II. Footnotes to tables should be indicated by raised letters (not numbers or asterisks) and set immediately below the table itself. Tables should be typed clearly for possible direct reproduction.

Footnotes to the text should be numbered consecutively with raised Arabic numerals; excessive use of footnotes should be avoided.

All equations should be typed as carefully as possible, with unavailable Greek letters and other symbols clearly inserted by hand. Specifically:

(1) To eliminate confusion between symbols with similar appearance (e.g. between ones, ells and primes), make them as distinct as possible, if necessary marking them clearly by hand. In manuscripts with handwritten formulas, all further sources of confusion (such as n's and u's, u's and v's, e's and l's, J's and I's) should also be marked.

(2) Indicate a vector by an arrow on top rather than by bold face lettering.

(3) Tensors of second rank should bear two arrows on top; if higher rank tensors are required, choose an appropriate symbol and explain it.

(4) Indicate the normal algebraic product by simple juxtaposition of symbols, i.e. without multiplication sign.

(5) Write scalar products of vectors with a raised point, e.g. $\vec{A} \cdot \vec{B}$.

(6) Use the multiplication sign ($\times$) solely to designate: (i) a vector product, (ii) an algebraic (but not a scalar) product in the case where an equation has to be split over two lines, and (iii) in expressions like $3 \text{ cm} \times 3 \text{ cm}$ or 2×10^6 cm.

(7) The nabla operator (∇) does not carry an arrow.

(8) When equations are split over two or more lines, place operational signs only at the beginning of each new line, not at the end of the preceding line. For direct reproduction of an equation, the length of the lines should not exceed 9 cm.

(9) Where it is impossible to split long fractions over two lines, use negative exponents: similarly, replace root signs by fractional exponents where appropriate.

(10) Do not use symbols, abbreviations and formulations that are recognizable only in a particular language.

Use SI units as far as possible; where this is not possible, please give the appropriate conversion factor.